

Doctoral Thesis

**Nano-architectures with hierarchical porosity
manufactured by colloidal techniques for application
in ceramic semiconductor-based supercapacitors**

Author:

Joaquín Luis Yus Domínguez

**A dissertation submitted by in partial fulfillment of the requirements
for the degree of Doctor of Philosophy in**

Materials Science and Engineering

Universidad Carlos III de Madrid

5Xvisors:

Dr. Zoilo González Granados

Dra. Begoña Ferrari Fernández

Tutor:

Prof. Elena Gordo Odériz

Leganés, July 2019

Esta tesis se distribuye bajo licencia “Creative Commons **Reconocimiento – No Comercial – Sin Obra Derivada**”





0

Published & Submitted Content

This PhD Thesis has been carried out at the Tailoring through Colloidal Processing Group, which belongs to the “Química Física de Superficies y Procesos” department of the Instituto de Cerámica y Vidrio (ICV) – Consejo Superior de Investigaciones Científicas (CSIC) during the period from April 2016 to July 2019.

The structure of this document consists of: i) a first Preface and Contribution statement with the brief description of the scientific articles which compounds this thesis. ii) The abstract, which is the common thread that connected the previous contributions. iii) The motivation and objectives for achieving the main goal. iv) The Executive Summary, which includes an introduction, and a summary of the results and the contributions of the doctoral student reported in the appended papers, and v) the conclusions of this work.

The results of this Doctoral Thesis are presented in detail in the following appended.

Publication 1

J. Yus, B. Ferrari, A.J. Sanchez-Herencia, Z. Gonzalez.

Emerging processing techniques for electrodes microarchitectures
tailoring in pseudocapacitors.

Sent to publish to the Journal of the European Ceramic Society.

Main Contributions: This revision provides a general knowledge for researchers who intend to introduce themselves into the use of ceramic semiconductor materials for pseudocapacitors (PCs) electrodes. Novel processing techniques reported from 2000, to tailor microstructures and hierarchical porous structures with high electrochemical performance, is also summarized. The increase of the surface of reaction and the optimization of conductivity, throughout the sintering of the transition metal oxides (TMOs) based electrodes, enhance the final electrochemical properties providing better chemical stability and higher specific capacitance. Moreover, this review paid specially attention on NiO as electroactive material, because of their intrinsic electrochemical properties and accessibility as raw material. Finally, the manuscript widely reviews technologies developed to shape PCs electrodes TMO-based, mixed with carbon-based materials, for the manufacture of hybrid capacitors or ultracapacitors.

Publication 2

**J. Yus, B. Ferrari, A.J. Sanchez-Herencia, A. Caballero, J. Morales,
Z. Gonzalez.**

In Situ Synthesis and Electrophoretic Deposition of NiO/Ni Core-
Shell Nanoparticles and Its Application as Pseudocapacitor.

Coatings **2017**, *7*, 193.

doi:10.3390/coatings7110193.

Main Contributions: The manuscript describes for the first time a colloidal processing technology applied to the fabrication of PC electrodes to explore electrochemical performance of the incorporation of non-noble metals, as Ni, in the NiO-based electrodes. NiO/Ni nanocomposites were prepared through a heterogeneous precipitation of metallic Ni nanospheres using NiO nanoplatelets stabilized in an aqueous suspension as synthesis seeds. The Electrophoretic Deposition (EPD) was employed as shaping method achieving homogeneous films over 3D Ni foams during the coating process. After the EPD, a subsequent mild heat treatment, 325°C-1 h, was optimized to obtain a well-connected and consolidated microstructure, which facilitates the movement of charges through it. The inclusion of metal nanoparticles into the microstructure of the semiconductor enhances the electron transfer by sharing the delocalized electrons with NiO. Finally, a high electrochemical performance was obtained, showing an elevated specific capacitance value of 755 F/g with a 62% of retention.

Publication 3

Z. Gonzalez, **J. Yus**, A. Caballero, J. Morales, A.J. Sanchez-Herencia, B. Ferrari.

Electrochemical performance of pseudo-capacitor electrodes fabricated by Electrophoretic Deposition inducing Ni(OH)₂ nanoplatelets agglomeration by Layer-by-Layer.

Electrochim. Acta **2017**, *247*, 333–343.

doi:10.1016/j.electacta.2017.07.043.

Main Contributions: The manuscript describes the modification of Ni(OH)₂ nanoplatelets surfaces with a polyelectrolyte multilayer, through a the sequential adsorption of cationic and anionic polymers. Those inorganic/organic core-shell nanostructures were used to fabricate PC electrodes with higher porosities by EPD method. The increase of the number of polyelectrolyte layers increased the hydrodynamic diameter of the core-shells and promoted their controlled agglomeration, resulting in a disordered packing during the deposition. The electrically driven assembly of the core-shells was herein evaluated in terms of specific surface area and porosity. The electrochemical response improved with the number of layers

adsorbed in the core-shell nanostructure. The disorder provoked during the deposition resulted in a hierarchical porous microstructure with micro, meso and macropores, favoring the electrolyte diffusion throughout the structure and increasing the number of reaction sites at the electroactive material. The obtained value of specific capacitance was close to 1000 F/g with a 60% of retention after 1000 cycles.

Publication 4

J. Yus, E. Chinarro, B. Ferrari, Z. Gonzalez.

The Effect of the Substrate on the Conductivity of NiO Electrodes in Electrochemical Capacitor Shaped by Electrophoretic Deposition.

ECS Transactions **2018**, 82(1):97-104.

doi: 10.1149/08201.0097ecst

Main Contributions: The manuscript deserves differences among collectors used to shape NiO-based electrodes for PCs. Nanoplatelets of NiO were deposited by EPD on stainless steel, copper and nickel collectors to study the effect of the substrate in the electrochemical performance of the electrode. Impedance spectroscopy (EIS) studies allow determining the charge-transfer resistance (R_{ct}) between the NiO coating and the substrate/collector. The lower R_{ct} was obtained for the electrodes shaped using Ni foil collectors (0.21 Ω). In addition, the shape of the collector was also tested. Although Ni foams have a larger specific surface area, the section through which the electrons flow is smaller and the R_{ct} resulted higher (1.71 Ω) than when foil substrates are used.

Publication 5

J. Yus, Z. Gonzalez, A.J. Sanchez-Herencia, A. Sangiorgi, N. Sangiorgi, D. Gardini, A. Sanson, C. Galassi, A. Caballero, J. Morales, B. Ferrari.

Semiconductor Water-based Inks: Miniaturized NiO Pseudocapacitor Electrodes by Inkjet Printing.

Journal of the European Ceramic Society. **2019**, 39, 2908-2914.

doi: 10.1016/j.jeurceramsoc.2019.03.020

Main Contributions: The manuscript illustrates a competitive colloidal approach to prepare aqueous NiO-based inks for Inkjet Printing (IJP) to design patterns for their use in energy storage micro-devices. After the optimization of inks parameters (surface tension, viscosity, density and particle size) as well as printing parameters, one-layer NiO patterns were successfully printed onto Ni foils and tested. Sintering allows

obtaining a NiO consolidated microstructure well adhered to the substrate, deserving a specific capacitance of 170 F/gr with 100% retention after 1000 cycles. Therefore, device miniaturization and the well-connected nanostructure of the printed NiO patterns result in a R_{ct} as low as 0.23 Ω . This work is the result of an international collaboration funded by a JECS Trust mobility grant that allowed the PhD student developing a research stay of three months at the Institute of Science and Technology for Ceramics.

Publication 6 **J. Yus, Y. Bravo, A.J. Sanchez-Herencia, B. Ferrari, Z. Gonzalez.**
Electrophoretic Deposition of rGO-NiO Core-Shell nanostructures
driven by Heterocoagulation Method with High Electrochemical
Performance.

Electrochim. Acta **2019**, 308, 363 – 372.

doi: 10.1016/j.electacta.2019.04.053

Main Contributions: The manuscript describes for the first time the heterocoagulation of colloidal suspensions of reduced graphene oxide (RGO) nanosheets and NiO nanoplatelets to prepare RGO/NiO composites, and deposit them by EPD to shape electrodes for hybrid supercapacitor (HSC). HSCs profit from both energy storage mechanisms, electrostatic and faradaic reactions, which can increase the achievable specific capacitance. After cathodic deposition and sintering, graphene maintains reduced. The incorporation of RGO favors the electron conductivity (decreasing R_{ct} until 1.13 Ω) and provides chemical stability to the electrode during the energy accumulation process, as well as the mechanical stability softening the volume changes of the ceramic semiconductor microstructure and lengthening the electrode lifetime and capacitance retention. A specific capacitance value of 920 F/g was finally obtained with a retention of 71% after 1000 cycles.

Publication 7 **J. Yus, B. Ferrari, A.J. Sanchez-Herencia, Z. Gonzalez.**
Understanding Electron Transport and Ion Diffusion on Ni-based
semiconductor microstructures shaped on 3D hierarchical networks
by EPD.

Sent to publish to the Journal of Power Sources

Main Contributions: The manuscript provides an extensive EIS study that allows evaluating the electrochemical performance of PC electrodes in terms of their physicochemical properties: the specific surface area and the degree of sintering of the ceramic semiconductors processed throughout different colloidal approaches. EIS analysis allows understanding and separate the influence of the electron transport and the ion diffusion on the final electrochemical response in PCs. EIS showed the specific contribution of nanoparticles morphology, composition, packing and consolidation of the nanostructure, to the electroactivity. 3D electrodes microarchitectures with high porosity (5LbL) presented better capacitive behavior, however they displayed also higher R_{ct} . The inclusion of electron donors in the microstructure of the semiconductor decreased the R_{ct} making easier the electronic movement through the electroactive material. Other way to improve the charge transfer consisted in the consolidation of the microstructure by sintering, employing a mild thermal without eliminate the mesoporosity. A compromise between porosity and connectivity should be established, favoring the electrolyte diffusion and the redox reactions throughout the porous microstructure, as well as the electronic conduction through the semiconductor nanostructure to improve the final electrochemical performance.

Other contributions not included in this doctoral thesis, where the PhD student has been strongly involved, deal with the colloidal processing ceramic semiconductors, as nano- TiO_2 particles, in energy generation and waste-water regeneration due to its photovoltaic and photocatalytic properties. This research line has generated a patent and two scientific articles also published in Q1 journals:

Z. Gonzalez, **J. Yus**, A.J. Sanchez-Herencia, J. Dewalque, L. Manceri, C. Henrist and B. Ferrari. A colloidal approach to prepare binder and crack-free TiO_2 multilayer coatings from particulate suspensions: Application in DSSCs (2019) *Journal of the European Ceramic Society*, 39 (2-3), pp. 366-375. DOI: 10.1016/j.jeurceramsoc.2018.09.018

A. Sangiorgi, Z. Gonzalez, A. Ferrandez-Montero, **J. Yus**, A.J. Sanchez-Herencia, C. Galassi, A. Sanson and B. Ferrari. 3D printing of photocatalytic filters using a biopolymer to immobilize TiO_2 nanoparticles (2019) *Journal of the Electrochemical Society*, 166 (5), pp. H3239-H3248. DOI: 10.1149/2.0341905jes

A. Ferrandez-Montero, B. Ferrari, A.J. Sánchez-Herencia, Z. Gonzalez, **J. Yus**, J.L. González and M. Lieblich. Method for obtaining a piece by fused deposition modeling. P201830503 (**2018**). PCT/ES2019/070348 (International framework).

This Doctoral Thesis has been carried out at the Instituto de Cerámica y Vidrio (ICV) - Consejo Superior de Investigaciones Científicas (CSIC) and it has been funded by the following projects:

Autonomic Projects:

CAMPD17_ICV_002. (PEJD-2017-PRE/IND-4593).



MULTIMAT Challenge: Materiales
Multifuncionales para retos de la Sociedad: S2013/MIT-2862



ADITIMAT: Additive Manufacturing: from Material to
Application. S2018/NMT-4411

National Projects:

MAT2015-70780-C4-1-P



International Projects:

JECS Trust of the European Ceramic Society (ECERS),
which financed my stay abroad. Contract 2017141



Esta memoria de tesis cumple los requisitos necesarios para obtener la Mención Internacional en el Título de Doctor que se describen en la normativa de enseñanzas universitarias de doctorado de la Universidad Carlos III de Madrid y que han sido establecidos en el artículo 15 del Real Decreto 99/2011 que establece la Ordenación de las Enseñanzas Universitarias Oficiales (BOE nº 35 del 28 de Enero de 2011, Págs. 13909-13926). Dicha Memoria de tesis ha sido informada por dos doctores que pertenecen a instituciones de educación superior internacionales:

Dr. Guillaume Toquer
Ecole Nationale Supérieure de Chimie de Montpellier
Institut de Chimie Séparative de Marcoule
France

Dra. Maria Isabel Gonzalo de Juan
Technische Universität Darmstadt
Materials Science Department
Germany

Content

1. Abstract	1
2. Motivations & Objectives	5
3. Executive Summary.....	13
3.1. Introduction to the ceramic-based pseudocapacitors.....	15
3.1.1. Profiting TMO electrochemical performance through the processing strategies.....	25
3.1.2. The parameters with implication in the TMO electrochemical performance.....	28
3.1.3. Strategies for the micro, nanostructure modification to maximize the electrochemical response of the TMO based electrodes	32
3.1.4. Based-synthesis strategies of the processing of TMO for pseudocapacitors	36
3.1.5. Microstructural modification by shaping and, sintering ceramic films. 41	
3.1.6. Hybrid capacitors.....	46
3.2 Summary of Results & Discusion	52
3.2.1 Standardization of the sonocrystallization and annealing processes to synthesize Ni(OH)₂ and NiO nanoplatelets	52
3.2.2 Shaping processes of PEI-modified Ni(OH)₂ nanoplatelets for pseudocapacitor (PC) electrodes: Electrophoretic Deposition and Inkjet Printing.....	59
3.2.2.1 3D electrodes for PC processed by Electrophoretic Deposition of PEI-modified Ni(OH)₂ nanoplatelets	62
3.2.2.2 2D electrodes for PC processed by Inkjet Printing of PEI-modified Ni(OH)₂ nanoplatelets	69
3.2.3 Colloidal Modification	76
3.2.3.1 Processing and electrochemical enhancement by the inclusion of a conductive phase in the nanostructure of NiO-based PC electrodes	79
3.2.3.2 Processing and electrochemical enhancement by assembling a porous hierarchical nanoarchitecture of NiO based PC electrodes.....	88
4. Concluding Remarks.....	95
5. Bibliography.....	101
6. Publications	120
7. Other Research Merits.....	313



1

Abstract

All the scientific contributions presented in this thesis have a main goal: to achieve science and technology challenges in the manufacture of energy storage devices based on a ceramic semiconductor employing colloidal processing strategies.

Needs of the renewable energy systems and portable devices have revolutionized research on energy storage systems. Development of more powerful devices able to store large amounts of energy is now the challenge. In this field, the research in supercapacitors (SC) based on ceramic semiconductors has been tackled as a relevant issue to improve the electrochemical response of the electrodes inducing better reactant–catalyst contacts through the design of complex structures with large surface-to-volume ratio. The structuring and electrochemical activity of the pseudocapacitors (PCs) electrodes can be controlled by tuning the physical properties of the electroactive material (particle size, crystalline phase, preferred orientation) but also, shaping and consolidating the ceramic microstructure (*publication 1*).

As a promising electroactive material (and non-strategic raw material), the NiO presents an elevated theoretical capacitance, high thermal and chemical stability and easy availability (*publication 1*). For these reasons, in this research work, the ultrasound aided synthesis of Ni(OH)₂ and NiO nanoplatelets was standardized, and the manufacture of tridimensional (3D) and bidimensional (2D) NiO-based electrodes for PCs was tackled throughout different colloidal processing strategies. The Electrophoretic Deposition (EPD) and inkjet printing (IJP) technologies have been employed as shaping techniques for the manufacturing of these electrodes. While EPD allows us to fully and homogeneously coat collectors with complex shapes, as 3D Ni foams, the IJP enables the miniaturization of 2D electrodes for their use in energy-storage microdevices (*publication 5*). Both techniques are based on the dispersion and stabilization of Ni(OH)₂ and NiO nanoplatelets in colloidal water-based suspensions, which were optimized for each application, leading to PC electrodes with specific capacitances of 250 and 160 F/g with retentions of 71 and 100%, respectively, where the remarkable low charge transfer resistance ($R_{ct} = 0.23\Omega$) of NiO patterns (IJP) has to be highlighted.

Moreover, the assembly of synthesized NiO nanoplatelets has been also addressed resulting in a cohort of semiconductor microarchitectures that improves the electrochemical response of PC electrodes shaped by EPD.

EPD is a well-known colloidal technique with remarkable performance in the coating of electrodes with complex shapes. However, for PC electrodes shaping, the nature and shape of the substrate have to be considered since collector has a relevant influence on electron transfer phenomena as well as the ion diffusion at the electrode/electrolyte interface (*publication 4 & 7*). The deposition and consolidation of the electroactive nanoplatelets through a mild heat treatment (sintering) connects the particles by the formation of sintering necks reducing Rct of these 3D electrodes to 1.71Ω . (*publication 2 & 7*).

To cover Ni-3D collectors improving electrochemical performance, one of the employed colloidal strategies in this thesis was the surface modification of NiO nanoplatelets by layer-by-layer deposition of polyelectrolytes, leading to the formation of organic/inorganic core-shell structures which strongly modified the NiO nanoplatelets assembly by EPD (*publication 3*). The resulting hierarchical nanostructure presents high Rct values (3.65Ω), while the capacitive response (CPE-p = 0.90) step up due to the enhancement of electrolyte wetting and faster ion diffusion. This fully ceramic porous nanostructure shows a specific capacitance of 982 F/g, with 60% retention after 1000 cycles, and relaxation times in the range of carbonaceous SC electrodes ($\tau_0 = 18\text{ s}$), demonstrating that the capacitance is strongly related to the surface exposure of the semiconductor to the electrolyte, in spite of a relative high Rct. This is because of the increase in resistance is compensated by a better capacitive behavior as well as a better rate capability (*publication 7*).

Finally, we also demonstrate that Rct can be reduced by the inclusion of materials capable of sharing their free electrons within the semiconductor microstructure such as metallic Ni or reduced graphene Oxide (RGO) (*publication 2, 6 & 7*), without deteriorating the capacitive response. In this way, NiO/Ni electrodes with specific capacitances of 755 F/gr and a retention of 71% was shaped by EPD in Ni foams, leading to Rct values of 1.55Ω and relaxation times of 11 s; while RGO/NiO hybrid supercapacitors (HSC) were prepared also by EPD, exhibiting specific capacitances of 920 F/g at a current density of 2 A/g with a retention of 71% and a Rct as low as 1.13Ω and a relaxation time of 4 s



2

Motivations & Objectives

The energy consumption in the world is growing every year, rising in 2015 until to an estimated value of 575 quadrillion in British thermal units (1 BTU = 1055 J = 0.29 W·h), being USA and China the main energy consumers. Up to 40% of all energy is consumed by both countries (figure 2-1).

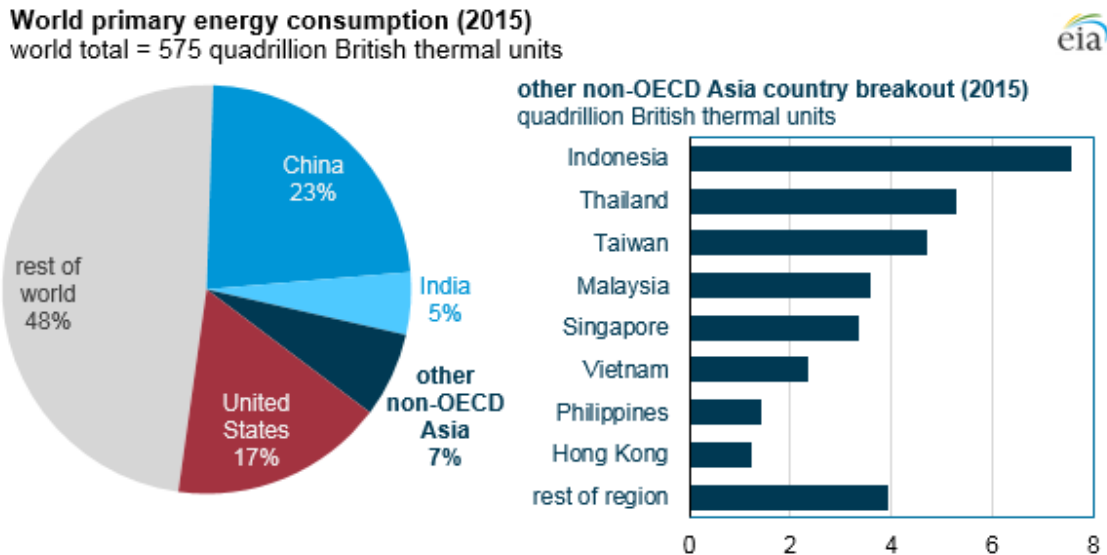


Figure 2-1. World primary energy consumption by regions in 2015. Data obtained from EIA website [1]
Last accessed on June 1st 2019.

Moreover, if these two world powers are compared, the use of fossil fuels far exceeds any other type of energy. China bases its energy system on coal and in the USA, oil and natural gas are the most used energy sources. However, the energy consumed from fossil fuels exceeds 80% in both cases (figure 2-2)

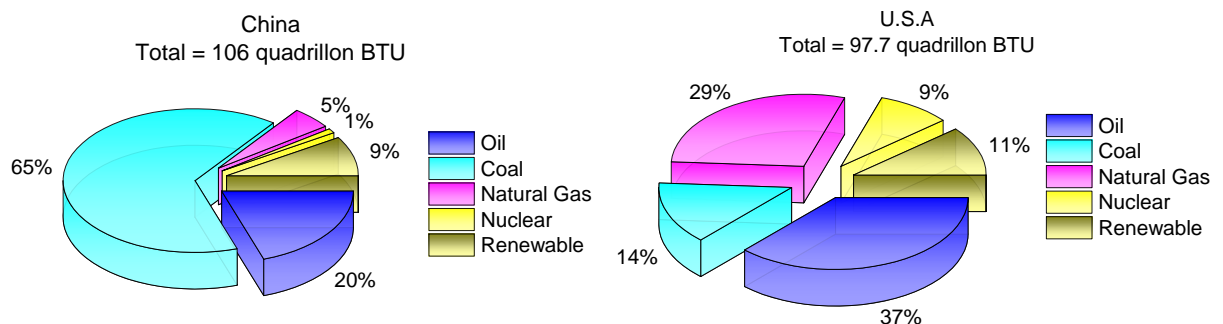


Figure 2-2. a) China and b) USA energy consumptions by source. *The percentages were obtained from the web site: www.eia.gov[2] and www.americanexperiment.org[3], respectively. Last accessed on June 1st2019.*

The abusive use and high demand of fossil fuels for energy production is one of the main causes of climate change. The high emission of greenhouse gases and pollution into the atmosphere are causing variations in the climate, which is bringing about an increase in the temperature of the entire planet, favoring the non-desirable global warming. Figure 2-3 shows the increase in the overall temperature of the planet in the last decades, which has risen until 4 °C in some specific areas. Moreover, it is estimated that, the thermometers could rise in 2.7 °C more by the end of the present Century.

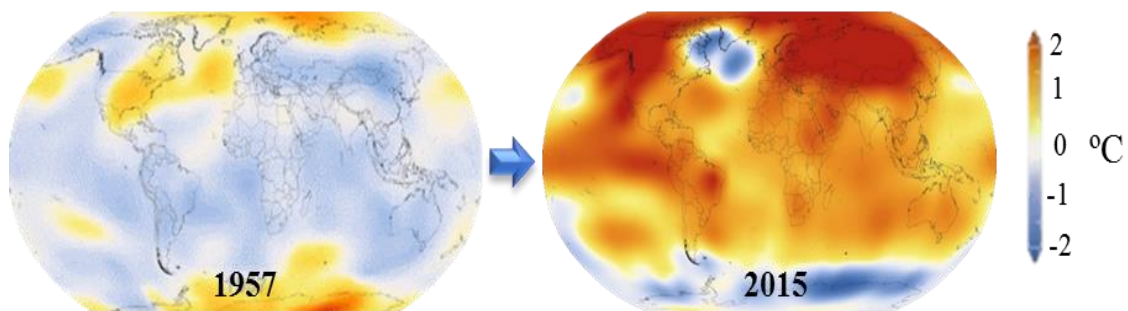


Figure 2-3. Comparison of how the Earth's climate has changed from 1957 until 2015. The data were obtained from acciona web page [4]. *Last accessed on June 1st 2019.*

In order to reduce the pollution produced by non-renewable energy sources, we need to change our current energy system into a greener one, where the cleaner energy generation systems pretend to be an alternative solution of this serious problem. In the last 20 years, the consumption of renewable energy has increased exponentially as can be observed in figure 2-4. At individually level of each country, these sources are already playing an important role in some places. For example, in Denmark the 68% of power comes from renewable energy sources. In Spain, however, its use only reaches up to 25% of the total energy consumed, ahead of Italy (23%) and behind Germany (30%).

The fast evolution of renewable energy production is already continuing. In 2017, the increase was resulted in 17%, and in terms of volume, the major growth of clean energies employment was in China in 2016, followed by USA, Germany, Japan, and India, which conformed the top five clean energy-producing countries. Thus, in 2017, the 8% of the consumed world's electricity came from renewable sources.

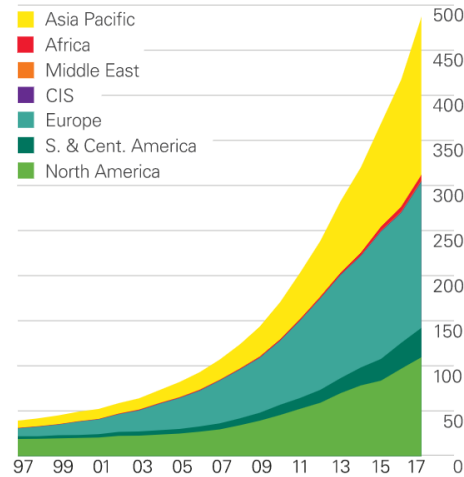


Figure 2-4. Growth in the renewable energies consumption by region from 1997 until 2017. Graphic obtained from BP web page [5] *Last accessed on June 1st 2019.*

Nevertheless, the main drawback related with the use of renewable energies, such as solar and wind energy, is their generation in an intermittent way. Thus, energy storage devices become necessary to accumulate the green energy and supply the power according to user's demand. Depending on the moment, the needs of energy consumption changes, being the peaks of demand difficult to palliate with the unique use of one device such as batteries, which supply the energy steadily over a long time. Thus, others alternative devices like supercapacitors arise as rapid loading and unloading systems of energy storage, being a promising strategy to increase the energetic efficiency in combination with batteries.

In this sense, the demand for energy-efficient storage devices is growing every day in key sectors such as automotive and consumer electronics. Thus, hybrid and electric vehicles, based on the combination of batteries and supercapacitors (SC), are increasingly requiring more autonomy and less charge time. In the automotive sector, in electric vehicles, the combination of lithium batteries with the use of SC is becoming more and more popular. Although, it is expected that the market of SC is leaded by transport applications, their use in others consumer electronic products is growing through the application in mobile phones memories, watches and so on.

The current state-of-the-art evidences that different materials have been investigated for applications as pseudocapacitor (PC) electrodes. Special attention is given to Nickel-based materials[6–13], in particular, nickel hydroxide ($\text{Ni}(\text{OH})_2$) and nickel oxide (NiO), have received extra attention due to their high theoretical specific capacitance (C_s), easy

oxidation process [14], high chemical and thermal stability, ready availability and low price. For these reasons, NiO has been used as an electroactive material for the manufacture of the electrodes studied in this thesis.

Additionally, the nanoscale and nanotechnology have played an important role in this work since the control of the size in the nanostructure results in the enhanced properties at the macroscale. Therefore, particles with nanometric size have been used as an initial concept in this thesis. The main reasons of this election are: i) nanoparticles have a high specific surface area, which provides a greater number of sites, where redox reactions are generated, and ii) the profit of the structural nano-effect which allows better withstanding the volumetric changes that the material undergoes in its microstructure during oxidation and reduction processes, extending the useful life of the device. Taking into account the use of dry nanopowders requires special equipment to avoid agglomeration flowing, float problems as well as a high health risk, an alternative wet route have been proposed, where most of these problems are solved when powders are immersed in a liquid media.

Most of the characteristics of the nanostructured electrodes depend on the shaping process. Properties as the active surface area, the conductivity, the macropores distribution, the microstructural connectivity and its mechanical stability, determine the electrochemical response and durability. New findings suggest the need to address the development of new strategies to control the nanoparticles arrangement during film growth and further achieve higher performance in terms of self-discharge, life expectancy, capacity, resistance, and so on. Therefore, in the electrode fabrication, shaping processes including patterning, coating or stacking of active materials are a key step profiting from the synthesis of raw nanomaterials and determining their sintering process [15].

From the final eighties, advances in colloidal chemistry knowledge have covered the necessary milestones for successfully applied colloidal processing methods in the reliable manufacture of nanostructures with final specific properties. The colloidal techniques involve the manipulation and control of the interparticle forces in the suspensions of powders in liquid media. This is a key step to break down weak agglomerates, stabilize and facilitate powders mixing, removing heterogeneities and defects in the shaped material, which avoid the degradation of relevant final properties. Moreover, it is critical to fit processing additives to modify suspensions properties apart from dispersion, such as the viscosity, flux, surface tension, wettability, etc., adapting their rheological behavior

to the forming technique [16,17] and also they are relevant to control the particles assembly.

Among the different colloidal processes, Electrophoretic Deposition (EPD) and Inkjet Printing (IJP) can be considered as two of the most promising techniques in the SC manufacture as industrial manufacturers can be integrated as safer, flexible, economical, and ecological processes in the context of green and sustainable engineering. IJP is an additive manufacturing technique that has exponentially grown during the last few years, especially in ceramic decoration [18] and more recently, in the manufacture of miniaturized devices and other industrial applications, such as microchips, LCD and plasma screens, by the development of novel and innovative functional inks [19–21]. However, it is mainly a 2D technique, and even through layer-by-layer printing it is possible to increase the pattern thickness.

EPD is proposed as an alternative technique for the fabrication of 3D electrodes. EPD stands out for being a powerful and versatile colloidal process that responds to the need to cover tridimensional complex shapes in order to enhance the specific capacitance by increasing of the specific surface area. This technique produces homogeneous films using low concentrated suspensions.

In this context, the main objective of this thesis is addressed the improvement of the specific properties of PC electrodes using Ni-based ceramic semiconductors processed by colloidal techniques as electroactive material. The developed research covers from the synthesis of Ni(OH)_2 and NiO nanoplatelets to the final characterization of electrodes shaped by different techniques for microstructures tailoring.

Scientific innovative short-term objectives face the cutting-edge technologies of electroactive electrodes, to produce new compositions and explore assembling of nanoplatelets, the micro/nanostructure building and its electrochemical performance. We especially tackled pseudocapacitors enhancement throughout increasing the specific surface area and reducing the charge transfer resistance, to achieve higher specific capacitances and good cycling properties.

For this purpose, the research work has consisted in the processing of ceramic semiconductor electrodes with hierarchical porous structures, using in all cases synthesized Ni-based nanoplatelets, as building block or main electroactive material. Nanoplatelets were then shaped by EPD and IJP onto 3D and 2D current collectors,

respectively. To achieve this objective a number of partial objectives have been considered:

- Scale-up of the synthesis process corresponding to our selected electroactive material, Ni(OH)_2 and NiO nanoplatelets.
- Development of novel modification colloidal strategies to build up complex composite nanostructures (core-shell type) with improved features.
- Formulation of water-based inks to the miniaturization of PC electrodes processed by IJP.
- Standardization of the EPD parameters to completely cover the surface of the 3D current collectors (Ni foams) with Ni-based nanoplatelets.
- Consolidation of the as-prepared microstructures focused on the capacity improvement, by optimizing the sintering process and the substrate for the manufacture of electrodes.
- Characterization of the electrochemical response of the manufactured PC electrodes, to determine the contribution of the main features of the ceramic semiconductor microstructure in the electrochemical yield.

3

Executive Summary

3.1. Introduction to the ceramic-based pseudocapacitors

The poles fusion, the migrations or even the extinction of some animal species are only a few of the consequences that global warming produces in our planet. Greenhouse effect, induced mainly by the atmospheric carbon dioxide, is considered the more direct responsible of the global warming. In this sense, the renewable energies pretend to be an alternative solution of these problems by substituting the fossil fuels for other non-emitting energy sources, like solar light or wind, that are intermittent. Thus, energy storage devices are necessary to retain the electrical energy and supply the power according to demand. Additionally, they must be considered uses where, according to the specific needs of each moment, accumulators must satisfy rapid electric loading and unloading without losing storage capacity. That is why batteries, or fuel cells, probably would be a lame duck solution without complementary devices such as supercapacitors (SCs). While batteries are capable of supplying energy steadily over a long time, SC can provide large amount of energy in milliseconds, being loading and unloading cycles truly fast.

Thus, hybrid and electric vehicles, based on the combination of lithium batteries and SCs, are increasingly requiring more autonomy and less charge time [22]. It should be noted that batteries offer a higher energy density and will continue to be responsible for us travelling more and more miles in our electric car. Although, if the batteries work beyond their power density possibilities, their temperature can rise, reducing their useful life. Here is where SC supports electronic motors, delivering the energy instantaneously and reducing the charging times. Nowadays, there are ongoing projects in which SC are already being applied in real conditions. For example, the TOSA Concept and Test Bus is the first 100% electric articulated bus in Switzerland with a high capacity that can recharge electric energy at every stop, in few seconds each time, without damaging the battery. Although the market for SC is expected to be led by transport applications their use in others consumer electronic products has grown through application in mobile phones memories, watches and so on.

The best way to compare the energy conversion and accumulation performances is the Ragone plot, where device types are grouped in terms of energy and power densities (Figure 3.1-1). The Power Density (W/Kg) which is the available energy that devices can supply per unit of mass, is represented at the vertical axis, while the Energy Density,

which determines the time rate of energy transfer per unit of mass (Wh/Kg), is represented at the horizontal axis. Therefore, in the Ragone plot, the necessary time for the charge and discharge is obtained by the quotient between energy density and power density.

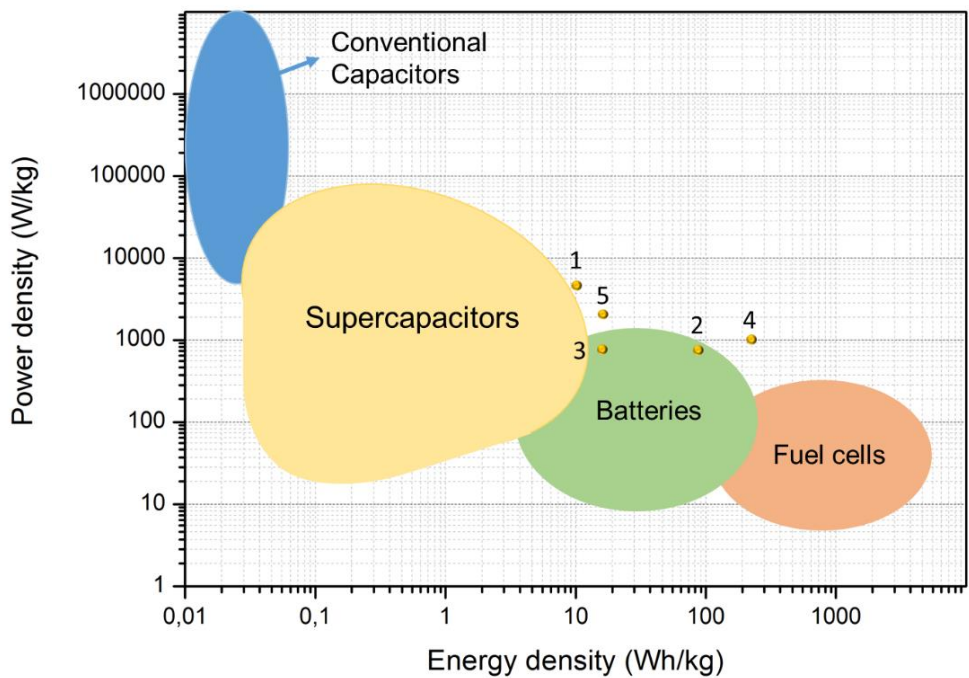


Figure 3.1-1. Ragone plot shows energy density vs power density grouping the most representative devices in energy storage. Random recent results of pseudocapacitors based on ceramic semiconductors (table 3.1-2).

SCs are located between traditional capacitors and batteries and combine properties of both. In devices with less volume and weight, SCs are able to store between 10 and 1000 times more energy than conventional capacitors and simultaneously, they can deliver a higher electrical power with a larger cycling lifespan, if compared with fuel cells and batteries. In other words, SCs can improve the performance of a battery in terms of power or increase the storage capacity of energy of the conventional capacitors. Table 3.1-1 summarizes accumulated energy, power delivery, charge/discharge time and cyclability of each group.

Table 3.1-1. Main features of batteries, fuel cells conventional capacitors and supercapacitors in terms of power and energy density and charge/discharge time

	Fuel cells	Battery	Supercapacitor	Conventional Capacitor
Power density (W/Kg)	5-500	10-10 ³	15- 1.5·10 ⁴	10 ⁴ -10 ⁷
Energy density (Wh/Kg)	>10 ²	10-120	0.1 - 10	<0.05
Charge/Discharge Time	∞	0.1 - 12 h	2.4 - 24 s	10 ⁻³ - 10 ms
Cycle life/ cyclability (n° cycles)	--	500 - 2000	> 100000	> 500000

Some data published in the last decade for semiconductor ceramic-based pseudocapacitors are also included in figure 3.1-1 and summarized in table 3.1-2. These compiled data show that the electrochemical response of this type of SCs approaches the top performance of batteries in terms of powder for energy densities ranging 10-100 Wh/Kg, being another advantage of these SCs the capability of making millions of charge/discharge cycles without losing their storage capability as capacitor.

Table 3.1-2. Data of SC's plotted in the Ragone diagram in Figure 3.1-1

Plot point	Based Material	Power density (W/Kg)	Energy density (Wh/Kg)	Ref
1	NiO	5332	10	[23]
2	Ni(OH) ₂ /MnO ₂	750	91.1	[24]
3	NiCl ₂	750	15.4	[25]
4	Mn ₂ O ₃	1000	147	[26]
5	CoO	2153	15	[27]

Depending on the application for which an energy storage device is required, it is necessary to evaluate the amount of energy and the time of charge/discharge. In order to respond efficiently to the requirements of each application, the combination of several systems could be the best solution, maximizing the strengths and minimizing the weakness they have separately. To understand the electrochemical performance and the main limitations for each systems, the four categories (Batteries, Fuel Cells, Conventional Capacitors and Supercapacitors) will be shortly introduced.

In **Batteries** chemical reactions transform high-energy reactants to lower-energy products, and the free-energy difference is supplied to the external circuit as electrical energy. Secondary batteries are based on reversible chemical reactions, and consequently are rechargeable. For example, the original composition of the electrodes in lithium-ion batteries (LIBs) can be restored by reversing the current. During the device charge, the

reduction and insertion of the Li ions takes place in the cathode producing a flow of ions from the cathode to the anode, while during the discharge, the oxidation and the disinsertion of ions occur in the anode, producing a flow of ions in the opposite way. These accumulators provide high energy density, but the volumetric changes associated to the insertion and disinsertion of Li ions produces the degradation of the electrodes due to the structure collapse, which is the main drawback of this devices.

The **Conventional Capacitor** chemically stores the energy through an electrostatic field generated between two electrodes. They are composed by two conductive surfaces (commonly metal foils) separated by vacuum or a dielectric material (for example a non-conductor ceramic). When a potential difference is applied between the electrodes, the transfer of charge takes place until the potential difference between the plates become equal to the potential difference applied by the charged device. The stored charge, q (C), is proportional to the developed potential, ΔV (V), being the constant of proportionality the capacity, C , expressed in Farads (F), according to equation 3.1-1.

$$C = \frac{q}{\Delta V} \text{ (eq. 3.1-1)}$$

Conventional capacitors can be classified depending on the material used as dielectric. Electrostatic capacitors employ an insulating material (ceramic, porcelain, teflon, etc.), being the electric field between the electrodes homogenous since the capacity is proportional to the dielectric constant of the medium and to the surface area of the electrodes and inversely proportional to the distance between them, as define the equation 2:

$$C = \epsilon_r \frac{A}{d} \text{ (eq. 3.1-2)}$$

where A (cm^2) is the area of the electrode, d (cm) the distance between them and ϵ_r (F/cm) the permittivity of the dielectric.

Electrolytic capacitors are a kind of capacitors having a conductive electrolyte between the electrodes, generally, boric acid or sodium borate. It maintains the serial connection between the two electrodes, which have a thin dielectric layer of oxide. This configuration leads to higher capacities than electrostatic capacitors, but they are also more hazardous when facing heating since the oxide can dissolve causing a short circuit when the polarity is inversed.

Supercapacitors (SCs), also known as ultracapacitors or electrochemical capacitors, are considered promising devices for energy storage and management due to their short-acting high power delivery. Parameters such as capacity, power density and energy density are usually adopted to evaluate the response of SCs.

The equations regularly used for the calculation of the Energy, E_d (eq. eq. 3.1-3), and Power, P_d (eq. 3.1-4), densities are:

$$E_d = \frac{1}{2 \cdot 3.6} C_s \cdot V^2 \quad (\text{eq. 3.1-3})$$

where C_s (F/g) is the specific capacitance (already divided by the mass) and V (V) is the nominal voltage, and:

$$P_d = \frac{E_d}{t} \cdot 3600 \quad (\text{eq. 3.1-4})$$

where E_d is the already calculated energy density and t (s) is the discharge time. The coefficients of the equations provide the results for E_d and P_d in terms of W·h/Kg and W/kg, respectively.

The specific capacitance, C_s , is determined from charging/discharging curves through chronopotentiometry analyses (CP) according to the equation 3.1-5:

$$C_s = \frac{I \cdot \Delta t}{m \cdot \Delta V} \quad (\text{eq. 3.1-5})$$

where C_s (F/g) is the specific capacitance, I (A) is the discharge current, Δt (s) is the charging/discharging time, ΔV (V) is the voltage window for discharge, and m (g) is the mass of the active material in the electrode. Another way to calculate the C_s is determining the charge value, Q (C), proportional to the integral of the cyclic voltammetry (CV) curve. In SCs, the accumulated charge represents the difference between the area under the charge curve and the area under the discharge curve for the upper and lower limits of the potential window (ΔV). Thus, the specific capacitance was obtained from the equations 3.1-6, 7 y 8:

$$Q = \int I \cdot dt; t = \frac{V}{v} \quad (\text{eq. 3.1-6})$$

$$Q = \frac{1}{v} \int I dV \quad (\text{eq. 3.1-7})$$

$$C_s = \frac{Q}{m \cdot \Delta V}; C_s = \frac{\int I \cdot dV}{v \cdot m \cdot I \cdot V} \quad (\text{eq. 3.1-8})$$

where I (A) is the current, t (s) is the time, V (V) is the voltage, v (V/s) is the scan rate, C_s (F/g) the specific capacitance, m (g) is the mass and Q (C) is the charge/discharge value.

According to the nature of the charge storage mechanism, the SCs are classified in two main groups, the electrochemical double layer capacitors (EDLCs) and pseudocapacitors (PCs). Additionally, a third group can be considered: the hybrid supercapacitors, where the energy accumulation is based on the combination of both charge storage mechanism. Figure 3.1-2 shows a scheme of the different electrochemical phenomena associated to their characteristic CV diagrams.

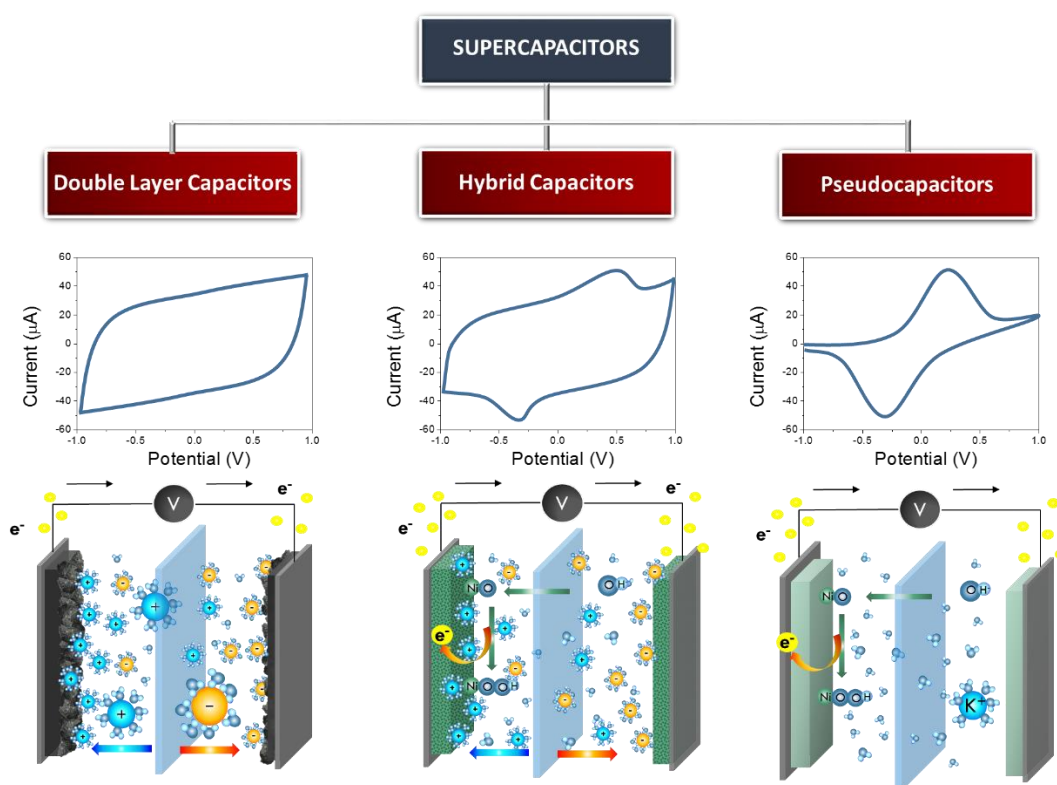


Figure 3.1-2. Hierarchical diagram of the supercapacitor classification attending to the energy storage mechanism. Charge storage principles and examples of the typical cyclic voltammograms are also included.

EDLCs store the energy through the accumulation of electric charges at the electrode/electrolyte interface. EDLCs are based on the electrochemical performance of carbonaceous materials with high specific surface area, which exhibit good conductivity and high electrochemical stability in solutions within a wide range of pH values[28]. In EDLCs, when the electrode is charged, opposite charged ions from the electrolyte are adsorbed to neutralize its surface. Ions will be desorbed once the potential changes in a

complete reversible ion adsorption/desorption process. This mechanism of energy accumulation by electrostatic charge provides both, fast energy loading and supply. Furthermore, these electrodes present a very long cyclic lifetime since the volume variations of the electroactive materials are avoided. The ions do not penetrate into the microstructure of the electroactive material, as occurs in storage systems based on redox reactions characteristic of batteries and PCs.

PCs storage the energy through a faradaic process based on reversible redox reactions between electrode and electrolyte, which take place on the surface of the electroactive material, involving electronic charge transfer processes by electrosorption. Thus, the cyclic voltammetries (CV) show the contribution of oxidation/reduction reactions and determine the redox reactions taking place at the electrode and its reversibility (Figure 3.1-2). In those electrodes, the rectangular shape typical from EDLCs disappears[29]. Although carbon-based EDLCs have many advantages such as higher specific surface area, good electronic conductivity, and high chemical stability, the capacitance of PCs can be 10–100 times higher than that achieved by EDLC[30].

Different materials have been investigated as PCs electrodes. Metal oxides (MO) and conducting polymers are the most common materials used[31]. Conducting polymers such as polypyrrole (PPy) and polyaniline (PANI) are easy of processing because its mechanical flexibility, but they have lower cyclability due to their easy degradability if they are compared with transition metal oxides (TMO). The poor cyclability of polymer-based PCs is attributed to large volumetric changes in the microstructure during cycling associated with doping and over-oxidation of chains at high potential. The limitations of these polymeric electrodes make TMO a reliable alternative as ceramic semiconductor-based PCs.

TMOs emerge as one of the best options for energy storage, since they exhibit a wide range of bandgaps, E_g , due to the diversity of electronic structure of the transition metals (Figure 3.1-3). The bandgap or energy gap describes the energy range in a solid material where electrons cannot exist due to the absence of energetic states. It is determined by the energy difference (eV) between the top of the valence band and the bottom of the conduction band, and it is related with the HOMO and LUMO gap in molecular chemistry. If some electrons promote from the valence to the conduction band then the material can be electrically conductor. Therefore, the bandgap determines the electrical conductivity of the material. In metals, there is not a bandgap because the valence band

overlaps the conduction band. However, conductivity in materials with $E_g < 0.01$ eV can be also considered essentially metallic. It is accepted that for insulators bandgap has to be higher than 5 eV, which is a gap too wide for the electron promotion. Then the E_g in semiconductors is consider to oscillate between 0.01 and 5 eV.

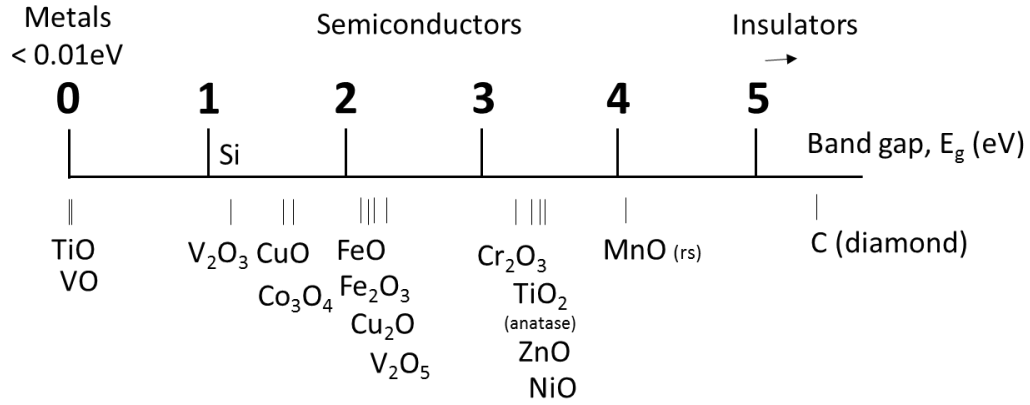


Figure 3.1-3. Relation between the band gap and electronic properties of TMOs.

TMO semiconductors are materials that can conduct electrical energy under especial conditions, depending on the voltage and current applied. The conductivity (S/m or $1/(\Omega \cdot m)$) is given by the equation 9:

$$\sigma = n \cdot e \cdot \mu \quad (\text{eq. 3.1-9})$$

where n is the number of current carriers, e is the absolute magnitude of the electrical charge on an electron (1.6×10^{-19} C) and μ their mobility ($m^2/(V \cdot s)$). In semiconductors, the number of mobile carriers is discrete, and they are classified in electrons, e , and holes, h . An intrinsic semiconductor possesses the same amount of electrons and holes ($n=e=h$) for each electron that is promoted into the conduction band, a hole is left behind in the valence band and therefore. A hole has a positive electric charge, equal and opposite to the charge on an electron, and the flow of holes occurs in a direction opposite to the flow of electrons. When an intrinsic semiconductor is doped in order to increase the number of charge carriers, adding either donor or acceptor dopants, then they are named type-n and type-p extrinsic semiconductor, respectively. The energies of electrons in the highest occupied levels and the conduction mechanisms are different depending on the whether the materials are doped to be either n-type or p-type.

The Fermi energy (E_F) refers to the maximum level of the energy where the electrons remain at low temperature. The Fermi's level position in regard to the conduction band is essential in the determination of the electrical behavior of TMO. This theoretical level is considered as a hypothetical energy level of an electron in thermodynamic equilibrium at 0 K.

Figure 3.1-4 shows a scheme of the structure of the semiconductor bands defining the bandgap (Figure 3.1-4a) and the position E_F level in the semiconductor structures depending on their electrochemical nature (Figure 3.1-4b). In TMO semiconductors the E_F level is inside the bandgap (Figure 3.1-4b) and the conduction and valance bands are near enough to the Fermi level to be thermally populated with electrons or holes. For intrinsic semiconductors, the E_F is located in the middle of the E_g , at the same distance from both bands. However, for extrinsic semiconductors, E_F is closer to the conducting band for the n-type semiconductors than in the p-type. This difference in the E_F level within the bandgap region of different TMO has been determined the entire evolution of microelectronics industry [32], and is a key-point of study in TMO-based devices for energy storage.

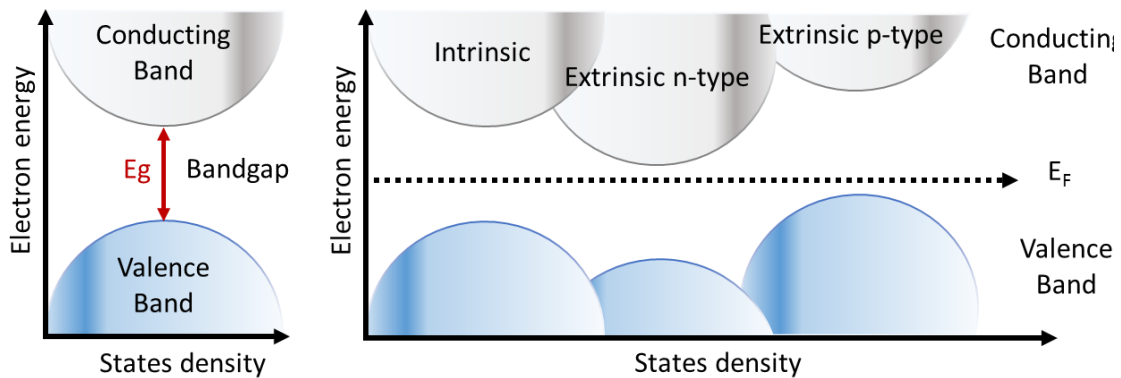


Figure 3.1-4. a) Semiconductor bands structures and bandgap. b) E_F position depending on the nature of TMO semiconductor.

In TMO an important aspect that affects the band structure and the final electronic properties is the partly occupied metal d orbitals in the electronic configuration. For example, TiO and Cu₂O are the beginning and the end of the $3d$ orbitals in TMO presenting an empty (d^0) and totally filled (d^{10}) valence layer, respectively [33]. Therefore, they are well known semiconductors because the last electron of the valence

band would reside in a more elevated hybrid orbital (in terms of energy), then the E_F increase when more electrons exist occupying the energy orbitals of less energy. Occasionally, if the d band(s) overlaps a higher conductivity can be obtained. In other cases, the overlap of d orbitals is limited, and the orbitals are effectively located in the individual atoms. NiO is often used as a prototypical example where this excitation is assumed to correspond either to the reaction $2\text{Ni}^{+2}\text{O}^{-2} \rightarrow \text{Ni}^{+1}\text{O}^{-2} + \text{Ni}^{+3}\text{O}^{-2}$ or to $\text{Ni}^{+2}\text{O}^{-2} \rightarrow \text{Ni}^{+1}\text{O}^{-1}$ (case of charge transfer insulator) [33]. Nevertheless, NiO can exhibit good p-type conduction, which makes it attractive as a transparent hole-transport layer with applications in energy accumulation. However, TiO and VO, that have the same crystallographic structure, exhibit d orbitals of the type d_{xy} , d_{xz} and d_{yz} on the metal ions strongly overlap creating a wide t_{2g} band only partly filled by electrons. Consequently, TiO and VO have metallic conductivity, $\sim 10^3 \text{ } 1/\Omega \cdot \text{cm}$ at 25°C [32], and an appropriate radiation light can promote the electrons transforming radiated light into other form of energy. Those ceramic semiconductors are the base of the photovoltaics, being its mayor limitation the low value of the quantum efficiency due to the high rate of recombination sites at the surface[32].

TMO can be considered intrinsic semiconductors since their charge is neutralized, which means that $n = p$, but even undoped MTO structures exhibit defects in the crystal lattice varying the proportion between the number of oxygen atoms and the number of metal atoms and hence breaking the balance of charges. Then, the TMO stoichiometry is declining itself to one side or the other making the conduction possible by vacancies or electrons. These defects are mainly produced during synthesis or sintering processes. It is the case of ZnO which is n-type intrinsically due to native oxygen vacancy inherently present in the crystal lattice. Each oxygen vacancy provides two free electrons. The number of vacancies created depends on the preparation of the ZnO-based material, i.e. an oxygen deficient environment during ZnO thermal processing [34]. A simple way to determine the intrinsic semiconductor nature of the TMO-based materials consists in the measurement of the capacitance at different voltages plotting the results in a $1/C^2$ vs V curve. If the linear range of the curve has a positive slope, then the TMO-based material is a p-type semiconductor, otherwise it is a n-type[35].

3.1.1. Profiting TMO electrochemical performance through the processing strategies

From the beginning of the XXI century, the knowledge on semiconductor ceramic oxides has become a key element when it comes to the evaluation of the PCs performance.

The graph in figure 3.1.1-1a shows the published reviews especially dedicated to PCs from 2000 until now. The first review on this topic appears in 2002 and it is not until 2013 when its popularity increases exponentially until the present. Around 40 reviews about these energy storage systems were published during this period, it is observed that studies of the electrode active material have been specifically emphasized, in terms of composition and morphology, while only a slight assessment of the electrolyte characteristics has been evaluated. Figure 3.1.1-1b illustrates how the fifty percent of these reviews recollected in table 3.1.1-1 are only focused on specific ceramic oxides compositions or/and their processing, while a 6% of them are targeted on the electrolyte, and the remaining publications mix polymers and carbon-based materials in different types of electrodes.

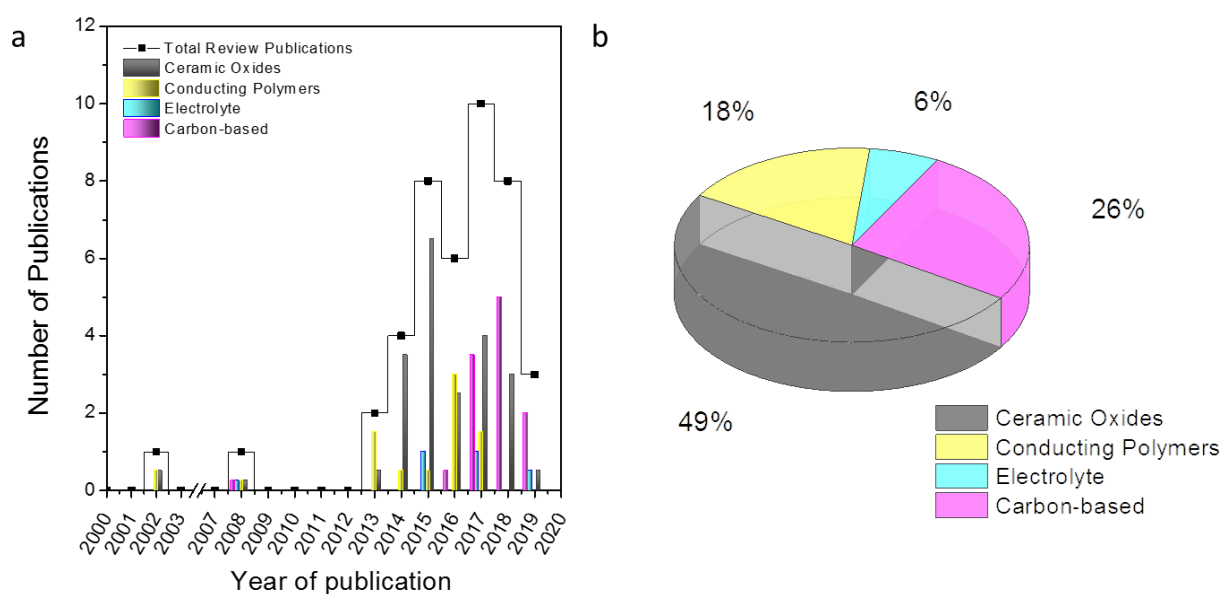


Figure 3.1.1-1. a) Overview of the published reviews since 2000 by year and main topic. b) Topic distribution of all the reviews about pseudocapacitors (Scopus) from 2000.

Table 3.1.1-1. List of the reviews published since 2000 ordered by the date of publication and classified depending on the main research topic assessed

Review	Topic	Ref	Date
Carbon-Based Metal-Free Catalysts for Energy Storage and Environmental Remediation	Carbon-based	[36]	March 2019
Background, fundamental understanding and progress in electrochemical capacitors	Carbon-based & Electrolyte	[37]	March 2019
A review on recent advances in hybrid supercapacitors: Design, fabrication and applications	Ceramic Oxides & Carbon-based	[38]	March 2019
Puzzles and confusions in supercapacitor and battery: Theory and solutions	Carbon-based	[39]	October 2018
Lignin in storage and renewable energy applications: A review	Carbon-based	[40]	September 2018
Review of Hybrid Ion Capacitors: From Aqueous to Lithium to Sodium	Ceramic Oxides & Carbon-based	[41]	July 2018
Emergent Pseudocapacitance of 2D Nanomaterials	Ceramic Oxides & Carbon-based	[42]	May 2018
Materials for supercapacitors: When Li-ion battery power is not enough	Ceramic Oxides & Carbon-based	[43]	May 2018
Energy Storage in Nanomaterials – Capacitive, Pseudocapacitive, or Battery-like?	Ceramic oxides & Carbon-based	[44]	March 2018
Overview of nanostructured metal oxides and pure nickel oxide (NiO) electrodes for supercapacitors: A review	Ceramic Oxides (Nickel)	[45]	February 2018
Recent advances of graphene-based materials for high-performance and new-concept supercapacitors	Carbon-based	[46]	January 2018
Three-Dimensional Binder-Free Nanoarchitectures for Advanced Pseudocapacitors	Ceramic oxide & Carbon-based	[47]	December 2017
Recent advances in nanostructured vanadium oxides and composites for energy conversion	Ceramic Oxide (Vanadium)	[48]	December 2017
Interlayer nanoarchitectonics of two-dimensional transition-metal dichalcogenides nanosheets for energy storage and conversion applications	Ceramic Oxides	[49]	December 2017
Tailoring pseudocapacitive materials from a mechanistic perspective.	Ceramic Oxides, electrolyte & Carbon-based	[50]	December 2017
Energy efficient graphene based high performance capacitors	Carbon-based	[51]	August 2017
Redox-electrodes for selective electrochemical separations	Ceramic Oxides & Conducting Polymers	[52]	June 2017
Carbon-based supercapacitors for efficient energy storage	Carbon-based	[53]	may-17
Electrical and electrochemical properties of conducting polymers	Conducting polymers	[54]	April 2017
Pseudocapacitive materials for electrochemical capacitors: From rational synthesis to capacitance optimization	Ceramic Oxides, electrolyte & Carbon-based	[55]	January 2017
Design and preparation of electrode materials for supercapacitors with high specific capacitance	Ceramic Oxides, electrolyte & Carbon-based	[56]	2017
Vanadium Based Materials As Electrode Materials For High Performance Supercapacitors	Ceramic Oxides (Vanadium)	[57]	October 2016
Conducting Polymers for Pseudocapacitive Energy Storage	Conducting Polymers	[58]	September 2016
Polyaniline-based electrodes: recent application in supercapacitors and next generation rechargeable batteries	Conducting Polymers	[59]	August 2016

Quinone and its derivatives for energy harvesting and storage materials	Conducting Polymers	[60]	June 2016
A mini review of designed mesoporous materials for energy-storage applications: From electric double-layer capacitors to hybrid supercapacitors	Ceramic Oxides & Carbon-based	[61]	April 2016
Review on advances in porous nanostructured nickel oxides and their composite electrodes for high-performance supercapacitors	Ceramic Oxide	[29]	March 2016
Understanding performance limitation and suppression of leakage current or self-discharge in electrochemical capacitors: A review	Ceramic Oxides & Conducting Polymers	[62]	November 2015
A review of electrolyte materials and compositions for electrochemical supercapacitors	Electrolyte	[63]	November 2015
MnO ₂ -based nanostructures for high-performance supercapacitors	Ceramic Oxides (Manganese)	[64]	September 2015
Rare earth and transitional metal colloidal supercapacitors	Ceramic Oxides	[65]	August 2015
Nanostructured electrode materials for electrochemical capacitor applications	Ceramic Oxides	[66]	June 2015
Nanostructured Mo-based electrode materials for electrochemical energy storage	Ceramic Oxides (Molybdenum)	[67]	April 2015
Nanostructured Mn-based oxides for electrochemical energy storage and conversion	Ceramic Oxides	[68]	February 2015
Recent development in spinel cobaltites for supercapacitor application	Ceramic Oxides	[69]	January 2015
Recent progress in nickel based materials for high performance pseudocapacitor electrodes	Ceramic Oxides	[70]	December 2014
Nanowire electrodes for electrochemical energy storage devices	Ceramic Oxides & Conducting Polymers	[71]	December 2014
Microwave-assisted synthesis of metal oxide/hydroxide composite electrodes for high power supercapacitors - A review	Ceramic Oxides	[72]	October 2014
Cu-based materials as high-performance electrodes toward electrochemical energy storage	Ceramic Oxides (Copper)	[73]	February 2014
Recent advances in conjugated polymer energy storage	Conducting Polymers	[74]	February 2013
Electrospinning technology for applications in supercapacitors	Ceramic Oxides & Conducting Polymers	[75]	2013
Materials for electrochemical capacitors	Ceramic Oxides, Carbon-based, electrolyte & Conducting Polymers	[76]	November 2008
Electrochemical capacitors	Ceramic Oxides, electrolyte & Conducting Polymers	[77]	September 2002

The election of the electroactive material plays a crucial role in the final response for the device. Among all metal oxides/hydroxides, TMOs have been regarded as promising electrode materials for SCs owing to their changeable valence and theoretical capacities[78] among others electrochemical properties. However, the selection of the electrode compound is not always based on their electrochemical response since the cost

and the availability are variables which should be considered for product fabrication scaling or its commercialization, i.e. ruthenium, indium, tungsten or vanadium are more expensive and less available than manganese, iron, titanium, nickel or copper, among other metals.

3.1.2. The parameters with implication in the TMO electrochemical performance

Depending on the valence and oxidation numbers, when binds to oxygen forming the semiconductor, the transition metal presents different semi-occupied *d* orbitals, determining the redox reactions through which the energy is stored. The theoretical capacitance, C_t , depends on the number of electrons exchanged participating in the redox reaction, and it can be calculated following equations (3.1.2-1) and (3.1.2-2):

$$C_t = n \cdot n^0_{e^-} \cdot F \quad (\text{eq. 3.1.2-1})$$

$$C_t/m = \frac{n^0_{e^-} \cdot F}{MW} \quad (\text{eq. 3.1.2-2})$$

where the molecular weight of the TMO, MW , and the number of exchanged electrons in the redox reaction, $n^0_{e^-}$, depend on the electrode composition and are related to the theoretical capacitance per the electrode mass, C_t/m , by the Faraday constant, F . The final units of C_t are F/g, if we assume 1 V of potential.

As theoretical capacity is based on intrinsic properties (eq. eq. 3.1.2-1 and 2) it has to be also considered an intrinsic characteristic of TMOs. In the table 3.1.2-1 the theoretical capacitance, C_t , was calculated for different metal oxides at their most common valences.

Table 3.1.2-1. Theoretical capacitance calculated by eq. 3.1.2-2 for different MO.

Metal oxide	Theoretical Capacitance (F/g)
RuO ₂	1450
MnO ₂	1109
Co ₃ O ₄	2003
Fe ₃ O ₄	416
V ₂ O ₅	530
NiO	2583
TiO	2416
SnO ₂	2560
In ₂ O ₃	708
Bi ₂ O ₃	418
WO ₃	416
MnO _x	>1300
MoO ₃	670
CuO	2425

Although metallic oxides such as NiO or TiO have high values of theoretical capacity, 2583 and 2416 F/g, respectively, the final electrochemical response also depends on other intrinsic properties of the material, such as the bands structure of the TMO and more precisely its band gap which determine its electronic conductivity. Thus, the capacitance of the electroactive material is usually lower than the theoretical value.

Intrinsically the charge transfer is intimately related to electron conductivity. Free electron mobility implies higher conductivity of the semiconductor. Therefore, n-type semiconductors (electron conduction) are better conductors than p-type conductors (hole conduction). The reason for this lies in the location of these electrons. For n-type the free electrons are in the conduction band, while p-type semiconductors have the holes in the valence band, and the movement of the holes is governed by the electrons movement that participate in the atomic bonds, then they have less freedom and thus, slowing down the charge transfer.

Moreover, the specific capacitance depends on extrinsic properties such as charge transfer, ion diffusion, reversibility of the redox reactions and cyclability. These extrinsic characteristics are directly related to both the electronic configuration of the metals, the crystallographic properties and related band gap of TMOs, but also on the electrode microstructure which define the interface of the electroactive material with the electrolyte and which mainly depends on the processing strategies (synthesis, shaping and consolidation).

Extrinsically, the electrochemical reversibility of redox reactions describes the rate of the electron transfer, being faster when the window of potential determining the redox reaction in CV is smaller. In other words, the distance between the oxidation and reduction peaks that can be seen in a PCs electrode CV is shorter. In this sense, the cyclability, considered as the number of times an electrode can be recharged before they begin to break down, and rate capability, considered as ratio of the galvanostatic discharge capacity to the total discharge capacity for various discharge rates [79], are electrochemical properties of the electrodes, related to the chemical and structural stability of their microstructures being then also extrinsic properties. Figure 6 shows common shape of a charge/discharge cycles (figure 3.1.2-1a) and rate capability plots

(figure .1.2-1ab) of different electrodes. The electrodes that keep constant their specific capacitance after several charge/discharge cycles exhibits a 100% cyclability, while the rate capability relates differences in the capacitance values registered for the electrode when it is cycled at different sweep rates.

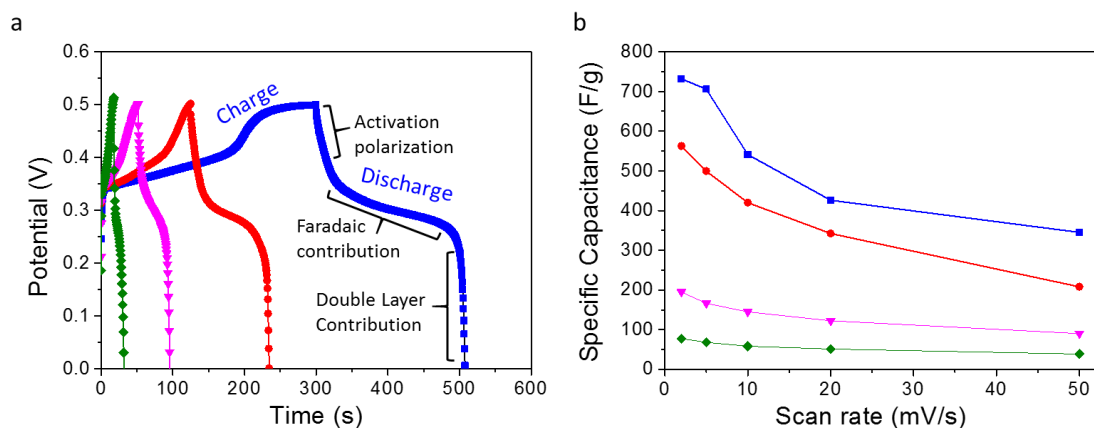


Figure 3.1.2-1 a) Charge – discharge curves of different electrodes at the same current density (2 A/g).
b) Rate capability obtained from the cyclic voltagrams for different electrodes at different scan rates.

The more resistive the electrode, the lower the rate capability. The resistance of the electrode varies depending on its microstructural characteristics, such as the ion diffusion in the electrolyte solution and the electron transfer resistance of boundaries between the electroactive particles in the ceramic semiconductor microstructure, as well as the interface resistance between the current collector and the electroactive material. All these properties can be modified acting on either the crystallography of the TMO and on the morphology and the microstructure of the electrode. **Consequently, the synthesis and shaping processes of the electrode has a crucial role in the development of high-performed electrodes.** Table 3.1.2-2 summarizes TMO-based PCs and their electrochemical performance described in the literature during the last decade, listed by the main metal transition in its composition, where the synthesis or shaping technologies used to fabricate the tested electrode have been highlighted. In this table, only TMO-based electrodes shaped onto metal substrates have been collected, since those electrodes shaped onto graphite substrates or carbonaceous species have been include in table 3.1.5-1 and considered hybrid devices due to the contribution of the substrate to the specific capacitance.

Shaping strategies, can differentiate between the current routes of electrode preparation by mixing as-synthesized electroactive particles with binders and conductive materials

(generally carbonaceous species), and one-step processing routes where synthesis and shaping are processes that take place simultaneously. In the current route of the electrode preparation, research efforts are focus on the control of the synthesis procedures, such as hydrothermal or solvothermal precipitation, colloidal sol-gel synthesis, etc. After the synthesis of particles, the resulting slurry/paste obtained by blending is applied onto the collector substrate by different shaping processes such as dip-coating, drop-casting, tape-casting, spin coating, electrophoretic deposition, etc.[80,81] Most of these synthesis techniques evolve to one-step processes, since coating technologies allows the proper film growth on the substrate during the synthesis of the nanostructure, resulting on binder-free electrodes. This is the case of process such as sol-gel coating, hydrothermal/solvothermal growth, electrodeposition, CVD, etc.[82–84]

Related to the composition of the TMO-based PCs, the RuO_2 has been the most widely investigated TMO because of its superior electrochemical properties such as high conductivity, highly reversible redox process in a large potential window and thermal stability, which lead to a worthy cyclability and rate capability (the specific capacitance remains stable after CV at different sweep rates)^{36,37}. However, its practical applicability is impeded by its toxicity, high costs and naturally less abundance as raw material. In fact, due to cost consideration, non-strategic TMO candidates with excellent theoretical capacitive values have attracted much attention such as manganese[87], nickel[78], cobalt [88], zinc [84], and iron [27].

Noteworthy is the widely use of manganese oxides for this type of devices due to their rapid cationic diffusion at high charge and discharge rates, environmental friendliness, and abundant raw materials. As a transition metal, manganese presents several oxidation states and therefore a great variety of stable oxides (MnO , Mn_3O_4 , Mn_2O_3 , MnO_2) showing ideal charge–discharge curves. For instance, Maiti, et al. [89] or Qiu, et al. [90] have achieved a more than the 95% of capacity retention of values of specific capacitance as higher as 840 and 775 F/g, respectively.

Other interesting metal, due to its abundance, is the iron. Fe_3O_4 has been employed to build electrodes, however this material possesses slower electron transport rates than other TMO because of their poor electrical conductivities. Co_3O_4 , is also employed for this kind of devices because it exhibits excellent reversible redox behavior, high conductivity, long-term performance, and good corrosion resistance [14]. V_2O_5 is the other promising candidate to replace the ruthenium. This strategic material is easier

available than ruthenium, but the price is still elevated. However, the unique layered structure and mixed oxidation states confer to this material a suitable option[91]. Finally Cu-based oxides are other candidates toward practical electrochemical energy storage devices due to their abundant, low cost, easy synthesis and environmentally friendly merits[92].

Special attention is given to Nickel-based materials[6–13], in particular, nickel hydroxide ($\text{Ni}(\text{OH})_2$) and nickel oxide (NiO) have attracted extra interest due to their high theoretical specific capacitance, easy oxidation process [14], high chemical and thermal stability, ready availability and low price. In 1996, Liu and Anderson for the first time used porous NiO as a possible electrode material for SC applications measuring specific capacitances ranging 50-60 F/g[93], far away from the theoretical value. Nowadays several studies of NiO -based electrodes have reported specific capacitances closer to the theoretical value, 2018 F/g[94], 2192 F/g[95], 2186 F/g[96]. It should be also noted that the published work to date with the highest capacity obtained is the supercapacitor developed by Chen et al. [4] It was fabricated by in situ electrochemical activation of Ni-based colloids from a NiCl_2 electrode, taking advantage of the different nickel oxidation states. The highest specific capacitance was 10286 F/g at a current density of 3 A/g, indicating that a three-electron Faradaic redox reaction ($\text{Ni}^{3+} \leftrightarrow \text{Ni}^0$) occurred.

3.1.3. Strategies for the micro, nanostructure modification to maximize the electrochemical response of the TMO based electrodes

As it has been mentioned above, the full profiting of the surface reactions of the TMO is still a challenge since the electrochemical response of the electrodes not only depends on the inherent properties of the selected material, such as their theoretical capacitance or their electronic band structure. Electrodes must present a high exposed surface area with abundant reaction sites and successfully impregnate the electrolyte along their electroactive microarchitecture, as well as they should promote the electrons mobility through the metal oxide microstructure reducing the resistance at the interface between the electroactive material and the conductive collector. Thus, an optimal performance of a PC requires of a consolidated nanostructure with a highly hierarchically organized macro-meso-microporosity, holding accessible redox active sites, to step up charge transfer and ion diffusion capability.

Table 3.1.2-2. Summary of PCs performances reported in recent publications

Ref	Material	Synthesis Strategies	Shaping Strategies	Morphology	Specific Capacitance	Capacitance retention
Manganese						
[27]	Mn ₃ O ₄	Hydrothermal	Pressed	nano-capsules	750 F/g at 5 A/g	107% after 9000 cycles
[26]	Mn ₂ O ₃	Solvothermal+ calcination	Pressed	nanobars	250 F/g at 0.2 A/g	~75% after 3000 cycles
[89]	MnO ₂	Hydrothermal	Pressed	nanowire net	775 F/g at 2 mV/s	97% after 5000cycles
[90]	Au/MnOx	Au sputtering & MnO electrodeposition		nanocone structure (MnO ₆ octahedra)	840.3 F/g at 2 A/g	96.5% after 2000 cycles
[97]	KMnO ₂	Hydrothermal	Drop-casting	--	303 F/g at 0.2 A/g	100-90% after 1000 cycles
Nickel						
[98]	Ni(OH) ₂ and NiO	Hydrothermal	Pressed	pompon-like spheres	1028.5 F/g at 2.22 A/g	98.5% after 1000 cycles
[99]	NiWO ₄ -CoWO ₄	Co-precipitation	Pressed	cauliflower-like	196.7 /g at 0.5 A/g	110% after 5000 cycles
[78]	NiO	Hydrothermal + calcination	Pressed	Flowerlike	1297.3 mAh/g a 200 mA/g	--
[100]	NiO	Hydrothermal + calcination	Pressed	Hollow nanosphere	612.5 F/g at 0.5 A/g	90% after 1000 cycles
[101]	NiO	Hydrothermal + calcination	Pressed	Mesoporous Spheres	1140 F/g at 10 A/g	100% after 1000 cycles
[102]	NiO	Hydrothermal + areogel	Pressed	--	901 F/g at 0.5 A/g	93% after 3000 cycles
[103]	LiNiVO ₄	Hydrothermal + calcination	Pressed	--	456 F/g at 0.5 A/g	99.6% after 1000 cycles
[104]	NiCoO	Hydrothermal + calcination	Pressed	microsheres	1884 F/g at 3 A/g	79.4% after 10000 cycles
[105]	NiCo ₂ O ₄	Hydrothermal + annealing + electrodeposition	Pressed	--	1080 F/g at 6 A/g	83% after 4000 cycles
[106]	NiCo ₂ (CO ₃) _{1.5} (OH) ₃ @NiCo ₂ S ₄	Hydrothermal	Pressed	urchin-like	956.4 F/g at 4 A/g	80.1% after5000 cycles
[107]	NiO	Precipitation	drop casting	--	243 F/g at 2 mV/s	--
[24]	Ni(OH) ₂ /MnO ₂	Soaking	Coating	nanorods	2937 F/g at 5 A/g	92.3% after 25000 cycles
[108]	Ni(OH) ₂	Precipitacion hydrotehm al /electrochemical deposition /CBD		nanoflakes	325 F/cm ³	80% after 1000
[109]	NiO	Sorvothermal	Spin-coating	nanospheres	1386 F/g at 1 A/g	78.5% after 5000 cycles
[110]	NiO	Sparking	drop coating	--	402.7 C/g at 1 A /g	88% after 1000 cycles
[111]	NiO	Sparking		Foam-like	920 C/g at 1 A/g	96% after 1000 cycles
[81]	Co-doped Ni(OH) ₂	LA laser-induced L	drop-casting	curly nanosheet	720 F/g at 6 A/g	92% after 1000 cycles
Cobalt						
[80]	ZnCo ₂ O ₄	Hydrothermal	Pressed	oval-like	2555.8 F/g at 2 mV/s	83.7% after 3000 cycles

Executive Summary

[88]	Co ₃ O ₄	Laser Ablation in Liquid	dropwise presed with gel	--	177 F/g at 1 mV/s	100% after 20000 cycles
[112]	LiCoO ₂	Solvothermal	Pressed	--	654 F/g at 2 A/g	86.9% after 4000 cycles
[83]	CoS	Hydrothermal + Anion exchange reaction		--	103 mAh/g at 2 A/g	79% after 16000 cycles
[113]	ZnCo _{1.5} (OH) _{4.5} C _{10.5} ·0.45H ₂ O	Precipitation	Deposition	nanosheets	3946.5 F/g at 3 A/g	81% after 5000 cycles
[82]	Co ₃ O ₄ CoOH Co(OH) ₂	Electrochemical precipitation		2D hexagonal platelet	627 F/g at 5 mA/cm ²	90% after 1000 cycles
[114]	Co(OH) ₂ –Au	Electroplating			1800 F/g at 20 A/g	78% after 3000 cycles
[115]	CoNiO ₂	Solvothermal	Pressed	microspheres	~854.9 and ~414.5 F/g at 1 and 20 A/g	100.8% after 10000 cycles
Ruthenium						
[116]	RuO ₂	Theoretical calculation				
Iron						
[117]	np-Ag@Fe ₂ O ₃	Electrodeposited			~608 F/g at 10 A/g	84.9 % after 6000 cycles
[118]	MnFe ₂ O ₄	Hydrothermal	Drop-casted		282.4 F/g at 0.5 A/g	85.8 % after 2000 cycles
Tungsten						
[119]	WO ₃	Electrodeposition /crimping	Pressed	flower-like	196 F/g 10 mV/s	85% after 5000 cycles
Molybdenum						
[120]	Ni/MoO/VO ₂	Electrochemical deposition		nanowires	477 mF/cm ² 1 mV/s	95% after 20000 cycles
Vanadium						
[121]	Na _{0.33} V ₂ O ₅	Co-precipitation	Pasted	nanorod-like	168 F/g at 0.5 A/g	81% after 50000 in NaCl
[122]	TiO ₂ -V ₂ O ₅	Forming gel	Drop casting	tube-like mesoporous nanostructure	310 F/g at 2 mV/s	94% after 1000 cycles
Tin						
[123]	Sn@SnO ₂	hydrothermal + calcination	Pressed	nanosphetres	906.8 F/g at 1mV/s	~100% after 2000 cycles
Zinc						
[84]	ZnO-Au NC	Solgel	Hydrothermal		205.7 F/g at 2 A/g	--
Cerium						
[124]	CeO ₂	Solvothermal + calcination 650°C 3h	Coating	brick-upon-tile	1204 F/g at 0.2 A/g	100% after 5000 cycles
Silver						
[125]	Nanoporous Au/AgO composite (NPAAC)	Dealloying–stripping		--	82 F/g at 5 A/g	94% after 10000 cycles

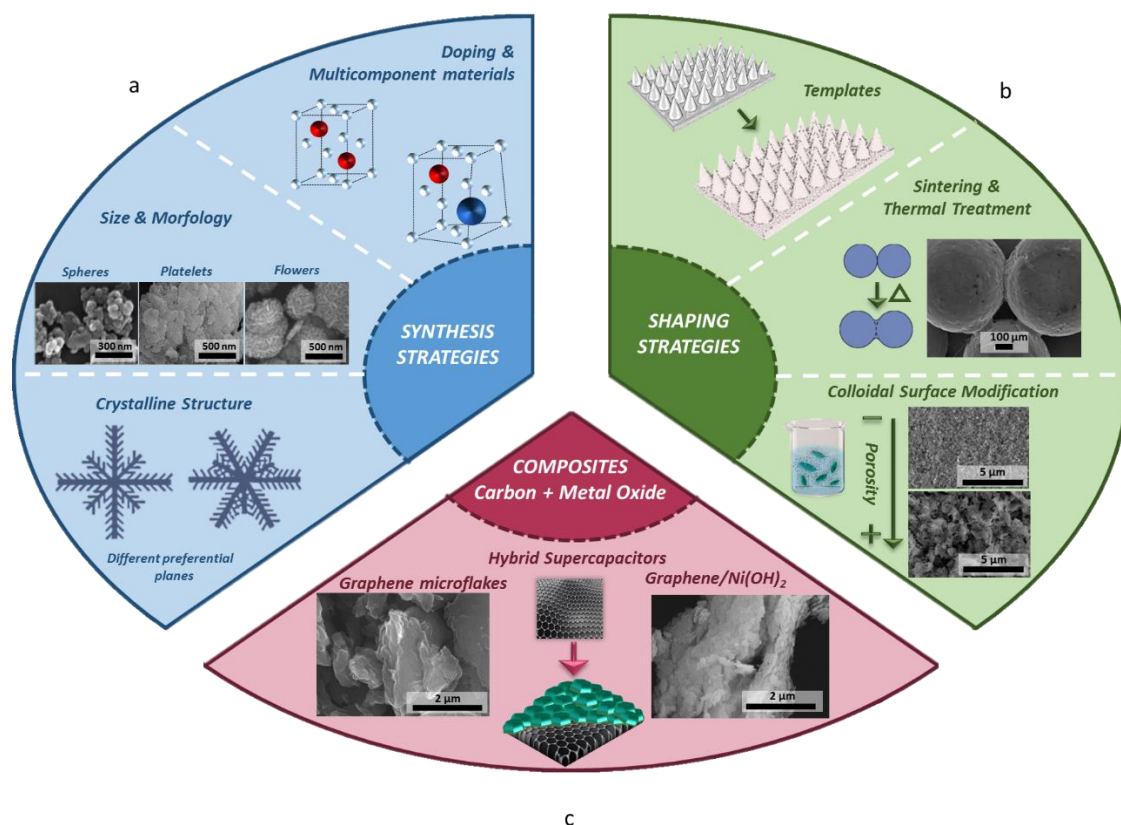


Figure 3.1.3-1. Current strategies for the improvement of the final electrochemical features in pseudocapacitors. a) In blue, synthesis modification of particles and 0D, 1D, 2D and 3D nanostructures, changing morphology, crystallography and defining new solid solutions. b) In green, shaping films and coating of metal collectors by the nanoparticles assembling and microstructure tailoring, designing porosity (specific surface area, including endo- and exo-templates and sintering. c) In red, technologies based on in situ synthesis of composites using carbon-based materials and TMO.

From decades, the researchers devoted to the study of PCs have focused their efforts on improving their electrochemical response by different routes. Figure 3.1.3-1 gives an overview of the current strategies employed to overcome this challenge. Processing strategies have been classified in three different groups: (i) Synthesis and modification of particles or nanostructures; (ii) Microstructure tailoring by shaping films or coating metal collectors; and (iii) Technologies based on the combination with carbon-based materials for the development of hybrid capacitors or ultracapacitors.

The first strategy (Figure 3.1.3-1 in blue sector) is related with the physic-chemical modification of the crystallography of the particles or the synthesis of nanostructures (0D

or nanocrystals and nanoparticles, 1D or nanofibers and nanotubes, 2D or nanoflakes or nanoplatelets, and 3D or tridimensional flower-like structures), or directional crystal growing, acting directly over the synthesis process [126]. These processing strategies are focused on the development of new applications of synthesis processes. Many review papers and articles demonstrate that the nanosize, the morphology (0D, 1D, 2D and 3D) and the crystallography modification at the atomic level, by the inclusion of dopants and the creation of vacancies, provides new opportunities to achieve higher efficiency.

In the second category (Figure 3.1.3-1 in green sector), the shaping strategies are included. The use of different process to shape thin or porous thick films employing the as-synthesized new nanostructures are the processing strategies considered in this category. Among available coating techniques[127], those based on the control of the colloidal-chemical parameters of sols, suspensions, inks or slurries should be highlighted due to their reliability, scalability and the wide range of possibilities for the microstructure tailoring. In those techniques, the use of templates or microstructural modifiers, the control on the shaping parameters and the further selection of specific sintering treatments could be managing to maximize the electrochemical properties of the active electrode microstructure. Some examples of the final properties that can be controlled through this collection of processing strategies to optimize the electrochemical response of PCs are: i) the exposed specific surface area, which determines the redox events profiting and ion diffusion through the electrolyte. ii) The connectivity between ceramic semiconductor particles, which largely regulates the charge transfer phenomena. And iii) the consolidation level and adherence/joining of the coating and the metal collector, which define the electrical resistance of the system.

Finally, the last group of the proposed strategies (Figure 3.1.3-1 in red sector) shows the combination of TMO with the materials used for the EDLC electrodes (carbon-based). This strategy defines a new family of storage devices based on carbonaceous composite structures, the hybrid supercapacitors, or also called ultracapacitors, which offer the combination of both energy storage mechanisms.

3.1.4. Based-synthesis strategies of the processing of TMO for pseudocapacitors

The first group of the proposed classification is based on the development of new synthetic routes in order to design nanoparticles with complex morphologies and crystallography. The 0D nanocrystals and/or nanoparticles are ideal systems for exploring

a large number of novel phenomena at the nanoscale and at the atomic level to investigate the effect of size and dimensionality dependence of the electrochemical properties. The 1D and 2D nanostructures exhibit unique shape-dependent characteristics and consequently, they have been used as building blocks to shaped electroactive films and understand the mechanism of the nanostructure growth and their implications in the enhancement of the electrochemical response of PCs. Finally 3D nanostructures attract intensive research interest because they present a high exposed surface area, supplying enough absorption sites for all involved molecules in a small space, while lead to a better transport of species through their well-connected microstructure [126]. Different features of as-synthesized microstructures with the same composition can be tuned by modifying the synthesis parameters [128,129]. Figure 3.1.4-1 shows different types of NiO nanostructures synthetized in our laboratory by ultrasound-aided chemical precipitation. The morphologies were obtained by changing the precursor's concentration, the ratio of reactants and the ultrasonic power [128,129].

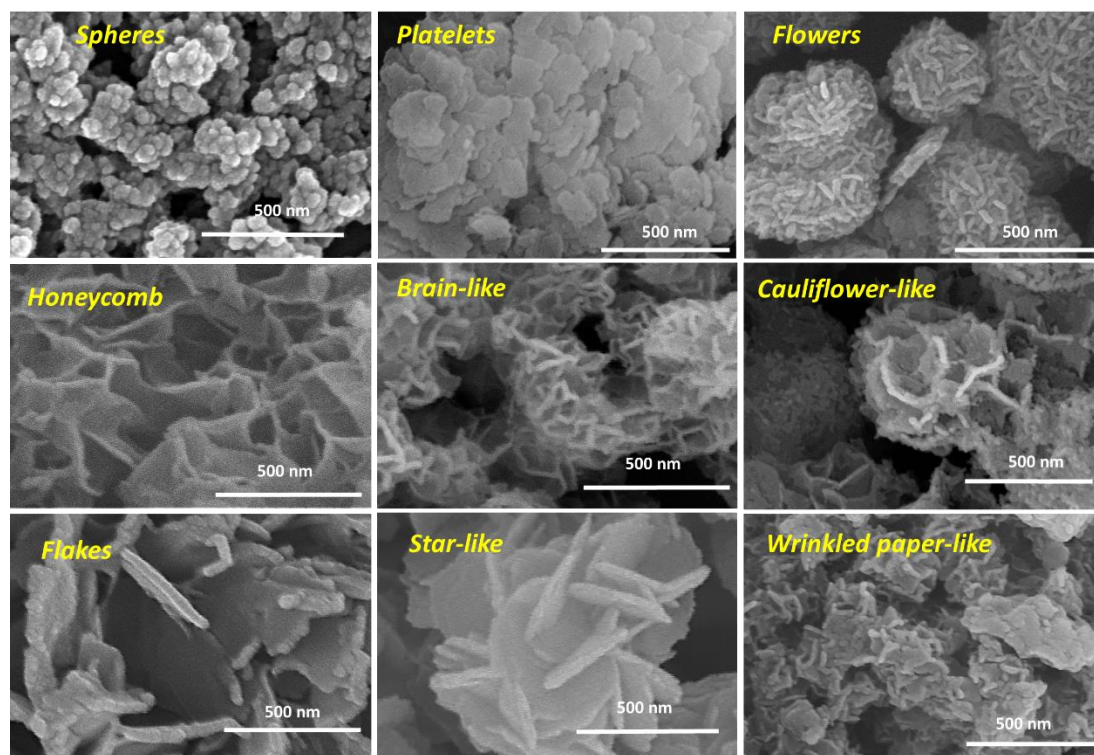


Figure 3.1.4-1. Typical SEM images of NiO nanoparticles with different types of morphology: spheres, platelets, flowers-like, etc.

Alternatively, the progress in new multicomponent electroactive materials have been significantly increased obtaining binary [112,130,131], ternary [82,99,120], quaternary [132] oxides, etc. Although, the description of new synthesis processes is not aimed in

this review, several physical and chemical methods have been analyzed to give the most recent overview about the topic.

The most common processing method for PCs electrodes consists on a first stage of synthesis of the electroactive material and its subsequent shaping onto the collector substrate. These collectors can range from metal substrates to glass coated with conductive ceramic films such as ITO or FTO. Conventionally, the preparation procedure for TMO-based electrodes lies on the formulation of a slurry by the blending of electroactive material with additives like carbon black (CB), acetylene black, PVDF, PTFE, etc. which act as binders to enhance the contact between particles of active material. And then, these mixtures are directly deposited, pasted or pressed onto conductive substrates[24,26,27,80,98,100,104]. Depending on the way the pressure is applied, two techniques are distinguished. The most used is called “die pressing” in the paste is put into a die and shaped by the punches under a load (see figure 3.1.4-2). Secondly, isostatic pressing, which consist in consolidating the powder by an isostatic pressure applied by a liquid on a shaped mold.

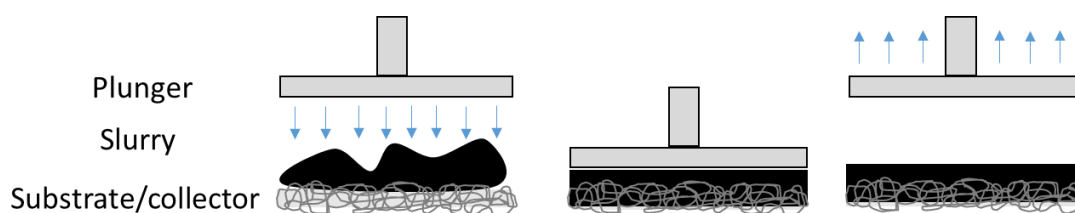


Figure 3.1.4-2. Scheme of the most commonly used conventional shaping method: The die pressing.

The sol-gel, solvothermal and hydrothermal syntheses, together with precipitation or co-precipitation, are the most common routes for particles synthesis and subsequent pressing. Nowadays, these syntheses are in continuous development for its application in SC. In view of the collected publications in table 3.1.2-2, the hydrothermal synthesis is the most employed. It consists in a chemical reaction of precipitation under the appropriate temperature and pressure conditions (normally above 100 °C and 1 bar) with water as liquid medium. Commonly reactions take place in an autoclave. Using this kind of synthesis, Maiti et al.[89] have prepared single-phase α -MnO₂ with an interconnected nanowire morphology forming a network, which results in a specific pseudocapacitance of 775 F/g. Furthermore, after 5000 cycles the capacitance retention of the pressed

electrode was 97%. However, the employment of Ni-based oxides shows better electrochemical responses. Wang et al.,[98] synthesized β -Ni(OH)₂ hollow microspheres which show excellent capacitance behavior (1028.5 F/g) at a charge/discharge current density of 2.22 A/g and 100% of coulombic efficiency after 1000 cycles. In the case of Li et al.,[104] the hydrothermal synthesis of bixide microspheres (NiCoO) was followed by a thermal treatment and then pressed with carbon black and PTFE onto a nickel foam. The obtained capacitance value was 1884 F/g at 3 A/g, retained the 79.4% of its initial capacitance after 10000 cycles. Solvothermal syntheses differs from Hydrothermal processes in the use of organic solvents as reaction media. Using organic solvents, Cai et al.[109] synthesized NiO nanospheres inside of an autoclave by a simple and low-cost solvothermal method, which were spin-coated onto different substrates forming homogeneous films. The electrodes presented a high capacitance (1386 F/g at 1 A/g) and a cyclability retention of 78.5% after 5000 cycles.

As synthesis techniques, the precipitation and co-precipitation synthesis must be taking into account because they are also widely employed for TMO-based electrodes preparation. The objective of these techniques consists on preparing ceramic oxides through the formation of intermediate compounds, such as hydroxides or oxalates achieving a perfect homogeneity even after as-synthesized powder calcination and annealing. The use of one metal salt, or more than one, as precursor allows obtaining of a single precipitation or a multicomponent suspension, respectively. Wang et al.[99] synthesized by co-precipitation a mesoporous NiWO₄-CoWO₄ nanocomposite. The electrochemical response of this compound after pressing was 196.7 C/g at 0.5 A/g, and less than one third of rate capability losses. Similarly, Yeager et al. reported how NiO nanoparticles deposited by dropping a suspension on a target substrate generates a rough surface, which implies a larger surface area but a non-uniform thickness of the coating. The pseudocapacitive behavior obtained was tested in three-electrode half-cells with a maximum specific capacitance value of 243 F/g. Yeager et [97] al. achieved a gravimetric capacitance of 303 F/g, at a charge/discharge current of 0.2 A/g employing also drop casting for the fabrication of the electrodes based on KMnO₂ as electroactive material. The capacitive retention obtained was 87.8% after 1000 cycles. Among other, described results suggest the relevance of the binder and the shaping processes in the electrochemical behavior of ceramic semiconductor electrodes.

In ceramics, the technological development in thin film is widespread due to the savings in material. Besides, in semiconductors for energy storage and in the electronic components industry, they also have a great application in the optic coatings for their application in photovoltaics, and in corrosion protection for their use to extend the life of cutting tools. In spite of the two-step conventional routes, where synthesis and shaping are separately performed, sometimes both steps go hand in hand. For example, when the growth of the particles can take place on the substrate inside the synthesis medium leading to the formation of a thin film. This is the case of Mahajan et al.,[84] who employed the sol-gel synthesis combined with the hydrothermal growth of ZnO-Au nanocomposites, and without further processing, resulting in a specific capacitance of 205.7 F/g at current density of 2 A/g. In fact, sol-gel is a well know technology to synthesize ceramic materials and final products with a controlled stoichiometry and high purity leading to interesting microstructures for electrochemical devices[133].

Moreover, other combinations of techniques are possible. Pu et al.[105] have combined hydrothermal synthesis with electrodeposition to grow oriented NiCo_2O_4 nanowires on ultralight nickel foams. As-synthesized specimens were directly measured obtaining a capacitance value of 1080 F/g with 17% lost after 4000 cycles. In this case, the tailored hydrothermal growth of a complex morphology results in an improved electrochemical performance, evading additional processing steps such as annealing treatments and the use of binders. In electrodeposition, the structure, morphology, and uniformity of the oxide layers can be controlled by adjusting the plating parameters such as deposition mode, applied potential, current density, bath temperature, concentration of precursors, and addition of complex/additive agents [134]. In the literature is easy to find authors using this processing technique to prepare PCs electrodes. This electrochemical one-step and cost-effective method precipitates the semiconductor nanoparticles at the same time that deposition take place onto the substrate. This technique also works as multicomponent precipitation if the precursor reactants are dissolved in the same solution. Ju et al. [82] synthetized by electrochemical precipitation, and controlling the pH, 2D hexagonal platelet based on Co onto a Ti plate obtaining 627 F/g as capacitance value and a 90% of retention after 1000 cycles.

The synthesis of metal organic frameworks (MOFs) have been also employed in developing of PCs. MOF derived CeO_2 showed a pseudocapacitance of 1204 F/g at 0.2

A/g with the maximum cyclability after 5000 cycles (100%). Maiti et al. [124] synthesized this MOF by solvothermal method and a subsequent calcination with a brick-upon-tile morphology. There are other specific thin film techniques, such as Laser ablation in Liquid (LAL) or Atomic Layer Deposition (ALD) also employed in this field. Liang et al. [81] employed LAL to develop curly nanosheets of Co-doped Ni(OH)₂ electrode obtaining an specific capacitance of 1421 F/g at a current density of 6 A/g, and a retention level of 76% after 1000 cycles. And Liu et al. [88], using the same method, have developed Co₃O₄ nanocrystals for PCs, which exhibits a capacitance of 177 F/g based on the mass, and 6.03 mF/cm² on a basis of the active material area at a scan rate of 1 mV/s. Furthermore, this electrode presents a long cyclability, 100% of capacitance retention after 20000 cycles. Other authors have used ALD. Xia [135] carried out an optimized PANI–RuO₂ core–shell nanostructured electrodes, which exhibit very high specific capacitance (710 F/g at 5 mV/s) and power density (42.2 kW/kg) at an energy density of 10 Wh/kg, with a capacitance retention of 88% over 10000 cycles (higher than that obtained for just PANI-based electrodes). Nonetheless, these methods require the use of strategic technology compared to other ceramic routes described below.

3.1.5. Microstructural modification by shaping and, sintering ceramic films

Following the trend of the thin films manufacture, other strategies have been proposed based on the use of binder-free techniques to modify the electrode microstructures. In those processing strategies shaping of electroactive materials is followed by a low temperature (<600°C) sintering process to consolidate the nanoceramic semiconductor structure to maximize connectivity by forming unions between particles (sintering necks).

Sintering is a well-known treatment in ceramics, which promotes the connectivity between particles and joining to the collector, making the electron transfer easier, and reducing the charge transfer resistance. Furthermore, the microstructure consolidation improves mechanical stability, which results in a longer lifetime of the device. In this sense, nanosized TMO can be consolidated by a mild sintering treatment after synthesis and shaping, achieving a stronger electrically connected electrodes, where at porous nanostructure also provides the structural tolerance needed to overpass the volume changes of the faradaic reactions. The formation of sintering necks between NiO nanoparticles in a thermal treatment of sintering at 325°C is showed in figure 3.1.5-1.

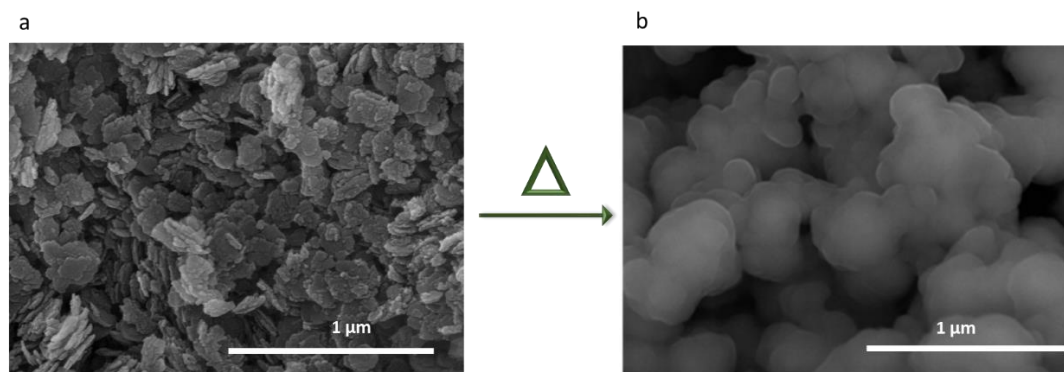


Figure 3.1.5-1. NiO nanoparticles before (a) and after (b) the sintering process at 325°C during 1h under Ar atmosphere.

This type of heat treatment also allows the use of endo- and exo-templates, for example, sponges or microstructural modifiers, that decompose during sintering leading to a porous microarchitecture which contributes to maximize the efficiency of the device increasing the contact between the electroactive material and the electrolyte. Moreover, the electrical conductivity can be enhanced by introducing metal [136] or nonmetal impurities [137] within the oxide nanostructure, generating donor or acceptor states in the bandgap and thereby increasing the concentration of charge carriers.

The table 3.1.5-1 shows publications describing PC electrodes processing route ending by a sintering process in a furnace to consolidate the electroactive material, where parameters such as temperature, pressure, time and atmosphere was controlled to reach the proper consolidation of the oxide structure and a porosity balance ad hoc for the final application.

The hydrothermal synthesis of a thin layer followed by a mild thermal treatment to strength oxides consolidation is one of the widely extended process. Lu et al. [138] developed NiO nanorod arrays on Ni collectors, and Yoo et al. [139] worked with Co_3O_4 on porous Ni substrates, achieving specific capacitances of 2018 F/g and 1591F/g, respectively.

In some cases, this type of synthesis is employed in combination with other techniques apart from the final sintering to drive the crystallographic growth. For instance, Cai et al. [109] employed a spin-coating technique to form the first layer and then by hydrothermal synthesis they grew the full microstructure.

Table 3.1.5-1- Summary of carbon-free PCs electrodes processed following a ceramic route ending by sintering process.

Ref	Material	Synthesis and shapping process		Thermal treatment	Morphology	Specific Capacitance	Capacitance retention
[140]	Co ₃ O ₄ @Au@MnO ₂	Electrochemical deposition		250°C 2h 1 °C/min	Porous nanowalls	1532.4 F/g at 1 A/g	~ 100% after 5000 cycles
[141]	NiO	Electrodeposition		250°C 2h	3D cross-linked grid	2558 F/g at 2 A/g	--
[23]	Ni ₂ PNS/NF	Hydrothermal+phosphorization		300°C 2h 5 °C/min	--	2400 F/g at 50 mV/s	67 % 5000 cycles
[142]	NP c-V ₂ O ₃ /r-VO _{2-x}	Electrodeposition + template calcination		300°C	--	1856 F/g at 5 mV/s	93% after 15000 cycles
[143]	TiO ₂ /Ni(OH) ₂	Hydrothermal+CBD		300°C	Core-shell nanorod arrays	482 F/g at 0.5 A/g	--
[7]	NiO	Precipitation US	EPD	325°C 15min Ar	Flower-like	363F/g at 10A/g	79 % after 1000 cycles
[144]	NiO/Ni	Precipitation US + calcination	EPD	325 °C 1h Ar	Nanoplatelets	755 F/g at 2 A/g	62% after 1000 cycles
[145]	NiO	Precipitation US	Inkjet Printing	325 °C 1h Ar	Nanoplatelets	160 F/g at 2 A/g	100% after 1200 cycles
[139]	Co ₃ O ₄	Hydrothermal		350°C 1h 3°C/min	Nanorods	1591 F/g at 5 mV/s	~100% after 90 cycles
[146]	Co ₃ O ₄ or ZnO and NiO	Hydrothermal + CBD Chemical bath deposition + sputtering of ZnO		350°C 1.5h Ar	Nanowires	853 F/g at 2 A/g	95.1% after 6000 cycles
[147]	MnO ₂ - NiO	hydrothermal		350°C 2h in Ar	Tubular arrays assembled by thin nanoflakes	0.35 F/cm ² at 8.5 mA/cm ²	97.4% after 1500 cycles
[138]	NiO	Hydrothermal US		250, 300, 350, or 400°C 3h Ar	Nanorod	2018 F/g at 2.27 A/g	92% after 100 cycles
[148]	MoO ₂	HFMOVD technique		400°C 60min 10 ⁻² Torr	Nanorod	98 F/g at 4A/g	71% after 5000 cycles
[149]	V ₂ O ₃ /MnO ₂	Electrodeposition + Template calcination		400 °C 2h Reductor atmosphere	Foam-like	1162 F/cm ³ at 1.56 A/cm ³	~100% after 15 000 cycles
[150]	Co ₃ O ₄ /Cu ₂ S//Co ₃ O ₄ /Cu ₂ S	Hydrothermal + SILAR		450°C	--	1080 mF/cm ² at 10 mV/s	98.2% after 2000 cycles
[151]	PVP modified NiCo ₂ O ₄	Hydrothermal		450 °C in air 2 h 3 °C/min	Flower-like	0.60356 mF/cm ²	86.9 % after 500 cycles
[152]	Nb ₂ O ₅	Solvothermal + Sol-gel	Aerogel deposition	600 °C	Different	400 F/g at 5, 10, 20 and 50 mV/s	--

In the same way, Zhou et al. [23] found a phosphorylation strategy to produce electrodes with high capacitance (2141 F/g at a scan rate of 50 mV/s). The electrode retains a high specific capacitance of 1437 F/g even after 5000 cycles at a current density of 10 A/g. They employed a hydrothermal process, before the phosphorylation, to grow the hydroxide precursors on nickel foams, and after all, the samples were calcined at 300°C for 2h under Ar flow. In the case of Xia X. et al., [146] $\text{Co}_3\text{O}_4/\text{NiO}$ core-shell nanostructures were firstly prepared. Two-step solution-based method was employed in order to synthesize these nanoparticles. It consists in a combination of a hydrothermal synthesis and a chemical bath deposition (CBD) with a final ZnO sputtering. The final calcination was at 350°C for 1.5 h and under Ar flow. Those electrodes exhibit a high specific capacitance of 853 F/g at 2 A/g and an excellent cycling stability (95% after 6000 cycles).

The sol-gel synthesis has also employed for the same purpose, in combination with aerogel deposition and spin-coating. In this way, Kim et al. [152] carried out the deposition of Nb_2O_5 as electroactive material by solvothermal sol-gel method. This metal oxide was then calcined at 400 °C in air for 2 h, reaching a specific capacitance of ~ 400 F/g.

Electrochemical deposition is largely used as well followed by sintering. Li et al. [140] deposited a 3D multicomponent electrode ($\text{Co}_3\text{O}_4@\text{Au}@\text{MnO}_2$) using a sequential electrochemical deposition process. Finally, after sintering at 200°C for 2 h under Ar atmosphere, the specific capacitance value obtained was 1532.4 F/g at 1 A/g with no degradation after 5000 cycles. This technique is also employed by Lang et al. [149] to deposit $\text{V}_2\text{O}_3/\text{MnO}_2$ using latex nanospheres as endo-templates, which decompose during the sintering process at 400°C. The specific capacitance achieved was 1162 F/cm³ at 1.56 A/cm³ and it retains this value after the long-term electrochemical cycling (100% after 15000 cycles). Moreover, Liu et al. [142] also employed templates to form hierarchical isomeric vanadium oxides, leading to a specific capacitance of ~1856 F/g and a high cyclability, 93% of capacitance retention after 15000 cycles.

Special attention should be paid to the Electrophoretic Deposition (EPD), a shaping method for thin and thick films, consisting in the application of an electric field to a suspension, which causes the migration of charged particles and their deposition to the electrode of opposite charge. The EPD is gaining increasing interest with other

electrochemical strategies for the deposition of multicomponent films and functional coatings. EPD offers many advantages for the deposition process, such as the easy control of the thickness changing the time or the operational potential, the versatility to cover complex shapes or 3D collectors and the generation of homogeneous layers. Many researchers are focused on the co-deposition of carbon-based materials and polymers with inorganic particles. However, authors like Hung et al. [153] and Gonzalez et al. [11] have developed electrodes based on MnO_2 and Ni(OH)_2 respectively, using this shaping method and obtaining capacitances of 481 F/g and 400 F/g and cyclability rates of 83% (after 15000cycles) and 100% (after 1000 cycles), respectively.

The synthesis by precipitation aided by the action of ultrasound (US) have been intensively explored by Gonzalez et al. [7,10]. They employed an US probe (inside of a precursor dissolution of Ni^{2+}) for the fabrication of nanoplatelets of Ni(OH)_2 , which were electrophoretically deposited and sintered, developing PCs electrodes with 79% of capacitance retention (424 F/g) during 1000 cycles at a scan rate of 10 A/g. Yus et al.[144] have employed the same process combined with the heteroprecipitation of Ni nanospheres in the suspension to obtain a NiO/Ni nanocomposites which were then deposited by EPD in Ni foams, exhibiting 755 F/g at 2 A/g.

As mentioned above, this technique is unique for coating 3D electrodes, however one of the research lines for raising the specific surface area is focus on promoting the porosity of the deposited electroactive material onto the surface of the electrodes. Nevertheless, the electrodes must present a robust structure, avoiding degradation during the charge and discharge processes, and resist small volumetric changes in their microstructure. Thus, larger specific surface area results in higher capacitance and ideal electrochemical behavior[6,128,154].

However, in terms of 2D, Direct Inkjet Printing as an additive manufacturing technology is becoming very popular. It is a mature technique widely employed in traditional ceramics industry for the tile's decoration. And nowadays, with the development of functional inks, their use in other industries such as microelectronics is growing. For instance, Yus et al.[145] have developed NiO electrodes through this powerful technique by printing Ni foils substrates with NiO nanoplatelets, and subsequent mild sintering process at 325 °C. The as-prepared electrodes showed a 160 F/g of capacitance and a 100% of retention after 1200 cycles.

All these electrochemical techniques are very useful in order to co-deposit two or more materials at the same time. And in the race for the manufacture of hybrid supercapacitors, they are widely used due to the easy ability to co-depositing semiconductor oxides and carbon species such as carbon nanotubes (CNT) or, oxidized (GO) or reduced (ERGO) graphene.

3.1.6. Hybrid capacitors

The development of hybrid capacitors (HSCs), also called “ultracapacitors”, is a novel strategy for the optimization of the electrochemical behavior. It consists in the combination of metal oxides with carbonaceous compounds with large specific surface such as graphene, carbon nanotubes, active carbon, etc. The presence of carbon-based materials as conductive additives may positively contribute to the improvement of the electrochemical response. This blend provides an increase of the final specific capacitance due to the combination of the pseudocapacitance of TMO and the electrochemical double-layer capacitance given by the carbonaceous component achieving better connectivity among the metal oxide phase. HSCs can accumulate higher energy densities compared with traditional PCs. The table 3.1.6-1 shows some interesting articles about this type of hybrid capacitors classified by the C-based material. Graphite substrates, graphene, graphene oxide or carbon nanotubes (CNT) are the most frequently used.

The processing routes for the manufacturing of these carbon-based pseudocapacitors electrodes do not differ from those mentioned above for PCs. The hydrothermal synthesis is the most commonly used. For instance, this synthesis was employed by Zhu et al. [155] for the development of self-assembled CoO nanorod cluster on three-dimensional graphene, reaching a specific capacitance of 980 F/g. In this case, hydrothermal synthesis is also used in combination with other such as electrodeposition, for example, Sawangphruk et al. [156] tailored Ag-doped MnO₂ by this method with a final sintering step at 400°C for 2 h on a carbon substrate. The specific capacitance values measured in 0.5 M Na₂SO₄ at a scan rate of 5 mV/s were 557 F/g achieving a high cyclability 98.6%.

Table 3.1.6-1. Summary of hybrid supercapacitors reported in literature classified attending to the employed carbon-based material.

Ref	Carbon-based Material	Metal Oxide	Synthesis & Layer formation	Specific Capacitance	Capacitance retention
[157]	Graphene	Mn ₃ O ₄ /graphene	Hydrothermal + Pressed	256 F/g	--
[158]	Graphene	MnNi (OH) _x /graphene	Hydrothermal + Pressed	2219 F/g at 0.73 A/g	90% after 1400 cycles
[159]	Graphene	GNS/Co ₃ O ₄	Microwave-assisted method+ Pressed	243.2 F/g at 10 mV/s	95.6% after 2000 cycles
[160]	Graphene	Co ₃ O ₄ /graphene	Solvothermal + Pressed	2435 F/g at 1 A/g	112% after 4500 cycles
[161]	Graphene	Co(OH) ₂ /graphene	Hummers and hydrothermal + Pressed	92 F/g	60% after 3000-6000 cycles
[155]	Graphene	CoO-Graphene	Hydrothermal + Ceramic TT at 450 °C for 2 h under Ar	980 F/g at 1 A/g	103% after 10000 cycles
[162]	Graphene O	MnO ₂ /GO (15:1)	Hummers + Sonication precipitation + Pressed	197.2 F/g	84.1% after 1000 cycles
[163]	Graphene O	MnO _x on Carbon Fibers	Electrodeposition + Reduction on substrate	1004.8 mF/cm (386.5 F/g) at 4 mA/cm	94% after 5000 cycles
[95]	Graphene O	Ni-MOFs@GO	Solvothermal + hummers + Pressed	2192.4 F/g	85.1% after 3000 cycles
[164]	Graphene O	GO/NiTAPc	Hummers + Pressed	163 F/g	70% after 1000 cycles
[165]	Graphene O	MoO ₃ /GO	Hydrothermal + Ceramic TT 600°C 3h Ar	321.8 F/cm ³ at 2 mV/s	97.6 % after 5000 cycles
[166]	rGO	CoS@rGO	Hydrothermal + Pasted	849 F/g at 1A/g	90.5% after 3000 cycles
[167]	rGO	rGO/Co ₃ O ₄	Hydrothermal + Pressed	207.2 F/g at 1A/g	--
[168]	rGO	NiPc NF-rGO	Solvothermal + drop casting	223.28 F/g at 1A/g	--
[169]	rGO	rGO-Co ₃ O ₄	Hydrothermal & Hummers + Aerogelification	136.6 mF/cm ² at a 2 mA/cm ²	~99-100% after 6000 cycles
[170]	rGO	CoO/RGO	Hydrothermal +ozonation + annealing N2	239.4 F/g at 10 A/g	93.2% after 10000 cycles
[171]	rGO	MoO ₂ -RGO	Hydrothermal + Drop casting	615 F/g	90% after 10 cycles
[172]	rGO	Au/ZnO/rGO	Hydrothermal + Pasted	875 F/g at 1 A/g	60% after 1000 cycles
[173]	rGO	NiO/RGO	Heterocoagulation + EPD + Sintering	885 F/g at 2 A/g	71% after 1000 cycles
[174]	ErGO	NiO/ERGO	Electrochemical co-deposition + Ceramic TT 300°C 2h Air	1715.5 F/g	78.8% after 2000 cycles
[175]	C. substate	MnO ₂	Hydrothermal + Pressed	212 F/g	88% after 10000 cycles
[130]	C. substate	LaMnO ₃	Solvothermal + Calcination 700 °C 4h dry air + Spin-casting 700 rpm	586.7 F/g and 609.8 F/g	--
[176]	C. substate	MnO ₂ /PANI	Hydrotherma l+ Pressed	873 F/g at 0.25 A/g	95% after 5000 cycles
[177]	C. Substrate	Mn ₃ O ₄ & MnOOH	Hydrothermal + Drop-casting	170 F/g at 500 mV/s	--
[178]	C. Substrate	MnO ₂ -Carbon	Electrodeposition	8 2.8 F/cm ² at 0.05 mV/s	80% after 1000 cycles
[97]	C. Substrate	KMnO ₂	Hydrothermal + Drop-csdting	303 F/g at 0.2 A/g	100-90% after 1000 cycles

Executive Summary

[110]	C. Substrate	NiO	Sparkling + Drop-casting	402.8 C/g at 1 A/g	88% after 1000 cycles
[179]	CNT	CNT-MnO ₂	Hydrothermal + Gelification	4.4 F/cm ³ at 0.04 A/cm ³	~50% after 3000 cycles
[153]	CNT	CNT/MnO ₂	Hydrothermal+ EPD	415 F/g at 3 A/g	83.3% after 15000 cycles
[180]	CNT	MnO ₂ /CNT//MoO ₃ /CNT	Drop-casting + Electrodeposition	507.2 F/g at 1 mA/cm ²	83% after 5000 cycles
[181]	CNT	MWCNT + MnO ₂ and RuO ₂	Dry painting method LbL	25 F/g at 0.2 A/g	82% after 5000 cycles
[182]	CNT	Ni/Ni(OH) ₂ & CNT	Hydrothermal + Pressed	1283 F/g at 2 A/g	~100% after 2000 cycles
[183]	CNT	NiO-CNT	hydrothermal & calcined in argon at 300 C for 2 h.	328 F/g at 0.33 A/g	64.3% after 300 cycles
[184]	CNT	CNT-NiO	Chemical Vapor Deposition (CVD) + Calcination + EPD	1.26 F/cm ³ at 100 mV/s	94.2% after 10000 cycles
[96]	CNT	β-Ni(OH) ₂ NS/ NWCT	Electrochemical deposition	2185.6 F/g at 5 A/g	95% 1000 cycles
[185]	CNT	NiCoAl-LDH// ERGO CNT	Hydrothermal & Hummers + Pressed	1188 F/g at 1A/g	88-91% after 1000 cycles
[186]	CNT	CNT/MO; M = Co, Zn, Mn	Microwave-assisted (MO) CVD (CNT) after annealed at 650 C	123.9 F/g at 377 μA/cm ²	95% after 1000 cycles
[187]	CNT	NiCo ₂ O ₄ Nanowire/CNT	Hydrothermal	277.3 mF/cm ² at 0.32 mA/cm ²	89% after 5000 cycles
[188]	CNT	RuO ₂ or MnO ₂ & CNT	Electrodeposition	72 and 98 F/g	86% and 93% after 1000 cycles
[189]	CNT	SWCNTs/Fe ₂ O ₃	Chemical Vapor Deposition (CVD) + Drop-casting	183 F/g at 0.01 V/s	--
[190]	CNT	H _x MoO _{3-y}	Hydrothermal	210 F/cm ³ at 1 A/g	93.3% after 4000 cycles
[191]	CNT	MoO ₃ @CNT	Hydrothermal-vacuum	100.04 F/g at 200 mA/g	90% after 600 cycles
[192]	CNT	V ₂ O ₅ /CNT	Hydrothermal + Pressed	~35 F/g	80% after 900 cycles
[193]	CNT	Mn-based	Electrodeposition + Dip-coating + Ceramic TT 600°C 2h	148 F/g 1 A/g	92% after 10000 cycles at 2 A/g
[194]	Graphyte pirolitic	Co(OH) ₂ -PG	Hydrothermal + US	642.5 F/g at 1.5 A/g	100% after 5000 cycles
[195]	Carbon nanofiber	(MCNs//NiCo ₂ O ₄)	solvothelmal + calcination	1631 F/g 1 at A/g	94.5% after 5000 cycles
[196]	Amorphous micron carbon ribbons (AMCR)	NiCo ₂ O ₄ @AMCRs	Hydrothermal + Pressed	1691 F/g at 3A/g	89 % after 10 000 cycles
[197]	Carbon nanoflakes	CoO@ f-C nanowire	Atomic Layer Deposition (ALD) + Glucose carbonization	3.4 F/cm ² 10 mA/cm ²	98.6 % after 5000 cycles

[85]	Mesoporous Carbon	RuO ₂ /carbon composite	Hydrothermal + Pressed	1733 F/g at 0.2 A/g	91% after 2500 cycles
[198]	Calcinated Mof	Fe ₃ O ₄ /carbon composite	Hydrothermal + Pressed	162 F/g at 1 A/g	83.3% after 4000 cycles
[199]	Glucose	α -Fe ₂ O ₃ @C	Hydrothermal + Pressed	288 F/g 1 A/g	72.3% after 2000 cycles
[200]	Polymer calcination	ZnO/carbon	ZnO Synthesis and in suspension + Polimerization + Calcination + Pressed	145 F/g at 2 mV/s	91% after 10000 cycles
[25]	Carbon spheres	Ni(OH) ₂	Precipitation + Electrodeposition	10286 F/g at 3 A/g	--
[201]	Calcinated Mof	Co/Ni oxide & carbon	MOF electrosynthesis + Electrodeposition + Ceramic TT 900 °C 12 h Ar	157 F/g at 1 mA /cm ²	92% after 4200 cycles
[81]	C. Substrate	Co-doped Ni(OH) ₂	LAL	720 F/g at 6 A/g	92% after 1000 cycles
[202]	C. Substrate carbon fiber paper	Co _x Ni _{1-x} (OH) ₂ /NiCo ₂ S ₄	Electrodeposition	2.7 F/cm ² at 4 mA/cm ²	96% after 2000 cycles
[203]	C. Substrate	Co ₃ O ₄	Solvothermal & calcination + Sprayed	476 F/g at 0.5 A/g	82% 2000 cycles
[204]	C. Substrate	Co-Ni	Coprecipitation + Electrodeposition	1123 F/g	78% after 2000 cycles
[131]	C. substrate	Co ₃ V ₂ O ₈	Hydrothermal (MHT)	4194 F/g at 1 A/g	85% after 10000 cycles
[135]	C. substrate	PAni-RuO ₂	Chemical oxidative polymerization + Atomic Laser Deposition ALD	710 F/g at 5 mV/s	88% after 10 000 cycles at 20 A/g
[132]	C. Substrate	Al _x Cu _y Co _z Fe ₂ O ₄	Sol-gel & calcination + Pressed	875 F/g at 5 mV/s	--
[205]	C. Substrate	MoO ₃	Sol-gel + Drop-casting	135 F/g	84% after 200 cycles
[134]	C. Substrate	VO _x /Carbon	Electrodeposition	167 F/g at 25 mV/s	--
[206]	C. substrate	Na ₂ Ti ₃ O ₇	Hydrothermal and annealing + Pasted	1.3 mWh/cm ³ and 70 mW/ cm ³	~ 80.3% after 2500 at 0.5 A/g
[207]	C. Substrate	Zn _x Co _{1-x} O	Hydrothermal on Carbon fiber paper CFP	450 F/g at 1 V/s	90.7% after 5000 cycles
[208]	C. Substrate	WO ₃ on carbon	Sol-gel + Spin-coating + Ceramic TT (300, 400, 500, 600 °C)	233.6 F/g at 2 mV/s	--
[209]	C. substrate	NiFe ₂ O ₄	Hydrothermal on template + Ceramic TT 350°C 2h Air	697 F/g at 5mV/s	93.6 % after 10000 cycles
[210]	C. substrate	MoO ₂ and V ₂ O ₃	Hydrothermal + Sintering 700–1000 °C N ₂	--	--
[156]	C. substrate	Ag-MnO ₂	Hidrothermal + Electrodeposition + Ceramic TT 400 °C 2h Air	557 F/g at 5mV/s	98.6 % after 2000 cycles
[211]	C. substrate	Ni/NiO	Sol-gel + Electrospinning + Pressed	526 F/g at 1 A/g	80% after 1000 cycles
[212]	C. Substrate	b-La ₂ Mo ₂ O ₉	Hydrothermal + Pressed	727.2 F/g at 0.5 A/g	98.7 % after 1000 cycles
[213]	C. substrate	SrFe ₁₂ O ₁₉	Hydrothermal + Calcination + Pasted	133.9 F/g 0.4 A/g	84% after 5000 cycles

In the case of Shim et al., [160] graphene was combined with Co_3O_4 (synthesized by solvothermal synthesis) and pressed onto a conductive collector given 2435 F/g (at current density 1 A/g) while after 4500 cycles, the specific capacitance increased until 112%. The solvothermal process is also employed in developing MOF, thus Zhou et al.[95] combined GO with a Ni-based MOF resulting in a capacitance of 2192.4 F/g and a retention of it of 85% during 3000 cycles. Zhang et al.[201] electrodeposited Ni-Co mixed MOF on Ni foam with a subsequent pyrolysis obtaining a carbon–metal oxide composite electrodes. The as-prepared electrodes exhibit a capacitance value of 2098 mF/cm^2 at a current density of $1\text{mA}/\text{cm}^2$ with a 93% of retention.

The co-precipitation or electrochemical co-deposition with graphene [155] have been also used by Shahrokhian et al.,[174] who fabricated directly, on a Nickel foam (substrate), ERGO/NiO electrodes in one-step. The heat treatment at 300°C for 2h leads to a maximum of specific capacitance around 1716 F/g and with a 78.8% of retention after 2000 cycles. And Jia et al. [163] combined GO and MnOx by electrodeposition onto carbon fibers showing a specific capacitance of 1004.8 mF/cm at a current density of 4 mA/cm during 5000 cycles with only a 6% of capacitance drop. Another electrochemical technique that has been used is the EPD. Yus et al.[173] prepared by heterocoagulation a NiO/RGO nanocomposite, which was electrophoretically deposited onto a Ni foam with a final stage of sintering at 352°C during 1h under Ar atmosphere. The final electrode showed a specific capacitance value of 940 F/g at 2 A/g.

Nanotubes are also used as template for growing TMO. Ma et al. [182] in 2015 grew $\text{Ni}(\text{OH})_2$ nanoplatelets on carbon nanotubes (CNT) by using hydrothermal synthesis to achieve a specific capacitance of 1283 F/g at 2 A/g, with a 100% retention after 2000 cycles. In this case the active material was mixed with poly(tetrafluoroethylene) and other carbonaceous species, and then spread and pressed onto a Ni foam in order to prepare the tested specimens. Another good example is the work developed by Chang et al. [193] They prepared a $\text{CNT}@\text{MnOOH}@\text{polypyrrole}$ by electrodeposition and dip coating techniques with a final calcination to conform a well-connected microstructure at 600°C for 2h. The reported specific capacitance was 148 F/g with a 92% of retention after 10000 cycles at 2 A/g. CNTs are, as graphene, widely used for the preparation of hybrid capacitors. Cha et al. [96] performed a ultracapacitor based on CNT and $\text{Ni}(\text{OH})_2$ synthesized by electrodeposition which showed 2185.6 F/g at current density of 5 A/g and a 95 % of retention over 1000 cycles.

Frequently, the combination of both species lies in the co-deposition of the carbon-based material and the metal oxide semiconductor. However, the combination of the TMO with an organic compound followed by calcination is also employed. Guan et al. [197] combined cellulose with CoO in order to manufacture CoO@C hybrid nanowires improving the capacitance of the CoO (from 1.6 F/cm² to 3.3 F/cm²) as well as the cycling life from 87.1% until 98.6% after 5000 cycles. In addition, sometimes the combination of a carbon phase consists only in the use of it as substrate. In those cases, the carbonaceous substrates generate a double-layer contribution. For instance, Sahoo et al.[131] grew by hydrothermal synthesis nanocrystals of Co₃V₂O₈, which showed a specific capacitance value of 4194 F/g measured at 1A/g with a capacitance retention after 10000 cycles of 85%. Yang et al.[195] performed a multicomponent HSC by impregnating carbon nanofibers with NiCo₂O₄ with a subsequent calcination obtaining 1631 F/g at 1 A/g with a capacitance retention of 94.5% after 5000 cycles. Moreover, the same bicomponent oxide was employed in combination with amorphous micro-carbon ribbons by Pang et al.[196] improving the specific capacitance in 60 units (1691 F/g at 3 A/g) which after 10 thousand of cycles it retains the 89% of the initial specific capacitance. And, Zhang et al. [201] prepared carbon-metal oxide (Ni and Co oxides) composite electrodes by electrosynthesis on Ni foam using MOF as a precursor. After the heat treatment (900 °C 12 h Ar), some carbon from the calcined MOF is mixed with the sintered oxides resulting in long-term electrochemical stability (93% retention of the capacitance from 1 to 20 mA/cm²). A different strategy consists in the deposition of oxides on carbonaceous substrates as is the case of Han et al. [204], who developed a multiphase composite film, composed of nickel(II) hydroxide and cobalt(II) hydroxide, synthesized by co-precipitation. The prepared a 3D network nanostructure showed 1123 F/g of capacitance with a 78% of retention after 2000 cycles.

Finally, highest specific capacitance values for hybrid capacitors were found 10286 F/g [25] combining carbon spheres with NiCl₂·H₂O ↔ Ni(OH)₂ colloids, and 2185.6 F/g [96] by electrodepositing Ni(OH)₂ nanoparticles onto non-woven conductive textile substrate.

3.2 Summary of Results & Discussion

3.2.1 Standardization of the sonocrystallization and annealing processes to synthesize $\text{Ni}(\text{OH})_2$ and NiO nanoplatelets

The $\text{Ni}(\text{OH})_2$ presents two polymorphs, α - and β - $\text{Ni}(\text{OH})_2$ (figure 3.2.1-1). The α - $\text{Ni}(\text{OH})_2$ polymorph is a stable metaphase due to the lack of hydroxyl groups within its structure, which is linked to the incorporation of anions to the crystalline network to maintain its electronegativity. These anions are located at the interlaminar spaces between the basal planes, disturbing the stacking of Ni planes aligned along the c-axis [128]. On the other hand, the β - $\text{Ni}(\text{OH})_2$ phase is a laminar hydroxide with hexagonal crystallographic structure, similar to brucite, $\text{Mg}(\text{OH})_2$, where each atom of Ni is coordinated with 6 hydroxyl groups forming an octahedron with laminar structure.

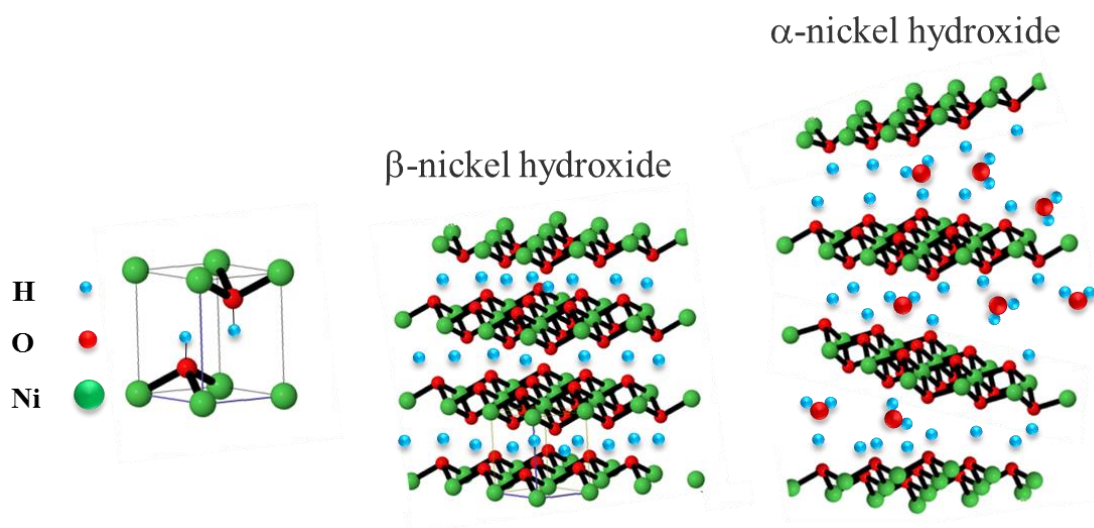


Figure 3.2.1-1. 3D-illustration of crystal structures of β - and α -nickel hydroxide.

From several decades, many researchers have focused their studies in the obtaining both α and β - $\text{Ni}(\text{OH})_2$ polymorphs by following different synthesis routes [214] such as chemical precipitation, electrochemical precipitation, sol-gel synthesis, chemical ageing, hydrothermal and solvothermal syntheses, layers growth, etc. (figure 3-2.1.2).

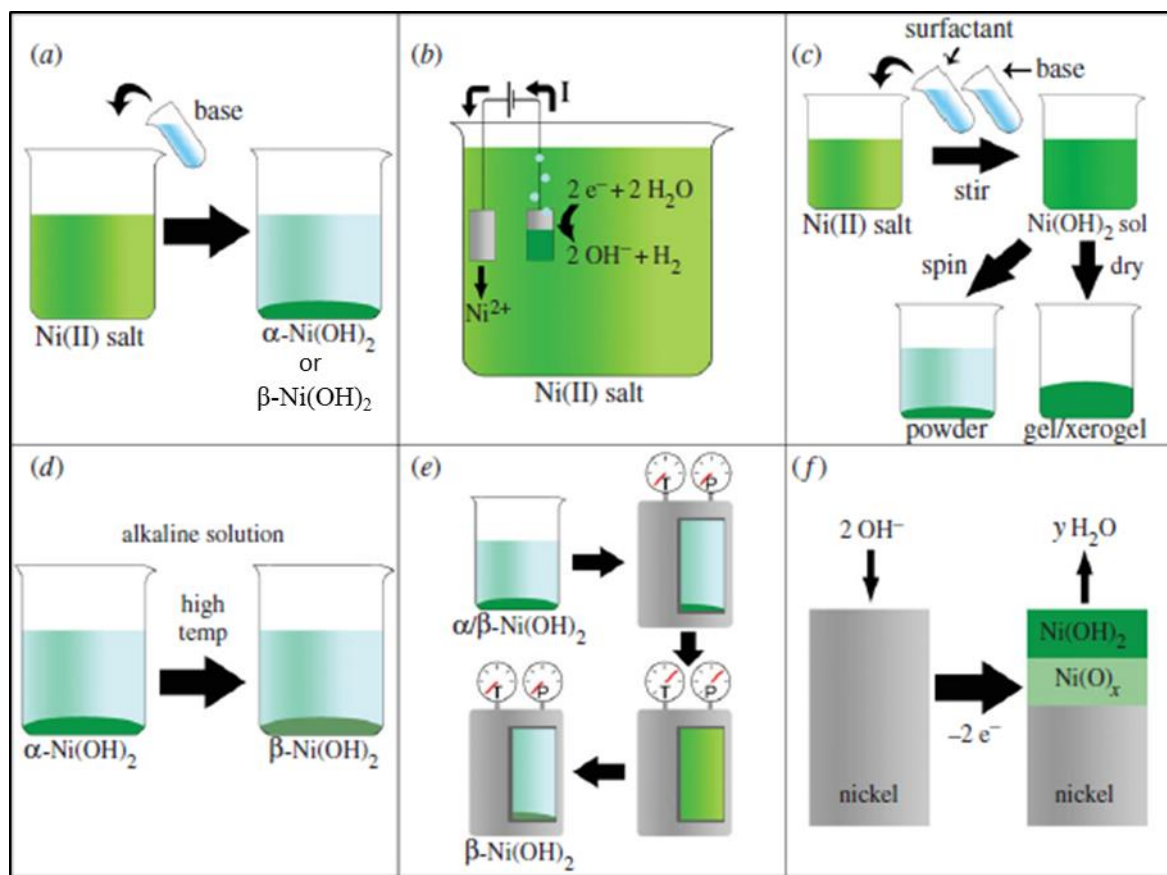
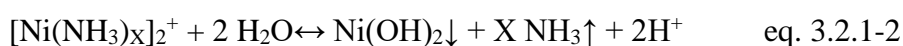
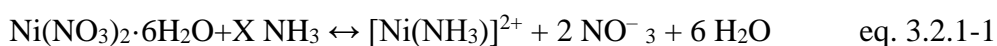


Figure 3.2.1-2. Schemes of different methods for obtaining α - and β -Ni(OH)₂ polymorphs. a) Chemical precipitation. b) Electrochemical precipitation. c) Sol-gel synthesis. d) Chemical ageing. e) Hydrothermal and solvothermal syntheses. f) Layers growth onto nickel.

Among all available routes, a chemical precipitation assisted by ultrasound, was chosen in this thesis as synthesis method for the obtaining of β -Ni(OH)₂ nanoplatelets. This methodology is based on the particles sonocrystallization by following the Ostwald Ripening theory, which consist on the competitive growth of their nuclei in the liquid media [129]. Under the ultrasound effects, a greater number of nuclei is generated, and the acoustic waves promote their dispersion in the whole reaction volume. In this way, a greater population of particles with a smaller size can be obtained. The reactions of the chemical precipitation of Ni(OH)₂ using nickel nitrate hexahydrate (Ni(NO₃)₂) as precursor salt and ammonia hydroxide as precipitant agent are:



The influence of different factors, such as the temperature, the concentration $X[\text{Ni}^{2+}]:Y[\text{NH}_3]$ ratio of precursors, the flow rate, the use of surfactants, additives or the action of ultrasounds, in the precipitation of the Ni(OH)₂ polymorph may vary the

physical features (crystallography, size and/or morphology) of the obtained nanoparticles [128,129]. For instance a strong morphological variation was found with the addition of some specific organic additives like PVP or PVA, leading to the precipitation of platelets and flower-like shapes of Ni(OH)_2 nanoparticles, respectively [6]. Under the selected conditions of synthesis, it is also important to consider that the flow rate and/or the temperature variations affect the concentration of NH_3 during the precipitation, which obviously can result in significant changes of the particles shape. Thus, for a high temperature or flow rate, the NH_3 concentration diminishes, which promotes the synthesis of Ni(OH)_2 nanoplatelets.

In addition, the use of ultrasound also contributes to determine the final size and morphology of particles, depending on the effectiveness of the sonication process. Noting that the synthesis yield can be adjusted by controlling the S-parameter, which have been previously described as the power applied through an US probe in the bosom of the suspension with a specific concentration ($\text{W/cm}^2\cdot\text{mol}$) [128]. The US application determines the nucleation of precipitates and its crystallization and growth, stepping up the number of crystalline domains at the Ni(OH)_2 platelets and reducing the size dimension while the specific surface area (SSA) increases. The US effect increases dispersion and decreases the size of viable nuclei resulting in the exponential rise of nucleation spots and leading to the manufacture of homogeneous nanopowders throughout a fast and reliable process.

In this thesis, the synthesis conditions of the chemical precipitation, assisted by US, has been optimized with aforementioned parameters achieving yields above 85%, with an average yield of 91.7% when the process was scaled [7]. In all cases, the volume of the precursor's solution as well as the applied US power were duplicated, fixing the S parameter to $12500 \text{ W/cm}^2\cdot\text{mol}$, while both, the concentration of the precursors and the molar ratio $[\text{Ni}^{2+}]/5[\text{NH}_3]$ were kept constant.

Figure 3.2.1-3 shows a general scheme of the synthesis of Ni(OH)_2 and annealing treatment of the nanopowder to achieve the corresponding NiO .

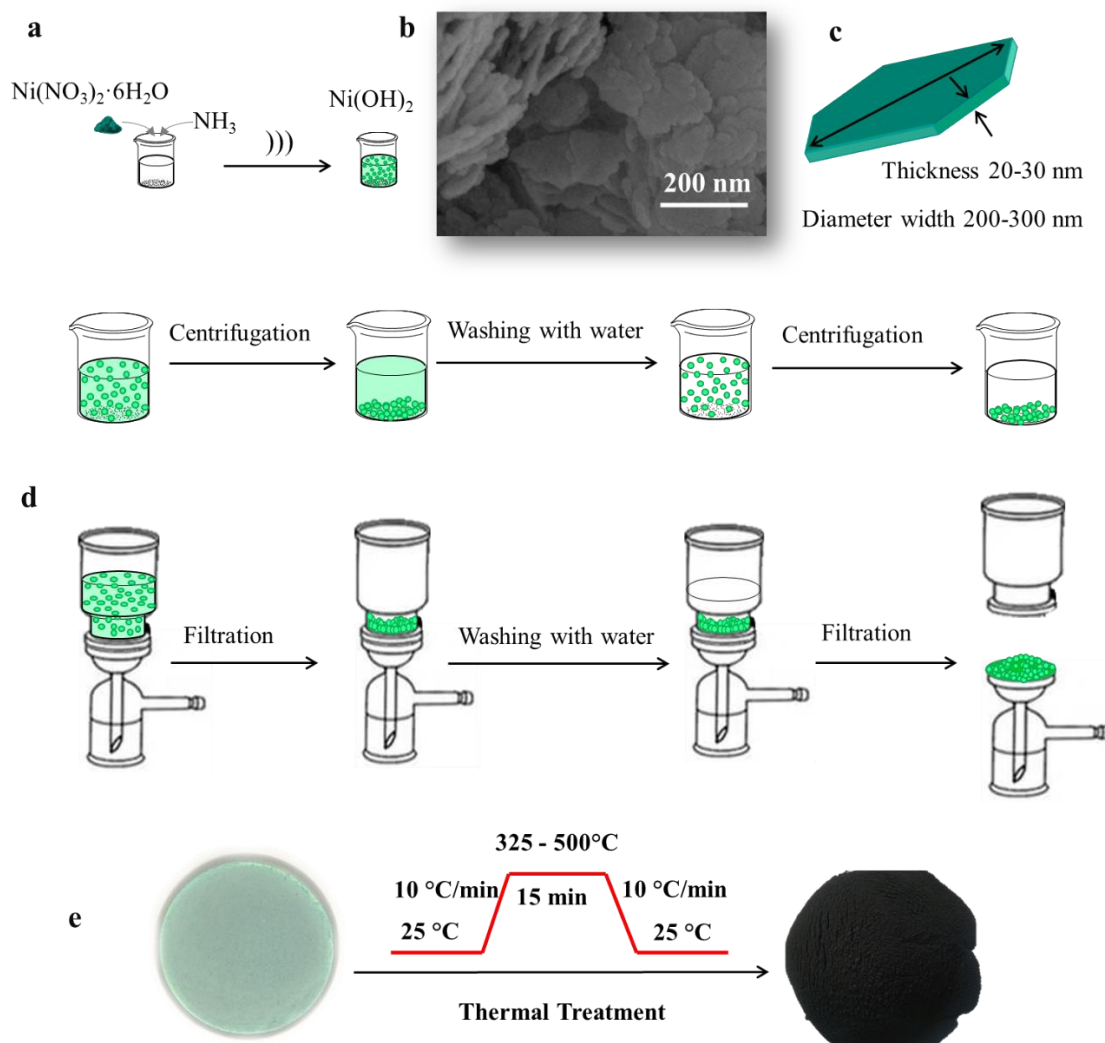
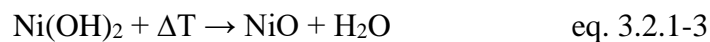


Figure 3.2.1-3. a) Diagram of the precipitation, b) FESEM image of the $\text{Ni}(\text{OH})_2$ nanoplatelets and c) dimension Scheme d) Separation process by centrifugation and filtration. And e) Thermal treatment.

The post-reaction medium, with the remain chemicals, was removed by filtration or centrifugation separating a green precipitate ($\text{Ni}(\text{OH})_2$) which was then washed with distilled water at pH ~10 (adjusted with tetramethyl ammonium hydroxide, TMAH) for several times. The obtained plate-like nanoparticles morphology is illustrated by the FESEM image in figure 3.2.1-3b. The obtained dimensions of the $\text{Ni}(\text{OH})_2$ nanostructures were 200-300 nm in diameter and 20-30 nm in thickness (figure 3.2.1-3c), similar to the obtained nanostructures when the volume of precursors was the middle. Reactants used for the synthesis were $\text{Ni}(\text{NO}_3)_2$ (99.9% purity; Panreac, Spain) and NH_3 (PA 25%, Panreac, Spain). Syntheses were conducted at room temperature using a high intensity

ultrasonic horn (45 W/cm², 24 kHz, titanium T13 tip, Sonopuls HD 2200, Bandelin Electronic, Germany) for 90 minutes.

After washing, the Ni(OH)₂ nanoparticles were dried at 80°C overnight and calcined to obtain NiO (eq. 3.2.1-3).



The thermal treatment of the Ni(OH)₂ calcination was chosen according to the thermogravimetric/dilatometric thermal analyses previously reported in the literature [7]. The phase change for the formation of the NiO takes place at 250-300°C, while still remaining residual nitrates that later decompose at a temperature close to 450°C. Consequently, two calcination temperatures, 325 °C and 500°C, were compared in air atmosphere, maintaining a dwell step during 15 min, with heating and cooling rates of 10°C/min. Figure 3.2.1-4 shows the FESEM images of NiO nanoplatelets after calcination at both temperatures.

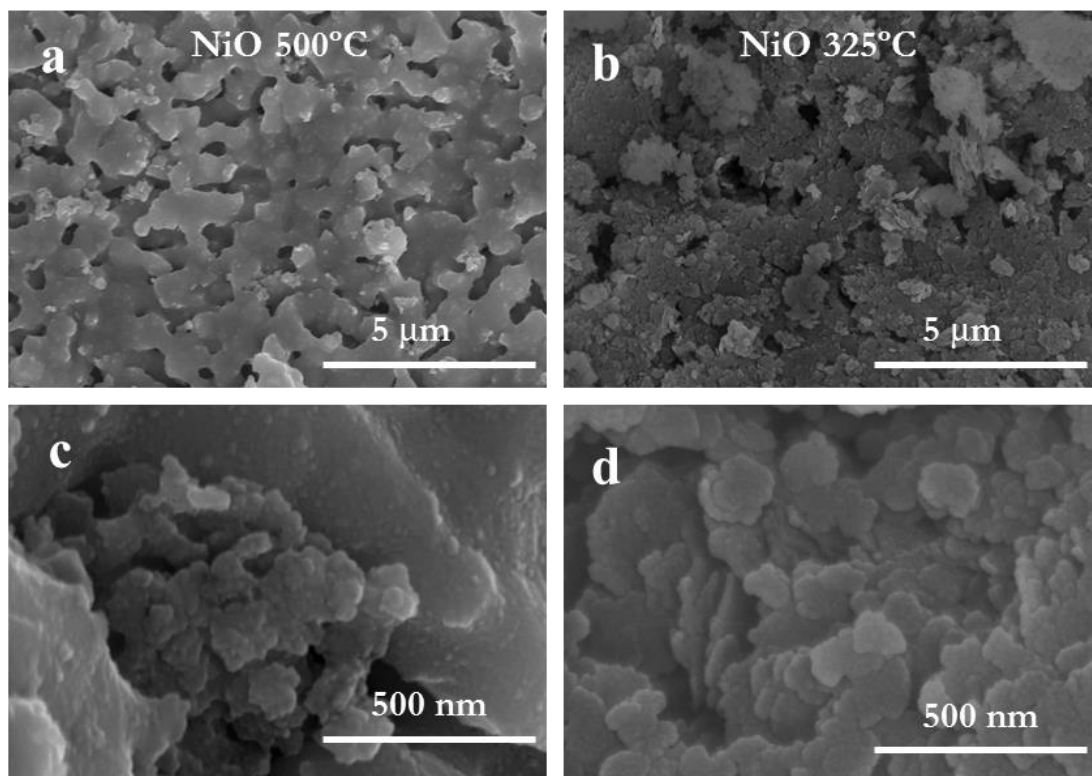


Figure 3.2.1-4. Morphological characterizations of the NiO powder of synthesis: a) and c) FESEM images taken at different magnifications of the calcined powder at 500°C and b) and d) calcined at 325°C.

The careful inspection of the micrographs evidences the formation of ceramic necks between particles when they are sintered at both temperatures. A higher degree of sintering of NiO nanoplatelets is found when they are treated at 500°C resulting in a significant increase of the size and densification level of the powder aggregates. Thus, a shorter thermal annealing of 15 min at 325 °C was selected for the processing of our synthesized NiO nanoplatelets.

Both, Ni(OH)₂ and NiO nanoplatelets, was used in this work directly as electroactive material or like building blocks for further microarchitecture design of the electrodes. The physical and crystallographic characterization of the Ni(OH)₂ and NiO nanoplatelets, synthesized by the scaled procedure, was summarizing in figure 3.2.1-5

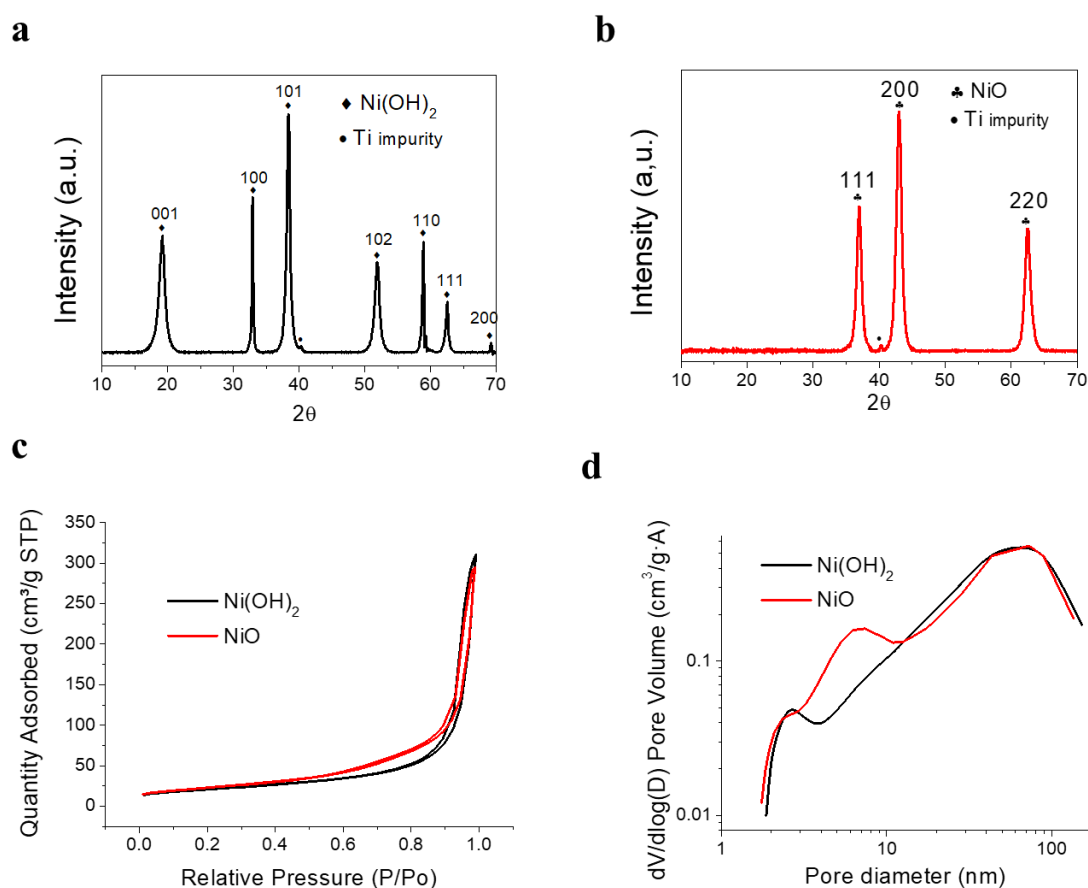


Figure 3.2.1-5. XRD patterns of the a) Ni(OH)₂ and b) NiO powders after the synthesis; c) N₂ gas adsorption-desorption isotherm and d) pore size distribution of as-prepared Ni(OH)₂ and NiO nanostructures.

All diffraction peaks of the XRD analysis of the Ni(OH)₂ powder were consistent with β-Ni(OH)₂ polymorph and they were indexed according with JCPDS Card file No 14-0117 in Figure 3.2.1-5a. The peak position and full width at half maximum (FWHM) of (001)

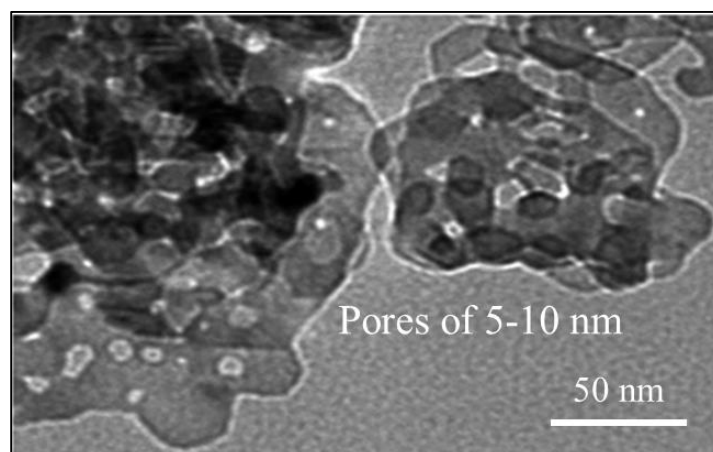
refractive plane (figure 3.2.1-5a), were employed for the calculations of the crystallite size along the c-axis, 8.1 ± 0.3 nm, and the cell unit dimension employing the Scherrer equation and Bragg's law, ranging 3.9 ± 0.6 Å.

Figure 3.2.1-5b shows the XRD pattern of the as-calcined NiO powders. The diffraction peaks were identified according to the XRD pattern (JCPDS Card file No 47-1049) as the cubic lattice of the NiO. The determined values for unit cell dimension and crystallite size for NiO nanoplatelets were 4.2 ± 0.1 Å and 9.9 ± 0.2 nm, respectively, being slightly larger than those measured for the precursor specie: Ni(OH)₂. Consequently, we could assume that the thermal treatment of calcination affects to the morphological and crystallographic dimensions of the electroactive material, always maintaining the nanometric scale of the platelets.

The SSA and the pore volume distribution as well as the open SSA and the micropore volume were determined by adsorption/desorption of N₂ for both species and shown at figure 3.2.1-5c and 5d respectively. The profile of the isotherms corresponds to the Type IV for both powders, exhibiting a narrow hysteresis loop at high relative pressures (0.8–1) which is characteristic of the presence of macroporosity. The pore size distributions plotted as a function of the adsorbed volume of N₂ confirm the presence of macroporosity with main diameters about 50-60 nm in both materials. However, the micro and mesoporosity of NiO (figure 3.2.1-5d) is considerably wider in size, since a fraction of mesopores with a main size of 10 nm is evidenced, and higher in amount, leading to slightly larger SSA ($82.4/83.7$ m²/g depending on the approximation method used). The absence of an open mesoporosity faction in Ni(OH)₂ powders enlarge the differences between calculated SSA from the BET (74.1 m²/g) to the t-plot (65.1 m²/g) modeling, evidencing the presence of a partially inaccessible surface at the hydroxide nanoplatelets. All these data are summarized and collected in table 3.2.1-1, as a percentage of the BET parameter. In addition, the density was measured by helium pycnometry resulting 5.76 ± 0.03 g/cm³ for NiO and 3.91 ± 0.01 g/cm³ for Ni(OH)₂ being in both cases quite far from the theoretical bulk densities of both species, which are 6.67 and 4.10 g/cm³, respectively. These density data confirm the higher porous structure of NiO powder (figure 3.2.1-6) since the apparent density of NiO is lower than Ni(OH)₂ (table 3.2.1-1).

Table 3.2.1-1. Morphological properties of the Ni(OH)₂ and NiO powders.

Morphology of β-Ni(OH)₂ and NiO nanoplatelets	Ni(OH)₂	NiO
BET SSA (m²/g)	74.1	83.7
Open SSA by t-plot (m²/g)	65.1	82.4
Total Pore Volume N₂ (cm³/g)	0.48	0.46
Micropore Volume by t-plot (cm³/g)	0.004	1.32
Apparent Density (%)	95	86

**Figure 3.2.1-6. TEM images of NiO. A. Caballero, *Energy Fuels* (2013).**

Once the particles have been synthesized, they have also been stabilized in aqueous medium according to the procedure described previously elsewhere [7]. Then, the stabilized particles (with Polyethylenimine, PEI of high molecular weight (Mw 25000)) have been shaped by EPD onto metallic substrates in order to manufacture the PC electrodes. In these previous works, the obtained NiO-based electrodes have been electrochemically tested showing specific capacitance values of 363 F/g [7] or 400 F/g [11]. In both cases the capacity obtained was far from the theoretical capacity of this material (2583 F/g within 0.5 V) [141]. In this thesis the study of several strategies for the surface modification of the electroactive material, Ni(OH)₂ or NiO nanoplatelets, or its combination with other materials, was tackled to improve their electrochemical behavior throughout the enhancement of the electrode microstructure.

3.2.2 Shaping processes of PEI-modified Ni(OH)₂ nanoplatelets for pseudocapacitor (PC) electrodes: Electrophoretic Deposition and Inkjet Printing

Tailoring the ceramic semiconductor microstructure and designing nano-architectures with hierarchical porosity to decrease the charge transfer resistance and increase the

specific capacitance of PC is the main objective in the research work. For this purpose, two colloidal processing techniques, the Electrophoretic Deposition (EPD) and the Inkjet Printing (IJP), were used to shape the electroactive materials and, the colloidal chemistry of the nanoplatelets suspensions was optimized to tune and optimize coating and patterning processes.

The stability of colloidal suspensions and inks for shaping is relevant in terms of dispersion and ageing. A stabilization process allows avoiding coagulation and sedimentation problems due to Brownian forces and the effect of gravity over agglomerates. In this sense, the electrosteric stabilization is the most efficient mechanism of dispersion since the combination of both steric and electrostatic repulsion forces offers a long term stability to the suspension [215–217]. Electrostatic repulsions forces among particles are mainly produced by the charges of functional groups of the adsorbed polyelectrolytes. Moreover, the steric effect is favored by the increase their hydrodynamic diameter on the surface of the suspended particles.

As we have mentioned in the previous section of this document, the optimization of the chemical and colloid-chemical stability of $\text{Ni}(\text{OH})_2$ nanoplatelets in aqueous medium was reported in others work of our research group [7]. Because of the $\text{Ni}(\text{OH})_2$ nanoplatelets usually dissolve under acid conditions, acid values of pH were avoided. Under basic conditions, the zeta potential values (ZP) of $\text{Ni}(\text{OH})_2$ are negative, and hence a cationic polyelectrolyte, such as PEI, was employed to protect and stabilize the nanoplatelets. This polyelectrolyte consists in a branched polycarbonate chain with primary, secondary and ternary amine functional groups. Branched PEI has three pKa values depending on the degree of substitution of the amines. The primary amine has a pKa value of 4.5, secondary: 6.7, and tertiary: 11.6. And the overall pKa value was 7.46 [218], which can be protonated within a wide pH range, maintaining the repulsion forces between particles and providing greater stability to the suspension.

Figure 3.2.2-1a illustrates the variation of ZP as a function of the pH of the suspension for the bare $\text{Ni}(\text{OH})_2$ and PEI- $\text{Ni}(\text{OH})_2$. The isoelectric point for the bare $\text{Ni}(\text{OH})_2$ is located around pH 9. At this pH, the surfaces of nanoplatelets are neutralized resulting in a ZP value closed to 0 mV, where the suspension is unstable, and particles are flocculated. However, at pH 10, the zeta potential of $\beta\text{-Ni}(\text{OH})_2$ nanoparticles is enough negative, closed to -20 mV, to adsorb the cationic polyelectrolyte. The variation of ZP as a function

of the amount of PEI added at pH 10 (not shown here) indicates significant changes in the sign of the charge. Nanoplatelet surfaces were saturated by the addition of 2.5 wt.% of PEI to a suspension deflocculated at pH 10, as it was reported by Gonzalez et al. [5]. In these conditions, the zeta potential value is close to 40 mV. The PEI at pH 10 is partially protonated and adsorbed onto the particles surface through protonated amine groups. The PEI addition shifts the isoelectric point, and the PEI-modified nanoplatelets maintain a positive charge in the whole pH range.

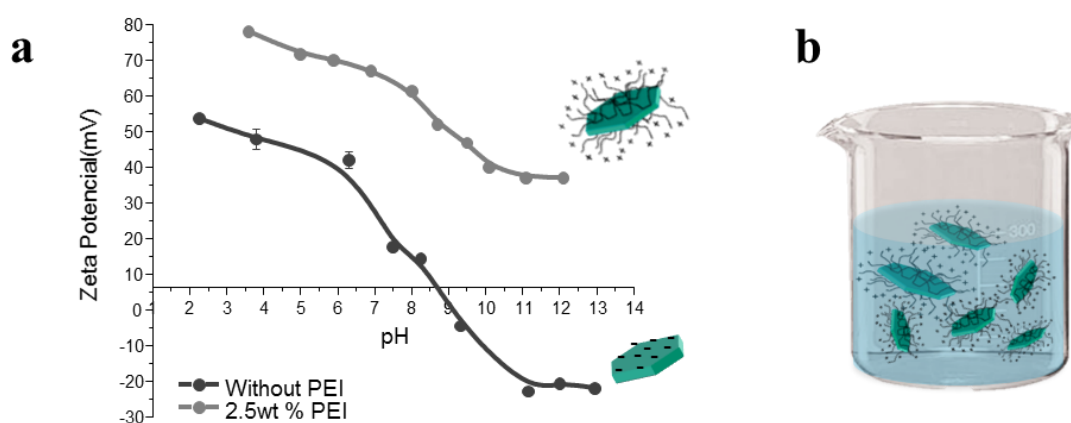


Figure 3.2.2-1. a) Evolution of Zeta potential of β -Ni(OH)₂ as a function of pH without PEI and with 2.5 wt% PEI. b) Scheme of the particles in suspension with PEI adsorbed. Z. Gonzalez. *J. Electrochem. Soc.* (2015).

Once the particles were stabilized in water through the pH adjustment and the adsorption of the PEI, the liquid media was removed by filtration and centrifugation (figure 3.2.1-3d) and the PEI-modified Ni(OH)₂ were re-dispersed in a new solvent depending on the subsequent shaping process, EPD or IJP. Both, coatings and patterning processes were optimized to achieve the highest exposed surface area at the electrode, using the least amount of electroactive material, thus improving the electrochemical yield per gram. In EPD, the thickness of the coating deposited was adjusted for the development of 3D electrodes (foams as current collectors) in order to provide the higher surface of reaction in the smaller volume, and mainly increase the specific capacitance in terms of energy accumulation. On the other hand, the IJP technique was chosen to miniaturize PC electrodes by printing patterns onto 2D substrates (foils) to increase the energy delivery rate by reducing the charge transfer resistance and availing print infinite areas.

In both processes, mixtures of water and an organic solvent were optimized to adjust the suspensions properties to the deposition mechanisms. The co-solvent EtOH:H₂O (in a

ratio 19:1) was used as liquid vehicle for EPD suspensions. The use of ethanol reduces the effects of collateral phenomena which hinders the EPD kinetics [220], by:

- i. reducing the suspension conductivity, thus increasing the electrochemical performance of the electrophoretic process by reducing the mobility of ions and promoting the movement of particles, and
- ii. screening the electrostatic component of the electrosteric mechanism of particles stabilization, and consequently reducing the electrostatic barrier for the nanoplatelets assembly during deposition.

The co-solvent employed in IJP inks was a mixture of diethylene glycol (DEG) with water (in a 50:50 ratio) which also screens the electrostatic effect of PEI-modification of the nanoplatelets, providing Newtonian suspensions at low solid contents, as well as proper values of viscosity, density and surface tension according to the ink requirements. These parameters are regarded as the key physical parameters to optimize the quality of jetting and deposition. In addition, DEG, which is also a humectant agent, minimizes the ink drying at the printer nozzles and delay pattern drying after inkjet deposition avoiding cracking effects.

Related to the deposition yield of the selected technologies, both EPD and IJP employ suspensions with low solid contents (<20 vol.%), contrarily to other shaping methods in which moderately or highly concentrated suspensions are used. In additions, they are zero waste processes allowing saving raw material. Both EPD and IJP can be considered additive-manufacturing technologies since both allows layer-by-layer growth of coatings and patterns, which would allow the manufacture of the PC devices (full-cell) by the staking of layers of similar or dissimilar materials. IJP is also a rapid prototyping technique since patterns can be designed, sliced and printing by layer-by-layer Computer Assisted Design(CAD) [221–223].

3.2.2.1 3D electrodes for PC processed by Electrophoretic Deposition of PEI-modified Ni(OH)₂ nanoplatelets

As we have previously mentioned in the introduction section, this powerful and versatile colloidal process is a room temperature and non-vacuum technology, easily scalable to the industry, which implies short processing time, zero wastes and low manufacturing

costs. Furthermore, it is one of the most suitable colloidal processes for shaping with organized structures at the nanoscale, especially when we are dealing with the coverage of 3D substrates and complex shapes. It offers the straight control over the deposited mass and over the thickness of the films controlling the applied potential and the deposition time.

In EPD, the positively charged particles (PEI-modified $\text{Ni}(\text{OH})_2$ nanoplatelets) were forced to migrate towards the electrode with opposite charge (PC electrode collector) under the influence of an electric field applied between two electrodes which were submerged in a stable suspension (figure 3.2.2.1-1). In producing homogeneous and reliable films, EPD performance strongly depends on the particle surface chemistry, the behaviour of the solid-liquid interface, the particle-particle and particle-substrate interactions during particle assembly and the applied electric field [224].

Consequently, the optimization of parameters describing stability, such as electrophoretic mobility, resistivity and particle size distribution in a nanoparticle suspension are parameters that govern the deposition kinetics and deposit characteristics. The control over all these parameters allows the organization (high packing degree, orientation, etc.) of the particles at the nanometric range in functional applications, leading to high structural integrity in materials, such as scaffolds, free-standing nanoparticle films, transparent films, etc. [225].

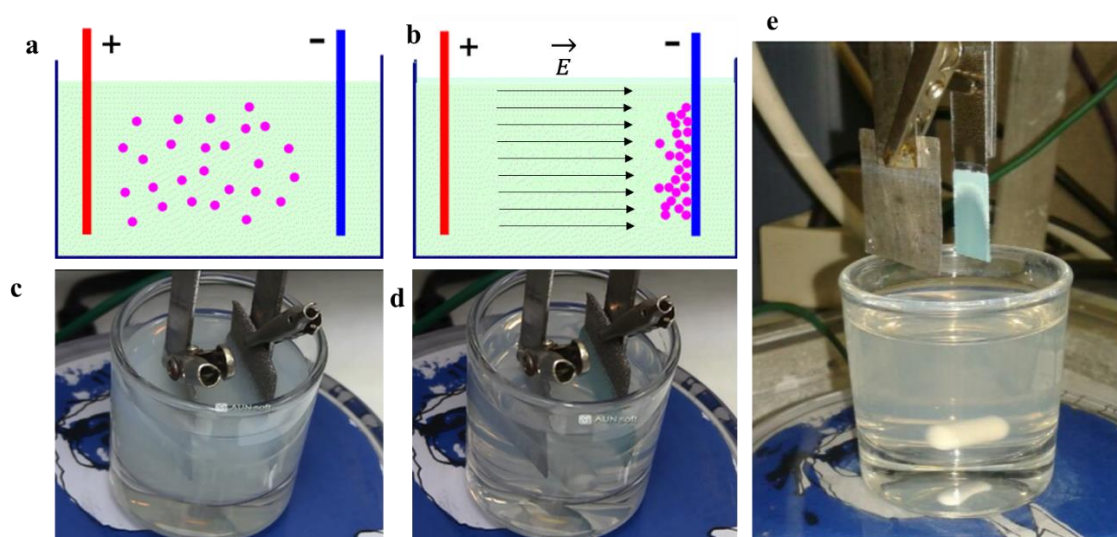


Figure 3.2.2.1-1. a) and b) EDP scheme before and after the potential application and the experimental picture c) and d), respectively. e) Picture of the $\text{Ni}(\text{OH})_2$ coating onto a conductor substrate.

The protocol and the formulation of a stable PEI-modified $\text{Ni}(\text{OH})_2$ nanoplatelets suspension for EPD, with a solid content of 1 g/L, were described elsewhere [7]. The parallel orientation of the $\text{Ni}(\text{OH})_2$ nanoplatelets along the substrate surface, illustrated in the cross section of the figure 3.2.2.1-2a and confirmed by the XRD analysis (figure. 3.2.2.1-2b), is due to the Van der Waals forces developed among particles and their interaction with the electro-hydrodynamic forces acting over them when approach to the substrate in the moderated electrophoresis of a low concentrated suspension of nanoplatelets. This phenomena has been reported in the literature for different flakes-like particles, in nature and size [6,226–228], as well as using different stabilizers, concluding that their orientation mainly depends on the solid content of the suspension and the particle morphology. In fact, the X-ray diffractogram of as-synthesized $\text{Ni}(\text{OH})_2$ platelets shows in figure 4b, how the peaks which correspond with (101), (102) and (101) miller reflections, disappeared when the nanoplatelets were deposited electrophoretically. At the same time, peaks belonging to the substrates ($\gamma(111)$ and $\gamma(200)$), appeared and the intensity of the (001) reflection highly increased.

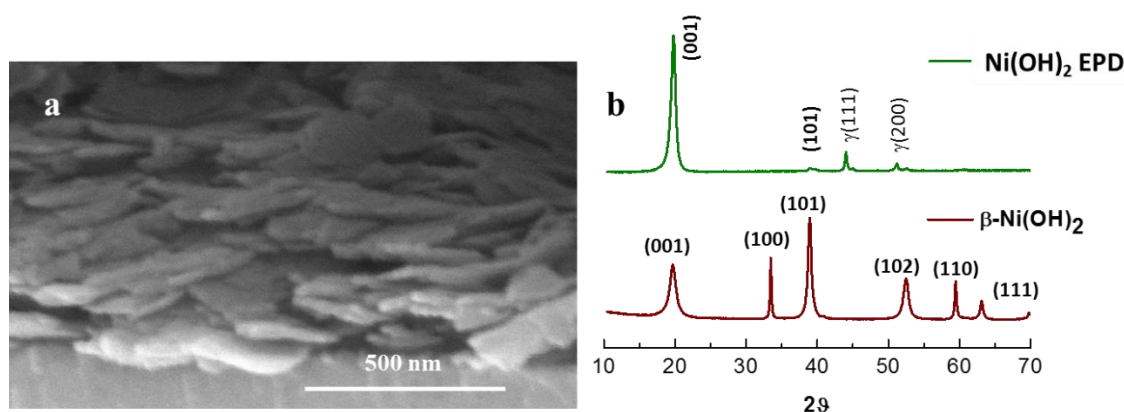


Figure 3.2.2.1-2. a) Cross section of the film where every particle presents a parallel configuration along the substrate surface. b) X-ray diffractogram of the $\text{Ni}(\text{OH})_2$ powder and shaped by EPD.

Therefore, it should be noted that in EPD, the parameters which control the deposition of PEI-modified $\text{Ni}(\text{OH})_2$ nanoplatelets depend on the particle morphology when suspension stability and electrical parameters were adjusted. However, from the point of view of the electrochemical performance, the nature and shape of the collector (EPD substrate) is also relevant.

The contribution of the developed research work, to the manufacture by EPD of the Ni-based PC electrodes, was the study of the electrochemical response of well-ordered PEI-modified $\text{Ni}(\text{OH})_2$ coating of Ni, Cu and stainless steel (SS) foils and Ni foams.

The different current collectors were covered with approximately 1 mg of electroactive material by EPD obtaining homogenous and crack-free coatings in all cases. The applied electrical conditions for each suspension-substrate system were: $50 \mu\text{A}/\text{cm}^2$ during 240 s for the SS foils, $1.5 \text{ mA}/\text{cm}^2$ during 120 s for Ni and Cu foils and $20 \mu\text{A}/\text{cm}^2$ for Ni foam) followed by a thermal treatment at 325°C during 60 minutes under Ar atmosphere (figure 3.2.2.1-3a-d). This heat treatment was carried out in order to achieve the oxidation of the $\text{Ni}(\text{OH})_2$ to NiO and also, to consolidate the nanoplatelets microstructure forming sintering necks (figure 3.2.2.1-3e) that confers adequate connectivity (low charge transfer resistance) and robustness to the deposited films for the use of this ceramic semiconductor structure in energy storage devices.

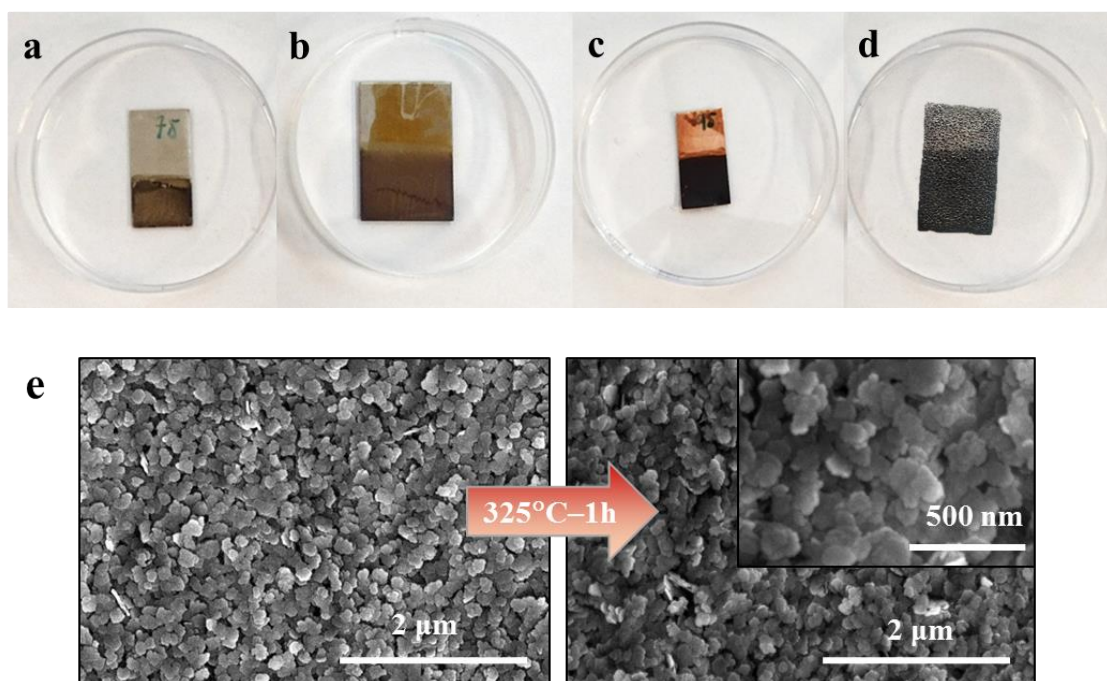


Figure 3.2.2.1-3. Picture of the Deposited and sintered Ni, SS and Cu foils and Ni foam electrodes at 325°C during 1h under Ar atmosphere. And FESEM images of e) their microstructure before and after the sintering.

Then each PC electrode was tested by Electrochemical Impedance Spectroscopy (EIS) in order to determine its electronic conductivity and capacity behavior. The results of these EIS measurements are included in table 3.2.2.1-4, where R_s is the resistance of electrolyte; R_{ct} is the resistance of charge transfer; and CPE is the constant phase element of capacitance. Nyquist and bode plots are displayed in figure 3.2.2.1-4a and 4b respectively. Typically, this kind of materials shows two differentiated parts on the Nyquist plot. In the high frequency range, the semicircle is related to the electronic resistance and the charge-transfer impedance. Meanwhile, in the low frequency region, the nearly vertical straight lines correspond to the ion diffusion process within the electrodes structure [101,139,229,230]. A vertical line of 90° phase angle indicates an ideal capacitor. The deviation from the vertical line to phase angles $< 90^\circ$ can indicate PC behavior. Additionally, the Bode plots allow comparing the maximum phase angle (Φ_{\max}) and relaxation time constant (τ_0) of the prepared electrodes, which define the ideal capacitor for $\Phi_{\max} = 90^\circ$ and the minimum time needed to discharge the stored energy with more than 50% efficiency respectively [231,232]. To determine τ_0 , the corresponding frequency is inversely related to the relaxation time constant at which the phase angle (Φ) is -45° [233,234]. It represents a transition for the PC from a resistive to a capacitive behavior and is related to the cell power. A lower τ_0 indicates a higher power capability (fast charge-discharge) of a PC. The equivalent circuit used to calculate the EIS parameters of the table 3.2.2-1 is included in Figure 3.2.2.1-4c.

Table 3.2.2-1. Fitted EIS parameters of the NiO films prepared onto different current collector.

Collector	Film	Mass	R_s (Ω)	R_{ct} (Ω)	CPE-P	τ_0 (ms)	Φ_{\max} ($^\circ$)
Ni foil	NiO	1.2	-	0.21	0.90	26.3	82
Cu foil		1.1	1.53	0.48	0.87	34.5	80
SS foil		1.6	1.17	2.14	0.77	83.3	74
Ni foam		1.1*	-	1.71	0.85	8.0	76

At the insert on figure 3.2.2.1-4a, both Ni current collectors, foil and foam (Fig 4d), do not show the arc corresponding to the electrolyte resistance at high frequencies, R_s . This resistance disappears due to the faradic reactions of the collector which compete with those provide by the electroactive material. In this case, the absence of semicircles would indicate that a diffusion process is prevailing beyond a capacitive one [41]. The biggest single depressed semicircle in the high frequency region observed for SS substrate

indicates that the resistance between the NiO films and the collector is higher than Cu and Ni substrates (table 3.2.2-1). Thus, the trend attending to the nature and the shape of the substrate continues as follows: $R_{SS} > R_{Cu} > R_{Ni}$. The Cu substrate is slightly more resistant than Ni, which can lie in the electronic configuration. Cu has the electrons in an energy state more stable (Ar, $3d^{10}$, $4s^1$) than Ni (Ar, $3d^8$, $4s^2$), what makes the electron sharing easier in Ni foils.

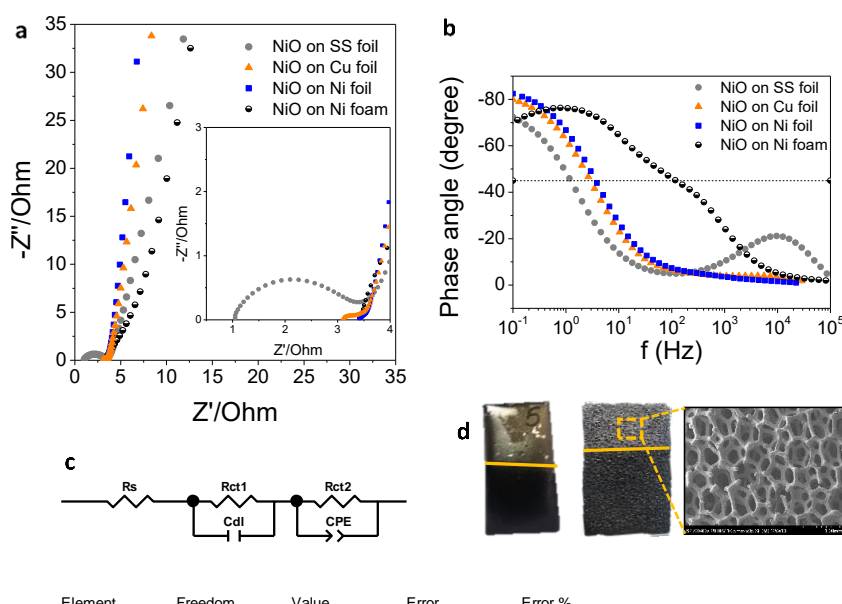


Figure 3.2.2.1-4. Nyquist plot and bode phase plot of NiO coatings onto different substrate a) and b) respectively. c) Equivalent circuit used to adjust the data. d) Images of the NiO films on Ni foil and foam.

At the insert on figure 3.2.2.1-4a, both Ni current collectors, foil and foam (Fig 4d), do not show the arc corresponding to the electrolyte resistance at high frequencies, R_s . This resistance disappears due to the faradic reactions of the collector which compete with those provide by the electroactive material. In this case, the absence of semicircles would indicate that a diffusion process is prevailing beyond a capacitive one [41]. The biggest single depressed semicircle in the high frequency region observed for SS substrate indicates that the resistance between the NiO films and the collector is higher than Cu and Ni substrates (table 3.2.2-1). Thus, the trend attending to the nature and the shape of the substrate continues as follows: $R_{SS} > R_{Cu} > R_{Ni}$. The Cu substrate is slightly more resistant than Ni, which can lie in the electronic configuration. Cu has the electrons in an energy

state more stable (Ar, $3d^{10}$, $4s^1$) than Ni (Ar, $3d^8$, $4s^2$), what makes the electron sharing easier in Ni foils.

In the Niquist curves the films onto Ni, Cu and SS-plates displayed steeper slopes at low frequencies than the film on Ni foam, which means an increase of the pseudo-capacitive behavior is produced. However, the value of R_{ct} corresponding to the coating on the Ni foam is higher than those of the Ni and Cu plates. This can be explained because the electronic charge transfer depends on the collector nature but also on the collector section. The section of a dense foil-collector is wider than the conductive section of the Ni foam, so the electronic transfer in foil-collectors is promoted [40].

On the other hand, Bode plots of the four electrodes are also drawn in figure 3.2.2.1-4d to analyze the relaxation time constant (τ_0) for determining the discharge rates of the electrodes. Ni foam electrode shows a lower τ_0 (8 ms) than Ni and Cu foils (26.3 and 34.5 ms respectively) being the SS foil electrode, which presents the highest value (83.3 ms). The rapid frequency response (low τ_0) as well as the shape and the phase angle of the Bode plot indicate that the Ni foam electrode has an improved rate capability and capacitance retention at high charging/discharging rate, which is attributed to higher ion accessible surface area and the more rapid ion transport in the unique hierarchical porous network [39]. Additionally, the τ_0 value is within the range of the electrochemical double layer capacitors (EDLC) and is lower than the commercial Carbon based EDLC ($\tau_0 = 10$ s) [42], which supports the presence of improved ion transport by the electrodes [43,44] when the porous structure of the Carbon is emulated.

Figure 3.2.2.1-5 shows as-deposited microstructures of 3D electrodes, in detail at different magnifications. Electrophoretically deposited $Ni(OH)_2$ nanoplatelets lay parallel to the substrate surface in Ni foams. The deposited mass of ~ 1 mg of $Ni(OH)_2$ nanoplatelets covers uniformly the 3D collector, where the thickness of the coating was found ~ 700 nm (figure 3.2.2.1-5f). After the thermal treatment (325°C -60 minutes under Ar atmosphere), the 3D electrodes exhibit a more effective profiting of the electrochemical performance than foil coatings. This is mainly reflected in the extremely lower relaxation time constant ($\tau_0 = 8$ ms) characteristic of the NiO nanoplatelets coating of Ni foams.

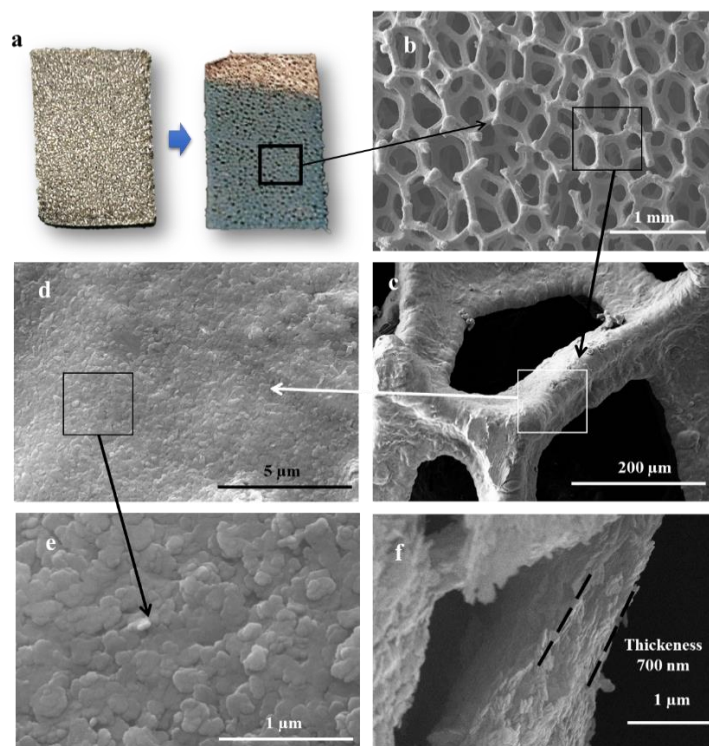


Figure 3.2.2.1-5. a) Picture of Ni foam before and after the EPD. b), c), d) and e) FESEM image taken at different magnification of the Ni(OH)_2 film onto the foam skeleton. f) Measurement of the thickness of a detached skeleton layer by FESEM.

3.2.2.2 2D electrodes for PC processed by Inkjet Printing of PEI-modified Ni(OH)_2 nanoplatelets

In this thesis, the IJP was proposed as a novel approach to prepare NiO patterns with reduced charge transfer resistant by the device miniaturization. Recently, the additive manufacturing in ceramic semiconductor has gain more and more relevance in industrial applications, such as the manufacturing of microchips, home printers, LCD and plasma screens, etc. This has led to the development of novel and innovative functional inks [19–21].

IJP consists in the deposition of suspensions or inks on a substrate following the path designed by the 2D modeling software. Nowadays, two mechanisms of drop generation are commonly employed: in continuous and drop on demand (DOD). The continuous system is equipped with a recirculation system to avoid the constant printing when it is needed. The DOD systems generate the drops through to a mechanical response only when it is required. This pulse can be produced by the use of a piezoelectric (drops diameter ranges from 10 to 100 μm) or by local heating (via a vapor pocket formation in

the ink) [20]. We focus on DOD based on a piezoelectric because it is easily transferable to industry for mass production of customized products. The high precision in the patterns design or the elimination of unwanted waste are some of the advantages of IJP but the quality of the pattern results from the combination of different effects of the ink and the nozzle diameter. The heads technology of the printer and the ink-substrate interaction during deposition and drying are in continuous development. Smaller nozzles allow smaller drops and higher resolutions, and it is generally accepted that particle size should be 50 times lower than the diameter of the nozzle to avoid clogging [235]. Talking about the ink, the more homogeneous and dispersed ink the more ensure the accuracy. A good jetting and drying feature is also required to obtain clear profiles and to maintain the functionality of the ink.

The selection of an aqueous ink lies in the need to replace full-organic inks with water-based inks [236] in order to be more environmentally friendly. However, the selection of co-solvents (in this case H₂O:DEG) and additives must provide ideal properties such as viscosity (2-20 mPa·s), surface tension (20-50 mN/m) and density (1.1-1.5 g/cm³). These ink properties are extremely relevant for printing and they define the Z-parameter which relates the ink physical parameters with the jetting nozzle through its Reynolds and Weber numbers, according to equation 3.2.2-1.

$$Z = \frac{1}{Oh} = \frac{Re}{\sqrt{We}} = \frac{\sqrt{\gamma \rho a}}{\eta} \quad \text{eq. 3.2.2-1}$$

where Oh is the Ohnesorge number, Re is the Reynolds number and We is the Weber number. γ (N·m), η (mPa·s) and ρ (g/cm³) are the surface tension, the viscosity and the density of the ink, respectively, and a (nm) is the diameter of the nozzle. So, the Z-parameter was used to predict a successful ink ejection. Experimentally, this non-dimensional parameter should be between 1 and 10 [237,238], however in some cases, the optimal range can change to $4 < Z < 14$ [239]. It depends on the technical requirements of the printers in terms of viscosity, particle size, density and surface tension.

Once the ink is correctly formulated, the next step, printing was carried out. A commercial XCEL System Aurel work cell printer (AUREL Automation, Italy) (figure 3.2.2.2-1a) was used to print the ceramic ink. This inkjet printer used a piezoelectric drive system (Figure 3.2.2.2-1b) and it was equipped with a print head with a nozzle diameter of 70 µm (figure 3.2.2.2-1c) and a static tank of 5 ml to storage the ink without recirculation.

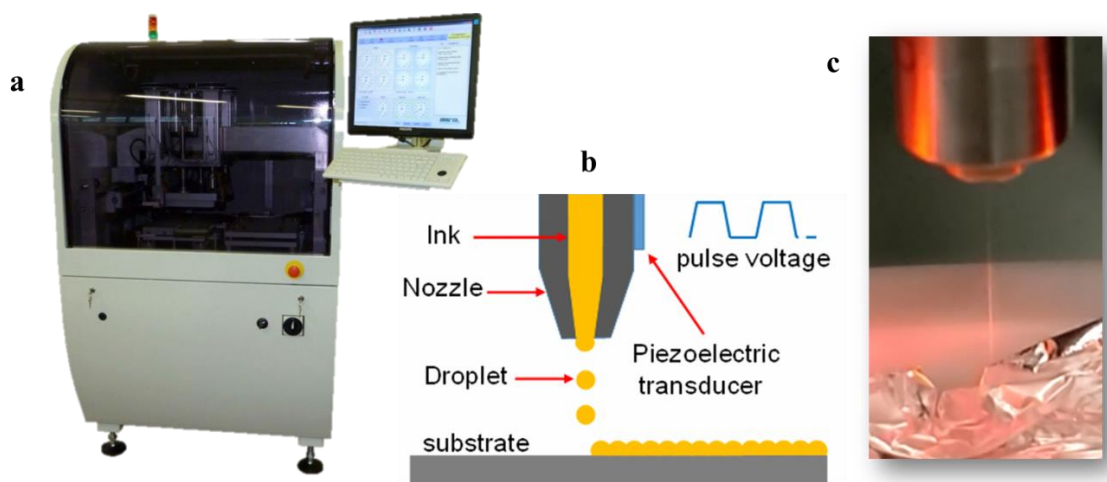


Figure 3.2.2.2-1. a) Picture of the employed printer. b) Scheme of how the IJP machine prints. c) Picture of the $\text{Ni}(\text{OH})_2$ ink jetting through the printer head.

In order to obtain high-quality prints, it was necessary to optimize certain intrinsic parameters of the printer, avoiding manufacturing defects, which deteriorate the microstructure, and the functional properties of the deposition. For example, if the separation of the lines was not enough, the droplets of contiguous lines could coalesce invading the free space. Additionally, the electrical parameters listed in table 3.2.2-2 were adjusted because of, for instance, if the oscillation frequency and pulse voltage were not adjusted, discontinuities and crooked lines could appear.

Table 3.2.2-2. Optimized Inkjet parameters

Ink-Jet parameters	Values
Pulse Volt	230 V
Pulse	135 us
Frequency	1036 Hz
Strobo Delay	227 us
Pressure	-20 mBar

Once the inkjet printer parameters were optimized, a well-defined grid was obtained (see figure 3.2.2.2-2a). The size of the printed grid was 1 cm x 1 cm, and the thicknesses were studied in terms of roughness resulting in 5 μm the average height per layer (figure 3.2.2.2-2b), while the wideness of the printed lines ranges 400-480 μm (figure 3.2.2.2-2d). FE-SEM images of figure 3.2.2.2-2e and 2f illustrates that the layer is free of cracking and other defects at different magnifications.

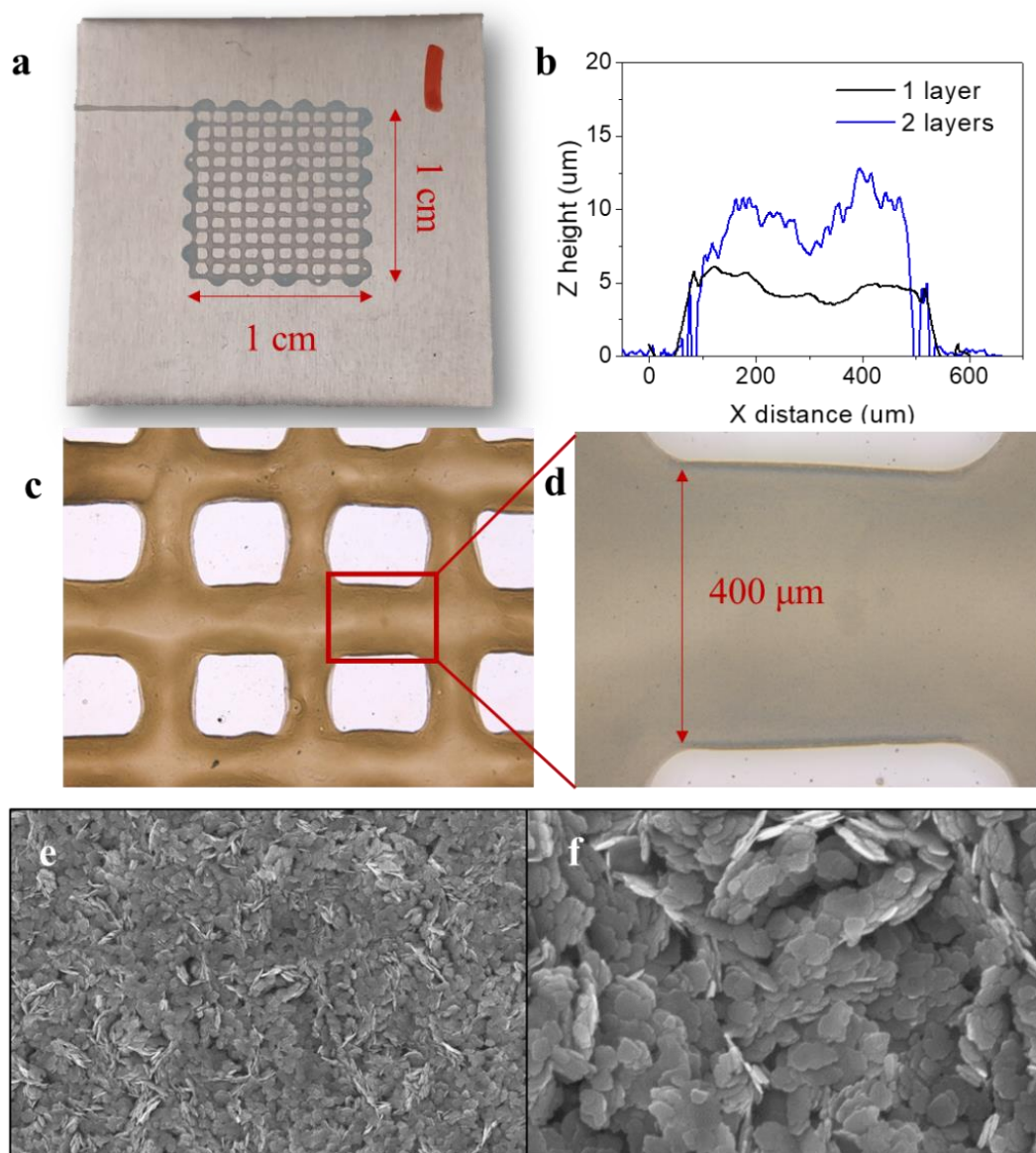


Figure 3.2.2.2-2. a) Photograph of the electrode NiO-IJP of 1 cm² patterns. b) and c) Optical microscopy images of the top view of the deposited patterns. d) and e) FE-SEM images of the printed pattern microstructure taken at different magnifications, f) the height of one and two layers patterns.

A thermal treatment similar to that followed to consolidate the NiO semiconductor microstructure of 3D electrodes shaped by EPD (NiO-EPD) was used for IJP patterns (NiO-IJP). The transformation of Ni(OH)₂ (Figure 3.2.2.2-3a and 3d) to NiO (Figure 3.2.2.2-3c and 3e) coatings and patterns is shown in figure 3.2.2.2-3. The sintered and consolidated microstructure of both, the 2D designed grid pattern and the 3D electrode, showed a continuous and homogeneous layer free of cracking after sintering.

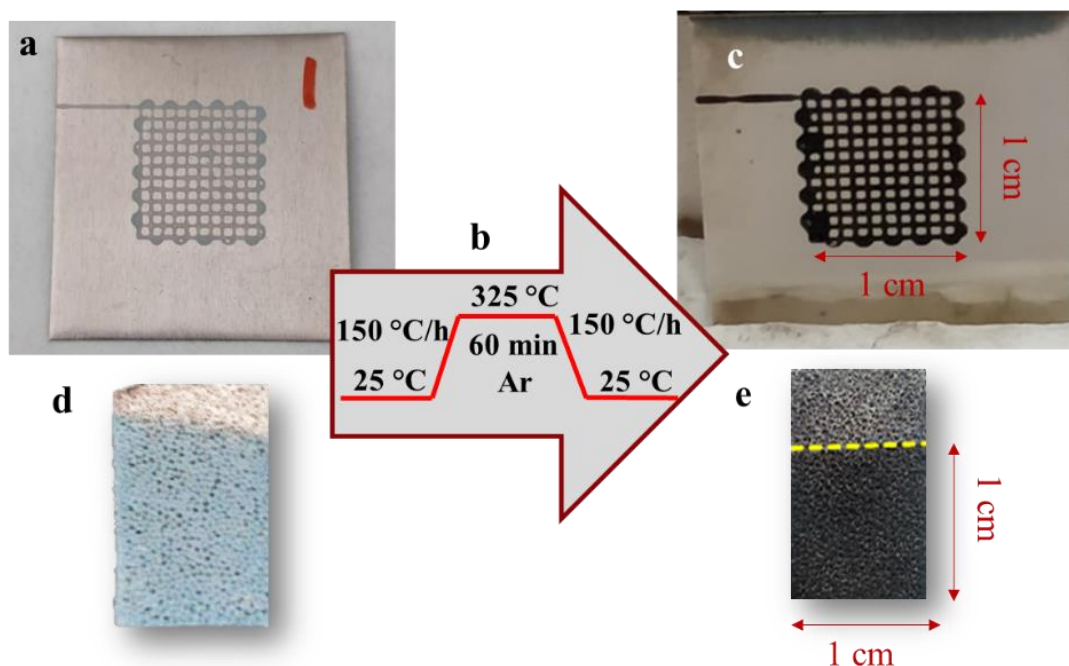
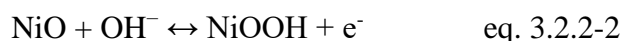


Figure 3.2.2.2-3. Picture of NiO-IJP before a) and after c) the thermal treatment indicated in b). Picture of NiO-EPD d) and e), after and before the thermal treatment, respectively.

After the thermal treatment, both electrodes were electrochemically characterized as PC. The electrochemical performance of the sintered coatings was evaluated in terms of faradaic capacitance. Figure 3.2.2.2-4a and 4b shows the cyclic voltammetry (CV) curves performed at different sweep rates (1, 2, 5, and 10 mV/s) for both electrodes NiO-IJP and NiO-EPD. In case of NiO-IJP, the quasi rectangle-shapes indicate that the electrodes have relatively large electric double layer capacitance (EDLC). In both cases, the redox peaks are distinguished, more clearly for the NiO-EPD electrode, determining the working potential window of 0.5 V (from 0 to -0.5V). These peaks were attributed to the following reversible redox reaction:



In CV, the reversibility of redox reaction is higher when reduction and oxidation peaks are closer. That means the NiO-EPD electrode was more reversible at rapid scan rates (>20 mV/s) and NiO-IJP electrode at slower scan rates (<20 mV/s).

In addition, specific capacitance values were also determined by galvanostatic measurements. Figure 3.2.2.2-4c presents the discharge curve, voltage vs. time plots at a potential ranging 0–0.5 V. The charge-discharge (C-D) curves are shown over a thousand

of cycles at 2 A/g for both electrodes. The specific capacitances were calculated from galvanostatic C-D curves, being 250 and 160 F/g the highest values of capacitance achieved for NiO-EPD and NiO-IJP electrodes, respectively. Then, the capacitance values were also plotted with the number of cycles (figure 3.2.2.2-4d), to show the long cycle-life of each electrode.

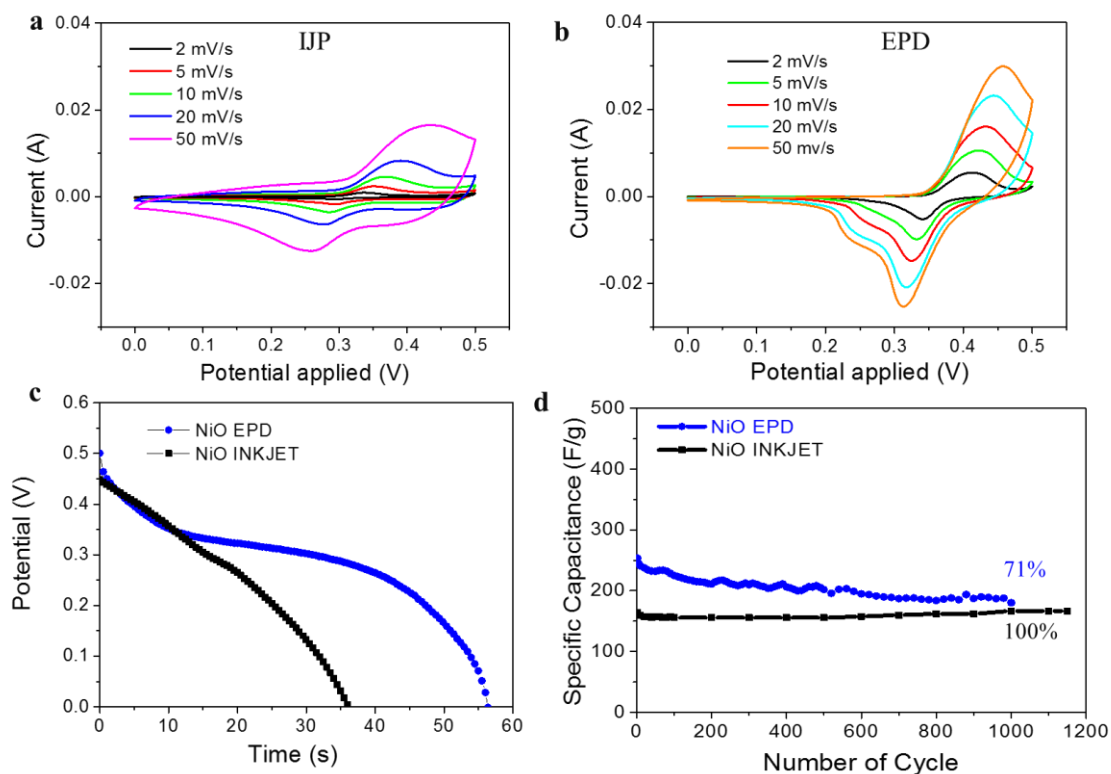


Figure 3.2.2.2-4. a) and b) Cyclic voltammeteries measured at different scan rates for NiO-IJP and NiO-EPD, respectively. c) Discharge curves at 2 A/g for both electrodes. And d) Specific capacitance retention as a function of number of cycles.

The cycling stability evidences the presence of a well-connected semiconductor structure as well as a firmly joined NiO layer to the Ni substrate for the NiO-IJP electrode, which facilitates the transport of electrons leading to a 100% of capacitance retention for more than 1000 cycles. On the other hand, NiO-EPD electrodes exhibits a 71% of capacitance retention after 1000 cycles of charge-discharge under similar conditions, achieving a similar value of capacitance than NiO-IJP electrodes, 160 F/g.

The EIS analyses are showed in Nyquist (figure 3.2.2.2-5a 5b) and Bode (figure 3.2.2.2-5d) plots. The resulting experimental values was fitted by Z-view using the equivalent circuit showed in figure 3.2.2.2-5c.

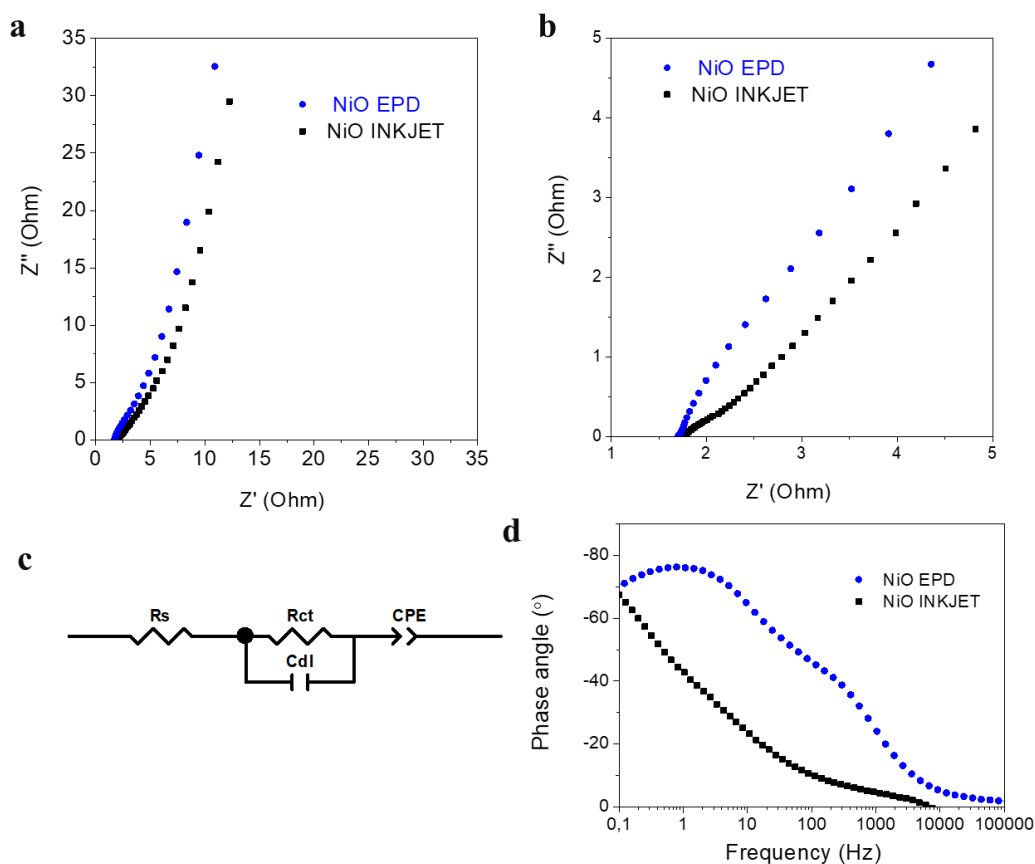


Figure 3.2.2.2-5. a) Nyquist plot of NiO electrodes and the zoom at high frequencies b). c) Equivalent circuit used for the fit. And d) Bode plot.

NiO-IJP electrodes were compared with electrodes shaped by EPD onto Ni foam (NiO-EPD). The values of the parameters R_{ct} , CPE-P, Φ_{max} and τ_0 were collected in table 3.2.2-3.

Table 3.2.2-3. Comparative of the fitted EIS parameters of the NiO- INKJET and NiO-EPD electrodes.

Substrate	Coating	Mass	R_{ct} (Ω)	CPE-P	τ_0	Φ_{max} ($^\circ$)
Ni foam	NiO-EPD	1.1	1.71	0.85	8.0 ms	76
Ni foil	NiO-IJP	0.7	0.23	0.60	1.3 s	67

The R_{ct} value for the IJP grid is lower than in NiO-EPD coating, however the CPE-P is also extremely lower. Moreover, related to the capacitance behavior, we can observe that the Φ_{max} achieved for NiO-IJP electrodes is 67° , much lower than that obtained by EPD on foam and foils. This can be expected since the exposed area of the electroactive material is greater for the EPD layers than for the IJP patterns (see figure 3.2.2.2-3), even on the foil collectors. Finally, the obtained value of the relaxation time, τ_0 , is two orders of magnitude higher for the IJP grid, which indicates that it displays a low charge/discharge rate.

However, the electrochemical performance of NiO-IJP patterns are similar to that reported for other NiO electrodes prepared by other methods [7,11]. The 100% retention factor and the low charge transfer (0.23Ω) of IJP patterns demonstrate that IJP is a reliable alternative to pattern PC electrodes with high resolution, but new designs of micro-PC should be printed to increase the exposed surface, providing simultaneously longer life-cycles and faster charge/discharge cycles than rechargeable micro-batteries [240].

3.2.3 Colloidal Modification

On view of the previous results and taking into account the advantage of covering fully the surfaces of 3D current collectors, EPD process was selected as shaping method to the manufacture of ceramic semiconductor-based PC electrodes with advanced microarchitectures. Three different colloidal strategies were proposed to tailor the final NiO-based electrode microstructure, trying to enhance the electrochemical response of the proposed devices. For this purpose, the surfaces of the $Ni(OH)_2$ and NiO nanoplatelets were tuned according to the requirements of each selected modification strategy, which were focused on:

- The synthesis of heteroprecipitated Ni nanospheres onto the surface of the NiO nanoplatelets to obtain in situ **NiO/Ni core-shell nanoparticles**. The precipitation of the metallic phase was carried out in the same liquid media where NiO nanoplatelets have been previously stabilized and dispersed.
- The heterocoagulation between NiO nanoplatelets and RGO nanosheets for the fabrication of **RGO/NiO nanostructures**. Two different stabilized suspensions (containing particles with opposite charge) were prepared separately and then mixed in the adequate ratio to facilitate the electrostatic interaction between both.

- The alternating adsorption of a polyelectrolyte multilayer onto the Ni(OH)₂ nanoplatelets (with 5 layers in total of cationic and anionic polyelectrolytes, **Ni(OH)₂-5LbL**) to increase their hydrodynamic diameter and produce relevant changes in the packing particles when they are shaped by EPD.

The optimization of the EPD parameters for each system was also tackle, in order to enhance the electrochemical response through the optimal amount of deposited mass onto the metallic substrate and their homogeneity. Cathodic electrophoresis was always employed for the deposits growth using a high voltage power source (2611 System Source Meter, Keithley Instruments Inc., USA). The theoretical adjust of the deposition kinetics were studied applying the general model proposed by Sarkar and Nicholson [220] where the exponential growth of the coatings is related to the characteristic time, τ through the most general equations (3.2.3-1 and 3.2.3-2) formulated up today to determine the deposition rate, and the EPD parameters.

$$m(t) = m_0(1 - e^{-t/\tau}) \quad \text{eq. 3.2.3-1}$$

where, m (g), is the deposition mass, m_0 (g), is the initial amount of powder in suspension and τ (s) is the characteristic time, calculated by:

$$\tau = \frac{V}{fSEu_e} \quad \text{eq. 3.2.3-2}$$

where, V (cm³), is the volume of suspension, S (cm²), is the conducting area, E (V/cm), is the applied electric field, u_e , (m²/V·s), is the electrophoretic mobility of the nanoparticles, and f ($0 < f < 1$), is the sticking factor. The sticking factor represents the percentage of depositing particles among the arriving particles to the work electrode by electrophoresis. The characteristic time determines the speed of the process and it was calculated from the main colloidal properties and starting conditions of each suspension.

Although the three colloidal strategies developed to formulate the nanocomposites suspensions (NiO/Ni, RGO/NiO and Ni(OH)₂-5LbL) will be described later in detail, all the parameters employed for their experimental deposition and to calculate their theoretical EPD kinetics curves are collected in table 3.2.3-1. In addition, the data corresponding to the Ni(OH)₂ nanoplatelets without any modification have also been included.

Table 3.2.3-1. Summary of the electrokinetics parameters of Ni(OH)₂, NiO/Ni, RGO/NiO and Ni(OH)₂-5LbL core-shells and the EPD electric conditions

Core-Shell Electrokinetics Parameters	Ni(OH) ₂	NiO/Ni	RGO/NiO	Ni(OH) ₂ 5LbL
Electrophoretic Mobility, u_e , ($\times 10^{-4}$ cm ² /V·s)	0.82	0.72	0.78	0.71
Suspension Conductivity, σ , (μ S/cm)	0.84	<1	2.20	0.50
Ratio of Mobility, σ/u_e	1.02	--	2.84	0.70
Current Density (μ A/cm ²)	20	13	67	8
Electric Field (V/cm)	71	15	--	60
Characteristic Time for EPD* (eq. 2)	308	7422	8516	423
Experimental Sticking Factor	0.64	<0.20	>1	0.20

*calculated for a volume of suspension of 30 ml and a sticking factor 1.

Lower characteristic time values indicate that faster deposition processes are happening. That means, theoretically, attending to the initial parameters of the suspension, the faster EPD kinetics follows this trend:

$$m(t) [\text{Ni(OH)}_2] > m(t) [\text{Ni(OH)}_2\text{-5LbL}] > m(t) [\text{NiO/Ni}] > m(t) [\text{RGO/NiO}]$$

Improvements on particles packing and EPD kinetics have been described for other systems when electrosteric mechanisms of dispersion and stabilization were used [224]. In those cases, similar coatings were obtained onto substrates of different nature, roughness and geometries [241]. Similarly to this research work happened for the optimized nanocomposites suspensions for EPD, where the co-solvent (H₂O: Ethanol) and the dispersant (PEI) were maintained and adjusted respectively for all systems. Nevertheless, although electrophoretic mobility is similar for all nanocomposite suspensions, conductivity differs and EPD parameters (electric field and deposition time) had to be then adjusted (table 3.2.3-1). Noting that only in the case of the EPD of RGO/NiO, the mechanism of flocculation described for other systems step up the coating growth. The PEI adsorbed onto the RGO/NiO core-shell reduces the exclusion volume and the electrostatic potential barrier when approach the work electrode (Ni foam) because of the decrease of pH promoted by the reactions which take place close to electrode. This mechanism of PEI neutralization at the electrode surroundings favours the flocculation of the nanocomposite. Consequently, attending to the sticking factors of the nanocomposites suspension, only the EPD of Ni(OH)₂ and RGO/NiO nanocomposites would achieve a 100% yield, depositing in a reasonable time all particles of the suspensions. The influence of the EPD kinetics in the packing degree of the PC electrode has been discussed in detail for each nanocomposites in related publications

[7,9,144,173]. The following paragraphs detail the processing and the electrochemical improvements of each modification strategy.

3.2.3.1 Processing and electrochemical enhancement by the inclusion of a conductive phase in the nanostructure of NiO-based PC electrodes

The inclusion of a conductive phase was studied as a way to reduce the charge-transfer resistance favoring the movement of the electrons through the electrode microstructure.

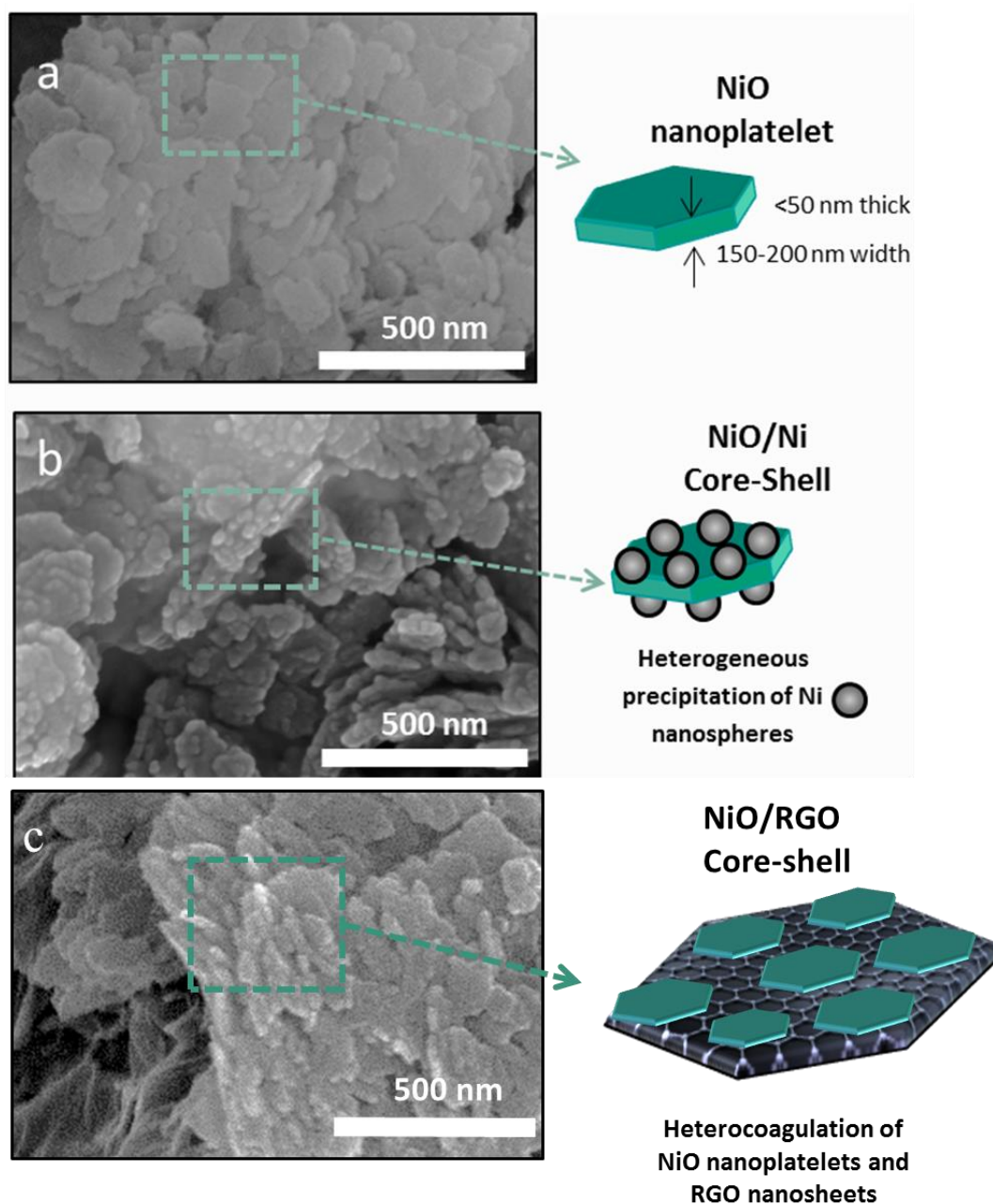


Figure 3.2.2.1-1. FESEM micrographs and schematic illustration of the synthesized powders of a) NiO nanoplatelets, b) core-shell NiO/Ni and c) core-shell NiO/RGO.

Both metallic Ni nanospheres and RGO nanosheets were incorporated to the ceramic semiconductor material as can be observed in figure 3.2.3.1-1.

The preparations of both types of nanostructures were carried out by using the ZP as the main tool to control the surfaces of the materials. Structural characterization illustrates the dimensions between 200-300 nm in diameter and 15-20 nm in thickness for the NiO nanoplatelets, 15-30 nm in diameter for the Ni metallic nanospheres and the RGO nanosheets shows 3 times more SSA per gram than NiO nanoplatelets.

More in detail, the inclusion of metallic Ni nanospheres onto the surface of the NiO consisted in a “one pot” reduction reaction under the action of an ultrasonic horn by using nickel nitrate as salt precursor and hydrazine monohydrate ($\text{N}_2\text{H}_4 \cdot \text{H}_2\text{O}$, 65% purity, Sigma-Aldrich, Madrid, Spain) as reductant and KOH as basifying agent. The temperature of the reaction was controlled through recirculation from a cryothermal bath at 50°C. The molar ratio of the reactants was $1[\text{Ni}^{+2}]:10[\text{KOH}]:39[\text{N}_2\text{H}_4]$ and the pH of the work was adjusted ranging 9-11 to favor the electrostatic interaction between the negative charge of the as-synthesized metallic Ni nanospheres and the positive charge of the NiO nanoplatelets dispersed with PEI.

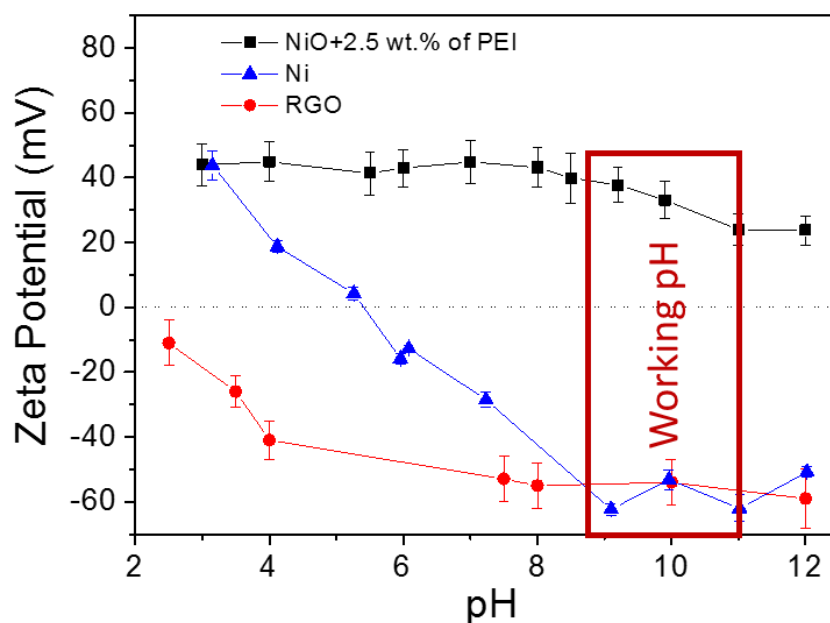


Figure 3.2.2.1-2. Zeta potential vs pH of NiO nanoplatelets with 2.5wt. % of PEI, Ni nanospheres and RGO nanosheets.

On the other hand, the preparation of the RGO/NiO structures were carried out by inducing heterocoagulation of the core-shell by mixing two different stabilized suspensions of NiO nanoplatelets and RGO nanosheets. Again, the working pH was adjusted ranging 9-11, where RGO nanoparticles presented ZP charges strongly negatives and the NiO nanoplatelets stabilized with PEI shows a positive charge at the same pH. See figure 3.2.2.1-2.

In order to deepen into the influence of the sintering treatment and the consolidation level of the final ceramic microstructure, different sintering times and temperatures were optimized. The adjustment of these parameters was made taking into account the compromise between having a high connection (forming sintering necks) among nanoparticles, which can reduce the electron transfer resistance, and/or maintaining a high meso- and microporosity, which can increase the exposed surface in the electrode microstructure. For this purpose, 1 mg of NiO/Ni core-shell nanostructures, deposited on 3D Ni foams by EPD, were sintered at three different heat treatments in Ar atmosphere figure 3.2.2.1-3. The heating and cooling rates were 10 °C/min. The modified parameters were temperature and dwell time.

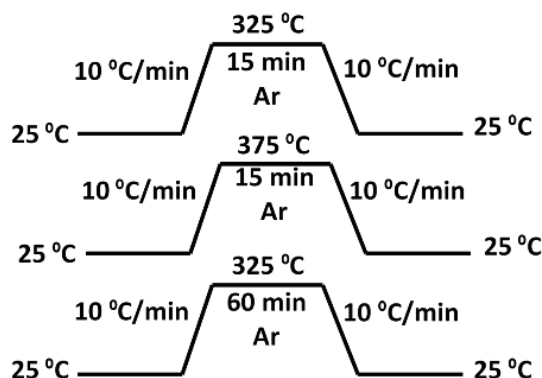


Figure 3.2.2.1-3. Diagram of different thermal treatments employed for the optimization process.

Both the electron transport and the ion diffusion can be affected by the connection pathways/channels inside of the semiconductor microarchitectures. If the coating is continuous and dense, then specific surface area and porosity are reduced and part of the deposited mass of the electroactive material is hidden to the faradaic reactions (not exposed to the liquid electrolyte). Looking at the FESEM images taken at x500 and x15K magnification (figures 3.2.2.1-3a, 3c and 3e; and 3b, 3d and 3f; respectively), all the as-

prepared electrodes showed an open microstructure that favors the electrolyte contact with the surface of the electroactive material [44–46]. However, different porosities were achieved in each sintering process. The most open porosity was given at 325 °C during 1 h as residence time. This open micro-architecture favors the number of sites where redox reactions may take place.

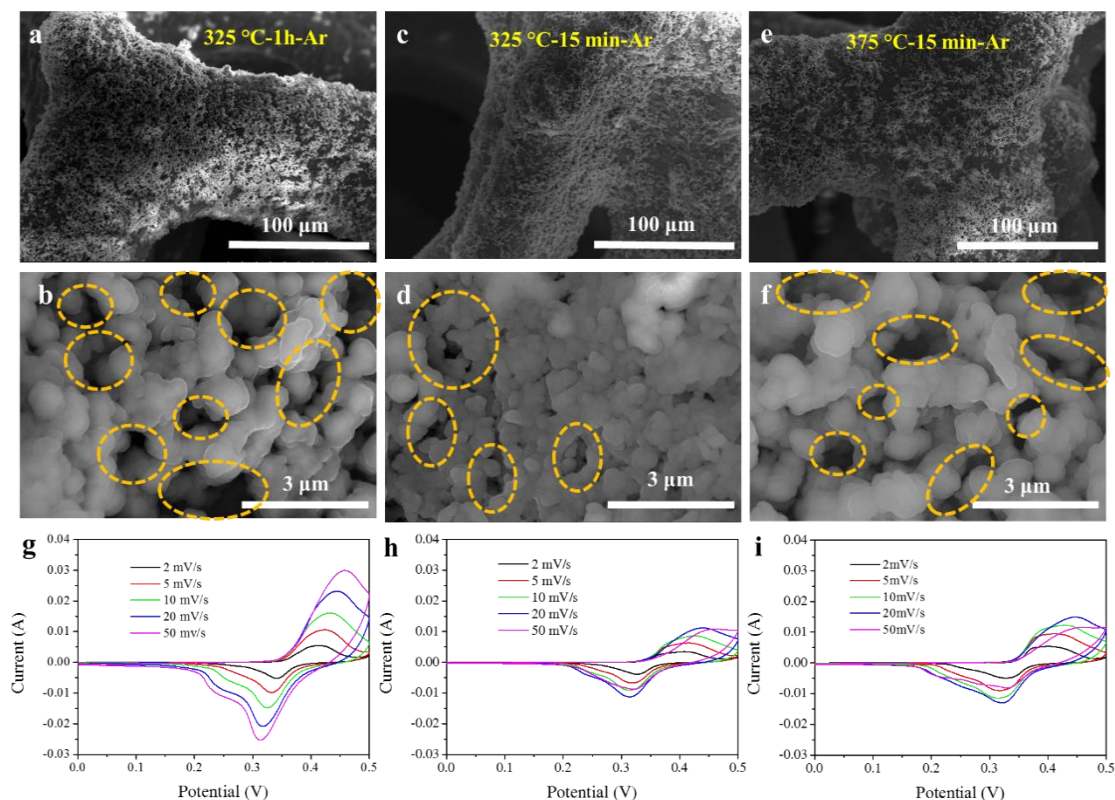


Figure 3.2.2.1-3. Final morphology and porosity of the NiO-Ni coating after the different heat treatment b) 325°C 15 min Ar, c) 375°C 15 min Ar and d) 325°C 60 min Ar. And cyclic voltammetry of NiO-Ni deposits calcined at g) 325°C 60 min, h) 325 °C 15min and i) 375°C 15 min.

The balance between particles connection and porosity affected directly to the electrochemical response of the electrode causing an increment in the C_s value, measured from the cyclic voltammetry (CV). In this graphs, the area under the curve is proportional to the specific capacitance. For the most open microstructure, corresponding to the electrodes sintered at 325°C during 60 min (figures 3.2.2.1-3a and 3b), the area was higher than the electrodes sintered by the others thermal treatments. Moreover, at the same time, CV tests harmonize with the specific capacitance obtained by the discharge curve at current density of 2 A/g. In figure 3.2.2.1-4a the typical voltage vs. time plots for each electrode sintered differently fall from 0.5 to 0 V, describing symmetric curves where

quasi-linear shapes with well-defined plateaus correspond with the pseudocapacitance behavior (see figure 3.1.2-1a of the introduction).

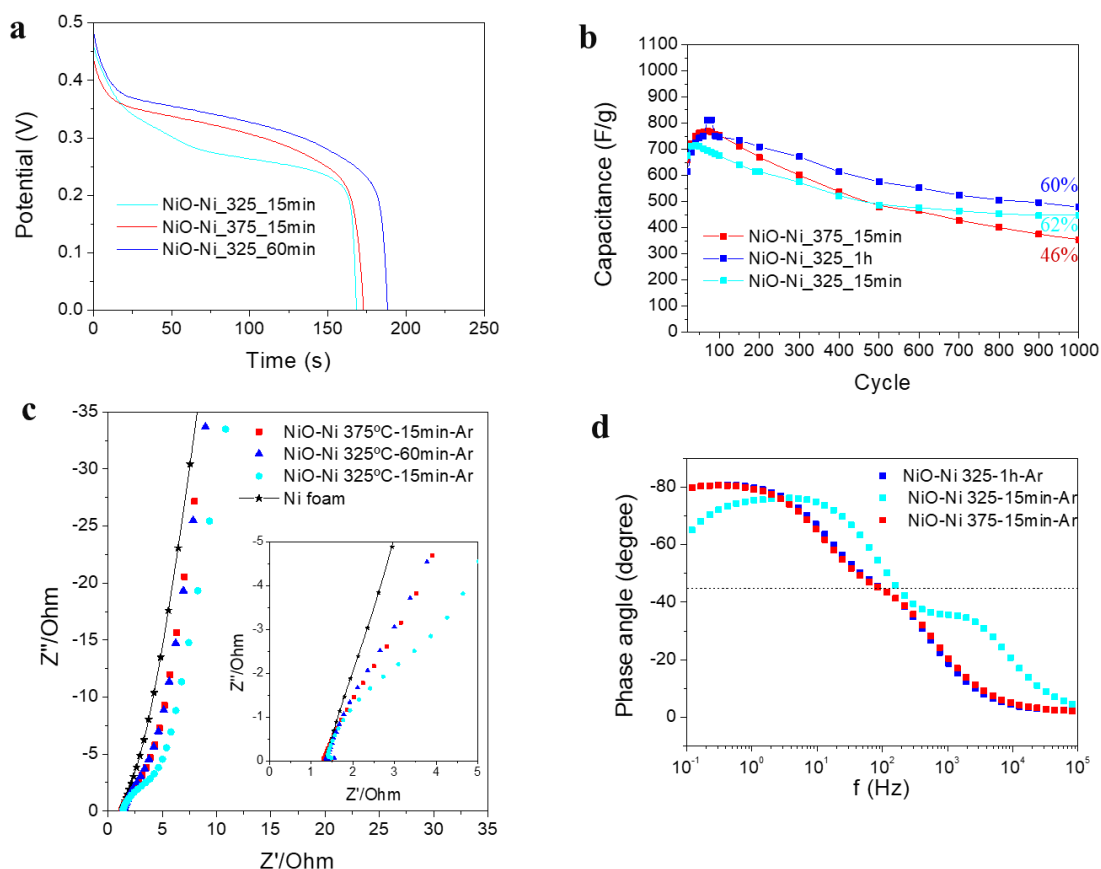


Figure 3.2.2.1-4. d) Galvanostatic discharge curves at 2 A/g of the different heat treatment electrodes. e) Cyclic chronopotentiometric measurement (CP). f) Nyquist plot, and g) Bodes plot of NiO-Ni electrodes at different TT.

The specific capacitance values for the NiO/Ni electrodes were 755, 688 and 668 F/g the Cs values obtained for the thermal treatment at 325°C - 1h, 325 °C -15min and 325 °C - 15min, respectively. The electrochemical responses of this electrodes were always better than the bare-NiO electrode processed previously by Gonzalez et al.[7] (363 F/g). This phenomenon can be explained through the EIS measurements performed in the same conditions for each electrode as can be observed in figures 3.2.2.1-ac and 4d. The electrode annealed at 325 °C during 15 minutes exhibits a higher transfer charge resistance ($R_{ct} = 2.43 \Omega$) than the electrodes treated at a higher temperature, 375°C ($R_{ct} = 1.64 \Omega$), or for a longer time, 60 minutes ($R_{ct} = 1.55 \Omega$), indicating that the softest

thermal conditions lead to less connectivity between the nanostructures [144]. Table 3.2.3-2 summarizes the EIS data and thermal conditions chosen for each electrode.

Table 3.2.3-2. Fitted values of the as-prepared NiO-Ni electrodes at different TT.

Collector	Film	Mass	Thermal Treatment	R _{ct} (Ω)	CPE-P	τ_0 (ms)	Φ_{\max} ($^\circ$)
Ni foam	NiO	1.1	325°C 60 min Ar	1.71	0.85	8	76
		1.0	325°C 15 min Ar	2.43	0.84	6	76
	NiO/Ni	1.1	325°C 60 min Ar	1.55	0.90	11	81
		1.1	375°C 15 min Ar	1.64	0.90	11	81

In the Nyquist plot (figure 3.2.2.1-4c) it can be observed that the electrode annealed at 325 °C during 15 minutes displayed less steep slope that the other two, which were very similar, confirming that its capacitive behavior can be improved by adjusting slightly the thermal treatment. The CPE-P value of this poor sintered electrode (0.84), and then the maximum phase angle achieved at the Bode plot ($\Phi_{\max} = -76$), were also lower than for the other sintering conditions, which evidences that the capacitive response can be deleterious when charge-transfer resistance increases, and it is not compensated in the microstructure by enough faster ion diffusion.

Bode plot in figure 3.2.2.1-4d shows how the effect of the resistance decreases when the thermal treatment temperature and time increase in the sintering process. Similar improvements are shown for sintering at 325°C during 60 min and 375°C during 15 min. These plots displayed phase angle values of -81° at low frequency, corroborating that the increasing of time or temperature modified the electrochemical behavior of the electrodes to ideal capacitor.

As consequence of this, we concluded that a low calcination temperature favors an open microstructure of the electroactive material allowing the creation of free spaces for a correct electrochemical behavior. In figure 3.2.2.1-5 at high magnification, the sintering necks are showed. It is not necessary to reach elevate values of temperature to obtain a well-defined and interconnected microstructure of NiO/Ni nanostructure.

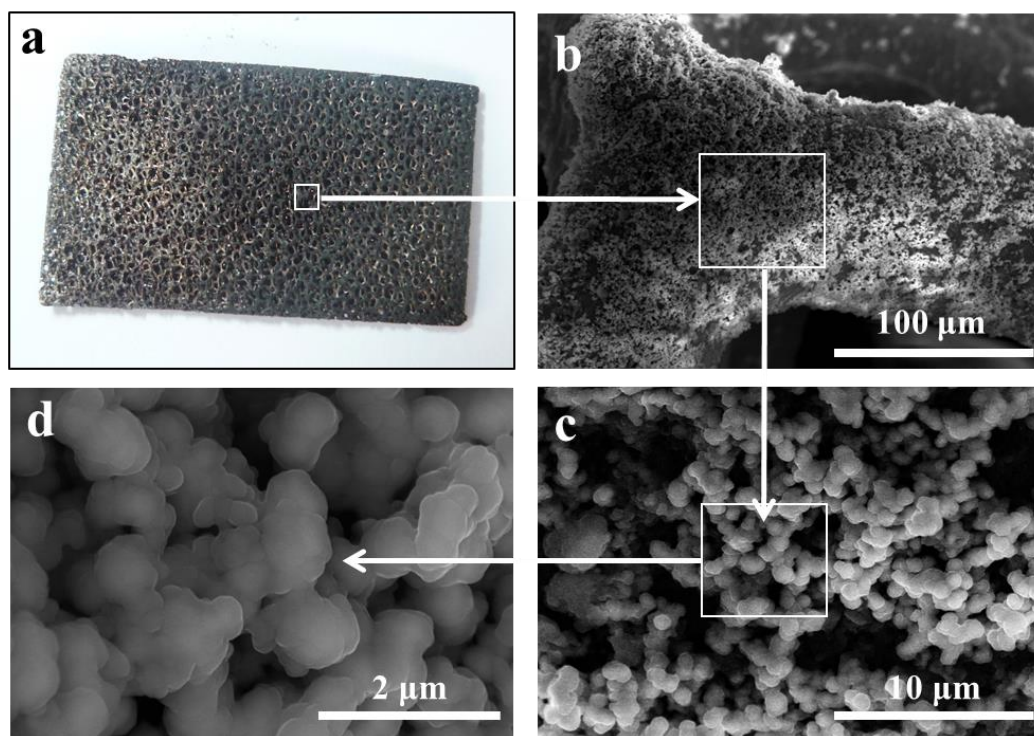


Figure 3.2.2-5. NiO/Ni coatings onto Ni foam deposited by EPD and sintered taken at different magnifications.

As mentioned before, the combination of the NiO with different materials decrease the R_{ct} . The inclusion of metal and non-metal impurities within the NiO microstructure has been analyzed to reduce R_{ct} increasing the specific capacitance. In this sense, the electrical conductivity can be enhanced generating donor or acceptor states in the bandgap and thereby increasing the concentration of charge carriers. This fact enhances the electron transport and reduces the R_{ct} values of the NiO-based electrodes.

Another widely studied electrical donor is RGO. When this nonmetal material is combined with NiO by heterocoagulation it forms nanostructures with high specific surface area. This composite was also used as electroactive material and ~1mg was electrophoretically deposited (figure 3.2.2.1-6a, b and c at different magnification) and sintered by the chosen thermal treatment (figure 3.2.2.1-6d).

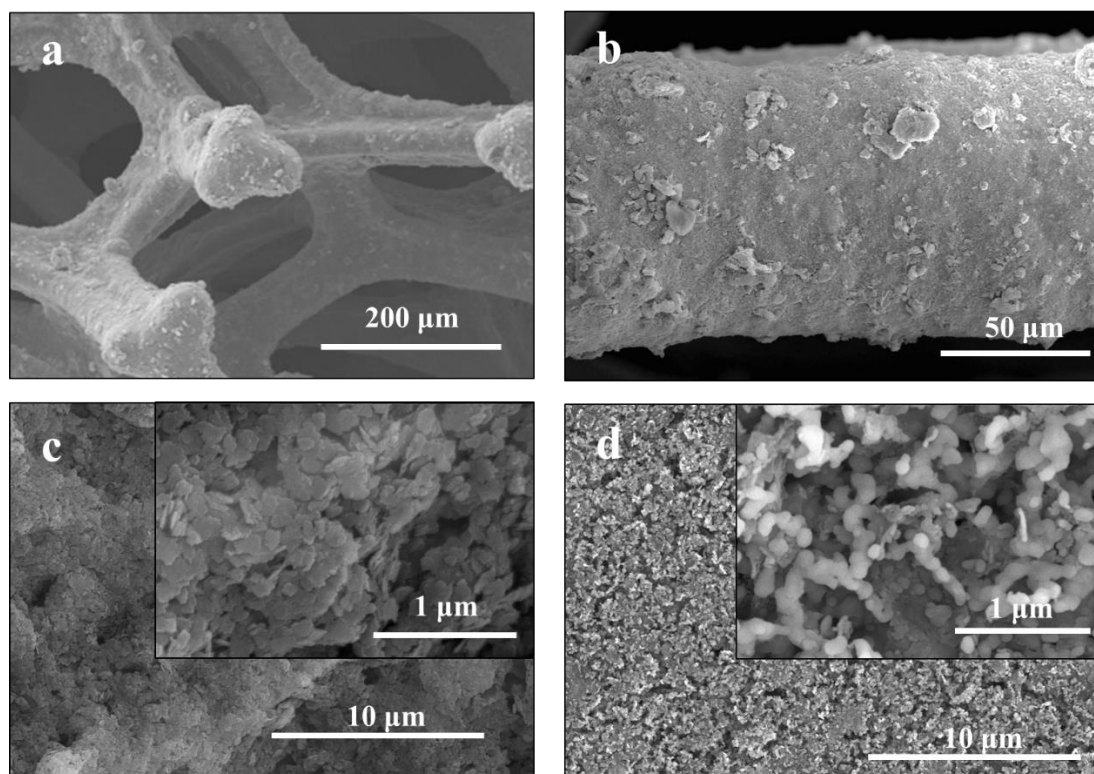


Figure 3.2.2.1-6. NiO/RGO coatings onto Ni foam deposited by EPD a), b) and c) before and d) after the sintering process.

These images confirmed that 1mg of this electroactive material (RGO/NiO) was also enough to cover the surface of the 3D current collector evidencing the absence of cracks and additional defects.

Then, the RGO/NiO electrode was electrochemically compared with NiO/Ni and bare NiO. In CV, the area under the curve of NiO/RGO, figure 3.2.2.1-7a, was larger than the area of NiO/Ni, figure 3.2.2.1-7b, which indicates that the specific capacitance of RGO composite was higher. The discharge profiles of the electrodes, parallel to the x-axis, confirmed also the typical pseudocapacitive contribution (figure 3.2.2.1-7c). And the specific capacitance determined for the NiO/Ni and NiO/RGO coatings at a scan rate of 2 A/g exhibited a specific capacitance of 755 F/g and 960 F/g respectively.

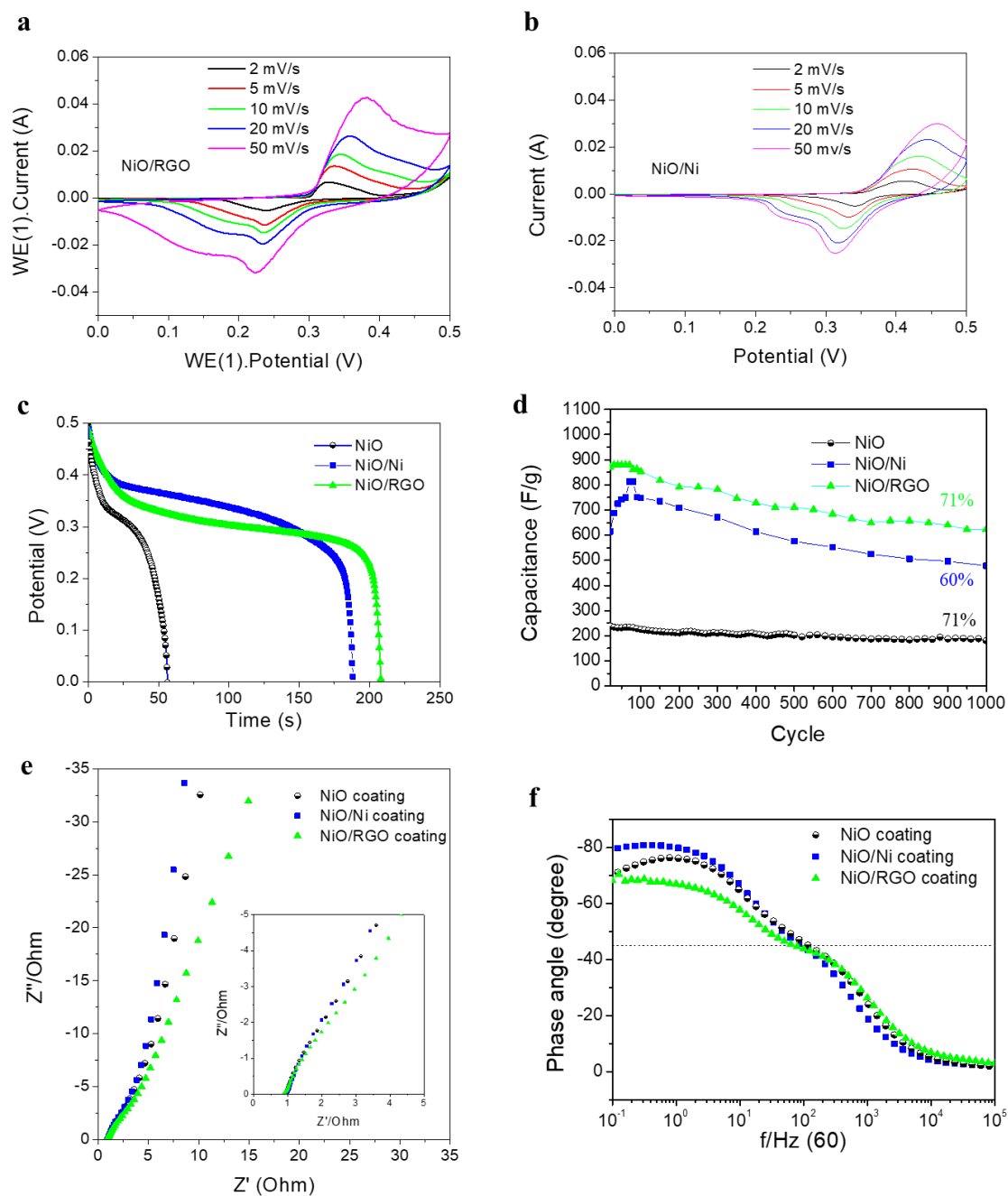


Figure 3.2.2.1-7. Cyclic voltammetry of a) NiO/RGO and b) NiO/Ni deposits calcined at 325°C 1h under Ar atmosphere c) Galvanostatic discharge curves at 2 A/g of the different composites. d) Nyquist and e) Bode plots of NiO and NiO/Ni and NiO/RGO coatings.

Figure 3.2.2.1-7d and 3.2.2.1-7e compare the Nyquist and Bode curves corresponding to the NiO/Ni and RGO/NiO electrodes and the NiO electrode as reference. Since electronic transport is easier on metal and graphene than semiconductors, NiO/Ni and RGO/NiO coatings exhibited smaller semicircles than those coated by NiO. In addition, RGO

impurities had even more depressed semicircle in the high frequency region due to their easiest electron transfer. This reason could also explain why the NiO/Ni core-shell nanocomposite had a charge-transfer resistance lower than NiO, 1.64 and 1.71 Ω respectively, and the RGO/NiO was the lowest, 1.13 Ω . The inclusion of the Ni and RGO NPs favored the electron transport through the semiconductor microstructure, reinforced by the contribution of the microporosity in the core-shells.

Table 3.2.3-3. Fitted values of the as-prepared NiO-based electrodes. Decreasing the Rct.

Coating	Mass (mg)	Cs (F/g)	Rs (Ω)	Rct (Ω)	CPE-P	τ_0 (MS)	Φ_{MAX} ($^\circ$)
Bare-NiO	1.1	250	-	1.71	0.85	8	76
NiO/Ni	~ 1	755	-	1.64	0.90	11	81
RGO/NiO	0.7	920	-	1.13	0.75	4	70

Moreover, the NiO/Ni electrode showed the best capacitive response than the other electrodes, without NPs and with RGO. The straight line in the low frequency region was steeper for the NiO/Ni electrode. The closer value to the unit means better capacity behavior, which was also confirmed by the CPE-P value of table 3.2.3-3. These CPE-P values varied from 0.75 to 0.90 while Φ_{max} also increased from -76° to -81° , when the Ni catalyst NPs were included. In this case, the relaxation time constants obtained from Bode curves were similar ($\tau_0 = 11$ ms), thus the variations of the capacitance retention at high charging/discharging rate were not significant.

3.2.3.2 Processing and electrochemical enhancement by assembling a porous hierarchical nanoarchitecture of NiO based PC electrodes

The adsorption of an alternative polyelectrolyte multilayer onto the Ni(OH)₂ nanoplatelets by using the Layer by layer (LbL) strategy aimed to increase the specific capacitance through the increase of the SSA and the porosity as a consequence of relevant changes in the coating organization (packing and distribution of their particles) during the EPD process of the modified particles.

The LbL technique is a self-assembly methodology [242], which consists in the functionalization of the solid particle with polyelectrolyte multilayers in a liquid media, as can be seen in figure 3.2.3.2-1. The polyelectrolytes used to build up the multilayer were branched Polyethylenimine (PEI, Mw 25,000, Sigma Aldrich, Germany) for odd layers,

and Polyacrylic Acid (PAA in a 63 wt.% solution in water, Mw 2000, Across, USA) for even layers. The growth of the multilayer was evaluated in terms of ZP by adsorption of the specific amount of polyelectrolyte (PEI or PAA) which saturates either the surface of nanoplatelets in the first layer or the previous layer in the subsequent additions. Moreover, to favour the adsorption of the following layer of opposite charge, the pH value of the suspension was adjusted. For the adsorption of PEI, pH 8 was selected to promote the protonation of the amino groups ($-\text{NH}_3^+$, $=\text{NH}_2^+$, $\equiv\text{NH}^+$), while at pH 10 the adsorption of PAA layer with deprotonated carboxyl groups (COO^-) was favoured.

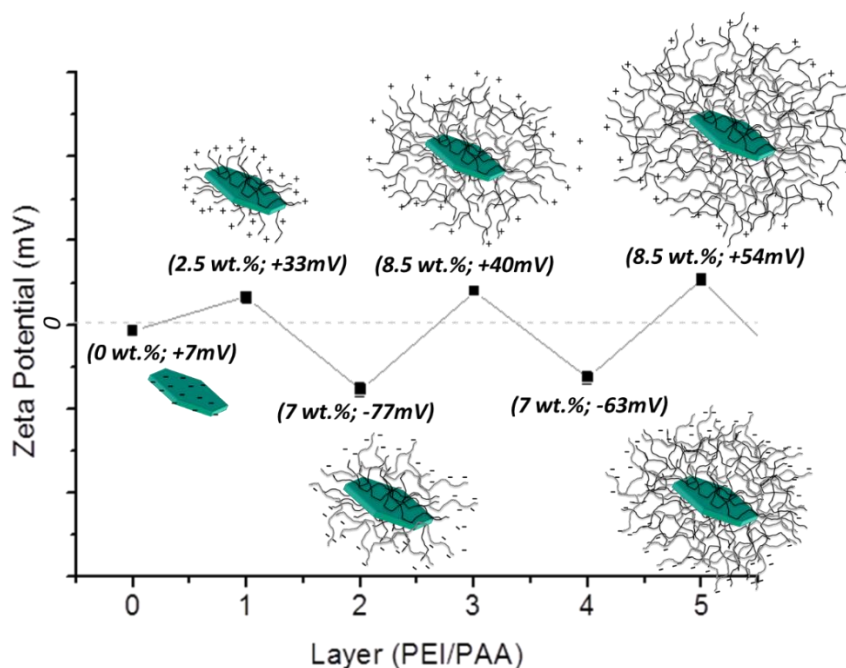


Figure 3.2.3.2-1. Scheme of polyelectrolyte adsorption LbL onto the $\text{Ni}(\text{OH})_2$ nanoplatelets and the Zeta potential evolution during the process.

The figure includes the percentages of the adsorbed polyelectrolytes in each layer. After the core-shell assembly with inorganic particles ($\text{Ni}(\text{OH})_2$) and organic shells (of 1, 3 and 5 Layers of polyelectrolyte), the remaining chemicals were eliminated by removing the supernatant after centrifugation and the resulting wet powder was washed. The cleaned and still wet precipitates were re-suspended in the solvent mix of ethanol:water (19:1 v/v) in order to perform the electrophoretic deposition.

After the shaping of the $\text{Ni}(\text{OH})_2$ nanoplatelets modified with 1, 3 and 5 layers, the resulting coatings were annealed by the selected thermal treatment at 325°C during 60min

to obtain a NiO consolidated structures and then the surface of as-deposited hydroxide-based films as well as that of the consolidated oxide-based structures were inspected by FESEM. Figure 3.2.3.2-2 illustrates the surface of the different coatings before and after the heat treatment. Moreover, three different schemes related with the packing nanoplatelets are also included. Low magnification micrographs evidence the uniform coatings built by EPD, and the increasing disorder promoted by the LbL modification of the nanoplatelets during deposition, even strikingly than those studied in a previous work for more intense EPD conditions [242]. These consolidated microstructures maintain their structural integrity after the sintering.

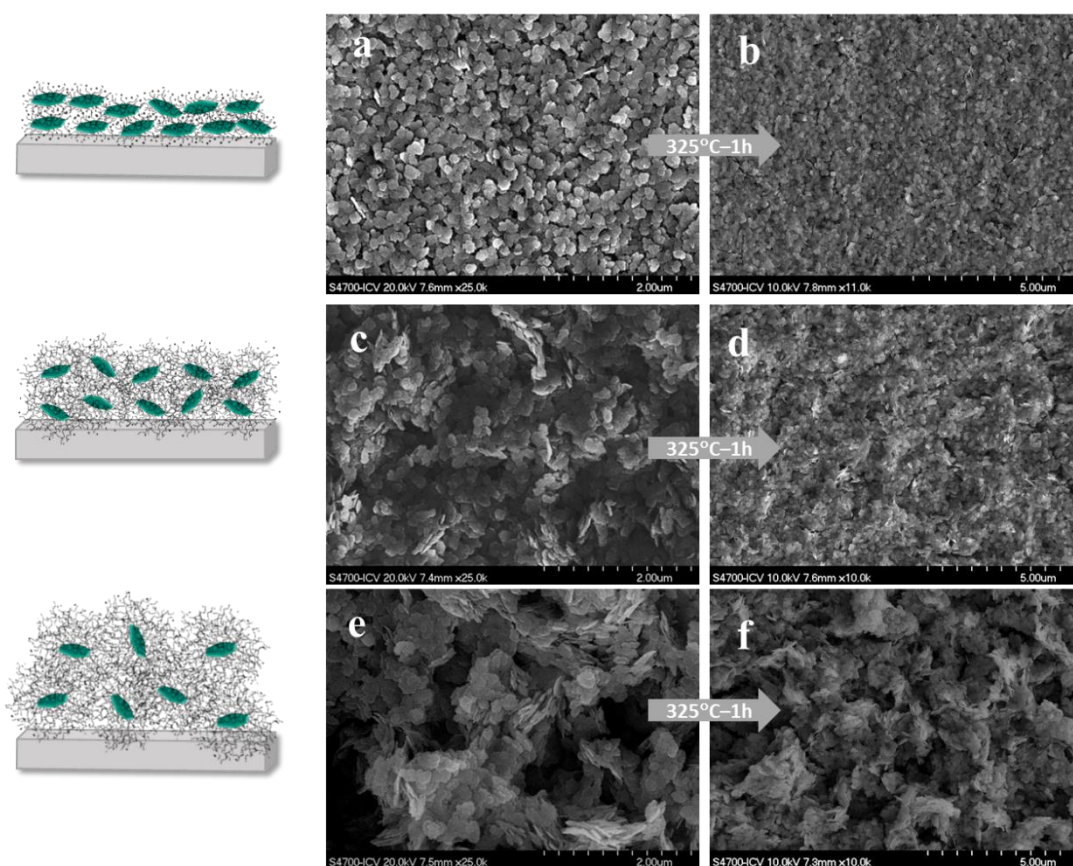


Figure 3.2.3.2-2. Schematic illustration of the coatings made with 1, 3 and 5LbL of NiO nanoparticles and FE-SEM images of electrodes before and after deposition of 1 LbL (a and b), 3LbL (c and d), and 5LbL (e and f) coatings onto Ni foams.

Although the electrochemical response of the electrodes (made with nanoparticles modified with 1 and 3 layers of polyelectrolyte) had already been evaluated in previous work [11], a new contribution of this thesis have consisted on comparing the electrochemical behavior of the electrodes prepared with nanoplatelets modified with 5

layers. The results of the cyclic voltammograms (CV) at different scan rates, galvanostatic charge/discharge tests (CP) at current density of 2 A/g and EIS, from 10^5 to 10^{-1} Hz, were performed in figure 3.2.3.2-3.

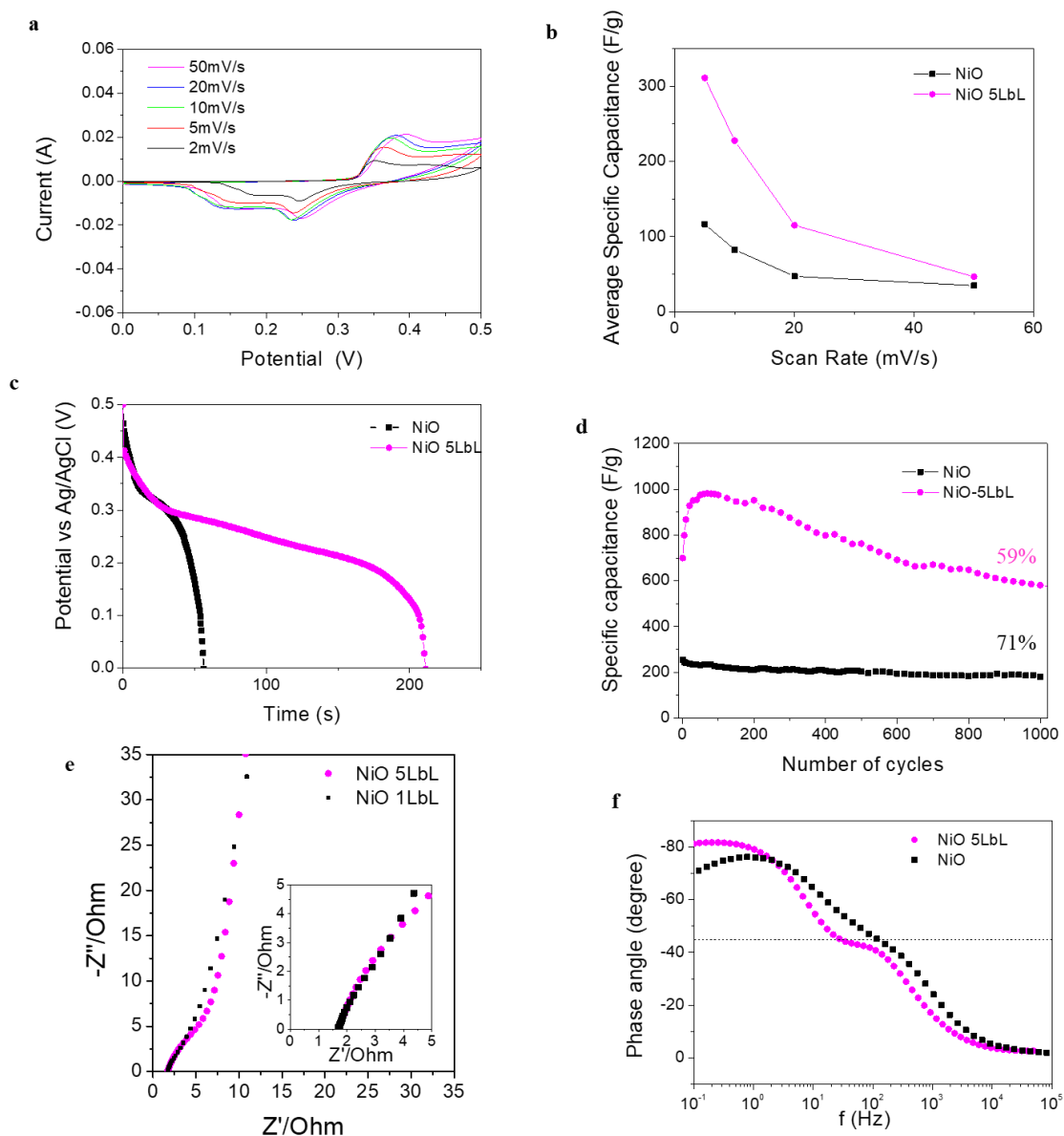


Figure 3.2.3.2-3. Electrochemical comparative between the NiO electrodes of 1 and 5 LbL. a) Cyclic voltametries of the sample NiO 5LbL at different scan rates. b) Variation of specific capacitance with scan rate. c) Galvanostatic discharge curves. d) Cyclic chronopotentiometric measurements at a current density of 2A/g. e) Nyquist and f) Bodes plot of NiO and NiO5LbLcoatings.

Figure 3.2.3.2-3a shows the CV curves in a potential window from 0 to 0.5 V. The identified redox peaks correspond to the previously described eq.3.2.2-2, showing a good reversibility. A shift of the redox peaks with the scan rate was observed. The anodic peaks

shifted to positive potentials and the cathodic peak to the negative potential due to the polarization in the electrode material and the OH^- ions intercalated quickly at the interface of electrode/electrolyte at the high scan rate (50 mV/s).

Figure 3.2.3.2-3b shows the variations of specific capacitance with the sweep rate for the electrodes made with nanoplatelets modified with 1 and 5 layers. Both curves show a gradual decrease of the capacitance values, although the coating of NiO-5LbL presents more elevated values of capacitance.

Additionally, the C_s value was calculated from the discharge curve (figure 3.2.3.2-3 c) taken at current density of 2 A/g in the same voltage range that the previous systems from 0 to 0.5 V. Both plots are also composed of three steps. The first step was assigned to fast initial potential drop in voltage due to internal resistance. The second slope (horizontal-like) was associated to the reduction reaction of Ni^{+2} and it was described as a slight potential. Finally, the third step, which illustrate a steeper voltage decay, corresponded to an electric double layer contribution. All the as-prepared electrodes presented similar curves, the main difference is the length of the second step, there are more contribution of pseudocapacitance. The macroporous microstructure of the NiO-5LbL leads in the increases of the active surface leading to a higher specific capacitance

The cycling stability of electrodes was evaluated by galvanostatic charge/discharge cycles at the same current density during 1000 cycles. Figure 3.2.3.2-3d shows the trend of the specific capacitance vs. the number of cycles. The specific capacitance increases with the number of organic layers, but also NiO-5LbL electrode exhibits a significant increase of the specific capacitance, from 650 to 1000 F/g, between the first 50-100 cycles due to the activation and stabilization of the opener microstructure. The electrolyte ions have to go through every nook to favour the contact with all the active sites in the semiconductor structure. After activation (first 100 cycles), the specific capacitance value starts to decrease until 650 F/g after 1000 cycles.

In addition, the EIS analyses were carried out to study the variations in R_{ct} CPE-p, ϕ_{max} and τ_o . Figure 3.2.3.2-3e and 3f shows a comparative of the Niquist and Bode plots respectively for the NiO reference electrode and the NiO-5LbL electrode. Both electrodes were coated with similar mass (~ 1 mg) and similar EPD conditions, using also Ni foam as collector. The characteristic parameters of NiO and NiO-5LbL electrodes obtained from the adjustments with Z-view of these EIS curves were summarized in table 3.2.3-4.

Table 3.2.3-4. Comparative of the fitted EIS parameters of the NiO-5LbL and the NiO electrodes.

Substrate	Coating	Mass	Rct (Ω)	CPE-P	τ_0 (s)	Φ_{\max} ($^\circ$)
Ni foam	Bare-NiO	1.1*	1.71	0.85	8.0	76
	NiO-5LbL	1.1	3.65	0.90	18.0	82

The CPE-P value of the NiO-5LbL electrode (0.90) was higher than the value of the NiO film indicating that benefits of the exposed surface and the porosity increase in the electrode microstructure, which was especially relevant in the electrochemical response despite the significant increase of Rct value (3.65 Ω). Although there were no significant differences in the slope of both Niquist curves, the results seen in the bode plots (Figure 3.2.2-10f) shows a phase angle value of -82° for NiO-5LbL, which is closer to -90° than the phase angle of the NiO reference, -76° . It implied that the porous NiO-5LbL electrode had stronger capacitive behavior [8, 26] than the NiO reference electrode, maintaining a lower τ_0 constant (18 ms) that was a quick charge/discharge rate.

Summarizing, the LbL surface modification of NiO nanoplatelets was a modification strategy addressed to enhance the electrode capacitance by increasing the macro and mesoporosity of the active material after depositing on Ni foams by EPD while charge-transfer resistances did not suppose significant changes in capabilities and the capacitance retention of NiO-5LbL electrodes. This was caused by major fraction of active sites and a better contact of the electrolyte with the electroactive material where diffusion of alkali cations access into the porous and disorganized microstructure.



4

Concluding Remarks

Concluding Remarks

The scientific development presented in this manuscript have allowed defining the desirable conditions to successfully carried out the processing of ceramic semiconductor electrodes with hierarchical porous microarchitectures, using in all cases synthesized Ni-based nanoplatelets, as building block or main electroactive material.

Described results demonstrate that the degree of consolidation and porosity, main microstructural features of the ceramic semiconductor material, play a crucial role in the energy storage process of pseudocapacitors (PC). This general conclusion is detailed as follow, regarding to the different topics studied in this research work.

The scale-up of the synthesis of $\text{Ni}(\text{OH})_2$ nanoplatelets, carried out during the ongoing of this thesis, provides a reliable methodology to obtain large batches of the effective electroactive material. These building blocks, $\text{Ni}(\text{OH})_2$ nanoplatelets, have been employed as main compound of different complex nanostructures (core-shell type) with improved features, and also used as electroactive materials to shape PC and hybrid supercapacitors (HSC) electrodes.

Two colloidal techniques have successfully been employed as shaping method for the fabrication of ceramic-based electrodes. Firstly, the Electrophoretic Deposition (EPD) was used for the manufacturing of 3D electrodes exhibiting a large and reactive surface in a small volume. After optimizing the EPD parameters (applied voltage, deposition time, etc.) for each complex nanostructure, homogeneous coatings covering the 3D collector were obtained.

Simultaneously, stable suspensions of $\text{Ni}(\text{OH})_2$ nanoplatelets were shaped by Ink-jet printing (IJP) in Ni foil. This thesis reports for the first time, that as-synthesized $\text{Ni}(\text{OH})_2$ nanoplatelets dispersed in an aqueous suspension is an useful ink, with a long-time stability for the IJP of ceramic-based electrodes in PC manufacture. The employment of DEG as a co-solvent resulted in optimal values of viscosity, surface tension and density of the ink for printing tailored NiO patterns.

All electrodes were electrochemically evaluated in terms of cyclability, specific capacitance and charge transfer resistance, showing the following results:

Electrodes shaped by EPD depend on the electronic charge-transfer of metallic collectors, mainly determined by its nature and conductive section. Cu and Ni foils as substrates present differences in the charge-transfer resistance as a consequence of the electronic

configuration, being Ni foil the electrode that shows the minimum R_{ct} value ($0.21\ \Omega$). And the highest resistance in foil configuration electrodes shaped by EPD is given by the stainless steel ($2.14\ \Omega$) further larger than Cu ($0.48\ \Omega$).

After depositing and sintering of the electroactive material, NiO nanostructured films on Ni foams improve the rate capability and capacitance retention at high charging/discharging rate, exhibiting a relaxation time constant ($\tau_0 = 8\text{ ms}$) in the same range of electric double layer capacitors (EDLC) capacitors. However, the charge-transfer resistance of electrodes shaped in this configuration is relatively high due to the lower conductive section of the 3D collector ($1.71\ \Omega$) and the larger interface collector/electroactive material (Ni/NiO). Nevertheless, this R_{ct} is compensated by the highly accessible surface which provides the rapid ion diffusion throughout the hierarchical porous 3D network of the electrode, leading to values of specific capacitance close to 250 F/g with retention of 71%.

However, NiO electrodes shaped by IJP illustrated a longer cycle-life, even when the electrochemical behavior, in terms of specific capacitance, is lower (160 F/g at the same current density) due to the minor exposed surface area of NiO patterns. A 100% of capacitance retention at 2 A/g during a thousand of cycles is obtained, which means that after 1000 cycles the electrodes manufactured by EPD achieve similar values of specific capacitance that this maintained by the JPI electrode. On the other hand, the lowest R_{ct} values is observed ($0.23\ \Omega$) for these NiO-based 2D electrodes, which show a better connection between the nanoparticles of the draw extremely flat patterns.

On the other hand, an extensive analysis of the physicochemical features of three different Ni-based microarchitectures allows understanding the influence of the electron transport and the ion diffusion on the final electrochemical response in the electrodes shaped by EPD.

NiO/Ni core-shell nanostructures were synthesized, with the aid of ultrasound, by heterogeneous precipitation of metallic Ni over NiO nanoplate-like seeds dispersed and stabilized in aqueous suspensions. The stabilization of as-synthesized core-shell nanostructures and the optimization of the EPD parameters allow controlling NiO/Ni nanoplatelets arrangement and the coating growth in 3D substrates (Ni foam). The Ni collector was fully and homogeneously covered with only 1 mg of electroactive material.

Then, binder-free electrodes were shaped avoiding the presence of cracks and other defects after sintering.

The inclusion of Ni nanospheres on the NiO/Ni electrode microstructure increases the specific capacitance from 250 (reference NiO coating onto Ni foam) to 755 F/g, which is more than three times the results for simple NiO nanoplatelets used as electroactive material. This improvement of the electrochemical performance is attributed to the presence of the metallic Ni nanoparticles in the microstructure which favors the electron transport through the semiconductor microstructure, leading to a lower R_{ct} (1.55 Ω). Moreover, the NiO/Ni electrode maintains a high capacitive response with $CPE-p = 0.90$, $\Phi_{max} = 0.81^\circ$ and a relaxation time, τ_0 , of 11 ms.

The optimization of the sintering process of NiO/Ni electrodes also influences the decrease in R_{ct} . A thermal treatment of 325°C during 1h in Ar atmosphere leads to a well-connected and consolidated NiO/Ni nanostructure, which is also well adhered to the Ni foam collector. The optimized thermal treatment results in a higher electrochemical performance, since it favors the electronic conduction through the ceramic semiconductor microstructure.

RGO/NiO nanostructures were provided throughout a heterocoagulation colloidal process. The full-covering of RGO nanosheets by NiO nanoplatelets is achieved by mixing both powders dispersed and stabilized in an aqueous suspension with a different charge by using a ligant: a branched polyethyleneimine with a high molecular weight. Core-shell nanostructures were achieved for a ratio of 20_[NiO]:1_[RGO]. The developed colloidal methodology to shape core-shell nanostructures could be applied to other carbonaceous materials and ceramic semiconductors.

It is remarkable the synergistic effect of RGO and NiO resulting in a superior electrochemical performance of the hybrid electrode due to the enhanced capacitance and the reduction of the R_{ct} value. The specific capacitance value of the homogeneous and thinner RGO/NiO electrode (~1 mg of coating of Ni foam) was 920 F/g at a current density of 2 A/g, which is more than three times the capacitance measured of the bare-NiO electrode shaped under similar EPD conditions. The intercalation of the RGO nanosheets among the NiO nanostructure reduces the R_{ct} from 1.71 to 1.13 Ω , while the capacity behavior is farer from the ideal ($CPE-p = 0.75$ and $\Phi_{max} = 70.4$) but the relaxation time is really low ($\tau_0 = 4$ ms). Moreover charge/discharge curves evidences

that the electrochemical performance of the hybrid electrodes is governed by the pseudocapacitive contribution provided by the well consolidated ceramic semiconductor nanostructure, showing a capacitance retention of 71% after 1000 cycles.

Ni(OH)₂ nanoplatelets modified by the adsorption of 1, 3 and 5 Layer-by-Layer organic shells were employed to manipulate the microstructure of the simple NiO-based EPD coatings. The layer-by-layer (LbL) strategy consists in the alternative adsorption of cationic and anionic layers of polyelectrolytes. The increase of the number of layers at the shell structure alters the hydrodynamics of the system and promotes fully nanoplatelets disorder during the deposition, resulting in an extremely open microstructure even under the reported smooth EPD conditions.

The adhesion of the film to the substrate as well as the own cohesion among the nanoplatelets, depend on the manipulation of the ionization and conformation of the surface modifiers at the organic corona of the organic-inorganic core-shell system. The manipulation of the stability conditions promotes the decrement of the inter-particles forces and leads to the electro-hydrodynamic forces govern the nanoparticles arrangement. In this way, the 2D nanostructures lay parallel to the substrate surface for the 1LbL core-shells, while they stack forming agglomerates and deposit perpendicularly to the electrode in the case of the 5LbL system.

After the sintering process, NiO-5LbL coatings exhibited a well-consolidated, interconnected and open microstructure with a larger microporosity in the range of 2–5 nm and a moderated mesoporosity of 30–100 nm. This extremely open porous microstructure results in a specific capacitance value of 982 F/g. However, due to the weakness of the porous microstructure this value decreases until 650 F/g after 1000 cycles (60% of capacitance retention). Moreover, the benefits of the exposed surface and porosity increase in the NiO-5LbL electrode strengthen the capacitive contribution of the electrochemical response ($CPE-p = 0.90$ and $\Phi_{max} = 0.82^\circ$) and τ_0 of 18 ms, in spite of the significant increase of R_{ct} value (3.65 Ω).

1. EIA Today energy in detail Available online:
<https://www.eia.gov/todayinenergy/detail.php?id=32972>.
2. EIA Renewable Energy Explained Available online:
<https://www.eia.gov/energyexplained/?page=renewable>.
3. American Experiment; Peter, F. Another report reluctantly-admits green energy disastrous flop Available online: <https://www.americanexperiment.org/2019/01/peter-foster-another-report-reluctantly-admits-green-energy-disastrous-flop/>.
4. Acciona Climate change Available online: <https://www.acciona.com/climate-change/>.
5. BP Review of world renewable-energy.
6. Cabanas-polo, S.; Gonzalez, Z.; Sanchez-herencia, A.J.; Ferrari, B.; Caballero, A. Cyclability of binder-free β -Ni(OH)₂ anodes shaped by EPD for Li-ion batteries. *J. Eur. Ceram. Soc.* **2015**, *35*, 573–584.
7. Gonzalez, Z.; Ferrari, B.; Sanchez-Herencia, A.J.; Caballero, A.; Morales, J. Relevance of the Semiconductor Microstructure in the Pseudocapacitance of the Electrodes Fabricated by EPD of Binder-Free β -Ni(OH)₂ Nanoplatelets. *J. Electrochem. Soc.* **2015**, *162*, D3001–D3012.
8. Gonzalez, Z.; Yus, J.; Caballero, A.; Morales, J.; Sanchez-Herencia, A.J.; Ferrari, B. Electrochemical performance of pseudo-capacitor electrodes fabricated by Electrophoretic Deposition inducing Ni(OH)₂ nanoplatelets agglomeration by Layer-by-Layer. *Electrochim. Acta* **2017**, *247*.
9. Gonzalez, Z.; Yus, J.; Caballero, A.; Morales, J.; Sanchez-Herencia, A.J.; Ferrari, B. Electrochemical performance of pseudo-capacitor electrodes fabricated by Electrophoretic Deposition inducing Ni(OH)₂ nanoplatelets agglomeration by Layer-by-Layer. *Electrochim. Acta* **2017**, *247*, 333–343.
10. Gonzalez, Z.; Filiatre, C.; Buron, C.C.; Sanchez-Herencia, A.J.; Ferrari, B. Electrophoretic Deposition of Ni(OH)₂ Nanoplatelets Modified by Polyelectrolyte Multilayers: Study of the Coatings Formation in a Laminar Flow Cell. *J. Electrochem. Soc.* **2017**, *164*, D436–D444.
11. Gonzalez, Z.; Ferrari, B.; Sanchez-Herencia, A.J.; Caballero, A.; Morales, J. Use of Polyelectrolytes for the Fabrication of Porous NiO Films by Electrophoretic Deposition for Supercapacitor Electrodes. *Electrochim. Acta* **2016**, *211*, 110–118.
12. Yus, J.; Chinarro, E.; Ferrari, B.; González, Z. The effect of the substrate on the conductivity of NiO electrodes in electrochemical capacitor shaped by electrophoretic deposition. In Proceedings of the ECS Transactions; 2018; Vol. 82.
13. Zhao, J.; Liu, H.; Zhang, Q. Applied Surface Science Preparation of NiO nanoflakes under different calcination temperatures and their supercapacitive and optical properties. *Appl. Surf. Sci.* **2017**, *392*, 1097–1106.

Bibliography

14. Jeong, G.H.; Baek, S.; Lee, S.; Kim, S.W. Metal Oxide/Graphene Composites for Supercapacitive Electrode Materials. *Chem. - An Asian J.* **2016**, *11*, 949–964.
15. Wang, G.; Zhang, L.; Zhang, J. A review of electrode materials for electrochemical supercapacitors. *Chem. Soc. Rev.* **2012**, *41*, 797–828.
16. Żółek-Tryznowska, Z. Additives for Ink Manufacture. In *Printing on Polymers*; Izdebska, J., Thomas, S., Eds.; William Andrew Publishing, 2016; pp. 57–66 ISBN 978-0-323-37468-2.
17. McManus, D.; Vranic, S.; Withers, F.; Sanchez-Romaguera, V.; Macucci, M.; Yang, H.; Sorrentino, R.; Parvez, K.; Son, S.-K.; Iannaccone, G.; et al. Water-based and biocompatible 2D crystal inks for all-inkjet-printed heterostructures. *Nat. Nanotechnol.* **2017**, *12*, 343–350.
18. Ferrari, G.; Zannini, P. VOCs monitoring of new materials for ceramic tiles decoration: GC-MS analysis of emissions from common vehicles and inkjet inks during firing in laboratory. *Bol. la Soc. Esp. Ceram. y Vidr.* **2017**, *56*, 226–236.
19. Cherrington, R.; Hughes, D.J.; Senthilarasu, S.; Goodship, V. Inkjet-Printed TiO₂ Nanoparticles from Aqueous Solutions for Dye-Sensitized Solar Cells (DSSCs). *Energy Technol.* **2015**, *3*, 866–870.
20. Derby, B. Additive Manufacture of Ceramics Components by Inkjet Printing. *Engineering* **2015**, *1*, 113–123.
21. Friederich, A.; Kohler, C.; Nikfalazar, M.; Wiens, A.; Sazegar, M.; Jakoby, R.; Bauer, W.; Binder, J.R. Microstructure and microwave properties of inkjet printed barium strontium titanate thick-films for tunable microwave devices. **2014**, *34*, 2925–2932.
22. Kouchachvili, L.; Yaïci, W.; Entchev, E. Hybrid battery/supercapacitor energy storage system for the electric vehicles. *J. Power Sources* **2018**, *374*, 237–248.
23. Zhou, K.; Zhou, W.; Yang, L.; Lu, J.; Cheng, S.; Mai, W.; Tang, Z.; Li, L.; Chen, S. Ultrahigh-Performance Pseudocapacitor Electrodes Based on Transition Metal Phosphide Nanosheets Array via Phosphorization: A General and Effective Approach. *Adv. Funct. Mater.* **2015**, *25*, 7530–7538.
24. Ren, Z.; Li, J.; Ren, Y.; Wang, S.; Qiu, Y.; Yu, J. Large-scale synthesis of hybrid metal oxides through metal redox mechanism for high-performance pseudocapacitors. *Sci. Rep.* **2016**, *6*, 20021.
25. Chen, K.; Xue, D. In situ electrochemical activation of Ni-based colloids from an NiCl₂ electrode and their advanced energy storage performance. *Nanoscale* **2016**, *8*, 17090–17095.
26. Maiti, S.; Pramanik, A.; Mahanty, S. Electrochemical energy storage in Mn₂O₃ porous nanobars derived from morphology-conserved transformation of benzenetricarboxylate-bridged metal-organic framework. *CrystEngComm* **2016**, *18*, 450–461.
27. Zhang, H.; Wang, X.; Chen, C.; An, C.; Xu, Y.; Dong, Y.; Zhang, Q.; Wang, Y.; Jiao, L.; Yuan, H. Facile synthesis of diverse transition metal oxide nanoparticles and electrochemical properties.

- Inorg. Chem. Front.* **2016**, *3*, 1048–1057.
28. Lu, X.; Wang, C.; Favier, F.; Pinna, N. Electrospun Nanomaterials for Supercapacitor Electrodes : Designed Architectures and Electrochemical Performance. *Adv. Energy Mater.* **2016**, *7*, 1–43.
 29. Sk, M.M.; Yue, C.Y.; Ghosh, K.; Jena, R.K. Review on advances in porous nanostructured nickel oxides and their composite electrodes for high-performance supercapacitors. *J. Power Sources* **2016**, *308*, 121–140.
 30. Kim, B.K.; Sy, S.; Yu, A.; Zhang, J. Electrochemical Supercapacitors for Energy Storage and Conversion. *Handb. Clean Energy Syst.* **2015**, 1–25.
 31. González, A.; Goikolea, E.; Barrena, J.A.; Mysyk, R. Review on supercapacitors: Technologies and materials. *Renew. Sustain. Energy Rev.* **2016**, *58*, 1189–1206.
 32. West, A.R. *Solid State Chemistry and its applications*; Wiley, Ed.; Second.; Wiley: Sheffield UK, 2014; ISBN 978-1-119-94294-8.
 33. Lany, S. Semiconducting transition metal oxides. *J. Phys. Condens. Matter* **2015**, *27*, 283203.
 34. Janotti, A.; Van De Walle, C.G. Fundamentals of zinc oxide as a semiconductor. *Reports Prog. Phys.* **2009**, *72*.
 35. Reynolds, N.D.; Panda, C.D.; Essick, J.M. Capacitance-voltage profiling : Research-grade approach versus low-cost alternatives. **2014**, 97202, 196–205.
 36. Hu, C.; Lin, Y.; Connell, J.W.; Cheng, H.M.; Gogotsi, Y.; Titirici, M.M.; Dai, L. Carbon-Based Metal-Free Catalysts for Energy Storage and Environmental Remediation. *Adv. Mater.* **2019**, *1806128*, 1–14.
 37. Kumar, Y.; Rawal, S.; Joshi, B.; Hashmi, S.A. Background, fundamental understanding and progress in electrochemical capacitors. *J. Solid State Electrochem.* **2019**, *23*, 667–692.
 38. Muzaffar, A.; Ahamed, M.B.; Deshmukh, K.; Thirumalai, J. A review on recent advances in hybrid supercapacitors: Design, fabrication and applications. *Renew. Sustain. Energy Rev.* **2019**, *101*, 123–145.
 39. Xie, J.; Yang, P.; Wang, Y.; Qi, T.; Lei, Y.; Li, C.M. Puzzles and confusions in supercapacitor and battery: Theory and solutions. *J. Power Sources* **2018**, *401*, 213–223.
 40. Espinoza-Acosta, J.L.; Torres-Chávez, P.I.; Olmedo-Martínez, J.L.; Vega-Rios, A.; Flores-Gallardo, S.; Zaragoza-Contreras, E.A. Lignin in storage and renewable energy applications: A review. *J. Energy Chem.* **2018**, *27*, 1422–1438.
 41. Ding, J.; Hu, W.; Paek, E.; Mitlin, D. Review of Hybrid Ion Capacitors: From Aqueous to Lithium to Sodium. *Chem. Rev.* **2018**, *118*, 6457–6498.
 42. Yu, X.; Yun, S.; Yeon, J.S.; Bhattacharya, P.; Wang, L.; Lee, S.W.; Hu, X.; Park, H.S. Emergent

Bibliography

- Pseudocapacitance of 2D Nanomaterials. *Adv. Energy Mater.* **2018**, 8, 1–33.
43. Lin, Z.; Goikolea, E.; Balducci, A.; Naoi, K.; Taberna, P.L.; Salanne, M.; Yushin, G.; Simon, P. Materials for supercapacitors: When Li-ion battery power is not enough. *Mater. Today* **2018**, 21, 419–436.
44. Gogotsi, Y.; Penner, R.M. Energy Storage in Nanomaterials – Capacitive, Pseudocapacitive, or Battery-like? *ACS Nano* **2018**, 12, 2081–2083.
45. Kate, R.S.; Khalate, S.A.; Deokate, R.J. Overview of nanostructured metal oxides and pure nickel oxide (NiO) electrodes for supercapacitors: A review. *J. Alloys Compd.* **2018**, 734, 89–111.
46. Shi, X.; Zheng, S.; Wu, Z.S.; Bao, X. Recent advances of graphene-based materials for high-performance and new-concept supercapacitors. *J. Energy Chem.* **2018**, 27, 25–42.
47. Kang, J.; Zhang, S.; Zhang, Z. Three-Dimensional Binder-Free Nanoarchitectures for Advanced Pseudocapacitors. *Adv. Mater.* **2017**, 29, 1–12.
48. Liu, M.; Su, B.; Tang, Y.; Jiang, X.; Yu, A. Recent advances in nanostructured vanadium oxides and composites for energy conversion. *Adv. Energy Mater.* **2017**, 7, 1–34.
49. Xu, J.; Zhang, J.; Zhang, W.; Lee, C.S. Interlayer nanoarchitectonics of two-dimensional transition-metal dichalcogenides nanosheets for energy storage and conversion applications. *Adv. Energy Mater.* **2017**, 7, 1–30.
50. Eftekhari, A.; Mohamedi, M. Tailoring pseudocapacitive materials from a mechanistic perspective. *Mater. Today Energy* **2017**, 6, 211–229.
51. Bae, J.; Kwon, O.S.; Lee, C.-S. Energy Efficient Graphene Based High Performance Capacitors. *Recent Pat. Nanotechnol.* **2017**, 11, 2019.
52. Su, X.; Hatton, T.A. Redox-electrodes for selective electrochemical separations. *Adv. Colloid Interface Sci.* **2017**, 244, 6–20.
53. Chen, X.; Paul, R.; Dai, L. Carbon-based supercapacitors for efficient energy storage. *Natl. Sci. Rev.* **2017**, 4, 453–489.
54. Le, T.H.; Kim, Y.; Yoon, H. Electrical and electrochemical properties of conducting polymers. *Polymers (Basel)*. **2017**, 9.
55. Wang, J.; Dong, S.; Ding, B.; Wang, Y.; Hao, X.; Dou, H.; Xia, Y.; Zhang, X. Pseudocapacitive materials for electrochemical capacitors: From rational synthesis to capacitance optimization. *Natl. Sci. Rev.* **2017**, 4, 71–90.
56. Wu, Z.; Zhang, X.B. Design and preparation of electrode materials for supercapacitors with high specific capacitance. *Wuli Huaxue Xuebao/Acta Phys. - Chim. Sin.* **2017**, 33, 305–313.
57. Yan, Y.; Li, B.; Guo, W.; Pang, H.; Xue, H. Vanadium based materials as electrode materials for

- high performance supercapacitors. *J. Power Sources* **2016**, 329, 148–169.
58. Bryan, A.M.; Santino, L.M.; Lu, Y.; Acharya, S.; D'Arcy, J.M. Conducting Polymers for Pseudocapacitive Energy Storage. *Chem. Mater.* **2016**, 28, 5989–5998.
 59. Simotwo, S.K.; Kalra, V. Polyaniline-based electrodes: recent application in supercapacitors and next generation rechargeable batteries. *Curr. Opin. Chem. Eng.* **2016**, 13, 150–160.
 60. Son, E.J.; Kim, J.H.; Kim, K.; Park, C.B. Quinone and its derivatives for energy harvesting and storage materials. *J. Mater. Chem. A* **2016**, 4, 11179–11202.
 61. Lim, E.; Jo, C.; Lee, J. A mini review of designed mesoporous materials for energy-storage applications: from electric double-layer capacitors to hybrid supercapacitors. *Nanoscale* **2016**, 8, 7827–7833.
 62. Ike, I.S.; Sigalas, I.; Iyuke, S. Understanding performance limitation and suppression of leakage current or self-discharge in electrochemical capacitors: a review. *Phys. Chem. Chem. Phys.* **2016**, 18, 661–680.
 63. Zhong, C.; Deng, Y.; Hu, W.; Qiao, J.; Zhang, L.; Zhang, J. A review of electrolyte materials and compositions for electrochemical supercapacitors. *Chem. Soc. Rev.* **2015**, 44, 7484–7539.
 64. Huang, M.; Li, F.; Dong, F.; Zhang, Y.X.; Zhang, L.L. MnO₂-based nanostructures for high-performance supercapacitors. *J. Mater. Chem. A* **2015**, 3, 21380–21423.
 65. Chen, K.; Xue, D. Rare earth and transitional metal colloidal supercapacitors. *Sci. China Technol. Sci.* **2015**, 58, 1768–1778.
 66. Choi, H.; Yoon, H. Nanostructured Electrode Materials for Electrochemical Capacitor Applications. *Nanomaterials* **2015**, 5, 906–936.
 67. Hu, X.; Zhang, W.; Liu, X.; Mei, Y.; Huang, Y. Nanostructured Mo-based electrode materials for electrochemical energy storage. *Chem. Soc. Rev.* **2015**, 44, 2376–2404.
 68. Zhang, K.; Han, X.; Hu, Z.; Zhang, X.; Tao, Z.; Chen, J. Nanostructured Mn-based oxides for electrochemical energy storage and conversion. *Chem. Soc. Rev.* **2015**, 44, 699–728.
 69. Chang, S.-K.; Zainal, Z.; Tan, K.-B.; Yusof, N.A.; Wan Yusoff, W.M.D.; Prabakaran, S.R.S. Recent development in spinel cobaltites for supercapacitor application. *Ceram. Int.* **2015**, 41, 1–14.
 70. Feng, L.; Zhu, Y.; Ding, H.; Ni, C. Recent progress in nickel based materials for high performance pseudocapacitor electrodes. *J. Power Sources* **2014**, 267, 430–444.
 71. Mai, L.; Tian, X.; Xu, X.; Chang, L.; Xu, L. Nanowire Electrodes for Electrochemical Energy Storage Devices. *Chem. Rev.* **2014**, 114, 11828–11862.
 72. Faraji, S.; Ani, F.N. Microwave-assisted synthesis of metal oxide/hydroxide composite electrodes for high power supercapacitors – A review. *J. Power Sources* **2014**, 263, 338–360.

Bibliography

73. Chen, K.; Xue, D. Cu-based materials as high-performance electrodes toward electrochemical energy storage. *Funct. Mater. Lett.* **2014**, *7*.
74. Mike, J.F.; Lutkenhaus, J.L. Recent advances in conjugated polymer energy storage. *J. Polym. Sci. Part B Polym. Phys.* **2013**, *51*, 468–480.
75. Chen, S.; He, S.; Hou, H. Electrospinning technology for applications in supercapacitors. *Curr. Org. Chem.* **2013**, *17*, 1402–1410.
76. Simon, P.; Gogotsi, Y. Materials for electrochemical capacitors. *Nat. Mater.* **2008**, *7*, 845–854.
77. Yu. M. Vol'fkovich and T. M. Serdyuk Electrochemical Capacitors. *Russ. J. Electrochem.* **2002**, *38*, 935–958.
78. Feng, F.; Zhao, S.; Liu, R.; Yang, Z.; Shen, Q. NiO Flowerlike porous hollow nanostructures with an enhanced interfacial storage capability for battery-to-pseudocapacitor transition. *Electrochim. Acta* **2016**, *222*, 1160–1168.
79. Buqa, H.; Goers, D.; Holzapfel, M.; Spahr, M.E.; Novák, P. High Rate Capability of Graphite Negative Electrodes for Lithium-Ion Batteries. *J. Electrochem. Soc.* **2005**, *152*, A474.
80. Tomboc, G.M.; Jadhav, H.S.; Kim, H. PVP assisted morphology-controlled synthesis of hierarchical mesoporous ZnCo₂O₄ nanoparticles for high-performance pseudocapacitor. *Chem. Eng. J.* **2017**, *308*, 202–213.
81. Liang, D. b; Wu, S.; Liu, J.; Tian, Z.; Liang, C. Co-doped Ni hydroxide and oxide nanosheet networks: Laser-assisted synthesis, effective doping, and ultrahigh pseudocapacitor performance. *J. Mater. Chem. A* **2016**, *4*, 10609–10617.
82. Ju, Y.T.; Cho, M.Y.; Park, S. min; Beack, S.H.; Lee, C.T.; Roh, K.C. Two-dimensional cobalt-based composites grown on Ti plates for application as pseudocapacitor materials. *Electron. Mater. Lett.* **2013**, *9*, 531–534.
83. Xia, X.; Zhu, C.; Luo, J.; Zeng, Z.; Guan, C.; Ng, C.F.; Zhang, H.; Fan, H.J. Synthesis of free-standing metal sulfide nanoarrays via anion exchange reaction and their electrochemical energy storage application. *Small* **2014**, *10*.
84. Mahajan, H.; Bae, J.; Yun, K. Facile synthesis of ZnO-Au nanocomposites for high-performance supercapacitors. *J. Alloys Compd.* **2018**, *758*, 131–139.
85. Zhang, C.; Xie, Y.; Zhao, M.; Pentecost, A.E.; Ling, Z.; Wang, J.; Long, D.; Ling, L.; Qiao, W. Enhanced Electrochemical Performance of Hydrous RuO₂/Mesoporous Carbon Nanocomposites via Nitrogen Doping. *ACS Appl. Mater. Interfaces* **2014**, *6*, 9751–9759.
86. Vellacheri, R.; Pillai, V.K.; Kurungot, S. Hydrous RuO₂-carbon nanofiber electrodes with high mass and electrode-specific capacitance for efficient energy storage. *Nanoscale* **2012**, *4*, 890–896.
87. Lv, Q.; Wang, S.; Sun, H.; Luo, J.; Xiao, J.; Xiao, J.; Xiao, F.; Wang, S. Solid-State Thin-Film

- Supercapacitors with Ultrafast Charge/Discharge Based on N-Doped-Carbon-Tubes/Au-Nanoparticles-Doped-MnO₂ Nanocomposites. *Nano Lett.* **2016**, *16*, 40–47.
88. Liu, X.Y.; Gao, Y.Q.; Yang, G.W. A flexible, transparent and super-long-life supercapacitor based on ultrafine Co₃O₄ nanocrystal electrodes. *Nanoscale* **2016**, *8*, 4227–4235.
 89. Maiti, S.; Pramanik, A.; Mahanty, S. Interconnected network of MnO₂ nanowires with a “cocoonlike” morphology: Redox couple-mediated performance enhancement in symmetric aqueous supercapacitor. *ACS Appl. Mater. Interfaces* **2014**, *6*, 10754–10762.
 90. Qiu, Y.; Zhao, Y.; Yang, X.; Li, W.; Wei, Z.; Xiao, J.; Leung, S.-F.; Lin, Q.; Wu, H.; Zhang, Y.; et al. Three-dimensional metal/oxide nanocone arrays for high-performance electrochemical pseudocapacitors. *Nanoscale* **2014**, *6*, 3626–31.
 91. Ghosh, A.; Ra, E.J.; Jin, M.; Jeong, H.K.; Kim, T.H.; Biswas, C.; Lee, Y.H. High pseudocapacitance from ultrathin V₂O₅ films electrodeposited on self-standing carbon-nanofiber paper. *Adv. Funct. Mater.* **2011**, *21*, 2541–2547.
 92. Chen, K.; Xue, D. Crystallisation of cuprous oxide. *Int. J. Nanotechnol.* **2013**, *10*, 4.
 93. Anderson, K.-C.L. and M.A. Porous Nickel Oxide/Nickel Films for Electrochemical Capacitors. *J. Electrochem. Soc.* **1996**, *143*, 124–130.
 94. Yan, H.; Zhang, D.; Xu, J.; Lu, Y.; Liu, Y.; Qiu, K.; Zhang, Y. Solution growth of NiO nanosheets supported on Ni foam as high-performance electrodes for supercapacitors. *Nano Res. Lett.* **2014**, *9*, 424.
 95. Zhou, Y.; Mao, Z.; Wang, W.; Yang, Z.; Liu, X. In-Situ Fabrication of Graphene Oxide Hybrid Ni-Based Metal – Organic Framework (Ni – MOFs @ GO) with Ultrahigh Capacitance as Electrochemical Pseudocapacitor Materials. **2016**.
 96. Cha, S.M.; Nagaraju, G.; Yu, J.S. Controlled Electrochemical Synthesis of Nickel Hydroxide Nanosheets Grown on Non-woven Cu/PET Fibers: A Robust, Flexible, and Binder-Free Electrode for High-Performance Pseudocapacitors. **2016**.
 97. Yeager, M.; Du, W.; Si, R.; Su, D.; Marinkovic, N.; Teng, X. Highly Efficient K^{0.15} MnO₂ Birnessite Nanosheets for Stable Pseudocapacitive Cathodes. *J. Phys. Chem. C* **2012**.
 98. Wang, Y.; Gai, S.; Li, C.; He, F.; Zhang, M.; Yan, Y.; Yang, P. Controlled synthesis and enhanced supercapacitor performance of uniform pompon-like β-Ni(OH)₂ hollow microspheres. *Electrochim. Acta* **2013**, *90*, 673–681.
 99. Wang, Y.; Shen, C.; Niu, L.; Sun, Z.; Ruan, F.; Xu, M.; Shan, S.; Li, C.; Liu, X.; Gong, Y. High rate capability of mesoporous NiWO₄ @ CoWO₄ nanocomposite as a positive material for hybrid supercapacitor. *Mater. Chem. Phys.* **2016**, *182*, 1–8.
 100. Yang, Z.; Xu, F.; Zhang, W.; Mei, Z.; Pei, B.; Zhu, X. Controllable preparation of multishelled NiO

Bibliography

- hollow nanospheres via layer-by-layer self-assembly for supercapacitor application. *J. Power Sources* **2014**, *246*, 24–31.
101. Abbas, S.A.; Jung, K.D. Preparation of mesoporous microspheres of NiO with high surface area and analysis on their pseudocapacitive behavior. *Electrochim. Acta* **2016**, *193*, 145–153.
102. Zhang, Z.; Gao, Q.; Gao, H.; Shi, Z.; Wu, J.; Zhi, M.; Hong, Z. Nickel oxide aerogel for high performance supercapacitor electrodes. *RSC Adv.* **2016**, *6*.
103. Hareendrakrishnakumar, H.; Chulliyote, R.; Joseph, M.G. Effect of crystallite size on the intercalation pseudocapacitance of lithium nickel vanadate in aqueous electrolyte. *J. Solid State Electrochem.* **2018**, *22*, 1–9.
104. Li, X.; Wang, L.; Shi, J.; Du, N.; He, G. Multishelled Nickel-Cobalt Oxide Hollow Microspheres with Optimized Compositions and Shell Porosity for High-Performance Pseudocapacitors. *ACS Appl. Mater. Interfaces* **2016**, *8*, 17276–17283.
105. Pu, J.; Liu, Z.; Ma, Z.; Wang, J.; Zhang, L.; Chang, S.; Wu, W.; Shen, Z.; Zhang, H. Structure design of NiCo₂O₄ electrodes for high performance pseudocapacitors and lithium-ion batteries. *J. Mater. Chem. A* **2016**, *4*, 1–3.
106. Yang, B.; Yu, L.; Yan, H.; Sun, Y.; Liu, Q.; Liu, J.; Song, D.; Hu, S.; Yuan, Y.; Liu, L.; et al. Fabrication of urchin-like NiCo₂(CO₃)(1.5)(OH)(3)@NiCo₂S₄ on Ni foam by an ion-exchange route and application to asymmetrical supercapacitors. *J. Mater. Chem. A* **2015**, *3*, 13308–13316.
107. Yeager, M.P.; Su, D.; Marinković, N.S.; Teng, X. Pseudocapacitive NiO fine nanoparticles for supercapacitor reactions. *J. Electrochem. Soc.* **2012**, *159*.
108. Kurra, N.; Alhebshi, N.A.; Alshareef, H.N. Microfabricated pseudocapacitors using Ni(OH)₂ electrodes exhibit remarkable volumetric capacitance and energy density. *Adv. Energy Mater.* **2015**, *5*, 1–9.
109. Cai, G.; Wang, X.; Cui, M.; Darmawan, P.; Wang, J.; Eh, A.L.-S.; Lee, P.S. Electrochromo-supercapacitor based on direct growth of NiO nanoparticles. *Nano Energy* **2015**, *12*.
110. Chuminjak, Y.; Daothong, S.; Reanpang, P.; Mensing, J.P.; Phokharatkul, D.; Jakmunee, J.; Wisitsoraat, A.; Tuantranont, A.; Singjai, P. Electrochemical energy-storage performances of nickel oxide films prepared by a sparking method. *RSC Adv.* **2015**, *5*.
111. Chuminjak, Y.; Daothong, S.; Kuntarug, A.; Phokharatkul, D.; Horprathum, M.; Wisitsoraat, A.; Tuantranont, A.; Jakmunee, J.; Singjai, P. High-performance Electrochemical Energy Storage Electrodes Based on Nickel Oxide-coated Nickel Foam Prepared by Sparking Method. *Electrochim. Acta* **2017**, *238*, 298–309.
112. Xu, Y.; Dong, Y.; Han, X.; Wang, X.; Wang, Y.; Jiao, L.; Yuan, H. Application for simply recovered LiCoO₂ material as a high-performance candidate for supercapacitor in aqueous system. *ACS Sustain. Chem. Eng.* **2015**, *3*, 2435–2442.

113. Pan, Z.; Jiang, Y.; Yang, P.; Wu, Z.; Tian, W.; Liu, L.; Song, Y.; Gu, Q.; Sun, D.; Hu, L. In Situ Growth of Layered Bimetallic ZnCo Hydroxide Nanosheets for High-Performance All-Solid-State Pseudocapacitor. *ACS Nano* **2018**, *12*, 2968–2979.
114. Chen, L.Y.; Hou, Y.; Kang, J.L.; Hirata, A.; Chen, M.W. Asymmetric metal oxide pseudocapacitors advanced by three-dimensional nanoporous metal electrodes. *J. Mater. Chem. A* **2014**, *2*, 8448.
115. Wang, Z.; Zhao, Z.; Zhang, Y.; Pang, G.; Sun, X.; Zhang, J.; Hou, L.; Yuan, C. Hierarchical flower-like conductive CoNiO₂ microspheres constructed with ultrathin mesoporous nanosheets towards long-cycle-life hybrid supercapacitors. *J. Alloys Compd.* **2019**, *779*, 81–90.
116. Zhan, C.; Jiang, D.-E. Understanding the pseudocapacitance of RuO₂ from joint density functional theory. *J. Phys. Condens. Matter* **2016**, *28*.
117. Seok, J.Y.; Lee, J.; Yang, M. Self-Generated Nanoporous Silver Framework for High-Performance Iron Oxide Pseudocapacitor Anodes. *ACS Appl. Mater. Interfaces* **2018**, *10*, 17223–17231.
118. Kwon, J.M.; Kim, J.H.; Kang, S.H.; Choi, C.J.; Rajesh, J.A.; Ahn, K.S. Facile hydrothermal synthesis of cubic spinel AB₂O₄ type MnFe₂O₄ nanocrystallites and their electrochemical performance. *Appl. Surf. Sci.* **2017**, *413*, 83–91.
119. Qiu, M.; Sun, P.; Shen, L.; Wang, K.; Song, S.; Yu, X.; Tan, S.; Zhao, C.; Mai, W. WO₃ nanoflowers with excellent pseudo-capacitive performance and the capacitance contribution analysis. *J. Mater. Chem. A* **2016**, *4*, 7266–7273.
120. Xu, C.; Liao, J.; Wang, R.; Zou, P.; Wang, R.; Kang, F.; Yang, C. MoO₃ @Ni nanowire array hierarchical anode for high capacity and superior longevity all-metal-oxide asymmetric supercapacitors. *RSC Adv.* **2016**, *6*, 110112–110119.
121. Manikandan, R.; Raj, C.J.; Rajesh, M.; Kim, B.C.; Sim, J.Y.; Yu, K.H. Electrochemical Behaviour of Lithium, Sodium and Potassium Ion Electrolytes in a Na_{0.33}V₂O₅ Symmetric Pseudocapacitor with High Performance and High Cyclic Stability. *ChemElectroChem* **2018**, *5*, 101–111.
122. Ray, A.; Roy, A.; Sadhukhan, P.; Chowdhury, S.R.; Maji, P.; Bhattacharya, S.K.; Das, S. Electrochemical properties of TiO₂-V₂O₅ nanocomposites as a high performance supercapacitors electrode material. *Appl. Surf. Sci.* **2018**, *443*, 581–591.
123. Yang, Y.; Ren, S.; Song, X.; Guo, Y.; Si, D.; Jing, H.; Ma, S.; Hao, C.; Ji, M. Sn@SnO₂ attached on carbon spheres as additive-free electrode for high-performance pseudocapacitor. *Electrochim. Acta* **2016**, *209*, 350–359.
124. Maiti, S.; Pramanik, A.; Mahanty, S. Extraordinarily high pseudocapacitance of metal organic framework derived nanostructured cerium oxide. *Chem. Commun.* **2014**, *50*.
125. Xu, J.; Wang, C.; Liu, J.; Xu, S.; Zhang, W.; Lu, Y. Facile fabrication of a novel nanoporous Au / AgO composite for electrochemical double-layer capacitor. *RSC Adv.* **2015**, *5*, 38995–39002.

Bibliography

126. Tiwari, J.N.; Tiwari, R.N.; Kim, K.S. Zero-dimensional, one-dimensional, two-dimensional and three-dimensional nanostructured materials for advanced electrochemical energy devices. *Prog. Mater. Sci.* **2012**, *57*, 724–803.
127. Pasquarelli, R.M.; Ginley, D.S.; O'Hayre, R. Solution processing of transparent conductors: from flask to film. *Chem. Soc. Rev.* **2011**, *40*, 5406.
128. Cabañas-Polo, S.; Gonzalez, Z.; Ferrari, B. Influence of ultrasound on the instantaneous synthesis of tridimensional α -Ni(OH)₂ nanostructures and derived NiO nanoparticles. *CrystEngComm* **2015**, *17*, 6193–6206.
129. Cabanas-Polo, S.; Suslick, K.S.; Sanchez-Herencia, A.J. Effect of reaction conditions on size and morphology of ultrasonically prepared Ni(OH)₂ powders. *Ultrason. Sonochem.* **2011**, *18*, 901–906.
130. Mefford, J.T.; Hardin, W.G.; Dai, S.; Johnston, K.P.; Stevenson, K.J. Anion charge storage through oxygen intercalation in LaMnO₃ perovskite pseudocapacitor electrodes. *Nat. Mater.* **2014**, *13*, 726–32.
131. Sahoo, R.; Roy, A.; Dutta, S.; Ray, C.; Aditya, T.; Pal, A.; Pal, T. Liquor ammonia mediated V (v) insertion in thin Co₃O₄ sheets for improved pseudocapacitors with high energy density and high specific capacitance value. *Chem. Commun.* **2015**, *51*, 15986–15989.
132. Bhujun, B.; Anandan, S.; Tan, M.T.T. Study of ternary metal oxides as supercapacitor electrodes. *WIT Trans. Ecol. Environ.* **2014**, *186*.
133. Das, D.; Bagchi, B.; Basu, R.N. Nanostructured zirconia thin film fabricated by electrophoretic deposition technique. *J. Alloys Compd.* **2017**, *693*, 1220–1230.
134. Hu, C.C.; Huang, C.M.; Chang, K.H. Anodic deposition of porous vanadium oxide network with high power characteristics for pseudocapacitors. *J. Power Sources* **2008**, *185*, 1594–1597.
135. Xia, C.; Chen, W.; Wang, X.; Hedhili, M.N.; Wei, N.; Alshareef, H.N. Highly stable supercapacitors with conducting polymer core-shell electrodes for energy storage applications. *Adv. Energy Mater.* **2015**, *5*.
136. Zheng, Z.; Huang, B.; Qin, X.; Zhang, X.; Dai, Y.; Whangbo, M.-H. Facile in situ synthesis of visible-light plasmonic photocatalysts M@TiO₂ (M = Au, Pt, Ag) and evaluation of their photocatalytic oxidation of benzene to phenol. *J. Mater. Chem.* **2011**, *21*, 9079.
137. Wu, H.; Li, D.; Zhu, X.; Yang, C.; Liu, D.; Chen, X.; Song, Y.; Lu, L. High-performance and renewable supercapacitors based on TiO₂ nanotube array electrodes treated by an electrochemical doping approach. *Electrochim. Acta* **2014**, *116*, 129–136.
138. Lu, Z.; Chang, Z.; Liu, J.; Sun, X. Stable ultrahigh specific capacitance of NiO nanorod arrays. *Nano Res.* **2011**, *4*, 658–665.
139. Yoo, C.Y.; Park, J.; Yun, D.S.; Yu, J.H.; Yoon, H.H.C.; Kim, J.N.; Yoon, H.H.C.; Kwak, M.; Kang,

- Y.C. Crucial role of a nickel substrate in Co_3O_4 pseudocapacitor directly grown on nickel and its electrochemical properties. *J. Alloys Compd.* **2016**, 676, 407–413.
140. Li, W.; Li, G.; Sun, J.; Zou, R.; Xu, K.; Sun, Y.; Chen, Z.; Yang, J.; Hu, J. Hierarchical heterostructures of MnO_2 nanosheets or nanorods grown on Au-coated Co_3O_4 porous nanowalls for high-performance pseudocapacitance. *Nanoscale* **2013**, 5, 2901–8.
 141. Wang, H.; Yi, H.; Chen, X.; Wang, X. Facile synthesis of a nano-structured nickel oxide electrode with outstanding pseudocapacitive properties. *Electrochim. Acta* **2013**, 105, 353–361.
 142. Liu, B.T.; Shi, X.M.; Lang, X.Y.; Gu, L.; Wen, Z.; Zhao, M.; Jiang, Q. Extraordinary pseudocapacitive energy storage triggered by phase transformation in hierarchical vanadium oxides. *Nat. Commun.* **2018**, 9, 1–9.
 143. Xia, X.; Luo, J.; Zeng, Z.; Guan, C.; Zhang, Y.; Tu, J.; Zhang, H.; Fan, H.J. Integrated photoelectrochemical energy storage: solar hydrogen generation and supercapacitor. *Sci. Rep.* **2012**, 2, 981.
 144. Yus, J.; Ferrari, B.; Sanchez-Herencia, A.; Caballero, A.; Morales, J.; Gonzalez, Z. In Situ Synthesis and Electrophoretic Deposition of NiO/Ni Core-Shell Nanoparticles and Its Application as Pseudocapacitor. *Coatings* **2017**, 7, 193.
 145. Yus, J.; Gonzalez, Z.; Sanchez-Herencia, A.J.; Sangiorgi, A.; Sangiorgi, N.; Gardini, D.; Sanson, A.; Galassi, C.; Caballero, A.; Morales, J.; et al. Semiconductor water-based inks: Miniaturized NiO pseudocapacitor electrodes by inkjet printing. *J. Eur. Ceram. Soc.* **2019**, 0–1.
 146. Xia, X. b; Tu, J.; Zhang, Y.; Wang, X.; Gu, C.; Zhao, X.-B.; Fan, H.J. High-quality metal oxide core/shell nanowire arrays on conductive substrates for electrochemical energy storage. *ACS Nano* **2012**, 6, 5531–5538.
 147. Liu, J.; Jiang, J.; Bosman, M.; Fan, H.J. Three-dimensional tubular arrays of MnO_2 –NiO nanoflakes with high areal pseudocapacitance. *J. Mater. Chem.* **2012**, 22, 2419.
 148. Pham, D. Van; Patil, R.A.; Yang, C.C.; Yeh, W.C.; Liou, Y.; Ma, Y.R. Impact of the crystal phase and 3d-valence conversion on the capacitive performance of one-dimensional MoO_2 , MoO_3 , and Magnéli-phase Mo_4O_{11} nanorod-based pseudocapacitors. *Nano Energy* **2018**, 47, 105–114.
 149. Lang, X.-Y.; Liu, B.-T.; Shi, X.-M.; Li, Y.-Q.; Wen, Z.; Jiang, Q. Ultrahigh-Power Pseudocapacitors Based on Ordered Porous Heterostructures of Electron-Correlated Oxides. *Adv. Sci.* **2016**, n/a-n/a.
 150. Pawar, S.A.; Patil, D.S.; Shin, J.C. Designing a Copper- and Silver-Sulfide Composite with Co_3O_4 for High-Performance Electrochemical Supercapacitors. *ChemElectroChem* **2019**, 6, 522–534.
 151. Tomboc, G.M.; Abebe, M.W.; Baye, A.F.; Kim, H. Utilization of the superior properties of highly mesoporous PVP modified NiCo_2O_4 with accessible 3D nanostructure and flower-like morphology towards electrochemical methanol oxidation reaction. *J. Energy Chem.* **2018**, 29, 136–146.

Bibliography

152. Kim, J.W.; Augustyn, V.; Dunn, B. The effect of crystallinity on the rapid pseudocapacitive response of Nb₂O₅. *Adv. Energy Mater.* **2012**, *2*.
153. Jung, C.; Lin, P.; Yuen, T. Electrophoretic fabrication and pseudocapacitive properties of graphene / manganese oxide / carbon nanotube nanocomposites. *J. Power Sources* **2013**, *243*, 594–602.
154. Caballero, A.; Hernán, L.; Morales, J.; González, Z.; Sánchez-Herencia, A.J.J.; Ferrari, B. A high-capacity anode for lithium batteries consisting of mesoporous NiO nanoplatelets. *Energy and Fuels* **2013**, *27*, 5545–5551.
155. Zhu, Y.G.; Wang, Y.; Shi, Y.; Huang, Z.X.; Fu, L.; Yang, H.Y. Phase transformation induced capacitance activation for 3D graphene-CoO nanorod pseudocapacitor. *Adv. Energy Mater.* **2014**, *4*, 1–8.
156. Sawangphruk, M.; Pinitsoontorn, S.; Limtrakul, J. Surfactant-assisted electrodeposition and improved electrochemical capacitance of silver-doped manganese oxide pseudocapacitor electrodes. *J. Solid State Electrochem.* **2012**, *16*, 2623–2629.
157. Wang, B.; Park, J.; Wang, C.; Ahn, H.; Wang, G. Mn₃O₄ nanoparticles embedded into graphene nanosheets: Preparation, characterization, and electrochemical properties for supercapacitors. *Electrochim. Acta* **2010**, *55*, 6812–6817.
158. Lee, I.; Jeong, G.H.; An, S.; Kim, S.W.; Yoon, S. Facile synthesis of 3D MnNi-layered double hydroxides (LDH)/graphene composites from directly graphites for pseudocapacitor and their electrochemical analysis. *Appl. Surf. Sci.* **2018**, *429*, 196–202.
159. Yan, J.; Wei, T.; Qiao, W.; Shao, B.; Zhao, Q.; Zhang, L.; Fan, Z. Rapid microwave-assisted synthesis of graphene nanosheet/Co₃O₄ composite for supercapacitors. *Electrochim. Acta* **2010**, *55*, 6973–6978.
160. Shim, J.; Ko, Y.; Lee, K.S.; Partha, K.; Lee, C.H.; Yu, K.; Koo, H.Y.; Lee, K.T.; Seo, W.S.; Son, D.I. Conductive Co₃O₄/graphene (core/shell) quantum dots as electrode materials for electrochemical pseudocapacitor applications. *Compos. Part B Eng.* **2017**, *130*, 230–235.
161. Cai, X.; Hua, S.; Kok, C.; Lai, L.; Lin, J.; Shen, Z. High-performance asymmetric pseudocapacitor cell based on cobalt hydroxide / graphene and polypyrrole / graphene electrodes. *J. Power Sources* **2015**, *275*, 298–304.
162. Chen, S.; Zhu, J.; Wu, X.; Han, Q.; Wang, X. Graphene oxide-MnO₂ nanocomposites for supercapacitors. *ACS Nano* **2010**, *4*, 2822–2830.
163. Jia, D.; Chen, X.; Tan, H.; Liu, F.; Yue, L.; Zheng, Y.; Cao, X.; Li, C.; Sun, Y.; Liu, H.; et al. Boosting Electrochemistry of Manganese Oxide Nanosheets by Ostwald Ripening during Reduction for Fiber Electrochemical Energy Storage Device. *ACS Appl. Mater. Interfaces* **2018**, *10*, 30388–30399.
164. Makgopa, K.; Ejikeme, P.M.; Ozoemena, K.I. Graphene oxide-modified nickel (II) tetra-

- aminophthalocyanine nanocomposites for high-power symmetric pseudocapacitor. *Electrochim. Acta* **2016**, *212*.
165. Ma, W.; Chen, S.; Yang, S.; Chen, W.; Weng, W.; Cheng, Y.; Zhu, M. Flexible all-solid-state asymmetric supercapacitor based on transition metal oxide nanorods/reduced graphene oxide hybrid fibers with high energy density. *Carbon N. Y.* **2017**, *113*, 151–158.
 166. Song, X.; Tan, L.; Wang, X.; Zhu, L.; Yi, X.; Dong, Q. Synthesis of CoS@rGO composites with excellent electrochemical performance for supercapacitors. *J. Electroanal. Chem.* **2017**, *794*, 132–138.
 167. Chang, M.S.; Kim, T.; Kang, J.H.; Park, J.; Park, C.R. The effect of surface characteristics of reduced graphene oxide on the performance of a pseudocapacitor. *2D Mater.* **2015**, *2*.
 168. Madhuri, K.P.; John, N.S. Supercapacitor application of nickel phthalocyanine nanofibres and its composite with reduced graphene oxide. *Appl. Surf. Sci.* **2018**, *449*, 528–536.
 169. Ghosh, D.; Lim, J.; Narayan, R.; Kim, S.O. High Energy Density All Solid State Asymmetric Pseudocapacitors Based on Free Standing Reduced Graphene Oxide-Co₃O₄ Composite Aerogel Electrodes. **2016**, 4–11.
 170. Bhattacharya, P.; Joo, T.; Kota, M.; Park, H.S. CoO nanoparticles deposited on 3D macroporous ozonized RGO networks for high rate capability and ultralong cyclability of pseudocapacitors. *Ceram. Int.* **2018**, *44*, 980–987.
 171. Kim, H.-S.; Cook, J.B.; Tolbert, S.H.; Dunn, B. The Development of Pseudocapacitive Properties in Nanosized-MoO₂. *J. Electrochem. Soc.* **2015**, *162*, A5083–A5090.
 172. Chaudhary, M.; Doong, R. an; Kumar, N.; Tseng, T.Y. Ternary Au/ZnO/rGO nanocomposites electrodes for high performance electrochemical storage devices. *Appl. Surf. Sci.* **2017**, *420*, 118–128.
 173. Yus, J.; Bravo, Y.; Sanchez-Herencia, A.J.; Ferrari, B.; Gonzalez, Z. Electrophoretic deposition of RGO-NiO core-shell nanostructures driven by heterocoagulation method with high electrochemical performance. *Electrochim. Acta* **2019**, *308*, 363–372.
 174. Shahrokhian, S.; Mohammadi, R.; Asadian, E. One-step fabrication of electrochemically reduced graphene oxide/nickel oxide composite for binder-free supercapacitors. *Int. J. Hydrogen Energy* **2016**, *41*, 17496–17505.
 175. Rakhi, R.B.; Ahmed, B.; Anjum, D.; Alshareef, H.N. Direct Chemical Synthesis of MnO₂ Nanowhiskers on Transition-Metal Carbide Surfaces for Supercapacitor Applications. *ACS Appl. Mater. Interfaces* **2016**, *8*, 18806–18814.
 176. Sumboja, A.; Foo, C.Y.; Yan, J.; Yan, C.; Gupta, R.K.; Lee, P.S. Significant electrochemical stability of manganese dioxide/polyaniline coaxial nanowires by self-terminated double surfactant polymerization for pseudocapacitor electrode. *J. Mater. Chem.* **2012**, *22*, 23921.

Bibliography

177. Hu, C.C.; Wu, Y.T.; Change, K.H. Low-temperature hydrothermal synthesis of Mn_3O_4 and MnOOH single crystals: Determinant influence of oxidants. *Chem. Mater.* **2008**, *20*, 2890–2894.
178. Hu L.; Chen, W.; Xie, X.; Liu, N.; Yang, Y.; Wu, H.; Yao, Y.; Pasta, M.; Alshareef, H.N.; Cui, Y. Symmetrical MnO_2 -Carbon Nanotube-Textile Nanostructures for Wearable Pseudocapacitors with High Mass Loading. *ACS Nano* **2011**, 8904–8913.
179. Shen, L.; Sun, P.; Zhao, C.; Tan, S.; Mai, W. Tailorable pseudocapacitors for energy storage clothes. *RSC Adv.* **2016**, *6*, 67764–67770.
180. Yang, P.; Chen, Y.; Yu, X.; Qiang, P.; Wang, K.; Cai, X.; Tan, S.; Liu, P.; Song, J.; Mai, W. Reciprocal alternate deposition strategy using metal oxide/carbon nanotube for positive and negative electrodes of high-performance supercapacitors. *Nano Energy* **2014**, *10*, 106–116.
181. Lee, D.W.; Lee, J.H.; Min, N.K.; Jin, J.H. Buckling Structured Stretchable Pseudocapacitor Yarn. *Sci. Rep.* **2017**, *7*, 1–8.
182. Ma, X.; Li, Y.; Wen, Z.; Gao, F.; Liang, C.; Che, R. Ultrathin $\beta\text{-Ni}(\text{OH})_2$ nanoplates vertically grown on nickel-coated carbon nanotubes as high-performance pseudocapacitor electrode materials. *ACS Appl. Mater. Interfaces* **2015**, *7*, 974–979.
183. Su, A.D.; Zhang, X.; Rinaldi, A.; Nguyen, S.T.; Liu, H.; Lei, Z.; Lu, L.; Duong, H.M. Hierarchical porous nickel oxide-carbon nanotubes as advanced pseudocapacitor materials for supercapacitors. *Chem. Phys. Lett.* **2013**, 561–562, 68–73.
184. Jiang, Y.Q.; Wang, P.B.; Zang, X.N.; Yang, Y.; Kozinda, A.; Lin, L.W. Uniformly Embedded Metal Oxide Nanoparticles in Vertically Aligned Carbon Nanotube Forests as Pseudocapacitor Electrodes for Enhanced Energy Storage (vol 13, pg 3524, 2013). *Nano Lett.* **2014**, *14*, 2230.
185. Yu, C.; Yang, J.; Zhao, C.; Fan, X.; Wang, G.; Qiu, J. Nanohybrids from NiCoAl-LDH coupled with carbon for pseudocapacitors: understanding the role of nano-structured carbon. *Nanoscale* **2014**, *6*, 3097–3104.
186. Mazloumi, M.; Shadmehr, S.; Rangom, Y.; Nazar, L.F.; Tang, X. Fabrication of three-dimensional carbon nanotube and metal oxide hybrid mesoporous architectures. *ACS Nano* **2013**, *7*, 4281–4288.
187. Wang, Q.; Zhang, D.; Wu, Y.; Li, T.; Zhang, A.; Miao, M. Fabrication of Supercapacitors from NiCo_2O_4 Nanowire/Carbon-Nanotube Yarn for Ultraviolet Photodetectors and Portable Electronics. *Energy Technol.* **2017**, *5*, 1449–1456.
188. Fam, D.W.H.; Azoubel, S.; Liu, L.; Huang, J.; Mandler, D.; Magdassi, S.; Tok, A.I.Y. Novel felt pseudocapacitor based on carbon nanotube/metal oxides. *J. Mater. Sci.* **2015**, *50*, 6578–6585.
189. Zuru, D.U.; Zainal, Z.; Hussein, M.Z.; Jaafar, A.M.; Lim, H.N.; Chang, S.K. Theoretical and experimental models for the synthesis of single-walled carbon nanotubes and their electrochemical properties. *J. Appl. Electrochem.* **2018**, *48*, 287–304.

190. Huang, L.; Gao, X.; Dong, Q.; Hu, Z.; Xiao, X.; Li, T.; Cheng, Y.; Yao, B.; Wan, J.; Ding, D.; et al. $\text{H}_x\text{MoO}_{3-y}$ nanobelts with sea water as electrolyte for high-performance pseudocapacitors and desalination devices. *J. Mater. Chem. A* **2015**, *3*.
191. Liang, R.; Cao, H.; Qian, D. MoO_3 nanowires as electrochemical pseudocapacitor materials. *Chem. Commun.* **2011**, *47*, 10305–10307.
192. Chen, Z.; Augustyn, V.; Jia, X.; Xiao, Q.; Dunn, B.; Lu, Y. High-performance sodium-ion pseudocapacitors based on hierarchically porous nanowire composites. *ACS Nano* **2012**, *6*, 4319–4327.
193. Chang, S.; Pu, J.; Wang, J.; Du, H.; Zhou, Q.; Liu, Z.; Zhu, C.; Li, J.; Zhang, H. Electrochemical Fabrication of Monolithic Electrodes with Core / Shell Sandwiched Transition Metal Oxide / Oxyhydroxide for High- Performance Energy Storage. **2016**.
194. Jiang, J.; Liu, J.; Ding, R.; Zhu, J.; Li, Y.; Hu, A.; Li, X.; Huang, X. Large-Scale Uniform $\beta\text{-Co}(\text{OH})_2$ Long Nanowire Arrays Grown on Graphite as Pseudocapacitor Electrodes. *ACS Appl. Mater. Interfaces* **2011**, *3*, 99–103.
195. Yang, Y.; Zeng, D.; Yang, S.; Gu, L.; Liu, B.; Hao, S. Nickel cobaltite nanosheets coated on metal-organic framework-derived mesoporous carbon nanofibers for high-performance pseudocapacitors. *J. Colloid Interface Sci.* **2019**, *534*, 312–321.
196. Pang, Y.; Zhang, S.; Chen, S.; Liang, J.; Li, M.; Ding, D.; Ding, S. Transition-Metal Oxides Anchored on Nitrogen-Enriched Carbon Ribbons for High-Performance Pseudocapacitors. *Chem. - A Eur. J.* **2018**, *24*, 16104–16112.
197. Guan, C.; Zeng, Z.; Li, X.; Cao, X.; Fan, Y.; Xia, X.; Pan, G.; Zhang, H.; Fan, H.J. Atomic-layer-deposition-assisted formation of carbon nanoflakes on metal oxides and energy storage application. *Small* **2014**, *10*, 300–307.
198. Meng, W.; Chen, W.; Zhao, L.; Huang, Y.; Zhu, M.; Huang, Y.; Fu, Y.; Geng, F.; Yu, J.; Chen, X.; et al. Porous Fe_3O_4 /carbon composite electrode material prepared from metal-organic framework template and effect of temperature on its capacitance. *Nano Energy* **2014**, *8*, 133–140.
199. Zhu, M.; Kan, J.; Pan, J.; Tong, W.; Chen, Q.; Wang, J.; Li, S. One-pot hydrothermal fabrication of $\alpha\text{-Fe}_2\text{O}_3$ @C nanocomposites for electrochemical energy storage. *J. Energy Chem.* **2019**, *28*, 1–8.
200. Zhao, Y.; Wang, Z.; Yuan, R.; Lin, Y.; Yan, J.; Zhang, J.; Lu, Z.; Luo, D.; Pietrasik, J.; Bockstaller, M.R. ZnO/carbon hybrids derived from polymer nanocomposite precursor materials for pseudocapacitor electrodes with high cycling stability. *Polymer (Guildf)*. **2018**, *137*, 370–377.
201. Zhang, X.; Luo, J.; Tang, P.; Ye, X.; Peng, X.; Tang, H.; Sun, S.G.; Fransaer, J. A universal strategy for metal oxide anchored and binder-free carbon matrix electrode: A supercapacitor case with superior rate performance and high mass loading. *Nano Energy* **2017**, *31*, 311–321.

Bibliography

202. Xiao, J.; Wan, L.; Yang, S.; Xiao, F.; Wang, S. Design hierarchical electrodes with highly conductive NiCo_2S_4 nanotube arrays grown on carbon fiber paper for high-performance pseudocapacitors. *Nano Lett.* **2014**, *14*.
203. Deori, K.; Ujjain, S.K.; Sharma, R.K.; Deka, S. Morphology controlled synthesis of nanoporous Co_3O_4 nanostructures and their charge storage characteristics in supercapacitors. *ACS Appl. Mater. Interfaces* **2013**, *5*.
204. Han, J.; Roh, K.C.; Jo, M.R.; Kang, Y.M. A novel co-precipitation method for one-pot fabrication of a Co-Ni multiphase composite electrode and its application in high energy-density pseudocapacitors. *Chem Commun* **2013**, *49*, 7067–7069.
205. Mahmood, Q.; Kim, W.S.; Park, H.S. Structure and compositional control of MoO_3 hybrids assembled by nanoribbons for improved pseudocapacitor rate and cycle performance. *Nanoscale* **2012**, *4*, 7855–60.
206. Dong, S.; Shen, L.; Li, H.; Pang, G.; Dou, H.; Zhang, X. Flexible Sodium-Ion Pseudocapacitors Based on 3D $\text{Na}_2\text{Ti}_3\text{O}_7$ Nanosheet Arrays/Carbon Textiles Anodes. *Adv. Funct. Mater.* **2016**, *26*, 3703–3710.
207. Ling, T.; Da, P.; Zheng, X.; Ge, B.; Hu, Z.; Wu, M.; Du, X.W.; Hu, W. Bin; Jaroniec, M.; Qiao, S.Z. Atomic-level structure engineering of metal oxides for high-rate oxygen intercalation pseudocapacitance. *Sci. Adv.* **2018**, *4*, 1–9.
208. Susanti, D.; Wibawa, R.N.D.; Tananta, L.; Purwaningsih, H.; Fajarin, R.; Kusuma, G.E. The effect of calcination temperature on the capacitive properties of WO_3 -based electrochemical capacitors synthesized via a sol-gel method. *Front. Mater. Sci.* **2013**, *7*, 370–378.
209. Javed, M.S.; Zhang, C.; Chen, L.; Xi, Y.; Hu, C. Hierarchical mesoporous NiFe_2O_4 nanocone forest directly growing on carbon textile for high performance flexible supercapacitors. *J. Mater. Chem. A* **2016**, *4*, 8851–8859.
210. Miyajima, N.; Jinguji, K.; Matsumura, T.; Matsubara, T.; Sakane, H.; Akatsu, T.; Tanaike, O. A simple synthesis method to produce metal oxide loaded carbon paper using bacterial cellulose gel and characterization of its electrochemical behavior in an aqueous electrolyte. *J. Phys. Chem. Solids* **2016**, *91*, 122–127.
211. Zhang, Y.; Park, M.; Kim, H.Y.; Park, S.J. Moderated surface defects of Ni particles encapsulated with NiO nanofibers as supercapacitor with high capacitance and energy density. *J. Colloid Interface Sci.* **2017**, *500*, 155–163.
212. Tomar, A.K.; Marichi, R.B.; Singh, G.; Sharma, R.K. Enhanced electrochemical performance of anion-intercalated lanthanum molybdenum oxide pseudocapacitor electrode. *Electrochim. Acta* **2018**.
213. Rezaie, E.; Rezanezhad, A.; Ghadimi, L.S.; Hajalilou, A.; Arsalani, N. Effect of calcination on

- structural and supercapacitance properties of hydrothermally synthesized plate-like $\text{SrFe}_{12}\text{O}_{19}$ hexaferrite nanoparticles. *Ceram. Int.* **2018**, *44*, 20285–20290.
214. Hall, D.S.; Lockwood, D.J.; Bock, C.; MacDougall, B.R. Nickel hydroxides and related materials: A review of their structures, synthesis and properties. *Proc. R. Soc. A Math. Phys. Eng. Sci.* **2015**, *471*.
 215. Moreno, R. Colloidal processing of ceramics and composites. *Adv. Appl. Ceram.* **2012**, *111*, 246–253.
 216. Sigmund, W.M.; Bell, N.S.; Bergström, L. Novel Powder-Processing Methods for Advanced Ceramics. *J. Am. Ceram. Soc.* **2004**, *83*, 1557–1574.
 217. Franks, G. V.; Tallon, C.; Studart, A.R.; Sesso, M.L.; Leo, S. Colloidal processing: enabling complex shaped ceramics with unique multiscale structures. *J. Am. Ceram. Soc.* **2017**, *100*, 458–490.
 218. Dickhaus, B.N.; Priefer, R. Determination of polyelectrolyte pKa values using surface-to-air tension measurements. *Colloids Surfaces A Physicochem. Eng. Asp.* **2016**, *488*, 15–19.
 219. Helgeson, M.E.; Hodgdon, T.K.; Kaler, E.W.; Wagner, N.J.; Vethamuthu, M.; Ananthapadmanabhan, K.P. Formation and rheology of viscoelastic “double networks” in wormlike micelle-nanoparticle mixtures. *Langmuir* **2010**, *26*, 8049–8060.
 220. Ferrari, B.; Moreno, R. EPD kinetics: A review. *J. Eur. Ceram. Soc.* **2010**, *30*, 1069–1078.
 221. Hirt, L.; Reiser, A.; Spolenak, R.; Zambelli, T. Additive Manufacturing of Metal Structures at the Micrometer Scale. *Adv. Mater.* **2017**, *29*.
 222. Nold, A.; Zeiner, J.; Assion, T.; Clasen, R. Electrophoretic deposition as rapid prototyping method. *J. Eur. Ceram. Soc.* **2010**, *30*, 1163–1170.
 223. Derby, B. Inkjet Printing of Functional and Structural Materials: Fluid Property Requirements, Feature Stability, and Resolution. *Annu. Rev. Mater. Res.* **2010**, *40*, 395–414.
 224. Mendoza, C.; González, Z.; Castro, Y.; Gordo, E.; Ferrari, B. Improvement of TiN nanoparticles EPD inducing steric stabilization in non-aqueous suspensions. *J. Eur. Ceram. Soc.* **2016**, *36*, 307–317.
 225. Moreno, R.; Ferrari, B. Nanoparticles Dispersion and the Effect of Related Parameters in the EPD Kinetics. **2011**, 73–128.
 226. Zhang, L.; Vleugels, J.; Van der Biest, O. Fabrication of textured alumina by orienting template particles during electrophoretic deposition. *J. Eur. Ceram. Soc.* **2010**, *30*, 1195–1202.
 227. Verde, M.; Peiteado, M.; Caballero, A.C.; Villegas, M.; Ferrari, B. Electrophoretic Deposition of Transparent ZnO Thin Films from Highly Stabilized Colloidal Suspensions. *J. Colloid Interface Sci.* **2012**, *373*, 27–33.

Bibliography

228. Verde, M.; Caballero, A.C.; Iglesias, Y.; Villegas, M.; Ferrari, B. Electrophoretic Deposition of Flake-Shaped ZnO Nanoparticles. *J. Electrochem. Soc.* **2009**, *157*, H55.
229. Zhou, G.; Wang, D.W.; Yin, L.C.; Li, N.; Li, F.; Cheng, H.M. Oxygen bridges between nio nanosheets and graphene for improvement of lithium storage. *ACS Nano* **2012**, *6*, 3214–3223.
230. Huang, M.L.; Gu, C.D.; Ge, X.; Wang, X.L.; Tu, J.P. NiO nanoflakes grown on porous graphene frameworks as advanced electrochemical pseudocapacitor materials. *J. Power Sources* **2014**, *259*, 98–105.
231. P. L. Taberna, P.S. and J.F.F. Electrochemical Characteristics and Impedance Spectroscopy Studies of Carbon- Carbon Supercapacitors. **2003**, *Volume 150*, A292–A300.
232. Inamuddin, Mohammad Faraz Ahmer, Abdullah M. Asiri, S.Z. *Electrochemical Capacitors: Theory, Materials and Applications*; 2018; ISBN 978-1-945291-56-2.
233. Yuan, L.; Lu, X.-H.; Xiao, X.; Zhai, T.; Dai, J.; Zhang, F.; Hu, B.; Wang, X.; Gong, L.; Chen, J.; et al. Flexible Solid-State Supercapacitors Based on Carbon Nanoparticles/MnO₂ Nanorods Hybrid Structure. *ACS Nano* **2012**, *6*, 656–661.
234. Xu, Y.; Lin, Z.; Zhong, X.; Huang, X.; Weiss, N.O.; Huang, Y.; Duan, X. Holey graphene frameworks for highly efficient capacitive energy storage. *Nat. Commun.* **2014**, *5*.
235. Valero, J.L.; Jarom, C.; Comas, E. Optimized Automatic Recovery of Nozzle Health in Inkjet Systems. *Program* **2018**, 766–770.
236. Bakarič, T.; Malič, B.; Kuscer, D. Lead-zirconate-titanate-based thick-film structures prepared by piezoelectric inkjet printing of aqueous suspensions. *J. Eur. Ceram. Soc.* **2016**, *36*, 4031–4037.
237. He, P.; Derby, B. Inkjet printing ultra-large graphene oxide flakes. *2D Mater.* **2017**, *4*.
238. Liu, Y.F.; Tsai, M.H.; Pai, Y.F.; Hwang, W.S. Control of droplet formation by operating waveform for inks with various viscosities in piezoelectric inkjet printing. *Appl. Phys. A Mater. Sci. Process.* **2013**, *111*, 509–516.
239. Nallan, H.C.; Sadie, J.A.; Kitsomboonloha, R.; Volkman, S.K. Systematic Design of Jettable Nonoparticle-Based Inkjet Rheology, Acoustics, and Jettability. *Langmuir* **2014**, *30*, 13470–13477.
240. Notten, P.H.L.; Roozeboom, F.; Niessen, R.A.H.; Baggetto, L. 3-D integrated all-solid-state rechargeable batteries. *Adv. Mater.* **2007**, *19*, 4564–4567.
241. Mendoza, C.; Gonzalez, Z.; Gordo, E.; Ferrari, B.; Castro, Y. Protective nature of nano-TiN coatings shaped by EPD on Ti substrates. *J. Eur. Ceram. Soc.* **2018**, *38*, 495–500.
242. Gonzalez, Z.; Ferrari, B.; Sanchez-Herencia, A.J.; Caballero, A.; Morales, J. Use of Polyelectrolytes for the Fabrication of Porous NiO Films by Electrophoretic Deposition for Supercapacitor Electrodes. *Electrochim. Acta* **2016**, *211*, 110–118.



6

Publications



Publication

1

J. Yus, B. Ferrari, A.J. Sanchez-Herencia, Z. Gonzalez

**Emerging processing techniques for electrodes microarchitectures
tailoring in pseudocapacitors.**

Sent to publish to the Journal of the European Ceramic Society

Manuscript Number:

Title: Emerging processing techniques for electrodes microarchitectures tailoring in pseudocapacitors

Article Type: Review Article

Keywords: Supercapacitors, Pseudocapacitors, Hybrid-capacitors, Ceramic semiconductor, Metal Oxides, Colloidal Processing, Sintering.

Corresponding Author: Mr. Joaquín Luis Yus, M.D.

Corresponding Author's Institution: Instituto de Ceramica y Vidrio. CSIC

First Author: Joaquin Yus, M.D.

Order of Authors: Joaquin Yus, M.D.; Begoña Y Ferrari, PhD; Antonio Javier Sanchez-Herencia, PhD; Zoilo Gonzalez, PhD

Abstract: Pseudocapacitor electrodes based on ceramic semiconductors has received special attention because their inherent electrochemical properties. The employment of transition-metal-oxides, especially nanomaterials, allows to reach excellent compromise between power and energy density in energy storage devices.

Most of the characteristics of nanostructured ceramic electrodes depend on the shaping process; active surface area, conductivity, microstructural connectivity and mechanical stability determine the electrochemical response. New findings suggest the development of new strategies to control the crystallographic growth or the nanoparticle arrangement during the growth of the film and the consolidation of the structure.

This review emphasizes the novel binder-free techniques dedicated to design complex microstructures in the electrodes. Complex shaping strategies and the sintering maximized the microstructure connectivity enhancing the electrochemical response. Processing strategies are classified in three different groups: (i)-Synthesis and modification of particles or nanostructures; (ii)-Microstructure tailoring by shaping films or coating metal collectors; and (iii)-Technologies based on hybrid capacitors fabrications.

Suggested Reviewers: Alessandra Sanson PhD
ISTEC-CNR

alessandra.sanson@istec.cnr.it

She is a researcher specialised on the production of powders for functional applications and their shaping processes, focused on the materials devoted to the production and storage of energy.

Isabel Gonzalo de Juan PhD

Postdoc Research Associate, Technische Universität Darmstadt
gonzalo@materials.tu-darmstadt.de

She has a wide expertise in processing of ceramics and carbon based materials by different techniques.

Alvaro Caballero PhD

Inorganic chemistry, University of Cordoba

alvaro.caballero@uco.es

He is an expert in electrochemical characterization, in particular in supercapacitors and Li-ion batteries



MINISTERIO
DE ECONOMÍA
Y COMPETITIVIDAD



CSIC
CONSEJO SUPERIOR DE INVESTIGACIONES CIENTÍFICAS



INSTITUTO DE CERÁMICA Y VIDRIO

Madrid, June 24th, 2019

Dear Editor,

Thank you for considering the publication of our manuscript. Please find enclosed the original manuscript entitled “**Emerging processing techniques for electrodes microarchitectures tailoring in pseudocapacitors**” by J. Yus; B. Ferrari; A.J. Sanchez-Herencia and Z. Gonzalez; which we submit for publication at the **Journal of the European Ceramic Society**.

The review deals with a deep bibliographic revision of the latest trends in the use of ceramic oxides as semiconductors in the field of energy storage. The most powerful strategies for the fabrication of supercapacitors electrodes were classified into three different groups, emphasizing the novel binder-free techniques. These methods are dedicated to the design of complex microstructures in the electrodes that will increase the merits of the materials through complex shaping strategies. Moreover, the consolidation by ceramic sintering maximized the structure connectivity to optimize the electrochemical response.

Hoping this work being at the scope of the journal, I acknowledge very much your interest.

Yours sincerely,

Joaquin Yus

Data of the corresponding author are:

Joaquin Yus
Institute for Ceramic and Glass. CSIC
Kelsen Street, 5. 28049, Madrid, Spain
email: joaquinluis.yus@icv.csic.es

SUMMARY OF NOVEL CONCLUSIONS

This document provides the reader with a novel vision of last trends in synthesis, shaping and sintering strategies in the development of Supercapacitors based on TMOs and hybrid capacitors.

**Emerging processing techniques for electrodes microarchitectures
tailoring in pseudocapacitors**

J. Yus*, B. Ferrari, A.J. Sanchez Herencia and Z. Gonzalez

*Corresponding autor:

Institute of Ceramic and Glass. CSIC. Tailoring through Colloidal Processing Group 5, Kelsen
28049.

Abstract

Pseudocapacitor electrodes based on ceramic semiconductors has received special attention because their inherent electrochemical properties. The employment of transition-metal-oxides, especially nanomaterials, allows to reach excellent compromise between power and energy density in energy storage devices.

Most of the characteristics of nanostructured ceramic electrodes depend on the shaping process; active surface area, conductivity, microstructural connectivity and mechanical stability determine the electrochemical response. New findings suggest the development of new strategies to control the crystallographic growth or the nanoparticle arrangement during the growth of the film and the consolidation of the structure.

This review emphasizes the novel binder-free techniques dedicated to design complex microstructures in the electrodes. Complex shaping strategies and the sintering maximized the microstructure connectivity enhancing the electrochemical response. Processing strategies are classified in three different groups: (i)-Synthesis and modification of particles or nanostructures; (ii)-Microstructure tailoring by shaping films or coating metal collectors; and (iii)-Technologies based on hybrid capacitors fabrications.

Keywords

Supercapacitors, Pseudocapacitors, Hybrid capacitors, Ceramic semiconductor, Metal Oxides, Colloidal Processing, Sintering.

1. Introduction to the ceramic-based pseudocapacitors

The poles fusion, the migrations or even the extinction of some animal species are only a few of the consequences that global warming produces in our planet. Greenhouse effect, induced mainly by the atmospheric carbon dioxide, is considered the more direct

1 responsible of the global warming. In this sense, the renewable energies pretend to be
2 an alternative solution of these problems by substituting the fossil fuels for other non-
3 emitting energy sources, like solar light or wind, that are intermittent. Thus, energy
4 storage devices are necessary to retain the electrical energy and supply the power
5 according to demand. Additionally, they must be considered uses where, according to
6 the specific needs of each moment, accumulators must satisfy rapid electric loading
7 and unloading without losing storage capacity. That is why batteries, or fuel cells,
8 probably would be a lame duck solution without complementary devices such as
9 supercapacitors (SCs). While batteries are capable of supplying energy steadily over a
10 long time, SC can provide large amount of energy in milliseconds, being loading and
11 unloading cycles truly fast.
12

13 Thus, hybrid and electric vehicles, based on the combination of lithium batteries and
14 SCs, are increasingly requiring more autonomy and less charge time[1]. It should be
15 noted that batteries offer a higher energy density and will continue to be responsible for
16 us travelling more and more miles in our electric car. Although, if the batteries work
17 beyond their power density possibilities, their temperature can rise, reducing their
18 useful life. Here is where SC supports electronic motors, delivering the energy
19 instantaneously and reducing the charging times. Nowadays, there are ongoing
20 projects in which SC are already being applied in real conditions. For example, the
21 TOSA Concept and Test Bus is the first 100% electric articulated bus in Switzerland
22 with a high capacity that can recharge electric energy at every stop, in few seconds
23 each time, without damaging the battery. Although the market for SC is expected to be
24 led by transport applications their use in others consumer electronic products has
25 grown through application in mobile phones memories, watches and so on.
26

27 The best way to compare the energy conversion and accumulation performances is the
28 Ragone plot, where device types are grouped in terms of energy and power densities
29 (Figure 1). The Power Density (W/Kg) which is the available energy that devices can
30 supply per unit of mass, is represented at the vertical axis, while the Energy Density,
31 which determines the time rate of energy transfer per unit of mass (Wh/Kg), is
32 represented at the horizontal axis. Therefore, in the Ragone plot, the necessary time
33 for the charge and discharge is obtained by the quotient between energy density and
34 power density.
35

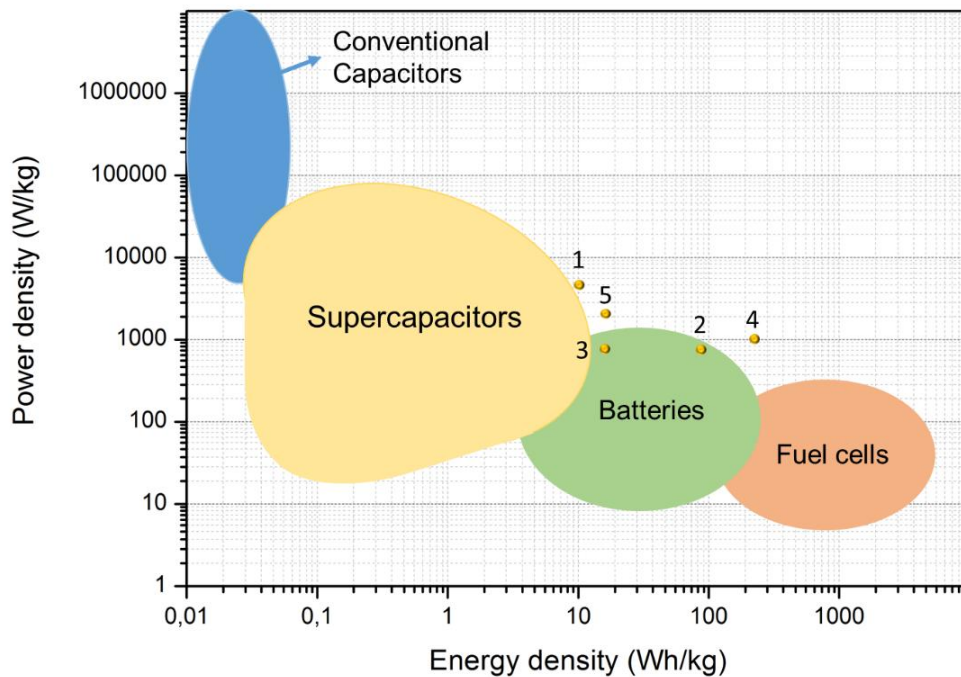


Figure 1. Ragone plot shows energy density vs power density grouping the most representative devices in energy storage. Random recent results of pseudocapacitors based on ceramic semiconductors (table 2)

SCs are located between traditional capacitors and batteries and combine properties of both. In devices with less volume and weight, SCs are able to store between 10 and 1000 times more energy than conventional capacitors and simultaneously, they can deliver a higher electrical power with a larger cycling lifespan, if compared with fuel cells and batteries. In other words, SCs can improve the performance of a battery in terms of power or increase the storage capacity of energy of the conventional capacitors. Table 1 summarizes accumulated energy, power delivery, charge/discharge time and cyclability of each group.

Table 1. Main features of batteries, fuel cells conventional capacitors and supercapacitors in terms of power and energy density and charge/discharge time

	Fuel cells	Battery	Supercapacitor	Conventional Capacitor
Power density (W/Kg)	5-500	$10-10^3$	$15-1.5 \cdot 10^4$	10^4-10^7
Energy density (Wh/Kg)	$>10^2$	10-120	0.1 - 10	<0.05

Charge/Discharge Time	∞	0.1 - 12 h	2.4 - 24 s	10^{-3} - 10 ms
Cycle life/ cyclability (n° cycles)	--	500 - 2000	> 100000	> 500000

Some data published in the last decade for semiconductor ceramic-based pseudocapacitors are also included in figure 1 and summarized in table 2. These compiled data show that the electrochemical response of this type of SCs approaches the top performance of batteries in terms of powder for energy densities ranging 10-100 Wh/Kg, being another advantage of these SCs the capability of making millions of charge/discharge cycles without losing their storage capability as capacitor.

Table 2. Data of SCs plotted in the Ragone diagram in Figure 1

Plot point	Based Material	Power density (W/Kg)	Energy density (Wh/Kg)	Ref
1	NiO	5332	10.0	[2]
2	Ni(OH) ₂ /MnO ₂	750	91.1	[3]
3	NiCl ₂	750	15.4	[4]
4	Mn ₂ O ₃	1000	147.0	[5]
5	CoO	2153	15.0	[6]

Depending on the application for which an energy storage device is required, it is necessary to evaluate the amount of energy and the time of charge/discharge. In order to respond efficiently to the requirements of each application, the combination of several systems could be the best solution, maximizing the strengths and minimizing the weakness they have separately. To understand the electrochemical performance and the main limitations for each systems, the four categories (Batteries, Fuel Cells, Conventional Capacitors and Supercapacitors) will be shortly introduced.

In **Batteries**, chemical reactions transform high-energy reactants to lower-energy products, and the free-energy difference is supplied to the external circuit as electrical energy. Secondary batteries are based on reversible chemical reactions, and consequently are rechargeable. For example, the original composition of the electrodes in lithium-ion batteries (LIBs) can be restored by reversing the current. During the device charge, the reduction and insertion of the Li ions takes place in the cathode producing a flow of ions from the cathode to the anode, while during the discharge, the oxidation and the disinsertion of ions occur in the anode, producing a flow of ions in the opposite way. These accumulators provide high energy density, but the volumetric

changes associated to the insertion and disinsertion of Li ions produces the degradation of the electrodes due to the structure collapse, which is the main drawback of this devices.

The **Conventional Capacitor** chemically stores the energy through an electrostatic field generated between two electrodes. They are composed by two conductive surfaces (commonly metal foils) separated by vacuum or a dielectric material (for example a non-conductor ceramic). When a potential difference is applied between the electrodes, the transfer of charge takes place until the potential difference between the plates become equal to the potential difference applied by the charged device. The stored charge, q (C), is proportional to the developed potential, ΔV (V), being the constant of proportionality the capacity, C , expressed in Farads (F), according to equation 1.

$$C = \frac{q}{\Delta V} \quad (1)$$

Conventional capacitors can be classified depending on the material used as dielectric. Electrostatic capacitors employ an insulating material (ceramic, porcelain, teflon, etc.), being the electric field between the electrodes homogenous since the capacity is proportional to the dielectric constant of the medium and to the surface area of the electrodes and, inversely proportional to the distance between them, as define the equation 2:

$$C = \epsilon_r \frac{A}{d} \quad (2)$$

where A (cm²) is the area of the electrode, d (cm) the distance between them and ϵ_r (F/cm) the permittivity of the dielectric.

Electrolytic capacitors is a kind of capacitors having a conductive electrolyte between the electrodes, generally, boric acid or sodium borate. It maintains the serial connection between the two electrodes, which have a thin dielectric layer of oxide. This configuration leads to higher capacities than electrostatic capacitors, but they are also more hazardous when facing heating since the oxide can dissolve causing a short circuit when the polarity is inversed.

Supercapacitors (SCs), also known as ultracapacitors or electrochemical capacitors, are considered promising devices for energy storage and management due to their short-acting high power delivery. Parameters such as capacity, power density and energy density are usually adopted to evaluate the response of SCs.

The equations regularly used for the calculation of the Energy, E_d (3), and Power, P_d (4), densities are:

$$E_d = \frac{1}{2 \cdot 3.6} C_s \cdot V^2 \quad (3)$$

where C_s (F/g) is the specific capacitance (already divided by the mass) and V (V) is the nominal voltage, and:

$$P_d = \frac{E_d}{t} \cdot 3600 \quad (4)$$

where E_d is the already calculated energy density and t (s) is the discharge time. The coefficients of the equations provide the results for E_d and P_d in terms of W·h/Kg and W/kg, respectively.

The specific capacitance, C_s , is determined from charging/discharging curves through chronopotentiometry analyses (CP) according to the equation 5:

$$C_s = \frac{I \cdot \Delta t}{m \cdot \Delta V} \quad (5)$$

where C_s (F/g) is the specific capacitance, I (A) is the discharge current, Δt (s) is the charging/discharging time, ΔV (V) is the voltage window for discharge, and m (g) is the mass of the active material in the electrode. Another way to calculate the C_s is determining the charge value, Q (C), proportional to the integral of the cyclic voltammetry (CV) curve. In SCs, the accumulated charge represents the difference between the area under the charge curve and the area under the discharge curve for the upper and lower limits of the potential window (ΔV). Thus, the specific capacitance was obtained from the equations 6, 7 y 8:

$$Q = \int I \cdot dt; t = \frac{V}{v} \quad (6)$$

$$Q = \frac{1}{v} \int I dV \quad (7)$$

$$C_s = \frac{Q}{m \cdot \Delta V}; C_s = \frac{\int I \cdot dV}{v \cdot m \cdot \Delta V} \quad (8)$$

where I (A) is the current, t (s) is the time, V (V) is the voltage, v (V/s) is the scan rate, C_s (F/g) the specific capacitance, m (g) is the mass and Q (C) is the charge/discharge value.

According to the nature of the charge storage mechanism, the SCs are classified in two main groups, the electrochemical double layer capacitors (EDLCs) and pseudocapacitors (PCs). Additionally, a third group can be considered: the hybrid supercapacitors, where the energy accumulation is based on the combination of both

charge storage mechanism. Figure 2 shows a scheme of the different electrochemical phenomena associated to their characteristic CV diagrams.

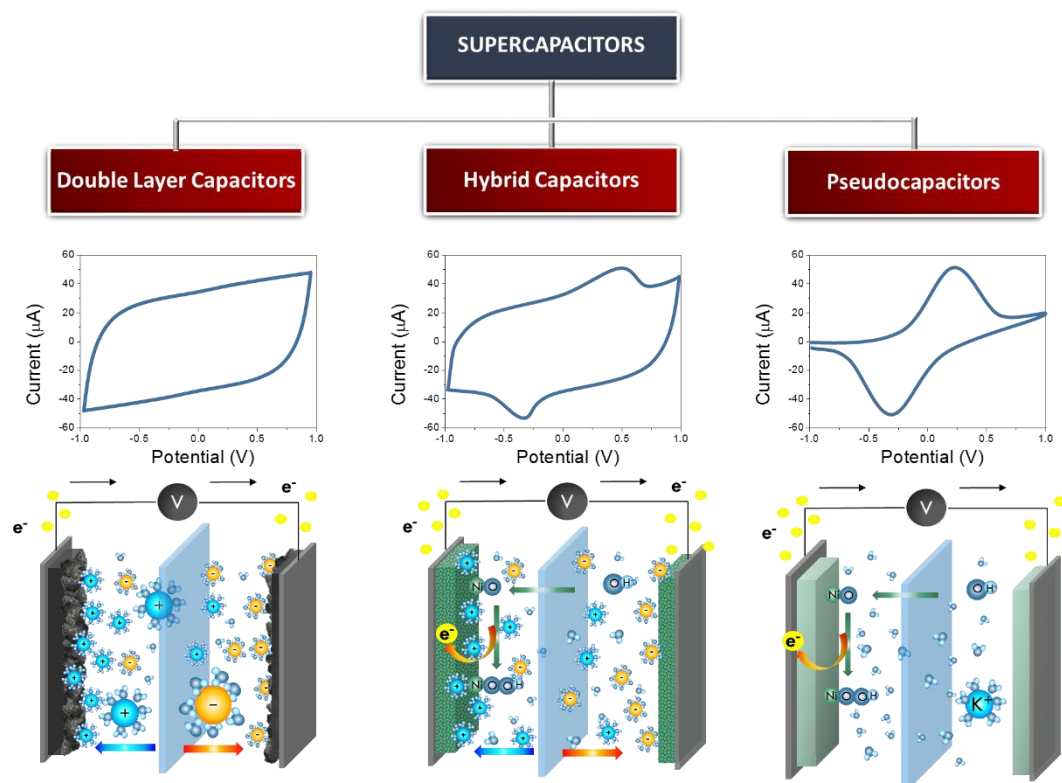


Figure 2. Hierarchical diagram of the supercapacitors classification attending to the energy storage mechanism. Charge storage principles and examples of the typical cyclic voltammograms are also included.

EDLCs store the energy through the accumulation of electric charges at the electrode/electrolyte interface. EDLCs are based on the electrochemical performance of carbonaceous materials with high specific surface area, which exhibit good conductivity and high electrochemical stability in solutions within a wide range of pH values[7]. In EDLCs, when the electrode is charged, opposite charged ions from the electrolyte are adsorbed to neutralize its surface. Ions will be desorbed once the potential changes in a complete reversible ion adsorption/desorption process. This mechanism of energy accumulation by electrostatic charge provides both, fast energy loading and supply. Furthermore, these electrodes present a very long cyclic lifetime since the volume variations of the electroactive materials are avoided. The ions do not penetrate into the microstructure of the electroactive material, as occurs in storage systems based on redox reactions characteristic of batteries and PCs.

PCs storage the energy through a faradaic process based on reversible redox reactions between electrode and electrolyte, which take place on the surface of the

1 electroactive material, involving electronic charge transfer processes by
2 electrosorption. Thus, the cyclic voltammetries (CV) show the contribution of
3 oxidation/reduction reactions and determine the redox reactions taking place at the
4 electrode and its reversibility (Figure 2). In those electrodes, the rectangular shape
5 typical from EDLCs disappears[8]. Although carbon-based EDLCs have many
6 advantages such as higher specific surface area, good electronic conductivity, and high
7 chemical stability, the capacitance of PCs can be 10–100 times higher than that
8 achieved by EDLC[9].
9

10
11
12
13 Different materials have been investigated as PCs electrodes. Metal oxides (MO) and
14 conducting polymers are the most common materials used[10]. Conducting polymers
15 such as polypyrrole (PPy) and polyaniline (PANI) are easy of processing because its
16 mechanical flexibility, but they have lower cyclability due to their easy degradability if
17 they are compared with transition metal oxides (TMO). The poor cyclability of polymer-
18 based PCs is attributed to large volumetric changes in the microstructure during cycling
19 associated with doping and over-oxidation of chains at high potential. The limitations of
20 these polymeric electrodes make TMO a reliable alternative as ceramic semiconductor-
21 based PCs.
22
23
24
25
26
27
28

29
30 TMOs emerge as one of the best options for energy storage, since they exhibit a wide
31 range of bandgaps, E_g , due to the diversity of electronic structure of the transition
32 metals (Figure 3). The bandgap or energy gap describes the energy range in
33 a solid material where electrons cannot exist due to the absence of energetic states. It
34 is determined by the energy difference (eV) between the top of the valence band and
35 the bottom of the conduction band, and it is related with the HOMO and LUMO gap in
36 molecular chemistry. If some electrons promote from the valence to the conduction
37 band then the material can be electrically conductor. Therefore, the bandgap
38 determines the electrical conductivity of the material. In metals, there is not a bandgap
39 because the valence band overlaps the conduction band. However, conductivity in
40 materials with $E_g < 0.01$ eV can be also considered essentially metallic. It is accepted
41 that for insulators bandgap has to be higher than 5 eV, which is a gap too wide for the
42 electron promotion. Then the E_g in semiconductors is consider to oscillate between
43 0.01 and 5 eV.
44
45
46
47
48
49
50
51
52
53
54
55
56
57
58
59
60
61
62
63
64
65

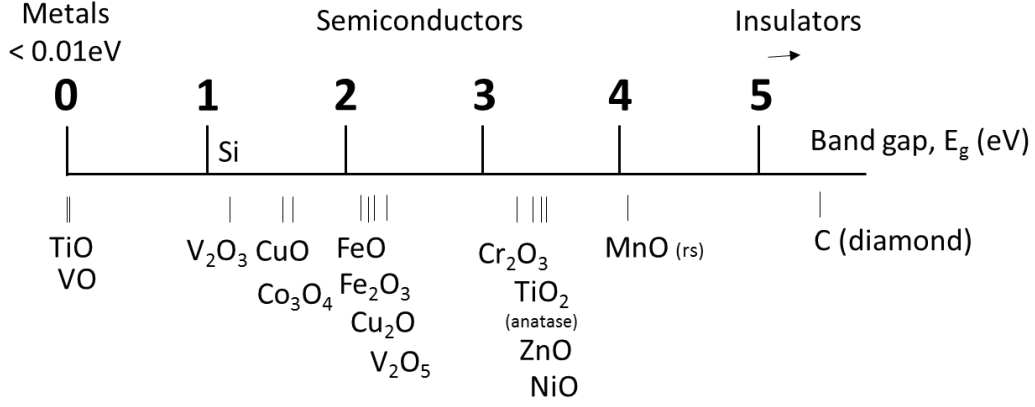


Figure 3. Relation between the band gap and electronic properties of TMOs.

TMO semiconductors are materials that can conduct electrical energy under especial conditions, depending on the voltage and current applied. The conductivity (S/m or $1/(\Omega \cdot m)$) is given by the equation 9:

$$\sigma = n \cdot e \cdot \mu \quad (9)$$

where n is the number of current carriers, e is the absolute magnitude of the electrical charge on an electron (1.6×10^{-19} C) and μ their mobility ($m^2/(V \cdot s)$). In semiconductors, the number of mobile carriers is discrete, and they are classified in electrons, e , and holes, h . An intrinsic semiconductor possesses the same amount of electrons and holes ($n=e=h$) for each electron that is promoted into the conduction band, a hole is left behind in the valence band and therefore. A hole has a positive electric charge, equal and opposite to the charge on an electron, and the flow of holes occurs in a direction opposite to the flow of electrons. When an intrinsic semiconductor is doped in order to increase the number of charge carriers, adding either donor or acceptor dopants, then they are named type-n and type-p extrinsic semiconductor, respectively. The energies of electrons in the highest occupied levels and the conduction mechanisms are different depending on the whether the materials are doped to be either n-type or p-type.

The Fermi energy (E_F) refers to the maximum level of the energy where the electrons remain at low temperature. The Fermi's level position in regard to the conduction band is essential in the determination of the electrical behavior of TMO. This theoretical level is considered as a hypothetical energy level of an electron in thermodynamic equilibrium at 0 K.

Figure 4 shows a scheme of the structure of the semiconductor bands defining the bandgap (Figure 4a) and the position E_F level in the semiconductor structures

depending on their electrochemical nature (Figure 4b). In TMO semiconductors, the E_F level is inside the bandgap (Figure 4b) and the conduction and valance bands are near enough to be thermally populated with electrons or holes. For intrinsic semiconductors, the E_F is located in the middle of the E_g , at the same distance from both bands. However, for extrinsic semiconductors, E_F is closer to the conducting band for the n-type semiconductors than in the p-type. This difference in the E_F level within the bandgap region of different TMO has been determined the entire evolution of microelectronics industry [11], and is a key-point of study in TMO-based devices for energy storage.

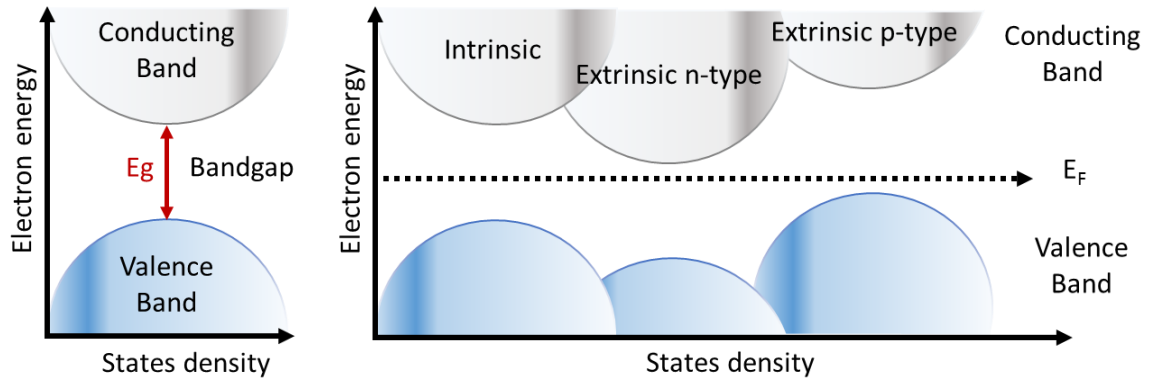


Figure 4. a) Semiconductor bands structures and bandgap. b) E_F position depending on the nature of TMO semiconductor.

In TMO, an important aspect that affects the band structure and the final electronic properties is the partly occupied metal d orbitals in the electronic configuration. For example, TiO and Cu₂O are the beginning and the end of the $3d$ orbitals in TMO presenting an empty (d^0) and totally filled (d^{10}) valence layer, respectively [12]. Therefore, they are well known semiconductors because the last electron of the valence band would reside in a more elevated hybrid orbital (in terms of energy), then the E_F increase when more electrons exist occupying the energy orbitals of less energy. Occasionally, if the d band(s) overlaps a higher conductivity can be obtained. In other cases, the overlap of d orbitals is limited, and the orbitals are effectively located in the individual atoms. NiO is often used as a prototypical example where this excitation is assumed to correspond either to the reaction $2\text{Ni}^{+2}\text{O}^{-2} \rightarrow \text{Ni}^{+1}\text{O}^{-2} + \text{Ni}^{+3}\text{O}^{-2}$ or to $\text{Ni}^{+2}\text{O}^{-2} \rightarrow \text{Ni}^{+1}\text{O}^{-1}$ (case of charge transfer insulator) [12]. Nevertheless, NiO can exhibit good p-type conduction, which makes it attractive as a transparent hole-transport layer[12] with applications in energy accumulation. However, TiO and VO, which have the same crystallographic structure, exhibit d orbitals of the type d_{xy} , d_{xz} and d_{yz} on the metal ions strongly overlap creating a wide t_{2g} band only partly filled by

1 electrons. Consequently, TiO and VO have metallic conductivity, $\sim 10^3 \text{ 1}/\Omega\cdot\text{cm}$ at 25 °C
2 [11], and an appropriate radiation light can promote the electrons transforming radiated
3 light into other form of energy. Those ceramic semiconductors are the base of the
4 photovoltaics, being its mayor limitation the low value of the quantum efficiency due to
5 the high rate of recombination sites at the surface[11].
6
7

8 TMO can be considered intrinsic semiconductors since their charge is neutralized,
9 which means that $n = p$, but even undoped MTO structures exhibit defects in the crystal
10 lattice varying the proportion between the number of oxygen atoms and the number of
11 metal atoms and hence breaking the balance of charges. Then, the TMO stoichiometry
12 is declining itself to one side or the other making the conduction possible by vacancies
13 or electrons. These defects are mainly produced during synthesis or sintering
14 processes. It is the case of ZnO, which is n-type intrinsically due to native oxygen
15 vacancy inherently present in the crystal lattice. Each oxygen vacancy provides two
16 free electrons. The number of vacancies created depends on the preparation of the
17 ZnO-based material, i.e. an oxygen deficient environment during ZnO thermal
18 processing [13]. A simple way to determine the intrinsic semiconductor nature of the
19 TMO-based materials consists in the measurement of the capacitance at different
20 voltages plotting the results in a $1/C^2$ vs V curve. If the linear range of the curve has a
21 positive slope, then the TMO-based material is a p-type semiconductor, otherwise it is
22 a n-type[14].
23
24
25
26
27
28
29
30
31
32
33

34 **2. Profiting TMO electrochemical performance through the processing** 35 **strategies** 36 37 38

39 From the beginning of the XXI century, the knowledge on semiconductor ceramic
40 oxides has become a key element when it comes to the evaluation of the PCs
41 performance.
42
43

44 The graph in figure 5a shows the published reviews especially dedicated to PCs from
45 2000 until now. The first review on this topic appears in 2002 and it is not until 2013
46 when its popularity increases exponentially until the present. Around 40 reviews about
47 these energy storage systems were published during this period, it is observed that
48 studies of the electrode active material have been specifically emphasized, in terms of
49 composition and morphology, while only a slight assessment of the electrolyte
50 characteristics has been evaluated. Figure 5b illustrates how the fifty percent of these
51 reviews recollected in table 3 are only focused on specific ceramic oxides compositions
52 or/and their processing, while a 6% of them are targeted on the electrolyte, and the
53
54
55
56
57
58
59
60
61
62
63
64
65

remaining publications mix polymers and carbon-based materials in different types of electrodes.

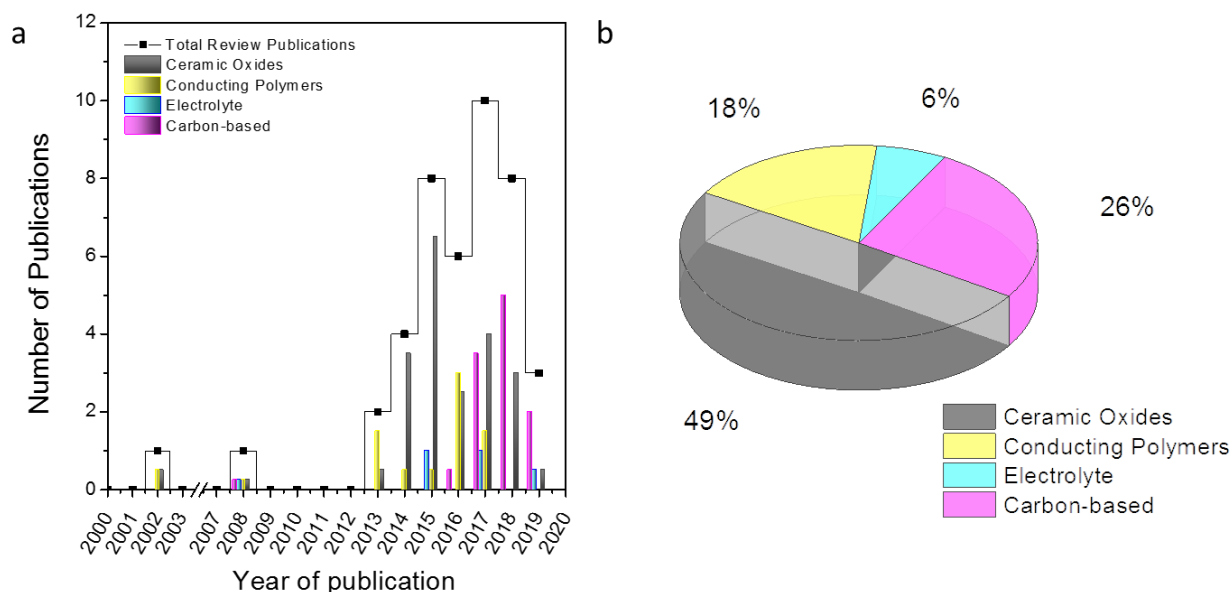


Figure 5. a) Overview of the published reviews since 2000 by year and main topic. b) Topic distribution of all the reviews about pseudocapacitors (Scopus) from 2000.

Table 3. List of the reviews published since 2000 ordered by the date of publication and classified depending on the main research topic assessed

Review	Topic	Ref	Publication Date
Carbon-Based Metal-Free Catalysts for Energy Storage and Environmental Remediation	Carbon-based	[15]	March 2019
Background, fundamental understanding and progress in electrochemical capacitors	Carbon-based & Electrolyte	[16]	March 2019
A review on recent advances in hybrid supercapacitors: Design, fabrication and applications	Ceramic Oxides & Carbon-based	[17]	March 2019
Puzzles and confusions in supercapacitor and battery: Theory and solutions	Carbon-based	[18]	October 2018
Lignin in storage and renewable energy applications: A review	Carbon-based	[19]	September 2018
Review of Hybrid Ion Capacitors: From Aqueous to Lithium to Sodium	Ceramic Oxides & Carbon-based	[20]	July 2018
Emergent Pseudocapacitance of 2D Nanomaterials	Ceramic Oxides & Carbon-based	[21]	May 2018
Materials for supercapacitors: When Li-ion battery power is not enough	Ceramic Oxides & Carbon-based	[22]	May 2018
Energy Storage in Nanomaterials – Capacitive, Pseudocapacitive, or Battery-like?	Ceramic oxides & Carbon-based	[23]	March 2018
Overview of nanostructured metal oxides and pure nickel oxide (NiO) electrodes for supercapacitors: A review	Ceramic Oxides (Nickel)	[24]	February 2018
Recent advances of graphene-based materials for high-performance and new-concept supercapacitors	Carbon-based	[25]	January 2018
Three-Dimensional Binder-Free Nanoarchitectures for	Ceramic oxide &	[26]	December 2017

	Advanced Pseudocapacitors	Carbon-based		
1	Recent advances in nanostructured vanadium oxides	Ceramic Oxide	[27]	December 2017
2	and composites for energy conversion	(Vanadium)		
3	Interlayer nanoarchitectonics of two-dimensional	Ceramic Oxides	[28]	December 2017
4	transition-metal dichalcogenides nanosheets for energy			
5	storage and conversion applications			
6	Tailoring pseudocapacitive materials from a	Ceramic Oxides,	[29]	December 2017
7	mechanistic perspective	electrolyte & Carbon-		
8		based		
9	Energy efficient graphene based high performance	Carbon-based	[30]	August 2017
10	capacitors			
11	Redox-electrodes for selective electrochemical	Ceramic Oxides &	[31]	June 2017
12	separations	Conducting Polymers		
13	Carbon-based supercapacitors for efficient energy	Carbon-based	[32]	may-17
14	storage			
15	Electrical and electrochemical properties of conducting	Conducting polymers	[33]	April 2017
16	polymers			
17	Pseudocapacitive materials for electrochemical	Ceramic Oxides,	[34]	January 2017
18	capacitors: From rational synthesis to capacitance	electrolyte & Carbon-		
19	optimization	based		
20	Design and preparation of electrode materials for	Ceramic Oxides,	[35]	2017
21	supercapacitors with high specific capacitance	electrolyte & Carbon-		
22		based		
23	Vanadium Based Materials As Electrode Materials For	Ceramic Oxides	[36]	October 2016
24	High Performance Supercapacitors	(Vanadium)		
25	Conducting Polymers for Pseudocapacitive Energy	Conducting Polymers	[37]	September 2016
26	Storage			
27	Polyaniline-based electrodes: recent application in	Conducting Polymers	[38]	August 2016
28	supercapacitors and next generation rechargeable			
29	batteries			
30	Quinone and its derivatives for energy harvesting and	Conducting Polymers	[39]	June 2016
31	storage materials			
32	A mini review of designed mesoporous materials for	Ceramic Oxides &	[40]	April 2016
33	energy-storage applications: From electric double-	Carbon-based		
34	layer capacitors to hybrid supercapacitors			
35	Review on advances in porous nanostructured nickel	Ceramic Oxide	[8]	March 2016
36	oxides and their composite electrodes for high-			
37	performance supercapacitors			
38	Understanding performance limitation and	Ceramic Oxides &	[41]	November 2015
39	suppression of leakage current or self-discharge in	Conducting Polymers		
40	electrochemical capacitors: A review			
41	A review of electrolyte materials and compositions for	Electrolyte	[42]	November 2015
42	electrochemical supercapacitors			
43	MnO₂-based nanostructures for high-performance	Ceramic Oxides	[43]	September 2015
44	supercapacitors	(Manganese)		
45	Rare earth and transitional metal colloidal	Ceramic Oxides	[44]	August 2015
46	supercapacitors			
47	Nanostructured electrode materials for electrochemical	Ceramic Oxides	[45]	June 2015
48	capacitor applications			
49	Nanostructured Mo-based electrode materials for	Ceramic Oxides	[46]	April 2015
50	electrochemical energy storage	(Molybdenum)		
51	Nanostructured Mn-based oxides for electrochemical	Ceramic Oxides	[47]	February 2015
52	energy storage and conversion			
53	Recent development in spinel cobaltites for	Ceramic Oxides	[48]	January 2015
54	supercapacitor application			
55	Recent progress in nickel based materials for high	Ceramic Oxides	[49]	December 2014
56	performance pseudocapacitor electrodes			
57	Nanowire electrodes for electrochemical energy storage	Ceramic Oxides &	[50]	December 2014
58	devices	Conducting Polymers		
59				
60				
61				
62				
63				
64				
65				

Microwave-assisted synthesis of metal oxide/hydroxide composite electrodes for high power supercapacitors - A review	Ceramic Oxides	[51]	October 2014
Cu-based materials as high-performance electrodes toward electrochemical energy storage	Ceramic Oxides (Copper)	[52]	February 2014
Recent advances in conjugated polymer energy storage	Conducting Polymers	[53]	February 2013
Electrospinning technology for applications in supercapacitors	Ceramic Oxides & Conducting Polymers	[54]	2013
Materials for electrochemical capacitors	Ceramic Oxides, Carbon-based, electrolyte & Conducting Polymers	[55]	November 2008
Electrochemical capacitors	Ceramic Oxides, electrolyte & Conducting Polymers	[56]	September 2002

The election of the electroactive material plays a crucial role in the final response for the device. Among all metal oxides/hydroxides, TMOs have been regarded as promising electrode materials for SCs owing to their changeable valence and theoretical capacities[57] among others electrochemical properties. However, the selection of the electrode compound is not always based on their electrochemical response since the cost and the availability are variables, which should be considered for product fabrication scaling or its commercialization, i.e. ruthenium, indium, tungsten or vanadium are more expensive and less available than manganese, iron, titanium, nickel or copper, among other metals.

2.1. The parameters with implication in the TMO electrochemical performance

Depending on the valence and oxidation numbers, when binds to oxygen forming the semiconductor, the transition metal presents different semi-occupied *d* orbitals, determining the redox reactions through which the energy is stored. The theoretical capacitance, C_t , depends on the number of electrons exchanged participating in the redox reaction, and it can be calculated following equations (10) and (11):

$$C_t = n \cdot n_{e^-}^0 \cdot F \quad (10)$$

$$C_t/m = \frac{n_{e^-}^0 \cdot F}{MW} \quad (11)$$

where the molecular weight of the TMO, *MW*, and the number of exchanged electrons in the redox reaction, $n_{e^-}^0$, depend on the electrode composition and are related to the theoretical capacitance per the electrode mass, C_t/m , by the Faraday constant, *F*. The final units of C_t are F/g, if we assume 1 V of potential.

As theoretical capacity is based on intrinsic properties (eq. 10 and 11) it has to be also considered an intrinsic characteristic of TMOs. In the table 4, the theoretical

capacitance, C_t , was calculated for different metal oxides at their most common valences.

Table 4. Theoretical capacitance calculated by the equation 11 for different MO

Metal oxide	Theoretical Capacitance (F/g)
RuO₂	1450
MnO₂	1109
Co₃O₄	2003
Fe₃O₄	416
V₂O₅	530
NiO	2583
TiO	2416
SnO₂	2560
In₂O₃	708
Bi₂O₃	418
WO₃	416
MnO_x	>1300
MoO₃	670
CuO	2425
Cu₂O	674

Although metallic oxides such as NiO or TiO have high values of theoretical capacity, 2583 and 2416 F/g, respectively, the final electrochemical response also depends on other intrinsic properties of the material, such as the bands structure of the TMO and more precisely its band gap, which determine its electronic conductivity. Thus, the capacitance of the electroactive material is usually lower than the theoretical value.

Intrinsically the charge transfer is intimately related to electron conductivity. Free electron mobility implies higher conductivity of the semiconductor. Therefore, n-type semiconductors (electron conduction) are better conductors than p-type conductors (hole conduction). The reason for this lies in the location of these electrons. For n-type the free electrons are in the conduction band, while p-type semiconductors have the holes in the valence band, and the movement of the holes is governed by the electrons movement that participate in the atomic bonds, then they have less freedom and thus, slowing down the charge transfer.

Moreover, the specific capacitance depends on extrinsic properties such as charge transfer, ion diffusion, reversibility of the redox reactions and cyclability. These extrinsic characteristics are directly related to both the electronic configuration of the metals, the crystallographic properties and related band gap of TMOs, but also on the electrode microstructure which define the interface of the electroactive material with the

electrolyte and which mainly depends on the processing strategies (synthesis, shaping and consolidation).

Extrinsically, the electrochemical reversibility of redox reactions describes the rate of the electron transfer, being faster when the window of potential determining the redox reaction in CV is smaller. In other words, the distance between the oxidation and reduction peaks that can be seen in a PCs electrode CV is shorter. In this sense, the cyclability, considered as the number of times an electrode can be recharged before they begin to break down, and rate capability, considered as ratio of the galvanostatic discharge capacity to the total discharge capacity for various discharge rates[58], are electrochemical properties of the electrodes, related to the chemical and structural stability of their microstructures being also extrinsic properties. Figure 6 shows common shape of a charge/discharge cycles (figure 6a) and rate capability plots (figure 6b) of different electrodes. The electrodes that keep constant their specific capacitance after several charge/discharge cycles exhibits a 100% cyclability, while the rate capability relates differences in the capacitance values registered for the electrode when it is cycled at different sweep rates.

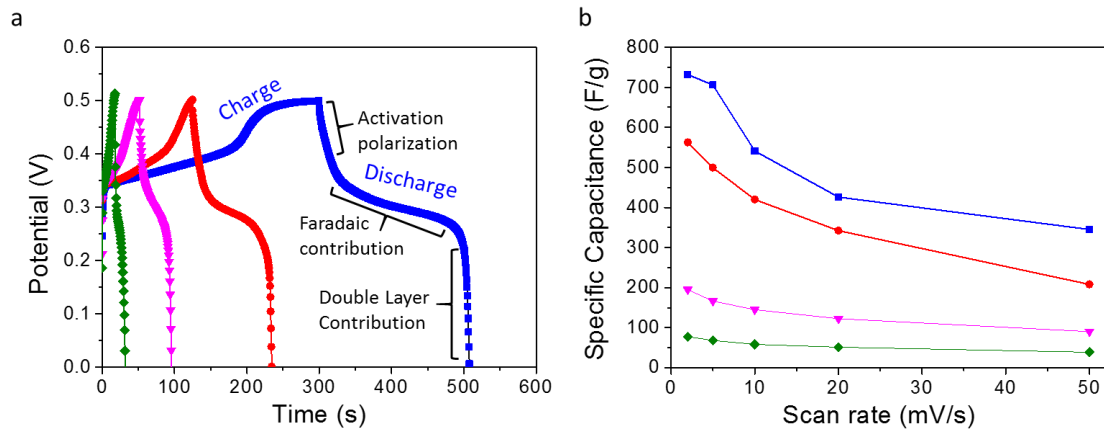


Figure 6 a) Charge – discharge curves of different electrodes at the same current density (2 A/g). b) Rate capability obtained from the cyclic voltagrams for different electrodes at different scan rates.

The more resistive the electrode, the lower the rate capability. The resistance of the electrode varies depending on its microstructural characteristics, such as the ion diffusion in the electrolyte solution and the electron transfer resistance of boundaries between the electroactive particles in the ceramic semiconductor microstructure, as well as the interface resistance between the current collector and the electroactive material. All these properties can be modified acting on either the crystallography of the

1 TMO, and on the morphology and the microstructure of the electrode. Consequently,
2 the synthesis and shaping processes of the electrode has a crucial role in the
3 development of high-performed electrodes.
4

5 Table 5 summarizes TMO-based PCs and their electrochemical performance described
6 in the literature during the last decade, listed by the main metal transition in its
7 composition, where the synthesis or shaping technologies used to fabricate the tested
8 electrode have been highlighted. In this table, only TMO-based electrodes shaped onto
9 metal substrates have been collected, since those electrodes shaped onto graphite
10 substrates or carbonaceous species have been include in table 6 and considered
11 hybrid devices due to the contribution of the substrate to the specific capacitance.
12
13
14
15
16

17 Shaping strategies, can differentiate between the current routes of electrode
18 preparation by mixing as-synthesized electroactive particles with binders and
19 conductive materials (generally carbonaceous species), and one-step processing
20 routes where synthesis and shaping are processes that take place simultaneously. In
21 the current route of the electrode preparation, research efforts are focus on the control
22 of the synthesis procedures, such as hydrothermal or solvothermal precipitation,
23 colloidal sol-gel synthesis, etc.[59–61] After the synthesis of particles, the resulting
24 slurry/paste obtained by blending is applied onto the collector substrate by different
25 shaping processes such as dip-coating, drop-casting, tape-casting, spin coating,
26 electrophoretic deposition, etc.[62,63] Most of these synthesis techniques evolve to one-
27 step processes, since coating technologies allows the proper film growth on the
28 substrate during the synthesis of the nanostructure, resulting on binder-free electrodes.
29 This is the case of process such as sol-gel coating, hydrothermal/solvothermal growth,
30 electrodeposition, CVD, etc.[59,64,65]
31
32
33
34
35
36
37
38
39
40
41

42 Related to the composition of the TMO-based PCs, the RuO_2 has been the most widely
43 investigated TMO because of its superior electrochemical properties such as high
44 conductivity, highly reversible redox process in a large potential window and thermal
45 stability, which lead to a worthy cyclability and rate capability (the specific capacitance
46 remains stable after CV at different sweep rates)^{36,37}. However, its practical
47 applicability is impeded by its toxicity, high costs and naturally less abundance as raw
48 material. In fact, due to cost consideration, non-strategic TMO candidates with
49 excellent theoretical capacitive values have attracted much attention such us as
50 manganese[68], nickel[57], cobalt[69], zinc[59], and iron[6].
51
52
53
54
55
56
57

58 Noteworthy is the widely use of manganese oxides for this type of devices due to their
59 rapid cationic diffusion at high charge and discharge rates, environmental friendliness,
60
61
62
63
64
65

and abundant raw materials. As a transition metal, manganese presents several oxidation states and therefore a great variety of stable oxides (MnO , Mn_3O_4 , Mn_2O_3 , MnO_2) showing ideal charge–discharge curves. For instance, Maiti et al.[70] or Qiu et al.[71] have achieved a more than the 95% of capacity retention of values of specific capacitance as higher as 840 and 775 F/g, respectively.

Other interesting metal, due to its abundance, is the iron. Fe_3O_4 has been employed to build electrodes, however this material possesses slower electron transport rates than other TMO because of their poor electrical conductivities. Co_3O_4 , is also employed for this kind of devices because it exhibits excellent reversible redox behavior, high conductivity, long-term performance, and good corrosion resistance[72]. V_2O_5 is the other promising candidate to replace the ruthenium. This strategic material is easier available than ruthenium, but the price is still elevated. However, the unique layered structure and mixed oxidation states confer to this material a suitable option[73]. Finally Cu-based oxides are other candidates toward practical electrochemical energy storage devices due to their abundant, low cost, easy synthesis and environmentally friendly merits[74].

Special attention is given to Nickel-based materials[75–82], in particular, nickel hydroxide ($\text{Ni}(\text{OH})_2$) and nickel oxide (NiO) have attracted extra interest due to their high theoretical specific capacitance, easy oxidation process[72], high chemical and thermal stability, ready availability and low price. In 1996, Liu and Anderson for the first time used porous NiO as a possible electrode material for SC applications measuring specific capacitances ranging 50-60 F/g[83], far away from the theoretical value. Nowadays several studies of NiO -based electrodes have reported specific capacitances closer to the theoretical value, 2018 F/g[84], 2192 F/g[85], 2186 F/g[86]. It should be also noted that the published work to date with the highest capacity obtained is the supercapacitor developed by Chen et al.[4] It was fabricated by in situ electrochemical activation of Ni-based colloids from a NiCl_2 electrode, taking advantage of the different nickel oxidation states. The highest specific capacitance was 10286 F/g at a current density of 3 A/g, indicating that a three-electron Faradaic redox reaction ($\text{Ni}^{3+} \leftrightarrow \text{Ni}^0$) occurred.

2.2. Strategies for the micro, nanostructure modification to maximize the electrochemical response of the TMO based electrodes

As it has been mentioned above, the full profiting of the surface reactions of the TMO is still a challenge since the electrochemical response of the electrodes not only depends on the inherent properties of the selected material, such as their theoretical capacitance or their electronic band structure. Electrodes must present a high exposed

Table 5. Summary of PCs performances reported in recent publications

Ref	Material	Synthesis Strategies	Shaping Strategies	Morphology	Specific Capacitance	Capacitance retention
Manganese						
[6]	Mn ₃ O ₄	Hydrothermal	Pressed	Nano-capsules	750 F/g at 5 A/g	107% after 9000 cycles
[5]	Mn ₂ O ₃	Solvothermal+ calcination	Pressed	Nanobars	250 F/g at 0.2 A/g	~75% after 3000 cycles
[7]	MnO ₂	Hydrothermal	Pressed	nanowire net	775 F/g at 2 mV/s	97% after 5000cycles
[7]	Au/MnOx	Au sputtering & MnO electrodeposition		Nanocone structure	840.3 F/g at 2 A/g	96.5% after 2000 cycles
[8]	KMnO ₂	Hydrothermal	Drop-casted	--	303 F/g at 0.2 A/g	100-90% after 1000 cycles
Nickel						
[6]	Ni(OH) ₂ and NiO	Hydrothermal	Pressed	Pompon-like spheres	1028.5 F/g at 2.22 A/g	98.5% after 1000 cycles
[8]	NiWO ₄ -CoWO ₄	Co-precipitation	Pressed	Cauliflower-like	196.7 C/g at 0.5 A/g	110% after 5000 cycles
[5]	NiO	Hydrothermal + calcination	Pressed	Flowerlike	1297.3 mAh/g at 200 mA/g	--
[8]	NiO	Hydrothermal + calcination	Pressed	Hollow nanosphere	612.5 F/g at 0.5 A/g	90% after 1000 cycles
[9]	NiO	Hydrothermal + calcination	Pressed	Mesoporous Spheres	1140 F/g at 10 A/g	100% after 1000 cycles
[9]	NiO	Hydrothermal + areogel	Pressed	--	901 F/g at 0.5 A/g	93% after 3000 cycles
[9]	LiNiVO ₄	Hydrothermal + calcination	Pressed	--	456 F/g at 0.5 A/g	99.6% after 1000 cycles
[9]	NiCoO	Hydrothermal + calcination	Pressed	Microspheres	1884 F/g at 3 A/g	79.4% after 10000 cycles
[9]	NiCo ₂ O ₄	Hydrothermal + annealing + electrodeposition	Pressed	--	1080 F/g at 6 A/g	83% after 4000 cycles
[9]	NiCo ₂ (CO ₃) _{1.5} (OH) ₃ @NiCo ₂ S ₄	Hydrothermal	Pressed	Urchin-like	956.4 F/g at 4 A/g	80.1% after5000 cycles

- 1
- 2
- 3
- 4
- 5
- 6
- 7
- 8
- 9
- 10
- 11
- 12
- 13
- 14
- 15
- 16
- 17
- 18
- 19
- 20
- 21
- 22
- 23
- 24
- 25
- 26
- 27
- 28
- 29
- 30
- 31
- 32
- 33
- 34
- 35
- 36
- 37
- 38
- 39
- 40
- 41
- 42
- 43
- 44

[9 6] [3]	NiO	Precipitation	Drop-casted	--	243 F/g at 2 mV/s	--
[9 7] [9 8] [9 9] [1 00]	Ni(OH) ₂ /MnO ₂	Soaking	Coate	Nanorods	2937 F/g at 5 A/g	92.3% after 25000 cycles
	Ni(OH) ₂	Hydrotehmal+ electrochemical deposition + CBD		Nanoflakes	325 F/cm ³	80% after 1000
	NiO	Sorvothermal	Spin-coated	Nanospheres	1386 F/g at 1 A/g	78.5% after 5000 cycles
	NiO	Sparking	Drop-coated	--	402.7 C/g at 1 A /g	88% after 1000 cycles
	NiO	Sparking		Foam-like	920 C/g at 1 A/g	96% after 1000 cycles
[6 3]	Co-doped Ni(OH) ₂	LA laser-induced L	Drop-casted	Curly nanosheet	720 F/g at 6 A/g	92% after 1000 cycles
Co						
[6 2] [6 9] [1 01]	ZnCo ₂ O ₄	Hydrothermal	Pressed	Oval-like	2555.8 F/g at 2 mV/s	83.7% after 3000 cycles
	Co ₃ O ₄	Laser Ablation in Liquid	Dropwise presed with gel	--	177 F/g at 1 mV/s	100% after 20000 cycles
	LiCoO ₂	Solvothermal	Pressed	--	654 F/g at 2 A/g	86.9% after 4000 cycles
[6 5] [1 02]	CoS	Hydrothermal + Anion exchange reaction		--	103 mAh/g at 2 A/g	79% after 16000 cycles
	ZnCo _{1.5} (OH) _{4.5} C _{10.5} ·0.45H ₂ O	Precipitation	Deposition	Nanosheets	3946.5 F/g at 3 A/g	81% after 5000 cycles
[6 4] [1 03]	Co ₃ O ₄ CoOH Co(OH) ₂	Electrochemical precipitation		2D hexagonal platelet	627 F/g at 5 mA/cm ²	90% after 1000 cycles
	Co(OH) ₂ -Au	Electroplating			1800 F/g at 20 A/g	78% after 3000 cycles
[6 1]	CoNiO ₂	Solvothermal	Pressed	Microspheres	~854.9 and ~414.5 F/g at 1 and 20 A/g	100.8% after 10000 cycles
Ru						

Table5

[1						
04	RuO ₂	Theoretical calculation				
]						
Fe						
[1						
05	np-Ag@Fe ₂ O ₃	Electrodeposition			~608 F/g at 10 A/g	84.9 % after 6000 cycles
]						
[1						
06	MnFe ₂ O ₄	Hydrothermal	Drop-casted		282.4 F/g at 0.5 A/g	85.8 % after 2000 cycles
]						
W						
[1						
07	WO ₃	Electrodeposition + crimping	Pressed	Flower-like	196 F/g 10 mV/s	85% after 5000 cycles
]						
Mo						
[1						
08	Ni/MoO/VO ₂	Electrochemical deposition		Nanowires	477 mF/cm ² 1 mV/s	95% after 20000 cycles
]						
V						
[1						
09	Na _{0.33} V ₂ O ₅	Co-precipitation	Pasted	Nanorod-like	168 F/g at 0.5 A/g	81% after 50000 in NaCl
]						
[1						
10	TiO ₂ -V ₂ O ₅	Forming gel	Drop-casted	Mesoporous tube-like	310 F/g at 2 mV/s	94% after 1000 cycles
]						
Sn						
[1						
11	Sn@SnO ₂	Hydrothermal + calcination	Pressed	Nanosphetres	906.8 F/g at 1mV/s	~100% after 2000 cycles
]						
Zn						
[5						
9]	ZnO-Au NC	Sol-gel	Hydrothermal		205.7 F/g at 2 A/g	--
Ce						
[1						
12	CeO ₂	Solvothermal + calcination	Coated	Brick-upon-tile	1204 F/g at 0.2 A/g	100% after 5000 cycles
]						
Ag						
[1						
13	Au/AgO (NPAAC)	Dealloying–stripping			82 F/g at 5 A/g	94% after 10000 cycles
]						

surface area with abundant reaction sites and successfully impregnate the electrolyte along their electroactive microarchitecture, as well as they should promote the electrons mobility through the metal oxide microstructure reducing the resistance at the interface between the electroactive material and the conductive collector. Thus, an optimal performance of a PC requires of a consolidated nanostructure with a highly hierarchically organized macro-meso-microporosity, holding accessible redox active sites, to step up charge transfer and ion diffusion capability.

From decades, the researchers devoted to the study of PCs have focused their efforts on improving their electrochemical response by different routes. Figure 7 gives an overview of the current strategies employed to overcome this challenge. Processing strategies have been classified in three different groups: (i) Synthesis and modification of particles or nanostructures; (ii) Microstructure tailoring by shaping films or coating metal collectors; and (iii) Technologies based on the combination with carbon-based materials for the development of hybrid capacitors or ultracapacitors.

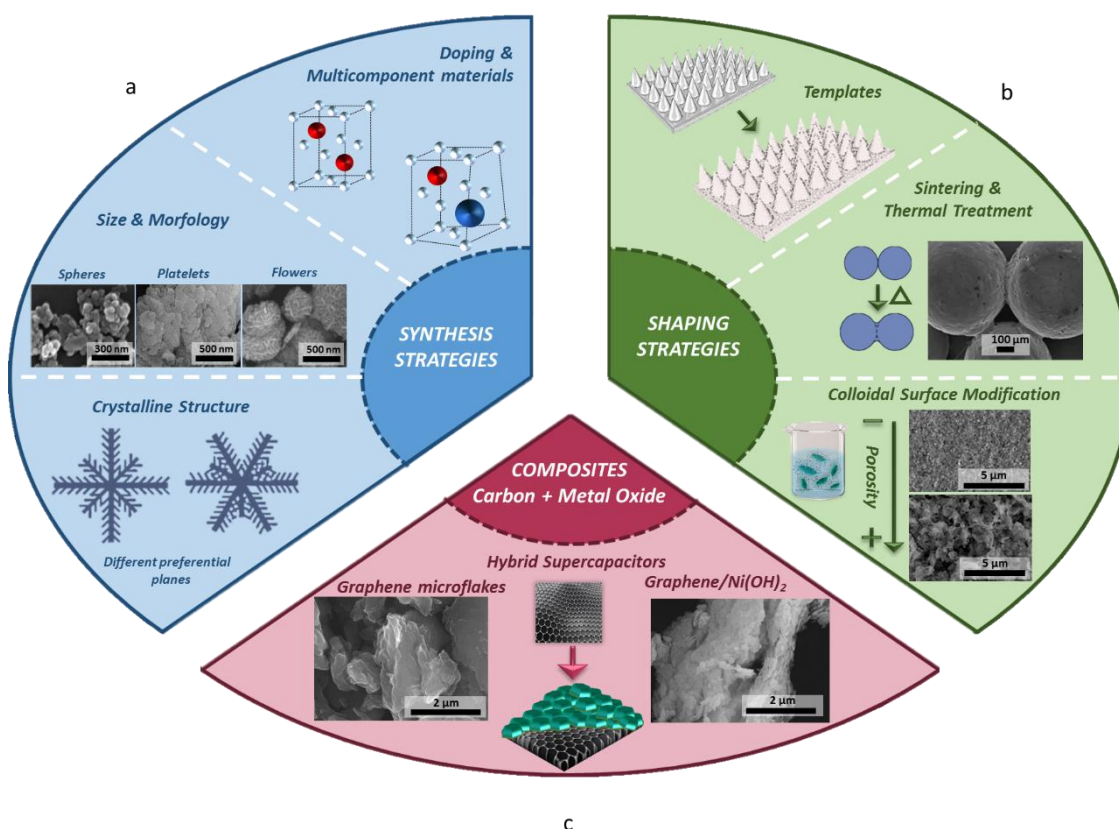


Figure 7. Current strategies for the improvement of the final electrochemical features in pseudocapacitors. a) In blue, synthesis modification of particles and 0D, 1D, 2D and 3D nanostructures, changing morphology, crystallography and defining new solid solutions. b) In green, shaping films and coating of metal collectors by the nanoparticles assembling and microstructure tailoring, designing porosity (specific

surface area, including endo- and exo-templates and sintering. c) In red, technologies based on in situ synthesis of composites using carbon-based materials and TMO.

The first strategy (Figure 7 in blue sector) is related with the physic-chemical modification of the crystallography of the particles or the synthesis of nanostructures (0D or nanocrystals and nanoparticles, 1D or nanofibers and nanotubes, 2D or nanoflakes or nanoplatelets, and 3D or tridimensional flower-like structures), or directional crystal growing, acting directly over the synthesis process [114]. These processing strategies are focused on the development of new applications of synthesis processes. Many review papers and articles demonstrate that the nanosize, the morphology (0D, 1D, 2D and 3D) and the crystallography modification at the atomic level, by the inclusion of dopants and the creation of vacancies, provides new opportunities to achieve higher efficiency.

In the second category (Figure 7 in green sector), the shaping strategies are included. The use of different process to shape thin or porous thick films employing the as-synthesized new nanostructures are the processing strategies considered in this category. Among available coating techniques[115], those based on the control of the colloidal-chemical parameters of sols, suspensions, inks or slurries should be highlighted due to their reliability, scalability and the wide range of possibilities for the microstructure tailoring. In those techniques, the use of templates or microstructural modifiers, the control on the shaping parameters and the further selection of specific sintering treatments could be managing to maximize the electrochemical properties of the active electrode microstructure. Some examples of the final properties that can be controlled through this collection of processing strategies to optimize the electrochemical response of PCs are: i) the exposed specific surface area, which determines the redox events profiting and ion diffusion through the electrolyte. ii) The connectivity between ceramic semiconductor particles, which largely regulates the charge transfer phenomena. And iii) the consolidation level and adherence/joining of the coating and the metal collector, which define the electrical resistance of the system.

Finally, the last group of the proposed strategies (Figure 7 in red sector) shows the combination of TMO with the materials used for the EDLC electrodes (carbon-based). This strategy defines a new family of storage devices based on carbonaceous composite structures: the hybrid supercapacitors, or also called ultracapacitors, which offer the combination of both energy storage mechanisms.

2.2.1. Based-synthesis strategies of the processing of TMO for pseudocapacitors

The first group of the proposed classification is based on the development of new synthetic routes in order to design nanoparticles with complex morphologies and crystallography. The 0D nanocrystals and/or nanoparticles are ideal systems for exploring a large number of novel phenomena at the nanoscale and at the atomic level, to investigate the effect of size and dimensionality dependence of the electrochemical properties. The 1D and 2D nanostructures exhibit unique shape-dependent characteristics and consequently, they have been used as building blocks to shaped electroactive films and understand the mechanism of the nanostructure growth and their implications in the enhancement of the electrochemical response of PCs. Finally, 3D nanostructures attract intensive research interest because they present a high exposed surface area, supplying enough absorption sites for all involved molecules in a small space, while lead to a better transport of species through their well-connected microstructure [114]. Different features of as-synthesized microstructures with the same composition can be tuned by modifying the synthesis parameters. Figure 8 shows different types of NiO nanostructures synthetized in our laboratory by ultrasound-aided chemical precipitation. The morphologies were obtained by changing the precursor's concentration, the ratio of reactants and the ultrasonic power [116,117].

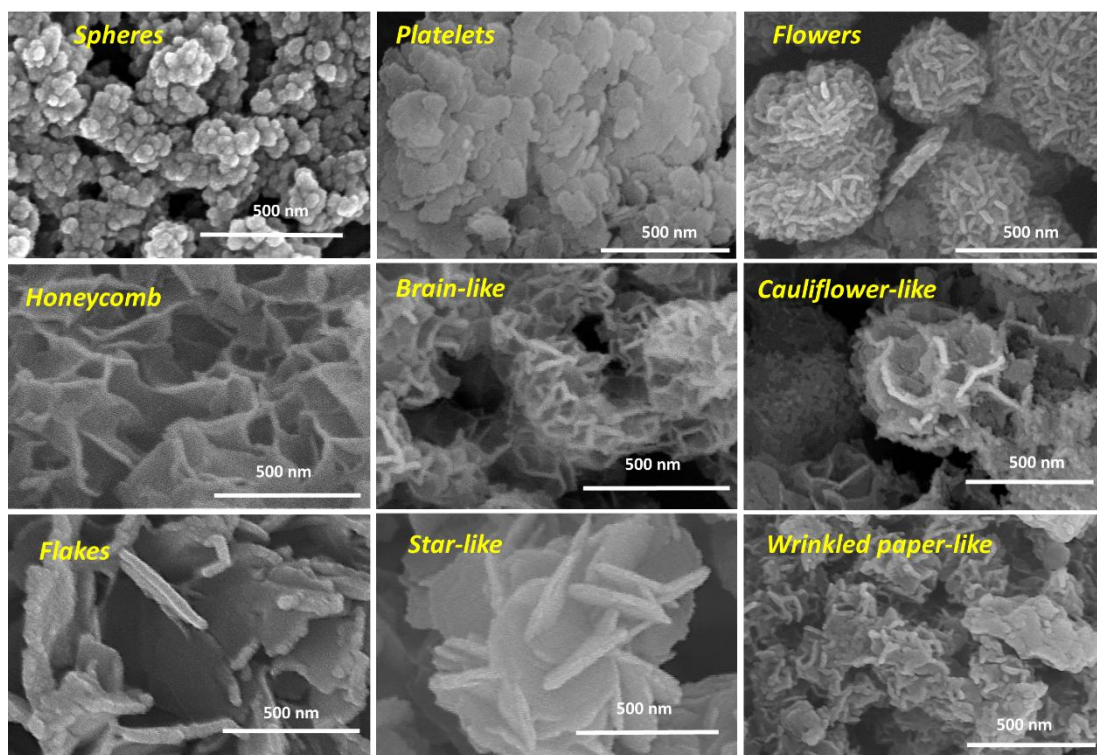


Figure 8. Typical SEM images of NiO nanoparticles with different types of morphology: spheres, platelets, flowers-like, etc.

Alternatively, the progress in new multicomponent electroactive materials have been significantly increased obtaining binary [101,118,119], ternary [64,88,108], quaternary [120] oxides, etc. Although, the description of new synthesis processes is not aimed this review, several physical and chemical methods have been analyzed to give the most recent overview about the topic.

The most common processing method for PCs electrodes consists on a first stage of synthesis of the electroactive material and its subsequent shaping onto the collector substrate. These collectors can range from metal substrates to glass coated with conductive ceramic films such as ITO or FTO. Conventionally, the preparation procedure for TMO-based electrodes lies on the formulation of a slurry by the blending of electroactive material with additives like carbon black (CB), acetylene black, PVDF, PTFE, etc. which act as binders to enhance the contact between particles of active material. And then, these mixtures are directly deposited, pasted or pressed onto conductive substrates[3,5,6,60,62,89,93]. Depending on the way the pressure is applied, two techniques are distinguished. The most used is called “die pressing” in the paste is put into a die and shaped by the punches under a load (see figure 9). Secondly, isostatic pressing, which consist in consolidating the powder by an isostatic pressure applied by a liquid on a shaped mold.

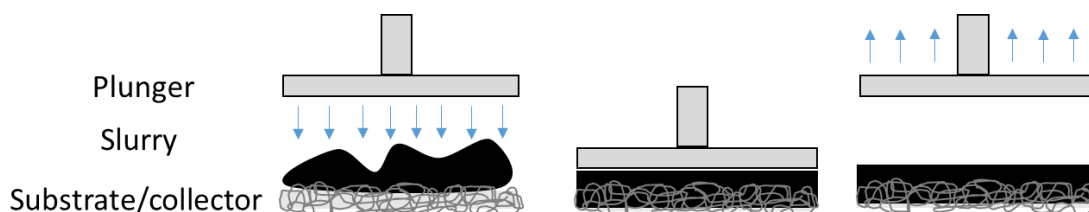


Figure 9. Scheme of the most commonly used conventional shaping method: The die pressing.

The sol-gel, solvothermal and hydrothermal syntheses, together with precipitation or co-precipitation, are the most common routes for particles synthesis and subsequent pressing. Nowadays, these syntheses are in continuous development for its application in SC. In view of the publications collected in table 5, the hydrothermal synthesis is the most employed. It consists in a chemical reaction of precipitation under the appropriate temperature and pressure conditions (normally above 100 °C and 1 bar) with water as liquid medium. Commonly, reactions take place in an autoclave. Using this kind of synthesis, Maiti et al.[70] prepared single-phase α - MnO_2 with an interconnected nanowire morphology forming a network, which results in a specific pseudocapacitance

of 775 F/g. Furthermore, after 5000 cycles the capacitance retention of the pressed electrode was 97%. However, the employment of Ni-based oxides shows better electrochemical responses. Wang et al.,[60] synthesized β -Ni(OH)₂ hollow microspheres, which show excellent capacitance behavior (1028.5 F/g) at a charge/discharge current density of 2.22 A/g and 100% of coulombic efficiency after 1000 cycles. In the case of Li et al.,[93] the hydrothermal synthesis of bixite microspheres (NiCoO) was followed by a thermal treatment and then pressed with carbon black and PTFE onto a nickel foam. The obtained capacitance value was 1884 F/g at 3 A/g, retained the 79.4% of its initial capacitance after 10000 cycles.

Solvothermal syntheses differs from hydrothermal processes in the use of organic solvents as reaction media. Using organic solvents, Cai et al.[98] synthesized NiO nanospheres inside of an autoclave by a simple and low-cost solvothermal method, which were spin-coated onto different substrates forming homogeneous films. The electrodes presented a high capacitance (1386 F/g at 1 A/g) and a cyclability retention of 78.5% after 5000 cycles.

As synthesis techniques, the precipitation and co-precipitation synthesis must be take into account because they are also widely employed for TMO-based electrodes preparation. The objective of these techniques consists on preparing ceramic oxides through the formation of intermediate compounds, such as hydroxides or oxalates achieving a perfect homogeneity even after as-synthesized powder calcination and annealing. The use of one metal salt, or more than one, as precursor allows obtaining of a single precipitation or a multicomponent suspension, respectively. Wang et al.[88] synthesized by co-precipitation a mesoporous NiWO₄-CoWO₄ nanocomposite. The electrochemical response of this compound after pressing was 196.7 C/g at 0.5 A/g, and less than one third of rate capability losses. Similarly, Yeager et al. reported how NiO nanoparticles deposited by dropping a suspension on a target substrate generates a rough surface, which implies a larger surface area but a non-uniform thickness of the coating. The pseudocapacitive behavior obtained was tested in three-electrode half-cells with a maximum specific capacitance value of 243 F/g. Yeager et [87] al., achieved a gravimetric capacitance of 303 F/g, at a charge/discharge current of 0.2 A/g employing also drop casting for the fabrication of the electrodes based on KMnO₂ as electroactive material. The capacitive retention obtained was 87.8% after 1000 cycles. Among other, described results suggest the relevance of the binder and the shaping processes in the electrochemical behavior of ceramic semiconductor electrodes.

1 In ceramics, the technological development in thin film is widespread due to the
2 savings in material. Besides, in semiconductors for energy storage and in the electronic
3 components industry, they also have a great application in the optic coatings for their
4 application in photovoltaics, and in corrosion protection for their use to extend the life of
5 cutting tools. In spite of the two-step conventional routes, where synthesis and shaping
6 are separately performed, sometimes both steps go hand in hand. For example, the
7 growth of the particles can take place on the substrate inside the synthesis medium
8 leading to the formation of a thin film. This is the case of Mahajan et al.,[59] who
9 employed the sol-gel synthesis combined with the hydrothermal growth of ZnO-Au
10 nanocomposites, and without further processing, resulting in a specific capacitance of
11 205.7 F/g at current density of 2 A/g. In fact, sol-gel is a well know technology to
12 synthesize ceramic materials and final products with a controlled stoichiometry and
13 high purity leading to interesting microstructures for electrochemical devices[121].
14
15
16
17
18
19
20
21
22

23 Moreover, other combinations of techniques are possible. Pu et al.[94] have combined
24 hydrothermal synthesis with electrodeposition to grow oriented NiCo_2O_4 nanowires on
25 ultralight nickel foams. As-synthesized specimens were directly measured obtaining a
26 capacitance value of 1080 F/g with 17% lost after 4000 cycles. In this case, the tailored
27 hydrothermal growth of a complex morphology results in an improved electrochemical
28 performance, evading additional processing steps such as annealing treatments and
29 the use of binders. In electrodeposition, the structure, morphology, and uniformity of
30 the oxide layers can be controlled by adjusting the plating parameters such as
31 deposition mode, applied potential, current density, bath temperature, concentration of
32 precursors, and addition of complex/additive agents [122]. In the literature is easy to
33 find authors using this processing technique to prepare PCs electrodes. This
34 electrochemical one-step and cost-effective method precipitates the semiconductor
35 nanoparticles at the same time that deposition take place onto the substrate. This
36 technique also works as multicomponent precipitation if the precursor reactants are
37 dissolved in the same solution. Ju et al. [64] synthesized by electrochemical
38 precipitation, and controlling the pH, 2D hexagonal platelet based on Co onto a Ti plate
39 obtaining 627 F/g as capacitance value and a 90% of retention after 1000 cycles.
40
41
42
43
44
45
46
47
48
49
50
51

52 The synthesis of metal organic frameworks (MOFs) have been also employed in
53 developing of PCs. MOF derived CeO_2 showed a pseudocapacitance of 1204 F/g at
54 0.2 A/g with the maximum cyclability after 5000 cycles (100%). Maiti et al.[112]
55 synthesized this MOF by solvothermal method and a subsequent calcination with a
56 brick-upon-tile morphology. There are other specific thin film techniques, such as Laser
57
58
59
60
61
62
63
64
65

ablation in Liquid (LAL) or Atomic Layer Deposition (ALD) also employed in this field. Liang et al.[63] employed LAL to develop curly nanosheets of Co-doped Ni(OH)₂ electrodes obtaining an specific capacitance of 1421 F/g at a current density of 6 A/g, and a retention level of 76% after 1000 cycles. And Liu et al.[69], using the same method, have developed Co₃O₄ nanocrystals for PCs, which exhibits a capacitance of 177 F/g based on the mass, and 6.03 mF/cm² on a basis of the active material area at a scan rate of 1 mV/s. Furthermore, this electrode presents a long cyclability, 100% of capacitance retention after 20000 cycles. Other authors have used ALD. Xia et al.[123] carried out an optimized PANI–RuO₂ core–shell nanostructured electrodes, which exhibit very high specific capacitance (710 F/g at 5 mV/s) and power density (42.2 kW/kg) at an energy density of 10 Wh/kg, with a capacitance retention of 88% over 10000 cycles (higher than that obtained for just Pani-based electrodes). Nonetheless, these methods require the use of strategic technology compared to other ceramic routes described below.

2.2.2. Microstructural modification by shaping and sintering ceramic films

Following the trend of the thin films manufacture, other strategies have been proposed based on the use of binder-free techniques to modify the electrode microstructures. In those processing strategies shaping of electroactive materials is followed by a low temperature (<600°C) sintering process to consolidate the nanoceramic semiconductor structure to maximize connectivity by forming unions between particles (sintering necks).

Sintering is a well-known treatment in ceramics, which promotes the connectivity between particles and joining to the collector, making the electron transfer easier, and reducing the charge transfer resistance. Furthermore, the microstructure consolidation improves mechanical stability, which results in a longer lifetime of the device. In this sense, nanosized TMO can be consolidated by a mild sintering treatment after synthesis and shaping, achieving a stronger electrically connected electrodes, where a porous nanostructure also provides the structural tolerance needed to overpass the volume changes of the faradaic reactions. The formation of sintering necks between NiO nanoparticles in a thermal treatment of sintering at 325°C is showed in figure 10.

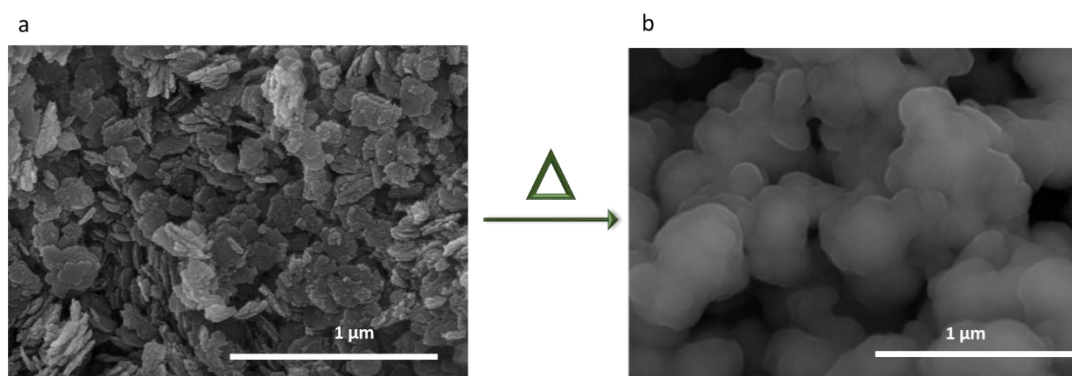


Figure 10. NiO nanoparticles before (a) and after (b) the sintering process at 325°C during 1h under Ar atmosphere.

This type of heat treatment also allows the use of endo- and exo-templates, for example, sponges or microstructural modifiers, that decompose during sintering leading to a porous microarchitecture which contributes to maximize the efficiency of the device increasing the contact between the electroactive material and the electrolyte. Moreover, the electrical conductivity can be enhanced by introducing metal [124] or nonmetal impurities [125] within the oxide nanostructure, generating donor or acceptor states in the bandgap and thereby increasing the concentration of charge carriers.

The table 6 shows publications describing PC electrodes processing routes ending by a sintering process in a furnace to consolidate the electroactive material, where parameters such as temperature, pressure, time and atmosphere was controlled to reach the proper consolidation of the oxide structure and a porosity balance ad hoc for the final application.

The hydrothermal synthesis of a thin layer followed by a mild thermal treatment to strength oxides consolidation is one of the widely extended process. Lu et al.[135] have developed NiO nanorod arrays on Ni collectors, and Yoo et al.[132] worked with Co_3O_4 on porous Ni substrates, achieving specific capacitances of 2018 F/g and 1591 F/g, respectively.

In some cases, this type of synthesis is employed in combination with other techniques apart from the final sintering to drive the crystallographic growth. For instance, Cai et al.[98] employed a spin-coating technique to form the first layer and then by hydrothermal synthesis they grew the full microstructure. In the same way, Zhou et al. [2] found a phosphorylation strategy to produce electrodes with high capacitance (2141 F/g at a scan rate of 50 mV/s).The electrode retains a high specific capacitance of 1437 F/g even after 5000 cycles at a current density of 10 A/g. They employed a hydrothermal process, before the phosphorylation, to grow the hydroxide precursors on nickel foams, and after all, the samples were calcined at 300°C for 2h under Ar flow. In

Table6

Table * - Summary of carbon-free PCs electrodes processed following a ceramic route ending by sintering process

Ref	Material	Synthesis and shapping process		Thermal treatment	Morphology	Specific Capacitance	Capacitance retention
[1 26]	Co ₃ O ₄ @Au@MnO ₂	Electrochemical deposition		250°C 2h 1 °C/min	Porous nanowalls	1532.4 F/g at 1 A/g	~ 100% after 5000 cycles
[1 27]	NiO	Electrodeposition		250°C 2h	3D cross-linked grid	2558 F/g at 2 A/g	--
[2]	Ni ₂ PNS/NF	Hydrothermal+ phosphorization strategy		300°C 2h 5 °C/min	--	2400 F/g at 50 mV/s	67 % 5000 cycles
[1 28]	NP c-V ₂ O ₃ /r-VO _{2-x}	Electrodeposition + template calcination		300°C	--	1856 F/g at 5 mV/s	93% after 15000 cycles
[1 29]	TiO ₂ /Ni(OH) ₂	Hydrothermal+CBD		300°C	Core-shell nanorod arrays	482 F/g at 0.5 A/g	--
[7 6]	NiO	Precipitation US	EPD	325°C 15min Ar	Flower-like	363F/g at 10A/g	79 % after 1000 cycles
[1 30]	NiO/Ni	Precipitation US + calcination		325 °C 1h Ar	Nanoplatelets	755 F/g at 2 A/g	62% after 1000 cycles
[1 31]	NiO	Precipitation US	Inkjet Printing	325 °C 1h Ar	Nanoplatelets	160 F/g at 2 A/g	100% after 1200 cycles
[1 32]	Co ₃ O ₄	Hydrothermal		350°C 1h 3°C/min	Nanorods	1591 F/g at 5 mV/s	~100% after 90 cycles
[1 33]	Co ₃ O ₄ or ZnO and NiO	Hydrothermal + Chemical bath deposition + sputtering of ZnO		350°C 1.5h Ar	Nanowires	853 F/g at 2 A/g	95.1% after 6000 cycles
[1 34]	MnO ₂ - NiO	hydrothermal		350°C 2h in Ar	Tubular arrays assembled by thin nanoflakes	0.35 F/cm ² at 8.5 mA/cm ²	97.4% after 1500 cycles
[1 35]	NiO	Hydrothermal US		250, 300, 350, or 400°C 3h Ar	Nanorod	2018 F/g at 2.27 A/g	92% after 100 cycles

- 1
- 2
- 3
- 4
- 5
- 6
- 7
- 8
- 9
- 10
- 11
- 12
- 13
- 14
- 15
- 16
- 17
- 18
- 19
- 20
- 21
- 22
- 23
- 24
- 25
- 26
- 27
- 28
- 29
- 30
- 31
- 32
- 33
- 34
- 35
- 36
- 37
- 38
- 39
- 40
- 41
- 42
- 43
- 44

the case of Xia et al.[133] $\text{Co}_3\text{O}_4/\text{NiO}$ core-shell nanostructures were firstly prepared. Two-step solution-based method was employed in order to synthesize these nanoparticles. It consists in a combination of a hydrothermal synthesis and a chemical bath deposition (CBD) with a final ZnO sputtering. The final calcination was at 350°C for 1.5 h and under Ar flow. Those electrodes exhibit a high specific capacitance of 853 F/g at 2 A/g and an excellent cycling stability (95% after 6000 cycles).

The sol-gel synthesis has also employed for the same purpose, in combination with aerogel deposition and spin-coating. In this way, Kim et al.[140] carried out the deposition of Nb_2O_5 as electroactive material by solvothermal sol-gel method. This metal oxide was then calcined at 400°C in air for 2 h, reaching a specific capacitance of ~ 400 F/g.

Electrochemical deposition is largely used as well followed by sintering. Li et al.[126] deposited a 3D multicomponent electrode ($\text{Co}_3\text{O}_4@\text{Au}@\text{MnO}_2$) using a sequential electrochemical deposition process. Finally, after sintering at 200°C for 2 h under Ar atmosphere, the specific capacitance value obtained was 1532.4 F/g at 1 A/g with no degradation after 5000 cycles. This technique is also employed by Lang et al.[137] to deposit $\text{V}_2\text{O}_3/\text{MnO}_2$ using latex nanospheres as endo-templates, which decompose during the sintering process at 400°C . The specific capacitance achieved was 1162 F/cm³ at 1.56 A/cm³ and it retains this value after the long-term electrochemical cycling (100% after 15000 cycles). Moreover, Liu et al.[128] also employed templates to form hierarchical isomeric vanadium oxides, leading to a specific capacitance of ~ 1856 F/g and a high cyclability, 93% of capacitance retention after 15000 cycles.

Special attention should be paid to the Electrophoretic Deposition (EPD), a shaping method for thin and thick films, consisting in the application of an electric field to a suspension, which causes the migration of charged particles and their deposition to the electrode of opposite charge. The EPD is gaining increasing interest with other electrochemical strategies for the deposition of multicomponent films and functional coatings. EPD offers many advantages for the deposition process, such as the easy control of the thickness changing the time or the operational potential, the versatility to cover complex shapes or 3D collectors and the generation of homogeneous layers. Many researchers are focused on the co-deposition of carbon-based materials and polymers with inorganic particles. However, authors like Hung et al.[141] and Gonzalez et al.[80] have developed electrodes based on MnO_2 and $\text{Ni}(\text{OH})_2$ respectively, using this shaping method and obtaining capacitances of 481 F/g and closed to 400 F/g and cyclability rates of 83% (after 15000 cycles) and 100% (after 1000 cycles), respectively.

The synthesis by precipitation aided by the action of ultrasound (US) have been intensively explored by Gonzalez et al.[76,79]. They employed an US probe (inside of a precursor dissolution of Ni^{2+}) for the fabrication of nanoplatelets of $\text{Ni}(\text{OH})_2$, which were electrophoretically deposited and sintered, developing PCs electrodes. Yus et al.[130] have employed the same process combined with the heteroprecipitation of Ni nanospheres in the suspension to obtain a NiO/Ni nanocomposites which were then deposited by EPD in Ni foams, exhibiting 755 F/g at 2 A/g.

As mentioned above, this technique is unique for coating 3D electrodes, however one of the research lines for raising the specific surface area is focus on promoting the porosity of the deposited electroactive material onto the surface of the electrodes. Nevertheless, the electrodes must present a robust structure, avoiding degradation during the charge and discharge processes, and resist small volumetric changes in their microstructure. Thus, larger specific surface area results in higher capacitance and ideal electrochemical behavior[75,116,142].

However, in terms of 2D, Direct Inkjet Printing as an additive manufacturing technology is becoming very popular. It is a mature technique widely employed in traditional ceramics industry for the tile's decoration. In addition, nowadays, with the development of functional inks, their use in other industries, such as microelectronics, is growing. For instance, Yus et al.[131] have developed NiO electrodes through this powerful technique by printing Ni foils substrates with NiO nanoplatelets, and a subsequent mild sintering process at 325 °C. The as-prepared electrodes showed a 160 F/g of capacitance and a 100% of retention after 1200 cycles.

All these electrochemical techniques are very useful in order to co-deposit two or more materials at the same time. And in the race for the manufacture of hybrid supercapacitors, they are widely used due to the easy ability to co-depositing semiconductor oxides and carbon species such as carbon nanotubes (CNT) or oxidized (GO) or reduced (ERGO) graphene.

2.2.3. Hybrid capacitors.

The development of hybrid capacitors (HSCs), also called "ultracapacitors", is a novel strategy for the optimization of the electrochemical behavior. It consists in the combination of metal oxides with carbonaceous compounds with large specific surface such as graphene, carbon nanotubes, active carbon, etc. The presence of carbon-based materials as conductive additives may positively contribute to the improvement of the electrochemical response. This blend provides an increase of the final specific capacitance due to the combination of the pseudocapacitance of TMO and the

1 electrochemical double-layer capacitance given by the carbonaceous component
2 achieving better connectivity among the metal oxide phase. HSCs can accumulate
3 higher energy densities compared with traditional PCs. The table 7 shows some
4 interesting articles about this type of hybrid capacitors classified by the C-based
5 material. Graphite substrates, graphene, graphene oxide or carbon nanotubes (CNT)
6 are the most frequently used.
7
8
9

10 The processing routes for the manufacturing of these carbon-based pseudocapacitors
11 electrodes do not differ from those mentioned above for PCs. The hydrothermal
12 synthesis is the most commonly used. For instance, this synthesis was employed by
13 Zhu et al.[148] for the development of self-assembled CoO nanorod cluster on three-
14 dimensional graphene, reaching a specific capacitance of 980 F/g. In this case,
15 hydrothermal synthesis is also used in combination with other such as
16 electrodeposition, for example, Sawangphruk et al.[194] tailored Ag-doped MnO₂ by
17 this method with a final sintering step at 400°C for 2 h on a carbon substrate. The
18 specific capacitance values measured in 0.5 M Na₂SO₄ at a scan rate of 5 mV/s were
19 557 F/g achieving a high cyclability 98.6%. In the case of Shim et al.,[146] graphene
20 was combined with Co₃O₄ (synthesized by solvothermal synthesis) and pressed onto a
21 conductive collector given 2435 F/g (at current density 1 A/g), while after 4500 cycles,
22 the specific capacitance increased until 112%. The solvothermal process is also
23 employed in developing MOF, thus Zhou et al.[85] combined GO with a Ni-based MOF
24 resulting in a capacitance of 2192.4 F/g and a retention of it of 85% during 3000 cycles.
25 Zhang et al.[184] electrodeposited Ni-Co mixed MOF on Ni foam with a subsequent
26 pyrolysis obtaining a carbon–metal oxide composite electrodes. The as-prepared
27 electrodes exhibit a capacitance value of 2098 mF/cm² at a current density of 1mA/cm²
28 with a 93% of retention.
29
30
31
32
33
34
35
36
37
38
39
40
41
42

43 The co-precipitation or electrochemical co-deposition with graphene [148] have been
44 also used by Shahrokhian et al.,[161] who fabricated directly, on a Nickel foam
45
46
47
48
49
50
51
52
53
54
55
56
57
58
59
60
61
62
63
64
65

Table 7. Summary of hybrid supercapacitors reported in literature classified attending to the employed carbon-based material.

Ref	Carbon-based Material	Metal Oxide	Synthesis & Layer formation	Specific Capacitance	Capacitance retention
[143]	Graphene	Mn ₃ O ₄ /graphene	Hydrothermal + Pressed	256 F/g	--
[144]	Graphene	MnNi (OH) _x /graphene	Hydrothermal + Pressed	2219 F/g at 0.73 A/g	90% after 1400 cycles
[145]	Graphene	GNS/Co ₃ O ₄	Microwave-assisted method + Pressed	243.2 F/g at 10 mV/s	95.6% after 2000 cycles
[146]	Graphene	Co ₃ O ₄ /graphene	Solvothermal + Pressed	2435 F/g at 1 A/g	112% after 4500 cycles
[147]	Graphene	Co(OH) ₂ /graphene	Hummers and hydrothermal + Pressed	92 F/g	60% after 3000- 6000 cycles
[148]	Graphene	CoO/Graphene	Hydrothermal + Ceramic TT at 450°C for 2 h under Ar	980 F/g at 1 A/g	103% after 10000 cycles
[149]	Graphene O	MnO ₂ /GO (15:1)	Hummers + Sonication precipitation + Pressed	197.2 F/g	84.1% after 1000 cycles
[150]	Graphene O	MnO _x on Carbon Fibers	Electrodeposition + Reduction on substrate	1004.8 mF/cm (386.5 F/g) at 4 mA/cm	94% after 5000 cycles
[85]	Graphene O	Ni-MOFs@GO	Solvothermal + hummers + Pressed	2192.4 F/g	85.1% after 3000 cycles
[151]	Graphene O	GO/NiTAPc	Hummers + Pressed	163 F/g	70% after 1000 cycles
[152]	Graphene O	MoO ₃ /GO	Hydrothermal + Ceramic TT 600°C 3h Ar	321.8 F/cm ³ at 2 mV/s	97.6 % after 5000 cycles
[153]	rGO	CoS@rGO	Hydrothermal + Pasted	849 F/g at 1A/g	90.5% after 3000 cycles
[154]	rGO	rGO/Co ₃ O ₄	Hydrothermal + Pressed	207.2 F/g at 1A/g	--
[155]	rGO	NiPc NF-rGO	Solvothermal + drop casting	223.28 F/g at 1A/g	--
[156]	rGO	rGO-Co ₃ O ₄	Hydrothermal & Hummers + Aerogelification	136.6 mF/cm ² at a 2 mA/cm ²	~99-100% after 6000 cycles
[157]	rGO	CoO/RGO	Hydrothermal +ozonation + annealing N2	239.4 F/g at 10 A/g	93.2% after 10000 cycles
[158]	rGO	MoO ₂ -RGO	Hydrothermal + Drop casting	615 F/g	90% after 10 cycles
[159]	rGO	Au/ZnO/rGO	Hydrothermal + Pasted	875 F/g at 1 A/g	60% after 1000 cycles
[160]	rGO	NiO/RGO	Heterocoagulation + EPD + Sintering	885 F/g at 2 A/g	71% after 1000 cycles
[161]	ErGO	NiO/ERGO	Electrochemical co-deposition + Ceramic TT 300°C 2h Air	1715.5 F/g	78.8% after 2000 cycles
[162]	CNT	CNT-MnO ₂	Hydrothermal + Gelification	4.4 F/cm at 0.03 A/cm ³	~50% after 3000 cycle
[141]	CNT	CNT/MnO ₂	Hydrothermal+ EPD	415 F/g at 3 A/g	83.3% after 15000 cycles
[163]	CNT	MnO ₂ /CNT//MoO ₃ /CNT	Drop-casting + Electrodeposition	507.2 F/g at 1 mA/cm ²	83% after 5000 cycles

[164]	CNT	MWCNT + MnO ₂ and RuO ₂	Dry painting method LbL	25 F/g at 0.2 A/g	82% after 5000 cycles
[165]	CNT	Ni/Ni(OH) ₂ & CNT	Hydrothermal + Pressed	1283 F/g at 2 A/g	~100% after 2000 cycles
[166]	CNT	NiO-CNT	hydrothermal & calcined in argon at 300 C for 2 h.	328 F/g at 0.33 A/g	64.3% after 300 cycles
[167]	CNT	CNT-NiO	Chemical Vapor Deposition (CVD) + Calcination + EPD	1.26 F/cm ³ at 100 mV/s	94.2% after 10000 cycles
[86]	CNT	β-Ni(OH) ₂ NS/ NWCT	Electrochemical deposition	2185.6 F/g at 5 A/g	95% 1000 cycles
[168]	CNT	NiCoAl-LDH// ERGO CNT	Hydrothermal & Hummers + Pressed	1188 F/g at 1A/g	88-91% after 1000 cycles
[169]	CNT	CNT/MO; M = Co, Zn, Mn	Microwave-assisted (MO) CVD (CNT) after annealed at 650°C	123.9 F/g at 377 μA/cm ²	95% after 1000 cycles
[170]	CNT	NiCo ₂ O ₄ Nanowire/CNT	Hydrothermal	277.3 mF/cm ² at 0.32 mA/cm ²	89% after 5000 cycles
[171]	CNT	RuO ₂ or MnO ₂ & CNT	Electrodeposition	72 and 98 F/g	86% and 93% after 1000 cycles
[172]	CNT	SWCNTs/Fe ₂ O ₃	Chemical Vapor Deposition (CVD) + Drop-casting	183 F/g at 0.01 V/s	--
[173]	CNT	H _x MoO _{3-y}	Hydrothermal	210 F/cm ³ at 1 A/g	93.3% after 4000 cycles
[174]	CNT	MoO ₃ @CNT	Hydrothermal	100.04 F/g at 200 mA/g	90% after 600 cycles
[175]	CNT	V ₂ O ₅ /CNT	Hydrothermal + Pressed	~35 F/g	80% after 900 cycles
[176]	CNT	Mn-based	Electrodeposition + Dip-coating + Ceramic TT 600°C 2h	148 F/g 1 A/g	92% after 10000 cycles at 2 A/g
[177]	Graphyte pirolitic	Co(OH) ₂ -PG	Hydrothermal + US	642.5 F/g at 1.5 A/g	100% after 5000 cycles
[178]	Carbon nanofiber	(MCNs//NiCo ₂ O ₄)	solvothelmal + calcination	1631 F/g 1 at A/g	94.5% after 5000 cycles
[179]	Amorphous micron carbon ribbons (AMCR)	NiCo ₂ O ₄ @AMCRs	Hydrothermal + Pressed	1691 F/g at 3A/g	89 % after 10 000 cycles
[180]	Carbon nanoflakes	CoO@ f-C nanowire	Atomic Layer Deposition (ALD) + Glucose carbonization	3.4 F/cm ² 10 mA/cm ²	98.6 % after 5000 cycles
[66]	Mesoporous Carbon	RuO ₂ /carbon composite	Hydrothermal + Pressed	1733 F/g at 0.2 A/g	91% after 2500 cycles
[181]	Calcinated Mof	Fe ₃ O ₄ /carbon composite	Hydrothermal + Pressed	162 F/g at 1 A/g	83.3% after 4000 cycles
[182]	Glucose	α-Fe ₂ O ₃ @C	Hydrothermal + Pressed	288 F/g 1 A/g	72.3% after 2000 cycles
[183]	Polymer calcination	ZnO/carbon	ZnO Synthesis + Polimerization + Calcination + Pressed	145 F/g at 2 mV/s	91% after 10000 cycles
[4]	Carbon spheres	NiCl ₂ and Ni(OH) ₂	Precipitation + Electrodeposition	10286 F/g at 3 A/g	--
[184]	Calcinated Mof	Co/Ni oxide & carbon	MOF electrosynthesis + Electrodeposition + Ceramic TT 900 °C 12 h Ar	157 F/g at 1 mA /cm ²	92% after 4200 cycles

[63]	C. Substrate	Co-doped Ni(OH) ₂	LAL	720 F/g at 6 A/g	92% after 1000 cycles
[185]	C. Substrate carbon fiber paper	Co _x Ni _{1-x} (OH) ₂ /NiCo ₂ S ₄	Electrodeposition	2.7 F/cm ² at 4 mA/cm ²	96% after 2000 cycles
[186]	C. Substrate	Co ₃ O ₄	Solvothermal & calcination + Sprayed	476 F/g at 0.5 A/g	82% 2000 cycles
[187]	C. Substrate	Co-Ni	Coprecipitation + Electrodeposition	1123 F/g	78% after 2000 cycles
[119]	C. substrate	Co ₃ V ₂ O ₈	Hydrothermal (MHT)	4194 F/g at 1 A/g	85% after 10000 cycles
[123]	C. substrate	PAni-RuO ₂	Chemical oxidative polymerization + Atomic Laser Deposition ALD	710 F/g at 5 mV/s	88% after 10 000 cycles at 20 A/g
[120]	C. Substrate	Al _x Cu _y Co _z Fe ₂ O ₄	Sol-gel & calcination + Pressed	875 F/g at 5 mV/s	--
[188]	C. Substrate	MoO ₃	Sol-gel + Drop-casting	135 F/g	84% after 200 cycles
[122]	C. Substrate	VO _x /Carbon	Electrodeposition	167 F/g at 25 mV/s	--
[189]	C. substrate	Na ₂ Ti ₃ O ₇	Hydrothermal and annealing + Pasted	1.3 mWh/cm ³ and 70 mW/ cm ³	~ 80.3% after 2500 at 0.5 A/g
[190]	C. Substrate	Zn _x Co _{1-x} O	Hydrothermal on Carbon fiber paper CFP	450 F/g at 1 V/s	90.7% after 5000 cycles
[191]	C. Substrate	WO ₃ on carbon	Sol-gel + Spin-coating + Ceramic TT (300, 400, 500, 600 °C)	233.6 F/g at 2 mV/s	--
[192]	C. substrate	NiFe ₂ O ₄	Hydrothermal on template + Ceramic TT 350 °C 2h Air	697 F/g at 5mV/s	93.6 % after 10000 cycles
[193]	C. substrate	MoO ₂ and V ₂ O ₃	Hydrothermal + Sintering 700–1000 °C N ₂	--	--
[194]	C. substrate	Ag-MnO ₂	Hydrothermal + Electrodeposition + Ceramic TT 400 °C 2h Air	557 F/g at 5mV/s	98.6 % after 2000 cycles
[195]	C. substrate	Ni/NiO	Sol-gel + Electrospinning + Pressed	526 F/g at 1 A/g	80% after 1000 cycles
[196]	C. Substrate	β-La ₂ Mo ₂ O ₉	Hydrothermal + Pressed	727.2 F/g at 0.5 A/g	98.7 % after 1000 cycles
[197]	C. substrate	SrFe ₁₂ O ₁₉	Hydrothermal + Calcination + Pasted	133.9 F/g 0.4 A/g	84% after 5000 cycles
[198]	C. substrate	MnO ₂	Hydrothermal + Pressed	212 F/g	88% after 10000 cycles
[118]	C. substrate	LaMnO ₃	Solvothermal + Calcination 700 °C 4h air + Spin-casting 700 rpm	586.7 F/g and 609.8 F/g	--
[199]	C. substrate	MnO ₂ /PANI	Hydrotherma l+ Pressed	873 F/g at 0.25 A/g	95% after 5000 cycles
[200]	C. Substrate	Mn ₃ O ₄ & MnOOH	Hydrothermal + Drop-casting	170 F/g at 500 mV/s	--
[201]	C. Substrate	MnO ₂ -Carbon	Electrodeposition	8 2.8 F/cm ² at 0.05 mV/s	80% after 1000 cycles
[87]	C. Substrate	KMnO ₂	Hydrothermal + Drop-csdting	303 F/g at 0.2 A/g	100-90% after 1000 cycles
[99]	C. Substrate	NiO	Sparking + Drop-casting	402.8 C/g at 1 A/g	88% after 1000 cycles

(substrate), ERGO/NiO electrodes in one-step. The heat treatment at 300°C for 2h leads to a maximum of specific capacitance around 1716 F/g and with a 78.8% of retention after 2000 cycles. And Jia et al.[150] combined GO and MnOx by electrodeposition onto carbon fibers showing a specific capacitance of 1004.8 mF/cm at a current density of 4 mA/cm during 5000 cycles with only a 6% of capacitance drop. Another electrochemical technique that has been used is the EPD. Yus et al.[160] prepared by heterocoagulation a NiO/RGO nanocomposite, which was electrophoretically deposited onto a Ni foam with a final stage of sintering at 352 °C during 1h under Ar atmosphere. The final electrode showed a specific capacitance value of 940 F/g at 2 A/g.

Nanotubes are also used as template for growing TMO. Ma et al. in 2015 [165] grew Ni(OH)₂ nanoplatelets on carbon nanotubes (CNT) by using hydrothermal synthesis to achieve a specific capacitance of 1283 F/g at 2 A/g, with a 100% retention after 2000 cycles. In this case the active material was mixed with poly(tetrafluoroethylene) and other carbonaceous species, and then spread and pressed onto a Ni foam in order to prepare the tested specimens. Another good example is the work developed by Chang et al.[176]. They prepared a CNT@MnOOH@polypyrrole by electrodeposition and dip coating techniques with a final calcination to conform a well-connected microstructure at 600°C for 2h. The reported specific capacitance was 148 F/g with a 92% of retention after 10000 cycles at 2 A/g. CNTs are, as graphene, widely used for the preparation of hybrid capacitors. Cha et al.[86] performed a ultracapacitor based on CNT and Ni(OH)₂ synthesized by electrodeposition which showed 2185.6 F/g at current density of 5 A/g and a 95 % of retention over 1000 cycles.

Frequently, the combination of both species lies in the co-deposition of the carbon-based material and the metal oxide semiconductor. However, the combination of the TMO with an organic compound followed by calcination is also employed. Guan et al.[180] combined cellulose with CoO in order to manufacture CoO@C hybrid nanowires improving the capacitance of the CoO (from 1.6 F/cm² to 3.3 F/cm²) as well as the cycling life from 87.1% until 98.6% after 5000 cycles. In addition, sometimes the combination of a carbon phase consists only in the use of it as substrate. In those cases, the carbonaceous substrates generate a double-layer contribution. For instance, Sahoo et al.[119] grew by hydrothermal synthesis nanocrystals of Co₃V₂O₈, which showed a specific capacitance value of 4194 F/g measured at 1A/g with a capacitance retention after 10000 cycles of 85%. Yang et al.[178] performed a multicomponent HSC by impregnating carbon nanofibers with NiCo₂O₄ with a subsequent calcination obtaining 1631 F/g at 1 A/g with a capacitance retention of

94.5% after 5000 cycles. Moreover, the same bicomponent oxide was employed in combination with amorphous micro-carbon ribbons by Pang et al.[179] improving the specific capacitance in 60 units (1691 F/g at 3 A/g) which after 10 thousand of cycles it retains the 89% of the initial specific capacitance. And, Zhang et al.[184] prepared carbon-metal oxide (Ni and Co oxides) composite electrodes by electrosynthesis on Ni foam using MOF as a precursor. After the heat treatment (900 °C 12 h Ar), some carbon from the calcined MOF is mixed with the sintered oxides resulting in long-term electrochemical stability (93% retention of the capacitance from 1 to 20 mA/cm²). A different strategy consists in the deposition of oxides on carbonaceous substrates as is the case of Han et al.[187], who developed a multiphase composite film, composed of nickel(II) hydroxide and cobalt(II) hydroxide, synthesized by co-precipitation. The prepared 3D network nanostructure showed 1123 F/g of capacitance with a 78% of retention after 2000 cycles.

Finally, highest specific capacitance values for hybrid capacitors were found 10286 F/g [4] combining carbon spheres with $\text{NiCl}_2 \cdot \text{H}_2\text{O} \leftrightarrow \text{Ni}(\text{OH})_2$ colloids, and 2185.6 F/g [86] by electrodepositing $\text{Ni}(\text{OH})_2$ nanoparticles onto non-woven conductive textile substrate.

Summary and Conclusion

Reaching future challenges of energetic demand will require a whole host of novel materials for the manufacture of more efficient devices. Among storage systems, ceramic-based pseudocapacitors (PCs) reach an excellent compromise between delivered power and stored energy. Although carbon-based EDLCs have many advantages such as higher specific surface area, good electronic conductivity, and high chemical stability, the capacitance of PCs can be 10–100 times higher.

Therefore, TMOs have been regarded as promising electroactive materials for PCs, since they exhibit a wide range of bandgaps, Eg, due to the diversity of electronic structure of the transition metals. Changeable valences and theoretical capacities of TMOs are considered, among others electrochemical properties, to select the appropriated electrode composition. However, this selection is not always based on their electrochemical response since the cost and the availability are variables, which should be considered for product fabrication scaling or its commercialization. In this sense, NiO-based electrodes have become one of the most promising compounds along with MnO₂. Both exhibit good p-type conduction, which makes it attractive as a transparent hole-transport layer stepping up their applications in energy accumulation. They exhibit excellent electrochemical properties, such as high theoretical capacitance,

1 electrical conductivity and chemical stability, leading to the highest specific capacitance
2 values reported until now in the literature. For example, several studies of NiO-based
3 electrodes have reported specific capacitances closer to the theoretical value, 2188
4 F/g, 2192 F/g, 2186 F/g.
5

6
7 Growing relevance of PCs is reflected in the number of published reviews. Around 40
8 reviews about these energy storage systems were published from 2002 until the
9 present, where studies of the electrode active material have been specifically
10 emphasized, in terms of composition and morphology, while only a slight assessment
11 of the electrolyte characteristics has been evaluated.
12
13
14
15

16 The specific capacitance of TMOs depends on extrinsic properties such as charge
17 transfer, ion diffusion, reversibility of the redox reactions and cyclability. These extrinsic
18 characteristics are directly related to both the electronic configuration of the metals, the
19 crystallographic properties and related band gap of TMOs, but also on the electrode
20 microstructure which define the interface of the electroactive material with the
21 electrolyte and which mainly depends on the processing strategies (synthesis, shaping
22 and consolidation).
23
24
25
26
27

28 In the current route of the electrode preparation, research efforts are focus on the
29 control of the synthesis procedures, such as hydrothermal or solvothermal
30 precipitation, colloidal sol-gel synthesis, etc. After the synthesis of particles, the
31 resulting slurry/paste obtained by blending is applied onto the collector substrate by
32 different shaping processes such as dip-coating, drop-casting, tape-casting, spin
33 coating, electrophoretic deposition, etc. Most of these synthesis techniques evolve to
34 one-step processes, since coating technologies allows the proper film growth on the
35 substrate during the synthesis of the nanostructure, resulting on binder-free electrodes.
36
37
38
39
40
41

42 Moreover, many review papers and articles demonstrate that the nanosize, the
43 morphology (0D, 1D, 2D and 3D) and the crystallography modification at the atomic
44 level, by the inclusion of dopants and the creation of vacancies, provides new
45 opportunities to achieve higher efficiency. But also, several studies determine that the
46 porous structure of the nanosized TMO should be consolidated by a mild sintering
47 treatment after synthesis and shaping, to prepare robust electrically connected
48 electrodes, where the porosity of the nanostructure provides the structural tolerance
49 needed to overpass the volume changes during faradaic reactions.
50
51
52
53
54
55

56 This review summarizes reported results of the electrochemical performance of TMOs
57 considering three processing strategies for specific capacitance enhancement:
58
59
60
61
62
63
64
65

1 synthesis modification, shaping and sintering developed technologies, and the
2 TMO/carbon-based composites.

3
4 The crystallographic modification during the synthesis in order to obtain complex
5 morphologies with higher specific surface areas and the development of
6 multicomponent materials exhibits excellent electrochemical performance owing to the
7 excellent conductivity. Binary and ternary metal composites for supercapacitor
8 materials can lead to highly beneficial synergistic effects among the components,
9 making possible greater electrochemical performance, cycling stability, and other
10 important properties than would be the case for each individual component. The
11 second widely studied alternative strategy is based on the surface modification of the
12 electroactive material microstructure during shaping. Porous structures lead to large
13 surfaces with more active sites where the redox reactions can take place. This results
14 in electrodes with enhanced specific capacitance. The lack of highly porous
15 microstructures is related to the loss of robustness. Thus, a consolidation stage is
16 mandatory to improve conductivity and reinforce mechanical properties. This
17 consolidation step is carried out by sintering.

18
19 Finally, hybrid capacitors combine both energy storage mechanism, electrostatic and
20 faradaic processes. Commonly the carbonaceous materials employed in these systems
21 have a high shape factor, being carbon nanotubes, graphene or porous carbon.
22 Moreover, due to their high surface area, they can support TMOs while improve
23 electrode conductivity.

24
25 Therefore, future research trends should focus on the following aspects:

26
27 (1) Preparation of TMO/carbon composites materials to achieve higher specific
28 capacitance maintaining it during cycling. (2) Optimization of the TMO robustness and
29 conductivity by sintering. (3) Combining non-strategic materials with the goal of
30 enabling lightweight, portable, safe, and environmentally friendly commercial devices.

31
32 We believe that as the technology matures and further breakthroughs in flexible
33 electrode material development are made, the introduction of intelligent wearable
34 devices in daily life in the near future is plausible. Concretely, the additive
35 manufacturing (AM) technology for the fabrication of flexible electronic products is
36 increasingly more and more interesting. This will bring a great future for the TMO and
37 carbon-based composite materials. How to achieve a power supply with high flexibility,
38 high energy density, excellent rate capacity, cycle stability, lightweight, safe operation,
39 low cost, and scalable production is the ultimate goal. One of the key challenges in AM
40 for the development of electrodes for flexible supercapacitors is their starting material

preparation. This is because loading inorganic particles into liquid suspension or polymeric composites are not trivial and require prior colloidal processing to obtain homogeneous and reproducible materials.

Acknowledges

Authors acknowledge the support to the projects ADITIMAT-CM S2018/NMT-4411 and MAT2015-70780-C4-1 (MINECO/FEDER). Z. Gonzalez acknowledges to the Spanish Ministry of Economy and Competitiveness for the Postdoctoral Fellowship: IJCI-2016-28538. J.Yus acknowledges to the Comunidad de Madrid the support from the Youth Employment Initiative, CAMPD17_ICV_002.

References

- [1] L. Kouchachvili, W. Yaïci, E. Entchev, Hybrid battery/supercapacitor energy storage system for the electric vehicles, *J. Power Sources*. 374 (2018) 237–248. doi:10.1016/j.jpowsour.2017.11.040.
- [2] K. Zhou, W. Zhou, L. Yang, J. Lu, S. Cheng, W. Mai, Z. Tang, L. Li, S. Chen, Ultrahigh-Performance Pseudocapacitor Electrodes Based on Transition Metal Phosphide Nanosheets Array via Phosphorization: A General and Effective Approach, *Adv. Funct. Mater.* 25 (2015) 7530–7538. doi:10.1002/adfm.201503662.
- [3] Z. Ren, J. Li, Y. Ren, S. Wang, Y. Qiu, J. Yu, Large-scale synthesis of hybrid metal oxides through metal redox mechanism for high-performance pseudocapacitors., *Sci. Rep.* 6 (2016) 20021. doi:10.1038/srep20021.
- [4] K. Chen, D. Xue, In situ electrochemical activation of Ni-based colloids from an NiCl₂ electrode and their advanced energy storage performance, *Nanoscale*. 8 (2016) 17090–17095. doi:10.1039/c6nr06325j.
- [5] S. Maiti, A. Pramanik, S. Mahanty, Electrochemical energy storage in Mn₂O₃ porous nanobars derived from morphology-conserved transformation of benzenetricarboxylate-bridged metal-organic framework, *CrystEngComm*. 18 (2016) 450–461. doi:10.1039/c5ce01976a.
- [6] H. Zhang, X. Wang, C. Chen, C. An, Y. Xu, Y. Dong, Q. Zhang, Y. Wang, L. Jiao, H. Yuan, Facile synthesis of diverse transition metal oxide nanoparticles and electrochemical properties, *Inorg. Chem. Front.* 3 (2016) 1048–1057. doi:10.1039/C6QI00096G.
- [7] X. Lu, C. Wang, F. Favier, N. Pinna, Electrospun Nanomaterials for Supercapacitor Electrodes : Designed Architectures and Electrochemical Performance, *Adv. Energy Mater.* 7 (2016) 1–43. doi:10.1002/aenm.201601301.
- [8] M.M. Sk, C.Y. Yue, K. Ghosh, R.K. Jena, Review on advances in porous nanostructured nickel oxides and their composite electrodes for high-performance supercapacitors, *J. Power Sources*. 308 (2016) 121–140. doi:10.1016/j.jpowsour.2016.01.056.
- [9] B.K. Kim, S. Sy, A. Yu, J. Zhang, Electrochemical Supercapacitors for Energy Storage and Conversion, *Handb. Clean Energy Syst.* (2015) 1–25. doi:10.1002/9781118991978.hces112.
- [10] A. González, E. Goikolea, J.A. Barrena, R. Mysyk, Review on supercapacitors: Technologies and materials, *Renew. Sustain. Energy Rev.* 58 (2016) 1189–1206. doi:10.1016/j.rser.2015.12.249.
- [11] A.R. West, *Solid State Chemistry and its applications*, Second, Wiley, Sheffield UK, 2014.

- [12] S. Lany, Semiconducting transition metal oxides, *J. Phys. Condens. Matter.* 27 (2015) 283203. doi:10.1088/0953-8984/27/28/283203.
- [13] A. Janotti, C.G. Van De Walle, Fundamentals of zinc oxide as a semiconductor, *Reports Prog. Phys.* 72 (2009). doi:10.1088/0034-4885/72/12/126501.
- [14] N.D. Reynolds, C.D. Panda, J.M. Essick, Capacitance-voltage profiling : Research-grade approach versus low-cost alternatives, 97202 (2014) 196–205.
- [15] C. Hu, Y. Lin, J.W. Connell, H.M. Cheng, Y. Gogotsi, M.M. Titirici, L. Dai, Carbon-Based Metal-Free Catalysts for Energy Storage and Environmental Remediation, *Adv. Mater.* 1806128 (2019) 1–14. doi:10.1002/adma.201806128.
- [16] Y. Kumar, S. Rawal, B. Joshi, S.A. Hashmi, Background, fundamental understanding and progress in electrochemical capacitors, *J. Solid State Electrochem.* 23 (2019) 667–692. doi:10.1007/s10008-018-4160-3.
- [17] A. Muzaffar, M.B. Ahamed, K. Deshmukh, J. Thirumalai, A review on recent advances in hybrid supercapacitors: Design, fabrication and applications, *Renew. Sustain. Energy Rev.* 101 (2019) 123–145. doi:10.1016/j.rser.2018.10.026.
- [18] J. Xie, P. Yang, Y. Wang, T. Qi, Y. Lei, C.M. Li, Puzzles and confusions in supercapacitor and battery: Theory and solutions, *J. Power Sources.* 401 (2018) 213–223. doi:10.1016/j.jpowsour.2018.08.090.
- [19] J.L. Espinoza-Acosta, P.I. Torres-Chávez, J.L. Olmedo-Martínez, A. Vega-Rios, S. Flores-Gallardo, E.A. Zaragoza-Contreras, Lignin in storage and renewable energy applications: A review, *J. Energy Chem.* 27 (2018) 1422–1438. doi:10.1016/j.jechem.2018.02.015.
- [20] J. Ding, W. Hu, E. Paek, D. Mitlin, Review of Hybrid Ion Capacitors: From Aqueous to Lithium to Sodium, *Chem. Rev.* 118 (2018) 6457–6498. doi:10.1021/acs.chemrev.8b00116.
- [21] X. Yu, S. Yun, J.S. Yeon, P. Bhattacharya, L. Wang, S.W. Lee, X. Hu, H.S. Park, Emergent Pseudocapacitance of 2D Nanomaterials, *Adv. Energy Mater.* 8 (2018) 1–33. doi:10.1002/aenm.201702930.
- [22] Z. Lin, E. Goikolea, A. Balducci, K. Naoi, P.L. Taberna, M. Salanne, G. Yushin, P. Simon, Materials for supercapacitors: When Li-ion battery power is not enough, *Mater. Today.* 21 (2018) 419–436. doi:10.1016/j.mattod.2018.01.035.
- [23] Y. Gogotsi, R.M. Penner, Energy Storage in Nanomaterials – Capacitive, Pseudocapacitive, or Battery-like?, *ACS Nano.* 12 (2018) 2081–2083. doi:10.1021/acsnano.8b01914.
- [24] R.S. Kate, S.A. Khalate, R.J. Deokate, Overview of nanostructured metal oxides and pure nickel oxide (NiO) electrodes for supercapacitors: A review, *J. Alloys Compd.* 734 (2018) 89–111. doi:10.1016/j.jallcom.2017.10.262.
- [25] X. Shi, S. Zheng, Z.S. Wu, X. Bao, Recent advances of graphene-based materials for high-performance and new-concept supercapacitors, *J. Energy Chem.* 27 (2018) 25–42. doi:10.1016/j.jechem.2017.09.034.
- [26] J. Kang, S. Zhang, Z. Zhang, Three-Dimensional Binder-Free Nanoarchitectures for Advanced Pseudocapacitors, *Adv. Mater.* 29 (2017) 1–12. doi:10.1002/adma.201700515.
- [27] M. Liu, B. Su, Y. Tang, X. Jiang, A. Yu, Recent advances in nanostructured vanadium oxides and composites for energy conversion, *Adv. Energy Mater.* 7 (2017) 1–34. doi:10.1002/aenm.201700885.
- [28] J. Xu, J. Zhang, W. Zhang, C.S. Lee, Interlayer nanoarchitectonics of two-dimensional transition-metal dichalcogenides nanosheets for energy storage and conversion applications, *Adv. Energy Mater.* 7 (2017) 1–30. doi:10.1002/aenm.201700571.

- [29] A. Eftekhari, M. Mohamedi, Tailoring pseudocapacitive materials from a mechanistic perspective, *Mater. Today Energy*. 6 (2017) 211–229. doi:10.1016/j.mtener.2017.10.009.
- [30] J. Bae, O.S. Kwon, C.-S. Lee, Energy Efficient Graphene Based High Performance Capacitors, *Recent Pat. Nanotechnol.* 11 (2017) 2019. doi:10.2174/1872210510666161027101910.
- [31] X. Su, T.A. Hatton, Redox-electrodes for selective electrochemical separations, *Adv. Colloid Interface Sci.* 244 (2017) 6–20. doi:10.1016/j.cis.2016.09.001.
- [32] X. Chen, R. Paul, L. Dai, Carbon-based supercapacitors for efficient energy storage, *Natl. Sci. Rev.* 4 (2017) 453–489. doi:10.1093/nsr/nwx009.
- [33] T.H. Le, Y. Kim, H. Yoon, Electrical and electrochemical properties of conducting polymers, *Polymers (Basel)*. 9 (2017). doi:10.3390/polym9040150.
- [34] J. Wang, S. Dong, B. Ding, Y. Wang, X. Hao, H. Dou, Y. Xia, X. Zhang, Pseudocapacitive materials for electrochemical capacitors: From rational synthesis to capacitance optimization, *Natl. Sci. Rev.* 4 (2017) 71–90. doi:10.1093/nsr/nww072.
- [35] Z. Wu, X.B. Zhang, Design and preparation of electrode materials for supercapacitors with high specific capacitance, *Wuli Huaxue Xuebao/ Acta Phys. - Chim. Sin.* 33 (2017) 305–313. doi:10.3866/PKU.WHXB201611012.
- [36] Y. Yan, B. Li, W. Guo, H. Pang, H. Xue, Vanadium based materials as electrode materials for high performance supercapacitors, *J. Power Sources*. 329 (2016) 148–169. doi:10.1016/j.jpowsour.2016.08.039.
- [37] A.M. Bryan, L.M. Santino, Y. Lu, S. Acharya, J.M. D'Arcy, Conducting Polymers for Pseudocapacitive Energy Storage, *Chem. Mater.* 28 (2016) 5989–5998. doi:10.1021/acs.chemmater.6b01762.
- [38] S.K. Simotwo, V. Kalra, Polyaniline-based electrodes: recent application in supercapacitors and next generation rechargeable batteries, *Curr. Opin. Chem. Eng.* 13 (2016) 150–160. doi:10.1016/j.coche.2016.09.001.
- [39] E.J. Son, J.H. Kim, K. Kim, C.B. Park, Quinone and its derivatives for energy harvesting and storage materials, *J. Mater. Chem. A*. 4 (2016) 11179–11202. doi:10.1039/C6TA03123D.
- [40] E. Lim, C. Jo, J. Lee, A mini review of designed mesoporous materials for energy-storage applications: from electric double-layer capacitors to hybrid supercapacitors, *Nanoscale*. 8 (2016) 7827–7833. doi:10.1039/C6NR00796A.
- [41] I.S. Ike, I. Sigalas, S. Iyuke, Understanding performance limitation and suppression of leakage current or self-discharge in electrochemical capacitors: a review, *Phys. Chem. Chem. Phys.* 18 (2016) 661–680. doi:10.1039/C5CP05459A.
- [42] C. Zhong, Y. Deng, W. Hu, J. Qiao, L. Zhang, J. Zhang, A review of electrolyte materials and compositions for electrochemical supercapacitors, *Chem. Soc. Rev.* 44 (2015) 7484–7539. doi:10.1039/C5CS00303B.
- [43] M. Huang, F. Li, F. Dong, Y.X. Zhang, L.L. Zhang, MnO₂-based nanostructures for high-performance supercapacitors, *J. Mater. Chem. A*. 3 (2015) 21380–21423. doi:10.1039/C5TA05523G.
- [44] K. Chen, D. Xue, Rare earth and transitional metal colloidal supercapacitors, *Sci. China Technol. Sci.* 58 (2015) 1768–1778. doi:10.1007/s11431-015-5915-z.
- [45] H. Choi, H. Yoon, Nanostructured Electrode Materials for Electrochemical Capacitor Applications, *Nanomaterials*. 5 (2015) 906–936. doi:10.3390/nano5020906.
- [46] X. Hu, W. Zhang, X. Liu, Y. Mei, Y. Huang, Nanostructured Mo-based electrode materials for electrochemical energy storage, *Chem. Soc. Rev.* 44 (2015) 2376–2404. doi:10.1039/C4CS00350K.

- [47] K. Zhang, X. Han, Z. Hu, X. Zhang, Z. Tao, J. Chen, Nanostructured Mn-based oxides for electrochemical energy storage and conversion., *Chem. Soc. Rev.* 44 (2015) 699–728. doi:10.1039/c4cs00218k.
- [48] S.-K. Chang, Z. Zainal, K.-B. Tan, N.A. Yusof, W.M.D. Wan Yusoff, S.R.S. Prabaharan, Recent development in spinel cobaltites for supercapacitor application, *Ceram. Int.* 41 (2015) 1–14. doi:10.1016/j.ceramint.2014.07.101.
- [49] L. Feng, Y. Zhu, H. Ding, C. Ni, Recent progress in nickel based materials for high performance pseudocapacitor electrodes, *J. Power Sources.* 267 (2014) 430–444. doi:10.1016/j.jpowsour.2014.05.092.
- [50] L. Mai, X. Tian, X. Xu, L. Chang, L. Xu, Nanowire Electrodes for Electrochemical Energy Storage Devices, *Chem. Rev.* 114 (2014) 11828–11862. doi:10.1021/cr500177a.
- [51] S. Faraji, F.N. Ani, Microwave-assisted synthesis of metal oxide/hydroxide composite electrodes for high power supercapacitors – A review, *J. Power Sources.* 263 (2014) 338–360. doi:10.1016/j.jpowsour.2014.03.144.
- [52] K. Chen, D. Xue, Cu-based materials as high-performance electrodes toward electrochemical energy storage, *Funct. Mater. Lett.* 7 (2014). doi:10.1142/S1793604714300011.
- [53] J.F. Mike, J.L. Lutkenhaus, Recent advances in conjugated polymer energy storage, *J. Polym. Sci. Part B Polym. Phys.* 51 (2013) 468–480. doi:10.1002/polb.23256.
- [54] S. Chen, S. He, H. Hou, Electrospinning technology for applications in supercapacitors, *Curr. Org. Chem.* 17 (2013) 1402–1410. doi:10.2174/1385272811317130007.
- [55] P. Simon, Y. Gogotsi, Materials for electrochemical capacitors, *Nat. Mater.* 7 (2008) 845–854. doi:10.1038/nmat2297.
- [56] Yu. M. Vol'fkovich and T. M. Serdyuk, Electrochemical Capacitors, *Russ. J. Electrochem.* 38 (2002) 935–958.
- [57] F. Feng, S. Zhao, R. Liu, Z. Yang, Q. Shen, NiO Flowerlike porous hollow nanostructures with an enhanced interfacial storage capability for battery-to-pseudocapacitor transition, *Electrochim. Acta.* 222 (2016) 1160–1168. doi:10.1016/j.electacta.2016.11.088.
- [58] H. Buqa, D. Goers, M. Holzapfel, M.E. Spahr, P. Novák, High Rate Capability of Graphite Negative Electrodes for Lithium-Ion Batteries, *J. Electrochem. Soc.* 152 (2005) A474. doi:10.1149/1.1851055.
- [59] H. Mahajan, J. Bae, K. Yun, Facile synthesis of ZnO-Au nanocomposites for high-performance supercapacitors, *J. Alloys Compd.* 758 (2018) 131–139. doi:10.1016/j.jallcom.2018.04.238.
- [60] Y. Wang, S. Gai, C. Li, F. He, M. Zhang, Y. Yan, P. Yang, Controlled synthesis and enhanced supercapacitor performance of uniform pompon-like-Ni(OH)₂ hollow microspheres, *Electrochim. Acta.* 90 (2013) 673–681. doi:10.1016/j.electacta.2012.11.136.
- [61] Z. Wang, Z. Zhao, Y. Zhang, G. Pang, X. Sun, J. Zhang, L. Hou, C. Yuan, Hierarchical flower-like conductive CoNiO₂ microspheres constructed with ultrathin mesoporous nanosheets towards long-cycle-life hybrid supercapacitors, *J. Alloys Compd.* 779 (2019) 81–90. doi:10.1016/j.jallcom.2018.11.249.
- [62] G.M. Tomboc, H.S. Jadhav, H. Kim, PVP assisted morphology-controlled synthesis of hierarchical mesoporous ZnCo₂O₄ nanoparticles for high-performance pseudocapacitor, *Chem. Eng. J.* 308 (2017) 202–213. doi:10.1016/j.cej.2016.09.056.
- [63] D.. b Liang, S.. Wu, J.. Liu, Z.. Tian, C.. b Liang, Co-doped Ni hydroxide and oxide nanosheet networks: Laser-assisted synthesis, effective doping, and ultrahigh pseudocapacitor performance, *J. Mater. Chem. A.* 4 (2016) 10609–10617.

doi:10.1039/c6ta03408j.

- [64] Y.T. Ju, M.Y. Cho, S. min Park, S.H. Beack, C.T. Lee, K.C. Roh, Two-dimensional cobalt-based composites grown on Ti plates for application as pseudocapacitor materials, *Electron. Mater. Lett.* 9 (2013) 531–534. doi:10.1007/s13391-013-0043-z.
- [65] X. Xia, C. Zhu, J. Luo, Z. Zeng, C. Guan, C.F. Ng, H. Zhang, H.J. Fan, Synthesis of free-standing metal sulfide nanoarrays via anion exchange reaction and their electrochemical energy storage application, *Small*. 10 (2014). doi:10.1002/sml.201302224.
- [66] C. Zhang, Y. Xie, M. Zhao, A.E. Pentecost, Z. Ling, J. Wang, D. Long, L. Ling, W. Qiao, Enhanced Electrochemical Performance of Hydrous RuO₂/Mesoporous Carbon Nanocomposites via Nitrogen Doping, *ACS Appl. Mater. Interfaces*. 6 (2014) 9751–9759. doi:10.1021/am502173x.
- [67] R. Vellacheri, V.K. Pillai, S. Kurungot, Hydrous RuO₂-carbon nanofiber electrodes with high mass and electrode-specific capacitance for efficient energy storage, *Nanoscale*. 4 (2012) 890–896. doi:10.1039/c2nr11479h.
- [68] Q. Lv, S. Wang, H. Sun, J. Luo, J. Xiao, J. Xiao, F. Xiao, S. Wang, Solid-State Thin-Film Supercapacitors with Ultrafast Charge/Discharge Based on N-Doped-Carbon-Tubes/Au-Nanoparticles-Doped-MnO₂ Nanocomposites, *Nano Lett.* 16 (2016) 40–47. doi:10.1021/acs.nanolett.5b02489.
- [69] X.Y. Liu, Y.Q. Gao, G.W. Yang, A flexible, transparent and super-long-life supercapacitor based on ultrafine Co₃O₄ nanocrystal electrodes, *Nanoscale*. 8 (2016) 4227–4235. doi:10.1039/c5nr09145d.
- [70] S. Maiti, A. Pramanik, S. Mahanty, Interconnected network of MnO₂ nanowires with a “cocoonlike” morphology: Redox couple-mediated performance enhancement in symmetric aqueous supercapacitor, *ACS Appl. Mater. Interfaces*. 6 (2014) 10754–10762. doi:10.1021/am502638d.
- [71] Y. Qiu, Y. Zhao, X. Yang, W. Li, Z. Wei, J. Xiao, S.-F. Leung, Q. Lin, H. Wu, Y. Zhang, Z. Fan, S. Yang, Three-dimensional metal/oxide nanocone arrays for high-performance electrochemical pseudocapacitors., *Nanoscale*. 6 (2014) 3626–31. doi:10.1039/c3nr06675d.
- [72] G.H. Jeong, S. Baek, S. Lee, S.W. Kim, Metal Oxide/Graphene Composites for Supercapacitive Electrode Materials, *Chem. - An Asian J.* 11 (2016) 949–964. doi:10.1002/asia.201501072.
- [73] A. Ghosh, E.J. Ra, M. Jin, H.K. Jeong, T.H. Kim, C. Biswas, Y.H. Lee, High pseudocapacitance from ultrathin V₂O₅ films electrodeposited on self-standing carbon-nanofiber paper, *Adv. Funct. Mater.* 21 (2011) 2541–2547. doi:10.1002/adfm.201002603.
- [74] K. Chen, D. Xue, Crystallisation of cuprous oxide, *Int. J. Nanotechnol.* 10 (2013) 4. doi:10.1504/IJNT.2013.050875.
- [75] S. Cabanas-polo, Z. Gonzalez, A.J. Sanchez-herencia, B. Ferrari, A. Caballero, Cyclability of binder-free β-Ni(OH)₂ anodes shaped by EPD for Li-ion batteries, *J. Eur. Ceram. Soc.* 35 (2015) 573–584. doi:10.1016/j.jeurceramsoc.2014.08.014.
- [76] Z. Gonzalez, B. Ferrari, A.J. Sanchez-Herencia, A. Caballero, J. Morales, Relevance of the Semiconductor Microstructure in the Pseudocapacitance of the Electrodes Fabricated by EPD of Binder-Free β-Ni(OH)₂ Nanoplatelets, *J. Electrochem. Soc.* 162 (2015) D3001–D3012. doi:10.1149/2.0101511jes.
- [77] Z. Gonzalez, J. Yus, A. Caballero, J. Morales, A.J. Sanchez-Herencia, B. Ferrari, Electrochemical performance of pseudo-capacitor electrodes fabricated by Electrophoretic Deposition inducing Ni(OH)₂ nanoplatelets agglomeration by Layer-by-Layer, *Electrochim. Acta*. 247 (2017). doi:10.1016/j.electacta.2017.07.043.
- [78] Z. Gonzalez, J. Yus, A. Caballero, J. Morales, A.J. Sanchez-Herencia, B. Ferrari,

- Electrochemical performance of pseudo-capacitor electrodes fabricated by Electrophoretic Deposition inducing Ni(OH)₂ nanoplatelets agglomeration by Layer-by-Layer, *Electrochim. Acta.* 247 (2017) 333–343. doi:10.1016/j.electacta.2017.07.043.
- [79] Z. Gonzalez, C. Filiatre, C.C. Buron, A.J. Sanchez-Herencia, B. Ferrari, Electrophoretic Deposition of Ni(OH)₂ Nanoplatelets Modified by Polyelectrolyte Multilayers: Study of the Coatings Formation in a Laminar Flow Cell, *J. Electrochem. Soc.* 164 (2017) D436–D444. doi:10.1149/2.0801707jes.
- [80] Z. Gonzalez, B. Ferrari, A.J. Sanchez-Herencia, A. Caballero, J. Morales, Use of Polyelectrolytes for the Fabrication of Porous NiO Films by Electrophoretic Deposition for Supercapacitor Electrodes, *Electrochim. Acta.* 211 (2016) 110–118. doi:10.1016/j.electacta.2016.06.014.
- [81] J. Yus, E. Chinarro, B. Ferrari, Z. González, The effect of the substrate on the conductivity of NiO electrodes in electrochemical capacitor shaped by electrophoretic deposition, in: *ECS Trans.*, 2018. doi:10.1149/08201.0097ecst.
- [82] J. Zhao, H. Liu, Q. Zhang, Applied Surface Science Preparation of NiO nanoflakes under different calcination temperatures and their supercapacitive and optical properties, *Appl. Surf. Sci.* 392 (2017) 1097–1106. doi:10.1016/j.apsusc.2016.09.128.
- [83] K.-C.L. and M.A. Anderson, Porous Nickel Oxide/Nickel Films for Electrochemical Capacitors, *J. Electrochem. Soc.* 143 (1996) 124–130. doi:10.1149/1.1836396.
- [84] H. Yan, D. Zhang, J. Xu, Y. Lu, Y. Liu, K. Qiu, Y. Zhang, Solution growth of NiO nanosheets supported on Ni foam as high-performance electrodes for supercapacitors, *Nano Res. Lett.* 9 (2014) 424. doi:10.1186/1556-276X-9-424.
- [85] Y. Zhou, Z. Mao, W. Wang, Z. Yang, X. Liu, In-Situ Fabrication of Graphene Oxide Hybrid Ni-Based Metal – Organic Framework (Ni – MOFs @ GO) with Ultrahigh Capacitance as Electrochemical Pseudocapacitor Materials, (2016). doi:10.1021/acsami.6b10640.
- [86] S.M. Cha, G. Nagaraju, J.S. Yu, Controlled Electrochemical Synthesis of Nickel Hydroxide Nanosheets Grown on Non-woven Cu/PET Fibers: A Robust, Flexible, and Binder-Free Electrode for High-Performance Pseudocapacitors, (2016). doi:10.1021/acs.jpcc.6b04611.
- [87] M. Yeager, W. Du, R. Si, D. Su, N. Marinkovic, X. Teng, Highly Efficient K 0.15 MnO₂ Birnessite Nanosheets for Stable Pseudocapacitive Cathodes, *J. Phys. Chem. C.* (2012).
- [88] Y. Wang, C. Shen, L. Niu, Z. Sun, F. Ruan, M. Xu, S. Shan, C. Li, X. Liu, Y. Gong, High rate capability of mesoporous NiWO₄ e CoWO₄ nanocomposite as a positive material for hybrid supercapacitor, *Mater. Chem. Phys.* 182 (2016) 1–8. doi:10.1016/j.matchemphys.2016.07.047.
- [89] Z. Yang, F. Xu, W. Zhang, Z. Mei, B. Pei, X. Zhu, Controllable preparation of multishelled NiO hollow nanospheres via layer-by-layer self-assembly for supercapacitor application, *J. Power Sources.* 246 (2014) 24–31. doi:10.1016/j.jpowsour.2013.07.057.
- [90] S.A. Abbas, K.D. Jung, Preparation of mesoporous microspheres of NiO with high surface area and analysis on their pseudocapacitive behavior, *Electrochim. Acta.* 193 (2016) 145–153. doi:10.1016/j.electacta.2016.02.054.
- [91] Z. Zhang, Q. Gao, H. Gao, Z. Shi, J. Wu, M. Zhi, Z. Hong, Nickel oxide aerogel for high performance supercapacitor electrodes, *RSC Adv.* 6 (2016). doi:10.1039/C6RA24436J.
- [92] H. Hareendrakrishnakumar, R. Chulliyote, M.G. Joseph, Effect of crystallite size on the intercalation pseudocapacitance of lithium nickel vanadate in aqueous electrolyte, *J. Solid State Electrochem.* 22 (2018) 1–9. doi:10.1007/s10008-017-3712-2.
- [93] X. Li, L. Wang, J. Shi, N. Du, G. He, Multishelled Nickel-Cobalt Oxide Hollow Microspheres with Optimized Compositions and Shell Porosity for High-Performance Pseudocapacitors, *ACS Appl. Mater. Interfaces.* 8 (2016) 17276–17283.

doi:10.1021/acsami.6b04654.

- [94] J. Pu, Z. Liu, Z. Ma, J. Wang, L. Zhang, S. Chang, W. Wu, Z. Shen, H. Zhang, Structure design of NiCo_2O_4 electrodes for high performance pseudocapacitors and lithium-ion batteries, *J. Mater. Chem. A*. 4 (2016) 1–3. doi:10.1039/C6TA08198C.
- [95] B. Yang, L. Yu, H. Yan, Y. Sun, Q. Liu, J. Liu, D. Song, S. Hu, Y. Yuan, L. Liu, J. Wang, Fabrication of urchin-like $\text{NiCo}_2(\text{CO}_3)(1.5)(\text{OH})(3)@\text{NiCo}_2\text{S}_4$ on Ni foam by an ion-exchange route and application to asymmetrical supercapacitors, *J. Mater. Chem. A*. 3 (2015) 13308–13316. doi:10.1039/c5ta02684a.
- [96] M.P. Yeager, D. Su, N.S. Marinković, X. Teng, Pseudocapacitive NiO fine nanoparticles for supercapacitor reactions, *J. Electrochem. Soc.* 159 (2012). doi:10.1149/2.025210jes.
- [97] N. Kurra, N.A. Alhebshi, H.N. Alshareef, Microfabricated pseudocapacitors using $\text{Ni}(\text{OH})_2$ electrodes exhibit remarkable volumetric capacitance and energy density, *Adv. Energy Mater.* 5 (2015) 1–9. doi:10.1002/aenm.201401303.
- [98] G. Cai, X. Wang, M. Cui, P. Darmawan, J. Wang, A.L.-S. Eh, P.S. Lee, Electrochromo-supercapacitor based on direct growth of NiO nanoparticles, *Nano Energy*. 12 (2015). doi:10.1016/j.nanoen.2014.12.031.
- [99] Y. Chuminjak, S. Daothong, P. Reanpang, J.P. Mensing, D. Phokharatkul, J. Jakmunee, A. Wisitsoraat, A. Tuantranont, P. Singjai, Electrochemical energy-storage performances of nickel oxide films prepared by a sparking method, *RSC Adv.* 5 (2015). doi:10.1039/c5ra09408a.
- [100] Y. Chuminjak, S. Daothong, A. Kuntarug, D. Phokharatkul, M. Horprathum, A. Wisitsoraat, A. Tuantranont, J. Jakmunee, P. Singjai, High-performance Electrochemical Energy Storage Electrodes Based on Nickel Oxide-coated Nickel Foam Prepared by Sparking Method, *Electrochim. Acta*. 238 (2017) 298–309. doi:10.1016/j.electacta.2017.03.190.
- [101] Y. Xu, Y. Dong, X. Han, X. Wang, Y. Wang, L. Jiao, H. Yuan, Application for simply recovered LiCoO_2 material as a high-performance candidate for supercapacitor in aqueous system, *ACS Sustain. Chem. Eng.* 3 (2015) 2435–2442. doi:10.1021/acssuschemeng.5b00455.
- [102] Z. Pan, Y. Jiang, P. Yang, Z. Wu, W. Tian, L. Liu, Y. Song, Q. Gu, D. Sun, L. Hu, In Situ Growth of Layered Bimetallic ZnCo Hydroxide Nanosheets for High-Performance All-Solid-State Pseudocapacitor, *ACS Nano*. 12 (2018) 2968–2979. doi:10.1021/acsnano.8b00653.
- [103] L.Y. Chen, Y. Hou, J.L. Kang, A. Hirata, M.W. Chen, Asymmetric metal oxide pseudocapacitors advanced by three-dimensional nanoporous metal electrodes, *J. Mater. Chem. A*. 2 (2014) 8448. doi:10.1039/c4ta00965g.
- [104] C. Zhan, D.-E. Jiang, Understanding the pseudocapacitance of RuO_2 from joint density functional theory, *J. Phys. Condens. Matter*. 28 (2016). doi:10.1088/0953-8984/28/46/464004.
- [105] J.Y. Seok, J. Lee, M. Yang, Self-Generated Nanoporous Silver Framework for High-Performance Iron Oxide Pseudocapacitor Anodes, *ACS Appl. Mater. Interfaces*. 10 (2018) 17223–17231. doi:10.1021/acsami.8b03725.
- [106] J.M. Kwon, J.H. Kim, S.H. Kang, C.J. Choi, J.A. Rajesh, K.S. Ahn, Facile hydrothermal synthesis of cubic spinel AB_2O_4 type MnFe_2O_4 nanocrystallites and their electrochemical performance, *Appl. Surf. Sci.* 413 (2017) 83–91. doi:10.1016/j.apsusc.2017.04.022.
- [107] M. Qiu, P. Sun, L. Shen, K. Wang, S. Song, X. Yu, S. Tan, C. Zhao, W. Mai, WO_3 nanoflowers with excellent pseudo-capacitive performance and the capacitance contribution analysis, *J. Mater. Chem. A*. 4 (2016) 7266–7273. doi:10.1039/C6TA00237D.
- [108] C. Xu, J. Liao, R. Wang, P. Zou, R. Wang, F. Kang, C. Yang, $\text{MoO}_3@\text{Ni}$ nanowire array

- hierarchical anode for high capacity and superior longevity all-metal-oxide asymmetric supercapacitors, *RSC Adv.* 6 (2016) 110112–110119. doi:10.1039/C6RA20579H.
- [109] R. Manikandan, C.J. Raj, M. Rajesh, B.C. Kim, J.Y. Sim, K.H. Yu, Electrochemical Behaviour of Lithium, Sodium and Potassium Ion Electrolytes in a $\text{Na}_{0.33}\text{V}_2\text{O}_5$ Symmetric Pseudocapacitor with High Performance and High Cyclic Stability, *ChemElectroChem.* 5 (2018) 101–111. doi:10.1002/celec.201700923.
- [110] A. Ray, A. Roy, P. Sadhukhan, S.R. Chowdhury, P. Maji, S.K. Bhattacharya, S. Das, Electrochemical properties of TiO_2 - V_2O_5 nanocomposites as a high performance supercapacitors electrode material, *Appl. Surf. Sci.* 443 (2018) 581–591. doi:10.1016/j.apsusc.2018.02.277.
- [111] Y. Yang, S. Ren, X. Song, Y. Guo, D. Si, H. Jing, S. Ma, C. Hao, M. Ji, Sn@SnO_2 attached on carbon spheres as additive-free electrode for high-performance pseudocapacitor, *Electrochim. Acta.* 209 (2016) 350–359. doi:10.1016/j.electacta.2016.05.105.
- [112] S. Maiti, A. Pramanik, S. Mahanty, Extraordinarily high pseudocapacitance of metal organic framework derived nanostructured cerium oxide, *Chem. Commun.* 50 (2014). doi:10.1039/c4cc05363j.
- [113] J. Xu, C. Wang, J. Liu, S. Xu, W. Zhang, Y. Lu, Facile fabrication of a novel nanoporous Au / AgO composite for electrochemical double-layer capacitor, *RSC Adv.* 5 (2015) 38995–39002. doi:10.1039/C5RA03564C.
- [114] J.N. Tiwari, R.N. Tiwari, K.S. Kim, Zero-dimensional, one-dimensional, two-dimensional and three-dimensional nanostructured materials for advanced electrochemical energy devices, *Prog. Mater. Sci.* 57 (2012) 724–803. doi:10.1016/j.pmatsci.2011.08.003.
- [115] R.M. Pasquarelli, D.S. Ginley, R. O'Hayre, Solution processing of transparent conductors: from flask to film, *Chem. Soc. Rev.* 40 (2011) 5406. doi:10.1039/c1cs15065k.
- [116] S. Cabañas-Polo, Z. Gonzalez, B. Ferrari, Influence of ultrasound on the instantaneous synthesis of tridimensional $\alpha\text{-Ni(OH)}_2$ nanostructures and derived NiO nanoparticles, *CrystEngComm.* 17 (2015) 6193–6206. doi:10.1039/C5CE00876J.
- [117] S. Cabanas-Polo, K.S. Suslick, A.J. Sanchez-Herencia, Effect of reaction conditions on size and morphology of ultrasonically prepared Ni(OH)_2 powders, *Ultrason. Sonochem.* 18 (2011) 901–906. doi:10.1016/j.ultsonch.2010.11.017.
- [118] J.T. Mefford, W.G. Hardin, S. Dai, K.P. Johnston, K.J. Stevenson, Anion charge storage through oxygen intercalation in LaMnO_3 perovskite pseudocapacitor electrodes., *Nat. Mater.* 13 (2014) 726–32. doi:10.1038/nmat4000.
- [119] R. Sahoo, A. Roy, S. Dutta, C. Ray, T. Aditya, A. Pal, T. Pal, Liquor ammonia mediated V (v) insertion in thin Co_3O_4 sheets for improved pseudocapacitors with high energy density and high specific capacitance value, *Chem. Commun.* 51 (2015) 15986–15989. doi:10.1039/C5CC06005B.
- [120] B. Bhujun, S. Anandan, M.T.T. Tan, Study of ternary metal oxides as supercapacitor electrodes, *WIT Trans. Ecol. Environ.* 186 (2014). doi:10.2495/ESUS140391.
- [121] D. Das, B. Bagchi, R.N. Basu, Nanostructured zirconia thin film fabricated by electrophoretic deposition technique, *J. Alloys Compd.* 693 (2017) 1220–1230. doi:http://dx.doi.org/10.1016/j.jallcom.2016.10.088.
- [122] C.C. Hu, C.M. Huang, K.H. Chang, Anodic deposition of porous vanadium oxide network with high power characteristics for pseudocapacitors, *J. Power Sources.* 185 (2008) 1594–1597. doi:10.1016/j.jpowsour.2008.08.017.
- [123] C. Xia, W. Chen, X. Wang, M.N. Hedhili, N. Wei, H.N. Alshareef, Highly stable supercapacitors with conducting polymer core-shell electrodes for energy storage applications, *Adv. Energy Mater.* 5 (2015). doi:10.1002/aenm.201401805.

- [124] Z. Zheng, B. Huang, X. Qin, X. Zhang, Y. Dai, M.-H. Whangbo, Facile in situ synthesis of visible-light plasmonic photocatalysts $M@TiO_2$ ($M = Au, Pt, Ag$) and evaluation of their photocatalytic oxidation of benzene to phenol, *J. Mater. Chem.* 21 (2011) 9079. doi:10.1039/c1jm10983a.
- [125] H. Wu, D. Li, X. Zhu, C. Yang, D. Liu, X. Chen, Y. Song, L. Lu, High-performance and renewable supercapacitors based on TiO_2 nanotube array electrodes treated by an electrochemical doping approach, *Electrochim. Acta.* 116 (2014) 129–136. doi:10.1016/j.electacta.2013.10.092.
- [126] W. Li, G. Li, J. Sun, R. Zou, K. Xu, Y. Sun, Z. Chen, J. Yang, J. Hu, Hierarchical heterostructures of MnO_2 nanosheets or nanorods grown on Au-coated Co_3O_4 porous nanowalls for high-performance pseudocapacitance., *Nanoscale.* 5 (2013) 2901–8. doi:10.1039/c3nr34140b.
- [127] H. Wang, H. Yi, X. Chen, X. Wang, Facile synthesis of a nano-structured nickel oxide electrode with outstanding pseudocapacitive properties, *Electrochim. Acta.* 105 (2013) 353–361. doi:10.1016/j.electacta.2013.05.031.
- [128] B.T. Liu, X.M. Shi, X.Y. Lang, L. Gu, Z. Wen, M. Zhao, Q. Jiang, Extraordinary pseudocapacitive energy storage triggered by phase transformation in hierarchical vanadium oxides, *Nat. Commun.* 9 (2018) 1–9. doi:10.1038/s41467-018-03700-3.
- [129] X. Xia, J. Luo, Z. Zeng, C. Guan, Y. Zhang, J. Tu, H. Zhang, H.J. Fan, Integrated photoelectrochemical energy storage: solar hydrogen generation and supercapacitor., *Sci. Rep.* 2 (2012) 981. doi:10.1038/srep00981.
- [130] J. Yus, B. Ferrari, A. Sanchez-Herencia, A. Caballero, J. Morales, Z. Gonzalez, In Situ Synthesis and Electrophoretic Deposition of NiO/Ni Core-Shell Nanoparticles and Its Application as Pseudocapacitor, *Coatings.* 7 (2017) 193. doi:10.3390/coatings7110193.
- [131] J. Yus, Z. Gonzalez, A.J. Sanchez-Herencia, A. Sangiorgi, N. Sangiorgi, D. Gardini, A. Sanson, C. Galassi, A. Caballero, J. Morales, B. Ferrari, Semiconductor water-based inks: Miniaturized NiO pseudocapacitor electrodes by inkjet printing, *J. Eur. Ceram. Soc.* (2019) 0–1. doi:10.1016/j.jeurceramsoc.2019.03.020.
- [132] C.Y. Yoo, J. Park, D.S. Yun, J.H. Yu, H.H.C. Yoon, J.N. Kim, H.H.C. Yoon, M. Kwak, Y.C. Kang, Crucial role of a nickel substrate in Co_3O_4 pseudocapacitor directly grown on nickel and its electrochemical properties, *J. Alloys Compd.* 676 (2016) 407–413. doi:10.1016/j.jallcom.2016.03.179.
- [133] X.. b Xia, J.. Tu, Y.. Zhang, X.. Wang, C.. Gu, X.-B.. Zhao, H.J.. Fan, High-quality metal oxide core/shell nanowire arrays on conductive substrates for electrochemical energy storage, *ACS Nano.* 6 (2012) 5531–5538. doi:10.1021/nn301454q.
- [134] J. Liu, J. Jiang, M. Bosman, H.J. Fan, Three-dimensional tubular arrays of MnO_2 –NiO nanoflakes with high areal pseudocapacitance, *J. Mater. Chem.* 22 (2012) 2419. doi:10.1039/c1jm14804d.
- [135] Z. Lu, Z. Chang, J. Liu, X. Sun, Stable ultrahigh specific capacitance of NiO nanorod arrays, *Nano Res.* 4 (2011) 658–665. doi:10.1007/s12274-011-0121-1.
- [136] D. Van Pham, R.A. Patil, C.C. Yang, W.C. Yeh, Y. Liou, Y.R. Ma, Impact of the crystal phase and 3d-valence conversion on the capacitive performance of one-dimensional MoO_2 , MoO_3 , and Magnéli-phase Mo_4O_{11} nanorod-based pseudocapacitors, *Nano Energy.* 47 (2018) 105–114. doi:10.1016/j.nanoen.2018.02.044.
- [137] X.-Y. Lang, B.-T. Liu, X.-M. Shi, Y.-Q. Li, Z. Wen, Q. Jiang, Ultrahigh-Power Pseudocapacitors Based on Ordered Porous Heterostructures of Electron-Correlated Oxides, *Adv. Sci.* (2016) n/a-n/a. doi:10.1002/adv.201500319.
- [138] S.A. Pawar, D.S. Patil, J.C. Shin, Designing a Copper- and Silver-Sulfide Composite with Co_3O_4 for High-Performance Electrochemical Supercapacitors, *ChemElectroChem.* 6 (2019) 522–534. doi:10.1002/celc.201801207.

- [139] G.M. Tomboc, M.W. Abebe, A.F. Baye, H. Kim, Utilization of the superior properties of highly mesoporous PVP modified NiCo_2O_4 with accessible 3D nanostructure and flower-like morphology towards electrochemical methanol oxidation reaction, *J. Energy Chem.* 29 (2018) 136–146. doi:10.1016/j.jechem.2018.08.009.
- [140] J.W. Kim, V. Augustyn, B. Dunn, The effect of crystallinity on the rapid pseudocapacitive response of Nb_2O_5 , *Adv. Energy Mater.* 2 (2012). doi:10.1002/aenm.201100494.
- [141] C. Jung, P. Lin, T. Yuen, Electrophoretic fabrication and pseudocapacitive properties of graphene / manganese oxide / carbon nanotube nanocomposites, *J. Power Sources.* 243 (2013) 594–602. doi:10.1016/j.jpowsour.2013.06.055.
- [142] A. Caballero, L. Hernán, J. Morales, Z. González, A.J.J. Sánchez-Herencia, B. Ferrari, A high-capacity anode for lithium batteries consisting of mesoporous NiO nanoplatelets, *Energy and Fuels.* 27 (2013) 5545–5551. doi:10.1021/ef400797r.
- [143] B. Wang, J. Park, C. Wang, H. Ahn, G. Wang, Mn_3O_4 nanoparticles embedded into graphene nanosheets: Preparation, characterization, and electrochemical properties for supercapacitors, *Electrochim. Acta.* 55 (2010) 6812–6817. doi:10.1016/j.electacta.2010.05.086.
- [144] I. Lee, G.H. Jeong, S. An, S.W. Kim, S. Yoon, Facile synthesis of 3D MnNi -layered double hydroxides (LDH)/graphene composites from directly graphites for pseudocapacitor and their electrochemical analysis, *Appl. Surf. Sci.* 429 (2018) 196–202. doi:10.1016/j.apsusc.2017.06.259.
- [145] J. Yan, T. Wei, W. Qiao, B. Shao, Q. Zhao, L. Zhang, Z. Fan, Rapid microwave-assisted synthesis of graphene nanosheet/ Co_3O_4 composite for supercapacitors, *Electrochim. Acta.* 55 (2010) 6973–6978. doi:10.1016/j.electacta.2010.06.081.
- [146] J. Shim, Y. Ko, K.S. Lee, K. Partha, C.H. Lee, K. Yu, H.Y. Koo, K.T. Lee, W.S. Seo, D.I. Son, Conductive Co_3O_4 /graphene (core/shell) quantum dots as electrode materials for electrochemical pseudocapacitor applications, *Compos. Part B Eng.* 130 (2017) 230–235. doi:10.1016/j.compositesb.2017.07.039.
- [147] X. Cai, S. Hua, C. Kok, L. Lai, J. Lin, Z. Shen, High-performance asymmetric pseudocapacitor cell based on cobalt hydroxide / graphene and polypyrrole / graphene electrodes, *J. Power Sources.* 275 (2015) 298–304. doi:10.1016/j.jpowsour.2014.10.204.
- [148] Y.G. Zhu, Y. Wang, Y. Shi, Z.X. Huang, L. Fu, H.Y. Yang, Phase transformation induced capacitance activation for 3D graphene- CoO nanorod pseudocapacitor, *Adv. Energy Mater.* 4 (2014) 1–8. doi:10.1002/aenm.201301788.
- [149] S. Chen, J. Zhu, X. Wu, Q. Han, X. Wang, Graphene oxide- MnO_2 nanocomposites for supercapacitors, *ACS Nano.* 4 (2010) 2822–2830. doi:10.1021/nn901311t.
- [150] D. Jia, X. Chen, H. Tan, F. Liu, L. Yue, Y. Zheng, X. Cao, C. Li, Y. Sun, H. Liu, J. Liu, Boosting Electrochemistry of Manganese Oxide Nanosheets by Ostwald Ripening during Reduction for Fiber Electrochemical Energy Storage Device, *ACS Appl. Mater. Interfaces.* 10 (2018) 30388–30399. doi:10.1021/acsami.8b09592.
- [151] K. Makgopa, P.M. Ejikeme, K.I. Ozoemena, Graphene oxide-modified nickel (II) tetra-aminophthalocyanine nanocomposites for high-power symmetric pseudocapacitor, *Electrochim. Acta.* 212 (2016). doi:10.1016/j.electacta.2016.07.027.
- [152] W. Ma, S. Chen, S. Yang, W. Chen, W. Weng, Y. Cheng, M. Zhu, Flexible all-solid-state asymmetric supercapacitor based on transition metal oxide nanorods/reduced graphene oxide hybrid fibers with high energy density, *Carbon N. Y.* 113 (2017) 151–158. doi:10.1016/j.carbon.2016.11.051.
- [153] X. Song, L. Tan, X. Wang, L. Zhu, X. Yi, Q. Dong, Synthesis of CoS@rGO composites with excellent electrochemical performance for supercapacitors, *J. Electroanal. Chem.* 794 (2017) 132–138. doi:10.1016/j.jelechem.2017.04.014.
- [154] M.S. Chang, T. Kim, J.H. Kang, J. Park, C.R. Park, The effect of surface characteristics

- of reduced graphene oxide on the performance of a pseudocapacitor, *2D Mater.* 2 (2015). doi:10.1088/2053-1583/2/1/014007.
- [155] K.P. Madhuri, N.S. John, Supercapacitor application of nickel phthalocyanine nanofibres and its composite with reduced graphene oxide, *Appl. Surf. Sci.* 449 (2018) 528–536. doi:10.1016/j.apsusc.2017.12.021.
- [156] D. Ghosh, J. Lim, R. Narayan, S.O. Kim, High Energy Density All Solid State Asymmetric Pseudocapacitors Based on Free Standing Reduced Graphene Oxide-Co₃O₄ Composite Aerogel Electrodes, (2016) 4–11. doi:10.1021/acsami.6b07511.
- [157] P. Bhattacharya, T. Joo, M. Kota, H.S. Park, CoO nanoparticles deposited on 3D macroporous ozonized RGO networks for high rate capability and ultralong cyclability of pseudocapacitors, *Ceram. Int.* 44 (2018) 980–987. doi:10.1016/j.ceramint.2017.10.032.
- [158] H.-S. Kim, J.B. Cook, S.H. Tolbert, B. Dunn, The Development of Pseudocapacitive Properties in Nanosized-MoO₂, *J. Electrochem. Soc.* 162 (2015) A5083–A5090. doi:10.1149/2.0141505jes.
- [159] M. Chaudhary, R. an Doong, N. Kumar, T.Y. Tseng, Ternary Au/ZnO/rGO nanocomposites electrodes for high performance electrochemical storage devices, *Appl. Surf. Sci.* 420 (2017) 118–128. doi:10.1016/j.apsusc.2017.05.088.
- [160] J. Yus, Y. Bravo, A.J. Sanchez-Herencia, B. Ferrari, Z. Gonzalez, Electrophoretic deposition of RGO-NiO core-shell nanostructures driven by heterocoagulation method with high electrochemical performance, *Electrochim. Acta.* 308 (2019) 363–372. doi:10.1016/j.electacta.2019.04.053.
- [161] S. Shahrokhian, R. Mohammadi, E. Asadian, One-step fabrication of electrochemically reduced graphene oxide/nickel oxide composite for binder-free supercapacitors, *Int. J. Hydrogen Energy.* 41 (2016) 17496–17505. doi:10.1016/j.ijhydene.2016.07.087.
- [162] L. Shen, P. Sun, C. Zhao, S. Tan, W. Mai, Tailorable pseudocapacitors for energy storage clothes, *RSC Adv.* 6 (2016) 67764–67770. doi:10.1039/C6RA11733C.
- [163] P. Yang, Y. Chen, X. Yu, P. Qiang, K. Wang, X. Cai, S. Tan, P. Liu, J. Song, W. Mai, Reciprocal alternate deposition strategy using metal oxide/carbon nanotube for positive and negative electrodes of high-performance supercapacitors, *Nano Energy.* 10 (2014) 106–116. doi:10.1016/j.nanoen.2014.08.018.
- [164] D.W. Lee, J.H. Lee, N.K. Min, J.H. Jin, Buckling Structured Stretchable Pseudocapacitor Yarn, *Sci. Rep.* 7 (2017) 1–8. doi:10.1038/s41598-017-12375-7.
- [165] X. Ma, Y. Li, Z. Wen, F. Gao, C. Liang, R. Che, Ultrathin -Ni(OH)₂ nanoplates vertically grown on nickel-coated carbon nanotubes as high-performance pseudocapacitor electrode materials, *ACS Appl. Mater. Interfaces.* 7 (2015) 974–979. doi:10.1021/am5077183.
- [166] A.D. Su, X. Zhang, A. Rinaldi, S.T. Nguyen, H. Liu, Z. Lei, L. Lu, H.M. Duong, Hierarchical porous nickel oxide-carbon nanotubes as advanced pseudocapacitor materials for supercapacitors, *Chem. Phys. Lett.* 561–562 (2013) 68–73. doi:10.1016/j.cplett.2013.01.023.
- [167] Y.Q. Jiang, P.B. Wang, X.N. Zang, Y. Yang, A. Kozinda, L.W. Lin, Uniformly Embedded Metal Oxide Nanoparticles in Vertically Aligned Carbon Nanotube Forests as Pseudocapacitor Electrodes for Enhanced Energy Storage (vol 13, pg 3524, 2013), *Nano Lett.* 14 (2014) 2230. doi:10.1021/nl5008129.
- [168] C. Yu, J. Yang, C. Zhao, X. Fan, G. Wang, J. Qiu, Nanohybrids from NiCoAl-LDH coupled with carbon for pseudocapacitors: understanding the role of nano-structured carbon, *Nanoscale.* 6 (2014) 3097–3104. doi:10.1039/C3NR05477B.
- [169] M. Mazloumi, S. Shadmehr, Y. Rangom, L.F. Nazar, X. Tang, Fabrication of three-dimensional carbon nanotube and metal oxide hybrid mesoporous architectures, *ACS Nano.* 7 (2013) 4281–4288. doi:10.1021/nn400768p.

- [170] Q. Wang, D. Zhang, Y. Wu, T. Li, A. Zhang, M. Miao, Fabrication of Supercapacitors from NiCo₂O₄ Nanowire/Carbon-Nanotube Yarn for Ultraviolet Photodetectors and Portable Electronics, *Energy Technol.* 5 (2017) 1449–1456. doi:10.1002/ente.201600726.
- [171] D.W.H. Fam, S. Azoubel, L. Liu, J. Huang, D. Mandler, S. Magdassi, A.I.Y. Tok, Novel felt pseudocapacitor based on carbon nanotube/metal oxides, *J. Mater. Sci.* 50 (2015) 6578–6585. doi:10.1007/s10853-015-9199-2.
- [172] D.U. Zuru, Z. Zainal, M.Z. Hussein, A.M. Jaafar, H.N. Lim, S.K. Chang, Theoretical and experimental models for the synthesis of single-walled carbon nanotubes and their electrochemical properties, *J. Appl. Electrochem.* 48 (2018) 287–304. doi:10.1007/s10800-018-1158-6.
- [173] L. Huang, X. Gao, Q. Dong, Z. Hu, X. Xiao, T. Li, Y. Cheng, B. Yao, J. Wan, D. Ding, Z. Ling, J. Qiu, J. Zhou, H_xMoO₃ nanobelts with sea water as electrolyte for high-performance pseudocapacitors and desalination devices, *J. Mater. Chem. A* 3 (2015). doi:10.1039/c5ta05251c.
- [174] R. Liang, H. Cao, D. Qian, MoO₃ nanowires as electrochemical pseudocapacitor materials, *Chem. Commun.* 47 (2011) 10305–10307. doi:10.1039/c1cc14030b.
- [175] Z. Chen, V. Augustyn, X. Jia, Q. Xiao, B. Dunn, Y. Lu, High-performance sodium-ion pseudocapacitors based on hierarchically porous nanowire composites, *ACS Nano* 6 (2012) 4319–4327. doi:10.1021/nn300920e.
- [176] S. Chang, J. Pu, J. Wang, H. Du, Q. Zhou, Z. Liu, C. Zhu, J. Li, H. Zhang, Electrochemical Fabrication of Monolithic Electrodes with Core / Shell Sandwiched Transition Metal Oxide / Oxyhydroxide for High- Performance Energy Storage, (2016). doi:10.1021/acsami.6b06073.
- [177] J. Jiang, J. Liu, R. Ding, J. Zhu, Y. Li, A. Hu, X. Li, X. Huang, Large-Scale Uniform α -Co(OH)₂ Long Nanowire Arrays Grown on Graphite as Pseudocapacitor Electrodes, *ACS Appl. Mater. Interfaces* 3 (2011) 99–103. doi:10.1021/am1009887.
- [178] Y. Yang, D. Zeng, S. Yang, L. Gu, B. Liu, S. Hao, Nickel cobaltite nanosheets coated on metal-organic framework-derived mesoporous carbon nanofibers for high-performance pseudocapacitors, *J. Colloid Interface Sci.* 534 (2019) 312–321. doi:10.1016/j.jcis.2018.09.037.
- [179] Y. Pang, S. Zhang, S. Chen, J. Liang, M. Li, D. Ding, S. Ding, Transition-Metal Oxides Anchored on Nitrogen-Enriched Carbon Ribbons for High-Performance Pseudocapacitors, *Chem. - A Eur. J.* 24 (2018) 16104–16112. doi:10.1002/chem.201802951.
- [180] C. Guan, Z. Zeng, X. Li, X. Cao, Y. Fan, X. Xia, G. Pan, H. Zhang, H.J. Fan, Atomic-layer-deposition-assisted formation of carbon nanoflakes on metal oxides and energy storage application, *Small* 10 (2014) 300–307. doi:10.1002/smll.201301009.
- [181] W. Meng, W. Chen, L. Zhao, Y. Huang, M. Zhu, Y. Huang, Y. Fu, F. Geng, J. Yu, X. Chen, C. Zhi, Porous Fe₃O₄/carbon composite electrode material prepared from metal-organic framework template and effect of temperature on its capacitance, *Nano Energy* 8 (2014) 133–140. doi:10.1016/j.nanoen.2014.06.007.
- [182] M. Zhu, J. Kan, J. Pan, W. Tong, Q. Chen, J. Wang, S. Li, One-pot hydrothermal fabrication of α -Fe₂O₃@C nanocomposites for electrochemical energy storage, *J. Energy Chem.* 28 (2019) 1–8. doi:10.1016/j.jechem.2017.09.021.
- [183] Y. Zhao, Z. Wang, R. Yuan, Y. Lin, J. Yan, J. Zhang, Z. Lu, D. Luo, J. Pietrasik, M.R. Bockstaller, K. Matyjaszewski, ZnO/carbon hybrids derived from polymer nanocomposite precursor materials for pseudocapacitor electrodes with high cycling stability, *Polymer (Guildf)* 137 (2018) 370–377. doi:10.1016/j.polymer.2018.01.024.
- [184] X. Zhang, J. Luo, P. Tang, X. Ye, X. Peng, H. Tang, S.G. Sun, J. Fransaer, A universal strategy for metal oxide anchored and binder-free carbon matrix electrode: A

- supercapacitor case with superior rate performance and high mass loading, *Nano Energy*. 31 (2017) 311–321. doi:10.1016/j.nanoen.2016.11.024.
- [185] J. Xiao, L. Wan, S. Yang, F. Xiao, S. Wang, Design hierarchical electrodes with highly conductive NiCo_2S_4 nanotube arrays grown on carbon fiber paper for high-performance pseudocapacitors, *Nano Lett.* 14 (2014). doi:10.1021/nl404199v.
- [186] K. Deori, S.K. Ujjain, R.K. Sharma, S. Deka, Morphology controlled synthesis of nanoporous Co_3O_4 nanostructures and their charge storage characteristics in supercapacitors, *ACS Appl. Mater. Interfaces*. 5 (2013). doi:10.1021/am4027482.
- [187] J. Han, K.C. Roh, M.R. Jo, Y.M. Kang, A novel co-precipitation method for one-pot fabrication of a Co-Ni multiphase composite electrode and its application in high energy-density pseudocapacitors, *Chem Commun.* 49 (2013) 7067–7069. doi:10.1039/c3cc43350a.
- [188] Q. Mahmood, W.S. Kim, H.S. Park, Structure and compositional control of MoO_3 hybrids assembled by nanoribbons for improved pseudocapacitor rate and cycle performance., *Nanoscale*. 4 (2012) 7855–60. doi:10.1039/c2nr32175k.
- [189] S. Dong, L. Shen, H. Li, G. Pang, H. Dou, X. Zhang, Flexible Sodium-Ion Pseudocapacitors Based on 3D $\text{Na}_2\text{Ti}_3\text{O}_7$ Nanosheet Arrays/Carbon Textiles Anodes, *Adv. Funct. Mater.* 26 (2016) 3703–3710. doi:10.1002/adfm.201600264.
- [190] T. Ling, P. Da, X. Zheng, B. Ge, Z. Hu, M. Wu, X.W. Du, W. Bin Hu, M. Jaroniec, S.Z. Qiao, Atomic-level structure engineering of metal oxides for high-rate oxygen intercalation pseudocapacitance, *Sci. Adv.* 4 (2018) 1–9. doi:10.1126/sciadv.aau6261.
- [191] D. Susanti, R.N.D. Wibawa, L. Tananta, H. Purwaningsih, R. Fajarin, G.E. Kusuma, The effect of calcination temperature on the capacitive properties of WO_3 -based electrochemical capacitors synthesized via a sol-gel method, *Front. Mater. Sci.* 7 (2013) 370–378. doi:10.1007/s11706-013-0220-x.
- [192] M.S. Javed, C. Zhang, L. Chen, Y. Xi, C. Hu, Hierarchical mesoporous NiFe_2O_4 nanocone forest directly growing on carbon textile for high performance flexible supercapacitors, *J. Mater. Chem. A*. 4 (2016) 8851–8859. doi:10.1039/C6TA01893A.
- [193] N. Miyajima, K. Jinguiji, T. Matsumura, T. Matsubara, H. Sakane, T. Akatsu, O. Tanaike, A simple synthesis method to produce metal oxide loaded carbon paper using bacterial cellulose gel and characterization of its electrochemical behavior in an aqueous electrolyte, *J. Phys. Chem. Solids*. 91 (2016) 122–127. doi:10.1016/j.jpcs.2016.01.007.
- [194] M. Sawangphruk, S. Pinitsoontorn, J. Limtrakul, Surfactant-assisted electrodeposition and improved electrochemical capacitance of silver-doped manganese oxide pseudocapacitor electrodes, *J. Solid State Electrochem.* 16 (2012) 2623–2629. doi:10.1007/s10008-012-1691-x.
- [195] Y. Zhang, M. Park, H.Y. Kim, S.J. Park, Moderated surface defects of Ni particles encapsulated with NiO nanofibers as supercapacitor with high capacitance and energy density, *J. Colloid Interface Sci.* 500 (2017) 155–163. doi:10.1016/j.jcis.2017.04.022.
- [196] A.K. Tomar, R.B. Marichi, G. Singh, R.K. Sharma, Enhanced electrochemical performance of anion-intercalated lanthanum molybdenum oxide pseudocapacitor electrode, *Electrochim. Acta.* (2018). doi:10.1016/j.electacta.2018.10.193.
- [197] E. Rezaie, A. Rezanezhad, L.S. Ghadimi, A. Hajalilou, N. Arsalani, Effect of calcination on structural and supercapacitance properties of hydrothermally synthesized plate-like $\text{SrFe}_{12}\text{O}_{19}$ hexaferrite nanoparticles, *Ceram. Int.* 44 (2018) 20285–20290. doi:10.1016/j.ceramint.2018.08.014.
- [198] R.B. Rakhi, B. Ahmed, D. Anjum, H.N. Alshareef, Direct Chemical Synthesis of MnO_2 Nanowhiskers on Transition-Metal Carbide Surfaces for Supercapacitor Applications, *ACS Appl. Mater. Interfaces*. 8 (2016) 18806–18814. doi:10.1021/acsami.6b04481.
- [199] A. Sumboja, C.Y. Foo, J. Yan, C. Yan, R.K. Gupta, P.S. Lee, Significant electrochemical

1 stability of manganese dioxide/polyaniline coaxial nanowires by self-terminated double
2 surfactant polymerization for pseudocapacitor electrode, J. Mater. Chem. 22 (2012)
3 23921. doi:10.1039/c2jm32456c.

4 [200] C.C. Hu, Y.T. Wu, K.H. Change, Low-temperature hydrothermal synthesis of Mn_3O_4 and
5 MnOOH single crystals: Determinant influence of oxidants, Chem. Mater. 20 (2008)
6 2890–2894. doi:10.1021/cm703245k.

7 [201] S. Mno, C. Nanotube, T. Nanostructures, W. Pseudocapacitors, H.M. Loading,
8 Symmetrical MnO_2 Å Carbon Nanotube Å Textile Nanostructures for Wearable
9 Pseudocapacitors with High, ACS Nano. (2011) 8904–8913. doi:10.1021/nn203085.

Table 1. Main features of batteries, fuel cells conventional capacitors and supercapacitors in terms of power and energy density and charge/discharge time

	Fuel cells	Battery	Supercapacitor	Conventional Capacitor
Power density (W/Kg)	5-500	10-10 ³	15- 1.5·10 ⁴	10 ⁴ -10 ⁷
Energy density (Wh/Kg)	>10 ²	10-120	0.1 - 10	<0.05
Charge/Discharge Time	∞	0.1 - 12 h	2.4 - 24 s	10 ⁻³ - 10 ms
Cycle life/ cyclability (nº cycles)	--	500 - 2000	> 100000	> 500000

Table 2. Data of SCs plotted in the Ragone diagram in Figure 1

Plot point	Based Material	Power density (W/Kg)	Energy density (Wh/Kg)	Ref
1	NiO	5332	10.0	[2]
2	Ni(OH) ₂ //MnO ₂	750	91.1	[3]
3	NiCl ₂	750	15.4	[4]
4	Mn ₂ O ₃	1000	147.0	[5]
5	CoO	2153	15.0	[6]

Table 3. List of the reviews published since 2000 ordered by the date of publication and classified depending on the main research topic assessed

Review	Topic	Ref	Publication Date
Carbon-Based Metal-Free Catalysts for Energy Storage and Environmental Remediation	Carbon-based	[15]	March 2019
Background, fundamental understanding and progress in electrochemical capacitors	Carbon-based & Electrolyte	[16]	March 2019
A review on recent advances in hybrid supercapacitors: Design, fabrication and applications	Ceramic Oxides & Carbon-based	[17]	March 2019
Puzzles and confusions in supercapacitor and battery: Theory and solutions	Carbon-based	[18]	October 2018
Lignin in storage and renewable energy applications: A review	Carbon-based	[19]	September 2018
Review of Hybrid Ion Capacitors: From Aqueous to Lithium to Sodium	Ceramic Oxides & Carbon-based	[20]	July 2018
Emergent Pseudocapacitance of 2D Nanomaterials	Ceramic Oxides & Carbon-based	[21]	May 2018
Materials for supercapacitors: When Li-ion battery power is not enough	Ceramic Oxides & Carbon-based	[22]	May 2018
Energy Storage in Nanomaterials – Capacitive, Pseudocapacitive, or Battery-like?	Ceramic oxides & Carbon-based	[23]	March 2018
Overview of nanostructured metal oxides and pure nickel oxide (NiO) electrodes for supercapacitors: A review	Ceramic Oxides (Nickel)	[24]	February 2018
Recent advances of graphene-based materials for high-performance and new-concept supercapacitors	Carbon-based	[25]	January 2018
Three-Dimensional Binder-Free Nanoarchitectures for Advanced Pseudocapacitors	Ceramic oxide & Carbon-based	[26]	December 2017
Recent advances in nanostructured vanadium oxides and composites for energy conversion	Ceramic Oxide (Vanadium)	[27]	December 2017
Interlayer nanoarchitectonics of two-dimensional transition-metal dichalcogenides nanosheets for energy storage and conversion applications	Ceramic Oxides	[28]	December 2017
Tailoring pseudocapacitive materials from a mechanistic perspective	Ceramic Oxides, electrolyte & Carbon-based	[29]	December 2017
Energy efficient graphene based high performance capacitors	Carbon-based	[30]	August 2017
Redox-electrodes for selective electrochemical separations	Ceramic Oxides & Conducting Polymers	[31]	June 2017
Carbon-based supercapacitors for efficient energy storage	Carbon-based	[32]	may-17
Electrical and electrochemical properties of conducting polymers	Conducting polymers	[33]	April 2017
Pseudocapacitive materials for electrochemical capacitors: From rational synthesis to capacitance optimization	Ceramic Oxides, electrolyte & Carbon-based	[34]	January 2017
Design and preparation of electrode materials for supercapacitors with high specific capacitance	Ceramic Oxides, electrolyte & Carbon-based	[35]	2017
Vanadium Based Materials As Electrode Materials For High Performance Supercapacitors	Ceramic Oxides (Vanadium)	[36]	October 2016
Conducting Polymers for Pseudocapacitive Energy Storage	Conducting Polymers	[37]	September 2016
Polyaniline-based electrodes: recent application in supercapacitors and next generation rechargeable batteries	Conducting Polymers	[38]	August 2016

Quinone and its derivatives for energy harvesting and storage materials	Conducting Polymers	[39]	June 2016
A mini review of designed mesoporous materials for energy-storage applications: From electric double-layer capacitors to hybrid supercapacitors	Ceramic Oxides & Carbon-based	[40]	April 2016
Review on advances in porous nanostructured nickel oxides and their composite electrodes for high-performance supercapacitors	Ceramic Oxide	[8]	March 2016
Understanding performance limitation and suppression of leakage current or self-discharge in electrochemical capacitors: A review	Ceramic Oxides & Conducting Polymers	[41]	November 2015
A review of electrolyte materials and compositions for electrochemical supercapacitors	Electrolyte	[42]	November 2015
MnO₂-based nanostructures for high-performance supercapacitors	Ceramic Oxides (Manganese)	[43]	September 2015
Rare earth and transitional metal colloidal supercapacitors	Ceramic Oxides	[44]	August 2015
Nanostructured electrode materials for electrochemical capacitor applications	Ceramic Oxides	[45]	June 2015
Nanostructured Mo-based electrode materials for electrochemical energy storage	Ceramic Oxides (Molybdenum)	[46]	April 2015
Nanostructured Mn-based oxides for electrochemical energy storage and conversion	Ceramic Oxides	[47]	February 2015
Recent development in spinel cobaltites for supercapacitor application	Ceramic Oxides	[48]	January 2015
Recent progress in nickel based materials for high performance pseudocapacitor electrodes	Ceramic Oxides	[49]	December 2014
Nanowire electrodes for electrochemical energy storage devices	Ceramic Oxides & Conducting Polymers	[50]	December 2014
Microwave-assisted synthesis of metal oxide/hydroxide composite electrodes for high power supercapacitors - A review	Ceramic Oxides	[51]	October 2014
Cu-based materials as high-performance electrodes toward electrochemical energy storage	Ceramic Oxides (Copper)	[52]	February 2014
Recent advances in conjugated polymer energy storage	Conducting Polymers	[53]	February 2013
Electrospinning technology for applications in supercapacitors	Ceramic Oxides & Conducting Polymers	[54]	2013
Materials for electrochemical capacitors	Ceramic Oxides, Carbon-based, electrolyte & Conducting Polymers	[55]	November 2008
Electrochemical capacitors	Ceramic Oxides, electrolyte & Conducting Polymers	[56]	September 2002

Table 4. Theoretical capacitance calculated by the equation 11 for different MO

Metal oxide	Theoretical Capacitance (F/g)
RuO₂	1450
MnO₂	1109
Co₃O₄	2003
Fe₃O₄	416
V₂O₅	530
NiO	2583
TiO	2416
SnO₂	2560
In₂O₃	708
Bi₂O₃	418
WO₃	416
MnO_x	>1300
MoO₃	670
CuO	2425
Cu₂O	674

Table5

Table 5. Summary of PCs performances reported in recent publications

Ref	Material	Synthesis Strategies	Shaping Strategies	Morphology	Specific Capacitance	Capacitance retention
Manganese						
[6]	Mn ₃ O ₄	Hydrothermal	Pressed	Nano-capsules	750 F/g at 5 A/g	107% after 9000 cycles
[5]	Mn ₂ O ₃	Solvothermal+ calcination	Pressed	Nanobars	250 F/g at 0.2 A/g	~75% after 3000 cycles
[70]	MnO ₂	Hydrothermal	Pressed	nanowire net	775 F/g at 2 mV/s	97% after 5000cycles
[71]	Au/MnOx	Au sputtering & MnO electrodeposition		Nanocone structure	840.3 F/g at 2 A/g	96.5% after 2000 cycles
[87]	KMnO ₂	Hydrothermal	Drop-casted	--	303 F/g at 0.2 A/g	100-90% after 1000 cycles
Nickel						
[60]	Ni(OH) ₂ and NiO	Hydrothermal	Pressed	Pompon-like spheres	1028.5 F/g at 2.22 A/g	98.5% after 1000 cycles
[88]	NiWO ₄ -CoWO ₄	Co-precipitation	Pressed	Cauliflower-like	196.7 C/g at 0.5 A/g	110% after 5000 cycles
[57]	NiO	Hydrothermal + calcination	Pressed	Flowerlike	1297.3 mAh/g at 200 mA/g	--
[89]	NiO	Hydrothermal + calcination	Pressed	Hollow nanosphere	612.5 F/g at 0.5 A/g	90% after 1000 cycles
[90]	NiO	Hydrothermal + calcination	Pressed	Mesoporous Spheres	1140 F/g at 10 A/g	100% after 1000 cycles
[91]	NiO	Hydrothermal + areogel	Pressed	--	901 F/g at 0.5 A/g	93% after 3000 cycles
[92]	LiNiVO ₄	Hydrothermal + calcination	Pressed	--	456 F/g at 0.5 A/g	99.6% after 1000 cycles
[93]	NiCoO	Hydrothermal + calcination	Pressed	Microspheres	1884 F/g at 3 A/g	79.4% after 10000 cycles
[94]	NiCo ₂ O ₄	Hydrothermal + annealing + electrodeposition	Pressed	--	1080 F/g at 6 A/g	83% after 4000 cycles
[95]	NiCo ₂ (CO ₃) _{1.5} (OH) ₃ @NiCo ₂ S ₄	Hydrothermal	Pressed	Urchin-like	956.4 F/g at 4 A/g	80.1% after5000 cycles

[96]	NiO	Precipitation	Drop-casted	--	243 F/g at 2 mV/s	--
[3]	Ni(OH) ₂ /MnO ₂	Soaking	Coate	Nanorods	2937 F/g at 5 A/g	92.3% after 25000 cycles
[97]	Ni(OH) ₂	Hydrotehmal+ electrochemical deposition + CBD		Nanoflakes	325 F/cm ³	80% after 1000
[98]	NiO	Sorvothermal	Spin-coated	Nanospheres	1386 F/g at 1 A/g	78.5% after 5000 cycles
[99]	NiO	Sparking	Drop-coated	--	402.7 C/g at 1 A /g	88% after 1000 cycles
[100]	NiO	Sparking		Foam-like	920 C/g at 1 A/g	96% after 1000 cycles
[63]	Co-doped Ni(OH) ₂	LA laser-induced L	Drop-casted	Curly nanosheet	720 F/g at 6 A/g	92% after 1000 cycles
Co						
[62]	ZnCo ₂ O ₄	Hydrothermal	Pressed	Oval-like	2555.8 F/g at 2 mV/s	83.7% after 3000 cycles
[69]	Co ₃ O ₄	Laser Ablation in Liquid	Dropwise presed with gel	--	177 F/g at 1 mV/s	100% after 20000 cycles
[101]	LiCoO ₂	Solvothermal	Pressed	--	654 F/g at 2 A/g	86.9% after 4000 cycles
[65]	CoS	Hydrothermal + Anion exchange reaction		--	103 mAh/g at 2 A/g	79% after 16000 cycles
[102]	ZnCo _{1.5} (OH) _{4.5} C _{10.5} ·0.45H ₂ O	Precipitation	Deposition	Nanosheets	3946.5 F/g at 3 A/g	81% after 5000 cycles
[64]	Co ₃ O ₄ CoOH Co(OH) ₂	Electrochemical precipitation		2D hexagonal platelet	627 F/g at 5 mA/cm ²	90% after 1000 cycles
[103]	Co(OH) ₂ –Au	Electroplating			1800 F/g at 20 A/g	78% after 3000 cycles
[61]	CoNiO ₂	Solvothermal	Pressed	Microspheres	~854.9 and ~414.5 F/g at 1 and 20 A/g	100.8% after 10000 cycles
Ru						

[1 04]	RuO ₂	Theoretical calculation				
Fe						
[1 05]	np-Ag@Fe ₂ O ₃	Electrodeposition			~608 F/g at 10 A/g	84.9 % after 6000 cycles
[1 06]	MnFe ₂ O ₄	Hydrothermal	Drop-casted		282.4 F/g at 0.5 A/g	85.8 % after 2000 cycles
W						
[1 07]	WO ₃	Electrodeposition + crimping	Pressed	Flower-like	196 F/g 10 mV/s	85% after 5000 cycles
Mo						
[1 08]	Ni/MoO/VO ₂	Electrochemical deposition		Nanowires	477 mF/cm ² 1 mV/s	95% after 20000 cycles
V						
[1 09]	Na _{0.33} V ₂ O ₅	Co-precipitation	Pasted	Nanorod-like	168 F/g at 0.5 A/g	81% after 50000 in NaCl
[1 10]	TiO ₂ -V ₂ O ₅	Forming gel	Drop-casted	Mesoporous tube-like	310 F/g at 2 mV/s	94% after 1000 cycles
Sn						
[1 11]	Sn@SnO ₂	Hydrothermal + calcination	Pressed	Nanosphetres	906.8 F/g at 1mV/s	~100% after 2000 cycles
Zn						
[5 9]	ZnO-Au NC	Sol-gel	Hydrothermal		205.7 F/g at 2 A/g	--
Ce						
[1 12]	CeO ₂	Solvothermal + calcination	Coated	Brick-upon-tile	1204 F/g at 0.2 A/g	100% after 5000 cycles
Ag						
[1 13]	Au/AgO (NPAAC)	Dealloying–stripping			82 F/g at 5 A/g	94% after 10000 cycles

Table6

Table * - Summary of carbon-free PCs electrodes processed following a ceramic route ending by sintering process

Ref	Material	Synthesis and shapping process		Thermal treatment	Morphology	Specific Capacitance	Capacitance retention
[1 26]	Co ₃ O ₄ @Au@MnO ₂	Electrochemical deposition		250°C 2h 1 °C/min	Porous nanowalls	1532.4 F/g at 1 A/g	~ 100% after 5000 cycles
[1 27]	NiO	Electrodeposition		250°C 2h	3D cross-linked grid	2558 F/g at 2 A/g	--
[2]	Ni ₂ PNS/NF	Hydrothermal+ phosphorization strategy		300°C 2h 5 °C/min	--	2400 F/g at 50 mV/s	67 % 5000 cycles
[1 28]	NP c-V ₂ O ₃ /r-VO _{2-x}	Electrodeposition + template calcination		300°C	--	1856 F/g at 5 mV/s	93% after 15000 cycles
[1 29]	TiO ₂ /Ni(OH) ₂	Hydrothermal+CBD		300°C	Core-shell nanorod arrays	482 F/g at 0.5 A/g	--
[7 6]	NiO	Precipitation US	EPD	325°C 15min Ar	Flower-like	363F/g at 10A/g	79 % after 1000 cycles
[1 30]	NiO/Ni	Precipitation US + calcination		325 °C 1h Ar	Nanoplatelets	755 F/g at 2 A/g	62% after 1000 cycles
[1 31]	NiO	Precipitation US	Inkjet Printing	325 °C 1h Ar	Nanoplatelets	160 F/g at 2 A/g	100% after 1200 cycles
[1 32]	Co ₃ O ₄	Hydrothermal		350°C 1h 3°C/min	Nanorods	1591 F/g at 5 mV/s	~100% after 90 cycles
[1 33]	Co ₃ O ₄ or ZnO and NiO	Hydrothermal + Chemical bath deposition + sputtering of ZnO		350°C 1.5h Ar	Nanowires	853 F/g at 2 A/g	95.1% after 6000 cycles
[1 34]	MnO ₂ - NiO	hydrothermal		350°C 2h in Ar	Tubular arrays assembled by thin nanoflakes	0.35 F/cm ² at 8.5 mA/cm ²	97.4% after 1500 cycles
[1 35]	NiO	Hydrothermal US		250, 300, 350, or 400°C 3h Ar	Nanorod	2018 F/g at 2.27 A/g	92% after 100 cycles

[1 36]	MoO ₂	HFMOVD technique		400 °C 60min 10 ⁻² Torr	Nanorod	98 F/g at 4A/g	71% after 5000 cycles
	V ₂ O ₃ /MnO ₂	Electrodeposition + Template calcination		400 °C 2h Reductor atmosphere	Foam-like	1162 F/cm ³ at 1.56 A/cm ³	~100% after 15 000 cycles
	Co ₃ O ₄ /Cu ₂ S// Co ₃ O ₄ /Cu ₂ S	Hydrothermal + SILAR		450 °C	--	1080 mF/cm ² at 10 mV/s	98.2% after 2000 cycles
	PVP modified NiCo ₂ O ₄	Hydrothermal		450 °C in air 2 h 3 °C/min	Flower-like	0.60356 mF/cm ²	86.9 % after 500 cycles
	Nb ₂ O ₅	Solvothermal + Sol- gel	Aerogel deposition	600 °C	Different	400 F/g at 5, 10, 20 and 50 mV/s	--

Table 7. Summary of hybrid supercapacitors reported in literature classified attending to the employed carbon-based material.

Ref	Carbon-based Material	Metal Oxide	Synthesis & Layer formation	Specific Capacitance	Capacitance retention
[143]	Graphene	Mn ₃ O ₄ /graphene	Hydrothermal + Pressed	256 F/g	--
[144]	Graphene	MnNi (OH) _x /graphene	Hydrothermal + Pressed	2219 F/g at 0.73 A/g	90% after 1400 cycles
[145]	Graphene	GNS/Co ₃ O ₄	Microwave-assisted method + Pressed	243.2 F/g at 10 mV/s	95.6% after 2000 cycles
[146]	Graphene	Co ₃ O ₄ /graphene	Solvothermal + Pressed	2435 F/g at 1 A/g	112% after 4500 cycles
[147]	Graphene	Co(OH) ₂ /graphene	Hummers and hydrothermal + Pressed	92 F/g	60% after 3000-6000 cycles
[148]	Graphene	CoO/Graphene	Hydrothermal + Ceramic TT at 450°C for 2 h under Ar	980 F/g at 1 A/g	103% after 10000 cycles
[149]	Graphene O	MnO ₂ /GO (15:1)	Hummers + Sonication precipitation + Pressed	197.2 F/g	84.1% after 1000 cycles
[150]	Graphene O	MnO _x on Carbon Fibers	Electrodeposition + Reduction on substrate	1004.8 mF/cm (386.5 F/g) at 4 mA/cm	94% after 5000 cycles
[85]	Graphene O	Ni-MOFs@GO	Solvothermal + hummers + Pressed	2192.4 F/g	85.1% after 3000 cycles
[151]	Graphene O	GO/NiTAPc	Hummers + Pressed	163 F/g	70% after 1000 cycles
[152]	Graphene O	MoO ₃ /GO	Hydrothermal + Ceramic TT 600°C 3h Ar	321.8 F/cm ³ at 2 mV/s	97.6 % after 5000 cycles
[153]	rGO	CoS@rGO	Hydrothermal + Pasted	849 F/g at 1A/g	90.5% after 3000 cycles
[154]	rGO	rGO/Co ₃ O ₄	Hydrothermal + Pressed	207.2 F/g at 1A/g	--
[155]	rGO	NiPc NF-rGO	Solvothermal + drop casting	223.28 F/g at 1A/g	--
[156]	rGO	rGO-Co ₃ O ₄	Hydrothermal & Hummers + Aerogelification	136.6 mF/cm ² at a 2 mA/cm ²	~99-100% after 6000 cycles
[157]	rGO	CoO/RGO	Hydrothermal +ozonation + annealing N2	239.4 F/g at 10 A/g	93.2% after 10000 cycles
[158]	rGO	MoO ₂ -RGO	Hydrothermal + Drop casting	615 F/g	90% after 10 cycles
[159]	rGO	Au/ZnO/rGO	Hydrothermal + Pasted	875 F/g at 1 A/g	60% after 1000 cycles
[160]	rGO	NiO/RGO	Heterocoagulation + EPD + Sintering	885 F/g at 2 A/g	71% after 1000 cycles
[161]	ErGO	NiO/ERGO	Electrochemical co-deposition + Ceramic TT 300°C 2h Air	1715.5 F/g	78.8% after 2000 cycles
[162]	CNT	CNT-MnO ₂	Hydrothermal + Gelification	4.4 F/cm at 0.03 A/cm ³	~50% after 3000 cycle
[141]	CNT	CNT/MnO ₂	Hydrothermal+ EPD	415 F/g at 3 A/g	83.3% after 15000 cycles
[163]	CNT	MnO ₂ /CNT//MoO ₃ /CNT	Drop-casting + Electrodeposition	507.2 F/g at 1 mA/cm ²	83% after 5000 cycles

[164]	CNT	MWCNT + MnO ₂ and RuO ₂	Dry painting method LbL	25 F/g at 0.2 A/g	82% after 5000 cycles
[165]	CNT	Ni/Ni(OH) ₂ & CNT	Hydrothermal + Pressed	1283 F/g at 2 A/g	~100% after 2000 cycles
[166]	CNT	NiO-CNT	hydrothermal & calcined in argon at 300 C for 2 h.	328 F/g at 0.33 A/g	64.3% after 300 cycles
[167]	CNT	CNT-NiO	Chemical Vapor Deposition (CVD) + Calcination + EPD	1.26 F/cm ³ at 100 mV/s	94.2% after 10000 cycles
[86]	CNT	β-Ni(OH) ₂ NS/ NWCT	Electrochemical deposition	2185.6 F/g at 5 A/g	95% 1000 cycles
[168]	CNT	NiCoAl-LDH// ERGO CNT	Hydrothermal & Hummers + Pressed	1188 F/g at 1A/g	88-91% after 1000 cycles
[169]	CNT	CNT/MO; M = Co, Zn, Mn	Microwave-assisted (MO) CVD (CNT) after annealed at 650°C	123.9 F/g at 377 μA/cm ²	95% after 1000 cycles
[170]	CNT	NiCo ₂ O ₄ Nanowire/CNT	Hydrothermal	277.3 mF/cm ² at 0.32 mA/cm ²	89% after 5000 cycles
[171]	CNT	RuO ₂ or MnO ₂ & CNT	Electrodeposition	72 and 98 F/g	86% and 93% after 1000 cycles
[172]	CNT	SWCNTs/Fe ₂ O ₃	Chemical Vapor Deposition (CVD) + Drop-casting	183 F/g at 0.01 V/s	--
[173]	CNT	H _x MoO _{3-y}	Hydrothermal	210 F/cm ³ at 1 A/g	93.3% after 4000 cycles
[174]	CNT	MoO ₃ @CNT	Hydrothermal	100.04 F/g at 200 mA/g	90% after 600 cycles
[175]	CNT	V ₂ O ₅ /CNT	Hydrothermal + Pressed	~35 F/g	80% after 900 cycles
[176]	CNT	Mn-based	Electrodeposition + Dip-coating + Ceramic TT 600°C 2h	148 F/g 1 A/g	92% after 10000 cycles at 2 A/g
[177]	Graphyte pirolitic	Co(OH) ₂ -PG	Hydrothermal + US	642.5 F/g at 1.5 A/g	100% after 5000 cycles
[178]	Carbon nanofiber	(MCNs//NiCo ₂ O ₄)	solvothetmal + calcination	1631 F/g 1 at A/g	94.5% after 5000 cycles
[179]	Amorphous micron carbon ribbons (AMCR)	NiCo ₂ O ₄ @AMCRs	Hydrothermal + Pressed	1691 F/g at 3A/g	89 % after 10 000 cycles
[180]	Carbon nanoflakes	CoO@ f-C nanowire	Atomic Layer Deposition (ALD) + Glucose carbonization	3.4 F/cm ² 10 mA/cm ²	98.6 % after 5000 cycles
[66]	Mesoporous Carbon	RuO ₂ /carbon composite	Hydrothermal + Pressed	1733 F/g at 0.2 A/g	91% after 2500 cycles
[181]	Calcinated Mof	Fe ₃ O ₄ /carbon composite	Hydrothermal + Pressed	162 F/g at 1 A/g	83.3% after 4000 cycles
[182]	Glucose	α-Fe ₂ O ₃ @C	Hydrothermal + Pressed	288 F/g 1 A/g	72.3% after 2000 cycles
[183]	Polymer calcination	ZnO/carbon	ZnO Synthesis + Polimerization + Calcination + Pressed	145 F/g at 2 mV/s	91% after 10000 cycles
[4]	Carbon spheres	NiCl ₂ and Ni(OH) ₂	Precipitation + Electrodeposition	10286 F/g at 3 A/g	--
[184]	Calcinated Mof	Co/Ni oxide & carbon	MOF electrosynthesis + Electrodeposition + Ceramic TT 900 °C 12 h Ar	157 F/g at 1 mA /cm ²	92% after 4200 cycles

[63]	C. Substrate	Co-doped Ni(OH) ₂	LAL	720 F/g at 6 A/g	92% after 1000 cycles
[185]	C. Substrate carbon fiber paper	Co _x Ni _{1-x} (OH) ₂ /NiCo ₂ S ₄	Electrodeposition	2.7 F/cm ² at 4 mA/cm ²	96% after 2000 cycles
[186]	C. Substrate	Co ₃ O ₄	Solvothermal & calcination + Sprayed	476 F/g at 0.5 A/g	82% 2000 cycles
[187]	C. Substrate	Co-Ni	Coprecipitation + Electrodeposition	1123 F/g	78% after 2000 cycles
[119]	C. substrate	Co ₃ V ₂ O ₈	Hydrothermal (MHT)	4194 F/g at 1 A/g	85% after 10000 cycles
[123]	C. substrate	PAni-RuO ₂	Chemical oxidative polymerization + Atomic Laser Deposition ALD	710 F/g at 5 mV/s	88% after 10 000 cycles at 20 A/g
[120]	C. Substrate	Al _x Cu _y Co _z Fe ₂ O ₄	Sol-gel & calcination + Pressed	875 F/g at 5 mV/s	--
[188]	C. Substrate	MoO ₃	Sol-gel + Drop-casting	135 F/g	84% after 200 cycles
[122]	C. Substrate	VO _x /Carbon	Electrodeposition	167 F/g at 25 mV/s	--
[189]	C. substrate	Na ₂ Ti ₃ O ₇	Hydrothermal and annealing + Pasted	1.3 mWh/cm ³ and 70 mW/ cm ³	~ 80.3% after 2500 at 0.5 A/g
[190]	C. Substrate	Zn _x Co _{1-x} O	Hydrothermal on Carbon fiber paper CFP	450 F/g at 1 V/s	90.7% after 5000 cycles
[191]	C. Substrate	WO ₃ on carbon	Sol-gel + Spin-coating + Ceramic TT (300, 400, 500, 600 °C)	233.6 F/g at 2 mV/s	--
[192]	C. substrate	NiFe ₂ O ₄	Hydrothermal on template + Ceramic TT 350 °C 2h Air	697 F/g at 5mV/s	93.6 % after 10000 cycles
[193]	C. substrate	MoO ₂ and V ₂ O ₃	Hydrothermal + Sintering 700–1000 °C N ₂	--	--
[194]	C. substrate	Ag-MnO ₂	Hydrothermal + Electrodeposition + Ceramic TT 400 °C 2h Air	557 F/g at 5mV/s	98.6 % after 2000 cycles
[195]	C. substrate	Ni/NiO	Sol-gel + Electrospinning + Pressed	526 F/g at 1 A/g	80% after 1000 cycles
[196]	C. Substrate	β-La ₂ Mo ₂ O ₉	Hydrothermal + Pressed	727.2 F/g at 0.5 A/g	98.7 % after 1000 cycles
[197]	C. substrate	SrFe ₁₂ O ₁₉	Hydrothermal + Calcination + Pasted	133.9 F/g 0.4 A/g	84% after 5000 cycles
[198]	C. substrate	MnO ₂	Hydrothermal + Pressed	212 F/g	88% after 10000 cycles
[118]	C. substrate	LaMnO ₃	Solvothermal + Calcination 700 °C 4h air + Spin-casting 700 rpm	586.7 F/g and 609.8 F/g	--
[199]	C. substrate	MnO ₂ /PANI	Hydrotherma l+ Pressed	873 F/g at 0.25 A/g	95% after 5000 cycles
[200]	C. Substrate	Mn ₃ O ₄ & MnOOH	Hydrothermal + Drop-casting	170 F/g at 500 mV/s	--
[201]	C. Substrate	MnO ₂ -Carbon	Electrodeposition	8 2.8 F/cm ² at 0.05 mV/s	80% after 1000 cycles
[87]	C. Substrate	KMnO ₂	Hydrothermal + Drop-csdting	303 F/g at 0.2 A/g	100-90% after 1000 cycles
[99]	C. Substrate	NiO	Sparking + Drop-casting	402.8 C/g at 1 A/g	88% after 1000 cycles

Figure1

[Click here to download high resolution image](#)

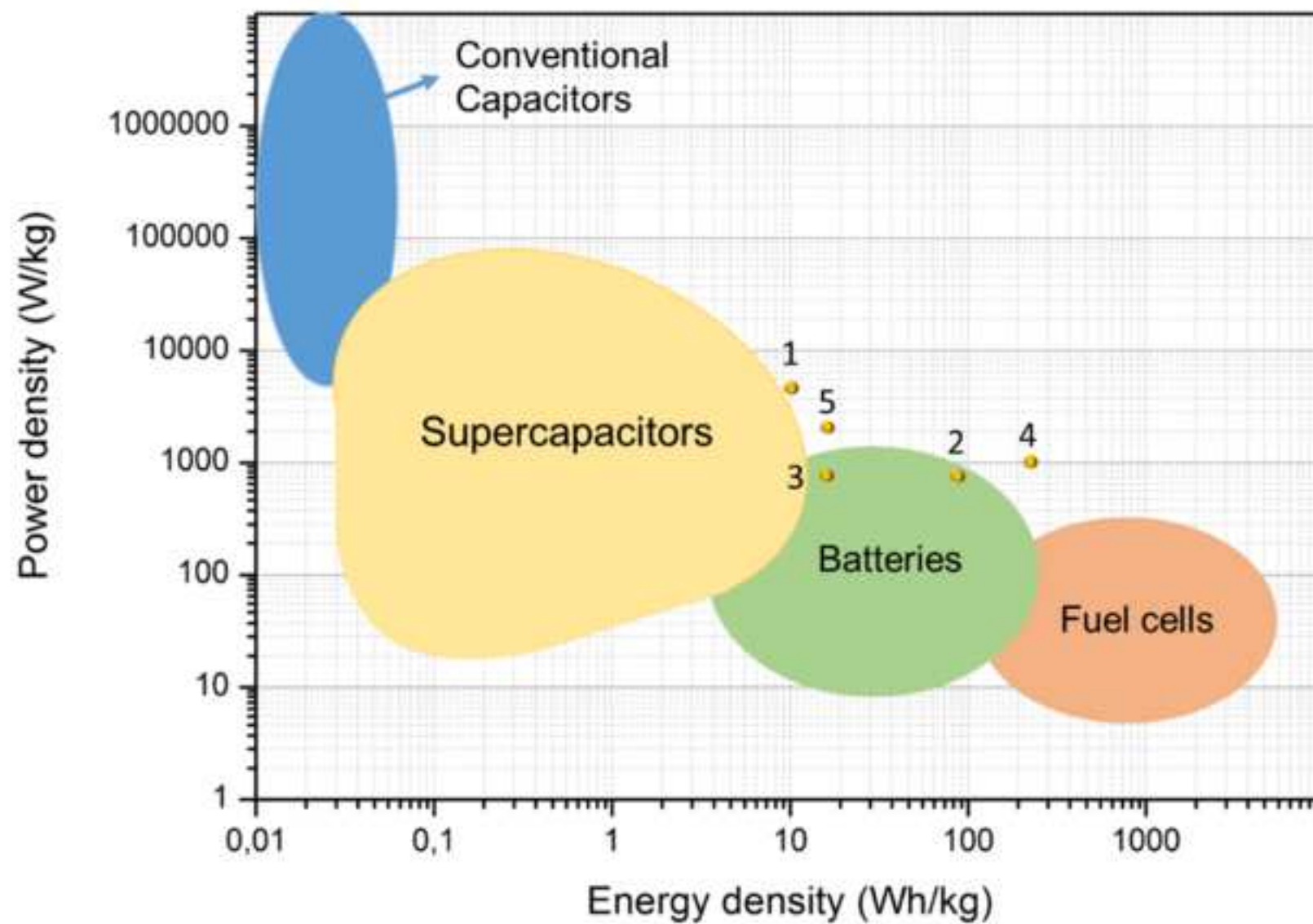


Figure2

[Click here to download high resolution image](#)

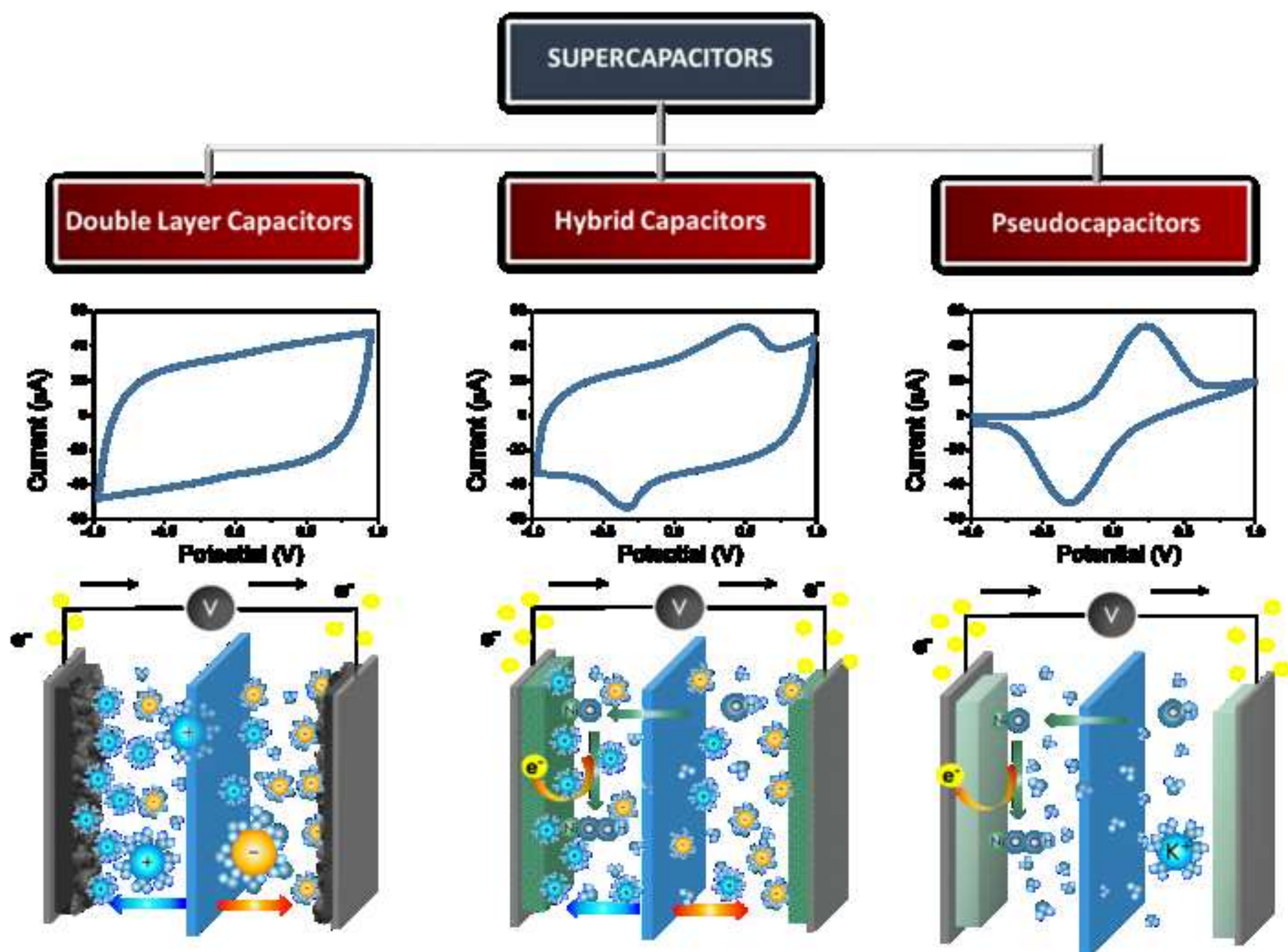


Figure3
[Click here to download high resolution image](#)

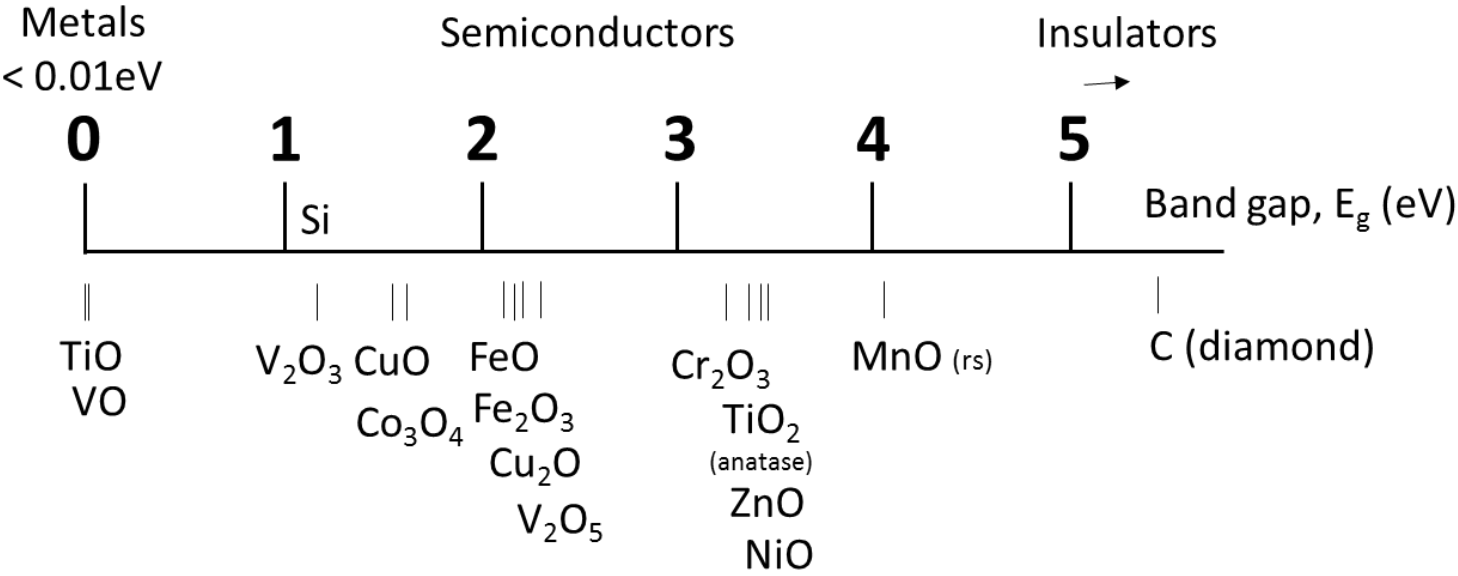


Figure4

[Click here to download high resolution image](#)

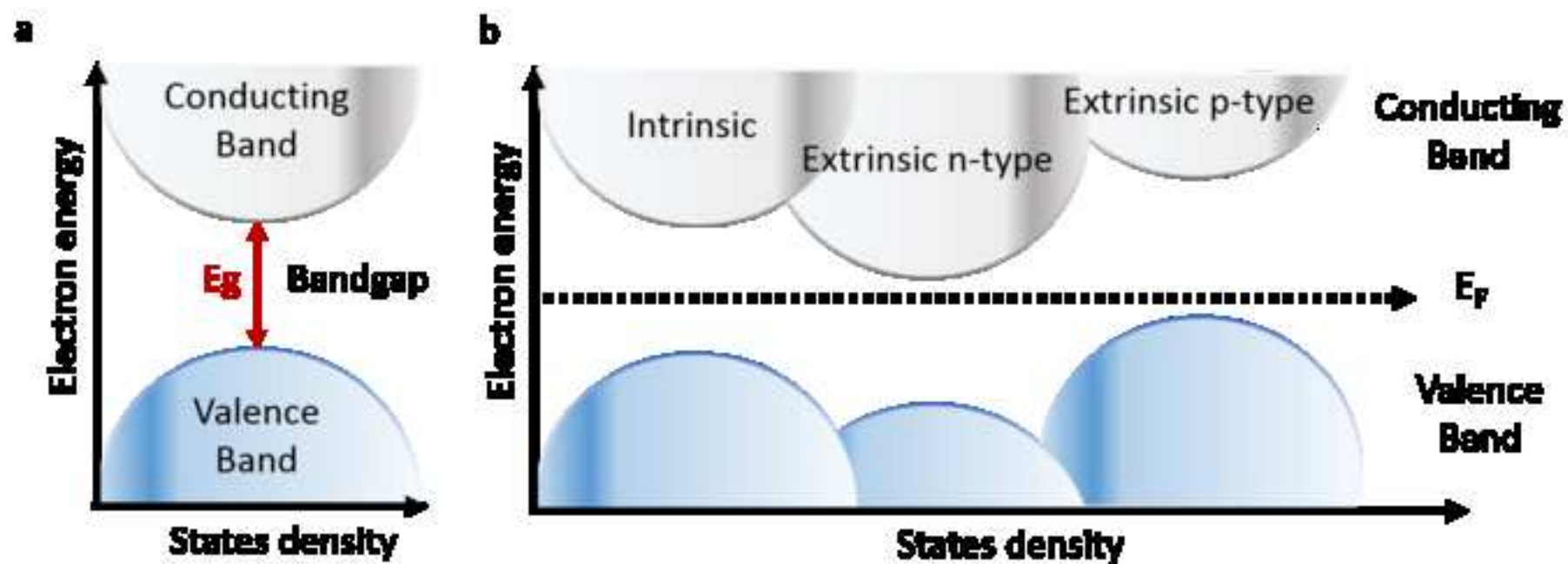


Figure5

[Click here to download high resolution image](#)

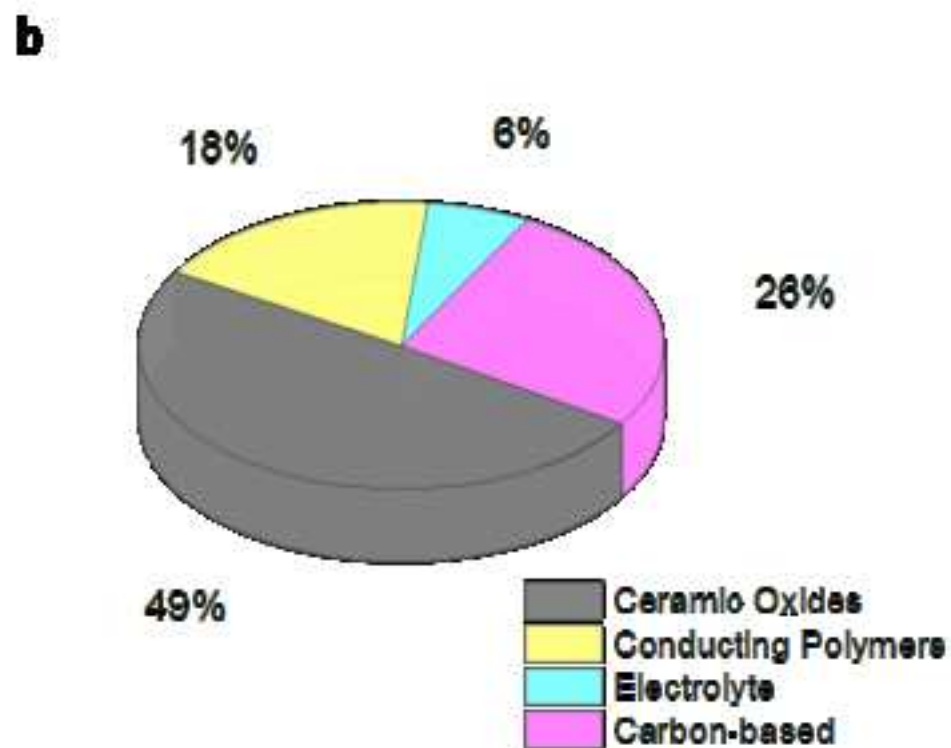
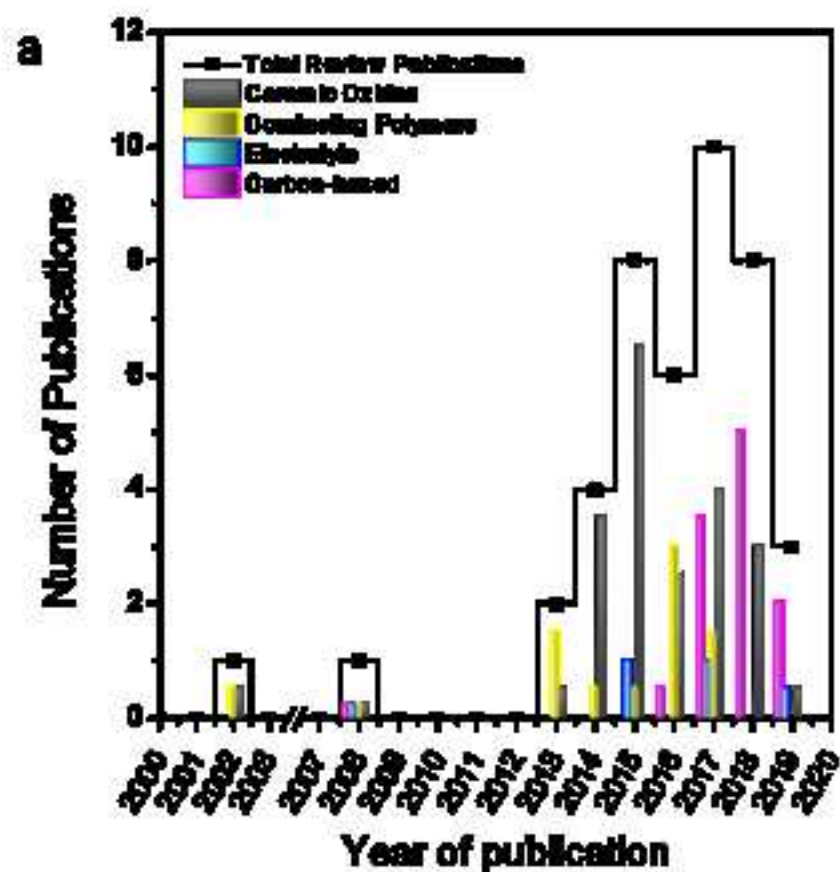


Figure6

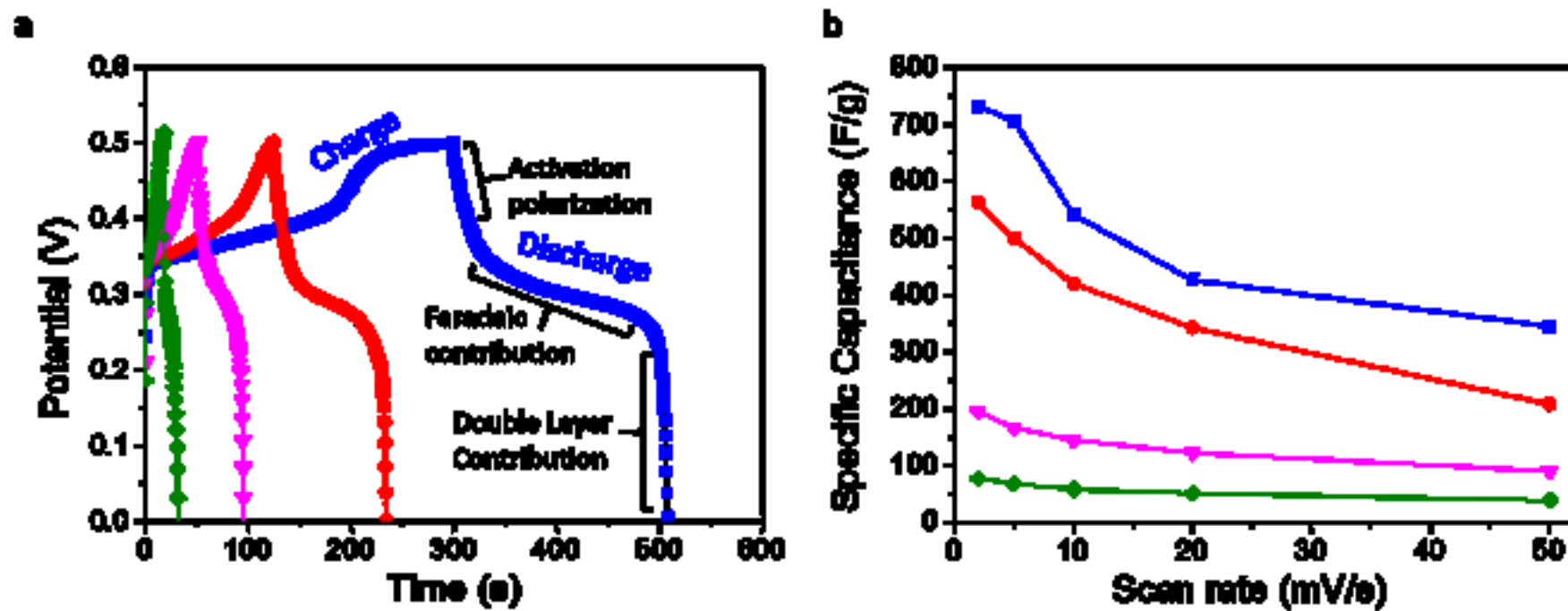
[Click here to download high resolution image](#)

Figure7

[Click here to download high resolution image](#)

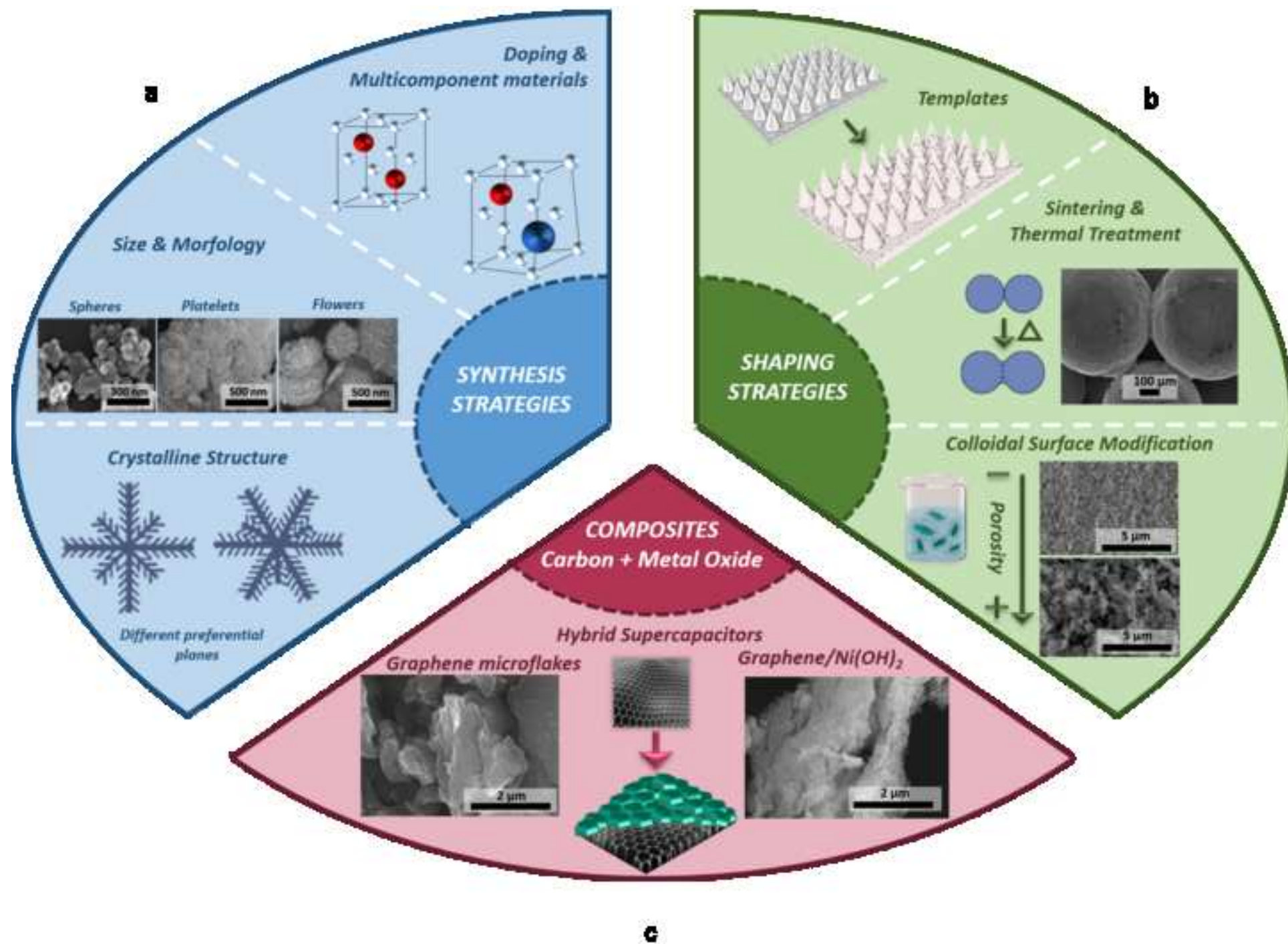


Figure8

[Click here to download high resolution image](#)

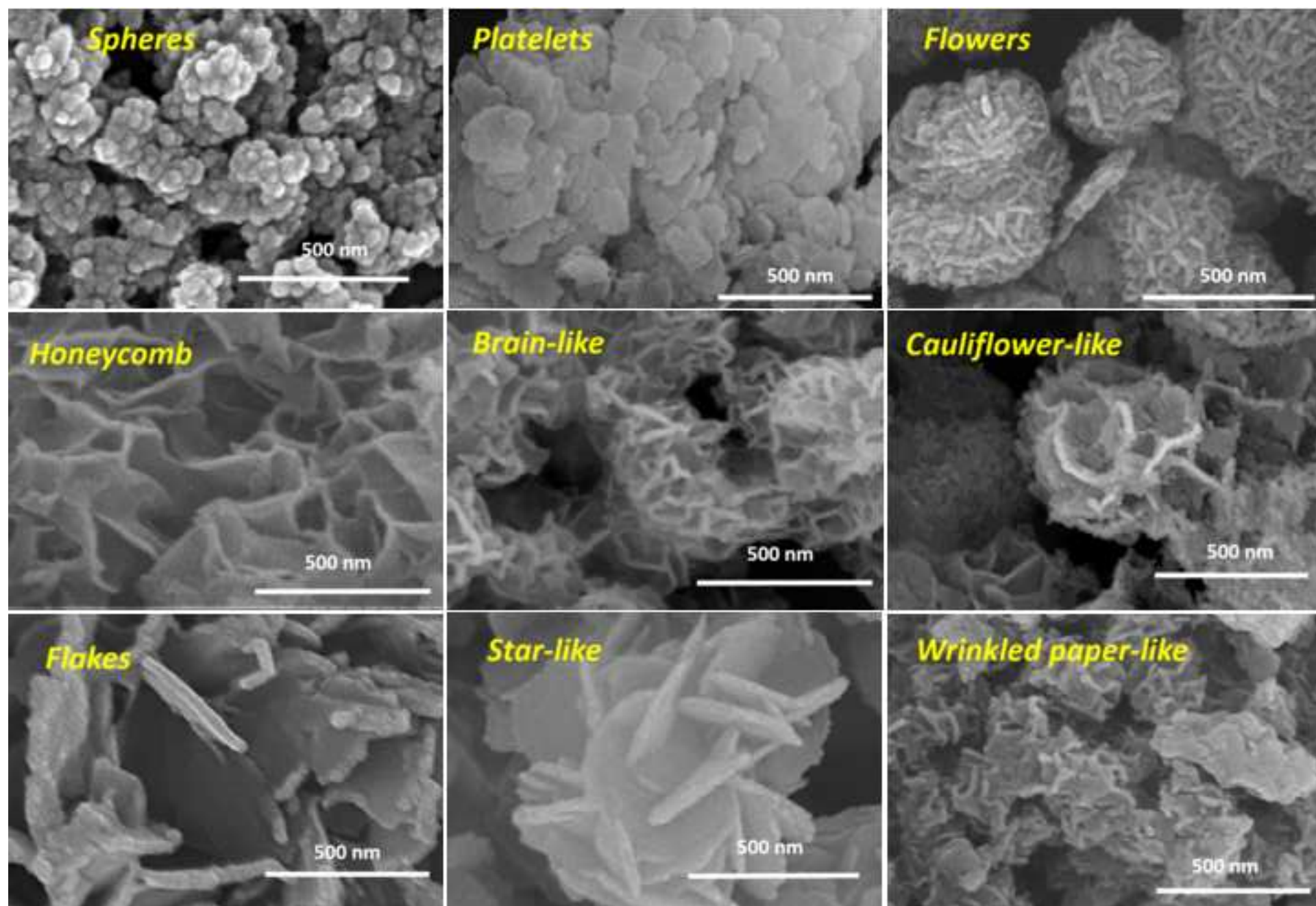


Figure9
[Click here to download high resolution image](#)

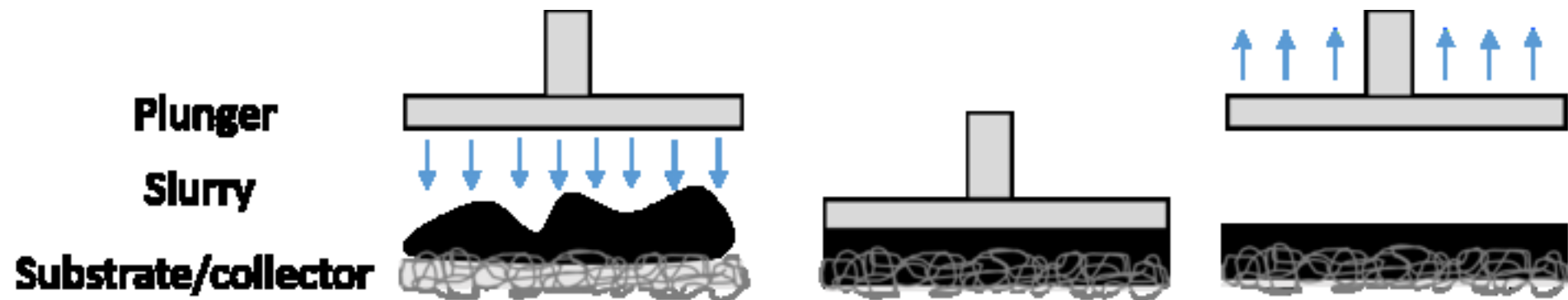
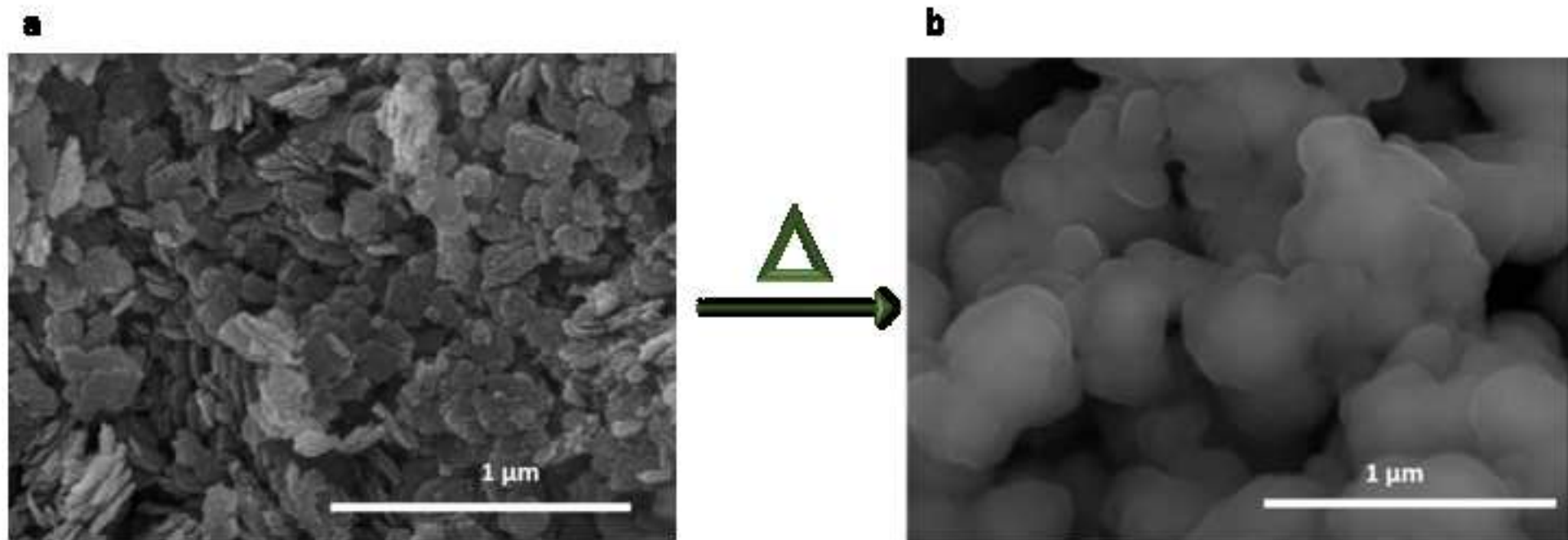
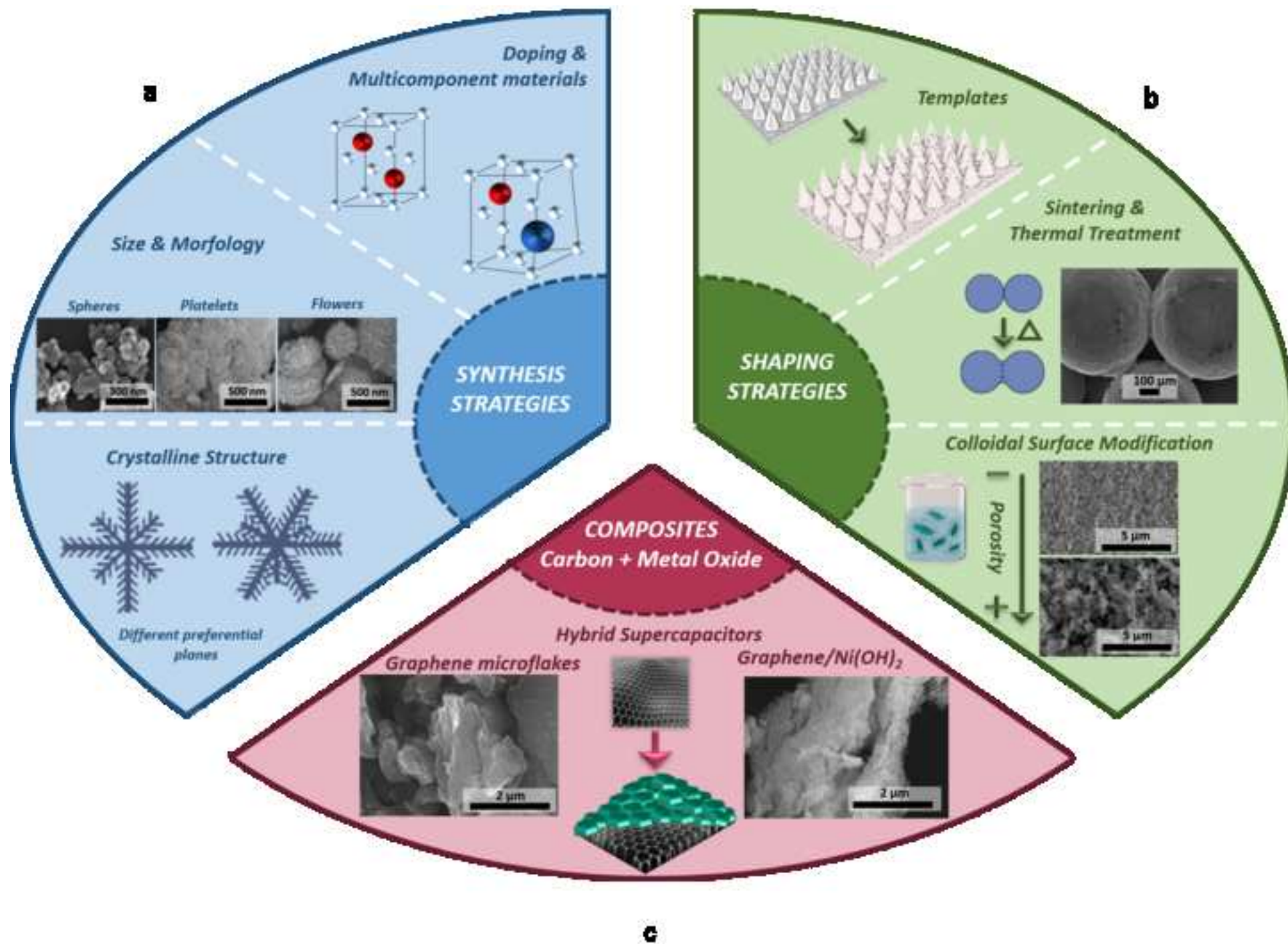


Figure10
[Click here to download high resolution image](#)





1

Figure 1. Ragone plot shows energy density vs power density grouping the most representative devices in energy storage. Random recent results of pseudocapacitors based on ceramic semiconductors (table 2)

Figure 2. Hierarchical diagram of the supercapacitors classification attending to the energy storage mechanism. Charge storage principles and examples of the typical cyclic voltammograms are also included.

Figure 3. Relation between the band gap and electronic properties of TMOs.

Figure 4. a) Semiconductor bands structures and bandgap. b) E_F position depending on the nature of TMO semiconductor.

Figure 5. a) Overview of the published reviews since 2000 by year and main topic. b) Topic distribution of all the reviews about pseudocapacitors (Scopus) from 2000.

Figure 6 a) Charge – discharge curves of different electrodes at the same current density (2 A/g). b) Rate capability obtained from the cyclic voltammograms for different electrodes at different scan rates.

Figure 7. Current strategies for the improvement of the final electrochemical features in pseudocapacitors. a) In blue, synthesis modification of particles and 0D, 1D, 2D and 3D nanostructures, changing morphology, crystallography and defining new solid solutions. b) In green, shaping films and coating of metal collectors by the nanoparticles assembling and microstructure tailoring, designing porosity (specific surface area, including endo- and exo-templates and sintering. c) In red, technologies based on in situ synthesis of composites using carbon-based materials and TMO.

Figure 8. Typical SEM images of NiO nanoparticles with different types of morphology: spheres, platelets, flowers-like, etc.

Figure 9. Scheme of the most commonly used conventional shaping method: The die pressing.

Figure 10. NiO nanoparticles before (a) and after (b) the sintering process at 325°C during 1h under Ar atmosphere.

2

J. Yus, B. Ferrari, A.J. Sanchez-Herencia, A. Caballero, J. Morales, Z. Gonzalez.

In Situ Synthesis and Electrophoretic Deposition of NiO/Ni Core-Shell Nanoparticles and Its Application as Pseudocapacitor.

Coatings **2017**, *7*, 193,

doi:10.3390/coatings7110193.

Article

In Situ Synthesis and Electrophoretic Deposition of NiO/Ni Core-Shell Nanoparticles and Its Application as Pseudocapacitor

Joaquín Yus ¹, Begoña Ferrari ¹, Antonio Javier Sanchez-Herencia ¹ , Alvaro Caballero ² , Julian Morales ² and Zoilo Gonzalez ^{1,*} 

¹ Instituto de Cerámica y Vidrio, Spanish National Research Council (CSIC) Madrid, 28049, Spain; joaquinluis.yus@icv.csic.es (J.Y.); bferrari@icv.csic.es (B.F.); ajsanchez@icv.csic.es (A.J.S.-H.)

² I.U.I Química Fina y Nanoquímica, Departamento Química Inorgánica e Ingeniería Química, Universidad de Córdoba, Córdoba, 14014, Spain; alvaro.caballero@uco.es (A.C.); iq1mopaj@uco.es (J.M.)

* Correspondence: zgonzalez@icv.csic.es; Tel.: +34-917-355-840

Academic Editor: Bill Clyne

Received: 29 September 2017; Accepted: 4 November 2017; Published: 8 November 2017

Abstract: A simple, low cost and transferable colloidal processing method and the subsequent heat treatment has been optimized to prepare binder-free electrodes for their application in supercapacitors. NiO/Ni core-shell hybrid nanostructures have been synthesized by heterogeneous precipitation of metallic Ni nanospheres onto NiO nanoplatelets as seed surfaces. The electrophoretic deposition (EPD) has been used to shape the electroactive material onto 3D substrates such as Ni foams. The method has allowed us to control the growth and the homogeneity of the NiO/Ni coatings. The presence of metallic Nickel in the microstructure and the optimization of the thermal treatment have brought several improvements in the electrochemical response due to the connectivity of the final microstructure. The highest specific capacitance value has been obtained using a thermal treatment of 325 °C during 1 h in Argon. At this temperature, necks formed among ceramic-metallic nanoparticles preserve the structural integrity of the microstructure avoiding the employment of binders to enhance their connectivity. Thus, a compromise between porosity and connectivity should be established to improve electrochemical performance.

Keywords: pseudocapacitor; EPD; NiO/Ni; core-shell; heterogeneous synthesis and binder free

1. Introduction

Recent studies on energy storage devices are giving rise to constant progresses in nanoscience. New features of hybrid/electric vehicles and the intermittent renewable energies production need storage devices, such as supercapacitors. For these applications, the electrodes should be able to provide high power density, excellent reversibility and long cycle life. Typically, supercapacitors exhibit 20–200 times larger capacitance per unit of mass or volume than conventional capacitors. Depending on the charge-storage mechanism there are electrical double-layer capacitors (EDLC), mainly based on carbon materials [1,2] which store the energy through ions accumulation at the electrode/electrolyte interface. In addition, pseudocapacitors, relayed on transition-metal oxides and conducting polymers, which store the energy through faradic reactions on the electrode surface in the appropriate potential window. Conducting polymers are easy to process due to its mechanical flexibility. However, polymers are easily degradable due to their bad stability, which results in a low cyclability. In contrast, transition metal oxides are robust and present higher capacitances and better cyclability. Because of these reasons, metal oxides have been proposed as an interesting alternative.

Among transition metals, the ruthenium oxides have showed the best capacitance response. It offers a very good cyclability during thousands of cycles, due to its high thermal and chemical stability, but the viability of those electrodes is limited because of its elevated cost [3]. The high price of this oxide have boosted the quest of new ones cheaper with high performances, for instance Cobalt, Manganese or Nickel oxides [4–7]. In particular, nickel oxide has received great attention due to its high theoretical specific capacitance of 3750 F/g [8], multiple reversible electrochemical reactions, ready availability and low cost [9].

There are many studies in the bibliography about synthesis, processing and characterization of pseudocapacitors based on Ni. Most authors usually carry out the processing of the electroactive material with subsequent mixing with binders for slurry formation and pressing onto metallic substrates. However, the consolidation of the electroactive material is not considered. The research works developed by Feng et al. [10], Zhang et al. [11] and Li et al. [12] are mainly focused on the synthesis of nanostructures, and they do not consider the influence of the processing parameters in the final electrochemical behavior.

Several studies have been developed in order to connect the effects of morphology, porosity and specific surface area with the electrochemical behavior. The main problem of these ceramic semiconductors (metallic oxides) is their low electrical connectivity between particles. Metal oxides are ceramic compounds, which microstructure should be consolidated by a sintering process with a specific heat treatment after shaping. This entails the obtaining of robust electrodes with well-connected particles, avoiding the use of well-known binders and/or additive like carbon black (CB), acetylene black, PVDF, PTFE used to increase the connectivity. In this way there are many published reports focusing on the improvement of the performance of the metal oxide electrodes in pseudocapacitors. In the case of NiO the use of different method to prepare electrodes for supercapacitor has been summarized previously in recent works [6,13]. Others authors prefer the application of sophisticated processing routes, which sometimes includes shaping and sintering simultaneously. For instance Kurra et al. employ CBD for the fabrication of micropseudocapacitors based on Ni(OH)₂ [14]. Liu et al. use laser ablation in liquid (LAL) [15] and Jiang et al. work with chemical vapor deposition (CVD) [16].

From the final eighties, advances in colloidal chemistry knowledge have provided the necessary milestones for successfully applied colloidal processing methods in the reliable manufacture of nanostructures with final specific properties. The colloidal techniques involve the manipulation and control of the interparticle forces in the suspensions of powders in liquid media. This is a key step to break down weak agglomerates, stabilize and facilitate powders mixing, removing heterogeneities and defects in the shaped material which avoid the degradation of relevant properties. Moreover, it is critical to fit processing additives to modify suspensions properties apart from dispersion, such as the viscosity, flux, etc., adapting their rheological behavior to the forming technique [17,18], and also they are relevant to control the particles assembly [19].

In comparison with other processing methods like paste/press method, slurry method and vacuum filtration method, EPD could be considered as an alternative which offers several advantages. This technique involves a non-vacuum method, room-temperature processing, short processing time, low cost, scalable to the industry, additive free and suitability for mass production. Furthermore, it also offers the control of the deposited mass, specifically the thickness of the films can be simply controlled by the concentration of the suspension, applied potential or deposition time. In relation to the engineering viability study, EPD processing is the most reasonable option to use to shape pseudocapacitor electrodes. Many examples of this method has already been studied in previous works [6,10,20–23] with the purpose of modify the surface of the final coating.

Therefore, substantial improvement in conductivity of NiO is needed for supercapacitor electrode materials. It is also well known that an increase in electrical conductivity of NiO can be achieved through introducing metal [23] or nonmetal impurities [10,11,24] into the oxide, which can generate donor or acceptor states in the bandgap and thereby increasing the concentration of charge carriers [25].

Among all possibilities, NiO/Ni nanocomposites are a good candidate for pseudocapacitor electrodes due to its outstanding properties.

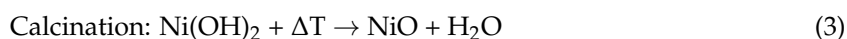
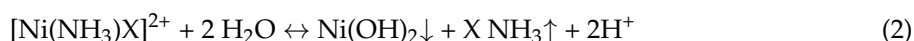
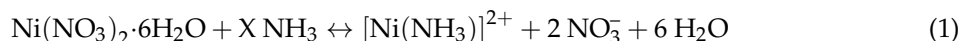
These semiconductor/metal hybrid nanostructures have been fabricated by different techniques. In one of our previous work we prepared core-shell nanostructures made on metallic nanoparticles covering the oxide nanoplatelets following an heterocoagulation process [21]. Wen et al. have been developed an eruption combustion synthesis enhanced properties for dye-absorption and Li-storage [26]. Song et al. made Ni-NiO composites by a chemical precipitation route of NiO after a further treated in pure hydrogen, in order to use it as catalyst [27]. In addition, finally, Lu et al. modified a polyol process to obtain Ni nanoparticles with an annealing process at low temperature (250 °C), obtaining monolithic NiO/Ni-Pt nanoporous composite electrodes which shows a specific capacitance of 900 F/g [28]. Anyone of these work consider the sintering of the semiconductor structure.

The novelty of this work is the direct one-pot processing of hybrid NiO/Ni core-shell nanostructures, where Ni has been precipitated by reduction onto the stabilized NiO nanoplatelets in a Ni precursor solution. As-synthesized NiO/Ni hybrid nanostructures were shaped by EPD for coating 3D substrates, such as Ni foams, to increase the exposed surface of the electroactive material and favour the contact with the liquid electrolyte in pseudocapacitors electrodes. Both strategies, the inclusion of a non-precious metal, such as Ni, and the consolidation of the semiconductor nanostructure, by a thermal treatment at low temperature (<500 °C), have been studied to improve the electrochemical response of the fabricated electrodes.

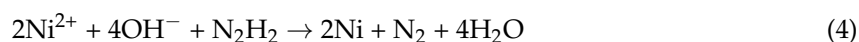
2. Materials and Methods

2.1. Synthesis of NiO Platelet Seeds and Metallic Ni (NPs)

On the one hand, the synthesis and the corresponding characterization of NiO nanoplatelets have been described previously elsewhere [13]. The procedure consisted on a chemical precipitation of the Ni(OH)₂ at room temperature using a high intensity ultrasonic horn (45 W/cm², 24 kHz, titanium T13 tip, Sonopuls HD 2200, Bandelin Electronic, Berlin, Germany) and with a subsequent calcination of the hydroxide powders into the oxide (NiO). The equation reactions of this synthesis are described below:



On the other hand, Ni NPs have been synthesized by the reduction of a nickel precursor (Ni(NO₃)₂·6H₂O) adding a mixture of monohydrated hydrazine/KOH following Equation (4):



This synthesis has already been described previously by Dios et al., using Ti(C,N) particles as seed [29].

2.2. Preparation of NiO/Ni Core/shell Nanoparticles

This synthesis of NiO/Ni nanostructures consist in a “one pot” reduction reaction by using Nickel Nitrate Hexahydrate (Ni(NO₃)₂·6H₂O, 99.9% purity, Panreac, Madrid, Spain) and hydrazine monohydrate (N₂H₄·H₂O, 65% purity, Sigma-Aldrich, Madrid, Spain) as a reductor agent. The synthesis took place in the same media where NiO nanoplatelets were previously dispersed in a concentration of 3.6 g/L, under the action of an ultrasonic horn (Ti horn, 24 kHz, 100 W/cm², UP 400 s, Dr. Hielscher, Teltow, Germany).

On the one hand, the NiO aqueous suspension was prepared using a 0.1M solution of Ni precursor as solvent (suspension A). In this way, a 0.5 NiO/Ni molar ratio was formulated in the suspension, considering a 100% synthesis reaction yield. Based on previous results [21], this NiO/Ni ratio will allow the completely covering of NiO platelets by Ni nanoparticles. On the other hand, one mixture 1 M in Potassium Hydroxide (KOH, Panreac, Madrid, Spain) and 3.9 M in monohydrate Hydrazine was prepared using deionized water (solution B). Then, solution B was poured into solution A while ultrasounds (US) were applied. The temperature was controlled through recirculation from a cryothermal bath at 50 °C. When the reaction is complete, the synthesis products were washed thoroughly three times with deionized water at pH 10 (adjusted by using tetramethyl ammonium hydroxide (TMAH), Sigma-Aldrich, Madrid, Spain) to remove residues. The molar ratio of the reactants was $[\text{Ni}^{+2}]:[\text{KOH}]:[\text{N}_2\text{H}_4]$, 1:10:39. This ratio was optimized in a previous work by Miguel et al. [21].

The identification of the crystal phases of the synthesized powders was carried out by D8 Advance Bruker X-ray diffractometer with Cu K α radiation ($\lambda = 1.5418 \text{ \AA}$) at 40 kV and 30 mA and $2\theta = 10\text{--}70^\circ$, Bruker, Bremen, Germany. The N₂ adsorption/desorption isotherms and BET specific surface area (SSA) of the NiO/Ni particles were carried out with a Micromeritics ASAP 2020 (Micromeritics Instrument Corp., Atlanta, GA, USA). In addition, the nanoparticles morphologies were observed with a Hitachi S-4700, Hitachi High-Technologies, Tokyo, Japan, Field emission scanning electron microscope (FESEM).

The surface charge of NiO/Ni nanoplatelets was evaluated in terms of zeta potential. A Zetasizer Nano ZS (Malvern Instruments Ltd., Malvern, UK) was used in order to determine zeta potential of all particles using laser Doppler velocimetry. Suspensions used for determination were prepared with concentrations of 0.1 g/L using 10^{-2} M KCl (Panreac) as solvent and inert electrolyte, to maintain the ionic strength of the medium. The pH adjustments of the suspensions were carried out by addition of small aliquots of 0.1 M HNO₃ (Panreac) or TMAH (Merck, Darmstadt, Germany) and controlled with a pH probe (Metrohm AG, Herisau, Switzerland). Subsequently, homogenization was achieved by sonication, using a UP400S Ultrasonic probe (Hielscher, Teltow, Germany) for 30 s.

After the synthesis, the remaining chemicals were eliminated by centrifugation and the resulting powder was washed several times with distilled water at pH 10 (adjusted with TMAH). The cleaned precipitate, still wet, was re-diluted in a desired amount of water at pH 11 where the polyelectrolytes are sequentially added in subsequent steps. The polyelectrolyte used for the modification of nanoplatelets surfaces was branched Polyethylenimine (PEI, M_w 25,000, Sigma Aldrich, Madrid, Spain). It confers a positive charge to the NiO/Ni particles which allows the use of cathodic deposition. To evaluate the pH of the work, zeta potential measurements were carried out at different values (from acid to basic). At this pH, the maximum amount of adsorbed additive was determined and then the surface charge of particles covered by PEI has been studied with the pH evolution.

To prepare the suspension for EPD the powder was re-dispersed in water and stabilized adding the appropriate amount of PEI (2.5 wt %) at pH 11 and then the aqueous suspension was diluted again in ethanol up to achieve a final ratio of 19:1 Ethanol:DI water with a solid content of 1 g/L.

The NiO/Ni core-shell particles (modified with 2.5 wt % of PEI) were deposited onto Ni foils of 25 mm \times 15 mm \times 0.5 mm for the study of the EPD kinetics, and onto Ni foams of 15 mm \times 10 mm \times 0.6 mm (SSA of 300 m²/g and 0.45 g/cm³ of density) and for the preparation of the supercapacitor electrodes. The counter electrode was a platinum foil separated from the work electrode by a distance of 20 mm in a volume of 30 mL of suspension in the electrophoretic cell. Also, previous to the deposition, foams and foils substrates were washed following an industrial cleaning protocol. The experimental EPD kinetics curves were determined under galvanostatic conditions using a high voltage power source (2611 System SourceMeter, Keithley Instruments Inc., Cleveland, OH, USA), applying current densities of 13.3, 26.6, 66.7 and 133.3 $\mu\text{A}/\text{cm}^2$ at deposition times from 0 to 5400 s. In addition, the foams were coated under potentiostatic conditions applying a voltage closed to 200 V at times from 10 s in order to achieve the desired amount of deposition. According to our previous experience, 1 mg coating was enough to completely cover the surface of the foam.

The most general equation formulated up today for the EPD kinetics was used to determine the theoretical deposition rate:

$$m = m_0(1 - e^{-\frac{t}{\tau}}) \quad (5)$$

where, m (g), is the deposition mass, m_0 (g), is the initial amount of powder in suspension and τ (s) is the characteristic time, calculated by:

$$\tau = \frac{V}{fSE\mu_e} \quad (6)$$

where, V (cm³), is the volume of suspension, S (cm²), is the conducting area, E (V/cm), is the applied electric field, C , (m²/V·s), is the electrophoretic mobility of the nanoparticles, and f ($0 < f < 1$), is the sticking factor. The sticking factor represents the percentage of depositing particles among the arriving particles to the work electrode by electrophoresis.

After the deposition, the coated substrates were sintered in Argon atmosphere, using the three different heating treatments (changing the dwell time and temperature) shown in Figure 1, with heating and cooling rates of 10 °C/min, resulting in consolidated NiO/Ni films.

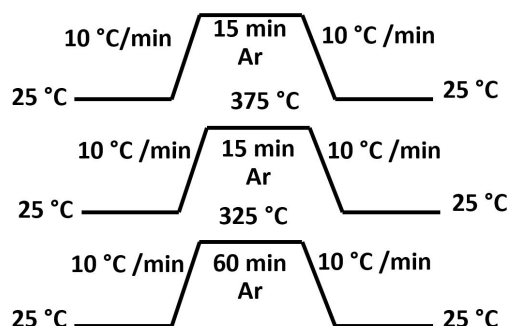


Figure 1. Diagram of different thermal treatments employed for the optimization process.

The film microstructure was examined by field emission scanning electron microscopy (FESEM) in an S-4700 microscope (Hitachi High-Technologies, Tokyo, Japan).

2.3. Electrochemical Tests

The capacitive performance of the electrodes was tested with Potenciostat/Galvanostat Autolab (PGSTAT204, Metrohm Autolab B.V., Utrecht, The Netherlands). For the Cyclic voltammetry (CV) and galvanostatic charge/discharge measurements, ten sequential cycles were programmed at a scan rate of 10 mV/s in a potential window of 0.0–0.5 V. A three-electrode configuration consisting of Ni/NiO composite as working electrode, Ag/AgCl as reference electrode and a Pt foil as counter electrode was used. The employed electrolyte was a 1 M KOH aqueous solution. The specific capacitance was determined from the charge value Q , proportional to the integral of the CV curve. Q represents the difference between the area under the charge curve and the area under the discharge curve for the upper and lower limits of the potential window. Thus, the specific capacitance was obtained from Equations (7)–(9):

$$Q = \int I \cdot dt; t = \frac{V}{v} \quad (7)$$

$$Q = \frac{1}{v} \int IdV \quad (8)$$

$$C = \frac{Q}{m \cdot \Delta V}; C = \frac{\int I \cdot dV}{v \cdot m \cdot A \cdot V} \quad (9)$$

where, I is the current (A), t , the time (s), V , the voltage (V), v , the scan rate (V/s), C , the specific capacitance (F/g), m , the mass (g) and Q , the charge/discharge value (C).

The charging/discharging measurement was carried out through chronopotentiometry analysis (CP) at a scan rate of 2 A/g using a multichannel potentiostat–galvanostat system (Arbin BT2000, Arbin Instruments, College Station, TX, USA). From CP measurements, the specific capacitance value was calculated according to Equation (10):

$$C = \frac{I \cdot \Delta t}{m \cdot \Delta V} \quad (10)$$

where C (F/g) is the specific capacitance, I (A) is the discharge current, Δt (s) is the charging/discharging time, ΔV (V) is the voltage window for discharge, and m (g) is the mass of the active NiO/Ni material in the electrode.

3. Results and Discussion

The characterization of the NiO seeds has been described previously elsewhere [13,23]. On the other hand, the NiO/Ni core-shell nanostructures were synthesized by inducing heteroprecipitation of Ni onto the NiO nanoplatelets suspension by reduction of the $\text{Ni}(\text{NO}_3)_2 \cdot 6\text{H}_2\text{O}$ with hydrazine in basic medium under US and temperature control (50 °C) during 5 min. Figure 2a shows the overall size of NiO/Ni core-shell nanoparticles with a length diameter ranging 200–300 nm and a thickness around 30 nm. It is important to notice that the NiO nanoplatelets, which acts as core, retains their initial shape and size, while they supports the metallic Ni nanospheres with diameters of 15–30 nm (similar to the scheme of Figure 2b).

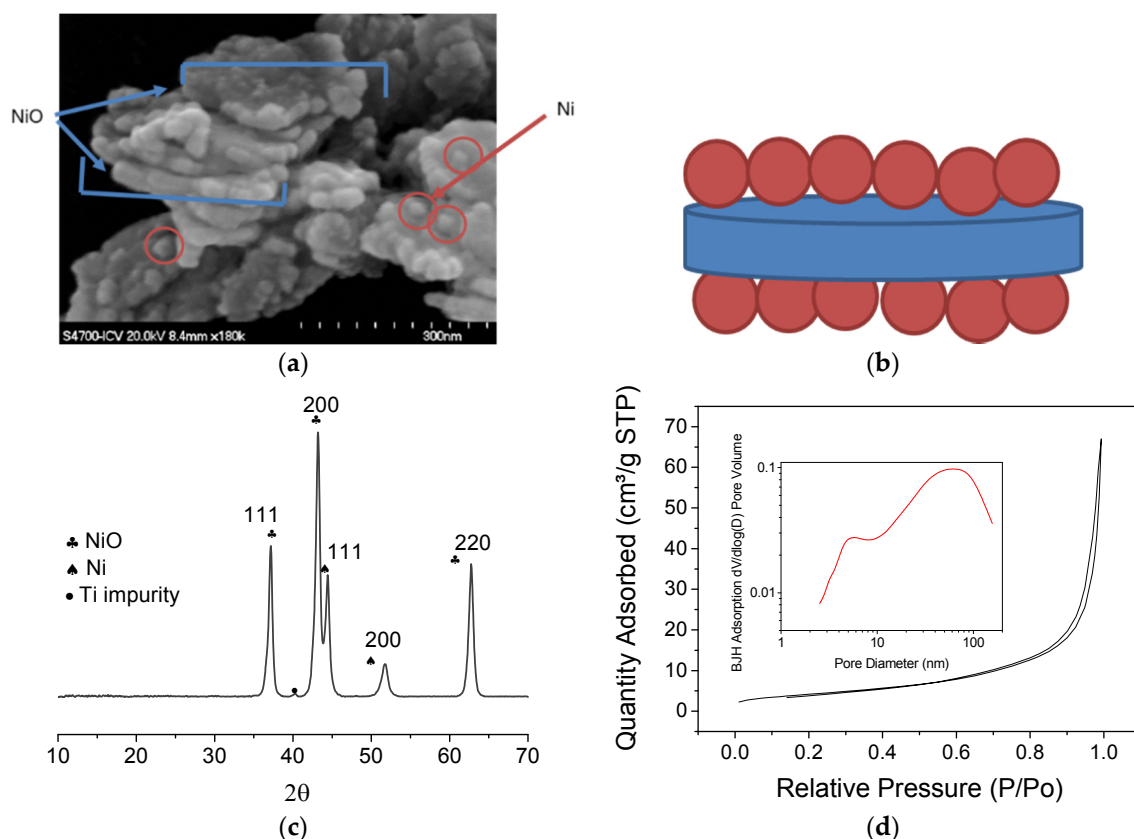


Figure 2. (a) FESEM images of the NiO-Ni powders; (b) scheme of the arrangement of NiO-Ni core-shell nanoparticles; (c) XRD patterns of the NiO-Ni powders after the synthesis process; and (d) N₂ gas adsorption-desorption isotherms and pore size distribution of as-prepared NiO-Ni nanostructure.

Additionally, the XRD analysis of Figure 2c confirmed the presence of the two crystallographic phases. On one side, the NiO peaks (200, 111 and 220) with a face-centered cubic lattice (Space group: Fm3m) with a unit cell dimension of 4.185 Å and a mean crystallite size of 28 nm. In addition, the metallic Ni peaks around 45° and 52.4° (111 and 200 respectively) according to the index card JCPDS No. 04-0850 and a face-centered cubic space group (Fm3m) with a unit cell dimension of 3.53 Å and a crystallite size of 14.5 nm.

Also, the N₂ adsorption/desorption isotherms and the corresponding pore size distribution are given in Figure 2d. The curve exhibits the IV isotherms with an H3-type hysteresis loop ($P/P_0 > 0.4$), indicative of the presence of mesopores. The specific surface area value of NiO/Ni was 16 m²/g. More than five times shorter than NiO seeds (BET SSA = 83.7 m²/g). In addition, the resultant average pore size and pore volume obtained was 21.42 nm and 0.104 cm³/g respectively. The results suggest that the presence of metallic Ni onto the surfaces of NiO nanoplatelets decreases their pore size and their specific surface area. However, the final capacitance of the NiO/Ni coatings should be discussed also considering sharing of the electronic cloud when the metallic Ni is incrustated, since it could provide efficient electronic transport pathways during the charge-discharge process, which could benefit for the final electrochemical performance.

3.1. EPD Deposition

The manipulation of the nanoparticles modified in aqueous suspension was carried out at room conditions following the one-pot approach, and thus avoiding separation and/or drying of the nanoparticles before the coating process to impede their agglomeration.

In the free-PEI curve (Figure 3a), two zones of maximum stability are displayed far from the isoelectric point located at pH 10.5. At acid pH (2–3), zeta potential is closed to +30 mV. Between the pH range 11–12 the NiO/Ni zeta potential is negative and the adsorption of the cationic polyelectrolyte on the surface of the core-shell should be promoted. Because of this the adsorption of PEI was determined at pH 11.

Consequently, the exactly concentration of polyelectrolyte (PEI) required to fully cover the surface of the nanoplatelets was determined. In Figure 3b the zeta potential trend shows that as the polyelectrolyte addition increases, its adsorption reverses the surface charge up to achieve a maximum value which is indicative of the surface saturation. It is evident that a low amount of the PEI (2.5 wt %) is needed to completely revers the surface charge of the NiO/Ni nanoplatelets.

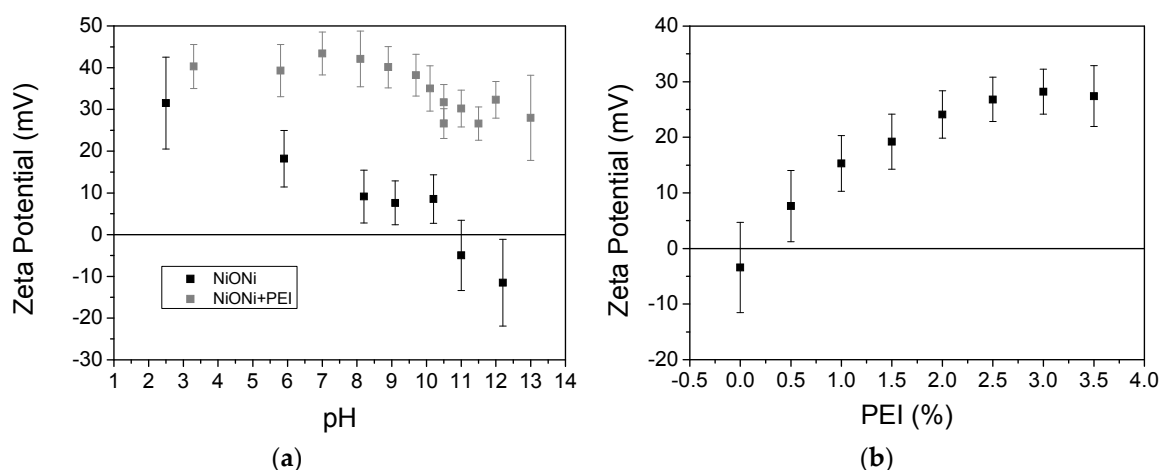


Figure 3. (a) Zeta potential vs pH curves for NiO-Ni nude nanoparticles and the stabilized with PEI; and (b) Zeta Potential of NiO-Ni nanoparticles as a function of the amount of added polyelectrolyte.

After PEI addition at pH 11, the variation of the zeta potential as a function of pH was measured again. Global charge balance at the particle surfaces was completely modified appearing positive sites in all pH range. From zeta potential determination, cathodic deposition will be favored in EPD through a stable suspension by means of an electro-steric mechanism.

After the dispersion and stabilization of the NiO/Ni powder in the suspension, the EPD kinetics was determined under galvanostatic conditions applying the current densities mentioned in the experimental section. When the applied current density value was higher than $26.6 \mu\text{A}/\text{cm}^2$, the deposition of particles onto foils did not take place due to the electrode polarization. The absence of other ions/particles in suspension (which indicates a low carrier concentration) and the low dielectric constant of the solvent (low resistance) resulted in a low conductivity ($<1 \mu\text{S}/\text{cm}$). Figure 4 compares the theoretical (lines) and experimental (full symbols) kinetics curves as a result of the EPD processes only at 13.3 and $26.6 \mu\text{A}/\text{cm}^2$. The theoretical curves were calculated following Equations (5) and (6) and considering a sticking factor of 1 and starting conditions summarized in Table 1. Deposited mass was normalized (in percentages) to the initial mass of powder in the suspension. No significant differences were observed between the kinetics of deposition under tested conditions. However, a large difference can be appreciated between theoretical and experimental data which could be attributable to the degradation of the suspension during the deposition, in terms of electrophoretic mobility, conductivity and solid concentration [30].

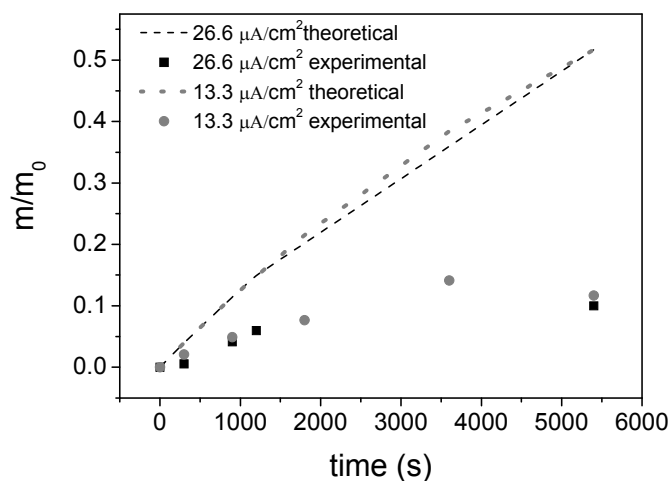


Figure 4. Experimental approximation of the EPD kinetics for NiO-Ni suspensions deposited on a Ni foil substrate.

Table 1. EPD parameters.

Volume of Suspension, V	Electrophoretic Mobility, μ_e	Deposition Surface, S	Electric Field, E	Sticking Factor, f	Characteristic Time, T
30 mL	$0.7186 \times 10^{-4} \text{ cm}^2 \text{ V}^{-1} \text{ s}^{-1}$	3.75 cm^2	$15 \text{ V}/\text{cm}$	1	7422 s

Based on the studied kinetics and our previous experience, EPD conditions were chosen to obtain coatings of 1 mg. Figure 5 shows the micrographs at different magnifications of Ni foam fully coated by NiO/Ni core-shell particles after a thermal treatment of 325°C and 60 min. The optimization of the work conditions for the suspension deposition resulted in a thin deposition yield. An open and interconnected porosity $100\text{--}500 \mu\text{m}$ is given by the foam substrate and a homogeneous and continuous film of the core-shell particles completely coats the complete surface of the foam. NiO/Ni particles ordering can be explained throughout the movement governed by the electro-hydrodynamics forces, when approach to the substrate surface and the binder role of PEI, which also reduces its ionized state forcing particles coagulation [31,32].

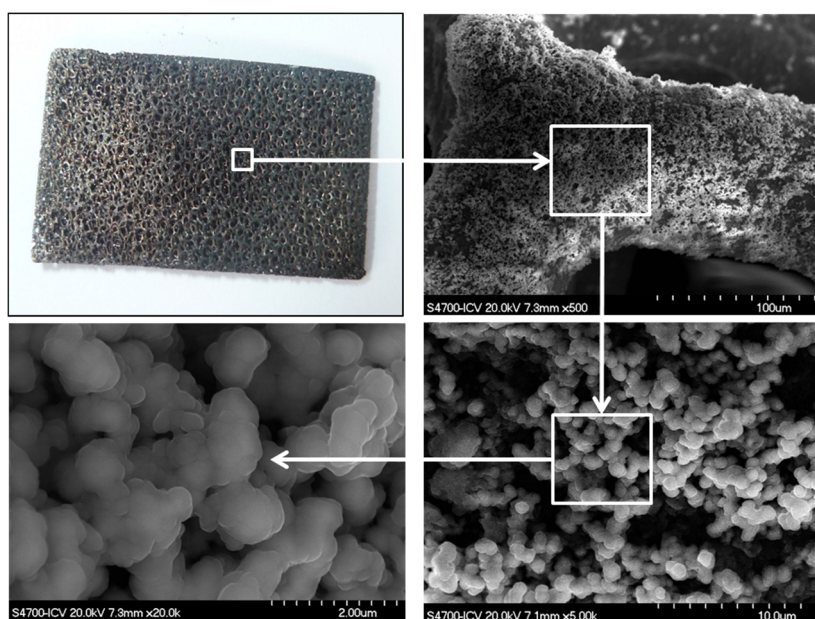


Figure 5. Picture and Micrographs at different magnifications of a Nickel foam coated with NiO/Ni particles.

3.2. Sintering Study

The fabrication of electrodes with an open microstructure and well-defined ion diffusion and electron pathways maximizes the electrolyte contact with the surface of the electroactive material [28,33,34]. In order to determine the optimum heat treatment, because of its influence on the electrochemical properties, we studied three different thermal processes, described in the experimental section in Figure 2.

FESEM images in Figure 6a–c show the plate-like morphology after the different heat treatments. In the three cases, the level of consolidation is high and all particles are well-connected, however the achieved porosity was different either produced by the increase of temperature or by the time of the dwell of the thermal treatment. According to these micrographs, the effect of the increase of the temperature prevails over the effect of the time and therefore the most closed porosity is given by the heat treatment at high temperature, 375 °C, Figure 6b. An opener micro-architecture (with the foam macroporosity) could favor the electrolyte diffusion defining pathways and improving the electrolyte impregnation in the microstructure. More porosity means higher exposed specific surface to the electrolyte, thus the number of redox reactions, which take place at the interface electrode/electrolyte increase. In addition, the size of the connected particles of Figure 6c seems to be bigger than the size of the particle forming the microstructure in Figure 6a,b. The increase of the dwell time leads to the growth of the sintered grains of the microstructure reducing the mesoporosity within the nanoplatelets while increase macroporosity among them, which could affect to the electrochemical response.

In addition, different coatings were analyzed by XRD to confirm the presence of Ni and NiO crystallographic phases after the sintering process. Figure 6d shows the diffractogram of one of the analyzed samples (all samples presented similar patterns independently from the thermal treatment followed, not shown here). The spectra verify that during the heat treatment under inert atmosphere, the metallic Ni did not suffer oxidation or other phase transformation.

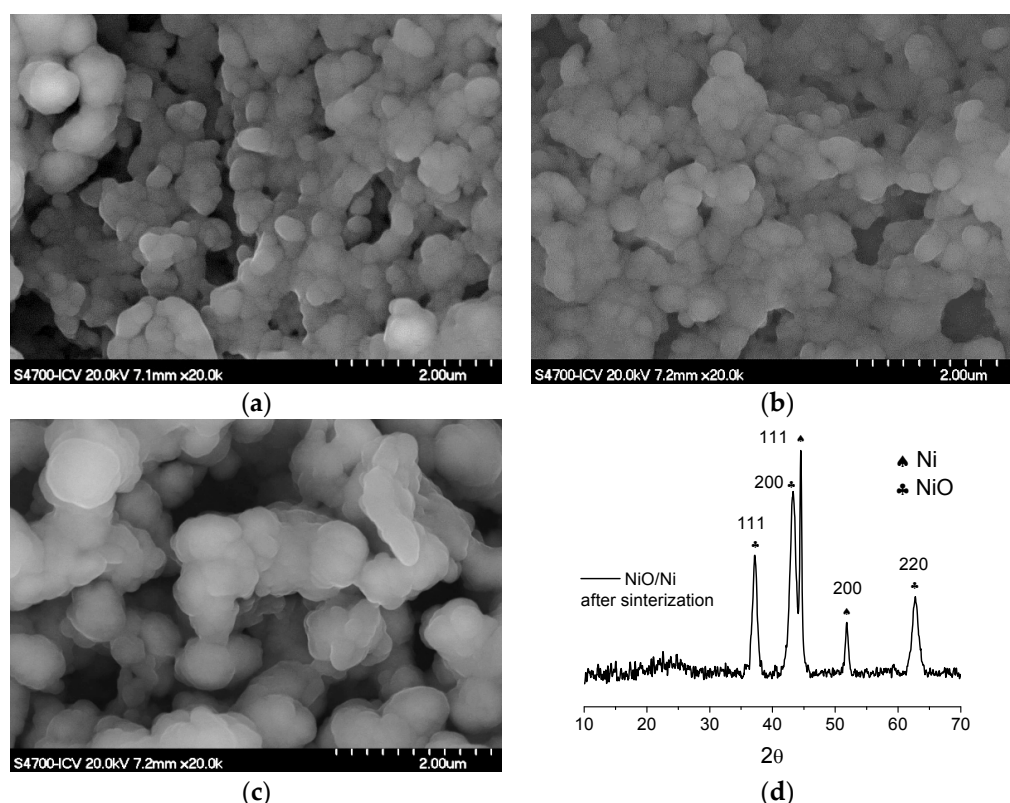


Figure 6. Final morphology and porosity of the NiO-Ni coating after the different heat treatment: (a) 325 °C 15 min Ar, (b) 375 °C 15 min Ar, and (c) 325 °C 60 min Ar; (d) XRD patterns of the NiO-Ni powders after calcination and scraping from the substrates.

3.3. Electrochemical Response

In order to study the influence of the nickel metallic, the thermal treatment, and later consolidation in the final properties, the electrochemical performance of the sintered coatings were evaluated in terms of faradaic capacity. Figure 7 shows the cyclic voltammetry (CV) curves of NiO/Ni electrodes calcined at 325 °C-15 min (Figure 7a), 375 °C-15 min (Figure 7b) and 325 °C-60 min (Figure 7c) at a sweep rate of 10 mV/s. A pair of redox current peaks with symmetrical shape can be identified during the cathodic and anodic sweeps, indicating the pseudocapacitance behavior. They can be attributed to the following reversible redox reaction with a potential window of 0.120 V:



It is well-known that the area under the curve in a cyclic voltagram is proportional to the specific capacitance and directly related with the specific surface area, where the redox reactions take place. In this study, the areas under the curves of Figure 7c were larger than the areas of Figure 7a,b which indicates that the thermal treatment most appropriated was 325 °C-60 min. These results can be discussed in accordance with the FESEM images of Figure 6 and the loading density of the electrodes. Although the size of the sintered grains is bigger and the nanoplatelets mesoporosity is lower (Figure 6c) the large macroporosity of the microstructure is the main responsible of the electrochemical response of this coating. However, also, the thin coating of Ni foams leads to a large active NiO/Ni surface at the electrode. In fact, the Ni foam has a specific surface of 300 m²/g and assuming that 0.1 g of foam is covered and tested, the 1 mg of NiO/Ni deposit results in a loading density in the order of 10^{−5} mg/cm². Thus, after a thermal treatment of 325 °C-60 min, low loading densities and the increase of macroporosity results that the most of the NiO/Ni grains are active surfaces linked to the Ni foam.

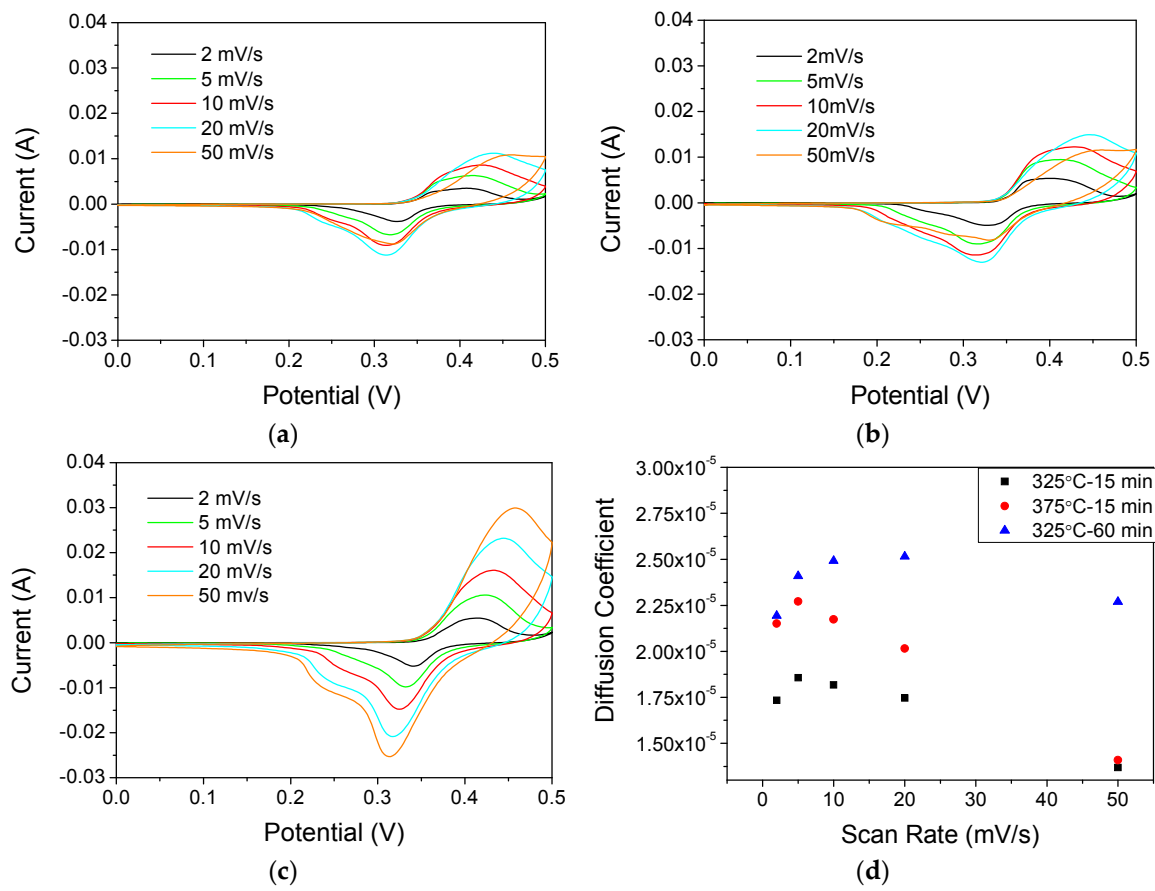


Figure 7. Cyclic voltammetry of NiO-Ni deposits calcined at 325 °C-15 min (a), 375 °C-15 min (b) and 325 °C-60 min (c). Diffusion coefficient calculated by the Randles–Sevcik equation for the different heat treatments (d).

To quantify the electrolyte diffusion through the microstructural pathways, the diffusion coefficients (D) were calculated by the Randles-Sevcik Equation (12).

$$i_p = 268.6 \times n^2 \times A \times D^{\frac{1}{2}} \times C \times v^{\frac{1}{2}} \quad (12)$$

where i_p is the current oxidation maximum in amperes, n is the number of electrons transferred in the redox reaction ($2 e^-$ in our case, Equation (11)). A is electrode area in cm^2 , D is the diffusion coefficient in cm^2/s , C is the electrolyte molar concentration and v is scan rate in V/s .

Figure 7d shows the calculated values at different scan-rates. The coating sintered at 325 °C-60 min displays the highest diffusion coefficient values, which confirm our previous hypothesis.

In addition, specific capacitance values were also determined by galvanostatic measurements. Figure 8a presents the typical discharge voltage vs. time plots for NiO/Ni at current densities of 2 A/g in the potential range of 0–0.5 V, from which symmetric and quasi-linear shapes with well-defined plateaus during the discharge processes are observed, suggesting electrodes have pseudocapacitive behavior, which is in agreement with the result of above CV test.

The specific capacitance determined for the thermal treatment at 325 °C-60 min exhibits a specific capacitance of 755 F/g, which is better than the 363 F/g corresponding to the NiO seeds [13]. Other authors have been reported specific capacitance values within our range, such as 900 F/g for NiO/Pt electrodes [28], or far from our values, such as 2018 F/g for hydrothermal NiO coatings [35] or 157 F/g for NiO + Carbon by electrodeposition [36]. The density of the NiO/Ni electrode on Ni foams is generally low, limiting the volumetric performance. The density of the whole electrode can

be considered that of the Ni foam (0.45 g/cm^3) and, as the deposited NiO/Ni coatings are 1 mg in weight, the volumetric performance is 13 F/cm^3 . A capacitance retention of 62% was achieved after 1000 cycles. In spite of having a decrease of the specific capacitance, the value still being higher than the previous reported. The discharge profiles of the electrodes, parallel to the x -axis, confirmed also the typical pseudocapacitive contribution.

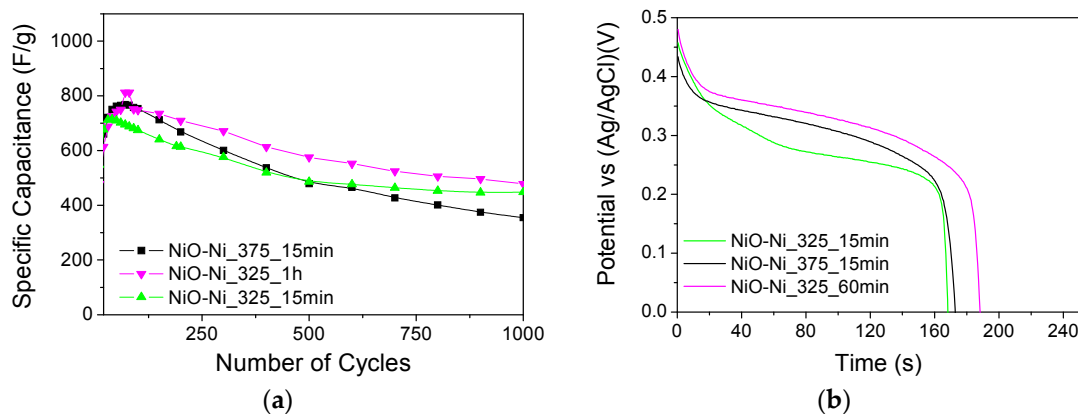


Figure 8. Galvanostatic discharge curves at mA cm^{-2} of the different heat treatment electrodes (a); and its cyclic voltammetry measurement (CV) (b).

4. Conclusions

The obtained specific capacitance of NiO/Ni electrodes is 755 F/g , which is more than twice the results for simple NiO nanoplatelets used as electroactive material. This improvement of the electrochemical performance can be attributed to the presence of the metallic Ni nanoparticles in the nanostructure.

A thermal treatment of 325°C -1 h leads a cohesive and consolidated NiO/Ni nanostructure well adhered to the Ni foam collector, with a macroporosity higher than $1 \mu\text{m}$, which results in a high electrochemical performance, favoring the electrolyte diffusion and reaction throughout the porous structure, as well as the electronic conduction through the semiconductor nanostructure.

NiO/Ni core-shell nanostructures were synthesized by heterogeneous precipitation of metallic Ni over NiO nanoplatelets seeds in aqueous suspensions. The stabilization of as-synthesized core-shell nanostructures and the optimization of the EPD parameters allow controlling nanoplatelets arrangement and the coating growth in 3D substrates. The Ni collector was fully and homogeneously covered by only 1 mg of electroactive NiO/Ni free-binders materials.

Acknowledgments: The authors acknowledge the support of the projects MAT2015-70780-C4-1-P and the program MULTIMAT-CHALLENGE, reference S2013/MIT-2862.

Author Contributions: Begoña Ferrari and Zoilo Gonzalez conceived and designed the experiments. Joaquin Yus performed the experiments. Joaquin Yus, Begoña Ferrari, Antonio Javier Sanchez-Herencia and Zoilo Gonzalez analyzed the data and wrote the paper. Alvaro Caballero and Julian Morales contributed electrochemical equipments and also analyzed the data.

Conflicts of Interest: The authors declare no conflict of interest.

References

1. Cuentas Gallegos, A.K.; Rincón, M.E. Carbon nanofiber and PEDOT-PSS bilayer systems as electrodes for symmetric and asymmetric electrochemical capacitor cells. *J. Power Sources* **2006**, *162*, 743–747. [[CrossRef](#)]
2. Sidhu, N.K.; Rastogi, A.C. Electrochemical performance of supercapacitors based on carbon nanofoam composite and microporous poly(3,4-ethylenedioxythiophene) thin film asymmetric electrodes. *Mater. Chem. Phys.* **2016**, *176*, 75–86. [[CrossRef](#)]

3. Xia, H.; Shirley Meng, Y.; Yuan, G.; Cui, C.; Lu, L. A symmetric RuO₂/RuO₂ supercapacitor operating at 1.6 V by using a neutral aqueous electrolyte. *Electrochem. Solid State Lett.* **2012**, *15*. [[CrossRef](#)]
4. Yoo, C.Y.; Park, J.; Yun, D.S.; Yu, J.H.; Yoon, H.; Kim, J.N.; Yoon, H.C.; Kwak, M.; Kang, Y.C. Crucial role of a nickel substrate in Co₃O₄ pseudocapacitor directly grown on nickel and its electrochemical properties. *J. Alloys Compd.* **2016**, *676*, 407–413. [[CrossRef](#)]
5. Argüello, J.A.; Cerpa, A.; Alanbari, M.H.; Fariñas, J.C.; Moreno, R. Preparation of manganese oxide-graphite electrodes by electrophoretic deposition. *Ceram. Int.* **2017**, *43*, 3231–3237. [[CrossRef](#)]
6. Gonzalez, Z.; Ferrari, B.; Sanchez-Herencia, A.J.; Caballero, A.; Morales, J. Use of Polyelectrolytes for the Fabrication of Porous NiO Films by Electrophoretic Deposition for Supercapacitor Electrodes. *Electrochim. Acta* **2016**, *211*, 110–118. [[CrossRef](#)]
7. Zhang, H.; Wang, X.; Chen, C.; An, C.; Xu, Y.; Dong, Y.; Zhang, Q.; Wang, Y.; Jiao, L.; Yuan, H. Facile synthesis of diverse transition metal oxide nanoparticles and electrochemical properties. *Inorg. Chem. Front.* **2016**, *3*, 1048–1057. [[CrossRef](#)]
8. Yang, Z.; Xu, F.; Zhang, W.; Mei, Z.; Pei, B.; Zhu, X. Controllable preparation of multishelled NiO hollow nanospheres via layer-by-layer self-assembly for supercapacitor application. *J. Power Sources* **2014**, *246*, 24–31. [[CrossRef](#)]
9. Bello, A.; Makgopa, K.; Fabiane, M.; Dodoo-Ahrin, D.; Ozoemena, K.I.; Manyala, N. Chemical adsorption of NiO nanostructures on nickel foam-graphene for supercapacitor applications. *J. Mater. Sci.* **2013**, *48*, 6707–6712. [[CrossRef](#)]
10. Feng, F.; Zhao, S.; Liu, R.; Yang, Z.; Shen, Q. NiO Flowerlike porous hollow nanostructures with an enhanced interfacial storage capability for battery-to-pseudocapacitor transition. *Electrochim. Acta* **2016**, *222*, 1160–1168. [[CrossRef](#)]
11. Zhang, Z.; Gao, Q.; Gao, H.; Shi, Z.; Wu, J.; Zhi, M.; Hong, Z. Nickel oxide aerogel for high performance supercapacitor electrodes. *RSC Adv.* **2016**, *6*. [[CrossRef](#)]
12. Li, X.; Wang, L.; Shi, J.; Du, N.; He, G. Multishelled Nickel-Cobalt Oxide Hollow Microspheres with Optimized Compositions and Shell Porosity for High-Performance Pseudocapacitors. *ACS Appl. Mater. Interfaces* **2016**, *8*, 17276–17283. [[CrossRef](#)] [[PubMed](#)]
13. Gonzalez, Z.; Ferrari, B.; Sanchez-Herencia, A.J.; Caballero, A.; Morales, J. Relevance of the Semiconductor Microstructure in the Pseudocapacitance of the Electrodes Fabricated by EPD of Binder-Free β-Ni(OH)₂ Nanoplatelets. *J. Electrochem. Soc.* **2015**, *162*, D3001–D3012. [[CrossRef](#)]
14. Kurra, N.; Alhebshi, N.A.; Alshareef, H.N. Microfabricated pseudocapacitors using Ni(OH)₂ electrodes exhibit remarkable volumetric capacitance and energy density. *Adv. Energy Mater.* **2015**, *5*, 1–9. [[CrossRef](#)]
15. Liu, X.Y.; Gao, Y.Q.; Yang, G.W. A flexible, transparent and super-long-life supercapacitor based on ultrafine Co₃O₄ nanocrystal electrodes. *Nanoscale* **2016**, *8*, 4227–4235. [[CrossRef](#)] [[PubMed](#)]
16. Jiang, Y.Q.; Wang, P.B.; Zang, X.N.; Yang, Y.; Kozinda, A.; Lin, L. Uniformly Embedded Metal Oxide Nanoparticles in Vertically Aligned Carbon Nanotube Forests as Pseudocapacitor Electrodes for Enhanced Energy Storage. *Nano Lett.* **2013**, *13*, 3524–3530. [[CrossRef](#)] [[PubMed](#)]
17. Żółek-Tryznowska, Z. Additives for Ink Manufacture. In *Printing on Polymers*; Izdebska, J., Thomas, S., Eds.; William Andrew Publishing: Norwich, NY, USA, 2016; pp. 57–66.
18. McManus, D.; Vranic, S.; Withers, F.; Sanchez-Romaguera, V.; Macucci, M.; Yang, H.; Sorrentino, R.; Parvez, K.; Son, S.K.; Iannaccone, G.; et al. Water-based and biocompatible 2D crystal inks for all-inkjet-printed heterostructures. *Nat. Nanotechnol.* **2017**, *12*, 343–350. [[CrossRef](#)] [[PubMed](#)]
19. Gonzalez, Z.; Yus, J.; Caballero, A.; Morales, J.; Sanchez-Herencia, A.J.; Ferrari, B. Electrochemical performance of pseudo-capacitor electrodes fabricated by Electrophoretic Deposition inducing Ni(OH)₂ nanoplatelets agglomeration by Layer-by-Layer. *Electrochim. Acta* **2017**, *247*, 333–343. [[CrossRef](#)]
20. Kazazi, M. Facile preparation of nanoflake-structured nickel oxide/carbon nanotube composite films by electrophoretic deposition as binder-free electrodes for high-performance pseudocapacitors. *Curr. Appl. Phys.* **2017**, *17*, 240–248. [[CrossRef](#)]
21. Dios, M.; Gonzalez, Z.; Gordo, E.; Ferrari, B. Semiconductor-metal core-shell nanostructures by colloidal heterocoagulation in aqueous medium. *Mater. Lett.* **2016**, *180*, 327–331. [[CrossRef](#)]
22. Wu, M.S.; Huang, C.Y.; Lin, K.H. Electrophoretic deposition of nickel oxide electrode for high-rate electrochemical capacitors. *J. Power Sources* **2009**, *186*, 557–564. [[CrossRef](#)]

23. Zheng, Z.; Huang, B.; Qin, X.; Zhang, X.; Dai, Y.; Whangbo, M.-H. Facile in situ synthesis of visible-light plasmonic photocatalysts $M@TiO_2$ ($M = Au, Pt, Ag$) and evaluation of their photocatalytic oxidation of benzene to phenol. *J. Mater. Chem.* **2011**, *21*, 9079. [[CrossRef](#)]
24. Chen, X.; Mao, S.S. Titanium Dioxide Nanomaterials: Synthesis, Properties, Modifications, and Applications. *Chem. Rev.* **2007**, *107*, 2891–2959. [[CrossRef](#)] [[PubMed](#)]
25. Wu, H.; Li, D.; Zhu, X.; Yang, C.; Liu, D.; Chen, X.; Song, Y.; Lu, L. High-performance and renewable supercapacitors based on TiO_2 nanotube array electrodes treated by an electrochemical doping approach. *Electrochim. Acta* **2014**, *116*, 129–136. [[CrossRef](#)]
26. Wen, W.; Wu, J.M. Eruption combustion synthesis of NiO/Ni nanocomposites with enhanced properties for dye-absorption and lithium storage. *ACS Appl. Mater. Interfaces* **2011**, *3*, 4112–4119. [[CrossRef](#)] [[PubMed](#)]
27. Song, S.; Yao, S.; Cao, J.; Di, L.; Wu, G.; Guan, N.; Li, L. Heterostructured Ni/NiO composite as a robust catalyst for the hydrogenation of levulinic acid to γ -valerolactone. *Appl. Catal. B Environ.* **2017**, *217*, 115–124. [[CrossRef](#)]
28. Lu, Q.; Lattanzi, M.W.; Chen, Y.P.; Kou, X.M.; Li, W.F.; Fan, X.; Unruh, K.M.; Chen, J.G.G.; Xiao, J.Q. Supercapacitor Electrodes with High-Energy and Power Densities Prepared from Monolithic NiO/Ni Nanocomposites. *Angew. Chem. Int. Ed.* **2011**, *50*, 6847–6850. [[CrossRef](#)] [[PubMed](#)]
29. Dios, M.; Gonzalez, Z.; Gordo, E.; Ferrari, B. Chemical precipitation of nickel nanoparticles on Ti (C,N) suspensions focused on cermet processing. *Int. J. Refract. Met. Hard Mater.* **2017**, *63*, 2–8. [[CrossRef](#)]
30. Ferrari, B.; Moreno, R. EPD kinetics: A review. *J. Eur. Ceram. Soc.* **2010**, *30*, 1069–1078. [[CrossRef](#)]
31. Mishra, M.; Bhattacharjee, S.; Besra, L.; Sharma, H.S.; Uchikoshi, T.; Sakka, Y. Effect of pH localization on microstructure evolution of deposits during aqueous electrophoretic deposition (EPD). *J. Eur. Ceram. Soc.* **2010**, *30*, 2467–2473. [[CrossRef](#)]
32. Besra, L.; Uchikoshi, T.; Suzuki, T.S.; Sakka, Y. Experimental verification of pH localization mechanism of particle consolidation at the electrode/solution interface and its application to pulsed DC electrophoretic deposition (EPD). *J. Eur. Ceram. Soc.* **2010**, *30*, 1187–1193. [[CrossRef](#)]
33. Xu, P.; Miao, C.; Cheng, K.; Ye, K.; Yin, J.; Cao, D.; Wang, G.; Zhang, X. Preparation of binder-free porous ultrathin $Ni(OH)_2$ nanoleafs using ZnO as pore forming agent displaying both high mass loading and excellent electrochemical energy storage performance. *Electrochim. Acta* **2016**, *216*, 499–509. [[CrossRef](#)]
34. Yan, H.; Zhang, D.; Xu, J.; Lu, Y.; Liu, Y.; Qiu, K.; Zhang, Y. Solution growth of NiO nanosheets supported on Ni foam as high-performance electrodes for supercapacitors. *Nano Res. Lett.* **2014**, *9*, 424. [[CrossRef](#)] [[PubMed](#)]
35. Lu, Z.; Chang, Z.; Liu, J.; Sun, X. Stable ultrahigh specific capacitance of NiO nanorod arrays. *Nano Res.* **2011**, *4*, 658–665. [[CrossRef](#)]
36. Zhang, X.; Luo, J.; Tang, P.; Ye, X.; Peng, X.; Tang, H.; Sun, S.G.; Fransaer, J. A universal strategy for metal oxide anchored and binder-free carbon matrix electrode: A supercapacitor case with superior rate performance and high mass loading. *Nano Energy* **2017**, *31*, 311–321. [[CrossRef](#)]



Z. Gonzalez, J. Yus, A. Caballero, J. Morales, A.J. Sanchez-Herencia, B. Ferrari.

**Electrochemical performance of pseudo-capacitor electrodes
fabricated by Electrophoretic Deposition inducing Ni(OH)₂
nanoplatelets agglomeration by Layer-by-Layer.**

Electrochim. Acta **2017**, 247, 333–343,

doi:10.1016/j.electacta.2017.07.043.



Electrochemical performance of pseudo-capacitor electrodes fabricated by Electrophoretic Deposition inducing Ni(OH)₂ nanoplatelets agglomeration by Layer-by-Layer

Z. Gonzalez^a, J. Yus^a, A. Caballero^b, J. Morales^b, A.J. Sanchez-Herencia^a, B. Ferrari^{a,*}

^a Institute for Ceramic and Glass, CSIC, Madrid, Spain

^b I.U.R Fine Chemistry and Nanochemistry, Inorganic Chemistry and Chemical Engineering Department, University of Córdoba, Córdoba, Spain

ARTICLE INFO

Article history:

Received 28 January 2017

Received in revised form 3 July 2017

Accepted 6 July 2017

Available online 8 July 2017

Keywords:

Nanoplatelets

Layer by Layer

Colloidal Processing

Electrophoretic Deposition

Ni-based materials and Pseudocapacitors

ABSTRACT

The electrochemical behaviour of ceramic semiconductors not only depends on the characteristics of the electroactive material but also on the processing method, the nanoparticles arrangement and the consolidation degree of the formed microstructure. In this sense, the use of nanoparticles with plane morphologies (disc, platelets, etc.) results interesting due to the formation of conduction pathways produced as a consequence of their laminar structures. Electrophoretic Deposition (EPD) is a shaping methodology which allows achieving high degrees in nanoplatelets packing by controlling their alignment during the coating process specifically over 3D substrates. In this work, we have studied the effect of a moderate nanoplatelets agglomeration, by tuning their surfaces with a polyelectrolyte multilayer following a Layer-by-Layer (LbL) methodology and fixing the electric conditions of the EPD process. Overcoming the destructive effects of the full agglomeration of nanoplatelets, NiO films with a stable and extremely open macroporous structure were processed to coat Ni foams, improving the capacitive performance of pseudocapacitors leading to values of specific capacitances of 650 F/g. Results collected in this work also evidence that an efficient ordering and orientation of nanoplatelets in EPD mainly depends on tuning the suspension parameters (solid contents, conductivity, electrophoretic mobility, etc.) to avoid the massive flux and interactions among interparticles and electro-hydrodynamic forces, as well as the interference of collateral electrode phenomena.

© 2017 Elsevier Ltd. All rights reserved.

1. Introduction

Among a large variety of nonspherical colloids, nanodiscs or nanoplatelets are particularly interesting as they enable the bottom-up assembly of layered nanocomposites, which enhances the ionic/electronic conduction throughout the formation of crystallographic pathways, or combines unmatched strength and toughness in laminar structures. Advances in nanoplatelets applications imply mastering their manipulation, during their assembly, orientation, packing, and the film deposition [1]. In these structures, the spontaneous organization of nanoentities is the key challenge. The nanosheets of graphite and graphene [2,3], hydroxides and oxides [4,5], chalcogenides [1] or metallic nanoclusters [6], have a tendency to vertically stack in suspension, forming aggregates, due to strong Van der Waals interactions

between the basal planes of their lattices. Dissimilar surface charge density can be also used to force nanoplatelets arrangement by a layer-by-layer strategy (LbL, i.e. alternating negatively charged nanosheets and cationic polyelectrolytes), or their reorientation in a magnetic or electric field. Then the formulation of stable dispersions of nanoplatelets can be used as slurries or inks to prepare tailored thin films by drop casting, inkjet printing, or electrophoretic deposition (EPD) [7].

In the EPD process, charged nanoparticles move toward the electrode with the opposite charge under the influence of an electric field, and deposit forming a compact film. The EPD behaviour of a large variety of nanoplatelets in nature and dimensions was studied during the last decade for different applications (Table 1). An example are the LbL assembly of alternate modified gibbsite nanoplatelets (100–200 nm in diameter) and polyelectrolyte multilayers, where the shaped smooth surfaces play a crucial role in the mechanical properties of the final lamellar structure [8] or the nanoplatelets alignment leads to optically transparent and flexible coatings [9]. In these works, Lin

* Corresponding author.

E-mail address: bferrari@icv.csic.es (B. Ferrari).

Table 1

Characteristic of nanoplatelets and thin films obtained by EPD described in the Literature.

Material	Diameter (nm)	Solvent	Stabilization mechanism	Electrophoretic kinetics conditions	Particle arrangement
Graphite [2]	1000	H ₂ O	Electro-steric (PEI + pH 9–10)	H ₂ bubbling	Random
Ni(OH) ₂ [24]	100	IPA	Electro-static (H ₂ O + I ₂)	High PZ (+30 mV) High solid content (10 g/L) H ₂ bubbling	Random
Gibbsite [9]	100–200	EtOH/H ₂ O	Electro-static (pH 7)	High PZ (+40 mV) Low electric field 11 V/cm	Aligned
ZnO [12,13]	35	H ₂ O	Electro-Steric (PEI)	Solid content: 1–10 g/L ZP = +22 mV (PEI)	Aligned & Perpendicular
SiO ₂ -Gibbsite [8]	100–200	EtOH	Electro-steric (H ₂ O + PEI pH 7)	High ZP (+28 mV) Low electric field 10 V/cm	Moderately aligned
GO [15]		H ₂ O	Electrostatic	PEI as binder Low solid content (1.5 g/L) Low electric field 10 V	Aligned
GdOCl [5]	200–400	Cyclohexane IPA	Electro-Steric (TOPO synthesis modifier)	H ₂ bubbling ZP = –66 mV (cyclohexane) ZP = +30, +48 mV (IPA, H ₂ O)	Aligned
TiO ₂ -Graphene [3]		H ₂ O IPA	Electrostatic (PVB-binder)	Electric field 25–400 V Low ZP (+10 mV) High solid content (>30 g/L)	Moderately aligned
Ni(OH) ₂ -CB [25]	200/10	H ₂ O	Electro-Steric (PVP, Igepal)	Composite clusters Solid content: 1	Aligned
Au-Cu [8]	>1000	Chloroform + Acetone	Electrostatic	ZP mixture = +40 mV Low solid content (<1 g/L)	Cu Aligned Au moderately Aligned
ZnO [11]	10	Acetonitrilo	Electrostatic	Electric field 200 V Low solid content (<1 g/L) Electric field 20–40 nV	Aligned

et al. [8,10] demonstrated how gibbsite can be oriented during EPD by the particular distribution of charges in their surfaces and edges, when they are electrostatically stabilised at pH 7 in a mixture of H₂O and EtOH. Further works of the same authors demonstrate that modified gibbsite-silica stabilised by the adsorption of high molecular weight Polyethylenimine (PEI) leads to crack-free coatings, but simultaneously nanoplatelets preferential alignment is slightly deteriorated. Those results suggest that the branched PEI molecule acts as flocculant disturbing the nanoplatelets ordering.

In a lower range of particle size [11–13], ZnO-based films made on aligned nanoparticles (20–35 nm in diameter) leads to high packing green density and room transparency even previously to the sintering process [12]. In those publications, the difference in charge of ZnO basal planes determines the massive adsorption of the stabilizer (branched PEI) in one side of the nanoflake, setting their hydrodynamic behaviour and then fashioning deposition. In a low concentrated suspension (1 g/L), hydrodynamic, polarization and also interparticles forces govern the arrangement of flake-like dispersed nanoparticles at the electrode. When the solid concentration increases, a massive arrival of particles prevents this ordering effect. This clearly opens the possibility of controlling the nanoplatelets orientation by EPD tuning their electrokinetics by designing the stabilization system.

The mechanisms of the deposit formation of graphene sheets have been also recently described in the literature. Most of the studies describe the stabilization of graphene by an electrostatic mechanism, and argue that the charge neutralisation is the main cause of the deposit formation [14]. But in the EPD of graphene sheets, side reactions, such as GO reduction, aqueous electrolysis, composite clusters (ceramic or metallic nanoparticles/graphene) have to be considered. Although low solid loadings deserve the graphene sheets alignment [15], even moderately for the deposition of composite clusters (TiO₂ nanoparticles and graphene nanoplatelets) [3], side reactions can disturb the nanoplatelets arrangement.

Finally, most recent studies of the EPD of flakes-like clusters of Au and Cu [6], in the micronic range, also suggest that the key for

governing the deposition efficiency is the lateral size of the sheets (the shape factor), inferring that the sheets with a large lateral size possess high electrophoretic mobility and strong face-to-face Van der Waals interactions, thus leading to high deposition efficiencies.

The experimental work described in those manuscripts (Table 1) suggests that there are several reasons that can explain the nanoplatelets alignment during EPD. Depending on the nanoflakes crystallography the charge distribution in basal planes is different than in the flake edges, or even different between both basal planes. That promotes strong Van der Waals interactions among the nanoplatelets and the electrode surface, but also among particles, during deposit growth. From the point of view of dispersion, the mechanism of stabilization (electrostatic/electrosteric) should promote the individual movement of dispersed nanoentities. However, it is necessary to consider that the yield rate prevail over other parameters, and the solid content, the electrophoretic mobility (zeta potential) and the conductivity should be adjusted to avoid the massive arrival of particles to the electrode, and also the premature agglomeration of nanoplatelets that can disturbs the contribution of the osmotic flow of the solvent to the nanoplatelets ordering, predicted by models [16–18]. Those premises should be considered in the fabrication by EPD of electrodes and structures based on nanoplatelets stacking.

On the other hand, in energy storage applications, electrodes based on NiO and Ni(OH)₂ nanostructures (3D and 2D nanoparticles) have demonstrated a high performance, especially when metallic foams were used as substrates of the active material or collectors [19,20]. It is well known the viability of EPD to cover 3D substrates or complex shapes, so the number of publications dealing with the preparation of films by EPD for energy storage and generation devices, and the functionalization of biostructures, is increasing. EPD is also recognised as the available technique to achieve the highest degrees of nanoparticles packing, even using diluted suspensions or sols, where rheological requirements are lowered [21]. Consequently, there are a strong research interest to transfer packing and ordering of the coatings achieved by EPD in

flat substrates, to cover the skeleton of 3D structures, especially scaffolds or metal foams [22–24].

In this line, Wu et al. [25] described the EPD of synthetic Ni(OH)₂ nanoplatelets, with a specific surface area of 170 m²/g and a mayor diameters of 50–150 nm, in which nanoplatelets are stabilized by means an electrostatic mechanisms, adding water, acetone and iodine to Isopropyl alcohol. These suspensions had an elevated conductivity (provided by the iodine addition) and zeta potential. Nanoflakes coagulate at the electrode due to the increases of solid content and the neutralisation (reduction) of the ionic double layer, since the pH of the cathode is mainly basic. But significant hydrogen bubbling had also observed. These EPD conditions and an elevated solid loading of the suspension (10 g/L) result on a random deposition of Ni(OH)₂ nanoplatelets, which promotes the formation of the mesoporous microstructures after the coating aneling (300 °C–1 h), achieving capacities of 1409 F/g at 1.0 A/g with 92% of capacity retention after 2500 cycles.

Ni(OH)₂ electrodes based on aligned nanoplatelets, and also built by a full yield EPD process on 3D substrates, have been recently reported in the literature for both pseudocapacitors and Li-Batteries (LIBS) [23,26]. Described results demonstrate the viability of the EPD process for replicate the nanoplatelets alignment in a dense and connected microstructure either in flat substrates or in 3D metallic foams. However, in those systems the high packing density limits the capacity performance of Ni(OH)₂ nanoplatelets. Consequently, in order to increases the open meso- and macroporosity in the semiconductor electrodes, evading the loss of connectivity, the surface modification of nanoplatelets by the Layer-by-Layer (LbL) approach has been proposed [22]. Recent results shown that in a porous microstructure shaped by EPD of Ni(OH)₂ modified by LbL adsorption of polyelectrolites, the direct contact between the electrolyte ions and the semiconductor material is favoured leading to a specific capacitance of 400 F/g at 2 A/g with 100% retention. The use of LbL approach as porous template seemed to be limited to the 3 layers assembly of polyanions and polycations, due to side effect of agglomeration induced by the LbL modification of nanoplatelets, which impedes the homogeneous deposition by EPD.

This work is aimed to overcome this agglomeration effect, by tuning nanoplatelets surface modification and EPD conditions, to coat 3D electrodes with a stable and extremely open mesoporous structure, which will increase the capacitive performance of the pseudocapacitor electrode.

2. Experimental

β-Ni(OH)₂ nanoplatelets were synthesized following the procedure described in a previous work [27] which consist on a chemical precipitation from a salt of nickel, (Ni(NO₃)₂·6H₂O Panreac, Spain), with ammonium hydroxide addition (NH₃, PA 28%, Panreac, Spain). The reaction was carried out at room temperature using a high intensity ultrasonic horn (45 W/cm², 24 kHz, titanium T13 tip, Sonopuls HD 2200, Bandelin Electronic, Germany). The obtained green precipitate was washed several times and re-diluted in a desired amount of distilled water at pH~10 (adjusted with tetramethyl ammonium hydroxide, TMAH, Merck, Germany).

The surface of the synthesized nanoplatelets were directly functionalized in the aqueous media with a polyelectrolyte multilayer through LbL self-assembly methodology [22]. The polyelectrolytes used were branched Polyethylenimine (PEI, Mw 25,000, Sigma Aldrich, Germany) for odd layers, and Polyacrylic Acid (PAA in a 63 wt.% solution in water, Mw 2000, Across, USA) for even layers. The built-up of the multilayer was evaluated in terms of zeta potential by adsorption of the specific amount of polyelectrolyte (PEI or PAA) which saturates either the surface

of nanoplatelets in the first layer or the previous layer in the subsequent additions. To favour the adsorption of the following layer of opposite charge, the pH value of the suspension was adjusted. A pH value of 8 was selected for the adsorption of PEI in order to promote the protonation of the amino groups (NH₂⁺), while a pH value of 10 was selected to promote the adsorption of the PAA layer with deprotonated carboxyl groups (COO⁻). All zeta potential measurements were made with a Zetasizer Nano ZS (Malvern, UK) by laser Doppler velocimetry with suspensions at a concentration value of 0.1 g/L. The pH was adjusted by adding HNO₃ or TMAH and determined with a pH probe (Metrohm AG, Germany).

Cathodic EPD were used as shaping technique to prepare the β-Ni(OH)₂ coatings. Considering the negative charge of the work electrode, suspensions of nanoplatelets modified with 1, 3 and 5 layers (charged positively) were only employed. After the polyanion adsorption suspensions was rinsed in order to eliminate the residual precursors, and then β-Ni(OH)₂ aqueous suspensions were diluted in ethanol with a volume ratio of 19:1 of EtOH:DI-Water to a concentration of 1 g/L of solid contents. The modified nanoplatelets were deposited onto as-received stainless steel foils (AISI 316L) of 30 × 20 × 0.5 mm and onto nickel foams of 15 × 10 × 1 mm with a specific surface at least 10 times higher than foils. The counter electrode was a platinum foil separated from the work electrode by a distance of 18 mm in the electrophoretic cell. Also, previous to the deposition, substrates (foils and foams) were washed following an industrial cleaning protocol. The experimental EPD kinetic curves were determined under galvanostatic/potenciostatic conditions using a high voltage power source (2611 System SourceMeter, Keithley Instruments Inc., USA), applying current densities from 50 to 100 μA with electric field values from 57 to 71 Vcm⁻¹, at deposition times from 0 to 900 seconds. In addition, the foams were coated under potenciostatic conditions applying a voltage closed to 200 V at times from 60 to 180 seconds in order to achieve the desired amount of deposition.

The most general equation [28] formulated up today was used to determine the theoretical deposition rate:

$$m(t) = m_0(1 - e^{-t/\tau}) \quad (1)$$

where, m (g), is the deposition mass, m_0 (g), is the initial amount of powder in suspension and τ (s) is the characteristic time, calculated by:

$$\tau = \frac{V}{fSEu_e} \quad (2)$$

where, V (cm³), is the volume of suspension, S (cm²), is the conducting area, E (V/cm), is the applied electric field, u_e (m²/Vs), is the electrophoretic mobility of the nanoparticles, and f ($0 < f < 1$), is the sticking factor. The sticking factor represents the percentage of depositing particles among the arriving particles to the work electrode by electrophoresis.

After EPD, all green coatings were firstly left to dry at room conditions and then they were calcined and sintered in Ar, maintaining a dwell temperature at 325 °C for 1 h, with heating and cooling rates of 10 °C/min, resulting in consolidated NiO films. Pore size distributions were characterized with scratched powders from NiO films by Mercury Intrusion Porosimetry (MIP) using a Micromeritics AutoPore IV 9510 (USA). X-Ray Diffraction analysis (XRD) were determined with a Siemens D5000 diffractometer (Germany) with a Kristalloflex 710 generator ($K\alpha(\text{Cu}) \lambda = 1.5405 \text{ \AA}$; 40 kV; 30 mA; $2\theta = 5\text{--}70$), and microstructural observations were examined by field emission scanning electron microscopy (FE-SEM) in an S-4700 microscope (Hitachi, JAPAN).

The capacitive performance of the electrodes was tested under different conditions. For the cyclic voltammetry (CV)

measurements carried out with a Potenciostat/Galvanostat Autolab (PGSTAT204), 5 sequential cycles were programmed at scan rates of 2, 5, 10, 20 and 50 mV/s in a potential window of 0.0–0.5 V. A three-electrode configuration consisting of Ni foam/NiO composite as working electrode, Ag/AgCl as reference electrode and a Pt foil as counter electrode, was used. The electrolyte employed was a 1 M KOH aqueous solution. The specific capacitance was determined from the charge value Q , proportional to the integral of the CV curve. Q represents the difference between the area under the charge curve and the area under discharge curve for the upper and lower limits of the potential window. Thus, the specific capacitance was obtained from the Eqs. (3)–(5).

$$Q = \int I \cdot dt \quad ; t = V/\nu \quad (3)$$

$$Q = \frac{1}{\nu} \int I \cdot dV \quad (4)$$

$$C = \frac{Q}{m \cdot \Delta V}; \quad C = \frac{\int I dV}{\nu \cdot m \cdot \Delta V} \quad (5)$$

where I is the current (A), t the time (s), V the voltage (V), ν the scan rate, C the specific capacitance (F/g), m the mass (g) and Q the charge/discharge value (C).

The charging/discharging measurement was carried out through chronopotentiometry analysis (CP) at a scan rate of 2 A/g using a multichannel potentiostat–galvanostat system (Arbin BT2000). From CP measurements, the specific capacitance value

was calculated according to the Eq. (4):

$$C = \frac{I \cdot \Delta t}{m \cdot \Delta V} \quad (6)$$

where C (F/g) is the specific capacitance, I (A) is the discharge current, Δt (s) is the charging/discharging time, ΔV (V) is the voltage window for discharge, and m (g) is the mass of the active NiO material in the electrode.

3. Results and Discussion

In this work, synthetic β -Ni(OH)₂ nanoplatelets superficially modified by a 1, 3 and 5 LbL organic shells were employed to manipulate the microstructure of the EPD coating. In a previous work, the successful assembling in a LbL system of PEI and PAA polyelectrolytes onto the surface of β -Ni(OH)₂ nanoparticles with platelet morphology was demonstrated [22]. Fig. 1a shows schematically the β -Ni(OH)₂ nanoplatelets stacking when precipitates during their synthesis with the aid of ultrasound. This particular kind of synthesis modifies the morphology and crystallography of the nanostructure at several levels [27,29]. The unit cell of nickel hydroxide stacks in a layer by layer structure of OH[−] and Ni along the c -axis. Ni atoms are superficially exposed when the nanoplatelets are fashioned thus the 2D nanostructures are negatively charged in aqueous media when the synthesis ends (pH > 8.5). So the branched polycation (PEI) added to the nanoplatelet suspension in the post-synthesis medium can be anchored to the hydrated Ni atoms in two different ways [12]. Depending on the pH, long PEI chains can acquire two different features as a function of their ionization state and the density of negative sites at the nanoplatelet surface (Fig. 1a). Schematically, the PEI adsorbs onto the β -Ni(OH)₂ surface in a mono- or multipoint way, and due

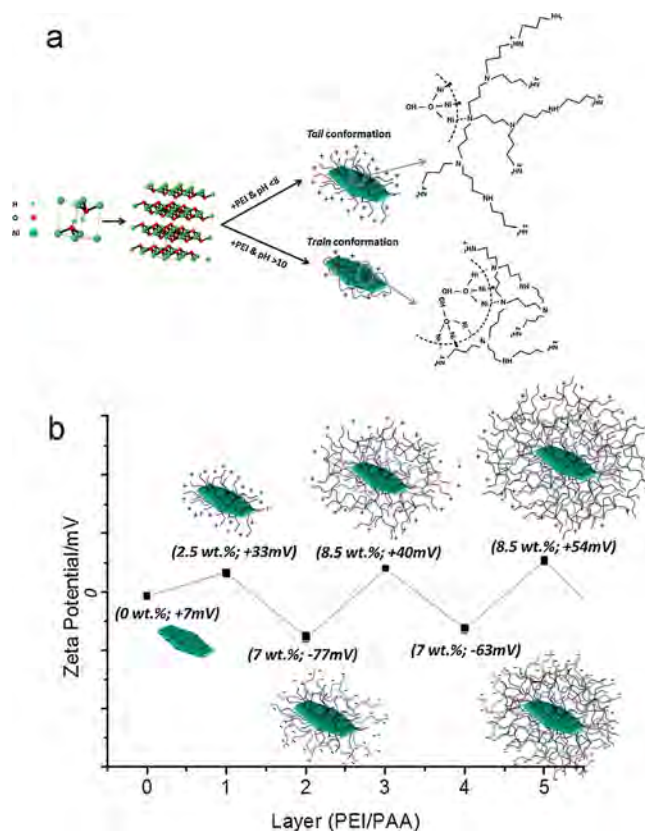


Fig. 1. Scheme of polycation adsorption onto the β -Ni(OH)₂ nanoplatelet adopting a tail or train conformation (a). Zeta potential evolution, core-shell scheme and added amount of polyelectrolyte in the LbL adsorption (b).

Table 2

Summary of the electrokinetics parameters of NH-1LbL, NH-3LbL and NH-5LbL core-shells and the EPD electric conditions.

Core-Shell Electrokinetics Parameters	NH-1L	NH-3L	NH-5L
Electrophoretic Mobility, u_e , ($\times 10^{-4}$ cm ² /V s)	0.82	0.77	0.71
Suspension Conductivity, σ , (μ S/cm)	0.84	0.63	0.50
Ratio of Mobility, σ/u_e	1.02	0.82	0.70
Current Density (μ A/cm ²)	40	12	8
Electric Field (V/cm)	75	76	80
Characteristic Time for EPD* (Eq. (2))	308	351	423

* Calculated for a volume of suspension of 30 ml and a sticking factor 1.

to their particular stereochemistry in each ionisation state, the branched chain adopts both conformations *tail* and *train*, respectively. For pH values higher than 8, we can consider that the PEI chain is completely ionized acquiring an open and strongly positive charged structure surrounding both faces of the nanoplatelets, while for pH values lower than 10, the PEI chain is multipoint adsorbed and becomes retracted onto the nanoplatelet surface, and then the whole system maintains a slightly positive charge.

Once the first layer of the PEI was formed, pH was accommodated to favour the deposition of the polyanion PAA. In this way, the LbL deposition of layers of PEI and PAA onto the nanoplatelet surfaces leads to an organic/inorganic core-shell nanostructure, where the organic corona will act as template in the further formation of a porous NiO-based structure. The exactly amount of each polyelectrolyte can be determined in terms of zeta potential in an aqueous suspension, and this parameter was used to modify in situ and massively the surface of β -Ni(OH)₂ nanoplatelets after their synthesis. Fig. 1b shows the zeta potential curve obtained after each polyanion and polycation addition. The plot also summarizes the amount of each polyelectrolyte added to the suspension in order to achieve a full covering or neutralization of the nanoplatelet surface or the previous polyelectrolyte layer, respectively.

When the nanoplatelet surfaces were massively modified in an aqueous suspension, they were diluted in EtOH up to achieve a EtOH:H₂O ratio of 19:1. Table 2 summarises the parameters which

define the electrokinetics behaviour of the modified nanoplatelets or core-shell nanostructures (NH-1LbL, NH-3LbL and NH-5LbL). Suspensions used for EPD have conductivities, σ , below 1 μ S/cm, and the electrophoretic mobility, u_e , of the core-shells ranges from 0.82 to 0.71×10^{-4} cm²/V s. The only current carriers in the suspension are the core-shells, which optimises the efficiency of the deposition process. Both electrokinetics properties results in different ratios of σ/u_e (from 1.02 to 0.70) and define the movement ability of the core-shells. In this sense, EPD tests were carried out applying current densities of 40, 30 and 20 μ A/cm², for the NH-1LbL (which implies electric fields ranging from 55 and 75 V/cm), and 40, 12 and 8 μ A/cm², for the NH-1LbL, NH-3LbL and NH-5LbL core-shells respectively, in order to maintain the electric field between 75–80 V/cm¹ and consider the decrease of σ/u_e values as the number of layers increases. Considering the starting conditions in the theoretical approach (Eqs. (1) and (2)), then characteristic times of the kinetics were adjusted to 308–423 1/s.

Plot in Fig. 2a shows the deposition kinetics of NH-1LbL suspensions when different current densities were applied (20, 30 and 40 mA/cm²). The straight line represents the theoretical kinetics of NH-1LbL suspensions, calculated considering the electrokinetics parameters listed in Table 2 and a sticking factor of 1 (Eqs. (1) and (2)), while dashed lines were used as eye guides for the experimental data plot. The increases of the applied electric field reasonably steps up the deposition process, and after 900 s the amount of deposited mass increases with the current density from the 25% to the 50% of the nanoplatelets in the suspension. However, in all cases the sticking factor of the NH-1LbL suspension barely achieves 0.1. Consequently, we can consider that nanoplatelets deposit discreetly under these conditions, compared to their electrokinetics ability of the dispersion. To determine the thickness range of the processed coatings, FE-SEM has been used to explore coatings in flat substrates. After the deposition of the 50% of powders (Fig. 2 a) in the NH-1LbL suspensions, 2.1 mg/cm² (4.6 mg) films with thicknesses of 5 μ m are obtained.

Plots in Fig. 2b, c and d show the kinetics of the deposition of the NH-1LbL, NH-3LbL and NH-5LbL core-shells respectively. Similarly to the plot in Fig. 2a, in all cases straight lines represent the theoretical kinetics of each system (following Eqs. (1) and (2)) and

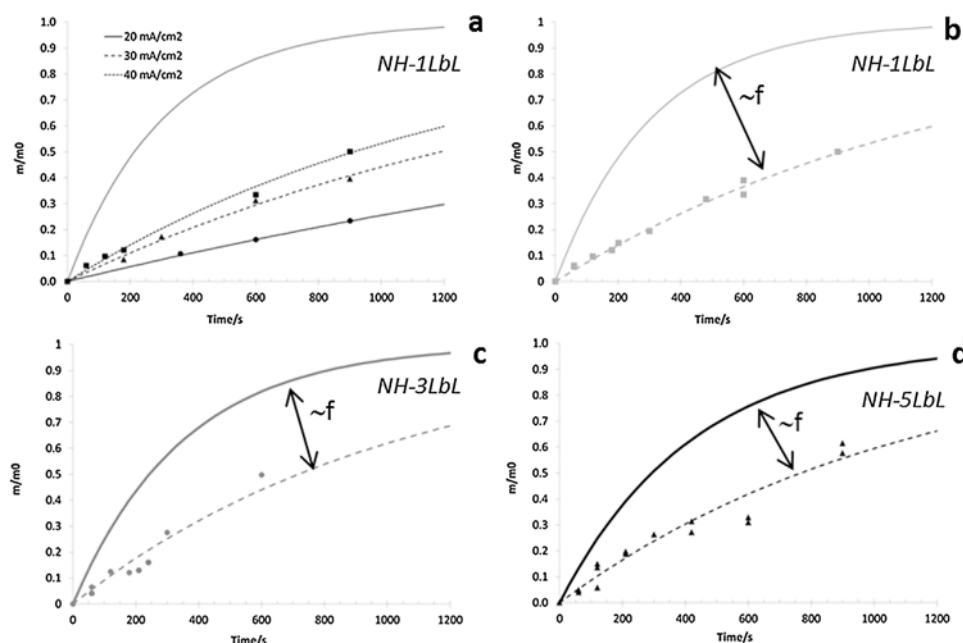


Fig. 2. EPD Kinetics for NH-1LbL core-shell deposition for current densities from 20–40 μ A/cm² (a), and for NH-1LbL (b), NH-3LbL (c) and NH-5LbL (d) at 10, 12, 8 μ A/cm², respectively.

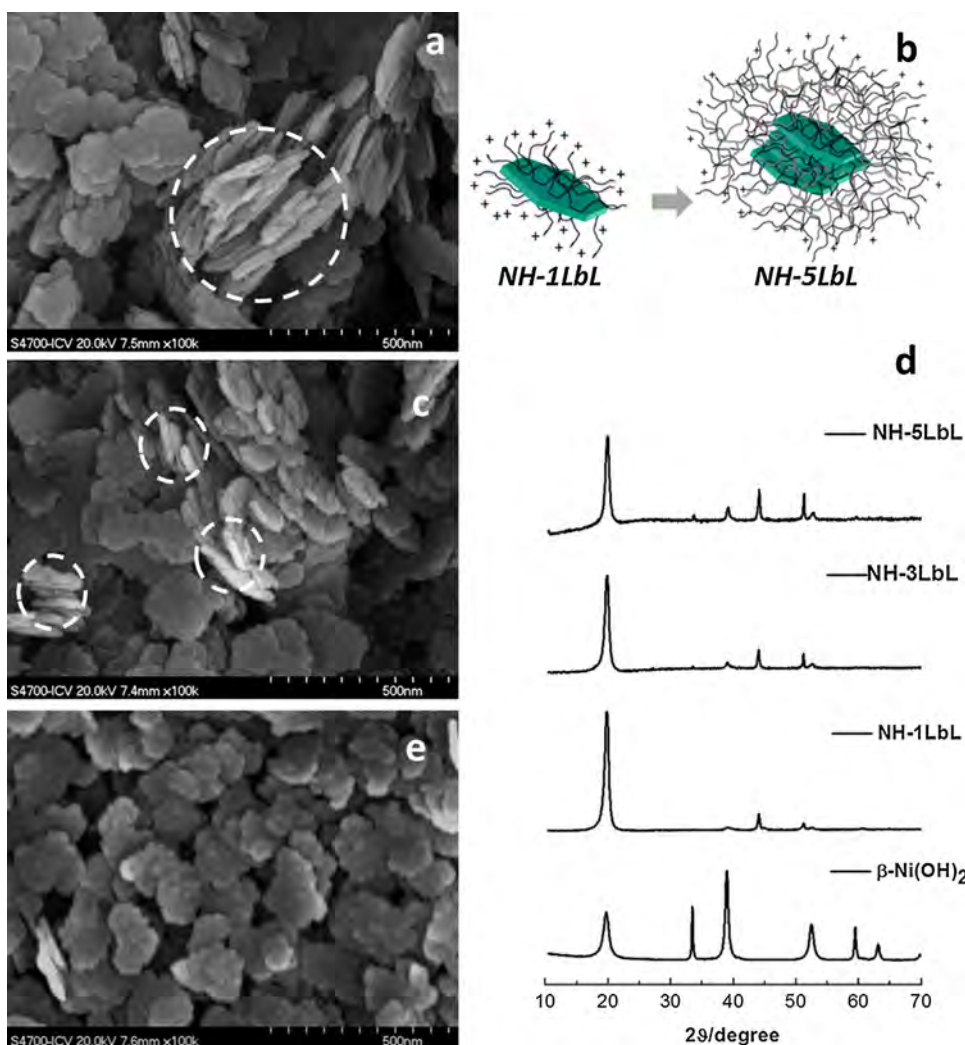


Fig. 3. FE-SEM micrographs of as-deposited NH-1LbL (a), NH-3LbL (c) and NH-5LbL (e) coatings, scheme of NH-1LbL and NH-5LbL core-shells (b) and XRD patterns of as-synthesized β -Ni(OH) $_2$ nanoplatelets and NH-1LbL, NH-3LbL and NH-5LbL coatings.

considering a sticking factor of 1 and starting conditions summarized in Table 2), while dashed lines represent the evolution of collected experimental data. Two facts can be corroborated associated to the deposit growth: deposition reliability slightly decreases, since the data of the deposited mass are more dispersed, and the sticking factor, f , doubles (from 0.10 to 0.2). So the deposition kinetics step up with the number of layers.

The low value of the sticking factor calculated for some systems is still matter of controversy in the literature. Stable suspensions should collapse at the working electrode to form the coating. So regularly the deposition takes place due to chemical changes in the electrode surroundings (increase of solid content, changes in pH, the increase of the ionic strength, etc.) [28]. Low ionic strength of the suspensions prepared in the present work softens collateral electrochemical phenomena at the working electrodes and stability of the core-shells prevail. So, electrostatic attraction with the electrode, hydrogen bridges and hydrodynamic forces could be some of the driving forces for the core-shell assembly and deposition, while the moderate agglomeration of the nanoplatelets could be the cause of the step up of the sticking factor with the number of layers of the LbL system.

Fig. 3 shows a detail of the NH-1LbL (Fig. 3a), NH-2LbL (Fig. 3c) and NH-5LbL (Fig. 3e) as-deposited microstructures where

differences in the nanoplatelets arrangement are evidenced. The 2D nanostructures lay parallel to the substrate surface for the NH-1LbL core-shells, while they seem to stack forming agglomerates deposited perpendicularly to the electrode in the case of the NH-5LbL system. In fact nanoplatelets agglomeration was pointed out as a reason of the deposition kinetics step up with the number of polyelectrolyte layers that form the core-shell. Fig. 3b schematise the nanoplatelets arrays as they can be imagine from the micrographs, while Fig. 3d shows the XRD of as-synthesized β -Ni(OH) $_2$ platelets as well as those of NH-1LbL, NH-3LbL and NH-5LbL coatings. In the coating spectra we can realise the presence of peaks belonging to the stainless steel used as substrates (γ (111) and γ (200)), but also if we compare the signals we can observe the intensity growth of (101), (102) and (101) reflections with the number of layers of polyanions/polycations. This can be definitely considered as an indicative of the increasing disorder. Indeed, the LbL approach seems to promote the agglomeration and certainly it determines the stacking behaviour of β -Ni(OH) $_2$ nanoplatelets in the suspension (Fig. 3b), and it affects to the core-shell arrangement during deposition.

As it is described in the introduction chapter, we should consider that the tendency of the β -Ni(OH) $_2$ platelets to align the (0 01) planes parallel to the substrate is due to the Van der Waals

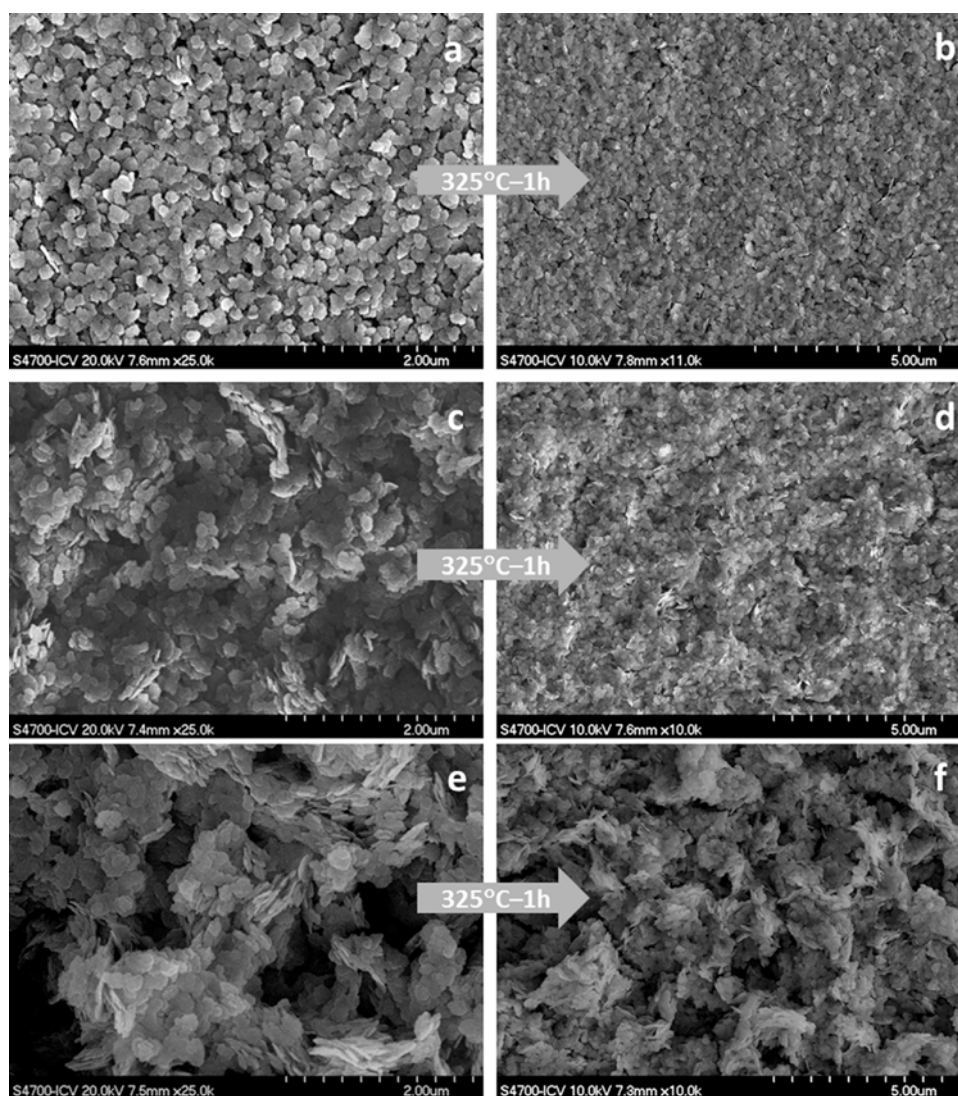


Fig. 4. FE-SEM micrographs of NH-1LbL and NO-1LbL (a and b), NH-3LbL and NO-3LbL (c and d), and NH-5LbL and NO-5LbL (e and f) coatings.

forces developed among particles and their interaction with the electro-hydrodynamic forces acting over them when approach to the substrate. Especially under smooth EPD conditions (for low current densities and low solid concentrations), their arrival to the working electrode slows down favouring nanoplatelets lying down. For LbL core-shell suspensions (NH-1LbL, NH-3LbL and NH-5LbL), the properties were adjusted not only to slow down the massive arrival of core-shells to the substrate (Table 2 and Fig. 3b), but for reduce as much as possible the conductivity of the suspension and avoid collateral phenomena derived from the electrophoretic movement of contra and co-ions, and the presence

Table 3

Morphological properties of the NiO powders and NO-1LbL, NO-3LbL and NO-5LbL core-shells.

Morphology of β -Ni(OH) ₂ and NiO nanoplatelets	NiO		
BET SSA (m ² /g)	83.71		
Open SSA by t-plot (m ² /g)	82.39		
Total Pore Volume N ₂ (cm ³ /g)	0.46		
Micropore Volume by t-plot (cm ³ /g)	1.32		
Morphology of the Core-Shell structures	NO-1L	NO-3L	NO-5L
SSA determined by MIP (m ² /g)	49.91	22.71	10.25
Total Pore Volume MIP (cm ³ /g)	1.27	1.37	0.79

of excessively charged nanostructures. On the other hand, low suspension conductivity relatively impedes the nanoplatelets flocculation in the suspension [29], and is enough to maintain a stable current density during EPD providing reliability to the mesostructures formation. Under these conditions, the electrostatic contribution to the nanoplatelets stability was reduced to the minimum necessary to assure the electrophoretic movement and the highest deposit yield. Thus, the flocculation of the nanoplatelets at the substrate is due to the PEI neutralization (at the 1st, 3st and 5th layer) under basic conditions at the electrode surroundings, and then nanoplatelets packing was favoured by the reduction of the interparticle depletion and the electrostatic repulsion among them [30,31]. Consequently, the adhesion of the film to the substrate as well as the own cohesion among the nanoplatelets, depends on the manipulation of the ionization and conformation of the surface modifiers at the organic corona of the core-shell system. Therefore, the decrement of the interparticles forces leads to that the electro-hydrodynamic forces govern the nanoentities arrangement. In this sense, micrographs in Fig. 3(a, c and e) show that the increase of the number of layers of the shell structure alters the hydrodynamics and promotes disorder under the reported smooth EPD conditions.

After β -Ni(OH)₂ nanoplatelets shaping, the EPD coatings were annealed by 1 h at 325 °C to obtain a NiO consolidated structure,

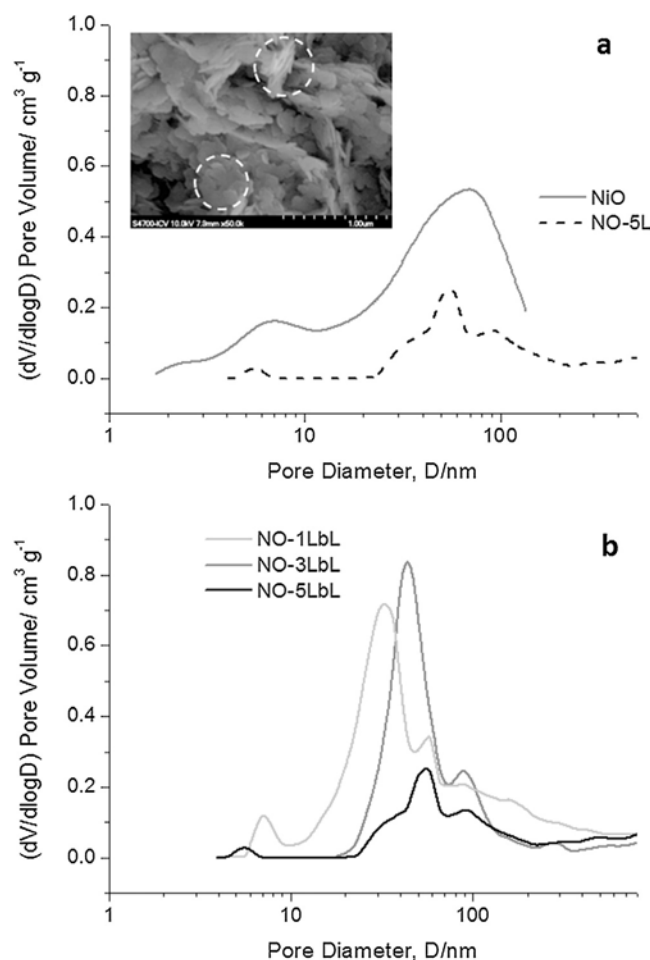


Fig. 5. Pore size distribution of NiO powders and NO-5LbL core-shell determined by N_2 isotherms and MIP, respectively, and a detail of the NO-5LbL microstructure (a). Pore size distribution of NO-1LbL, NO-3LbL and NO-5LbL core-shells determined by MIP (b).

and then the surfaces of as-deposited hydroxide-based films as well as that of the consolidated oxide-based structures were inspected by SEM. Fig. 4 shows the surface of NH-1LbL and NO-1LbL (a and b), NH-3LbL and NO-3LbL (c and d), and NH-5LbL and NO-5LbL (e and f) coatings. Low magnification micrographs evidence the uniform coatings built by EPD, and the increasing disorder promoted by the LbL modification of the nanoplatelets during deposition, even strikingly than those studied in a previous work for more intense EPD conditions [22]. However, a common factor for all of the LbL coatings is that their microstructures maintain their structural integrity after the thermal annealing.

To determine the microstructural sturdiness of the NO-5LbL coatings, NiO-based electrodes were electrochemically tested in terms of capacity, and the micro, meso and macroporosity of the consolidated microstructures after the thermal treatment was characterised.

First at all, micro and mesoporosity of the as-synthesized (unmodified) and calcined NiO powder was determined by N_2 adsorption/desorption isotherm. Main morphological properties, such as the specific surface area (SSA) and pore size distribution (PSD), were summarised in Table 3, while PSD are plotted in Fig. 5a (straight line). Results reveal that the thermal annealing leads to powders with an open SSA of $83.71 \text{ m}^2/\text{g}$, with a fraction of small mesopores with diameters ranging 4–10 nm, which corresponds to voids among nanoparticles forming the nanoplatelets [27], and a wide fraction of the large macro- mesoporosity (30–100 nm) that represents the inter-nanoplatelets spaces.

On the other hand, meso and macroporosity of the core-shells scrapped from the substrate after the EPD coating calcination was determined by Mercury Intrusion Porosimetry (MIP). Results of MIP are also shown in Table 3 and Fig. 5a (dashed line) and Fig. 5b. The SSA of the core-shells decreases with the number of polyelectrolyte layers, as well as the volume of pores. Nevertheless, the PSD obtained by MIP for the analysis of NO-5L core-shells verifies the presence of a fraction of macro- mesoporosity (30–100 nm) in the NO-5LbL coating after the thermal treatment. The detail of the microstructure in the inset identifies the nanoplatelets stacking in the sintered microstructure of the NO-5LbL semiconductor film. Plot in Fig. 5b shows the population of mesopores and small macropores of NO-1LbL, NO-3LbL and NO-5LbL coatings after the thermal treatment. The plot quantifies the decrease of the porous volume with the increase of the number polyelectrolyte layers in this range of porosity, and also it shows the increasing tendency of the size of the residual spaces among platelets formed during the coating sintering.

Those results evidence the consolidation of the nanoplatelets stacking during the thermal treatment, which confers the structural integrity to the porous coating, and also corroborate the presence of agglomerates (marked in the micrographs in Fig. 3). In this sense, we can consider that the SSA of the nanoentities decreases from $83.71 \text{ m}^2/\text{g}$ for unmodified NiO powder to $10.25 \text{ m}^2/\text{g}$ of the NO-5LbL nanoplatelets staking, but it is still enough to favors electrolyte impregnation and ion diffusion. The decreasing of SSA and the volume of porous in the meso- macro-range (30–100 nm) is a consequence of the

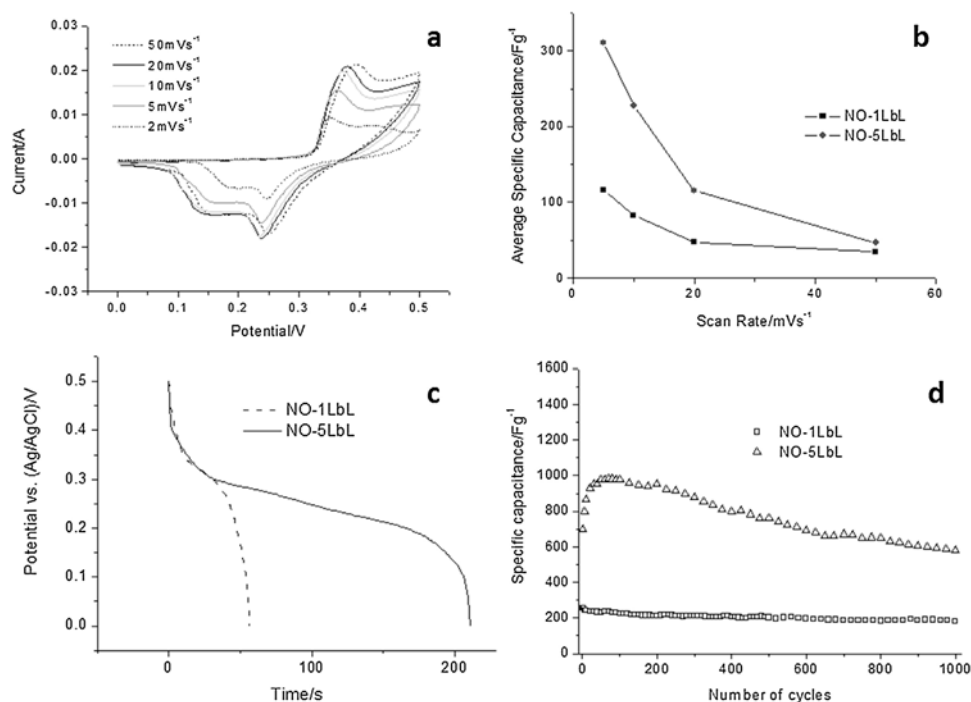


Fig. 6. Comparative of the electrochemical tests between the samples NO-5LbL and NO-1LbL [22]. Cyclic voltammograms of the sample NO-5LbL at different scan rates (a), variation of specific capacitance with scan rate (b), Galvanostatic discharge curves (c) and Cyclic Chronopotentiometric measurements at a current density of 2 A/g (d).

nanoplatelets agglomeration promoted by the LbL modification, and further sintering of the coating.

Consequently, for further characterization we should consider that the NO-5LbL coating exhibits a well consolidated and interconnected but also open macroporous microstructure, with a larger macroporosity in the range of 2–5 μm (Fig. 4f) and a moderated mesoporosity of 30–100 nm.

Electrochemical performance of the sample NO-5LbL was evaluated by cyclic voltammograms (CV) and galvanostatic charge/discharge tests (CP). The results were compared with a NO-1LbL electrode with a similar deposited mass [21] in Fig. 6. The CV curves for NO-5LbL were measured at different sweep rate 5, 10, 20 and 50 mV/s (Fig. 6a). All plots present faradic profile with oxidation and reduction peaks associated to the charge and discharge processes, respectively. The redox reaction is identified with the following equation:



An increase of the window of potential (ΔV) was observed. The anodic peaks shifted to positive potentials and the cathodic peak to the negative potential with scan rate due to the polarization in the electrode material and the OH^- ions intercalated quickly at the interface of electrode/electrolyte at the high scan rate (50 mV/s). The values of peaks separation mean a high rate capability and a good reversibility, exhibiting a fast kinetic of the indicated faradaic reaction.

Fig. 6b shows the variations of specific capacitance (calculated by the integration of the cathodic peak area shown in Eqs. (3)–(6) of the experimental section) with the scan rate for the two modified electrodes. Both curves show a gradual decrease of the capacitance values, however, the data of the sample NO-5LbL is above the sample NO-1LbL displaying a higher diffusion of alkali cations into the porous and disorganized microstructure, and thereby the access to a major fraction of active sites and a better contact of the electrolyte with the electroactive material.

On the other hand, the cycling stability of the NO-5LbL electrode was evaluated by galvanostatic charge/discharge curves at the current density of 2 A/g in the voltage range of 0–0.5 V for 1000 cycles. The discharge plots (Fig. 6c) are composed of three steps. The first two processes are assigned with the reduction of Ni^{+2} and are subdivided in a fast initial potential drop followed by a slow potential decay. Contrarily the third, which shows a faster voltage drop, corresponds to an Electric Double Layer Contribution (EDLC). Both electrodes presented similar slopes for the first and second step, and main differ in the discharge rate of the second step (slower in NO-5LbL coating), which indicates a higher redox contribution for the opener microstructure in the NO-5LbL electrode. The macroporous microstructure of the NO-5LbL results in the increases of the active surface leading to a higher specific capacitance. The high density of macropores produced by the LbL surface modification generates new diffusion pathways which favor the electrolyte impregnation, while the ceramic microstructure connectivity maintains by sintering. The higher surface area exposed to the electrolyte solution maximize the insertion of the OH^- ions favoring the faradaic reaction.

In addition, Fig. 6d shows the trend of the specific capacitance vs. the number of cycles. The specific capacitance increases with the number of organic layers, but also NO-5LbL electrode exhibits a significant increase of the specific capacitance, from 650 to 1000 F/g, between the first 50–100 cycles due to the activation and stabilization of the opener microstructure. The electrolyte ions have to go through every nook to favor the contact with all the active sites in the semiconductor structure. After 100 cycles, the specific capacitance value starts to decrease down to 650 F/g, stabilizing the capacitance retention (100%) after 1000 cycles.

4. Conclusions

Synthetic $\beta\text{-Ni}(\text{OH})_2$ nanoplatelets superficially modified by a 1, 3 and 5 LbL organic shells were employed to manipulate the

microstructure of the EPD coating. In β -Ni(OH)₂ deposition, we demonstrated that the new microstructural arrangement of nanoparticles with 2D morphology is a consequence of both processing strategies: (i) the LbL modification of their surfaces and (ii) their electrically-driven deposition.

The dispersion of core-shell structures was adjusted to slow down the massive arrival of modified nanoplatelets to the substrate, in order to reduce as much as possible the collateral phenomena derived from the electrophoretic movement of contra and co-ions. The electrostatic contribution to the nanoplatelets stability was also reduced to the minimum necessary to assure the electrophoretic movement and the highest deposit yield, while smooth EPD conditions (for low current densities and low solid concentrations) favor nanoplatelets lying down. Nanoplatelets deposit discreetly compared to their electrokinetics ability (sticking factor of 0.1), and only a 50% of the nanoplatelets in the suspension can be deposited after 900 s.

Results demonstrate that under these conditions, the LbL modification of the nanoplatelets surfaces promotes a moderated agglomeration, and specifically determines their stacking behavior in the suspension and their arrangement during deposition. The increase of the number of layers at the shell structure alters the hydrodynamics and promotes disorder, and the formation of an open microstructure, even under the reported smooth EPD conditions. Achieved moderated agglomeration allows the full and homogeneous coating of 3D substrates.

NO-5LbL coatings of 2D Ni substrates exhibit a well consolidated and interconnected but also open macroporous microstructure with a larger macroporosity in the range of 2–5 μ m and a moderated mesoporosity of 30–100 nm. **This extremely open porous microstructure can be reproduced in coatings of 3D Ni foams**, stabilizing a specific capacitance of 650 F/g measured at 2 A/g after 1000 cycles.

Once the stability conditions of the NH-5LbL suspensions were optimized for a successful EPD, the amount of deposited mass will depend on the deposition time and the electric field applied over the suspension. Further work should be done to study the electrochemical efficiency of the electrode as a function of the deposited mass and the free surface able to react with the electrolyte.

This clearly opens the possibility of controlling the nanoplatelets orientation by designing the stabilization system in EPD. The adhesion of the film to the substrate as well as the own cohesion among the nanoplatelets, depend on the manipulation of the ionization and conformation of the surface modifiers at the organic corona of the core-shell system. The manipulation of the stability conditions promote the decrement of the interparticles forces and leads to that the electro-hydrodynamic forces govern the nanoentities arrangement. In this way, the 2D nanostructures lay parallel to the substrate surface for the NH-1LbL core-shells, while they stack forming agglomerates and deposit perpendicularly to the electrode in the case of the NH-5LbL system.

Acknowledgements

The authors acknowledge the support of the project S2013/MIT-2862 and MAT2015-70780-C4-1 and Dr. Z Gonzalez acknowledges to JECS-TRUST fund contract 201481.

References

- [1] M. Nasilowski, B. Mahler, E. Lhuillier, S. Ithurria, B. Dubertret, Two-Dimensional Colloidal Nanocrystals, *Chem. Rev.* 116 (2016) 10934–10982, doi:http://dx.doi.org/10.1021/acs.chemrev.6b00164.
- [2] J.K. Park, I.H. Do, P. Askeland, L.T. Drzal, Electrodeposition of exfoliated graphite nanoplatelets onto carbon fibers and properties of their epoxy composites,

- Compos. Sci. Technol.* 68 (2008) 1734–1741, doi:http://dx.doi.org/10.1016/j.compscitech.2008.02.002.
- [3] J.H. Park, J.M. Park, Photo-generated cathodic protection performance of electrophoretically Co-deposited layers of TiO₂ nanoparticles and graphene nanoplatelets on steel substrate, *Surf. Coat. Technol.* 258 (2014) 62–71, doi: http://dx.doi.org/10.1016/j.surfcoat.2014.10.002.
- [4] Y. Zhang, J.R.G. Evans, Morphologies developed by the drying of droplets containing dispersed and aggregated layered double hydroxide platelets, *J. Colloid Interface Sci.* 395 (2013) 11–17, doi:http://dx.doi.org/10.1016/j.jcis.2012.09.089.
- [5] K.R. Kort, S. Banerjee, Oriented electrophoretic deposition of GdOCl nanoplatelets, *J. Phys. Chem. B* 117 (2013) 1585–1591, doi:http://dx.doi.org/10.1021/jp3051142.
- [6] J. Liu, Z. Wu, T. Li, D. Zhou, K. Zhang, Y. Sheng, J. Cui, H. Zhang, B. Yang, Electrophoretic deposition of fluorescent Cu and Au sheets for light-emitting diodes, *Nanoscale* 8 (2016) 395–402, doi:http://dx.doi.org/10.1039/c5nr06599b.
- [7] F. Withers, H. Yang, L. Britnell, A.P. Rooney, E. Lewis, A. Felten, C.R. Woods, V. Sanchez Romaguera, T. Georgiou, A. Eckmann, Y.J. Kim, S.G. Yeates, S.J. Haigh, A. K. Geim, K.S. Novoselov, C. Casiraghi, Heterostructures produced from nanosheet-based inks, *Nano Lett.* 14 (2014) 3987–3992, doi:http://dx.doi.org/10.1021/nl501355j.
- [8] T.H. Lin, W.H. Huang, I.K. Jun, P. Jiang, Bioinspired assembly of surface-roughened nanoplatelets, *J. Colloid Interface Sci.* 344 (2010) 272–278, doi: http://dx.doi.org/10.1016/j.jcis.2009.12.060.
- [9] T.H. Lin, W.H. Huang, I.K. Jun, P. Jiang, Electrophoretic deposition of biomimetic nanocomposites, *Electrochem. Commun.* 11 (2009) 14–17, doi:http://dx.doi.org/10.1016/j.elecom.2008.10.018.
- [10] T.H. Lin, W.H. Huang, I.K. Jun, P. Jiang, Bioinspired assembly of colloidal nanoplatelets by electric field, *Chem. Mater.* 21 (2009) 2039–2044, doi:http://dx.doi.org/10.1021/cm802372f.
- [11] R. Hoffmann, S. Sanctis, E. Erdem, S. Weber, Zinc diketones as single source precursors for ZnO nanoparticles: microwave-assisted synthesis, electrophoretic deposition and field-effect transistor device, *J. Mater.* (2016) 7345–7352, doi:http://dx.doi.org/10.1039/c6tc02489k.
- [12] M. Verde, M. Peiteado, A.C. Caballero, M. Villegas, B. Ferrari, Electrophoretic Deposition of Transparent ZnO Thin Films from Highly Stabilized Colloidal Suspensions, *J. Colloid Interface Sci.* 373 (2012) 27–33, doi:http://dx.doi.org/10.1016/j.jcis.2011.09.039.
- [13] M. Verde, A.C. Caballero, Y. Iglesias, M. Villegas, B. Ferrari, Electrophoretic Deposition of Flake-Shaped ZnO Nanoparticles, *J. Electrochem. Soc.* 157 (2010) H55–H59, doi:http://dx.doi.org/10.1149/1.3247343.
- [14] M. Diba, D.W.H. Fam, A.R. Boccaccini, M.S.P. Shaffer, Electrophoretic deposition of graphene-related materials: A review of the fundamentals, *Prog. Mater. Sci.* 82 (2016) 83–117, doi:http://dx.doi.org/10.1016/j.pmatsci.2016.03.002.
- [15] S.J. An, Y. Zhu, S.H. Lee, M.D. Stoller, T. Emilsson, S. Park, A. Velamakanni, J. An, R.S. Ruoff, Thin film fabrication and simultaneous anodic reduction of deposited graphene oxide platelets by electrophoretic deposition, *J. Phys. Chem. Lett.* 1 (2010) 1259–1263, doi:http://dx.doi.org/10.1021/jz100080c.
- [16] B. Giera, L.A. Zepeda-Ruiz, A.J. Pascall, T.H. Weisgraber, Mesoscale Particle-Based Model of Electrophoretic Deposition, *Langmuir* 33 (2) (2017) 652–661, doi:http://dx.doi.org/10.1021/acs.langmuir.6b04010.
- [17] C.L. Wirth, R.M. Rock, P.J. Sides, D.C. Prieve, Single and pairwise motion of particles near an ideally polarizable electrode, *Langmuir* 27 (2011) 9781–9791, doi:http://dx.doi.org/10.1021/la2017038.
- [18] L. Jankovic, H. Pálková, V. Hronsky, The effect of acid treatment on the structure and surface acidity of tetraalkylammonium-montmorillonites, *Journal of Colloid and Interface Science* 95 (2013) 166–175, doi:http://dx.doi.org/10.1016/j.jcis.2012.12.027.
- [19] M.M. Sk, C.Y. Yue, K. Ghosh, R.K. Jena, Review on advances in porous nanostructured nickel oxides and their composite electrodes for high-performance supercapacitors, *J. Power Sources* 308 (2016) 121–140, doi: http://dx.doi.org/10.1016/j.jpowsour.2016.01.056.
- [20] C. Hua, K. Changa, T. Hsub, The Synergistic Influences of OH[−] Concentration and Electrolyte Conductivity on the Redox Behavior of Ni(OH)₂/NiOOH, *J. Electrochem. Soc.* 155 (2008) F196–F200, doi:http://dx.doi.org/10.1149/1.2945911.
- [21] Y. Castro, B. Ferrari, R. Moreno, A. Durán, Coatings produced by electrophoretic deposition from nano-particulate silica sol-gel suspensions, *Surf. Coatings Technol.* 182 (2004) 199–203, doi:http://dx.doi.org/10.1016/j.surfcoat.2003.07.001.
- [22] Z. Gonzalez, B. Ferrari, A.J. Sanchez-Herencia, A. Caballero, J. Morales, Use of Polyelectrolytes for the Fabrication of Porous NiO Films by Electrophoretic Deposition for Supercapacitor Electrodes, *Electrochim. Acta* 211 (2016) 110–118, doi:http://dx.doi.org/10.1016/j.electacta.2016.06.014.
- [23] Z. Gonzalez, B. Ferrari, A.J. Sanchez-Herencia, A. Caballero, J. Morales, Relevance of the Semiconductor Microstructure in the Pseudocapacitance of the Electrodes Fabricated by EPD of Binder-Free β -Ni(OH)₂ Nanoplatelets, *J. Electrochem. Soc.* 162 (2015) D3001–D3012, doi:http://dx.doi.org/10.1149/2.010151jes.
- [24] K.T. Sullivan, C. Zhu, D.J. Tanaka, J.D. Kuntz, E.B. Duoss, A.E. Gash, Electrophoretic deposition of thermally onto micro-engineered electrodes prepared by direct-ink writing, *J. Phys. Chem. B* 117 (2013) 1686–1693, doi: http://dx.doi.org/10.1021/jp306440t.

- [25] M.-S. Wu, C.-Y. Huang, K.-H. Lin, Electrophoretic deposition of nickel oxide electrode for high-rate electrochemical capacitors, *J. Power Sources* 186 (2009) 557–564, doi:<http://dx.doi.org/10.1016/j.jpowsour.2008.10.049>.
- [26] S. Cabanas-Polo, Z. Gonzalez, A.J. Sanchez-Herencia, B. Ferrari, A. Caballero, L. Hernán, J. Morales, Cyclability of binder-free β -Ni(OH)₂ anodes shaped by EPD for Li-ion batteries, *J. Eur. Ceram. Soc.* 35 (2015) 573–584, doi:<http://dx.doi.org/10.1016/j.jeurceramsoc.2014.08.014>.
- [27] A. Caballero, L. Hernán, J. Morales, Z. González, A.J. Sánchez-Herencia, B. Ferrari, A high-capacity anode for lithium batteries consisting of mesoporous NiO nanoplatelets, *Energy and Fuels* 27 (2013) 5545–5551, doi:<http://dx.doi.org/10.1021/ef400797r>.
- [28] B. Ferrari, R. Moreno, EPD kinetics: A review, *J. Eur. Ceram. Soc.* 30 (2010) 1069–1078, doi:<http://dx.doi.org/10.1016/j.jeurceramsoc.2009.08.022>.
- [29] S. Cabanas-Polo, Z. Gonzalez, A.J. Sanchez-Herencia, B. Ferrari, Influence of ultrasound on the instantaneous synthesis of tridimensional α -Ni(OH)₂ nanostructures and derived NiO nanoparticles, *CrystEngComm* 17 (2015) 6193–6206, doi:<http://dx.doi.org/10.1039/C5CE00876J>.
- [30] A. Dietrich, A. Neubrand, Effects of Particle Size and Molecular Weight of Polyethylenimine on Properties of Nanoparticulate Silicon Dispersions, *J. Am. Ceram. Soc.* 84 (2001) 806–812, doi:<http://dx.doi.org/10.1111/j.1151-2916.2001.tb00745.x>.
- [31] C. Mendoza, Z. González, Y. Castro, E. Gordo, B. Ferrari, Improvement of TiN nanoparticles EPD inducing steric stabilization in non-aqueous suspensions, *J. Eur. Ceram. Soc.* 36 (2016) 307–317, doi:<http://dx.doi.org/10.1016/j.jeurceramsoc.2015.06.023>.

J. Yus, E. Chinarro, B. Ferrari, Z. Gonzalez.

The Effect of the Substrate on the Conductivity of NiO Electrodes in Electrochemical Capacitor Shaped by Electrophoretic Deposition.

ECS Transactions **2018**, 82(1):97-104.

doi: 10.1149/08201.0097ecst

The Effect of the Substrate on the Conductivity of NiO Electrodes in Electrochemical Capacitor Shaped by Electrophoretic Deposition

J. Yus^a, E. Chinarro^a, B. Ferrari^a, and Z. González^a

^a Institute of Ceramics and Glass, CSIC, Madrid 28049, SPAIN

In order to study the effect of the substrate on the electrochemical performance of pseudocapacitor electrodes, NiO nanoparticles have been deposited by EPD on different substrates, such as Ni foams and Ni, Cu and stainless steel foils. The electrochemical impedance spectroscopy was used to determine the electron charge-transfer resistance as well as the ion-diffusion resistance of the different substrate/coating systems. Lower charge-transfer resistance and higher ion-diffusion rates were measured when Ni foils are used as substrate or collector. That means NiO/Ni foil system has the highest charge-transfer and the best electrolyte accessibility, which is an evidence of the excellent electrochemical performance of the semiconductor coating and the metallic substrate. On the other hand, the shape of the electrode has been also studied because it is strongly related with the ion-diffusion rate. Although the Ni foams have a larger specific surface area, their charge-transfer resistance results higher than in foil substrates.

Introduction

In the last decade pseudocapacitors have been extensively studied due to their promising applications as energy storage devices. This kind of supercapacitors is based on transition-metal oxides and conducting polymers, which store the energy through redox reactions which take place on the electrode surface. The mechanical flexibility of conducting polymers makes them easy to process. However, they are not stable in time because their easy degradation, which results in a low cyclability. In contrast, metal oxides present better cyclability because of their higher robustness.

Among transition metals, ruthenium oxides have shown the best capacitance response. It offers a very good cyclability during thousands of cycles, due to its high thermal and chemical stability, but the viability of those electrodes is limited because of the elevated cost of ruthenium [1]. The high price of this oxide has boosted the quest of cheaper new ones. Nickel oxide is a good option due to its high theoretical specific capacitance of 3750 F/g [2], ready availability and low cost [3].

Electrophoretic deposition (EPD) is in comparison with other conventional methods a very interesting alternative which offers several advantages, such as low cost, suitable production, low processing time, and its easy transference to the industry[1]. In addition, EPD is a non-vacuum and room-temperature method which also offers the control of the deposited mass, the thickness of the films by the concentration of the suspension, applied potential and deposition time. In previous works, this method has been used to shape supercapacitors electrodes. [4–7]

In this study, EPD processing is employed in the fabrication of pseudocapacitor electrodes, which consist of a metallic substrate covered by a NiO layer. The Nickel oxide

has been synthesized through a calcination of $\text{Ni}(\text{OH})_2$ obtained by the precipitation of a dissolved Ni salt in presence of NH_3 . [8]

After the electrophoretic deposition and subsequent calcination, a well-connected and robust microstructure was achieved by the necks formation among packed nanoparticles. The pseudocapacitor electrochemical behavior of as-prepared electrodes was determined by Electrochemical Impedance Spectroscopy (EIS) in order to determine charge transfer between the active material (NiO) and the collector (substrate) in EPD electrodes. [9]

Materials and Methods

Ni foam and Ni, stainless steel (SS) and Cu foils were electrophoretically coated by $\text{Ni}(\text{OH})_2$ nanoplatelets stabilized in $\text{EtOH} : \text{H}_2\text{O} 19 : 1 + \text{PEI} 2.5\%$ (1g/L). The potentiostatic parameters were Bias Voltage - 200 V applied for 15 s, achieving a current intensity of 0.02 A. All experiments were carried out using a power source Keithley 2660 (United States). The volume of suspension per EPD experiment was 30 ml and the distance between the electrodes in the electrophoretic cell was kept constant at 2 cm. Moreover, no binder was added to the mixture.

After the deposition, coatings were calcined at 325 °C during 1 h, under inert atmosphere, with heating and cooling rates of 10 °C/min, resulting in consolidated NiO films as figure 1 shows.

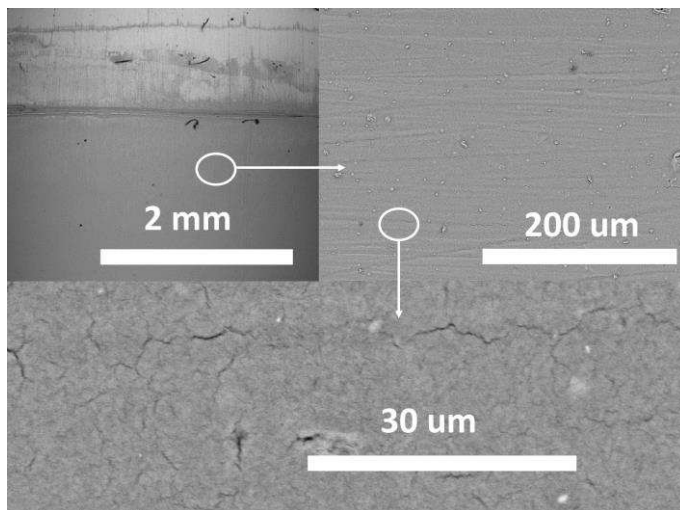


Figure 1. SEM image of the deposited and sintered electrodes at 325 °C during one hour under argon atmosphere.

Surface morphology and microstructure of the electrodes were assessed by field emission scanning electron microscopy (FESEM) in an S-4700 microscope (Hitachi, JAPAN) employing an accelerating voltage of 20 kV. The N_2 adsorption/desorption isotherms and BET specific surface area of the NiO powders were determined with a Micromeritics ASAP 2020 (USA). The crystallographic identification of the powder was carried out by D8 Advance Bruker X-ray diffractometer with Cu $K\alpha$ radiation ($\lambda = 1.5418 \text{ \AA}$) at 40KV and 30 mA and $2\theta = 10\text{--}70^\circ$, (Bruker, Germany). The crystal size and the crystallographic cell parameters were calculated by the Scherrer method.

Electrochemical impedance spectroscopy (EIS) measurements were done using an Autolab PGSTAT302N potentiostat, Metrohm (Switzerland) in 1 M NaOH electrolyte, at

room temperature, using a 3-electrode cell configuration. The as-prepared electrodes were used as working electrodes, a platinum foil as counter electrode and an Ag/AgCl electrode as reference. The frequency was swept from 10^5 down to 10^{-1} Hz. All the experiments were carried out at the open circuit potential.

Results and Discussion

NiO coatings were characterized before shaping and sintering. Figure 2 shows the overall size of NiO nanoplatelets forming the electrodes. The lengths of the platelets are 100-300 nm and the thickness is around 20-30 nm.

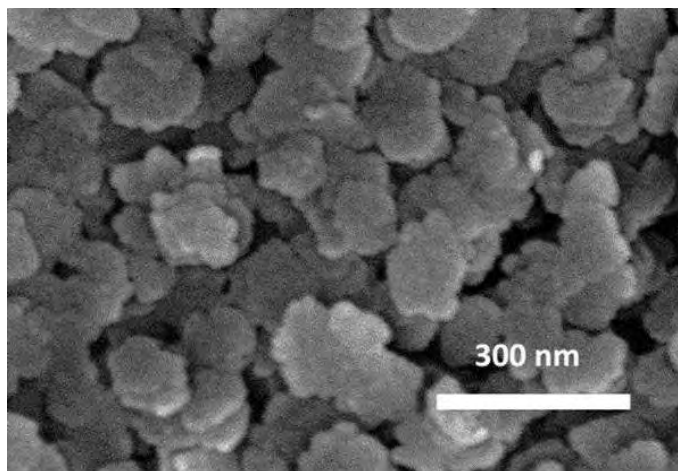


Figure 2. FESEM image of as-sintered NiO coating.

The NiO powder was scratched after the thermal treatment and analyzed by XRD and N_2 Adsorption/desorption. In Figure 3a, the peaks identified at the XRD diffractogram of NiO powders correspond to the Miller indices (111), (200) and (220). NiO presents a face-centered cubic lattice (space group: $Fm\bar{3}m$) with a unit cell dimension of 4.204 Å and a mean crystallite size of 13 nm calculated from the Scherrer equation.

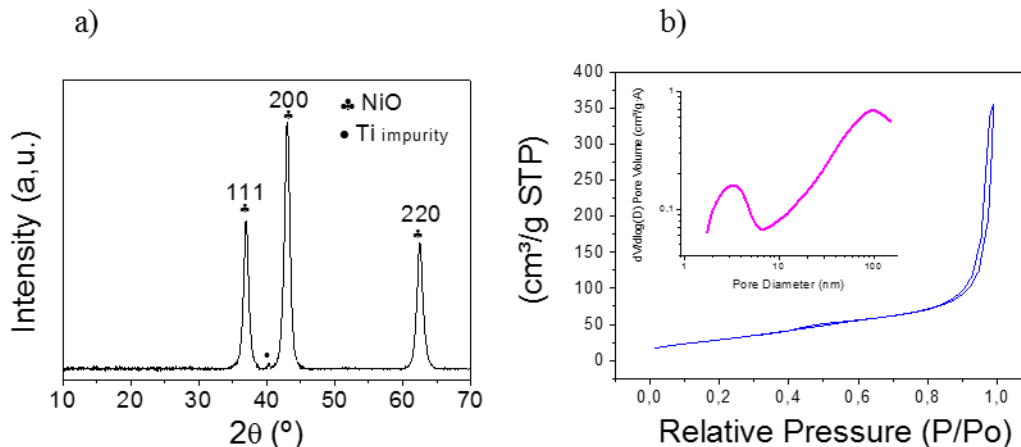


Figure 3. a) XRD patterns of the NiO powders after the synthesis and calcined. b) N_2 gas adsorption-desorption isotherms and pore size distribution of NiO.

The N₂ adsorption/desorption isotherms and the corresponding pore size distributions of NiO are presented in figure 3b. The curve exhibits the IV isotherms with an H1-type hysteresis loop ($P/P_0 > 0.8$), typical in materials which exhibit a narrow range of mesopores. The low adsorbed volume at very low relative pressure ($P/P_0 < 0.01$) evidences the absence of micropores. In addition, we can find a small hysteresis loop between 0.4 and 0.7 P/P_0 which indicates the presence of mesoporosity with different sizes. In fact a bimodal pore distribution centered in 3 and 100 nm can be observed in the plot at the inset. The resultant average pore size and pore volume were 18.2 nm and 0.460 cm³/g, respectively, while the specific surface area corresponding to this NiO structure is as high as 83.7 m²/g.

The EIS has been measured in order to determine the electrochemical response of our electrodes and the difference resistance obtained depending on the characteristics and the nature of the substrate. Nyquist plots exhibit two differentiated parts. At high values of frequencies there is a depressed semicircle which represents the charge-transfer resistance and, a straight line in the low frequency region which corresponds to the faradaic effect. Thus, a steeper slope signifies higher ion-diffusion rate and an ideal capacitive behavior. [11]

The figure 4 presents the Nyquist plots determined for NiO electrodes of 1 mg weight deposited by EPD covering Ni foams and Ni foil. Foil-shaped substrate exhibits a steeper slope at low frequencies indicating that the total resistance of the system is higher in foam than in foil substrates. However, the depressed semicircle does not appear in the high frequency region because the nature of the substrate and the electrode in the same. Thus, the substrate is oxidized and reduced contributing to the faradaic effect of the Ni-based electrodes.

The electronic charge transfer depends on the conductor section. Larger sections imply easier electronic transfer and a smaller semicircle is obtained, which sometimes can be even negligible. In this case, the foil has a larger section than the foam. Therefore, the transference of electrons through the foil is easier than through the foam.

On the other hand, charge transfer depends on other factors related to the microstructure of the coating, such as the continuity of the consolidated structure or the porosity of the layer. In fact, NiO layers should cover uniformly the entire substrate and, if the redox reactions take place on the surface, when the layer is too dense, part of deposited NiO cannot be considered as active material. Although, the exposed NiO surface is larger in the foam, the electron charge transfer is higher in the foil. Consequently, the diffusion not only depends on the specific surface area of the substrate, it should mainly depend on the microstructural connectivity and exposed surface of the NiO coating.

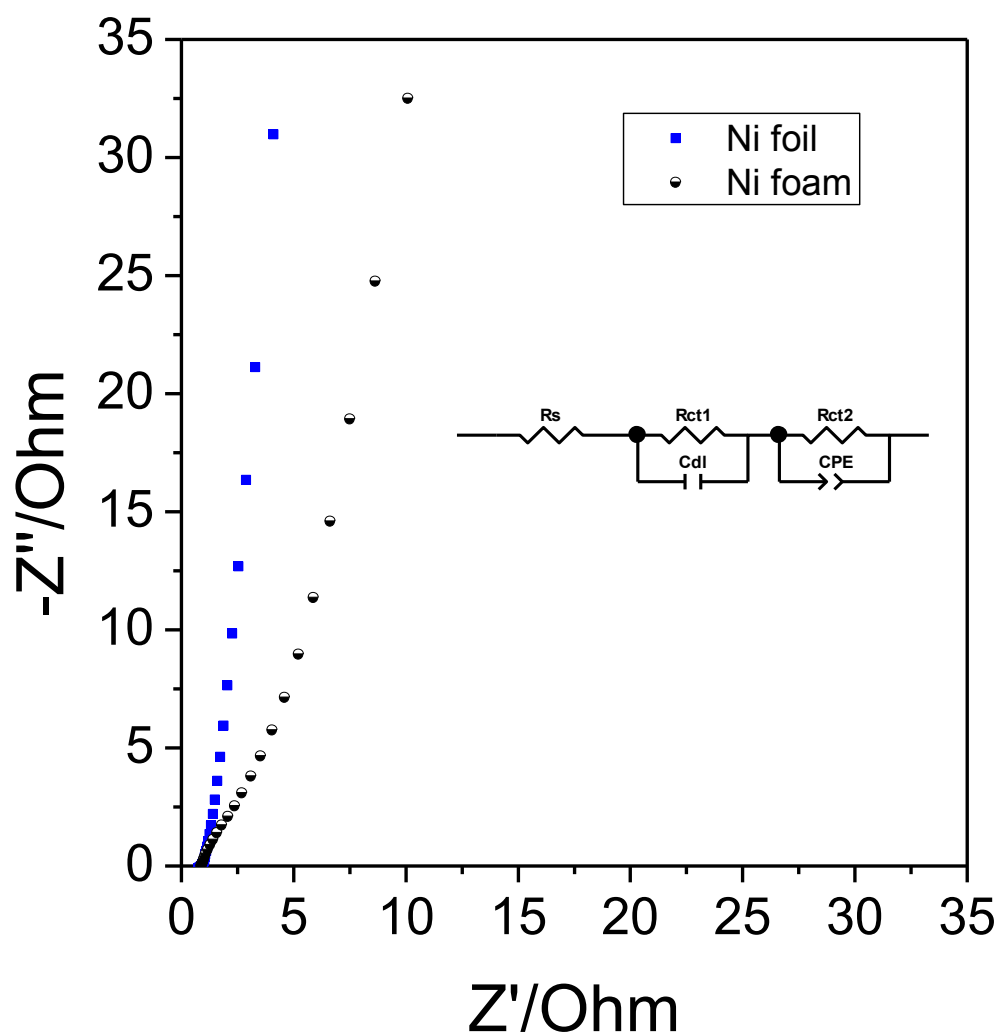


Figure 4. EIS results of Ni foam and Ni foil substrates covered by NiO nanoplatelets

The Nyquist plots corresponding to the Ni, Cu and SS substrates, showed in figure 5, present a single depressed semicircle in the high frequency region (for Cu and SS electrodes) and an inclined line at low frequency. The high frequency semicircle in Cu and SS substrates is attributed to the charge-transfer resistance between the metallic substrate and the NiO coating. A larger semicircle means a higher charge-transfer resistance [11]. In the plot, triangles corresponding to the SS form the largest semicircle, which means that the connectivity between this substrate and the NiO layer is poorer than with Cu and Ni foils.

Z-view software has been used to calculate the impedance values of the electrodes based on an equivalent circuit [12] shown at an inset in figure 5. Where R_s is the connections resistance, R_{ct} is the interface coating/substrate resistance and CPE is the pseudocapacitance used instead of pure capacitance due to the depressed semicircle. The calculated values of R_{ct} are described in table I.

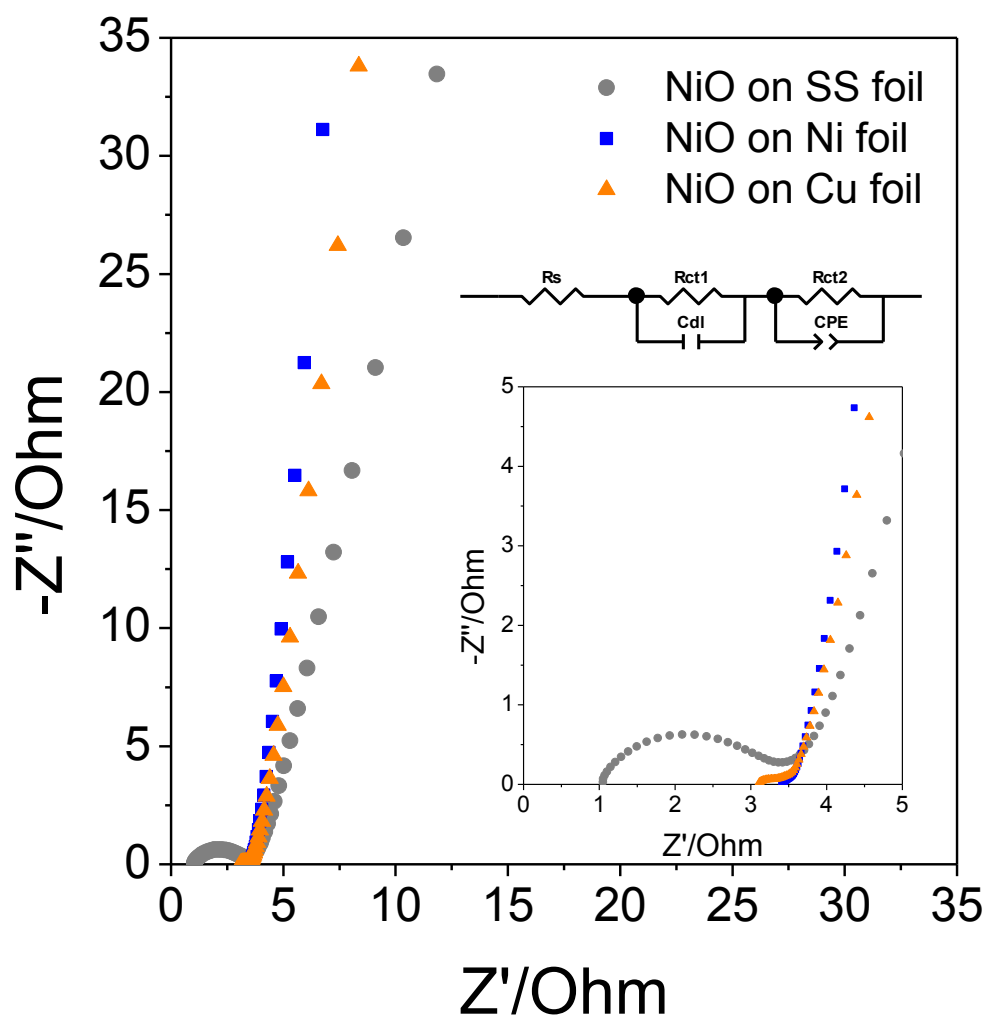


Figure 5. EIS results of Ni, Cu, and SS foil substrates covered by NiO nanoparticles.

Additionally, the low-frequency tail, which represents CPE, is related to faradaic reactions in the electrode, and they are also different for the three tested substrates. The slope of inclined line for the NiO film on the Ni substrate is steeper than the others, which can be identified with an ideal capacitance [12]. Fitted by Zview, the values are described in table I.

TABLE I. Values of the interface coating/substrate resistance and the slope of the curve in the low frequency region per foil electrode substrate.

Substrate	Rct (Ohm)	Slope
Ni	0.18	9.8
Cu	0.48	6.6
SS	2.53	4.2

The data obtained by the fitting in Z-view shows how the coating/substrate resistance (Rct) changes significantly, being the SS substrate the most resistive element and Ni the most conductive connector.

$$R_{SS} > R_{Cu} > R_{Ni}$$

The slope at low frequencies also follows a similar trend, in which the SS has the less ideal capacity behavior.

Cu is an intermediate collector between Ni and SS. The reason because of Cu is more resistant than Ni can lie in the electronic configuration of those atoms. Cu has the electrons in an energy state more stable (Ar, 3d¹⁰, 4s¹) than Ni (Ar, 3d⁸, 4s²), and for this reason the electron sharing is easier in Ni foils.

Lower resistance and higher ion-diffusion rate for NiO on metallic Ni substrate mean a faster charge-transfer process and better electrolyte accessibility, which should be attributed to the better connectivity of the electroactive material.

Conclusions

Ni foil exhibits the best properties as collector to be covered by the ceramic semiconductor NiO. This pseudocapacitor electrode presents the smallest charge transfer resistance among the three substrates studied (SS, Cu and Ni).

The shape of the substrate has also been studied. Ni foils present lower charge-transfer resistance than Ni foams. Moreover, Ni foil has steeper slope at low frequencies than Ni foam, which means that Ni foil is the electrode with the closest ideal capacity behavior.

NiO nanoplatelets have been successfully deposited by EPD on different substrates, and the electrodes were sintered at 325 °C during 1h under Argon atmosphere, obtaining a well-connected, uniform and robust NiO layer with a visible electrochemical response in all cases.

References

- [1] H. Xia, Y. Shirley Meng, G. Yuan, C. Cui, L. Lu, A symmetric RuO₂ RuO₂ supercapacitor operating at 1.6 v by using a neutral aqueous electrolyte, *Electrochem. Solid-State Lett.* 15 (2012).
- [2] Z. Yang, F. Xu, W. Zhang, Z. Mei, B. Pei, X. Zhu, Controllable preparation of multishelled NiO hollow nanospheres via layer-by-layer self-assembly for supercapacitor application, *J. Power Sources.* 246 (2014) 24–31.
- [3] A. Bello, K. Makgopa, M. Fabiane, D. Dodoo-Ahrin, K.I. Ozoemena, N. Manyala, Chemical adsorption of NiO nanostructures on nickel foam-graphene for supercapacitor applications, *J. Mater. Sci.* 48 (2013) 6707–6712.
- [4] M. Kazazi, Facile preparation of nanoflake-structured nickel oxide/carbon nanotube composite films by electrophoretic deposition as binder-free electrodes for high-performance pseudocapacitors, *Curr. Appl. Phys.* 17 (2017) 240–248.
- [5] M. Dios, Z. Gonzalez, E. Gordo, B. Ferrari, Semiconductor-metal core-shell nanostructures by colloidal heterocoagulation in aqueous medium, *Mater. Lett.* 180 (2016) 327–331.
- [6] M.-S. Wu, C.-Y. Huang, K.-H. Lin, Electrophoretic deposition of nickel oxide electrode for high-rate electrochemical capacitors, *J. Power Sources.* 186 (2009) 557–564.
- [7] Z. Gonzalez, B. Ferrari, A.J. Sanchez-Herencia, A. Caballero, J. Morales, Use of Polyelectrolytes for the Fabrication of Porous NiO Films by Electrophoretic Deposition for Supercapacitor Electrodes, *Electrochim. Acta.* 211 (2016) 110–118.
- [8] Z. Gonzalez, B. Ferrari, A.J. Sanchez-Herencia, A. Caballero, J. Morales, Relevance

- of the Semiconductor Microstructure in the Pseudocapacitance of the Electrodes Fabricated by EPD of Binder-Free β -Ni(OH)₂ Nanoplatelets, *J. Electrochem. Soc.* 162 (2015) D3001–D3012.
- [9] J. Yus, B. Ferrari, A.J. Sanchez-Herencia, A. Caballero, J. Morales and Z. Gonzalez, In-situ Synthesis and Electrophoretic Deposition of NiO/Ni Core-Shell nanoparticles and its Application as Pseudocapacitor *Coatings* (ISSN 2079-6412) (under review).
- [10] S.A. Abbas, K.D. Jung, Preparation of mesoporous microspheres of NiO with high surface area and analysis on their pseudocapacitive behavior, *Electrochim. Acta.* 193 (2016) 145–153.
- [11] J. Huang, J. Zhu, K. Cheng, Y. Xu, D. Cao, G. Wang, Preparation of Co₃O₄ nanowires grown on nickel foam with superior electrochemical capacitance, *Electrochim. Acta.* 75 (2012) 273–278.
- [12] M.L. Huang, C.D. Gu, X. Ge, X.L. Wang, J.P. Tu, NiO nanoflakes grown on porous graphene frameworks as advanced electrochemical pseudocapacitor materials, *J. Power Sources.* 259 (2014) 98–105.

J. Yus, Z. Gonzalez, A.J. Sanchez-Herencia, A. Sangiorgi, N. Sangiorgi, D. Gardini, A. Sanson, C. Galassi, A. Caballero, J. Morales, B. Ferrari.

Semiconductor Water-based Inks: Miniaturized NiO Pseudocapacitor Electrodes by Inkjet Printing.

Journal of The Electrochemical Society. **2019**, 39, 2908 - 2914,

doi: 10.1016/j.jeurceramsoc.2019.03.020



Original Article

Semiconductor water-based inks: Miniaturized NiO pseudocapacitor electrodes by inkjet printing



J. Yus^{a,*}, Z. Gonzalez^a, A.J. Sanchez-Herencia^a, A. Sangiorgi^b, N. Sangiorgi^b, D. Gardini^b,
A. Sanson^b, C. Galassi^b, A. Caballero^c, J. Morales^c, B. Ferrari^a

^a Instituto de Cerámica y Vidrio, CSIC, Madrid, Spain

^b Institute of Science and Technology for Ceramics, ISTE-CNR, Faenza, Italy

^c Departamento de Química Inorgánica, Universidad de Córdoba, Spain

ARTICLE INFO

Keywords:

Water-based inks

Ceramic semiconductor

Inkjet printing

Path design

Miniaturized pseudocapacitor electrodes

ABSTRACT

The formulation, development and optimization of water-based inks of platelet-like nanoparticles are the main objective of this work. As-synthesized Ni(OH)₂ nanoparticles were dispersed and stabilized in aqueous suspension by PEI addition. The combination of DEG (cosolvent) with H₂O shows the ideal values of surface tension and viscosity for piezoelectric inkjet printing, which exhibits a homogeneous jetting flow of the nanoplatelets suspension. The printed nanostructure was sintered at low temperature (325 °C) and the electrochemical overview of NiO electrode behavior was described. These printable pseudocapacitors tested by a three-electrode cell have showed a competitive specific capacitance, leading 92% and 78% of capacitance retention for 2000 cycles at scan rates of 1 and 2 A/g respectively, and a coulombic efficiency of 100%. The initial performance of this printed NiO pseudocapacitor can be compared with others prepared by conventional methods. This new finding is expected to be particularly useful for the designing of micro-pseudocapacitors.

1. Introduction

The development of InkJet Printing technology (IJP) has exponentially grown during the last few years, especially in ceramic decoration [1]. Recently, IJP of semiconductor ceramic compounds in the manufacture of miniaturized devices and other industrial applications, such as microchips, home printers, LCD and plasma screens, etc., has led to the development of novel and innovative functional inks [2–4]. IJP consists in the deposition of suspensions or inks on a substrate following the path designed by the 2D or 3D modelling software. Although it is mainly a 2D technique, layer-by-layer printing can be also employed in order to increase the pattern thickness. Among the advantages of this technique there are the exhaustive control over the amount of deposited material, the high precision in the patterns design or the elimination of unwanted waste. In this sense, the IJP is considered an un-expensive processing technique easy to be adapted for mass production of customized products.

IJP patterns result from the combined effects of the ink flowing properties, the heads technology of the printer and the ink-substrate interaction during deposition and drying. In commercial piezoelectric printers the nozzle diameter changes with the application. It is well known that smaller nozzles allow smaller droplets and higher

resolutions, and it is generally accepted that particle size should be 50 times lower than the diameter of the nozzle to avoid clogging [5]. Homogeneously dispersed nanoparticles will ensure the accuracy, while a good jetting and drying feature is required to obtain clear profiles and to keep the desired functionality of the inks.

The solvent must carry the nanoparticles in suspension until printing, and then it should evaporate at the prefixed drying rates. In order to optimize the formulations of the inks, the combination of solvents and the use of additives is widely spread [6–8]. Wetting and drying behavior, the drop formation and the successful jetting, are the most relevant characteristics of the inks in this process. Organic solvents provide low values of surface tension and reduce the interactions among particles, promoting lower viscosities and Newtonian behaviors [9]. However, due to the need to substitute organic inks with water based ones [10] the selection of solvents and additives providing the inks with ideal properties is extremely relevant in water-based inks. Printable aqueous inks require viscosities in the range of 2–20 mPa s and Newtonian behavior. The behaviour of water-based suspensions is normally non-Newtonian, typically pseudoplastic. Because inkjet printers operate in the frequency range of 1–10 kHz, the strain rates are expected to be in the range 10³–10⁴ 1/s, and it is difficult to measure the fluid viscosity in this range of shear rates [11]. However, applying

* Corresponding author.

E-mail address: joaquinluis.yus@icv.csic.es (J. Yus).

<https://doi.org/10.1016/j.jeurceramsoc.2019.03.020>

Received 19 September 2018; Received in revised form 7 March 2019; Accepted 9 March 2019

Available online 12 March 2019

0955-2219/ © 2019 Elsevier Ltd. All rights reserved.

the Cross model to the thinning or pseudoplastic behaviour allows extrapolating the viscosity for an infinite shear rate.

On the other hand, the surface tension has to be high enough to keep the suspension in the nozzle and avoid premature drop generation, and low enough to enable the spread of the drop onto the substrate surface. The use of cosolvents, in particular water, helps to reduce the evaporation rate of solvent mix and provides proper values of surface tension and viscosity [12]. In particular, glycol as water cosolvent is widely employed in the literature [2,12,13]. This solvent is used as a humectant to minimize drying at the printer nozzles [2] as well.

The surface tension and viscosity can be regarded as the key physical parameters to optimize the quality of jetting and deposition. Both parameters are related by the Z parameter which is the inverse of the Ohnesorge number. This number is defined by the equation:

$$Z = \frac{1}{Oh} = \frac{Re}{\sqrt{We}} = \frac{\sqrt{\gamma \rho a}}{\eta} \quad (1)$$

where Oh is the Ohnesorge number, Re is the Reynolds number and We is the Weber number. γ (N/m), η (mPa·s) and ρ (g/cm³) are the surface tension, the viscosity and the density of the ink, respectively, and a (nm) is the diameter of the nozzle.

This non-dimensional parameter is used in the literature to predict a successful ejection. Commonly $1 < Z < 10$ is considered the optimal range [14,15]; Yang et al. [16] defined the printable range as $4 < Z < 14$, while for other authors, such as Mogalicherla et al. [17], this parameter does not seem really relevant.

Regarding to energy storage devices, IJP meets the challenges involved in printing the electrodes, interconnections and contacts by reducing electrical loss Delannoy et al. [18] and Gu et al. [19] developed LiFePO₄ water-based inks for jetting, achieving similar discharge capacities and cyclability features (150 and 130 mAh/g) for patterns 4 and 20 μ m thick, printed onto aluminum and CNT mats.

Carbonaceous materials, especially graphene-based inks, were also printed and characterized.

Usually pseudocapacitors are made by transition metal oxides (TMO's) or conducting polymers as a functional material. TMOs have a high electrical conduction and accumulate the energy through redox reactions. Among others TMO's, NiO nanoparticles (NPs) inks have been proposed for the manufacture of different electronic devices. Lee et al. [12] first reported the Ni electrode fabrication by laser direct writing of NiO ink, while Li et al. [20] utilized a multi-color desktop inkjet printer to print Ni electrodes, and more recently, Huang et al. [21] reported inkjet-printed NiO films for application as a thermistor. Finally, Rho et al. [22] have developed an inkjet-printable NiO ink containing precrystallized ultra-small NPs, evidencing an arbitrary patterning of NiO electrodes.

In our work, as-synthesized Ni(OH)₂ plate-like NPs were used to formulate a water-based ink used to prepare miniaturized pseudocapacitor electrodes based on ceramic semiconductors. The ink formulation was optimized in terms of viscosity, surface tension and particle size to achieve printable compositions with high level of reproducibility. In addition, the printer parameters (frequency, voltage, pulse, etc.) were adjusted to reach homogeneous patterns deposition with a high accuracy. The microstructural properties of these patterns onto Ni foils were also analyzed by FESEM and the optimized designs were sintered at 325 °C under N₂ atmosphere to consolidate the NiO porous nanostructure. Finally, the electrochemical behavior of the developed electrodes was tested by different techniques, such as cyclic voltammetry and chronopotentiometry.

2. Experimental

All chemicals were of reagent grade and employed without any further purification. The β -Ni(OH)₂ nanoplatelets used for the inks formulations were synthesized by a chemical precipitation route,

assisted by ultrasound, which has been described elsewhere [23,24]. The ultrasonic horn used was Sonopuls HD 2200 (45 W/cm², 24 kHz, Bandelin Electronic, Germany) with a Ti tip. The as-synthesized Ni(OH)₂ nanoparticles were dispersed in a mixture of diethylene glycol (DEG) and water 1:1. 2.5%wt. (respect to the weight of Ni(OH)₂) polyethylenimine (PEI) was added as deflocculant and the pH of the suspension was adjusted at 10. Then, the suspension was ball-milled for 2–36 h in order to break agglomerates and homogenize the inks. Part of this suspension was diluted down to 0.1 g/L in 1:1 DEG:H₂O at pH 10 to determine the zeta potential in a Zetasizer Nano ZS (Malvern Instruments Ltd., UK).

The rheology of the solvent and the as-prepared inks with solid content ranging from 10 wt.% to 25 wt.% was studied. A Bohlin C-VOR viscometer (Malvern Instruments Ltd., UK) with coaxial cylinders (C25) with bob of 25 mm of diameter and gap 1.25 mm (the height of the bob is 37.5 mm) was used. Tests were performed with a pre-shear in a control rate mode (CR) from 0 to 1000 1/s in 2 min, dwelling at 1000 1/s for 2 min and shearing down to 0 in 2 min. And control stress from 0 Pa to the values obtained in the previous control rate in 2 min and down back to 0 Pa in the same time. All tests were done at a constant temperature of 25 \pm 0.5 °C. The applied high-shear rates during up-ramps are enough to achieve a reproducible suspension microstructure, and consider the same starting point to compare the inks formulations. Hence the plotted curves in the rheology study were the down-ramps, and the log–log plot was fitted following the Cross model (Eq. 2) in order to extrapolate the main parameters of the behavior of the inks flux. Cross model is:

$$\eta = \eta_{\infty} \frac{\eta_0 - \eta_{\infty}}{1 + C_{\dot{\gamma}}^n} \quad (2)$$

where η_0 (mPa·s) and η_{∞} (mPa·s) are the viscosities extrapolated at rest and at high shear rates respectively, $C_{\dot{\gamma}}$ is a time constant and n is the rate constant, a parameter related to the viscosity dependence on the shear rate. The Cross model describes the limit behavior of the suspension (viscosity at rest), and at an infinite shear rate which could be equivalent to the ink viscosity when it is jetted through the nozzle.

In addition, it has been found that the Krieger-Dougherty Model (K-D) provides a semi-empirical correlation of the effective viscosity with the maximum packing volume fraction of solid-liquid suspensions as follows [25]:

$$\eta = \eta_s \left(1 - \frac{\phi}{\phi_m} \right)^{-n} \quad (3)$$

where ϕ_m is the maximum packing fraction, n is an empirical exponent and η_s is the viscosity of the solvent (mPa·s). The exponent n and the maximum packing fraction, ϕ_m , for the suspension were estimated by using the K–D equation.

The Ni(OH)₂ nanoplatelets and aggregate sizes in suspension were evaluated in terms of volume fraction. A Zetasizer Nano ZS (Malvern Instruments Ltd., UK) was used in order to determine the particle size in a diluted suspension of H₂O:DEG (1:1), using Dynamic Light Scattering (DLS). The inks were filtered in three steps with a 5.0, 1.2 and 0.8 μ m Minisart® filters in order to avoid clogging of the nozzle. The thermogravimetric (TG) analysis of the inks was carried out from room temperature until 300 °C at a heating rate of 5 °C/min in a simultaneous thermal analyzer (STA 449, Netzsch, Germany).

The surface tension of the Ni(OH)₂ inks was measured at ambient conditions using a Drop Shape Analyzer – DSA30 Tensiometer (Krüss) in pendant drop configuration system. In addition, the suspension density was obtained by measuring the mass of 10 mL of suspension with a graduate test tube and a microbalance. The average density of the suspension was determined after five different measures, being 1.1 g/mL.

The Ni foils (0.2 mm thick, 99.0% purity, Goodfellow) were used as substrates and they were cleaned with acetone and ethanol several

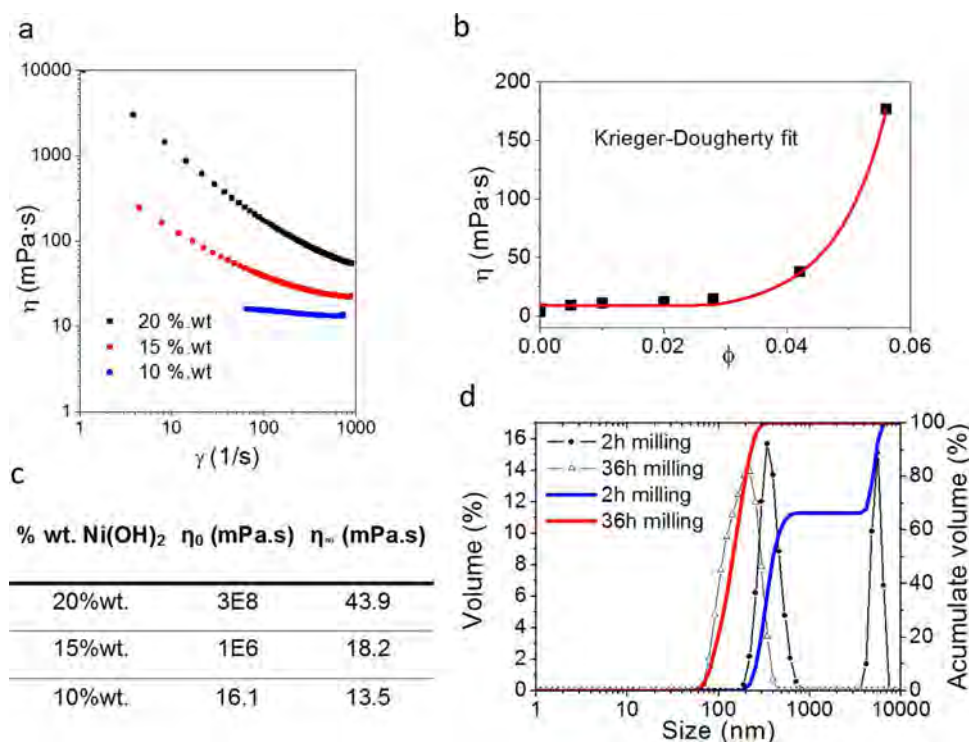


Fig. 1. (a) Flow curves and (b) Krieger-Dougherty fitting curve of the prepared inks, (c) the summary of the values of the viscosity at rest and at infinite shear rate calculated by Eq. (2) and, (d) DLS measurements after the 2 and 36 h ball-milling process.

times using an ultrasonic bath (15 s) and dried prior to print. The Ni(OH)₂ ink was then printed directly onto the Ni foil forming different patterns of 1 cm². A commercial XCEL System Aurel work cell printer (AUREL Automation, Italy) was used to print the ceramic ink. This inkjet printer uses piezoelectric actuation, the nozzle diameter is 70 μ m and the storage system is a tank of 5 ml, without recirculation. The topography of the surface of the deposition was also studied by 3D reconstructions by Zeta3D™ Optical Profiler (ZETA), and the morphology of the deposited particles by Field Emission Gun – Scanning Electron Microscopy (FEG-SEM, SIGMA Zeiss, Germany). Then, the inkjet-printed Ni(OH)₂ electrodes were sintered at 325 °C for 1 h under N₂ atmosphere according to previous studies [26]. The uniformity and surface morphology of the resulting NiO electrodes were also characterized by FE-SEM (Hitachi S-4700, Japan).

Finally, the electrochemical behavior of the IJP electrodes was evaluated with cyclic voltammetry (CV) at different scan rates, from 2 to 10 mV/s, in a potential window of 0.0–0.5 V, using a Potentiostat/GalvanostatAutolab (PGSTAT204, Netherlands) in a three-electrodes configuration cell. A NiO printed on the Ni foil was used as working electrode, Pt foil as counter electrode and Ag/AgCl as a reference. The employed electrolyte was 1 M KOH aqueous solution. The charging/discharging measurements were carried out through chronopotentiometry analysis (CP) at a scan rate of 1 and 2 A/g using a multichannel potentiostat-galvanostat system (Arbin BT2000, Arbin Instruments, TX, USA). From CP measurements, the specific capacitance value was calculated according to equation:

$$C = \frac{I \cdot \Delta t}{m \cdot \Delta V} \quad (4)$$

where C is the specific capacitance (F/g), I is the discharge current (A), Δt is the discharging time (s), ΔV is the voltage window (V), and m is the mass (g) of the printed active NiO material. The NiO active mass was determined calculating the mass of the Ni(OH)₂ patterns, weighting the substrate and the sample before and after the IJP process respectively, and considering the full transformation of Ni(OH)₂ into NiO after the thermal treatment. All measurements were carried out at room

temperature.

3. Results and discussion

The Ni(OH)₂ particles were synthesized by chemical precipitation in aqueous medium with the help of ultrasound [23,24]. The Ni(OH)₂ particles are nanoplatelets of 200–300 nm in diameter with a thickness of 20–30 nm, while the micro and mesoporosity of obtained NiO nanoplatelets after calcination ranges 2–3 nm and 40–50 nm, respectively. The chemical and colloidal stabilization of Ni(OH)₂ nanoplatelets in water was optimized in previous works [23,24,27] where nanoplatelets dispersion was adjusted by the PEI adsorption. The branched and cationic nature of this polyelectrolyte contributes to develop the electrostatic interaction among Ni(OH)₂ nanoplatelets in water. The colloidal stability of the as-synthesized nanoplatelets was estimated from the study of the zeta potential evolution with the pH. The isoelectric point (IEP) is at pH 8.5 and the maximum stability was at pH 10 where the zeta potential is –20 mV. At pH 10, the adsorption of 2.5 wt.% of PEI changes the zeta potential to a positive and higher absolute value (+50 mV) conferring a better stability to the suspension by improving both steric and electrostatic contributions.

In this work, the medium of the suspension consisted in a mixture of H₂O and DEG (1:1 vol.). The flux curve of this solvent was also determined, showing a Newtonian behavior and viscosity of 4 mPa.s. The dielectric constant (55.1) was calculated by the Law of Mixtures, considering that H₂O and DEG have dielectric constants of 78.5 and 31.7, respectively. If compared with water, the higher viscosity and the lower dielectric constant of the H₂O:DEG mixture limits the electrostatic interaction among particles, slightly decreasing the zeta potential of the suspension of Ni(OH)₂ nanoplatelets stabilized with 2.5 wt.% PEI to +42 mV.

Different solid contents were tested in the Ni(OH)₂ suspensions stabilized with 2.5 wt.% of PEI in the H₂O:DEG solvent. Fig. 1a shows the rheograms relating the viscosity of the inks with the shear rate for the Ni(OH)₂ suspensions with solid loadings of 10, 15 and 20 wt.%. As expected, the increase of solid content effectively increased the

viscosity. The viscosity curves clearly show the pseudoplastic behavior of the inks with solid contents of 15 wt.% and 20 wt.%, while the 10 wt.% suspension is quasi-newtonian. Fig. 1b illustrates the K-D fit for the $\text{Ni}(\text{OH})_2$ suspensions stabilized with PEL, confirming a maximum packing fraction (ϕ_m) of 7.5%, slightly low due to the high viscosity of the solvent (4 mPa s) if it is compared with that of the water. The flow curves were also fitted to the Cross model to define the limit behavior of the starting suspension (η_0) and at infinite shear rate (η_∞). The table at the inset (Fig. 1c) summarizes the values of η_0 and η_∞ for all the inks. Thinning or pseudoplastic behavior is desirable when the storage system is a tank and suspensions will keep at rest during the printing process. However, if the resting viscosity is very high it will be difficult to start moving the suspension from idle state. In our case the inks prepared at 15 and 20 wt.% solid contents achieve viscosities at rest exceeding 1 Pa·s, and for this reason the ink with 10 wt.% of solid content, showing viscosities of 13–16 mPa s in all the shear rate range, was selected for the print test.

Fig. 1d shows a bi-modal distribution of particles after 2 h milling with $5.4 \mu\text{m}$ of D_{v90} . After 36 h milling, the volume size distribution changes into a mono-modal distribution. The aggregates corresponding to the second peak with a mean size of 3000 nm after the first 2 h disappears after 36 h of milling. DLS determination shows that after 36 h milling, particle size of $\text{Ni}(\text{OH})_2$ is below 450 nm, with a large fraction under 200 nm ($\sim 70\%$ vol.), while particles size measured by FESEM is 200–300 nm [23]. Differences between both DLS and FESEM measurements are due to the shape of $\text{Ni}(\text{OH})_2$, since the measurement by DLS are based on the determination of the diffusion coefficient due to the Brownian movement of the particles, and the radius of the particles is calculated using the Stokes-Einstein equation which assumes that spherical particles have the same diffusion coefficient than the particles in the suspension. Consequently, the values collected in the particle size distribution in Fig. 1d can be only considered as an approximation to the real value showed by the FESEM images.

In any case, it was observed that the particle size after 36 h milling was not larger than 450 nm, smaller than the minimum required, which is 1400 nm (~ 50 times smaller than the nozzle diameter [28]). For this reason, a milling process of 36 h was fixed for the preparation of this ink. The loss of mass due to the filtration steps was studied by thermal analysis following a heating/cooling schedule of $5^\circ\text{C}/\text{min}$ until 300°C . TGA analysis (Figure S1) of the filtered inks shows two mass losses, which take place from 80 to 120°C and from 180 to 240°C and correspond to the boiling point of the water and DEG, 100°C and 245°C respectively. The total residual mass is 7 wt.% that is lower than expected (10 wt.%) after the evaporation of the solvents. This is because a chemical oxidation reaction takes place during the thermal analysis according to the calcination process of the $\text{Ni}(\text{OH})_2$ into NiO . The loss of a molecule of water leads to a nominal mass loss of 30 wt.% respect to the mass of the hydroxide. This reaction takes place at 250°C [24] and it is confirmed by the final black color of the residue of the TGA analysis. This result confirms that no significant amount of solid is retained in the filter and $\text{Ni}(\text{OH})_2$ nanoplatelets are fully dispersed in the ink.

To verify the applicability of these $\text{Ni}(\text{OH})_2$ -based inks the Z number was studied. This parameter is calculated by the inverse of the Ohnesorge number, ($Z = 1/\text{Oh}$), and relates the viscosity, density and surface tension parameters. Considering that the viscosity at infinite shear rate is 13.5 mPa·s, the average value of surface tension is 50 mN/m and the density of the suspension is 1.1 g/ml, the Z parameter was calculated by the Eq. (1) resulting in 3, being within the printable range [14,15].

To avoid macroscopic and microscopic manufacturing defects, which can deteriorate the structural, microstructural, and functional properties of the deposition patterns, and with the objective to define suitable printing conditions, the optimization of the printer parameters was necessary. Fig. 2 shows pictures of different defects obtained during the optimization. On one side, the inkjet printing at room conditions produced the coalescence of the ink, forming small drops along the

pattern. Fig. 2a shows the defects of printing when the substrate was not enough heated or the bed temperature was not controlled. A constant bed temperature of 70°C was required to get a homogenous path. Nevertheless, an intermediate thermal stabilization step was also necessary between the sequentially deposited layers. Fig. 2b illustrates similar defects when the area where the deposition takes place is gradually cooling. For this reason, in Fig. 2b the first line shows a single and homogeneous path, while at the second line some defects appeared and the last line presented the most accentuated defects. Additionally, in Fig. 2c, the lines were too close and some free spaces were closed by the ink. This problem was related with the diameter of the nozzle, which conditions, to a certain extent, the size of the drop. Moreover, other classical defect, Fig. 2d, is due to not adjusted oscillation frequency and pulse, producing crooked lines or discontinuities. Finally, a well-defined grid was created by adjusting the frequency, the pulse voltage and the speed movement of the printer head Table.1. Fig. 2e shows an image of a pattern without defects, where the sizes of the lines and the distance between them were 400 and 300 μm respectively.

The size of the printed grid was $1 \text{ cm} \times 1 \text{ cm}$, and the thicknesses were studied in terms of roughness. Fig. 3 presents the optical microscopy images of patterns made depositing one layer (Fig. 3a and c) and two layers (Fig. 3b and d) at different magnifications. Fig. 3e and f show the 3D reconstruction of one path for one and two layers samples, respectively. In addition, Fig. 3g illustrates the Z-height of the printed samples, being $5 \mu\text{m}$ the average height for one layer and $10 \mu\text{m}$ for two layers, and the maximum values 6.8 and 12.9 μm , respectively. In addition, the diameter of the printed lines ranges 400–480 μm , following a uniform pattern. Looking at the same figure, the well-known coffee stain effect is slightly perceived. This phenomenon was explained by Deegan et al. [29], who observed that the solute distribution after the drying was strongly influenced by the evaporation process of the solvent.

This reliable process allowed us to print multilayered $\text{Ni}(\text{OH})_2$ films with different deposition thicknesses. The thickness of these prints is proportional to the number of deposited layers. After the profilometer analysis, the morphology of the surface of the deposition on Ni foils at 70°C with one layer was studied by FESEM microscopy. The FESEM images of the top view of the green grid (Fig. 4) reveal a porous microstructure fully covering the Ni substrate. The FESEM images corresponding to the printed pattern depositing three layers (Figure S2 of the supplementary info) show that raising the number of printed layers does not affect the pattern microstructure. The surface microstructure of the one and three layers grids is similar, and the morphology and porosity do not change.

After the printing process, the electrodes were dried during 15 min on a heating plate at 70°C . Afterwards they were thermally treated at 325°C for one hour under N_2 atmosphere (Fig. 5b). This heat treatment was performed in order to achieve the oxidation of the $\text{Ni}(\text{OH})_2$ (Fig. 5a) to NiO (Fig. 5b) and also, to consolidate the nanoplatelets microstructure that will confer the adequate connectivity and robustness to the printed patterns for the use of this ceramic semiconductor structure in energy storage devices.

The structure of the designed pattern shows a continuous network not completely homogeneous (Fig. 5d) because some lines are slightly thinner and present a curvilinear (not straight) edge (Fig. 5e). In the Fig. 5f, both the crack-free microstructure of the pattern and the sintering necks among NiO nanoplatelets are evidenced. If we compare the FESEM images in Fig. 4, it looks that the surface morphology and the pore size of the deposition are preserved after the thermal treatment, while the sintering necks among NiO nanoplatelets can be observed.

In order to study the NiO electrodes manufactured by IJP, the electrochemical performance of the sintered coatings were evaluated in terms of faradaic capacity. Fig. 6a shows the cyclic voltammetry (CV) curves performed at different sweep rates (1, 2, 5, and 10 mV/s). The quasi symmetrical rectangle-shapes indicate that the NiO electrodes have relatively large electric double layer capacitance (EDLC) and only

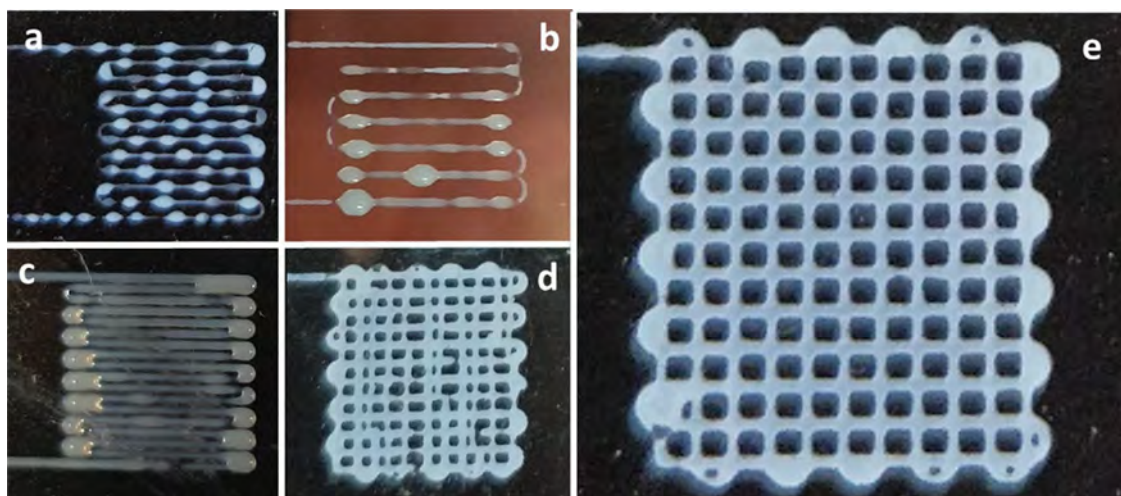


Fig. 2. Pictures showing printing defects during the IJP optimization of 1 cm² patterns.

Table 1
Optimized Inkjet parameters.

Ink-Jet parameters	Values
Pulse Volt	230 V
Pulse	135 us
Frequency	1036 Hz
Strobo Delay	227 us
Pressure	−20 mBar

a lower faradaic contribution, even at the slowest applied sweep rate (1 mV/s), which can be attributed to the following reversible redox reaction:



In addition, specific capacitance values were also determined by galvanostatic measurements. Fig. 6b presents the typical charge-discharge (C–D) voltage vs. time plots at a potential ranging 0–0.5 V. The C–D curves are shown for the cycle number 10 and 2000 at 1 and 2 A/g, respectively. The specific capacitances were calculated from galvanostatic charge/discharge curves (at 1 and 2 A/g) by the Eq. (4), during 2000 cycles, being 70.4 and 50.4 F/g the highest values of capacitance

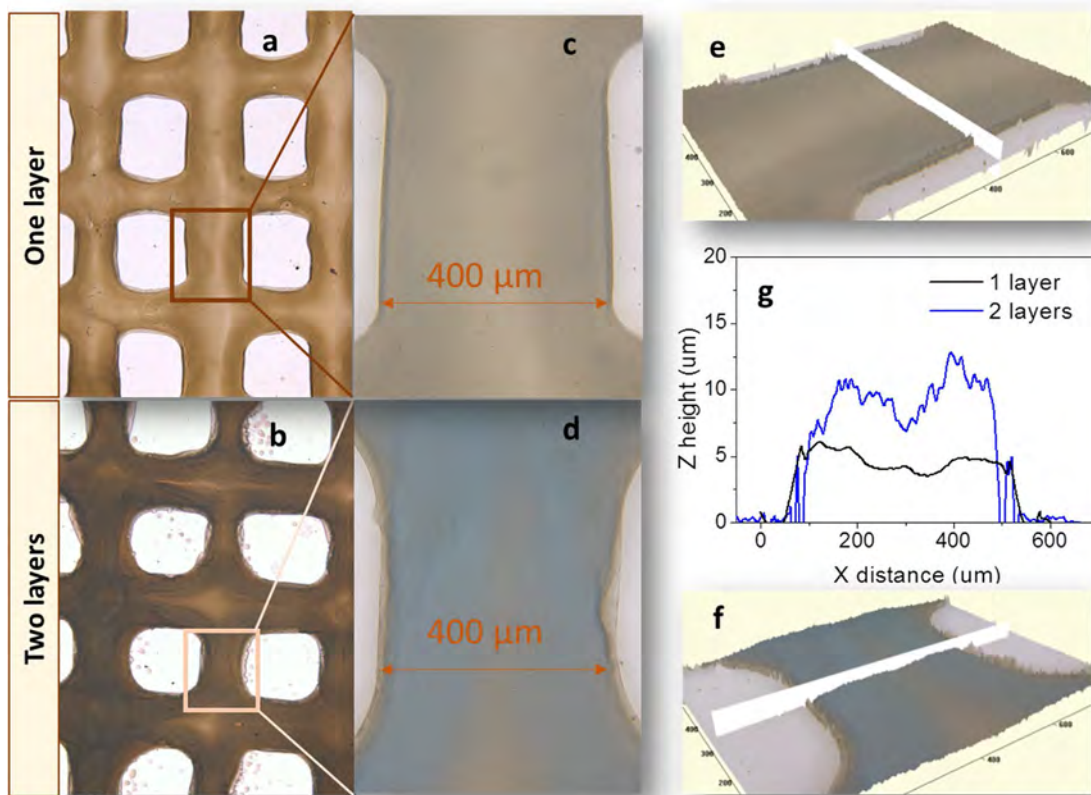


Fig. 3. (a–d) Optical microscopy images of the top view of the deposited one and two layers patterns, (e–f) their 3D reconstruction of the cross section and, (g) the height of one and two layers patterns.

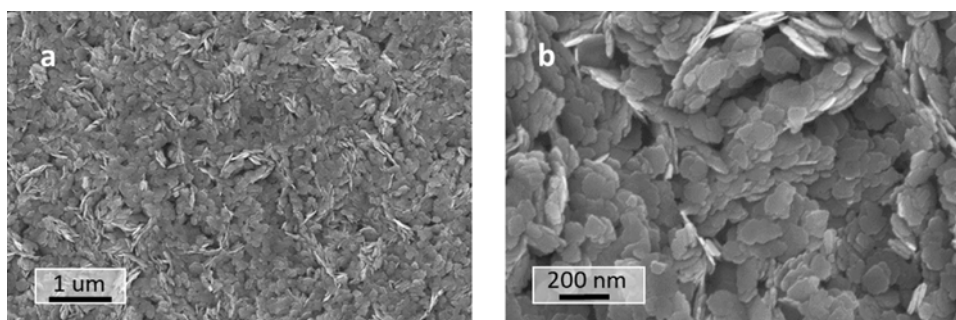


Fig. 4. FESEM images of patterns printed depositing one layer.

achieved, respectively. Then, the capacitance values were plotted in terms of percentage (Fig. 6c and d), in order to show the long cycle-life of the electrode.

The good cycling stability evidences the presence of a well-connected semiconductor structure as well as a firmly joined NiO layer to the Ni substrate, which facilitates the transport of electrons leading to a 92% and 78% of capacitance retention for 2000 cycles at scan rates of 1 and 2 A/g, respectively. The coulombic efficiency was calculated from the measured charge-discharge curves, as a function of the quotient in percent between the discharge and the charge capacity. The horizontal blue lines in the graphics 6c and 6d show a 100% coulombic efficiency during thousands of cycles.

The electrochemical performance of IJP NiO patterns was similar to that reported for other NiO electrodes prepared by other methods [23,27]. Our results suggest that the IJP of NiO nanoplatelets is a reliable alternative to pattern supercapacitor electrodes with a high resolution. New designs of micro-supercapacitors could be printed to increase the exposed surface, providing longer life-cycles and faster charge/discharge cycles than rechargeable micro-batteries [30].

4. Conclusions

For the first time it was shown that as-synthesized $\text{Ni}(\text{OH})_2$ nanoplatelets dispersed in an aqueous suspension is an useful ink for IJP of ceramic electrodes for pseudocapacitors. The employment of DEG as a co-solvent results in optimal viscosity and surface tension values as well

as the ink Z-number. The formulated inks show long time stability and can be used for inkjet printing without any further processing. The waveform function of the piezoelectric nozzle operation was adjusted in order to jet the printable water-based ink. Grid-like printed Ni-based pseudocapacitor electrodes were obtained by IJP. The amount of layers does not affect the morphology and connectivity between the deposited nanoplatelets. A path free of discontinuities with only one layer deposit can be printed, avoiding unnecessary waste of material.

In this work, we show an innovative design of Ni-based electrode obtained by IJP with a subsequent thermal treatment of the printings at 325 °C, which produces electrically conductive TMO electrodes. The electrochemical behavior of NiO electrodes show a long life during thousands of cycles (92% of capacitance retention at 1 A/g) and the specific capacitance is comparable to the performance of NiO electrodes fabricated by traditional techniques. Furthermore, as an additive manufacturing, IJP offers several advantages for environmental health and safety thanks to the reduction of both waste generation and potentially expensive and toxic raw nanomaterials.

Acknowledgments

The authors thank ECERS for funding this project through the JECS Trust grant under the contract 2017141, and the support to the projects S2018/NMT-4411 (Comunidad de Madrid) and MAT2015-70780-C4-1 and MAT2017-87541-R (MINECO/FEDER). J. Yus acknowledges the Comunidad de Madrid for the support from the Youth Employment

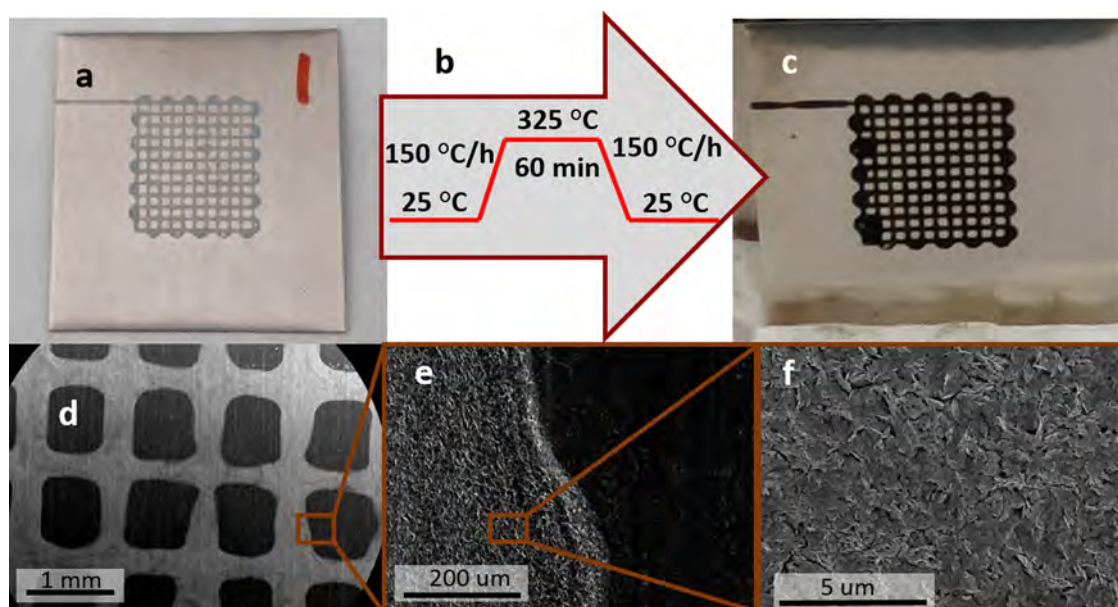


Fig. 5. (a–c) Pictures of one layer printed pattern before and after the thermal treatment indicated in (b) and, (d–f) FESEM images of the sintered electrode at different magnifications.

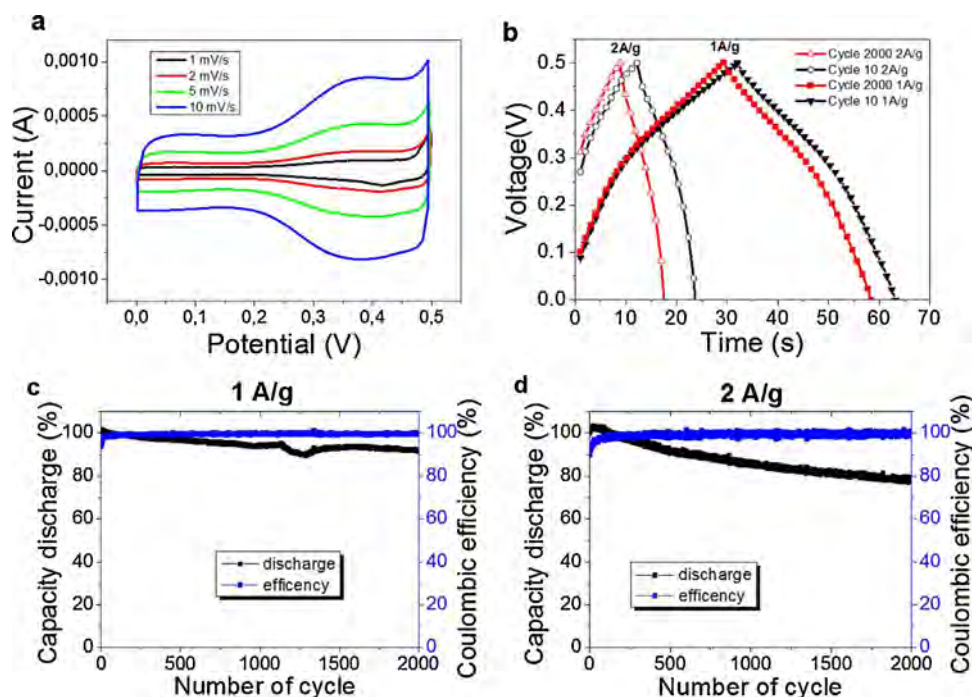


Fig. 6. a) Cyclic voltammograms measured at different scan rates. (b) C–D constant current charge/discharge curves at 1 and 2 A/g, respectively for the 10th and 2000th cycle. (c) & (d) Specific capacitance retained as a function of number of cycles and the efficiency for 1 and 2 A/g, respectively.

Initiative, CAMPD17_ICV_002. Z. Gonzalez acknowledges the Postdoctoral Fellowship: IJCI-2016-28538.

Appendix A. Supplementary data

Supplementary material related to this article can be found, in the online version, at doi:<https://doi.org/10.1016/j.jeurceramsoc.2019.03.020>.

References

- [1] G. Ferrari, P. Zannini, VOCs monitoring of new materials for ceramic tiles decoration: GC-MS analysis of emissions from common vehicles and inkjet inks during firing in laboratory, *Bol. Soc. Esp. Ceram. y Vid.* 56 (2017) 226–236.
- [2] R. Cherrington, D.J. Hughes, S. Senthilarasu, V. Goodship, Inkjet-printed TiO₂ nanoparticles from aqueous solutions for dye-sensitized solar cells (DSSCs), *Energy Technol.* 3 (2015) 866–870.
- [3] B. Derby, Additive manufacture of ceramics components by inkjet printing, *Engineering* 1 (2015) 113–123.
- [4] A. Friederich, C. Kohler, M. Nikfalazar, A. Wiens, M. Sazegar, R. Jakoby, W. Bauer, J.R. Binder, Microstructure and microwave properties of inkjet printed barium strontium titanate thick-films for tunable microwave devices, *J. Eur. Ceram. Soc.* 34 (2014) 2925–2932.
- [5] J.L. Valero, C. Jarom, E. Comas, Optimized automatic recovery of nozzle health in inkjet systems, *Program* (2018) 766–770.
- [6] M. Arin, P. Lommens, S.C. Hopkins, G. Pollefeijt, J. Van Der Eycken, S. Ricart, X. Granados, B.A. Glowacki, I. Van Driessche, Deposition of photocatalytically active TiO₂ films by inkjet printing of TiO₂ nanoparticle suspensions obtained from microwave-assisted hydrothermal synthesis, *Nanotechnology* 23 (2012).
- [7] C. Gadea, Q. Hanniet, A. Lesch, D. Marani, S.H. Jensen, V. Esposito, Aqueous metal-organic solutions for YSZ thin film inkjet deposition, *J. Mater. Chem. C* 5 (2017) 6021–6029.
- [8] M. Liu, J. Wang, M. He, L. Wang, F. Li, L. Jiang, Y. Song, Inkjet printing controllable footprint lines by regulating the dynamic wettability of coalescing ink droplets, *ACS Appl. Mater. Interfaces* 6 (2014) 13344–13348.
- [9] F. Zhang, M. Wei, V.V. Viswanathan, B. Swart, Y. Shao, G. Wu, C. Zhou, 3D printing technologies for electrochemical energy storage, *Nano Energy* 40 (2017) 418–431.
- [10] T. Bakarić, B. Malić, D. Kuscer, Lead-zirconate-titanate-based thick-film structures prepared by piezoelectric inkjet printing of aqueous suspensions, *J. Eur. Ceram. Soc.* 36 (2016) 4031–4037.
- [11] B. Derby, N. Reis, Inkjet printing of highly loaded particulate suspensions, *MRS Bull.* 28 (2003) 815–818.
- [12] H.H. Lee, K. Sen Chou, K.C. Huang, Inkjet printing of nanosized silver colloids, *Nanotechnology* 16 (2005) 2436–2441.
- [13] D. Pech, M. Brunet, P.L. Taberna, P. Simon, N. Fabre, F. Mesnilgrente, V. Conédéra, H. Durou, Elaboration of a microstructured inkjet-printed carbon electrochemical capacitor, *J. Power Sources* 195 (2010) 1266–1269.
- [14] P. He, B. Derby, Inkjet printing ultra-large graphene oxide flakes, *2D Mater.* 4 (2017).
- [15] Y.F. Liu, M.H. Tsai, Y.F. Pai, W.S. Hwang, Control of droplet formation by operating waveform for inks with various viscosities in piezoelectric inkjet printing, *Appl. Phys. A Mater. Sci. Process.* 111 (2013) 509–516.
- [16] H.C. Nallan, J.A. Sadie, R. Kitsomboonloha, S.K. Volkman, Systematic design of jettable nanoparticle-based inkjet rheology, acoustics, and jetability, *Langmuir* 30 (2014) 13470–13477.
- [17] M. Bienia, M. Lejeune, M. Chambon, V. Baco-Charles, C. Dossou-Yovo, R. Noguera, F. Rossignol, Inkjet printing of ceramic colloidal suspensions: filament growth and breakup, *Chem. Eng. Sci.* 149 (2016) 1–13.
- [18] P.E. Delannoy, B. Riou, T. Brousse, J. Le Bideau, D. Guyomard, B. Lestriez, Ink-jet printed porous composite LiFePO₄ electrode from aqueous suspension for micro-batteries, *J. Power Sources* 287 (2015) 261–268.
- [19] Y. Gu, A. Wu, H. Sohn, C. Nicoletti, Z. Iqbal, J.F. Federici, Fabrication of re-chargeable lithium ion batteries using water-based inkjet printed cathodes, *J. Manuf. Process.* 20 (2015) 198–205.
- [20] D. Li, D. Sutton, A. Burgess, D. Graham, P.D. Calvert, Conductive copper and nickel lines via reactive inkjet printing, *J. Mater. Chem.* 19 (2009) 3719–3724.
- [21] C.-C. Huang, Z.-K. Kao, Y.-C. Liao, Flexible miniaturized nickel oxide thermistor arrays via inkjet printing technology, *ACS Appl. Mater. Interfaces* 5 (2013) 12954–12959.
- [22] Y. Rho, K.-T. Kang, D. Lee, Highly crystalline Ni/NiO hybrid electrodes processed by inkjet printing and laser-induced reductive sintering under ambient conditions, *Nanoscale* 8 (2016) 8976–8985.
- [23] Z. Gonzalez, B. Ferrari, A.J. Sanchez-Herencia, A. Caballero, J. Morales, Relevance of the Semiconductor Microstructure in the Pseudocapacitance of the Electrodes Fabricated by EPD of Binder-Free β -Ni(OH)₂ Nanoplatelets, *J. Electrochem. Soc.* 162 (2015) D3001–D3012.
- [24] S. Cabanas-Polo, Z. Gonzalez, A.J. Sanchez-Herencia, B. Ferrari, A. Caballero, Cyclability of binder-free β -Ni(OH)₂ anodes shaped by EPD for Li-ion batteries, *J. Eur. Ceram. Soc.* 35 (2015) 573–584.
- [25] R. Deepak Selvakumar, S. Dhinakaran, Effective viscosity of nanofluids — a modified Krieger–Dougherty model based on particle size distribution (PSD) analysis, *J. Mol. Liq.* 225 (2017) 20–27.
- [26] J. Yus, B. Ferrari, A. Sanchez-Herencia, A. Caballero, J. Morales, Z. Gonzalez, In situ synthesis and electrophoretic deposition of NiO/Ni core-shell nanoparticles and its application as pseudocapacitor, *Coatings* 7 (2017) 193.
- [27] Z. Gonzalez, B. Ferrari, A.J. Sanchez-Herencia, A. Caballero, J. Morales, Use of Polyelectrolytes for the fabrication of porous NiO films by electrophoretic deposition for supercapacitor electrodes, *Electrochim. Acta* 211 (2016) 110–118.
- [28] P. Sundriyal, S. Bhattacharya, Inkjet-printed electrodes on A4 paper substrates for low-cost, disposable, and flexible asymmetric supercapacitors, *ACS Appl. Mater. Interfaces* 9 (2017) 38507–38521.
- [29] R.D. Deegan, O. Bakajin, T.F. Dupont, G. Huber, S.R. Nagel, T.A. Witten, Capillary flow as the cause of ring stains from dried liquid drops, *Nature* 389 (1997) 827–829.
- [30] P.H.L. Notten, F. Roozeboom, R.A.H. Niessen, L. Baggetto, 3-D integrated all-solid-state rechargeable batteries, *Adv. Mater.* 19 (2007) 4564–4567.

J. Yus, Y. Bravo, A.J. Sanchez-Herencia, B. Ferrari, Z. Gonzalez.

Electrophoretic Deposition of rGO-NiO Core-Shell nanostructures driven by Heterocoagulation Method with High Electrochemical Performance.

Electrochim. Acta **2019**, 308, 363 - 372,

doi: 10.1016/j.electacta.2019.04.053



Electrophoretic deposition of RGO-NiO core-shell nanostructures driven by heterocoagulation method with high electrochemical performance

J. Yus, Y. Bravo, A.J. Sanchez-Herencia, B. Ferrari, Z. Gonzalez*

Instituto de Cerámica y Vidrio, CSIC, Madrid, Spain

ARTICLE INFO

Article history:

Received 8 February 2019

Received in revised form

8 April 2019

Accepted 8 April 2019

Available online 9 April 2019

Keywords:

RGO

NiO

Heterocoagulation

Core-shell

Electrophoretic deposition

Supercapacitors

ABSTRACT

A heterocoagulation route is proposed to prepare Reduced Graphene Oxide-Nickel Oxide (RGO/NiO) hybrid structures for their application as supercapacitor electrodes. The RGO intercalation among the NiO nanoplatelets was carried out by electrostatic interactions of the synthesized particles which were previously dispersed and stabilized in aqueous media to improve the assembly between both materials forming core-shell structures. The electrophoretic deposition (EPD) was used to shape the composite onto 3D collector (Ni foams) controlling their growth and homogeneity. Electrodes were thermal treated at 325 °C during 1 h to improve the electrochemical response since the formation of ceramic necks among NiO semiconductor nanoparticles preserves the microstructural integrity to enhance their connectivity avoiding the employment of binders, while RGO contributes with the electrochemical double layer effect to step up the specific capacitance by reducing the charge transfer resistance. FESEM results confirmed that RGO nanosheets were full-covered by the NiO nanoplatelets and suggested that ~1 mg of the electroactive composite homogeneously covers the Ni foam and it is the optimum among of electroactive material to avoid microstructural defects that produce ohmic drops limiting the capacitance. The electrochemical characterization of the resulting binder-free RGO/NiO electrodes was compared with the bare-NiO electrode. The hybrid composite exhibited excellent performance with a high specific capacitance of 940 F g⁻¹ at 2 Ag⁻¹ and a higher rate capability.

© 2019 Elsevier Ltd. All rights reserved.

1. Introduction

Due to the energy crisis and the abuse of fossil fuel sources, a huge amount of emissions are promoting the greenhouse effect and increasing the global warming. That is why changing our current energy system is a priority and therefore we are in an urgent need for efficient, clean, and sustainable sources of energy [1]. The main inconvenient of this renewable energy is currently their intermittent production. For this reason, new technologies associated with the conversion and the storage of energy have acquired an especial relevance in the last few decades [2]. Additionally, the demand for high-efficiency energy storage devices is growing every day in other key sectors such as automotive and consumer electronics where a wider autonomy and a lower charge time are demanded [3]. Among all energy storage devices, supercapacitors (SCs) are

widely studied due to their promising properties such as their high power density and excellent cycling stability. They are able to deliver the power energy instantaneously and reduce the recharging times [4]. Attending to their energy storage mechanisms, SCs can be divided into two different groups: i) Electrochemical Double Layer Capacitors (EDLCs) which store energy by an electrostatic phenomena based on the ions accumulation in the double layer growing in the interface of the electroactive material and the electrolyte and ii) Pseudocapacitors (PCs) that store energy through redox reactions which take place on the surface of the electroactive material. EDLCs, usually based on carbonaceous materials, are electrochemically stable and present good conductivity [2,5]. Nevertheless, the power density delivered is limited by the available surface area of the electrode, which used to be lower than that for materials used for PCs, such as metal oxides (especially nanoparticles) or conducting polymers. This is the reason why PCs exhibits more elevated values of specific capacitance, although they present shorter cycle life, lower rate capability (substantial drop of capacitance with an increasing of scan rate) and poorer electrical

* Corresponding author.

E-mail address: zgonzalez@icv.csic.es (Z. Gonzalez).

conductivity than EDLCs. The specific capacitance of PCs can be 10–100 times higher than EDLCs, which significantly enhance their energy density [6,7]. A third group of SCs based on the combination of carbonaceous materials and transition metal oxide/hydroxide can be also found in the literature. The development of hybrid capacitors may result in a superior performance since both storage energy phenomena (ionic double layer and redox reactions) take place at the same time [8,9].

Among all the transition metal oxides, NiO is considered a promising candidate in the manufacturing of supercapacitors due to their high theoretical specific capacitance (3750 F/g), chemical and thermal stability and low cost [10,11]. However, it presents some common drawbacks of the semiconductor materials since delivers poor reversibility at the charge–discharge process due to the volumetric alteration of the crystalline structure during the redox reactions. Besides, it is also considered a ceramic compound, with low electronic conductivity, which is typically mixed by many authors with binders (carbon black, acetylene black or so on) to favor the particles connectivity [12–15]. The improvement of the microstructure connectivity in PCs is one of the reason why some authors have proposed alternative routes based on different processing strategies such as the inclusion of metal phases in the semiconductor material [10,16], the application of a post-sintering heat treatment after a specific shaping process [17–19] or the mentioned combination of the metal oxide with carbon-based materials, such as activated carbon, carbon nanotubes, or other mesoporous materials. Among all of them, graphene-based materials are good candidates due to its two-dimensional hexagonal network and their delocalized electrons show an elevated electronic conductivity, an intrinsic mechanical strength (flexible material), transparency and high specific surface area, which transform them into promising co-material to fabricate the electrodes with higher electrochemical performances [20,21]. However, graphene electrodes are limited due to the re-stacking problem caused by the strong π - π interaction and Van der Waals forces between their sheets, resulting in non-desirable properties like loss of exposed surface area, loss of the electric conductivity, and inferior ion accessibility. It is, therefore, crucial to fabricate a reduced graphene structure (RGO) which keeps the suitability of the material to avoid any possible limitation [22,23].

The integration of RGO together with the NiO in a film requires a preparation method on a large-scale with a good uniform film in order to achieve high electrochemical performance with the two contributions, the EDLC and pseudocapacitance. By far RGO-NiO composites have been synthesized by using different processing techniques. Gao, F. et al. described the synthesis of a RGO/NiO composite by a hydrothermal route exhibiting a specific capacitance of 1139 F g⁻¹ at 0.5 Ag⁻¹ [24]. Li, W. et al. reported the preparation of flower-like NiO/RGO by a hydrogen gas reduction method obtaining a specific capacitance of 428 F g⁻¹ at 0.3 Ag⁻¹ [25]. Chen, Y. et al. informed about the synthesis of NiO nanoparticles/RGO by a combination of hydrothermal and microwave irradiation methods showing a specific capacitance of 617 F g⁻¹ at 1 Ag⁻¹ [26]. Kahimbi et al. described simultaneous synthesis of NiO/RGO composites by ball milling method achieving a capacitance of 590 F g⁻¹ at 1 Ag⁻¹ [27]. Luan, V.H reported the preparation of a RGO/Ni hydrogel with a specific capacitance of 351 F g⁻¹ at 0.625 Ag⁻¹ [28]. Liu, A. informed more recently about the use of sandwich-like RGO/NiO nano-architectures in an asymmetric supercapacitor configuration [29]. However, these approaches often require the preparation of slurries or pastes by mixing the electroactive material with binders and other additives that are essential to connect the electroactive material within the electrode microstructures. Neither any shaping methods nor any thermal treatments have been considered for the preparation and the consolidation of the electroactive materials in

hybrid supercapacitors. In comparison with the pressing of slurries or pastes, or other methods like vacuum filtration, used to shape electroactive materials in tridimensional electrodes (foams or scaffolds), the Electrophoretic Deposition (EPD) could be considered as an alternative which offers several advantages. This room-temperature and non-vacuum processing can be easily transferable to the industry due to their suitability for mass production, in a short time and low cost. EPD also presents a facile control of the deposited mass. The modification of the solid content of the suspension, the deposition time or the applied potential is enough to vary the thickness of the deposited electroactive layer. This technique allows the total and homogeneous coating of complex shapes on the whole exposed surface [30,31]. However, until now, the RGO/NiO films prepared by EPD are still a challenge. Only Xia, X. et al. have reported the preparation of a RGO/porous NiO hybrid film made by a combination of EPD and CBD methods exhibiting a specific capacitance of 400 F g⁻¹ at 2 Ag⁻¹ [32], while Wu, M.S. et al. informed about the formation of nano-scaled crevices and spacers in NiO-attached graphene oxide nanosheets by sequential EPD in bath with different compositions showing a specific capacitance of 569 F g⁻¹ at 5 Ag⁻¹ [33].

In this report, we propose a new route to prepare RGO/NiO structures which consist on the intercalation of the RGO and the NiO by a heterocoagulation method. The improved assembly of both nanoparticles by electrostatic interaction, using a polyelectrolyte as ligand, was successfully implemented. In a first step, both as-synthesized NiO and RGO form a core-shell structure when mixing suspensions in the adequate ratio. Then, the resulting RGO-NiO composite was shaped using EPD in order to full covering metallic 3D substrates (Ni foams) and a subsequent mild thermal treatment process was applied. The fabricated electrodes were tested as electrode supercapacitor.

2. Experimental

All reagents were of analytical grade and used as received without further purification.

Reduced Graphene oxide (RGO) was prepared by the FQM-175 group from the Inorganic department at the University of Cordoba (Spain) following a modified Hummers method described previously elsewhere [34]. Graphite powder (Merck), H₂SO₄ (98%, Panreac), and NaNO₃ (Sigma–Aldrich) were mixed during 20 min under magnetic stirring controlling the temperature and then KMnO₄ (Sigma–Aldrich) was added drop by drop. After the total addition, the suspension was stirred for 30 min at 35 °C. The resulting slurry was diluted in deionized water, and subsequently, H₂O₂ (3%, Sigma–Aldrich) was slowly added and stirred during 15 min at 90 °C. Afterward, the obtained brown gel was filtered and washed with 10%aq. HCl (37%Panreac) and finally with distilled at pH 7. The produced graphite oxide (GO) was dried overnight at 60 °C. Subsequently, a solvothermal process was carried out reducing the GO in a microwave (Milestone flexiWAVE) at 350 W and 200 °C during 6 h. The resulting hydrogel was dried (-80 °C) obtaining the final RGO.

On the other hand, NiO nanoplatelets were obtained after the polymorph β -Ni(OH)₂ annealing in air at 325 °C during 15 min with a heating rate of 10 °C/min. β -Ni(OH)₂ nanoplatelets was synthesized by chemical precipitation at room temperature under the ultrasound action as an external energy source (45 W/cm², 24 kHz, titanium T13 tip, Sonopuls HD 2200, Bandelin Electronic, Germany). The synthesis was made by mixing 8 mmol of nickel nitrate hexahydrated (Ni(NO₃)₂, 99.9% purity; Panreac, Spain), and 40 mmol of ammonia (NH₃, 28%, Panreac, Spain) in a total volume of 80 ml of aqueous solution. This procedure was previously described more in detail elsewhere [10,31,35].

After the powder calcination, the NiO nanoparticles were dispersed in distilled water, assisted by the use of US and employing a polyelectrolyte as dispersant. The polyelectrolyte used for the modification of nanoplatelets surfaces was branched Poly-ethylenimine (PEI, Mw 25,000, Sigma Aldrich, Germany). The maximum amount of additive able to be adsorbed on the NiO nanoplatelets was determined by the zeta potential evolution at pH 10 (adjusted by using tetramethyl ammonium hydroxide (TMAH), Sigma-Aldrich, Germany). The surface charge of the NiO nanoplatelets, before and after the addition of the optimized amount of PEI, as well as that of the RGO nanosheets were evaluated in terms of zeta potential. A Zetasizer Nano ZS (Malvern, UK) was used in order to determine the particle size distribution and zeta potential using Dynamic Light Scattering (DLS) and laser Doppler velocimetry, respectively. For zeta potential determination, suspensions used for determination were prepared with concentrations of 0.2 g/L using 10^{-2} M of KCl as solvent and inert electrolyte to maintain the ionic strength of the suspension medium. The pH adjustments of the suspensions were carried out by addition of small aliquots of 0.1 M HNO₃ or TMAH and controlled with a pH probe (Metrohm AG, Germany). The application of ultrasounds was carried out on the aqueous NiO suspensions (prepared at pH = 10) to evaluate the effect of nanoplatelets dispersion. The particle size distributions were measured at different times of ultrasound (0–150s) and the variation of the suspension concentration (0.2, 0.02 and 0.002 g/L) was additionally considered to determine the stability of the measurement and dispersion degree. The US effect was studied by sonication, using the mentioned high-intensity ultrasonic horn. Finally, zeta potential measurements also help to determine the amount of NiO nanoparticles needed to completely coat the large specific surface of the RGO.

Then the preparation of the RGO-NiO core-shell nanostructures was carried out by inducing heterocoagulation of NiO nanoparticles and RGO. After the composite assembly, the remaining chemicals were eliminated by removing the supernatant after centrifugation and the resulting wet powder was washed several times with ethanol. The cleaned precipitate, still wet (without drying process to avoid the agglomerates formation), was re-suspended in the desired amount ethanol:water (19:1 v/v) solution in order to perform the electrophoretic deposition studio of the nano-composite onto a Ni foam (Goodfellow, thickness: 1.6 mm, bulk density: 0.45 g cm⁻³, porosity: 95%, pores/cm: 20 and purity: 99.5%).

The electrophoretic deposition was carried out under the following conditions:

- Concentration: 1 g L⁻¹ suspension in EtOH: H₂O 19:1 v/v.
- Substrate: Nickel Foam, counter electrode: Pt foil.
- Potentiostatic conditions: Bias Voltage up to 200 V and 15 s.

The distance between the electrodes at the electrophoretic cell was kept constant at 2 cm and the volume of suspension per EPD experiment was 30 ml. No binder was added to the mixture. All experiments were performed using a power source (Keithley 2660, United States). EPD kinetic curves were calculated by following the theoretical adjust proposed by Sarkar and Nicholson model [36].

$$m = m_0 \left(1 - e^{-t/\tau}\right) \quad (1)$$

$$\tau = \frac{V}{f \cdot \mu_e \cdot S \cdot E} \quad (2)$$

where m is the deposited mass (g), m₀ the total mass in suspension (g), t the time (s), V the volume (ml), f the sticking factor, μ_e the

electrophoretic mobility (cm²/V·s), S the surface (cm²) and E the applied electric field (V/cm).

After the EPD process, the electrodes (substrate + electroactive layer) were sintered by a mild thermal treatment at 325 °C for 1 h under Argon atmosphere, with heating and cooling rates of 10 °C/min, in order to consolidate the RGO-NiO films.

The identification of the crystal phases in the coating was carried out by D8 Advance Bruker X-ray diffractometer with Cu K α radiation ($\lambda = 1.5418$ Å) at 40 kV and 30 mA and $2\theta = 10$ –70 (Bruker, Germany). The N₂ adsorption/desorption isotherms and BET specific surface area of the RGO nanosheets were carried out with an Accelerated Surface Area & Porosimetry (ASAP) system (Micromeritics ASAP 2020 (USA)) and the thermogravimetry (DTA-TG) measurements for both initial materials were carried out using a thermal analyzer (Perkin Elmer, USA). Both nanoparticles and core-shell nanostructures morphologies were also observed with a field emission scanning electron microscope (FESEM, Hitachi S-4700, Japan).

The specific capacitance of the electrodes was tested in a three-electrode cell configuration with the Autolab PGSTAT302 N potentiostat/Galvanostat (Autolab, Switzerland). The as-prepared RGO-NiO working electrode was directly tested after the thermal treatment, Ag/AgCl (saturated KCl) reference electrode (CH Instruments, Inc.) was used as reference electrode and a Pt foil as counter electrode. The electrolyte was a 1 M KOH aqueous solution. Cyclic voltammetry (CV) was performed in ten sequential cycles at a scan rate ranging from 2 to 50 mV/s in a potential window of 0.0–0.5 V. The specific capacitance was determined from the charge value Q, proportional to the integral of the CV curve. Q represents the difference between the area under the charge curve and the area under the discharge curve for the upper and lower limits of the potential window. Thus, the specific capacitance was obtained from equations (3)–(5):

$$Q = \int I \cdot dt; t = \frac{V}{v} \quad (3)$$

$$Q = \frac{1}{v} \int I dV \quad (4)$$

$$C = \frac{Q}{m \cdot \Delta V}; C = \frac{\int I \cdot dV}{v \cdot m \cdot \Delta V} \quad (5)$$

where I is the current (A), t the time (s), V the voltage (V), v the scan rate (V/s), C the specific capacitance (F/g), m the mass (g) and Q the charge/discharge value (C).

The charging/discharging measurement was carried out through chronopotentiometry analysis (CP) at 2 A/g using a multichannel potentiostat–galvanostat system (Arbin BT2000). From CP measurements, the specific capacitance value was calculated according to equation (6):

$$C = \frac{I \cdot \Delta t}{m \cdot \Delta V} \quad (6)$$

where C (F·g⁻¹) is the specific capacitance, I (A) is the discharge current, Δt (s) is the charging/discharging time, ΔV (V) is the voltage window for discharge, and m (g) is the mass of the active material in the electrode.

Further electrochemical impedance spectroscopy (EIS) measurements were performed in a potentiostatic mode at ambient temperature in the frequency range 0.1–10⁶ Hz with a rms value of sinusoidal AC Voltage of 50 mV.

3. Results and discussion

Although the syntheses of both materials of our electroactive composite (RGO-NiO) were previously described separately elsewhere [31,34], additional characterization was carried out to understand better their colloidal behavior. The particle size distributions of the NiO nanoplatelets, obtained by annealing the β -Ni(OH)₂, were measured in terms of volume of particles at different ultrasound (US) time to evaluate the maximum dispersion level in the liquid media and favor their effective and homogeneous mixture during the heterocoagulation with the RGO particles. Fig. 1a shows a decrease of the particle size (Dv50) with the increase of the US time achieving a minimum size of 227 nm after 90 s of US, which coincides with the diameter of the particle measured by FESEM (inset of Fig. 1a). Additionally, the measured particle size (Dv50) for the NiO nanoplatelets did not exhibit any significant variation when the suspension concentration increases, which means that the measure and the nanoplatelets dispersion are stable when solid content ranges from 0.002 to 0.2 g L⁻¹.

Furthermore, zeta potential analyses were made in order to adapt the nanoplatelets surfaces to get specific charge values (suitable for the electrostatic interaction with the surfaces of RGO with opposite charge) as well as to stabilize the nanoparticles in the suspension media. Fig. 1c includes the variation of the zeta potential as a function of pH for the NiO suspension dispersed with and without PEI addition. The blue line corresponds to the evolution of NiO nanoplatelet surfaces before adding the polyelectrolyte. The NiO nanoplatelets show a positive zeta potential for the whole pH range. As the zeta potential of the NiO nanoparticles is higher at acid pH values, then pH 10 was selected to work since the surface charge balance of the nanoplatelets is closed to 11 mV. At this pH, the exact concentration of polyelectrolyte (PEI) required to fully cover the surface of the NiO nanoplatelets was determined. In these operation conditions, the PEI is partially protonated (pK_a 8.6) and can be adsorbed onto the surface of NiO through its protonated amine groups resulting in a slightly increase of the positive surface charge (Fig. 1d). Although the NiO nanoplatelets surfaces are

positive at pH 10, the low absolute value of zeta potential indicates the existence of negatives sites in the NiO nanoplatelets surface, where the partially protonated PEI chains can be adsorbed. For pH > 10, the polyelectrolyte deprotonates while for pH < 10 the higher zeta potential values indicate a decrease of the negative sites at the NiO surface. Consequently, a compromise should be adopted in order to stabilize electrostatically the suspension. In Fig. 1d the zeta potential trend shows that the polyelectrolyte adsorption increases the surface charge up to a maximum value of ~30 mV, which is indicative of the surface saturation [37]. That means PEI adsorbs adopting a branched configuration conferring better stability to the suspension and avoiding the coagulation/agglomeration of NiO nanoplatelets. It is relevant to remark that a low amount of the PEI (1.5 wt %) is needed to enhance the positive charge of the NiO nanoplatelets that should interact with the opposite charge RGO particles. After PEI addition, the variation of the zeta potential as a function of pH was measured (black line in Fig. 1c) stabilising a wider range, from 9 to 12, in which the positive surface charge of NiO modified nanoplatelets increases.

The surface area and pore morphology of RGO was investigated by N₂ adsorption-desorption measurements. Fig. 2b shows that the isotherm has a type IV shape with a wide hysteresis loop observed between 0.45 and 1.0 of relative pressure, according to the BDDT classification and suggesting mono/multilayer and capillary condensation, owing to mesoporous morphology. The estimated BET specific surface area (243 m²g⁻¹) and the pore-size distribution were also included in the inset of Fig. 2b revealing the presence of mesopores >10 nm as well as a small portion of micropores of approximately 2 nm, which suggest an abundant open pore structure that would facilitate the ion diffusion and the electron transport for electrochemical reactions. Additional thermal analysis (TGA-DTA) is included in Fig. 2b to demonstrate that any significant weight loss took place when the as-synthesized RGO powder was treated in Argon up to 600 °C. We fixed the temperature below 600 °C to sinter the electrodes. Further XRD spectra in Fig. 2c shows the characteristic peak at 25° after the calcination process revealing that the RGO powder keeps the structure and there is no evidence

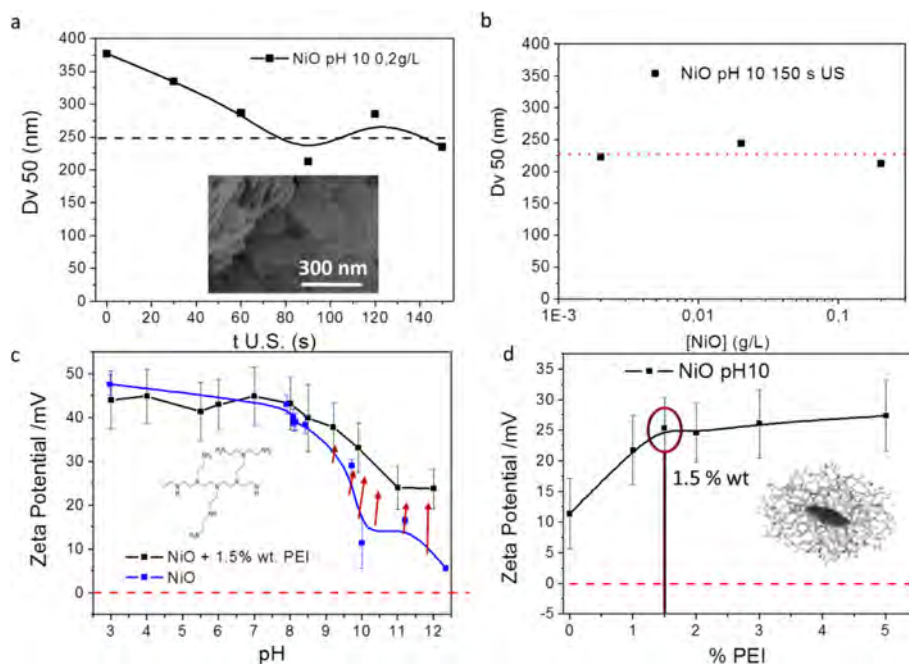


Fig. 1. Dv50 values of the NiO nanoplatelets at a) different US times (the inset includes FESEM image of the nanoplatelets) and b) different concentrations at the same US time. c) Evolution of Zeta potential of NiO as a function of pH and d) evolution of Zeta potential vs amount of adsorbed PEI onto the particle surface.

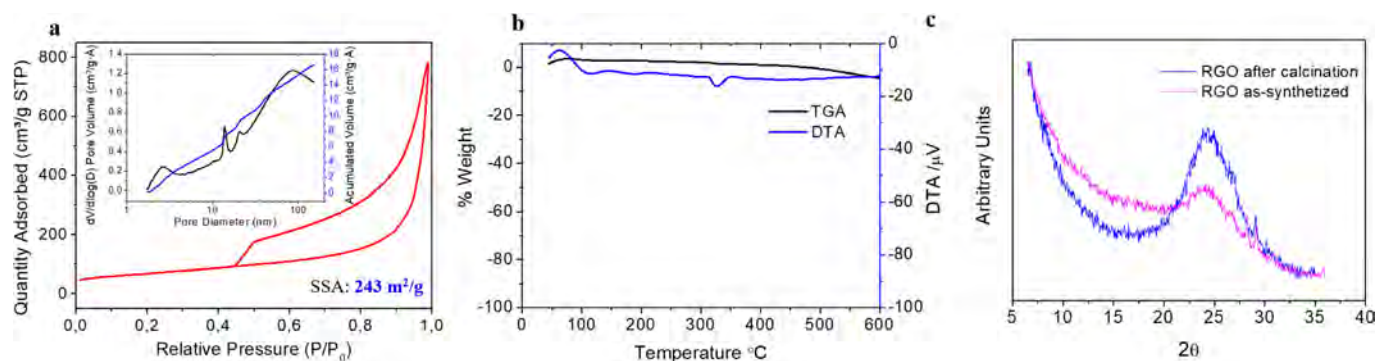


Fig. 2. a) N₂ adsorption/desorption isotherms and pore size distribution. b) TGA-DTA analysis of as-synthesized RGO powder. c) XRD patterns of the as-synthesized RGO powder before and after the calcination process.

of oxidation.

To facilitate the electrostatic interaction between the NiO nanoparticles (Fig. 3a) and the RGO nanosheets (Fig. 3b) in the heterocoagulation process, two different stabilized suspensions should be prepared separately and then mixed. Fig. 3c compares the zeta potential variations as a function of the pH for both components, NiO and RGO. While the surface charge balance of the NiO-PEI nanoplatelets was positive, the surface of the RGO nanosheets was negative throughout the pH range. Thus, a pH value of ~9 (dash square in Fig. 3c) was selected where the electrostatic interaction between them was maximized. The zeta potential of NiO-PEI particles was +40 mV, whereas the value for the RGO nanosheets was -50 mV.

Consequently, the RGO nanosheets were dispersed in distilled water at pH 9 where the opposite charge of RGO nanosheets allows the heterocoagulation with NiO. The formation of the RGO/NiO core-shell structures was also evaluated by monitoring the zeta potential changes. Fig. 3d shows the saturation curve of the RGO surfaces in terms of zeta potential by the addition of different amounts of NiO nanoplatelets, which were previously modified with the polyelectrolyte PEI. Similarly to the saturation bare-NiO

surfaces nanoplatelets with PEI (Fig. 1d the complete adsorption of NiO-PEI particles increases until reaching a value of approximately 40 mV for a ratio of 20 [NiO]:1 [RGO]). This zeta potential value of the RGO/NiO-PEI particles matches the zeta potential value of the NiO-PEI nanoparticles, which indicates that the full coverage of the negative surface of RGO particles. The inserted pictures of Fig. 3d schematize the progressive adsorption of NiO-PEI nanoplatelets onto the RGO nanosheets, Fig. 3e illustrates in detail a FESEM micrograph of a RGO/NiO core-shell structure.

From zeta potential determination, galvanostatic cathodic deposition was favored through the preparation of a stable suspension of the positive core-shell nanostructures, which is favorable since previous studies reported that the cathodic EPD of graphene colloidal suspensions lead to a partial reduction of GO materials [38]. Thus, after the heterocoagulation step and without drying, the powder was re-dispersed in 19:1 v/v EtOH:DI-water. Table 1 summarizes the parameters which define the electrokinetics behavior of the core-shell RGO/NiO structures in EtOH:DI-water medium, as well as the electric conditions: the applied current intensity and the considered deposition time.

Fig. 4 compares the evolution of deposition with time under

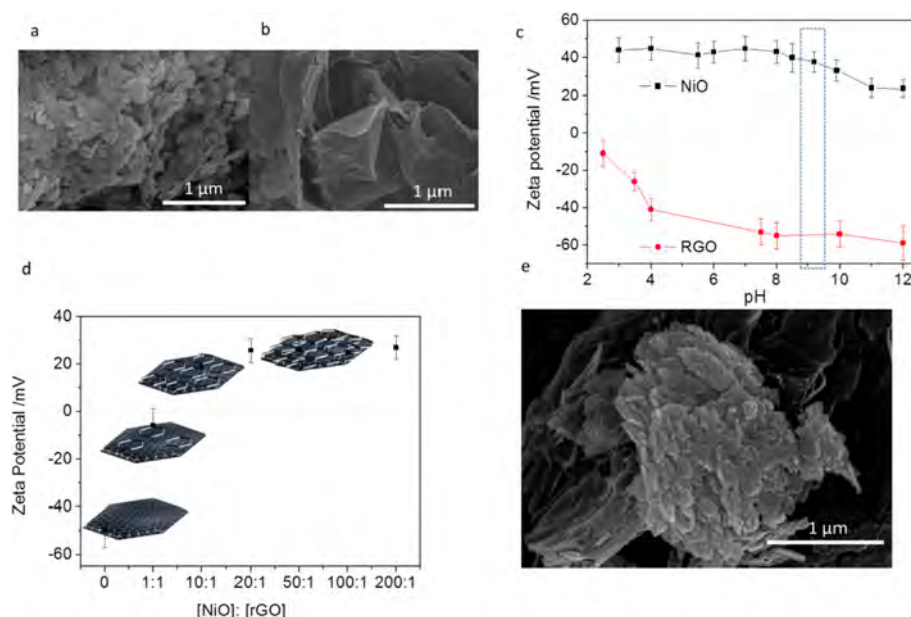


Fig. 3. FESEM images of the as-synthesized a) NiO nanoplatelets and b) RGO nanosheets. c) Evolution of Zeta potential of NiO-PEI and RGO as a function of pH. d) Evolution of Zeta potential vs amount of NiO nanoparticles and e) FESEM image of a resulting RGO/NiO Core-Shell structure.

Table 1
Starting conditions of the suspension for the theoretical approximation for the EPD.

Parameters of the EPD Kinetics	Suspensions		
Electrophoretic mobility, μ_e	$7.75 \cdot 10^{-5} \text{ cm}^2/\text{V} \cdot \text{s}$		
Conductivity, σ	$2.2 \cdot 10^{-6} \text{ S/cm}$		
Initial current intensity, I	0.10 mA	0.15 mA	0.20 mA
Deposition Time, t	30–900 s	30–900 s	30–900 s
Characteristic time for EPD ^a , τ (eq. (2))	8516 s	5677 s	4258 s

^a Calculated for a Volume of suspension of 30 ml, a sticking factor of 1 and an arbitrary area of 1 cm^2 .

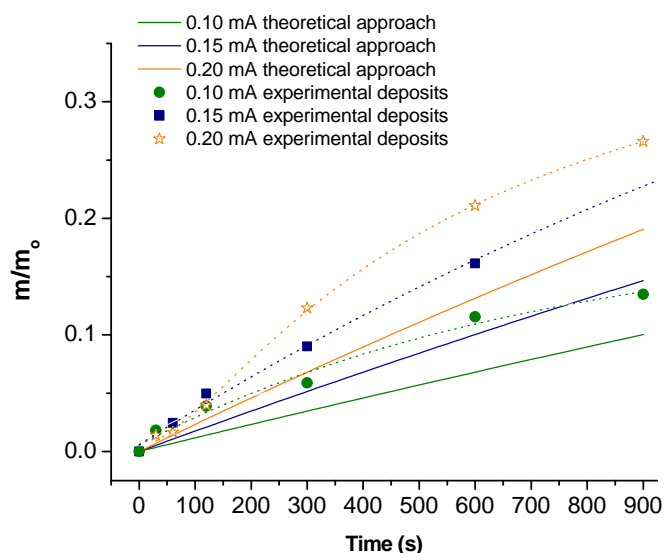


Fig. 4. Theoretical and experimental approximation of the EPD kinetics for NiO/GO suspensions deposited on a Ni foil substrate at different current densities (0.1; 0.15; 0.2 mA).

different applied current intensities (0.10, 0.15 and 0.20 mA) with the experimental data. The solid lines represent the theoretical kinetics of the RGO/NiO nanostructures, calculated considering the electrokinetics parameters listed in Table 1, while dotted lines were used as eye guides for the experimental data plot. The speed of the deposition is related with τ , the characteristic time, which varies depending on the applied current intensity.

In order to calculate the characteristic time and plot the theoretical approaches, sticking factor of 1 was considered in all cases that means, a 100% of the particles arriving to the electrode are deposited onto the substrate. On the other hand, the conduction area and the surface exposed to deposition in the Ni foam were considered similar (S in equation (2)), since the roughness of the foam filament referred to the particle size of the RGO/NiO core-shell allows to assume it [39]. Then the electric field applied during deposition can be calculated as follow:

$$E = \frac{I}{S \cdot \sigma} \quad (7)$$

where I is the applied current intensity (A), and σ is the suspension conductivity (S/cm). The substitution of the electric field in equation (2) leads to a characteristic time expression like follow:

$$\tau = \frac{\sigma V}{f \cdot \mu_e \cdot I} \quad (8)$$

Hence calculated characteristic times were adjusted to 5712, 4032 and 3427 s^{-1} considering current intensities of 0.10, 0.15 and

0.20 mA, respectively. As expected, the stronger electrical conditions promoted the faster deposition process. Similarly occurs with the deposits growths and EPD kinetics step up with the applied intensities following a similar trend. However, experimental data overpassed the theoretical data unexpectedly. As it has been reported elsewhere [40], the proposed model used to approach the theoretical kinetics only considers the parameters mainly involved in the electrophoretic behavior of the particles and does not quantify the phenomena taking place at the interface solid-liquid-solid during deposition, which is represented in this model by the sticking factor, f , which maximum value is 1. In our EPD tests, electrical conditions and some fixed stability conditions contribute to normalize the procedure [41]. For example, the conductivity of the suspension was reduced as much as possible in order to diminish the effect of secondary reactions at the workelectrode (current transients, overpotentials, etc.) and similar conduction and deposition areas can be considered. Consequently, in our system, the deposition and particles packing exclusively depend on the evolution of the colloidal chemistry of the suspension during deposition. The RGO/NiO core-shell nanostructures were stabilized throughout an electro-steric mechanism. The PEI was adsorbed onto NiO (the external layer of the core-shell nanostructure) in a previous step of the RGO nanosheets coverage, providing the whole system (RGO/NiO core-shells) with a positive charge (Fig. 3d). In a cathodic deposition, the increase of pH at the Ni foam surroundings promotes the neutralization of the amine groups of PEI leading to the decrease of the electrostatic contribution to the electro-steric mechanism of stability and promoting a better and faster packing. The film growth was then favored by the own stabilization of the core-shell nanostructure, and this is the reason for the anomalous fast kinetics exhibited by this system if compare with the theoretical approach.

Thus these conditions were selected to prepare the electrodes to evaluate the electrochemical properties. In addition, taking into account the relevance of the deposited mass in order to fully cover the whole specific surface area of Ni foams, further FESEM analyses were carried out. Fig. 5 shows a detail of the as-deposited nanocomposite microstructures shaped by EPD with a deposited mass of 0.5 up to 8.0 mg. All coatings were annealed at 325°C during 1 h under Ar atmosphere to consolidate the RGO/NiO microstructure.

The micrographs 5a and 5e show that the Ni foam is not fully coated (blue arrows), resulting in a discontinuous film which could decrease the final electrochemical response of the composite electrode. Nevertheless, an increase of the amount of the deposited mass around 1 mg (Fig. 5b and 5f) totally covered the 3D collector surface originating cracks and others defects (white arrows in Fig. 5c, 5d and 5g, 5h) when the mass is above 3 mg. These discontinuities reduce the particles connectivity and could affect the specific capacitance values and other electrochemical properties of the composite. Therefore, the optimal mass for the maximization of the electrochemical response was $\sim 1 \text{ mg}$.

To measure this effect, the electrochemical behavior of the RGO/NiO electrodes, prepared at different deposited mass (from 0.7 to 4.8 mg of deposited mass), were evaluated in terms of cyclic voltammetry (CV), galvanostatic charge/discharge test (CP) and electrochemical impedance spectroscopy. The incorporation of the RGO as conductive phase together with the semiconductor compound was also analyzed by comparing with the electrochemical properties of a bare-NiO electrode made with 1.1 mg by following the same EPD procedure. Fig. 6a shows the cyclic voltograms of an electrode example RGO/NiO at different sweep rate 2, 5, 10, 20 and 50 mV/s . The redox reaction of RGO/NiO is due to an interaction between the semiconductor material and the OH^- ions from the electrolyte according to the following equation (7):

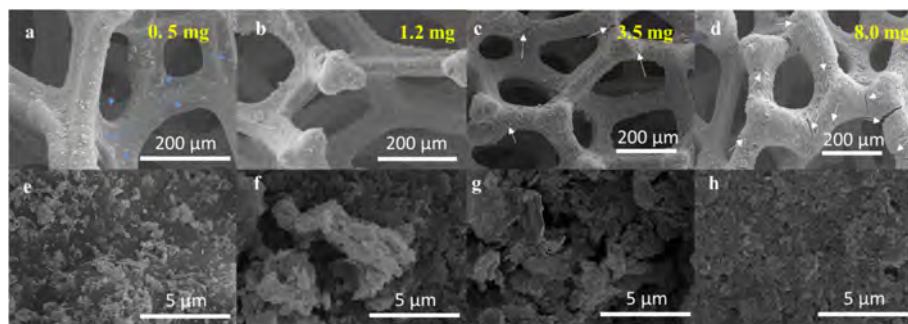


Fig. 5. FESEM images at different magnifications of the RGO/NiO electrodes prepared by EPD at different deposition times (30, 120, 300 and 900 s to obtain 0.5, 1.2, 3.5 and 8.0 mg of deposited mass, respectively).

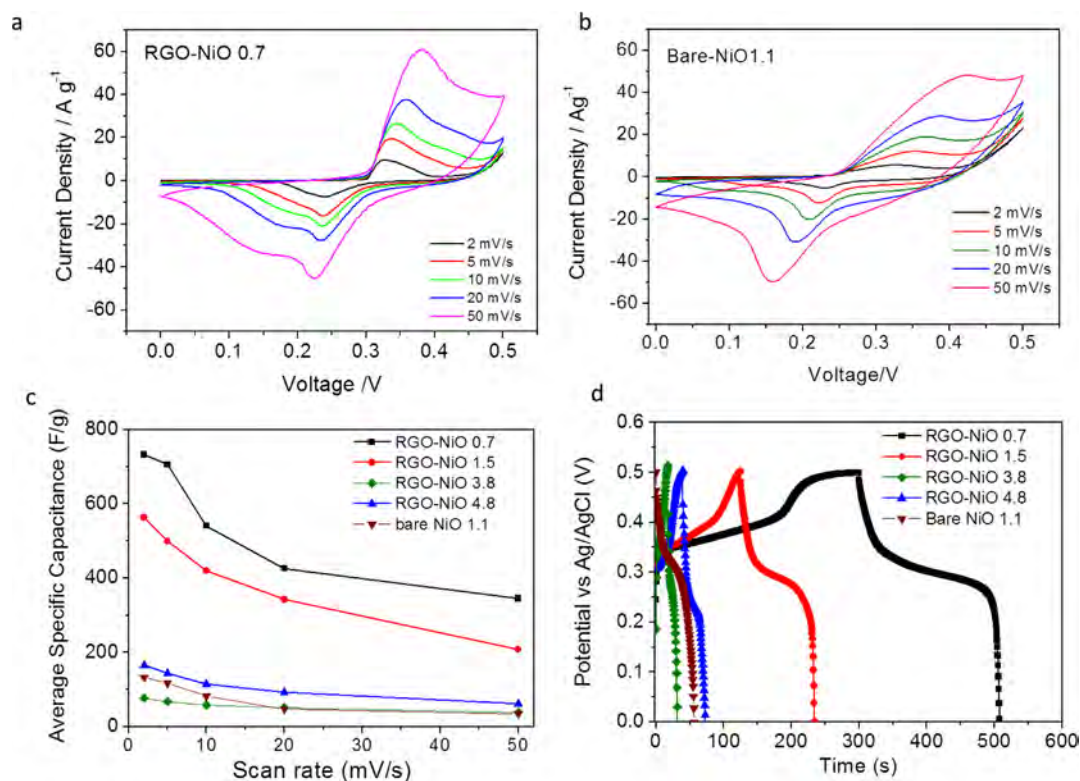


Fig. 6. CV curves at scan rates of 2–50 mV/s of the samples a) RGO/NiO 0.7 mg and b) bare-NiO 1.1 mg. c) variation of the specific capacitance values with the scan rates and d) Galvanostatic discharge profiles of the NiO and RGO/NiO electrodes with different mass.



For all the CVs an increase of potential windows was observed with the increase of the scan rate. The anodic peaks shifted to more positive potentials and the cathodic peak to more negative potentials because of the rapid intercalation of hydroxyl groups in between the interface of electrode/electrolyte at the high scan rate and the polarization of the electroactive material. Although the area under the curves of the others prepared electrodes (RGO/NiO-1.5, 3.8 and 4.8 mg not showed here) were different, the shapes of all voltammograms also showed oxidation and reduction peaks in the successive charge/discharge cycles. Moreover, the shape of these CV curves is partially different from the CV curve corresponding to the bare-NiO electrode, Fig. 6b. The presence of the RGO resulted in a widening of the cathodic peaks which could be attributed to a slight EDLC contribution. In addition, the peaks separation was

lower in the RGO/NiO electrodes which mean a higher rate capability and better reversibility, resulting in faster kinetic for the redox reaction. Fig. 6c summarizes the relation of specific capacitance (calculated by the integration of the cathodic peak area shown in Eqs. (5)–(7) of the experimental section) with the scan rate for the four as-prepared electrodes and compares the results with the specific capacitance (C_s) of a single NiO electrode. All curves show a gradual decrease of the capacitance values with the increase of sweep rate, being the RGO/NiO-0.7 the sample that offers higher results due to the access to a major fraction of active sites and a greater contact of the electrolyte with the electroactive material. It is important to remark that the presence of the RGO improved the electrochemical behavior of the semiconductor material and only the C_s of the RGO/NiO-3.8 electrode was below of the C_s corresponding to the single NiO electrode.

Furthermore, the galvanostatic charge/discharge (C/D) curves measured at the current density of 2 Ag^{-1} under a potential window

of 0–0.5 V were plotted in Fig. 6d. The discharge curves for all the tested electrodes present similar profiles which are divided into three different processes. The first one is assigned to fast initial potential drop in voltage due to internal resistance, a second slope (horizontal-like) is associated to the reduction reaction of Ni^{+2} and finally, a third step that illustrates a steeper voltage decay, corresponding to an electric double layer contribution. The main difference among our electrodes profiles was found in the second step of the discharge, which indicates that their C_s values are governed for the pseudocapacitive effect of the semiconductor material. The similar contribution of the double layer, seen in the third slope of the curves, could be attributed to the full cover of the RGO nanoparticles. From all these measurements, the corresponding specific capacitances were also calculated by equation (8) resulting in values of 920 F g^{-1} , 484 F g^{-1} , 60 F g^{-1} and 128 F g^{-1} for the RGO/NiO electrodes with 0.7, 1.5, 3.8 and 4.8 mg respectively. An excess of deposited mass onto the 3D collector higher than 1.5 mg led to larger contraction effect during drying and sintering of the EPD film which produces microstructural defects with important losses of particles connectivity and thus a decrease of the specific capacitance values. Consequently, the presence of cracks and detached material (seen in Fig. 5) originated resistance rise which result in low C_s values. Moreover, the increase of the mass during the EPD process produced a high level of packaging particles, which reduces the exposed surface area and the inner active sites of the electroactive material being less accessible and therefore decreasing their energy storage capability. Anyway, it is remarkable the synergistic effect of RGO and NiO resulting in a superior electrochemical performance of the supercapacitor electrode.

EIS analysis was additionally carried out to study the effect of the RGO/NiO structures connectivity and the contact resistance between the electroactive composite and current collector in the electrochemical response of the as-prepared electrodes with different deposited mass. All measurements were made at their open circuit potential in the 0.1 Hz – 100 kHz frequency range. Nyquist and Bode plots were displayed in Fig. 7a and b respectively.

Normally, this kind of material shows two parts well-defined on the Nyquist plot. At high frequency, the semicircle is related to the electronic resistance and the charge-transfer impedance R_{ct} . Bigger semicircle results in a large R_{ct} [42]. Therefore, at low frequencies, the nearly vertical but inclined straight lines correspond to the ion

diffusion process within the electrodes structure [43–46]. An ideal capacitor would show a vertical line of 90° phase angle. For the case of pseudocapacitors and due to de R_{ct} resistance this vertical line decays to phase angles smaller than 90° . Furthermore, the Bode plots allow comparing the maximum phase angle (Φ_{\max}) and relaxation time constant (τ_0) of the prepared electrodes. The τ_0 is defined as the minimum time needed to discharge the stored energy with more than 50% efficiency respectively [47,48] and it corresponds with the inverse of the frequency at phase angle (Φ) of -45° [9,49]. It represents the transition from a resistive to a capacitive behavior. A higher τ_0 indicates a lower power capability (slow charge-discharge).

The obtained data were adjusted by the Zview fitting software employing the equivalent circuit included in Fig. 7c. The results were included in Table 2, where R_s is the resistance of electrolyte; R_{ct} is the resistance of charge transfer; and CPE-P is the constant phase element of capacitance. Notice that the results of the bare-NiO were also incorporated herein to evaluate the electron transfer movement through the shaped microstructure in comparison with the RGO/NiO electrodes.

First of all, it is important to note the R_s values for RGO/NiO electrodes if compare with the null electrolyte resistance registered for the bare-NiO electrodes, that means in absence of RGO. RGO/NiO-0.7 and RGO/NiO-1.5 electrodes delivered higher C_s values (920 – 484 F g^{-1}) as well as presented lower R_{ct} values (0.75 – 1.13Ω) than bare-NiO electrode (1.71Ω) confirming that in a well-interconnected microstructure the intercalation of the RGO in the electrode increases the capacitance while provides a shortened electron diffusion path decreasing the charge transfer resistance among semiconductor NiO nanoplatelets, as well as between the electroactive material and the collector ($R_s = 0.94$ – 0.99Ω). Although the RGO/NiO3.8 and RGO/NiO4.8 electrodes also showed low R_{ct} values (0.78 – 0.81Ω), in both cases the R_s increases (1.34 – 1.50Ω) while C_s decreases (60 – 128 F g^{-1}). Probably this effect is associated with the presence of the already mentioned microstructural defects (cracks and non-adhered material) produced by the excess of deposited mass.

In addition, it is noteworthy to mention that the relaxation time constants corresponding to the 3D foam coated with thinner and more homogeneous layers (RGO/NiO-0.7 and RGO/NiO-1.5) maintain low values ($< 9 \text{ ms}$) as NiO-bare electrode, exhibiting a more

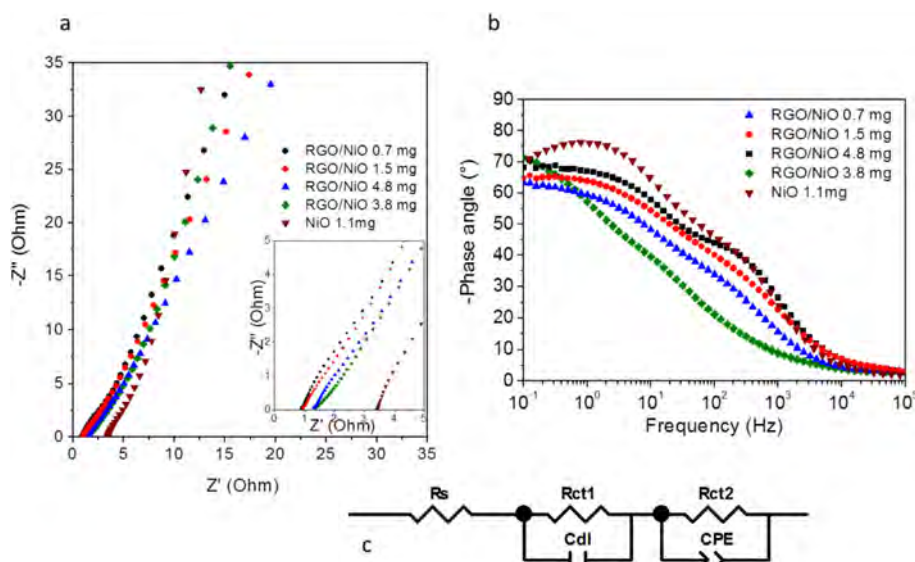


Fig. 7. a) Nyquist and b) Bode plots of the NiO and RGO/NiO electrodes fabricated with different mass. c) Equivalent circuit used to fit the data.

Table 2

Comparative of the fitted EIS parameters of the RGO/NiO electrodes with a different mass. Specific Capacitance values are also included.

Sample	Deposition Time (s)	Mass (mg)	C (Fg ⁻¹)	R _s (Ω)	R _{ct} (Ω)	CPE-P	T ₀ (MS)	Φ _{MAX} (°)
Bare-NiO	60	1.1	250	—	1.71	0.85	8.0	76
RGO/NiO	60	0.7	920	0.94	1.13	0.75	4	70.4
	120	1.5	484	0.99	0.75	0.72	9	65.5
	300	3.8	60	1.50	0.81	0.73	21	71.4
	600	4.8	128	1.34	0.78	0.69	25	63.4

effective profiting of the electrochemical performance although the capacity behavior decay (reflected by lower values of CPE-P and Φ_{MAX}). Consequently we can conclude that the improvement of the RGO/NiO capacitance is mainly due to the faster electron transfer through the hybrid structure, contrarily that occurs in a pseudocapacitor, where the capacitance is strongly dependent on the exposed surface area as it has been reported for the NiO films modified by a layer-by-layer system of polyelectrolytes, and deposited by EPD in similar conditions [30].

4. Conclusions

The C_s value of the homogeneous and thinner RGO/NiO electrode (~1 mg coating) was 920 Fg⁻¹ at a current density of 2 Ag⁻¹ which is more than three times the measured capacitance of the bare-NiO electrode shaped under similar EPD conditions.

It is remarkable the synergistic effect of RGO and NiO resulting in superior electrochemical performance of the hybrid electrode. The intercalation of the RGO nanoplatelets among the NiO nanostructure reduces the transfer charge resistance from 1.71 to 1.13Ω, while capacity performance is farther from the ideal effect (CPE-P = 0.75 and Φ_{MAX} = 70.4). Moreover, charge/discharge curves evidences that the electrochemical performance of the hybrid electrodes is governed by the pseudocapacitive effect provided by the semiconductor nanostructure.

The efficacy of the EPD method to completely cover the 3D Ni collectors with RGO/NiO core-shell nanostructures was also demonstrated by preparing hybrid films with different mass. There is a mass threshold (in our case ~1 mg) to avoid microstructural defects after sintering, such as cracks or material detachments, which affect the final electrochemical performance.

The heterocoagulation process results on a competitive method to intercalate the RGO sheets with the NiO nanoplatelets. The formation of the RGO/NiO core-shell structures was monitored by the zeta potential determination. The complete covering of RGO by NiO nanoplatelets is achieved for a ratio of 20 [NiO]:1 [RGO]. Although the hybrid structures were formed with two specific components (RGO and NiO), the methodology could be applied to other carbonaceous materials and ceramic semiconductors. Different [NiO]:[RGO] ratios can be also processed to evaluate both the EDLC and the pseudocapacitance contributions in the final electrochemical response of the hybrid electrodes.

Acknowledgments

The authors thank the support to the projects S2018/NMT-4411 (Comunidad de Madrid) and MAT2015-70780-C4-1 (MINECO/FEDER). J. Yus acknowledges the Comunidad de Madrid for the support from the Youth Employment Initiative, CAMPD17_ICV_002. Z. Gonzalez acknowledges the Postdoctoral Fellowship: IJCI-2016-28538.

References

- [1] B.K. Kim, S. Sy, A. Yu, J. Zhang, Electrochemical supercapacitors for energy storage and conversion, *Handb. Clean Energy Syst.* (2015) 1–25.
- [2] A. González, E. Goikolea, J.A. Barrena, R. Mysyk, Review on supercapacitors: technologies and materials, *Renew. Sustain. Energy Rev.* 58 (2016) 1189–1206.
- [3] X. Li, B. Wei, X. Li, B. Wei, Supercapacitors based on nanostructured carbon, *Nano Energy* 2 (2013) 159–173.
- [4] Y. Chuminjak, S. Daothong, A. Kuntarug, High-performance electrochemical energy storage electrodes based on nickel oxide-coated nickel foam prepared by sparking method, *Electrochim. Acta* 238 (2017) 298–309.
- [5] J. Han, N. Yoshimoto, Y.M. Todorov, K. Fujii, M. Morita, Characteristics of the electric double-layer capacitors using organic electrolyte solutions containing different alkylammonium cations, *Electrochim. Acta* 281 (2018) 510–516.
- [6] M. Karnan, K. Subramani, P.K. Srividhya, M. Sathish, Electrochemical studies on corn cob derived activated porous carbon for supercapacitors application in aqueous and non-aqueous electrolytes, *Electrochim. Acta* 228 (2017) 586–596.
- [7] Y. Chen, J. Zhang, M. Li, C. Yang, L. Zhang, C. Wang, et al., Strong interface coupling and few-crystalline MnO₂/Reduced graphene oxide composites for supercapacitors with high cycle stability, *Electrochim. Acta* 292 (2018) 115–124.
- [8] P. Yang, Y. Chen, X. Yu, P. Qiang, K. Wang, X. Cai, et al., Reciprocal alternate deposition strategy using metal oxide/carbon nanotube for positive and negative electrodes of high-performance supercapacitors, *Nano Energy* 10 (2014) 106–116.
- [9] L. Yuan, X.-H. Lu, X. Xiao, T. Zhai, J. Dai, F. Zhang, et al., Flexible solid-state supercapacitors based on carbon nanoparticles/MnO₂ nanorods hybrid structure, *ACS Nano* 6 (2012) 656–661.
- [10] J. Yus, B. Ferrari, A. Sanchez-Herencia, A. Caballero, J. Morales, Z. Gonzalez, In situ synthesis and electrophoretic deposition of NiO/Ni core-shell nanoparticles and its application as pseudocapacitor, *Coatings* 7 (2017) 193.
- [11] Z. Yang, F. Xu, W. Zhang, Z. Mei, B. Pei, X. Zhu, Controllable preparation of multishelled NiO hollow nanospheres via layer-by-layer self-assembly for supercapacitor application, *J. Power Sources* 246 (2014) 24–31.
- [12] Z. Zhang, Q. Gao, H. Gao, Z. Shi, J. Wu, M. Zhi, et al., Nickel oxide aerogel for high performance supercapacitor electrodes, *RSC Adv.* 6 (2016).
- [13] F. Feng, S. Zhao, R. Liu, Z. Yang, Q. Shen, NiO Flowerlike porous hollow nanostructures with an enhanced interfacial storage capability for battery-to-pseudocapacitor transition, *Electrochim. Acta* 222 (2016) 1160–1168.
- [14] H. Zhang, X. Wang, C. Chen, C. An, Y. Xu, Y. Dong, et al., Facile synthesis of diverse transition metal oxide nanoparticles and electrochemical properties, *Inorg. Chem. Front.* 3 (2016) 1048–1057.
- [15] M.P. Yeager, D. Su, N.S. Marinković, X. Teng, Pseudocapacitive NiO fine nanoparticles for supercapacitor reactions, *J. Electrochem. Soc.* 159 (2012).
- [16] M. Sawangphruk, S. Pinitsoontorn, J. Limtrakul, Surfactant-assisted electrodeposition and improved electrochemical capacitance of silver-doped manganese oxide pseudocapacitor electrodes, *J. Solid State Electrochem.* 16 (2012) 2623–2629.
- [17] Z. Gonzalez, B. Ferrari, A.J. Sanchez-Herencia, A. Caballero, J. Morales, Use of polyelectrolytes for the fabrication of porous NiO films by electrophoretic deposition for supercapacitor electrodes, *Electrochim. Acta* 211 (2016) 110–118.
- [18] Z. Lu, Z. Chang, J. Liu, X. Sun, Stable ultrahigh specific capacitance of NiO nanorod arrays, *Nano Res.* 4 (2011) 658–665.
- [19] S. Shahrokhian, R. Mohammadi, E. Asadian, One-step fabrication of electrochemically reduced graphene oxide/nickel oxide composite for binder-free supercapacitors, *Int. J. Hydrogen Energy* 41 (2016) 17496–17505.
- [20] C. Yu, J. Yang, C. Zhao, X. Fan, G. Wang, J. Qiu, Nanohybrids from NiCoAl-LDH coupled with carbon for pseudocapacitors: understanding the role of nanostructured carbon, *Nanoscale* 6 (2014) 3097–3104.
- [21] K. Makgopa, P.M. Ejikeme, K.I. Ozoemena, Graphene oxide-modified nickel (II) tetra-aminophthalocyanine nanocomposites for high-power symmetric pseudocapacitor, *Electrochim. Acta* 212 (2016) 876–882.
- [22] C. Jiang, B. Zhan, C. Li, W. Huang, X. Dong, Synthesis of three-dimensional self-standing graphene/Ni(OH)₂ composites for high-performance supercapacitors, *RSC Adv.* 4 (2014) 18080–18085.
- [23] N.B. Trung, T.V. Tam, D.K. Dang, K.F. Babu, E.J. Kim, J. Kim, et al., Facile synthesis of three-dimensional graphene/nickel oxide nanoparticles composites for high performance supercapacitor electrodes, *Chem. Eng. J.* 264 (2015) 603–609.
- [24] F. Gao, Q. Wei, J. Yang, H. Bi, M. Wang, Synthesis of graphene/nickel oxide composite with improved electrochemical performance in capacitors, *Ionics* 19 (2013) 1883–1889.

- [25] W. Li, Y. Bu, H. Jin, J. Wang, W. Zhang, S. Wang, et al., The preparation of hierarchical flowerlike NiO/reduced graphene oxide composites for high performance supercapacitor applications, *Energy Fuel*. 27 (2013) 6304–6310.
- [26] Y. Chen, Z. Huang, H. Zhang, Y. Chen, Z. Cheng, Y. Zhong, et al., Synthesis of the graphene/nickel oxide composite and its electrochemical performance for supercapacitors, *Int. J. Hydrogen Energy* 39 (2014) 16171–16178.
- [27] H. Kahimbi, S.B. Hong, M. Yang, B.G. Choi, Simultaneous synthesis of NiO/reduced graphene oxide composites by ball milling using bulk Ni and graphite oxide for supercapacitor applications, *J. Electroanal. Chem.* 786 (2017) 14–19.
- [28] V.H. Luan, J.S. Chung, S.H. Hur, Preparation of a reduced graphene oxide hydrogel by Ni ions and its use in a supercapacitor electrode, *RSC Adv.* 5 (2015) 22753–22758.
- [29] A. Liu, H. Zhang, G. Wang, J. Zhang, S. Zhang, Sandwich-like NiO/rGO nano-architectures for 4 V solid-state asymmetric-supercapacitors with high energy density, *Electrochim. Acta* 283 (2018) 1401–1410.
- [30] Z. Gonzalez, J. Yus, A. Caballero, J. Morales, A.J. Sanchez-Herencia, B. Ferrari, Electrochemical performance of pseudo-capacitor electrodes fabricated by Electrophoretic Deposition inducing Ni(OH)₂ nanoplatelets agglomeration by Layer-by-Layer, *Electrochim. Acta* 247 (2017) 333–343.
- [31] Z. Gonzalez, B. Ferrari, A.J. Sanchez-Herencia, A. Caballero, J. Morales, Relevance of the semiconductor microstructure in the pseudocapacitance of the electrodes fabricated by EPD of binder-free β -Ni(OH)₂ nanoplatelets, *J. Electrochem. Soc.* 162 (2015) D3001–D3012.
- [32] X. Xia, J. Tu, Y. Mai, R. Chen, X. Wang, C. Gu, et al., Graphene sheet/porous NiO hybrid film for supercapacitor applications, *Chem. Eur. J.* 17 (2011) 10898–10905.
- [33] M.-S. Wu, Y.-P. Lin, C.-H. Lin, J.-T. Lee, Formation of nano-scaled crevices and spacers in NiO-attached graphene oxide nanosheets for supercapacitors, *J. Mater. Chem.* 22 (2012) 2442–2448.
- [34] A. Benítez, D. Di Lecce, G.A. Elia, Á. Caballero, J. Morales, J. Hassoun, A lithium-ion battery using a 3 D-array nanostructured graphene–sulfur cathode and a silicon oxide-based anode, *ChemSusChem* 11 (2018) 1512–1520.
- [35] M. Dios, Z. Gonzalez, E. Gordo, B. Ferrari, Semiconductor-metal core-shell nanostructures by colloidal heterocoagulation in aqueous medium, *Mater. Lett.* 180 (2016) 327–331.
- [36] Partho Sarkar Patrick S. Nicholson, Electrophoretic Deposition (EPD): Mechanisms, Kinetics, and Application to Ceramics, 1996.
- [37] M.E. Helgeson, T.K. Hodgdon, E.W. Kaler, N.J. Wagner, M. Vethamuthu, K.P. Ananthapadmanabhan, Formation and rheology of viscoelastic “double networks” in wormlike micelle-nanoparticle mixtures, *Langmuir* 26 (2010) 8049–8060.
- [38] H. Zhang, X. Zhang, D. Zhang, X. Sun, H. Lin, C. Wang, et al., One-step electrophoretic deposition of reduced graphene oxide and Ni(OH)₂ composite films for controlled syntheses supercapacitor electrodes, *J. Phys. Chem. B* 117 (2013) 1616–1627.
- [39] R. Moreno, B. Ferrari, Nanoparticles dispersion and the effect of related parameters in the EPD kinetics, in: *Electrophor. Depos. Nanomater*, Springer, 2012.
- [40] C. Mendoza, Z. González, Y. Castro, E. Gordo, B. Ferrari, Improvement of TiN nanoparticles EPD inducing steric stabilization in non-aqueous suspensions, *J. Eur. Ceram. Soc.* 36 (2016) 307–317.
- [41] R. Moreno, B. Ferrari, Aqueous electrophoretic deposition of ceramics: the controlling parameters, in: *Electrophoretic Deposition: Fundamentals and Applications*, 2002. Edition.
- [42] X. Feng, J. Zhou, L. Wang, Y. Li, Z. Huang, S. Chen, et al., Synthesis of shape-controlled NiO–graphene nanocomposites with enhanced supercapacitive properties, *New J. Chem.* 39 (2015) 4026–4034.
- [43] G. Zhou, D.W. Wang, L.C. Yin, N. Li, F. Li, H.M. Cheng, Oxygen bridges between nio nanosheets and graphene for improvement of lithium storage, *ACS Nano* 6 (2012) 3214–3223.
- [44] M.L. Huang, C.D. Gu, X. Ge, X.L. Wang, J.P. Tu, NiO nanoflakes grown on porous graphene frameworks as advanced electrochemical pseudocapacitor materials, *J. Power Sources* 259 (2014) 98–105.
- [45] S.A. Abbas, K.D. Jung, Preparation of mesoporous microspheres of NiO with high surface area and analysis on their pseudocapacitive behavior, *Electrochim. Acta* 193 (2016) 145–153.
- [46] C.Y. Yoo, J. Park, D.S. Yun, J.H. Yu, H.H.C. Yoon, J.N. Kim, et al., Crucial role of a nickel substrate in Co₃O₄ pseudocapacitor directly grown on nickel and its electrochemical properties, *J. Alloy. Comp.* 676 (2016) 407–413.
- [47] P.L. Taberna, P. Simon, J.F. Fauvarque, Electrochemical characteristics and impedance spectroscopy studies of carbon-carbon supercapacitors, *J. Electrochem. Soc.* 150 (3) (2003) A292–A300.
- [48] S.Z. Inamuddin, Mohammad Faraz Ahmer, Abdullah M. Asiri, *Electrochemical Capacitors: Theory, Materials and Applications*, 2018.
- [49] Y. Xu, Z. Lin, X. Zhong, X. Huang, N.O. Weiss, Y. Huang, et al., Holey graphene frameworks for highly efficient capacitive energy storage, *Nat. Commun.* 5 (2014).



Publication

7

J. Yus, B. Ferrari, A.J. Sanchez-Herencia, Z. Gonzalez.

Understanding Electron Transport and Ion Diffusion on Ni-based semiconductor microstructures shaped on 3D hierarchical networks by EPD.

Sent to publish to the Journal of Power Sources

Manuscript Number:

Title: Understanding Electron Transport and Ion Diffusion on Ni-based ceramic semiconductor microstructures shaped on 3D hierarchical networks by EPD

Article Type: Research Paper

Keywords: Semiconductor, Pseudocapacitors, Ni-based electrodes, Electron Transport, Capacitive behavior.

Corresponding Author: Dr. Zoilo Gonzalez, Ph.D.

Corresponding Author's Institution: ICV-CSIC

First Author: Joaquin Yus, PhD student

Order of Authors: Joaquin Yus, PhD student; Begoña Ferrari, PhD; Antonio Javier Sanchez-Herencia, PhD; Zoilo Gonzalez, Ph.D.

Manuscript Region of Origin: SPAIN

Abstract: The particles connectivity or the consolidation level of the nanostructure play a relevant role in the electrodes to enhance the final device behaviour. The nanostructure design of a sintered ceramic film allow us to deliver specific capacitances up to 1000 F/g, overpassing thermal and mechanical mismatches between semiconductors and collectors providing a robust microstructure with a high performance and cyclability. The modification of the Ni-based electrodes nanostructures allow understanding and differencing the contribution of the specific features on the electron transport and the ion diffusion. EIS analysis show the specific contribution of nanoparticles morphology, composition, packing and consolidation, to the electroactivity. This characterization proves that the unique hierarchical porous 3D NiO network improves the rate capability and capacitance retention at high charging/discharging rate, exhibiting a relaxation time constant in the same range of EDLC capacitors, while the high charge-transfer resistances is negligible if the exposed surface is high enough to maintain a high ion transport. The inclusion of Ni NPs in the NiO semiconductor microstructure and the selection of the optimal deposited mass and sintering treatment creates a metal-ceramic electrode that enhances both the electron transport resistance and the capacitive behavior maintaining a quick charge/discharge rate.



MINISTERIO
DE ECONOMÍA
Y COMPETITIVIDAD



CSIC
CONSEJO SUPERIOR DE INVESTIGACIONES CIENTÍFICAS



INSTITUTO DE CERÁMICA Y VIDRIO

Madrid, March 4th, 2019

Dear Editor,

Please find enclosed the original manuscript entitled “**Understanding Electron Transport and Diffusion on Ni-based semiconductor shaped on 3D hierarchical networks by EPD**” by J. Yus; B. Ferrari; A.J. Sanchez-Herencia and Z. Gonzalez which we submit for publication at the **Journal of Power Sources**.

In this work we are discussing for the first time in the literature by electrochemical impedance spectroscopy (EIS) the relevance of totally different microarchitecture configurations and the specific contribution of nanoparticles morphology, composition, packing and consolidation, in the electrochemical response of three-dimensional electrodes based on transition metal oxides (TMO).

We would like to remark that we are not claiming the best high specific capacitance values during the cycling for our electrodes (already reported and cited several times along the manuscript), but the main reasons why these capacitance values are delivered, that is, how a rise of specific surface area or an increase of nanoparticles connectivity, can affect to the electrochemical behavior of a semiconductor electroactive material, with a consolidated microstructure, shaped by EPD and sintered at different thermal treatments. Just a few authors have been able to separate the influence of each physicochemical contribution to justify the final electrochemical performance.

Although the conclusions of the work are focused on NiO structures, they could be extended to the rest of TMO. Thus, we expect to have an important impact on others authors that they are working with other semiconductor-based compositions

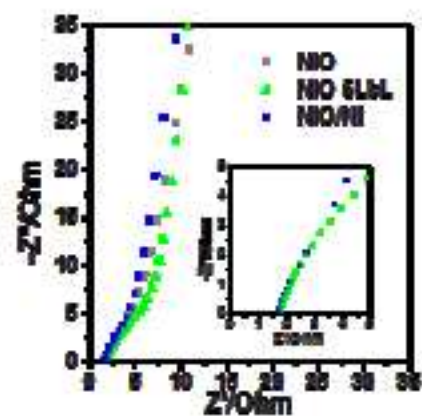
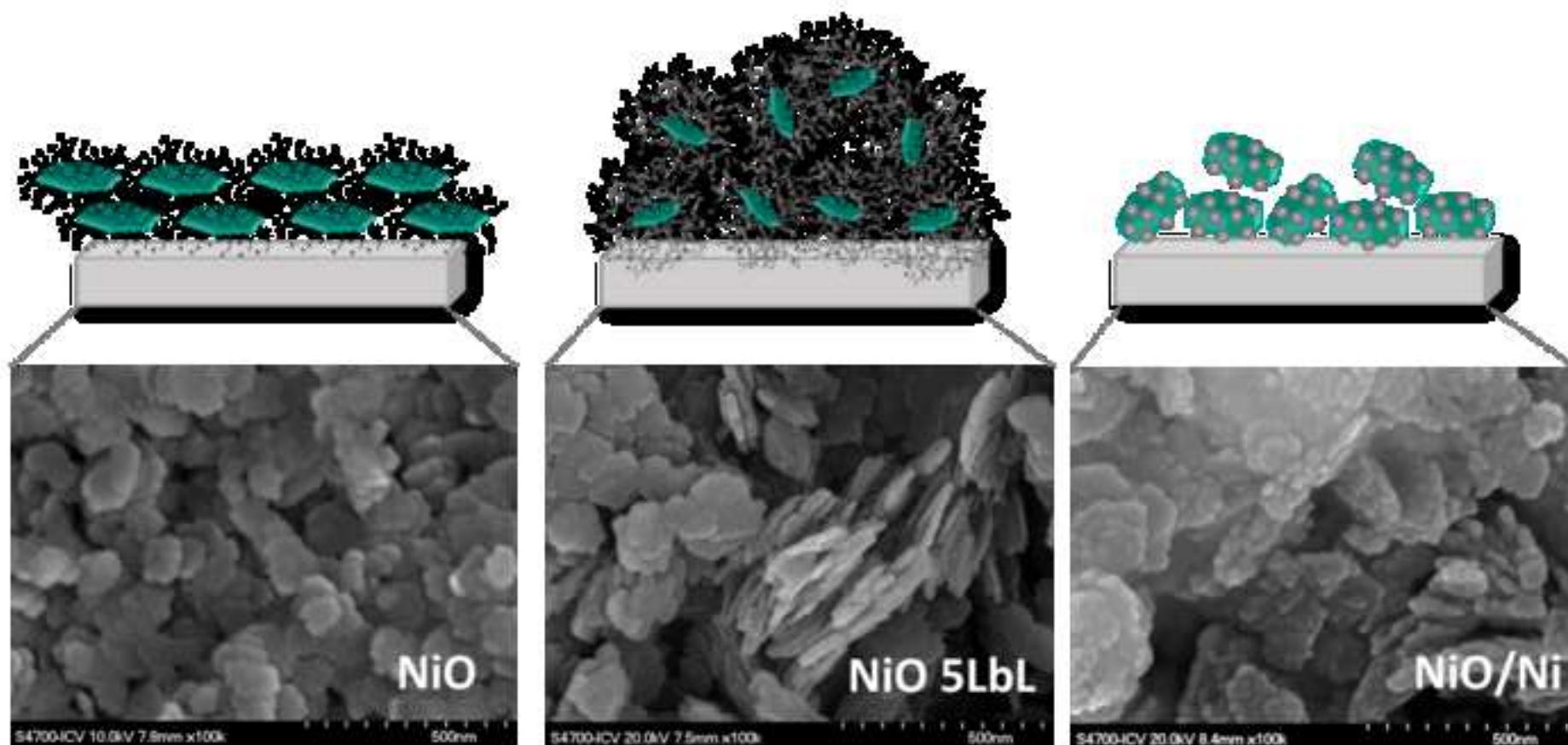
Hoping this work being at the scope of the journal and have the expected impact, I acknowledge very much your interest.

Yours sincerely,

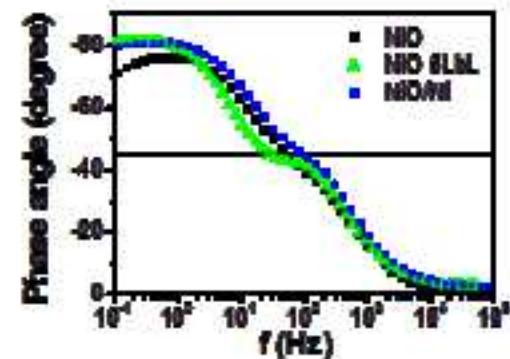
Dr. Zoilo González

Data of the corresponding author are:

Dr. Zoilo González
Institute for Ceramic and Glass. CSIC
Kelsen Street, 5. 28049, Madrid, Spain
email: zgonzalez@icv.csic.es



Coating	R_{ct} (Ω)	CPE-P	τ_0 (s)	Φ_{max} ($^\circ$)
NiO	1.71	0.85	8.0	76
NiO5LbL	3.65	0.90	18.0	82
NiO/Ni	1.55	0.90	11	81



Research Highlights

- Layer by Layer strategy and Core-Shells deposition were used to build different NiO-based microarchitectures
- Benefits of the exposed SSa and porosity increase the CPE in spite of increase of R_{ct} value
- Ni NPs favor the electron transport through the NiO microstructure (with lower R_{ct} value)
- The thermal consolidation level and the active mass affect to electrical response of electrodes

Understanding Electron Transport and Ion Diffusion on Ni-based ceramic semiconductor microstructures shaped on 3D hierarchical networks by EPD

J. Yus, B. Ferrari, A.J. Sanchez-Herencia and Z. Gonzalez*

Instituto de Ceramica y Vidrio, CSIC, Kelsen 5, 28049 Madrid, Spain.

*Corresponding author: zgonzalez@icv.csic.es

Abstract

The current state of the art for supercapacitors based on ceramic semiconductors (NiO, MnO, etc.) evidences that its electrochemical response is affected by the effect of the nanoscale, the morphology and the specific surface area of the electroactive material. However, other significant parameters such as the particles connectivity or the consolidation level of the nanostructure also play a relevant role offering alternative routes to enhance the final device behaviour. The nanostructure design of a sintered ceramic film can improve the pseudocapacitance, being a clear alternative to EDLC supercapacitors, since the use of nanoparticles can help to overpass thermal and mechanical mismatches between ceramic semiconductors (active electrodes) and the metal substrates (collectors) providing a robust microstructure with a high electrochemical performance and cyclability. In this work, the design and modification of the Ni-based electrodes nanostructures allow understanding and differencing the contribution of the specific features on the electron transport and the ion diffusion, and definitely in the final electrochemical response of a pseudocapacitor. NiO nanoplatelets have been modified superficially by the adsorption of a polyelectrolyte multilayer and by the heterogeneous precipitation of metallic Ni nanoparticles before being deposited on different metal collectors by electrophoretic deposition (EPD). Processed electrodes deliver specific capacitances up to 1000 F/g at 2A/g. A deep analysis through electrochemical impedance spectroscopy (EIS) show the specific contribution of nanoparticles morphology, composition, packing and consolidation, to the electroactivity of three-dimensional-NiO based electrodes. This characterization proves that the unique hierarchical porous 3D NiO network improves the rate capability and capacitance retention at high charging/discharging rate, exhibiting a relaxation time constant in the same range of EDLC capacitors (τ_0 = 8-18 ms), while the high charge-transfer resistances (R_{ct} = 3.65 Ω) is negligible if the exposed surface is high enough to maintain a high ion transport. Additionally the inclusion of Ni NPs in the NiO semiconductor microstructure and the selection of the optimal deposited mass and sintering treatment creates a metal-ceramic electrode that enhances both the

electron transport resistance ($R_{ct} = 1.55 \, \Omega$) and the capacitive behavior (CPE-P = 90) maintaining a quick charge/discharge rate ($\tau_0 = 11 \, \text{ms}$).

Keywords: Semiconductor, Pseudocapacitors, Ni-based electrodes, Electron Transport, Capacitive behavior.

Introduction

Pseudocapacitive materials growing attention is due to their capacity to enhanced energy density, improving simultaneously cycling stability with high capacity retention in hybrid supercapacitors and outdistancing traditional electrical double-layer capacitors [1,2]. These storage devices have several advantages over batteries in terms of power density, long cycle life and efficiency and thermal stability [3]. For these reasons, pseudocapacitors are now strong candidates to be used in wearable electronic devices [4] or energy harvesters [5], as well as in electric vehicles [6] or storing of intermittent renewable energy sources such as wind and solar[7].

Semiconductor nanomaterials based on RuO_2 , MnO_2 , Fe_3O_4 and Co_3O_4 have been intensively studied as pseudocapacitors [8,9] while the electrochemical performance of new compositions, such as nitrides or mixed oxides, as well as 3D nanostructures are matter of study [10–12]. Among the electroactive materials, Ni-based electrodes are promising candidates due to the high theoretical specific capacitance of NiO (3750 F/g), its ready availability and low cost, and its good thermal and chemical stability [2,8,13–15]. However full profiting of the Ni surface reactions to achieve the theoretical value of the capacity is still a challenge since the electrochemical response of the semiconductor electrodes not only depends on the inherent properties of the selected material. They should have high surface area with plentiful reaction sites and achieve a successful electrolyte impregnation through the porous nanostructure, while conducting electrons through the metal oxide. Consequently an optimal performance requires of a 3D nanostructure with mixed meso- and macro interconnected pores to hold easy accessible redox active sites as well as reinforced charge transfer and ion diffusion capability.

Traditionally the fabrication of semiconductors (mainly metal oxides) lies on the formulation of a mixture of the electroactive material with binder additives like carbon black (CB), acetylene black, PVDF, PTFE, etc. which are used to improve contact between particles. The resulting pastes are directly applied and pressed onto conductive substrates such as metallic or carbon [16–20]. Nevertheless, the poor electrical connectivity and the weakness of the resulting electrodes lead the development of fabrication routes of alternative binder-free electrodes where the electron transfer movement through the shaped microstructure is favored. In this sense nanosized metal oxides such as Ni-based nanocompounds can be consolidated by a sintering (annealing) treatment at low temperature after synthesis and shaping [2,11,21–23], leading to a stronger electrically connected electrodes, where the porous nanostructure

provides the structural tolerance needed to overpass the volume changes of the faradaic reactions. It is well known that the formation of ceramic necks between particles provides a better electron transport and improve the electrochemical response. Also the electrical conductivity can be improved by including metal [10], [24] or nonmetal impurities [11], [25] within the oxide nanostructure, generating donor or acceptor states in the bandgap and thereby increasing the concentration of charge carriers.

The use of a simple, reliable, controllable, as well as green and cost-effective colloidal technique such as EPD allows obtaining nanostructures tailoring and strengthening the control over deposited mass onto the 3D metallic collector. Opposite to other coating techniques, the EPD is able to cover difficult access surfaces in the 3D architectures. Moreover, significant physical parameters such as the films thickness, the amount of the deposited electroactive material as well as the particles packing can be easily tuned by EPD parameters like the concentration of the suspension, the applied potential and/or the deposition time.

In previous works [22,23,26,27] the specific capacitance and the reversibility of synthesized NiO nanoplatelets were evaluated. Resulting electrodes showed a robust 3D electroactive electrodes with micro-, meso- and macroporosity hierarchically ordered in different microarchitectures and achieved specific capacitances up to 1000 F/g at 2 A/g. In these studies, the NiO nanoplatelets surface was modified by either the alternative adsorption of polyanions and polycations forming a polyelectrolyte multilayer or the in situ heterogeneous precipitation of metallic Ni nanoparticles (NPs). The control on the processing parameters like the amount of deposited mass, thickness, temperature and time of the thermal treatment of sintering, etc., resulted in different features of the Ni-based coatings which improve the film quality as well as pseudocapacitor performance in many senses.

In this new paper the key role of tuning the microstructure of a shaped material is presented at the light of the electrochemical measurements. On one side the microstructural design of the two levels of porosity achieved by the Layer-by-Layer (LbL) [26] surface manipulation which is determinant in the capacitance values achieved. But also different thermal treatments promote different degrees of the nanoparticles connectivity in pure ceramics or in metal-ceramic composites which affects to the final electrochemical contributions [23]. Electrochemical impedance spectroscopy (EIS) is a steady state method used to obtain electric response of an electrochemical cell to an applied AC potential over a range of frequencies. It is usually measured with a very small input signal, which does not perturb the system much [28]. In the present work, EIS was used as a diagnostic tool to study the effect of the semiconductor nanoparticles connectivity in the electrochemical response of NiO-based electrodes with

different microstructures, especially those with different pore-channel openness and interconnection. The different microstructures were obtained by covering different collector substrates (2D and 3D structures), followed by sintering at 325 °C or 375 °C under Ar atmosphere during 15 or 60 minutes. EIS data were compared by using an appropriate equivalent circuit and analyzing the circuit parameters extracted from the experimental data.

Experimental Section

All chemicals were of reagent grade and used without any further purification. The Ni(OH)₂ nanoplatelets and NiO/Ni core-shell nanoparticles were synthesized by chemical precipitation and reduction reactions at room temperature under the ultrasound action as an external energy source (45 W/cm², 24 kHz, titanium T13 tip, Sonopuls HD 2200, Bandelin Electronic, Germany). The β-Ni(OH)₂ was synthesized by mixing 8 mmol of nickel nitrate hexahydrated (Ni(NO₃)₂, 99.9% purity; Panreac, Spain), and 40 mmol of ammonia (NH₃, PA 25%, Panreac, Spain) in a total volume of 80 ml of aqueous solution. The annealing of Ni(OH)₂ powder to obtain NiO was carried out in Air at 325 °C during 15 minutes with a heating rate of 10°C/min. Metallic Ni nanoparticles (NPs) have been synthesized onto the surface of the NiO nanoplatelets by heterogeneous reduction of a nickel precursor (Ni(NO₃)₂·6H₂O) in the same media where NiO nanoplatelets were previously dispersed at pH 10. The NP's were precipitated by the chemical reduction by adding a mixture of monohydrate Hydrazine (N₂H₄·H₂O, Sigma-Aldrich, Germany), with Potassium Hydroxide (KOH, Panreac, Spain), also sonicating with the same ultrasonic horn (SonopulsHD2200). The temperature was controlled through the recirculation from a cryothermal bath. Both procedures have been previously described more in detail elsewhere [23,27,29].

The identification of the crystal phases of the synthesized powders was carried out with a X-ray diffractometer (D8 Advance, Bruker, Bremen, Germany) using Cu K radiation (λ= 1.5418 Å) at 40 kV and 30 mA and 2θ = 10–70). Crystallite size (L_{hkl}) and unit cell dimensions (c) were determined by using the following equations:

$$L_{hkl} = \frac{k \cdot \lambda}{FWHM \cdot \cos \theta} \quad [\text{Eq.1}]$$

$$c = \frac{\lambda \cdot \sqrt{h^2 \cdot k^2 \cdot l^2}}{2 \cdot \sin(\theta)} \quad [\text{Eq.2}]$$

Where L_{hkl} is the size of the crystallite; k is a dimensionless shape factor, with a value close to unity, λ is the X-ray wavelength; FWHM, is the width of the peak at half height after subtracting the instrumental line broadening, in radians; and θ is the Bragg angle in radians.

And c is the unit cell dimension in Armstrong, and θ is the Bragg angle in radians, λ is the X-ray wavelength; and hkl the miller index for the family of lattice planes.

The N_2 adsorption/desorption isotherms and BET specific surface area (SSA) determination for the $Ni(OH)_2$, NiO and NiO/Ni nanoparticles were carried out with an accelerated surface area and porosimetry system (ASAP 2020, Micromeritics Instrument Corp., Atlanta, GA, USA). The nanoparticles morphologies were observed with a field emission scanning electron microscope (FESEM), (S-4700, Hitachi High-Technologies, Tokyo, Japan). High resolution transmission electron microscopy (HRTEM) images were recorded operating at 200 kV using a (Jeol JEM 2100F) electron microscope equipped with a CCD camera (Orian Gatan). To avoid degradation of the material, TEM images were recorded at low energy conditions.

After the synthesis, the resulting powder were separated from the reaction waters by centrifugation and washed several times with distilled water at pH 10, adjusted with trimethylamine, TMAH (Merck, Darmstadt, Germany). The washed precipitate, still wet, was re-diluted in a desired amount of water at pH 10 where the polyelectrolytes are sequentially added. The polyelectrolyte used for the modification of nanoplatelets surfaces was branched Polyethylenimine (PEI, Mw 25000, Sigma Aldrich, Darmstadt, Germany). It confers a positive charge to the $Ni(OH)_2$ and NiO/Ni nanoparticles which stabilizes the suspension and allows the use of cathodic deposition.

Ni-based electrodes were prepared following the EPD method described previously elsewhere[22,23]. Ni foams, Ni foils, Cu foils and SS foils substrates were introduced in a 1g/L suspension of Ni-based nanoparticles in Ethanol:DI water 19:1, during the necessary time to deposit around 1 mg of electroactive material. After drying the electrodes were sintered in air at different temperatures and dwell times ($\leq 325^\circ\text{C}$ and ≤ 60 minutes).

The electrochemical measurements were carried out in an electrochemical half-cell equipped with an Ag/AgCl (saturated KCl) reference electrode (CH instruments, Inc.) and a platinum-plate counter electrode. A KOH solution (1M) was used as electrolyte. The capacitive performance of the electrodes was tested under different conditions. Cyclic voltammetry (CV) tests were carried out with a Potenciostat/Galvanostat Auto-lab (PGSTAT204), 10 sequential cycles were programmed at a scan rates of 2, 5, 10, 20 and 50 mV/s in a potential window of 0.0–0.5 V. The specific capacitance was determined from the charge value Q , proportional to the integral of the CV curve. Q represents the difference between the area under the charge curve and the area under discharge curve for the upper and lower limits of the potential window [22]. The charging/discharging measurement was carried out through

chronopotentiometry analysis (CP) at a scan rate of 2 A/ g during 1000 cycles using a multichannel potentiostat–galvanostat system (Arbin BT2000).

Finally, the Electrochemical Impedance Spectroscopy (EIS) measurements were performed in potentiostatic mode at room temperature employing an Autolab PGStat302 N instrument (Switzerland) in the frequency range 0.1 - 10⁶ Hz with an applied voltage of 50 mV.

Results and Discussion

NiO nanoplatelets of Fig. 1.a were obtained after annealing in Ar from the polymorph Ni(OH)₂ nanopowders synthesized by a chemical precipitation with ammonium hydroxide as precipitating agent and free of any type of additive [27]. The precipitation reaction was carried out at basic pH, ranging from 9 to 10, at room temperature with the aids of ultrasound. Figure 1.b shows the NiO/Ni powders obtained by reduction of Ni²⁺ with hydrazine directly as Ni NPs onto the surface of the NiO nanoplatelets [23]. Detailed process descriptions for syntheses, which were ultrasound aided, are published elsewhere[27],[23].

The surface of the bare NiO nanoplatelets of figure 1a is a completely flat plate with a size ranging 150-200 nm of diameter and 20-30 nm in thickness. The heterogeneous synthesis of smaller metallic Ni nanospheres, 30 nm in diameter, partially covers the NiO nanoplatelets resulting in NiO/Ni nanostructure core-shell like, as shown and illustrated on figure 1b.

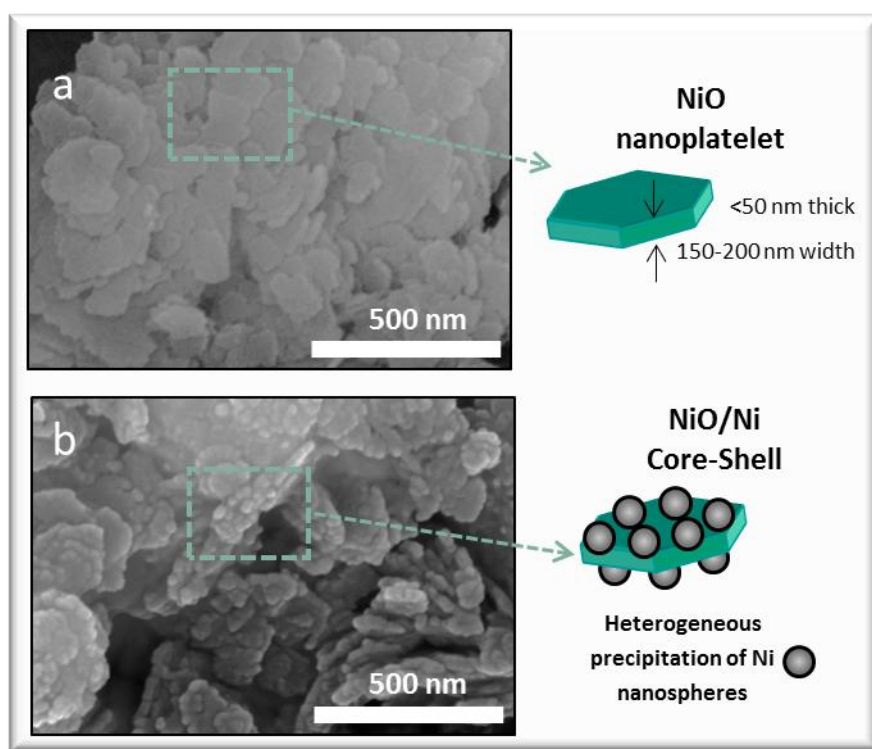


Fig. 1. FESEM micrographs and schematic illustration of the synthesized powders of a) NiO

A detailed physical characterization of the starting powders was made to monitor the changes before and after Ni NPs synthesis (Fig. 2). The XRD curves for the different species synthesized, Fig. 2a, indicate the presence of Ni(OH)₂ and two crystallographic phases after annealing, both with a face-centered cubic lattice (space group: Fm3m). According to the index card JCPDS No 47-1049, correspond to Ni, and No. 22- 1189 corresponds to NiO. There are no other peaks, suggesting that the Ni(OH)₂ was mainly turned into NiO and Ni during the thermal annealing and the heterogeneous synthesis, respectively [22,23]. Crystallite size of NiO and Ni nanoparticles calculated from the Scherrer equation (Eq.1) were 9.54 and 16.33 nm respectively. The unit cell dimensions (calculated by Eq.2) were 4.20 and 3.53 Å and the interplanar distances were 2.43 and 1.80 Å respectively. The BET specific surface area (SSA), the total pore volume as well as the open SSA and the micropore volume determined by the t-plot method for the three nanopowders (the Ni(OH)₂ precursor of NiO, NiO nanoplatelets and NiO/Ni core-shells) are compiled in Table 1. Figure 2b (main and inset) show the N₂ adsorption/desorption isotherms and the pore size distribution of the hierarchical nanostructures, respectively. The shape of the isotherm indicates that the Ni(OH)₂ and NiO nanoplatelets have higher porosity than NiO/Ni and a small but representative population of micropores. The amount of N₂ adsorbed at high-relative pressure for NiO/Ni is very low indicating that the porosity of the NiO nanoplatelets changes because of the Ni nanospheres precipitation onto their surfaces. This could be also the main reason of the differences in BET SSA from 83.7 m²/g for NiO to 16.1 m²/g of NiO/Ni. Moreover, the pore-size distribution plot (Fig. 2b inset) confirms a significant region of mesopores in the NiO nanostructures, which correspond to the voids seen on the nanoplatelets surfaces in TEM image of figure 2c. This mesoporous distribution was not detected in the pore-size distribution plot corresponding to the NiO/Ni core-shells particles, which is due to the presence of the metallic phase onto the semiconductor material surfaces (see Figure 1b).

Differences in SSA and pore volume values can be correlated to the SSA and volume associated with the micropores (porosity below 2 nm in diameter). The analysis of the data in Table 1 summarizes the SSA and the micropores volume calculated by BET and t-plot methodologies. All micropore volumes are lower than 2% of the total pore volume and they don't exceed the 18% of the total exposed surface, being microporosity the lowest representative fraction in NiO nanoplatelets where micropores are only 0.1% of the total porosity and 1.5% of the SSA. Focusing on the electrolyte impregnation, we can conclude that although all porosities (from

macroporosity to microporosity through mesoporosity) are relevant the high specific surface area value of the NiO calcined at 325 °C is mainly due to the mesoporosity (5-10 nm). On the other hand, the microporosity was recently related with electron transfer [12] and, although the volume of micropores is relatively low in both nanostructures, it is important to notice that the precipitation of metallic Ni NPs onto NiO nanoplatelets produces the decrease in the SSA while highlight the relevance of bare-NiO microporosity. These data also evidence the filling of macro and mesopores of NiO nanoplatelets with Ni NPs.

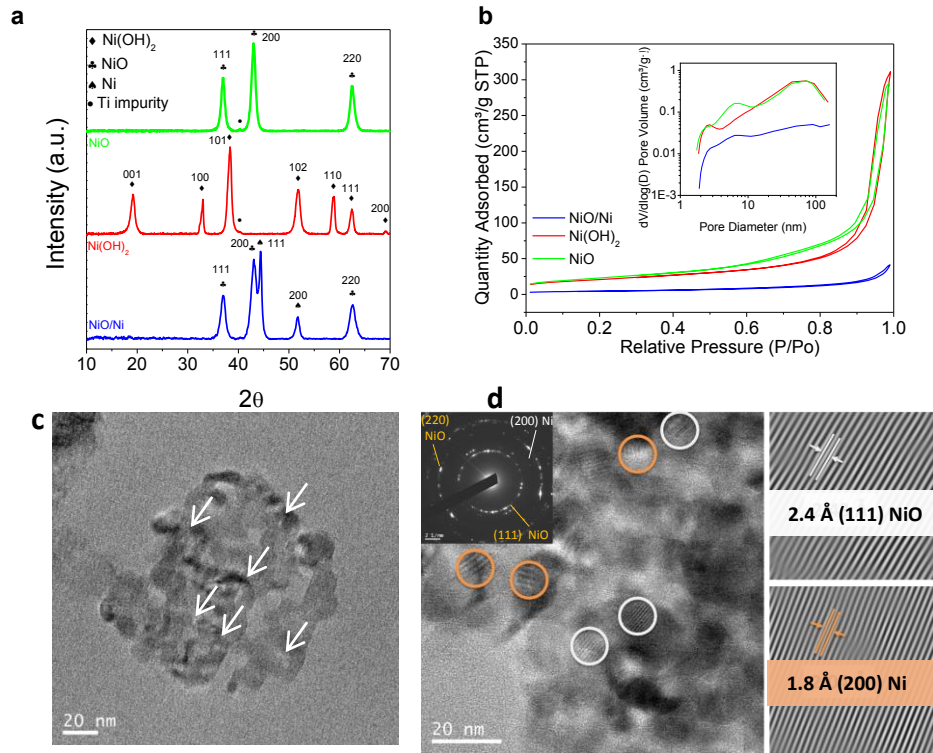


Fig. 2. a) XRD patterns of the β -Ni(OH)₂, NiO and NiO/Ni powders. b) N₂ gas adsorption-desorption isotherms and pore size distribution of as-prepared β -Ni(OH)₂, NiO calcined at 325 °C and NiO/Ni powders. And c) and d) HRTEM images of NiO/Ni powders (where different interplanar distance can be observed depending on the nanoparticle NiO and Ni respectively). Electron diffraction pattern of the sample was included at the inset.

Table 1. Textural properties of as-synthesized nanoparticles

	Ni(OH) ₂	NiO	NiO/Ni
BET SSA (m²/g)	74.1	83.7	16.1
Open SSA by t-plot (m²/g)	65.1	82.4	13.2
SSA contributed by micropores	12 %	1.5 %	18 %
Total Pore Volume N₂ (cm³/g)	0.481	0.457	0.064
Micropore Volume by t-plot (cm³/g)	0.004	0.000	0.001

The HR-TEM micrographs of Fig. 2c and 2d corroborate the growth of metallic NPs onto the NiO nanoplatelets in NiO/Ni core-shell nanostructures as well as the presence of micropores (white arrows). The measurements of the interplanar distances at the c-axis confirmed the results seen by XRD where the presence of the Ni nanospheres was justified by the presence of the main peaks (111 and 200). The interplanar distances in the Fourier transform (FFT) (Fig. 2d) were 2.43 Å and 1.80 Å for the NiO nanostructures and Ni nanospheres respectively. Both distances match with that of the well-defined cubic phase of NiO and metallic Ni. The electron diffraction pattern (also in Fig. 2d) shows diffraction effect with some bright spots that lay on the diffractions rings. Both the rings and spots confirm the polycrystallinity of the species, and also evidence the mixture of the NiO and Ni in NiO/Ni nanopowders. The metallic Ni nanoparticles are very unstable under the electron beam. The structure degrades as observed in the diffuse streaking appearing in the FFT. The rings were identified and assigned with the planes (220) and (111) which lattice distances corresponds to ~ 2.04 and 2.43 Å, respectively, at the SAED (Selected Area Diffraction) patterns of NiO. Additionally, the diffraction pattern of Ni was more difficult to be observed due to the mentioned liability and its lower crystallinity, but faint points corresponding to (200) lattice distance of Ni ~ 1.80 Å are also identified. The surfaces of the bare NiO nanoplatelets were also modified with a polyelectrolytes multilayer to induce changes in their packing in the electrode microstructure, especially in the exposed specific surface and the porosity, when they were shaped by EPD. The multilayer was built up following the layer by layer methodology which consisted on the alternative adsorption of polyethilenimine and polyacrylic acid as polycation and polyanion respectively. The details of the process have been previously reported elsewhere[22,26]. The samples here analyzed were prepared with NiO nanoplatelets modified with a final polyelectrolyte multilayer of 5 layers, here labelled as NiO-5LbL.

The electrochemical response of Ni foams fully covered by NiO, NiO/Ni and NiO-5LbL nanostructures were firstly determined with comparative purposes and to evaluate their performances as pseudocapacitor electrodes. Figure 3 shows the results of these analyses.

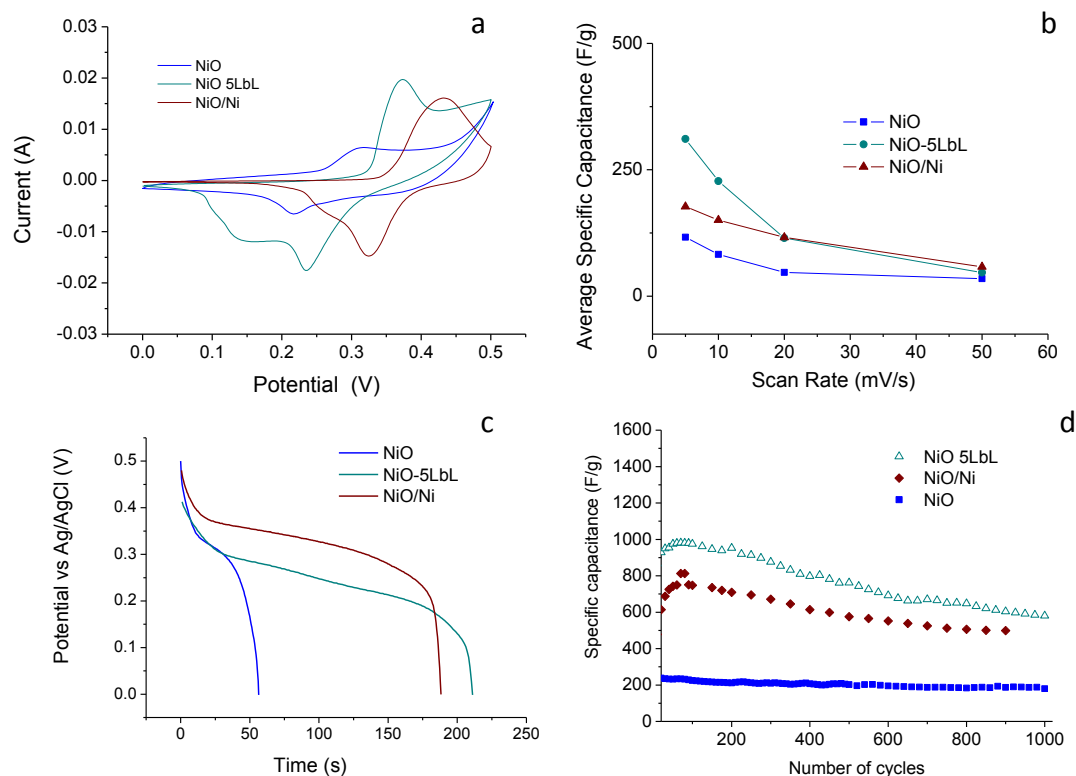


Figure 3. Comparative of the electrochemical response of the three electrodes NiO, NiO/Ni and NiO-5LbL. a) Cyclic Voltammograms (CV) at a scan rate of 10mV/s, b) variation of the specific capacitance values with the scan rates, c) Galvanostatic discharge profiles and d) Cyclic Chronopotentiometric measurements made at a current density of 2A/g.

Here the specific capacitance is mainly caused by the redox contribution since the shape of the CVs is distinguished from that of EDLC, which is usually close to an ideal rectangle. All CV curves of the figure 3a presented faradic profile with oxidation and reduction peaks associated to the charge and discharge processes corresponding to the following redox reaction:



where, the NiOOH is formed at the surface of the NiO during the cycling in the KOH aqueous solutions [30].

According to the voltammograms, the current density of the NiO-5LbL electrode is higher than the NiO and NiO/Ni electrodes and suggests a higher intercalation rate of electrolyte ions into the electrode surface leading to a higher rate of hydroxide/oxide formation. The larger area under the curve for the NiO-5 LbL electrode also indicates higher efficiency in the capacitive characteristics at the electrode/electrolyte interface. This suggests that the increase of the specific surface area, produced as a consequence of the electrode modification (by the

adsorption of the polyelectrolyte multilayer), generates more active sites where reactions take place.

In addition, a significant shift of the potential window was found for the NiO/Ni electrode. Both the center of the oxidation and reduction peaks shifted toward higher potentials. Such phenomena are related to the roughness on the surface of NiO/Ni due to the precipitation of the metallic phase onto the semiconductor nanostructured surface, as well as the fast ionic/electronic diffusion rates during the charge and discharge processes [31].

These results sustain that the capacitive properties of the NiO electrode can be improve both by the increase of porosity, and by the precipitation of metallic Ni onto de surface of the NiO nanoplatelets. This is also supported by the capacity vs scan rate curves. Figure 3b displays the variations of specific capacitance values (calculated by the integration of the cathodic peak areas) with the scan rate for the three types of electrodes, Similar tendencies with gradual decreases of the capacitance values were herein observed. In addition, the cycling stability of the electrodes was measured by galvanostatic charge/discharge curves. The three discharge profiles of the cycles tenth were plotted in figure 3c. All curves showed three similar processes. A first one corresponds to a fast initial potential drop followed by a slow potential decay, both assigned to the reduction of Ni^{+2} (Faradaic contribution). And a third, which shows a faster voltage drop, corresponds to an Electric Double Layer Contribution (EDLC). The main difference among them was identified on the second step which means that significant variations in the effective profiting of the Faradaic contribution were observed during cycling. The specific capacitance values were also calculated and plotted vs. the number of cycles in figure 3d leading to expected different results in values and retention capacity.

Table 2 collects the specific capacitance values corresponding to the 10th cycle, and also the energy density and power density values for the different NiO-based electrodes shaped by electrophoretic deposition (EPD) on Ni foams, and sintered at temperatures $\leq 375^\circ\text{C}$ in Ar. These values of capacitance were considered with comparative proposes since the EIS graphs were also measured for the 10th cycle.

Table 2. Capacity data collected from the three types of Ni-based electrodes.

Coating	Substrate	Capacitance of the 10 th cycle at 2 A/g	Energy Density [(W·h)/kg]	Power Density [W/kg]	Ref
NiO/Ni	Ni foam	755 F/g	52.4	1008	[23]
NiO	Ni foam	250 F/g	17.4	1085	[26]

EIS was performed to discriminate between the contribution of the electron charge-transfer resistance and the ions diffusion processes in the electrochemical performance of the Ni-based electrodes shaped by EPD, in films with the two different microarchitectures: (i) NiO-5LbL modified nanoplatelets and (ii) NiO/Ni core-shell nanostructures. These analyses allowed us to understand the contribution of these two effects to the capacitance values previously measured.

Before studying these mentioned systems, the influence of the type of substrate/collector was firstly analyzed by using the bare NiO films, considered as the initial reference film. Current collectors of SS foil, Cu foil, Ni foil and Ni foam were covered with ~ 1 mg of bare NiO deposited by EPD ($50 \mu\text{A}/\text{cm}^2$ and 240 s for the SS foils and $1.5 \text{ mA}/\text{cm}^2$, 120 s for Ni and Cu Substrates) followed by a thermal treatment at 325°C during 60 minutes.

The results of these EIS measurements are included in table 3, where R_s is the resistance of electrolyte; R_{ct} is the resistance of charge transfer; and CPE is the constant phase element of capacitance. Nyquist plots and bode phase plots are displayed in Fig. 4a and 4b respectively. The equivalent circuit used is included in Fig. 4c. Typically, this kind of materials shows two differentiated parts on the Nyquist plot. In the high frequency range, the semicircle is related to the electronic resistance and the charge-transfer impedance. It is well-known that a big semicircle represents a large resistance in the electronic charge-transfer [32]. Meanwhile, in the low frequency region, the nearly vertical straight lines corresponds to the ion diffusion process within the electrodes structure [9,33–35]. A vertical line of 90° phase angle indicates an ideal capacitor. The deviation from the vertical line to phase angles $< 90^\circ$ can indicate pseudocapacitive behavior. Additionally, the Bode plots allow comparing the maximum phase angle (Φ_{\max}) and relaxation time constant (τ_0) of the prepared electrodes, which define the ideal capacitor for $\Phi_{\max} = 90^\circ$ and the minimum time needed to discharge the stored energy with more than 50% efficiency respectively [36],[37]. To determine τ_0 , the corresponding frequency is inversely related to the relaxation time constant at which the phase angle (Φ) is -45° [38,39]. It represents a transition for the pseudocapacitor from a resistive to a capacitive behavior and is related to the cell power. A lower τ_0 indicates a higher power capability (fast charge-discharge) of a pseudocapacitor.

Table3. Fitted EIS parameters of the NiO films prepared onto different current collector.

Collector	Film	Mass	$R_s (\Omega)$	$R_{ct} (\Omega)$	CPE-P	τ_0 (ms)	$\Phi_{\max} (^\circ)$
-----------	------	------	----------------	-------------------	-------	------------------	------------------------

Ni foil		1.2	-	0.21	0.90	26.3	82
Cu foil	NiO	1.1	1.53	0.48	0.87	34.5	80
SS foil		1.6	1.17	2.14	0.77	83.3	74
Ni foam		1.1 [*]	-	1.71	0.85	8.0	76

^{*}This electrode is considered the reference and its characterization is also included in table 4 and 5

The NiO films onto Ni and Cu foil-shaped substrates exhibit the lower R_{ct} values while the NiO film made on SS substrate shows the highest one. The value of R_{ct} corresponding to the coating on the Ni foam is higher than that of the Ni plate. This can be explained because the electronic charge-transfer depends on the collector nature but also on the collector section. The section of a dense foil-collector is wider than the conductive section of the Ni foam, so the electronic transfer in foil-collectors is promoted [40] and a smaller arc is obtained in the Nyquist plot, which can be considered even negligible. Nevertheless, the use of the 3D Ni substrates as collector, with an interconnected macroporosity of about 200 μm , is justified due to the increase of exposed surface that compensates the final electrochemical response [21]. In addition, the use of the EPD process allows distributing the same amount of electroactive material (~ 1 mg) onto the 3D foam instead over one side of the 2D foil, resulting in homogeneous and continuous films covering Ni threads of the foam skeleton with a controllable and lower thicknesses (as lower as 760 nm) [27]. Then 3D foam coatings exhibit a more effective profiting of the electrochemical performance of a determined deposited mass. This is reflected in the extremely lower relaxation time constant ($\tau_0 = 8$ ms) characteristic of the NiO nanoplatelets coating Ni foams as we will discuss later.

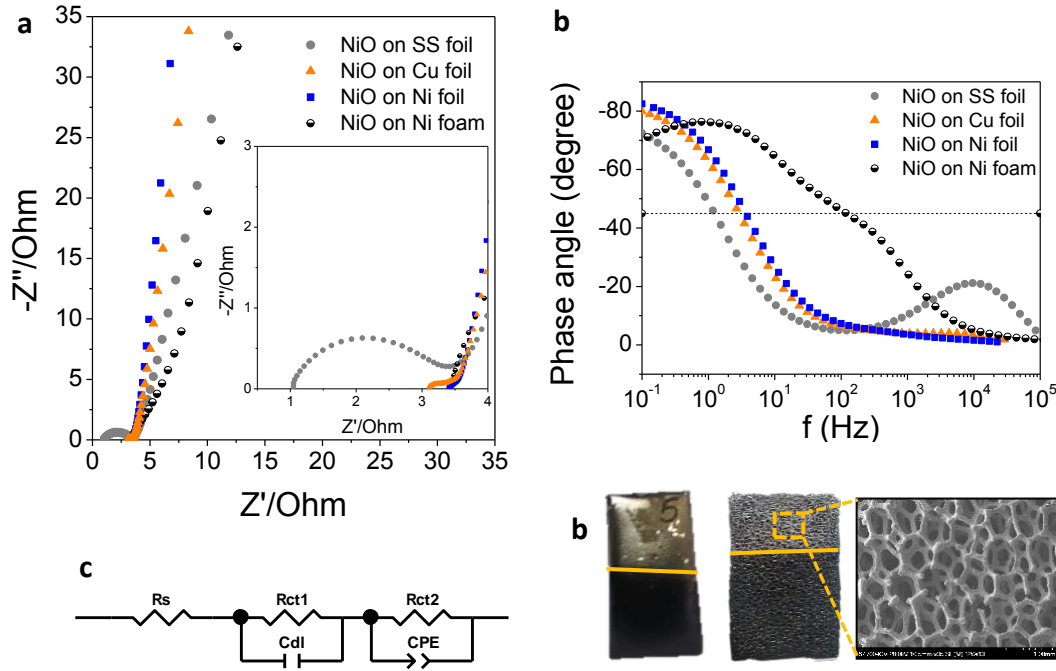


Fig. 4 Nyquist plot (a) and bode phase plot (b) of NiO coatings onto different substrate. Equivalent circuit used to adjust the data c) and images and detail of the NiO films on Ni foil and foam respectively d).

In the Niquist curves the films onto Ni, Cu and SS-plates displayed steeper slopes at low frequencies than the film on Ni foam which means an increase of the pseudo-capacitive behavior is produced.

At the insert on figure 4a it can be seen that, both of the metallic Ni current collector, foil and foam (Fig 4d), do not show the arc corresponding to the electrolyte resistance at high frequencies, R_s . This resistance can disappear due to the faradic reactions of the collector which compete with those provide by the electroactive material. In this case, the absence of semicircles would indicate that a diffusion process is prevailing beyond a capacitive one [41]. The biggest single depressed semicircle in the high frequency region observed for SS substrate indicates that the resistance between the NiO films and the collector is higher than Cu and Ni substrates (table 3). Thus, the trend attending to the nature and the shape of the substrate continues as follows: $R_{SS} > R_{Cu} > R_{Ni}$. The Cu substrate is slightly more resistant than Ni, which can lie in the electronic configuration. Cu has the electrons in an energy state more stable (Ar, $3d^{10}, 4s^1$) than Ni (Ar, $3d^8, 4s^2$), what makes the electron sharing easier in Ni foils.

Bode plots of the four electrodes are also drawn in figure 4d to analyze the relaxation time constant (τ_0) for determining the discharge rates of the electrodes. Ni foam electrode shows a

1 lower τ_0 (8 ms) than Ni and Cu foils (26.3 and 34.5 ms respectively) being the SS foil electrode
2 which presents the highest value (83.3 ms). The rapid frequency response (low τ_0) as well as
3 the shape and the phase angle of the Bode plot indicate that the Ni foam electrode has an
4 improved rate capability and capacitance retention at high charging/discharging rate, which is
5 attributed to higher ion accessible surface area and the more rapid ion transport in the unique
6 hierarchical porous network [39]. Additionally, the τ_0 value is within the range of the
7 electrochemical double layer capacitors (EDLC) and is lower than the commercial Carbon based
8 EDLC ($\tau_0 = 10$ s) [42], which supports the presence of improved ion transport by the electrodes
9 [43,44] when the porous structure of the Carbon is emulated.

10 However, the bode plot of the NiO deposited on Ni foams shows a protuberance in the
11 resistive range, for phase angles ranging $-45^\circ < |\Phi| < 25^\circ$, not visible for NiO films deposited on
12 2D foil-collectors. This resistive effect decay the capacitive behavior evidenced by the lower
13 values of CPE-P and Φ_{\max} collected in the table 3, which vary from 85 and 76° for the NiO film
14 in Ni foam to 90 and 82° in the Ni foil. The slightly increase of the charge-transfer resistance in
15 electrodes shaped on Ni foams reflects the presence of a large Ni-NiO interface due to the
16 tridimensional structure of the NiO film. Consequently, the 3D foam-collectors increases the
17 active surface and clearly favors the ion transport increasing charge/discharge rates while
18 simultaneously increase the Ni-NiO interface area which promotes the increase of charge-
19 transfer resistance and then the pseudocapacitance response deleterious.

20 Once the effect of different current collectors was analyzed, the electrochemical performance
21 of the NiO-5LbL microarchitecture was also measured by EIS. The LbL surface modification of
22 NiO nanoplatelets is a processing strategy addressed to enhance the electrode capacitance by
23 increasing the macro- mesoporosity of the active material deposited by EPD in Ni foams. In
24 fact NiO-5LbL electrodes achieve specific capacitances above 600 F/g at 2 A/g (figure 3). Figure
25 5a and 5b shows a comparative of the Niquist and Bode plots respectively for the NiO
26 reference electrode and theNiO-5LbL electrode. Both electrodes have the same mass and they
27 were made in similar conditions of EPD by using the Ni foam as collector. The modification on
28 the surface of the NiO nanoplatelets by the polyelectrolyte multilayer modifies the packing in
29 the deposited material which are also shown in the micrographs and in the schematic
30 illustration of figure 5c.

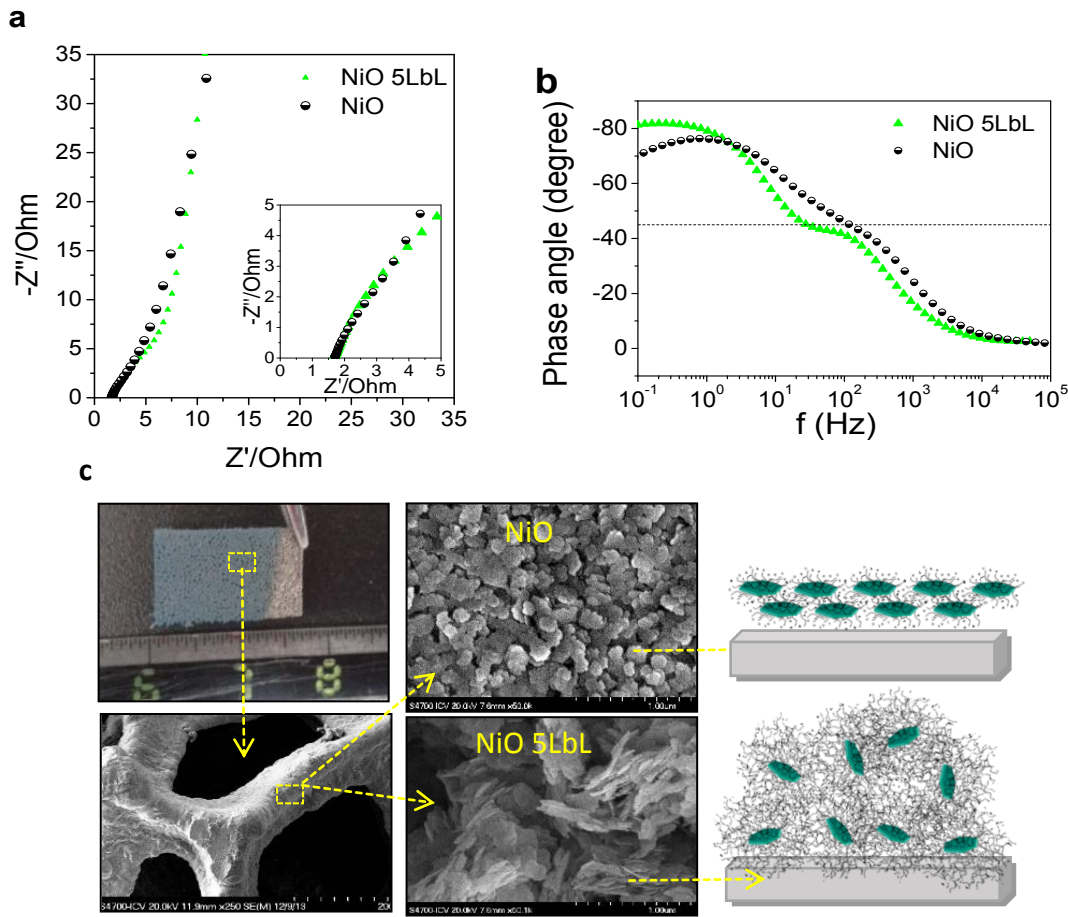


Fig. 5. (a) Nyquist plot, (b) Bode plot of NiO and NiO-5LbL coatings and (c) FESEM images and schematic illustration of the coatings made with NiO and 5LbL nanoparticles onto Ni foams

Characteristic parameters of NiO and NiO-5LbL electrodes obtained from the adjustments with Z-view of these EIS curves are summarized in table 4.

Table 4. Comparative of the fitted EIS parameters of the NiO-5LbL and the NiO electrodes

Substrate	Coating	Mass	R_{ct} (Ω)	CPE-P	τ_0 (s)	Φ_{max} ($^\circ$)
Ni foam	NiO	1.1*	1.71	0.85	8.0	76
	NiO-5LbL	1.1	3.65	0.90	18.0	82

- * This electrode is considered the reference and its characterization is also included in table 3 and 5

The CPE-P value of the NiO-5LbL electrode (0.90) is higher than the value of the NiO film indicating that benefits of the exposed surface and the porosity increase in the electrode microstructure, which is especially relevant in the electrochemical response in spite of the significant increase of R_{ct} value (3.65 Ω). Although there was no significant differences in the slope of both Nyquist curves, the results seen in the bode plots (Figure 5b) showed a phase angle value of -82° for NiO-5LbL, which is closer to -90° than the phase angle of the NiO

reference, -76° . It implies that the porous NiO-5LbL electrode has stronger capacitive behavior [8, 26] than the NiO reference electrode, maintaining a lower τ_0 constant (18 ms) that is a quick charge/discharge rate. Consequently, high charge-transfer resistances do not suppose significant changes in capabilities and the capacitance retention of NiO-5LbL electrodes.

To enhance the electron transport and reduce the R_{ct} values of the NiO-based electrodes, the main challenging presented by semiconductors, Ni NPs were included in its microstructure by synthesizing NiO/Ni core-shell nanostructures. Figures 6a and 6b compare the Niquist and Bode curves corresponding to the NiO/Ni electrode and the NiO reference electrode. The data of the naked collector has also been included herein. The compared electrodes were also shaped by EPD (15 mA/cm² and times ranging from 30-90 s) followed by the same thermal treatment at 325°C during 60 minutes in Ar atmosphere.

Since electronic transport is easier on metal than semiconductors, naked Ni foam exhibited a steeper slope and a smaller semicircle than those coated by NiO and NiO/Ni nanoparticles. Naked nickel foam has no depressed semicircle in the high frequency region due to the absence of coating. This reason could also explain why the NiO/Ni core-shell nanocomposite has a charge-transfer resistance lower than NiO, 1.55 and 1.71 Ω respectively. The inclusion of the Ni NPs favors the electron transport through the semiconductor microstructure, reinforced by the contribution of the microporosity in the NiO/Ni core-shell (Figure 2).

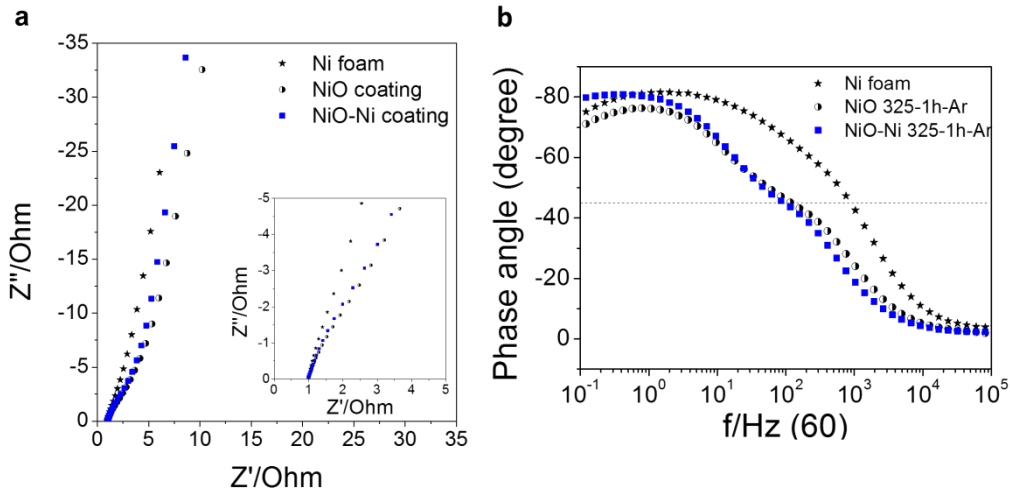


Fig. 6. (a)Nyquist and (b)Bode plots of NiO and NiO/Ni coatings onto Ni foam

Moreover, the NiO/Ni electrode showed better capacitive response than the electrode without Ni NPs. The straight line in the low frequency region was steeper than the slope of the NiO/Ni electrode. The closer value to the unit means a best capacity which is also confirmed by the

CPE-P value of table 5. These CPE-P values increased from 0.85 to 0.90 while Φ_{\max} also increased from -76° to -81° , when the Ni catalyst NPs were included. In this case, the relaxation time constants obtained from Bode curves were similar ($\tau_0 = 11$ ms), thus the variations of the capacitance retention at high charging/discharging rate were not significant.

Table 5. Fitted values of the as-prepared NiO/Ni electrodes with different coatings onto Ni foam.

Collector	Film	Mass	Thermal Treatment	Rct (Ω)	CPE-P	τ_0 (ms)	Φ_{\max} ($^\circ$)
Ni foam	bare	0.0	-	-	0.87	1	82
	NiO	1.1 [*]	325°C 60 min Ar	1.71	0.85	8	76
	NiO/Ni	1.0	325°C 15 min Ar	2.43	0.84	6	76
		1.1	325°C 60 min Ar	1.55	0.90	11	81
		1.1	375°C 15 min Ar	1.64	0.90	11	81
	NiO/Ni	0.6	325°C 60 min Ar	2.19	0.86	3	76
		0.6	375°C 15 min Ar	3.30	0.85	6	75

^{*}This electrode is considered the reference and its characterization is also included in table 3 and 4

In order to deepen into the behavior of the metal-ceramic system, the influence of the sintering treatment and the consolidation level of the ceramic microstructure were also investigated. Both the electron transport and the ion diffusion can be affected by the pathways or channels of connection inside of the semiconductor microarchitectures. If the film is continuous and too dense, the specific surface area and the porosity are reduced and part of the deposited mass of the active material is hidden to the faradaic reactions. Sintering times and/or temperatures should be optimized to form necks among nanoplatelets and NPs avoiding their complete densification so maintaining the meso- and microporosity. For this purpose, 1 mg films of NiO/Ni core-shell nanostructures deposited on Ni 3D foams were sintered at three different thermal treatments in Ar atmosphere. Table 5 summarizes the EIS data and the details the thermal conditions chosen for each electrode. The electrode annealed at 325 °C during 15 minutes exhibits a higher transfer charge resistance ($R_{ct} = 2.43 \Omega$) than the electrodes treated at a higher temperature, 375°C ($R_{ct} = 1.64 \Omega$), or for a longer time, 60 minutes ($R_{ct} = 1.55 \Omega$), indicating that the softest thermal conditions lead to a lower connected nanostructures[23].

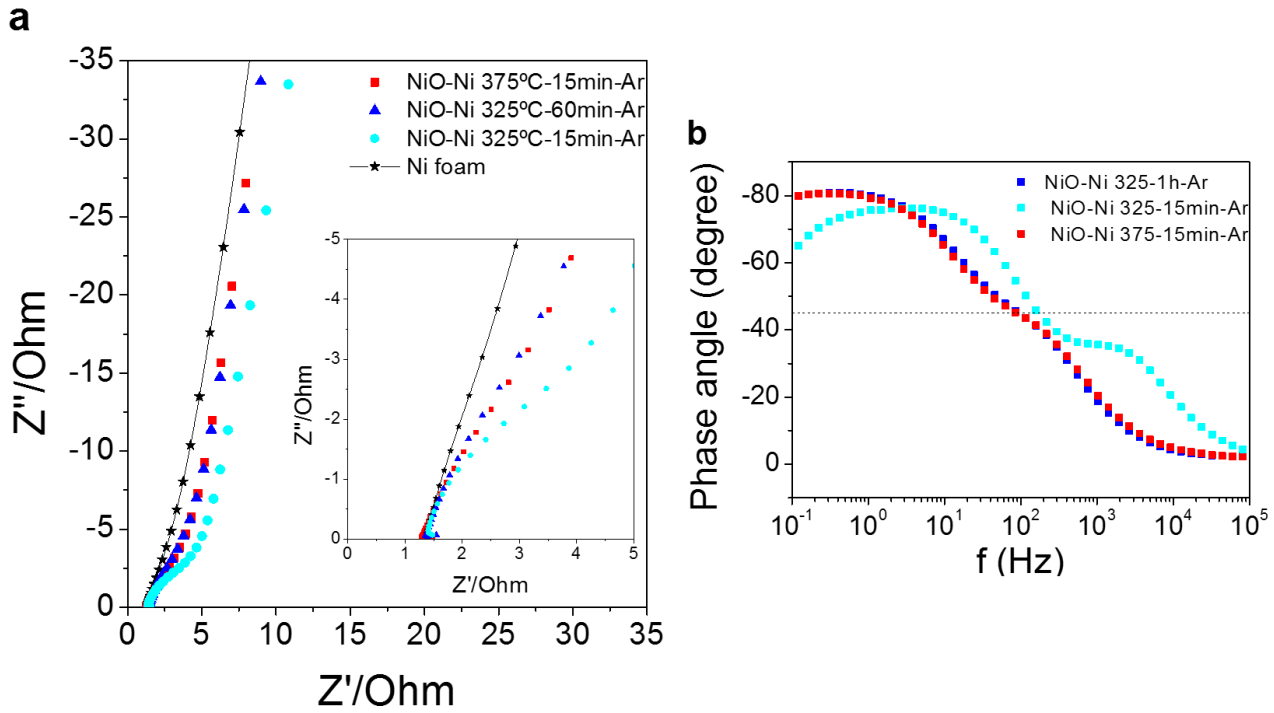


Fig. 7. (a) Nyquist plot and (b) Bodes plot of NiO/Ni electrodes at different TT.

In the Nyquist plot recorded for this NiO/Ni at different thermal conditions on figure.7a it can be observed that the electrode annealed at 325 °C during 15 minutes displayed less steep slope that the other two, which were very similar, confirming that its capacitive behavior can be improved by adjusting slightly the thermal treatment. The CPE-P value of this poor sintered electrode (0.84), and then the maximum phase angle achieved at the Bode plot ($\Phi_{\max} = -76$), were also lower than for the other sintering conditions, which evidences that the capacitive response can be deleterious when charge-transfer resistance increases and it is not compensated in the microstructure by enough faster ion diffusion, like occurs in the case of the NiO-5LbL electrodes.

Bode plot in figure 7b shows how the effect of the resistance decreases when the thermal treatment temperature and time increase in the sintering process. Similar improvements are shown for sintering at 325°C during 60 min and 375°C during 15 min. These plots displayed phase angle values of -81° at low frequency, corroborating that the increase of the time and temperature approaches the electrochemical behavior of the electrodes to that of the ideal capacitor.

Finally, the influence of the deposited mass in the electron transfer and ion diffusion was also evaluated. For this purpose, electrodes with less amount of electroactive mass, 0.6 mg, were

prepared and sintered. The EIS measurements were compared with the obtained data for prior electrodes of ~ 1 mg of mass (table 5). Plots in figure 8a and 8b compare Nyquist curves at sintering conditions of 325 °C - 60 min and 375 °C -15 min respectively. For both, the higher is the deposited mass the steeper is the straight part of the Nyquist curve at lower frequencies, being the difference larger for the NiO/Ni electrodes annealed at 375 °C for 15 min. Also the R_{ct} values increases, being higher the charge-transfer resistance for the electrode treated at a higher temperature. The detriment of the whole electrochemical response determined for the lower deposited mass for both thermal treatments evidences the presence of small naked surfaces on partially uncover Ni foams which limits the NiO/Ni nanostructure connectivity, figure 8d, confirming that a minimum amount of deposited mass is needed to fully cover the collector, which in our case is close to 1 mg.

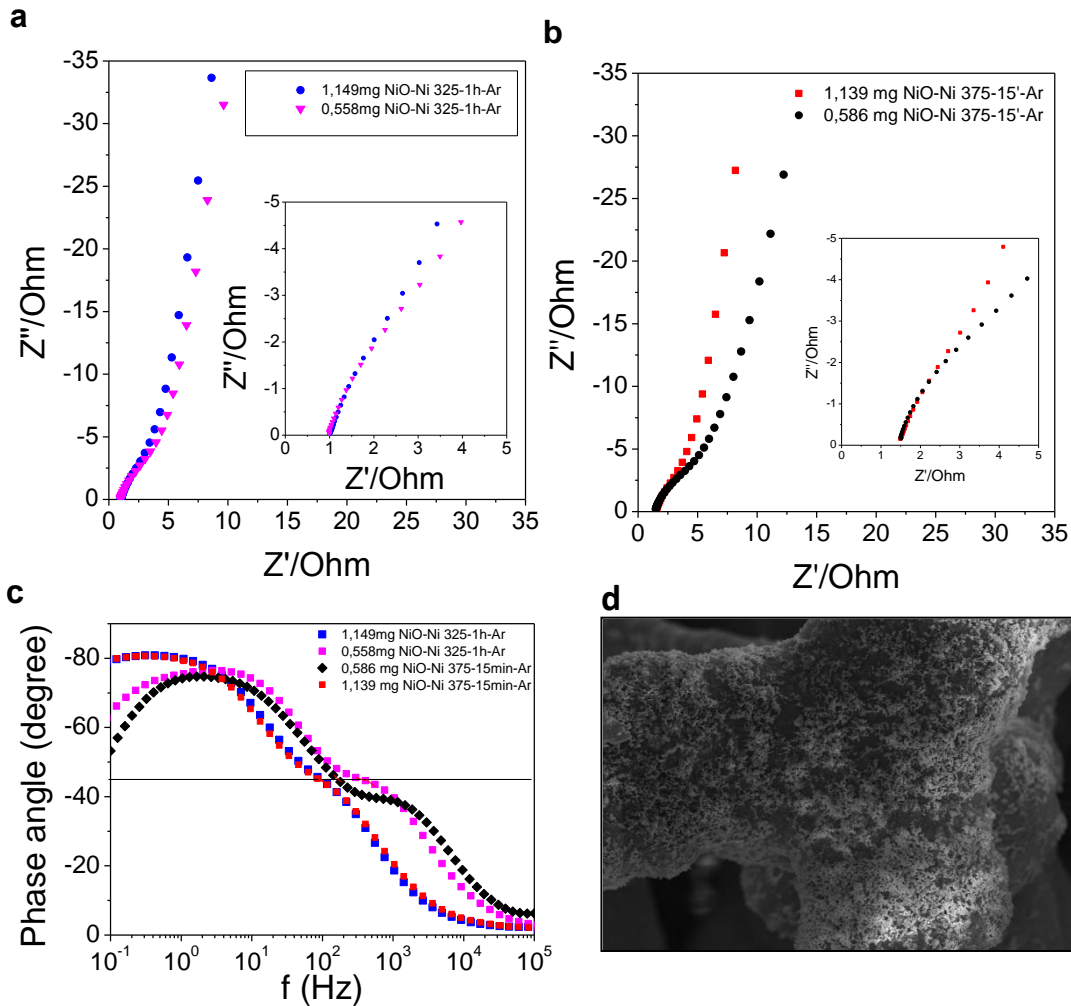


Fig. 8. a) and b) Nyquist plot, and (c) Bodes plot of different NiO/Ni deposit mass onto Ni foams. d) FESEM image of a Ni foam partially coated with 0.6mg of NiO/Ni nanoparticles

Conclusions

An extensive analysis of the physicochemical features (exposed SSA and nanoparticles connectivity by separately) of different Ni-based semiconductor 3D electrodes microarchitectures allowed to understand the contribution of the electron transport and the ion diffusion to the final electrochemical response.

The two different colloidal strategies followed allowed tuning the 3D electrodes microstructures in order to discriminate the effects produced by both electrochemical contributions. Firstly, increasing the SSA by the adsorption of a polyelectrolyte multilayer onto nanoplatelets surfaces (NiO-5LbL) and later enhancing the nanoparticles connectivity by the inclusion of a metallic phase in the semiconductor material (NiO/Ni). Moreover, the study about the influence of the collectors used minimized the additional resistances values due to the electrochemical performance of the NiO nanoplatelets.

Electrodes shaped by EPD depend on the electronic charge-transfer of collectors, mainly determined by its nature and conductive section. For a similar collector configuration, in Cu and Ni foils, differences in the charge-transfer resistance is a consequence of the electronic configuration. Considering Ni collectors, NiO nanostructured films on Ni foams improve rate capability and capacitance retention at high charging/discharging rate, exhibiting a relaxation time constant ($\tau_0 = 8$ ms) in the same range of EDLC capacitors. However, the charge-transfer resistance of electrodes shaped in this configuration is relatively high ($R_{ct} = 1.71 \Omega$) due to the lower conductive section of the 3D collector (Ni foam) and the larger interface collector/electroactive material (Ni/NiO), which is widely compensated by the high accessible surface area which provides a rapid ion transport in the unique hierarchical porous 3D network.

The results obtained in EIS analysis are in concordance with the CV and CP curves and confirms the benefits of having a high exposed surface area and porosity increase in the NiO-5LbL electrode microstructure. This strengthen the capacitive contribution of the electrochemical response ($CPE = 0.90$ and $\Phi_{max} = 0.82^\circ$) and τ_0 of 18 ms, in spite of the significant increase of R_{ct} value (3.65Ω).

On the other hand, the precipitation of Ni NPs and micropores favor the electron transport through the semiconductor NiO microstructure, leading to a lower charge-transfer resistance (1.55Ω) for electrodes shaped by NiO/Ni core-shells deposition. Moreover, the NiO/Ni electrode maintains a high capacitive response with $CPE = 0.90$, $\Phi_{max} = 0.81^\circ$ and τ_0 of 11 ms.

The deep study of the thermal consolidation of the ceramic microstructure of the active mass of the NiO/Ni electrodes demonstrates that the capacitive response can be deleterious when charge transfer resistance increases and it is not compensated in the microstructure by enough faster ion diffusion, like occurs in the case of the NiO-5LbL electrodes. Finally, a minimum amount of deposited mass is needed to fully cover the collector and enhance the capacitive response and limits the charge-transfer resistance.

Conflicts of interest

There are no conflicts to declare.

Acknowledges

Authors acknowledge the support to the projects S2013/MIT-2862 (Comunidad de Madrid) and MAT2015-70780-C4-1 (MINECO/FEDER). J.Yus acknowledges to the Comunidad de Madrid the support from the Youth Employment Initiative, CAMPD17_ICV_002. Z. Gonzalez acknowledges to the Spanish Ministry of Economy and Competitiveness for the Postdoctoral Fellowship: IJCI-2016-28538.

References

- [1] E. Lim, C. Jo, J. Lee, A mini review of designed mesoporous materials for energy-storage applications: from electric double-layer capacitors to hybrid supercapacitors, *Nanoscale*. 8 (2016) 7827–7833. doi:10.1039/C6NR00796A.
- [2] G. Meng, Q. Yang, X. Wu, P. Wan, Y. Li, X. Lei, et al., Hierarchical mesoporous NiO nanoarrays with ultrahigh capacitance for aqueous hybrid supercapacitor, *Nano Energy*. 30 (2016) 831–839. doi:10.1016/j.nanoen.2016.09.012.
- [3] P. Simon, Y. Gogotsi, Materials for electrochemical capacitors, *Nat. Mater.* 7 (2008) 845–854. doi:10.1038/nmat2297.
- [4] S. Kim, J. Kang, S. Kim, J. Jang, Nano Energy A new approach to high-performance flexible supercapacitors : Mesoporous, *Nano Energy*. 39 (2017) 639–646. doi:10.1016/j.nanoen.2017.07.050.
- [5] A. Maitra, S.K. Karan, S. Paria, A.K. Das, R. Bera, L. Halder, et al., Nano Energy Fast charging self-powered wearable and flexible asymmetric supercapacitor power cell with fish swim bladder as an efficient natural bio-piezoelectric separator, *Nano Energy*. 40 (2017) 633–645.
- [6] D. Su, H.S. Kim, W.S. Kim, G. Wang, Mesoporous nickel oxide nanowires: Hydrothermal synthesis, characterisation and applications for lithium-ion batteries and supercapacitors with superior performance, *Chem. - A Eur. J.* 18 (2012) 8224–8229. doi:10.1002/chem.201200086.
- [7] D.Y. Lee, S.J. Yoon, N.K. Shrestha, S.H. Lee, H. Ahn, S.H. Han, Unusual energy storage and charge retention in Co-based metal-organic-frameworks, *Microporous Mesoporous Mater.* 153 (2012) 163–165. doi:10.1016/j.micromeso.2011.12.040.
- [8] Y. Chuminjak, S. Daothong, A. Kuntarug, D. Phokharatkul, M. Horprathum, A. Wisitsoraat, et al., High-performance Electrochemical Energy Storage Electrodes Based on Nickel Oxide-coated Nickel Foam Prepared by Sparking Method, *Electrochim. Acta*. 238 (2017) 298–309. doi:10.1016/j.electacta.2017.03.190.
- [9] C.Y. Yoo, J. Park, D.S. Yun, J.H. Yu, H.H.C. Yoon, J.N. Kim, et al., Crucial role of a nickel substrate in Co3O4 pseudocapacitor directly grown on nickel and its electrochemical properties, *J. Alloys Compd.* 676 (2016) 407–413. doi:10.1016/j.jallcom.2016.03.179.
- [10] P. Mei, Y.V. Kaneti, M. Pramanik, T. Takei, Ö. Dag, Y. Sugahara, et al., Two-dimensional mesoporous vanadium phosphate nanosheets through liquid crystal templating method toward supercapacitor application, *Nano Energy*. 52 (2018) 336–344. doi:10.1016/j.nanoen.2018.07.052.
- [11] S. Chandra Sekhar, G. Nagaraju, J.S. Yu, High-performance pouch-type hybrid supercapacitor based on hierarchical NiO-Co3O4-NiO composite nanoarchitectures as an advanced electrode material, *Nano Energy*. 48 (2018) 81–92. doi:10.1016/j.nanoen.2018.03.037.
- [12] A. Djire, J.B. Siegel, O. Ajenifujah, L. He, L.T. Thompson, Nano Energy Pseudocapacitive storage via micropores in high-surface area molybdenum nitrides, *Nano Energy*. 51 (2018) 122–127.

- [13] S.A. Abbas, K.D. Jung, Preparation of mesoporous microspheres of NiO with high surface area and analysis on their pseudocapacitive behavior, *Electrochim. Acta.* 193 (2016) 145–153. doi:10.1016/j.electacta.2016.02.054.
- [14] G. Meng, Q. Yang, X. Wu, P. Wan, Y. Li, X. Lei, et al., Hierarchical mesoporous NiO nanoarrays with ultrahigh capacitance for aqueous hybrid supercapacitor, *Nano Energy.* (2016). doi:10.1016/j.nanoen.2016.09.012.
- [15] Y. Wang, S. Gai, C. Li, F. He, M. Zhang, Y. Yan, et al., Controlled synthesis and enhanced supercapacitor performance of uniform pompon-like β -Ni(OH)₂ hollow microspheres, *Electrochim. Acta.* 90 (2013) 673–681. doi:http://dx.doi.org/10.1016/j.electacta.2012.11.136.
- [16] Y. Wang, S. Gai, C. Li, F. He, M. Zhang, Y. Yan, et al., Controlled synthesis and enhanced supercapacitor performance of uniform pompon-like β -Ni(OH)₂ hollow microspheres, *Electrochim. Acta.* 90 (2013) 673–681. doi:10.1016/j.electacta.2012.11.136.
- [17] Z. Yang, F. Xu, W. Zhang, Z. Mei, B. Pei, X. Zhu, Controllable preparation of multishelled NiO hollow nanospheres via layer-by-layer self-assembly for supercapacitor application, *J. Power Sources.* 246 (2014) 24–31. doi:10.1016/j.jpowsour.2013.07.057.
- [18] Z. Ren, J. Li, Y. Ren, S. Wang, Y. Qiu, J. Yu, Large-scale synthesis of hybrid metal oxides through metal redox mechanism for high-performance pseudocapacitors., *Sci. Rep.* 6 (2016) 20021. doi:10.1038/srep20021.
- [19] X. Li, L. Wang, J. Shi, N. Du, G. He, Multishelled Nickel-Cobalt Oxide Hollow Microspheres with Optimized Compositions and Shell Porosity for High-Performance Pseudocapacitors, *ACS Appl. Mater. Interfaces.* 8 (2016) 17276–17283. doi:10.1021/acsami.6b04654.
- [20] G.M. Tomboc, H.S. Jadhav, H. Kim, PVP assisted morphology-controlled synthesis of hierarchical mesoporous ZnCo₂O₄ nanoparticles for high-performance pseudocapacitor, *Chem. Eng. J.* 308 (2017) 202–213. doi:10.1016/j.cej.2016.09.056.
- [21] S.-I. Kim, J.-H. Kang, S.-W. Kim, J.-H. Jang, A new approach to high-performance flexible supercapacitors: Mesoporous three-dimensional Ni-electrodes, *Nano Energy.* 39 (2017) 639–646. doi:10.1016/j.nanoen.2017.07.050.
- [22] Z. Gonzalez, J. Yus, A. Caballero, J. Morales, A.J. Sanchez-Herencia, B. Ferrari, Electrochemical performance of pseudo-capacitor electrodes fabricated by Electrophoretic Deposition inducing Ni(OH)₂ nanoplatelets agglomeration by Layer-by-Layer, *Electrochim. Acta.* 247 (2017) 333–343. doi:10.1016/j.electacta.2017.07.043.
- [23] J. Yus, B. Ferrari, A. Sanchez-Herencia, A. Caballero, J. Morales, Z. Gonzalez, In Situ Synthesis and Electrophoretic Deposition of NiO/Ni Core-Shell Nanoparticles and Its Application as Pseudocapacitor, *Coatings.* 7 (2017) 193. doi:10.3390/coatings7110193.
- [24] Z. Zheng, B. Huang, X. Qin, X. Zhang, Y. Dai, M.-H. Whangbo, Facile in situ synthesis of visible-light plasmonic photocatalysts M@TiO₂ (M = Au, Pt, Ag) and evaluation of their photocatalytic oxidation of benzene to phenol, *J. Mater. Chem.* 21 (2011) 9079. doi:10.1039/c1jm10983a.
- [25] H. Wu, D. Li, X. Zhu, C. Yang, D. Liu, X. Chen, et al., High-performance and renewable supercapacitors based on TiO₂ nanotube array electrodes treated by an electrochemical doping approach, *Electrochim. Acta.* 116 (2014) 129–136. doi:10.1016/j.electacta.2013.10.092.
- [26] Z. Gonzalez, B. Ferrari, A.J. Sanchez-Herencia, A. Caballero, J. Morales, Use of Polyelectrolytes for the Fabrication of Porous NiO Films by Electrophoretic Deposition for Supercapacitor Electrodes, *Electrochim. Acta.* 211 (2016) 110–118. doi:10.1016/j.electacta.2016.06.014.
- [27] Z. Gonzalez, B. Ferrari, A.J. Sanchez-Herencia, A. Caballero, J. Morales, Relevance of the Semiconductor Microstructure in the Pseudocapacitance of the Electrodes Fabricated by EPD of Binder-Free β -Ni(OH)₂ Nanoplatelets, *J. Electrochem. Soc.* 162 (2015) D3001–D3012. doi:10.1149/2.0101511jes.
- [28] S. Phadke, A. Du Pasquier, D.P. Birnie, Enhanced Electron Transport through Template-Derived Pore Channels in Dye-Sensitized Solar Cells, *J. Phys. Chem. C.* 115 (2011) 18342–18347. doi:10.1021/jp204974d.
- [29] M. Dios, Z. Gonzalez, E. Gordo, B. Ferrari, Semiconductor-metal core-shell nanostructures by colloidal heterocoagulation in aqueous medium, *Mater. Lett.* 180 (2016) 327–331. doi:10.1016/j.matlet.2016.05.179.
- [30] A.I. Inamdar, Y. Kim, S.M. Pawar, J.H. Kim, H. Im, H. Kim, Chemically grown, porous, nickel oxide thin-film for electrochemical supercapacitors, *J. Power Sources.* 196 (2011) 2393–2397. doi:10.1016/j.jpowsour.2010.09.052.
- [31] H. Sun, Z. Ma, Y. Qiu, H. Liu, G.-G. Gao, Ni@NiO Nanowires on Nickel Foam Prepared via “Acid Hungry” Strategy: High Supercapacitor Performance and Robust Electrocatalysts for Water Splitting Reaction, *Small.* 14 (2018). doi:10.1002/smll.201800294.
- [32] X. Feng, J. Zhou, L. Wang, Y. Li, Z. Huang, S. Chen, et al., Synthesis of shape-controlled NiO–graphene nanocomposites with enhanced supercapacitive properties, *New J. Chem.* 39 (2015) 4026–4034. doi:10.1039/C5NJ00040H.
- [33] G. Zhou, D.W. Wang, L.C. Yin, N. Li, F. Li, H.M. Cheng, Oxygen bridges between nio nanosheets and graphene for improvement of lithium storage, *ACS Nano.* 6 (2012) 3214–3223. doi:10.1021/nn300098m.
- [34] M.L. Huang, C.D. Gu, X. Ge, X.L. Wang, J.P. Tu, NiO nanoflakes grown on porous graphene frameworks as advanced electrochemical pseudocapacitor materials, *J. Power Sources.* 259 (2014) 98–105. doi:10.1016/j.jpowsour.2014.02.088.

- [35] S.A. Abbas, K.D. Jung, Preparation of mesoporous microspheres of NiO with high surface area and analysis on their pseudocapacitive behavior, *Electrochim. Acta.* 193 (2016) 145–153. doi:10.1016/j.electacta.2016.02.054.
- [36] P.S. and J.F.F. P. L. Taberna, *Electrochemical Characteristics and Impedance Spectroscopy Studies of Carbon- Carbon Supercapacitors*, Volume 150 (2003) A292–A300. doi:10.1149/1.1543948.
- [37] S.Z. Inamuddin, Mohammad Faraz Ahmer, Abdullah M. Asiri, *Electrochemical Capacitors: Theory, Materials and Applications*, 2018. doi:10.21741/9781945291579.
- [38] L. Yuan, X.-H. Lu, X. Xiao, T. Zhai, J. Dai, F. Zhang, et al., Flexible Solid-State Supercapacitors Based on Carbon Nanoparticles/MnO₂ Nanorods Hybrid Structure, *ACS Nano.* 6 (2012) 656–661. doi:10.1021/nn2041279.
- [39] Y. Xu, Z. Lin, X. Zhong, X. Huang, N.O. Weiss, Y. Huang, et al., Holey graphene frameworks for highly efficient capacitive energy storage, *Nat. Commun.* 5 (2014). doi:10.1038/ncomms5554.
- [40] A.B. Oskouyi, U. Sundararaj, P. Mertiny, Tunneling conductivity and piezoresistivity of composites containing randomly dispersed conductive nano-platelets, *Materials (Basel).* 7 (2014) 2501–2521. doi:10.3390/ma7042501.
- [41] A. Danine, L.M. Mancieru, A. Fargues, A. Danine, L.M. Mancieru, A. Fargues, et al., Eco-friendly redox mediator gelatin-electrolyte for simplified TiO₂ -viologen based electrochromic devices To cite this version : HAL Id : hal-01646260, (2017).
- [42] M.F. El-Kady, V. Strong, S. Dubin, R.B. Kaner, Laser Scribing of High-Performance and Flexible Graphene-Based Electrochemical Capacitors, *Science (80-.).* 335 (2012) 1326 LP-1330.
- [43] V.H. Pham, T.-D. Nguyen-Phan, X. Tong, B. Rajagopalan, J.S. Chung, J.H. Dickerson, Hydrogenated TiO₂ @reduced graphene oxide sandwich-like nanosheets for high voltage supercapacitor applications, *Carbon N. Y.* 126 (2018) 135–144. doi:10.1016/j.carbon.2017.10.026.
- [44] V.H. Pham, T. Gebre, J.H. Dickerson, Facile electrodeposition of reduced graphene oxide hydrogels for high-performance supercapacitors, *Nanoscale.* 7 (2015) 5947–5950. doi:10.1039/C4NR07508K.

Figure Captions

Fig. 1. FESEM micrographs and schematic illustration of the synthesized powders of a) NiO nanoplatelets and b) core-shell NiO/Ni.

Fig. 2. a) XRD patterns of the β -Ni(OH)₂, NiO and NiO/Ni powders. b) N₂ gas adsorption-desorption isotherms and pore size distribution of as-prepared β -Ni(OH)₂, NiO calcined at 325 °C and NiO/Ni powders. And c) and d) HRTEM images of NiO/Ni powders (where different interplanar distance can be observed depending on the nanoparticle NiO and Ni respectively) Electron diffraction pattern of the sample has been included inset.

Fig. 3. Comparative of the electrochemical tests of the three electrodes NiO, NiO/Ni and NiO-5LbL. a) Cyclic Voltammograms (CV) at a scan rate of 10mV/s, b) variation of the specific capacitance values with the scan rates, c) Galvanostatic discharge profiles and d) Cyclic Chronopotentiometric measurements made at a current density of 2A/g.

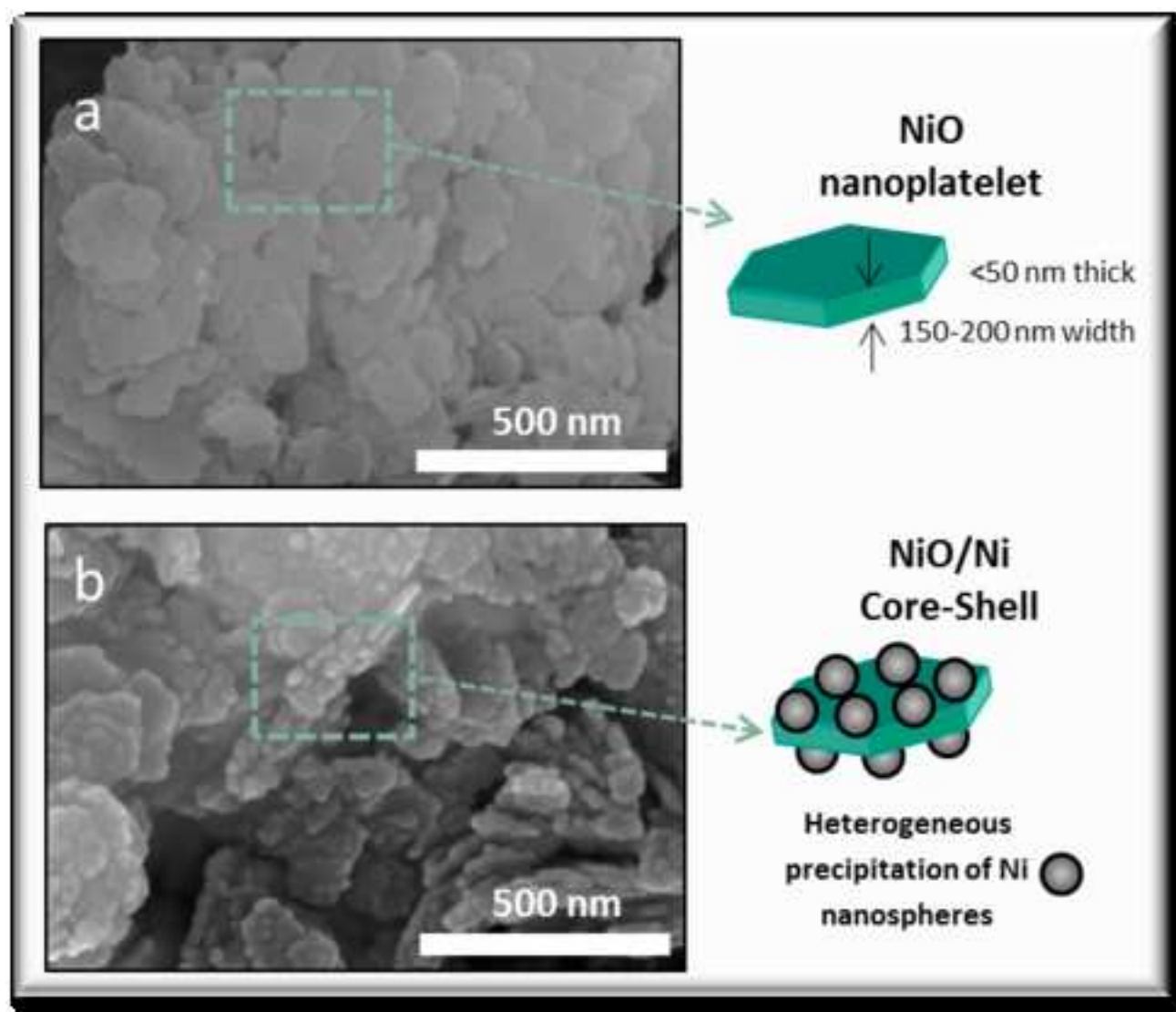
Fig. 4 Nyquist plot (a) and bode phase plot (b) of NiO coatings onto different substrate. Equivalent circuit used to adjust the data c) and images and detail of the NiO films on Ni foil and foam respectively d).

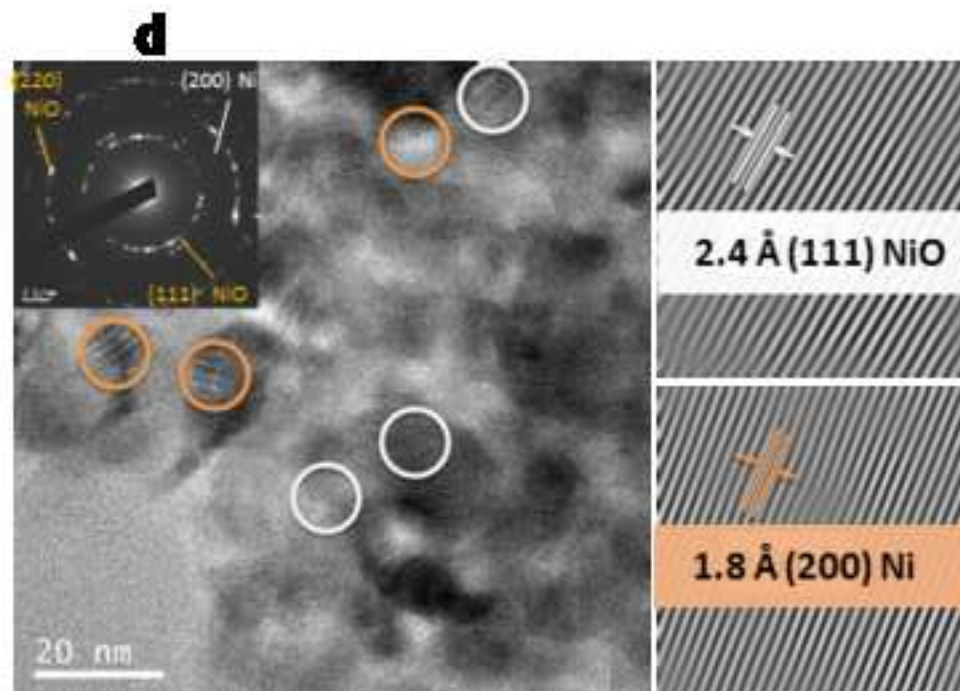
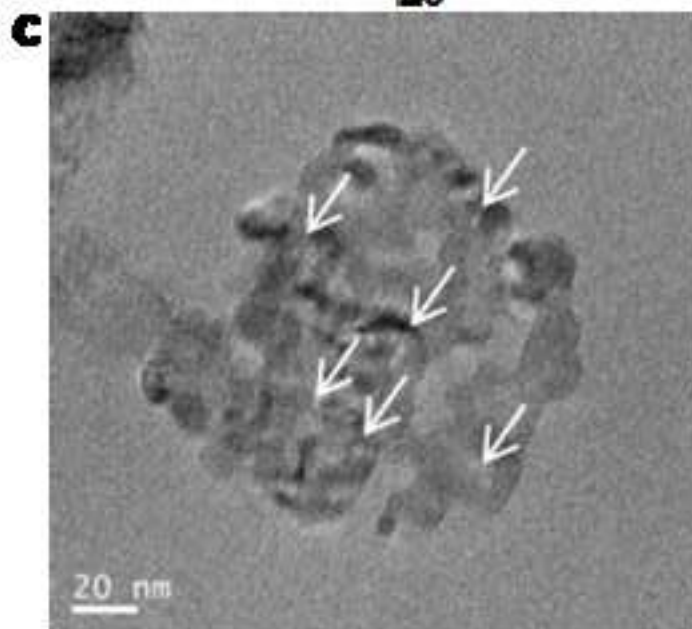
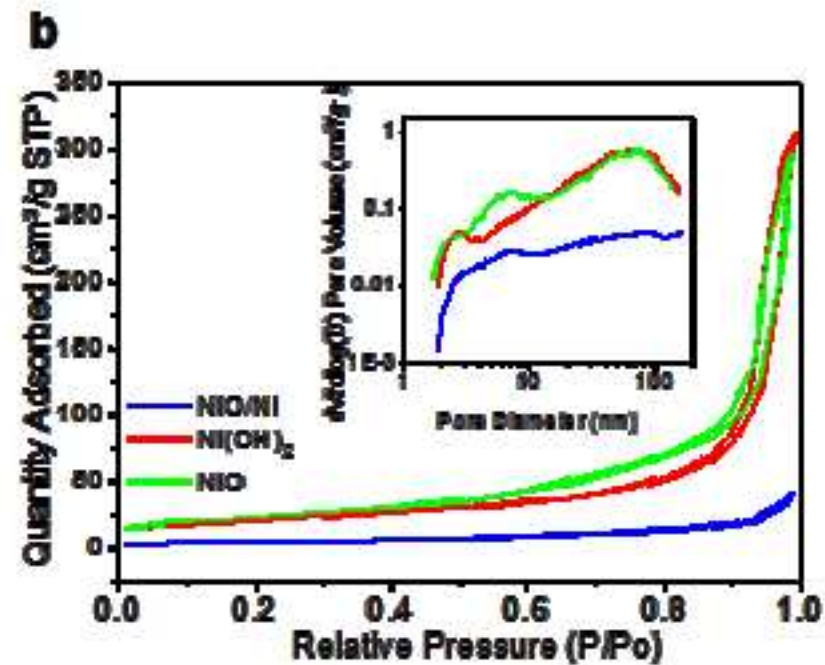
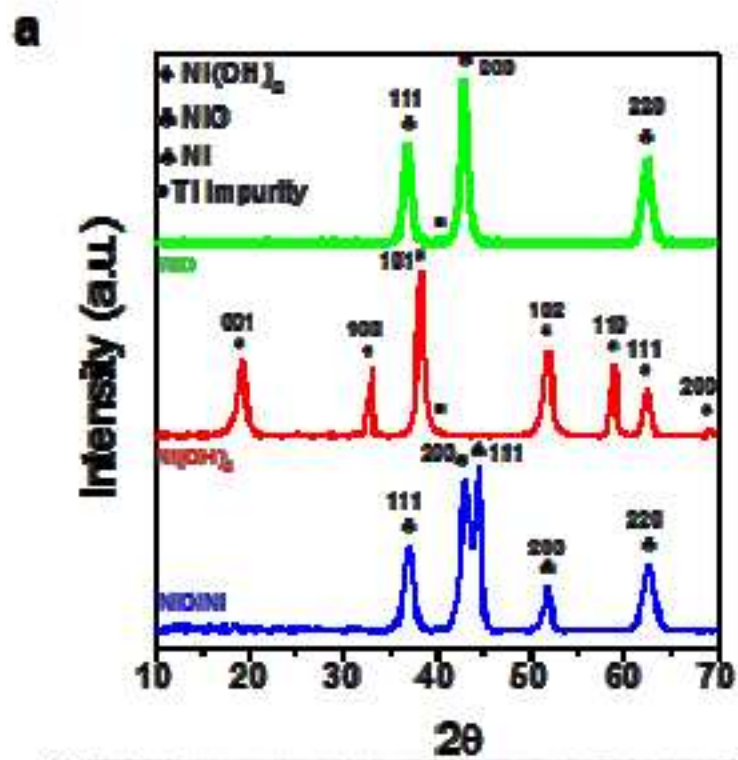
Fig. 5. (a) Nyquist plot, (b) Bodes plot of NiO and NiO5LbLcoatings and (c) FESEM images and schematic illustration of the coatings made with NiO and 5LbL nanoparticles onto Ni foams

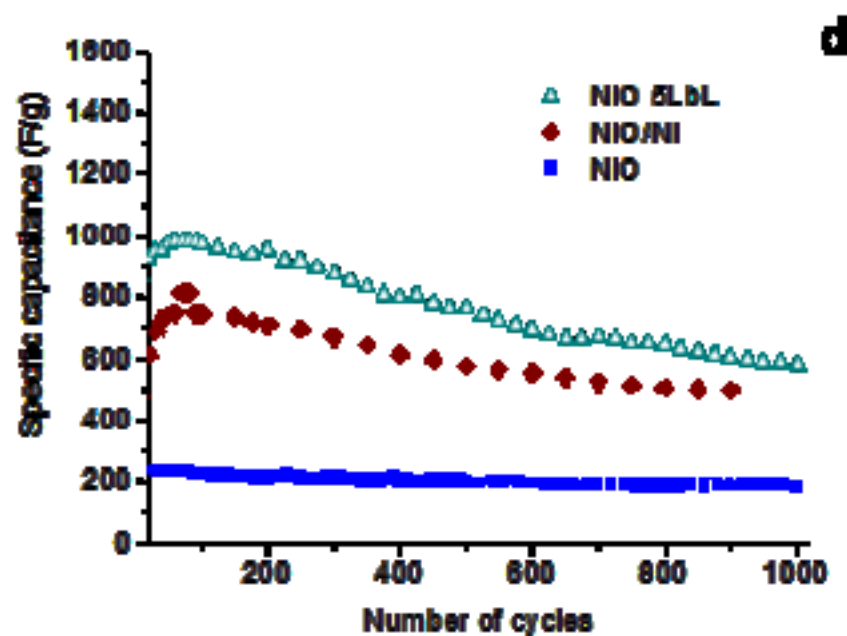
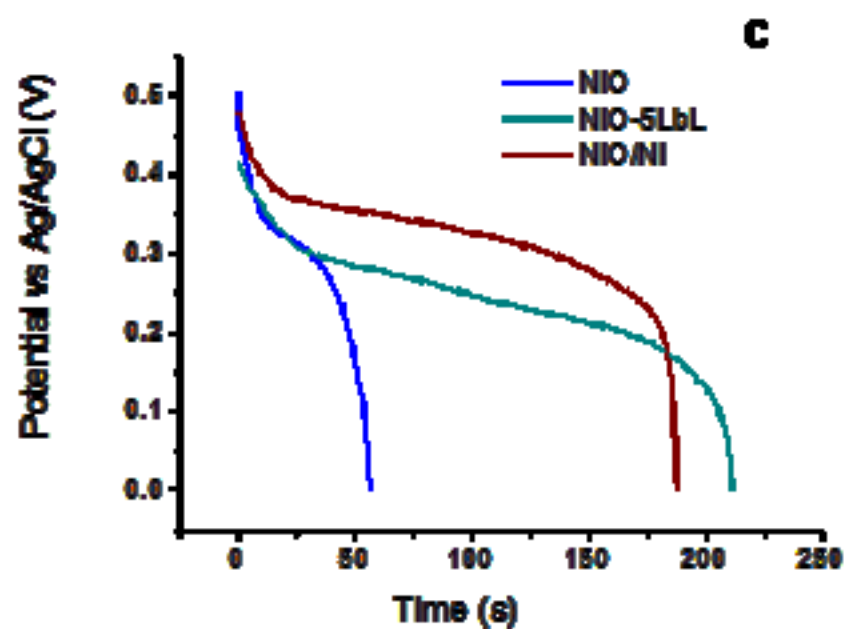
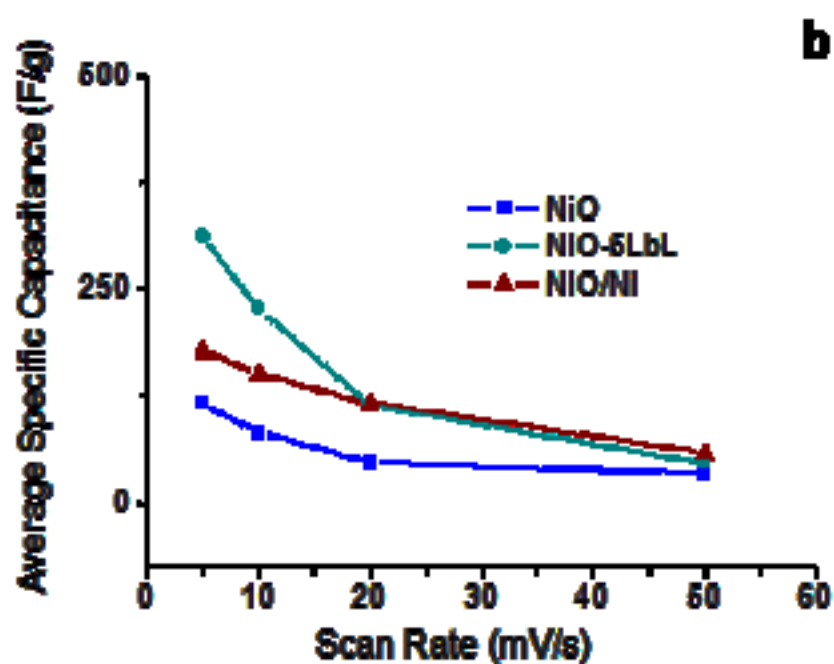
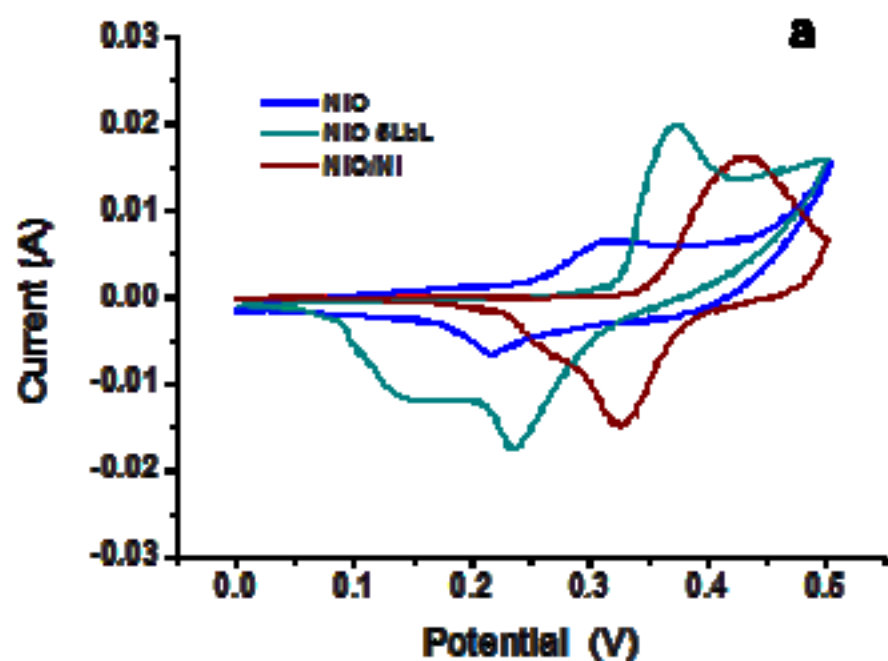
Fig. 6. (a)Nyquist and (b)Bode plots of NiO and NiO/Ni coatings onto Ni foam

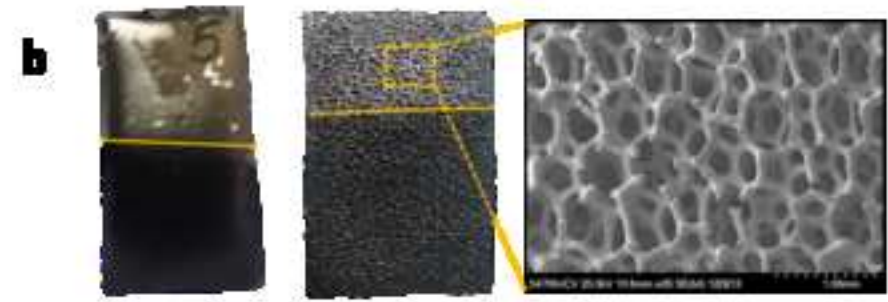
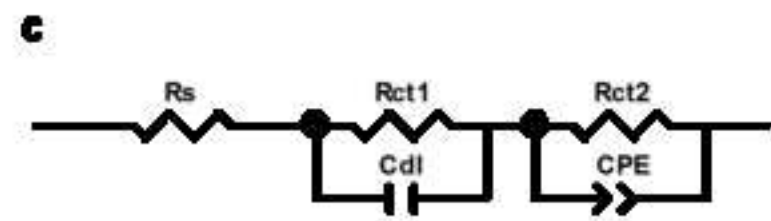
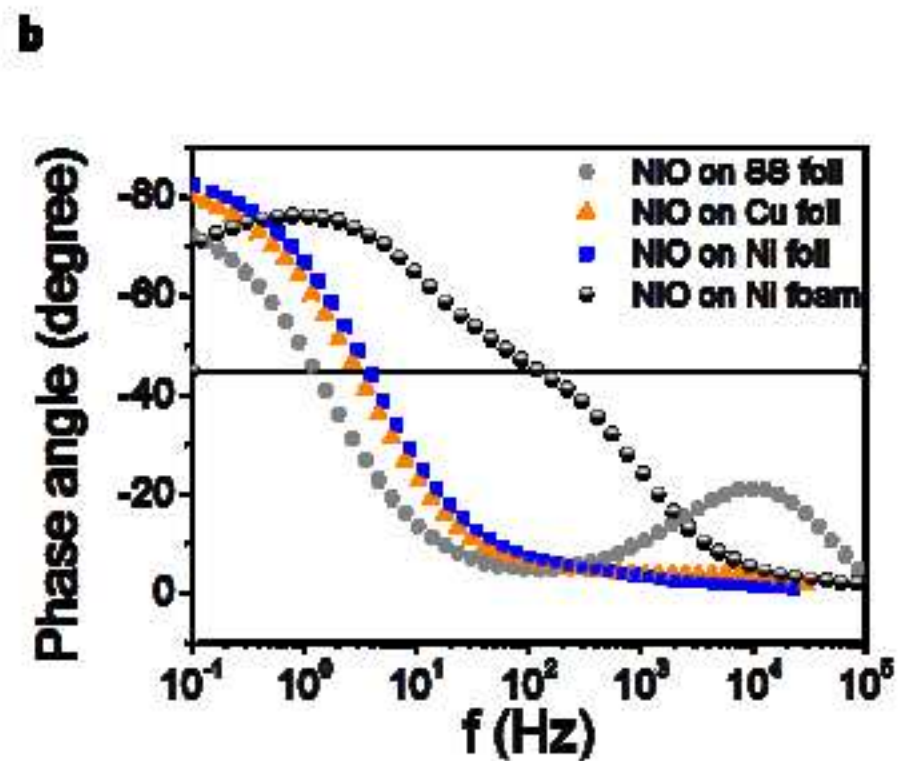
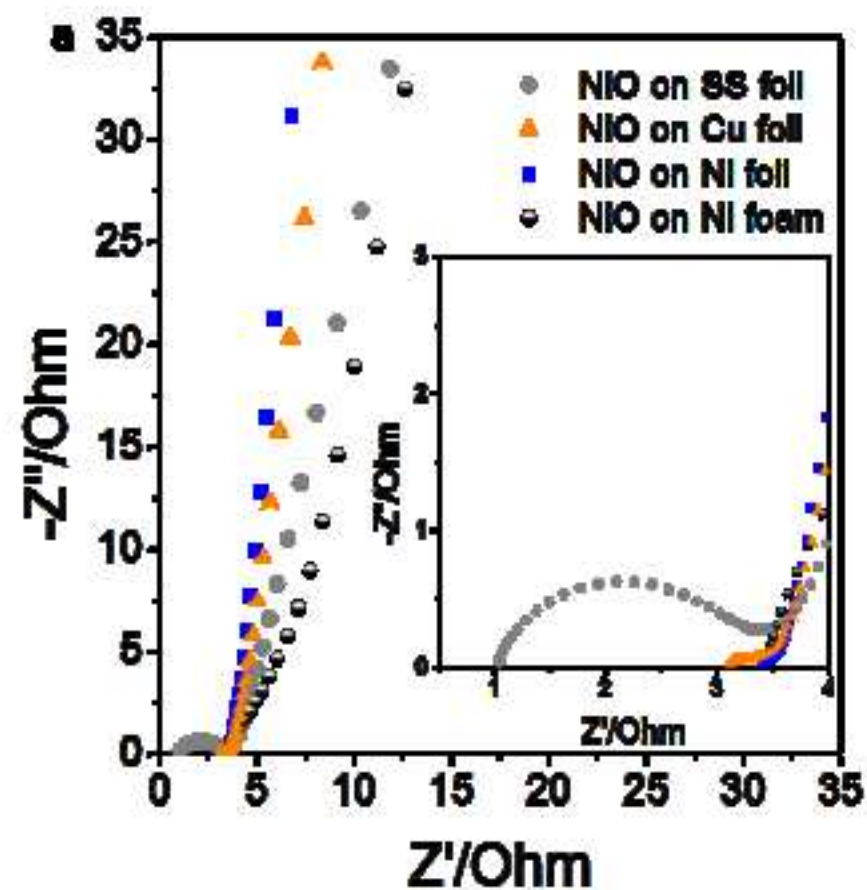
Fig. 7. (a) Nyquist plot, and (b) Bodes plot of NiO/Ni electrodes at different TT

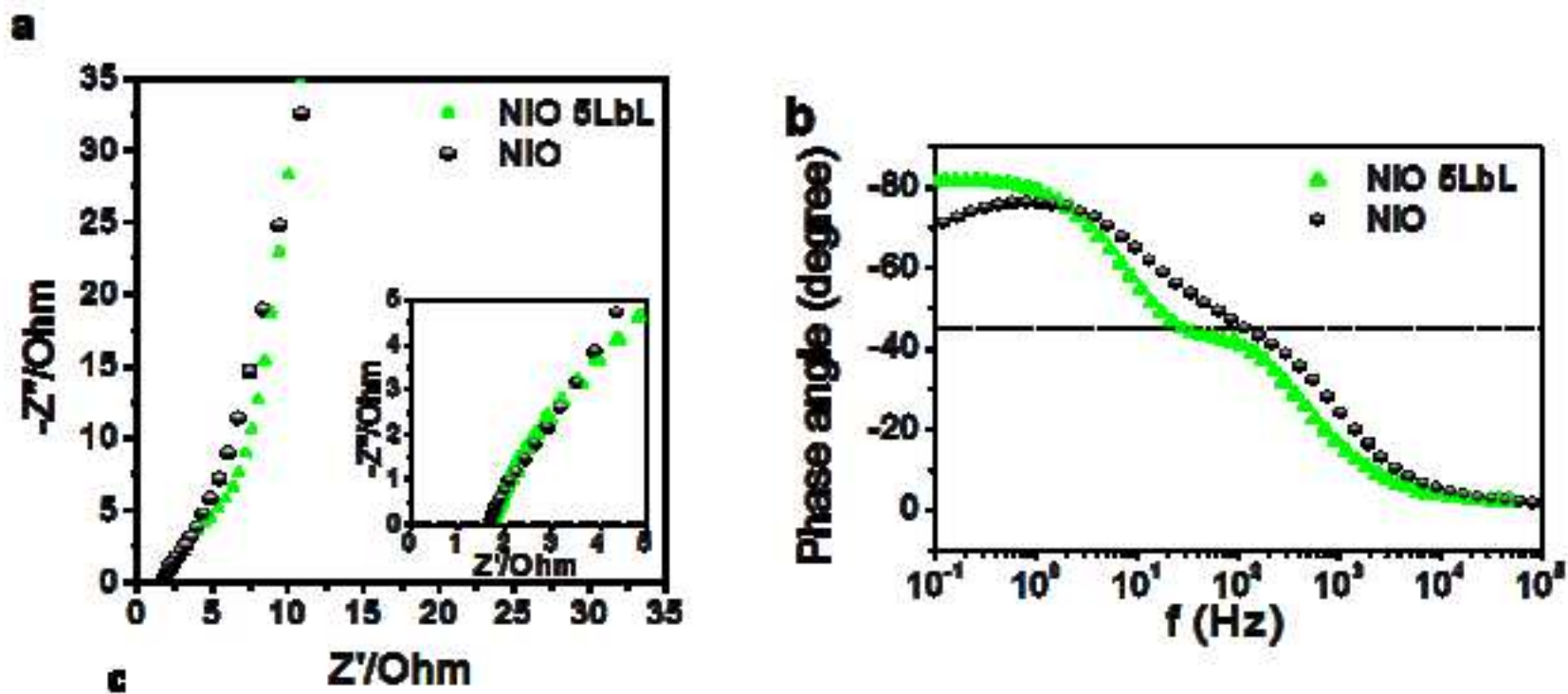
Fig. 8. a) and b) Nyquist plot, and (c) Bodes plot of different NiO/Ni deposit mass onto Ni foams. d) FESEM image of a Ni foam partially coated with 0.6mg of NiO/Ni nanoparticles

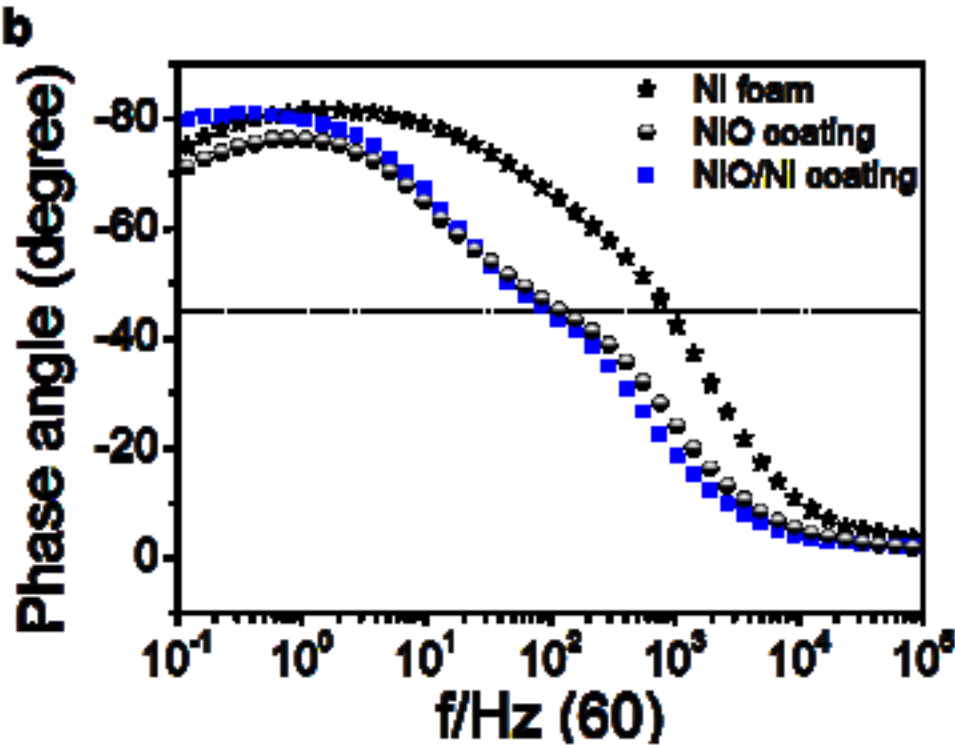
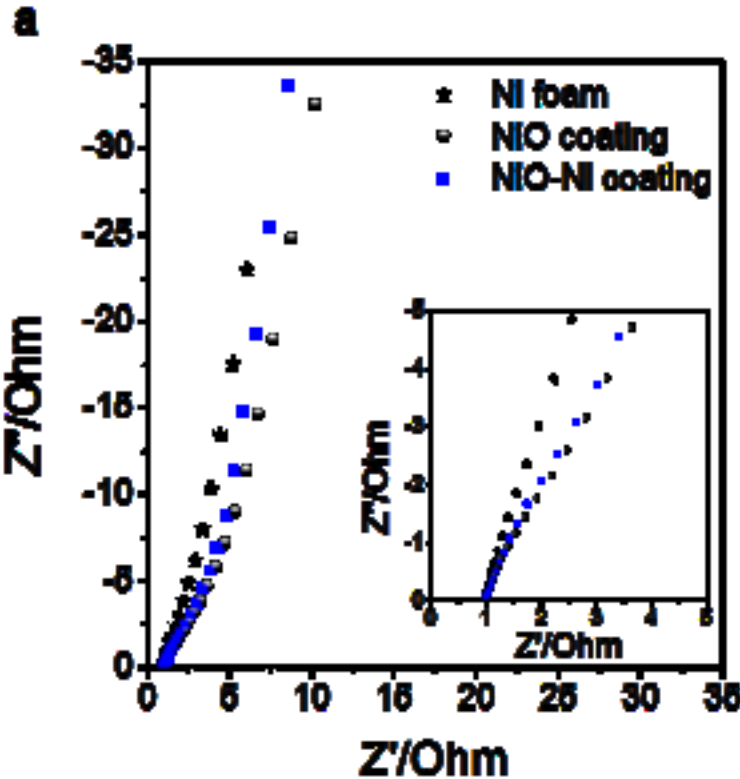


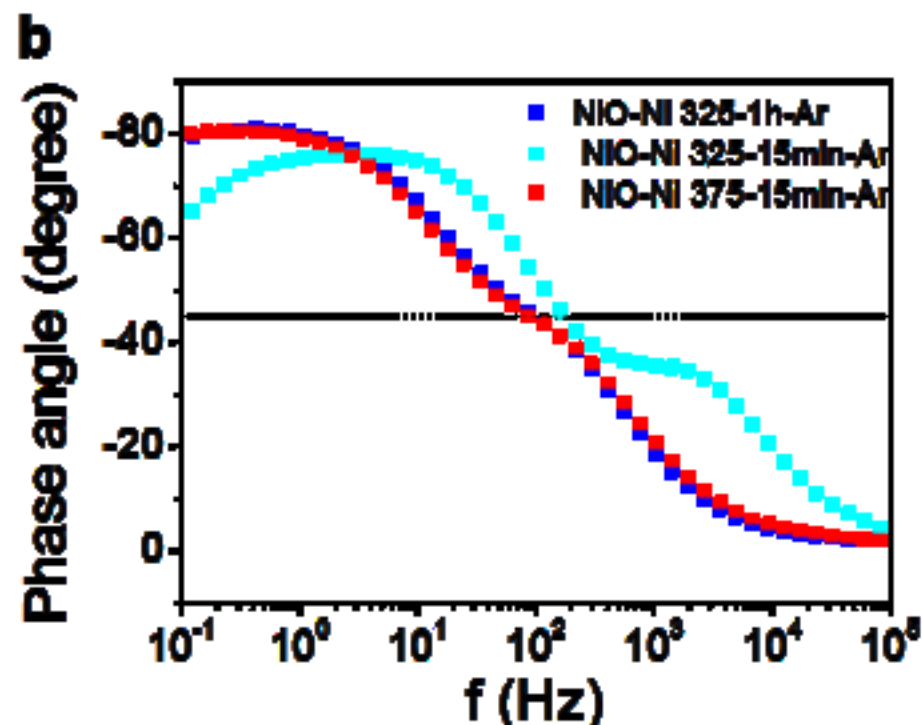
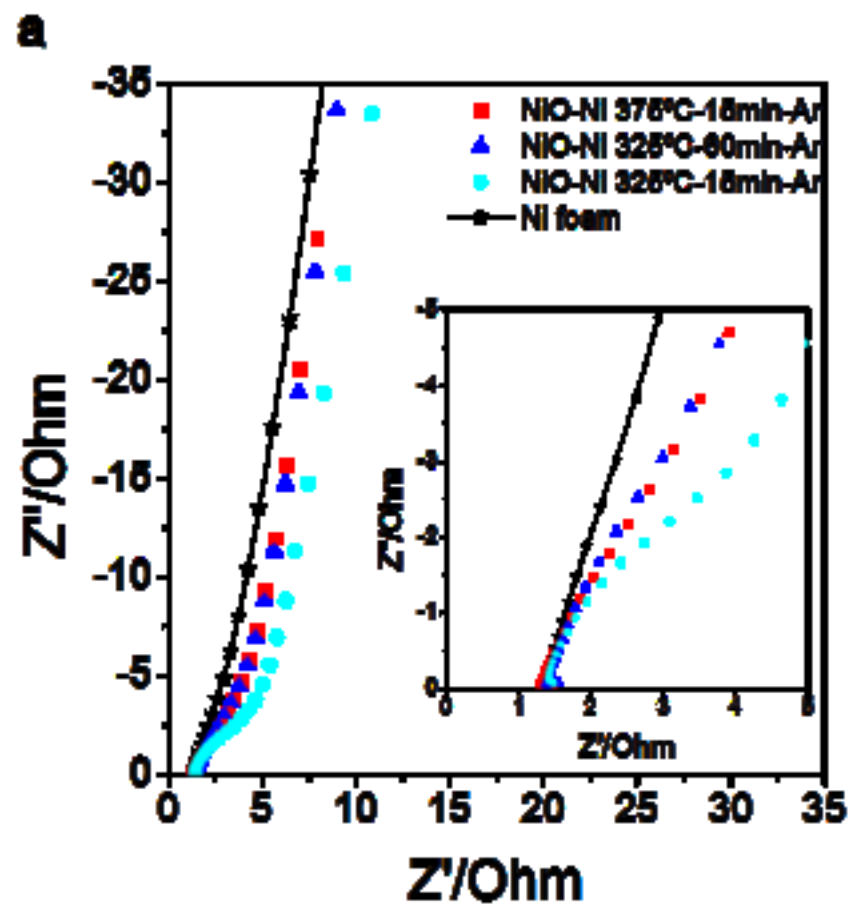


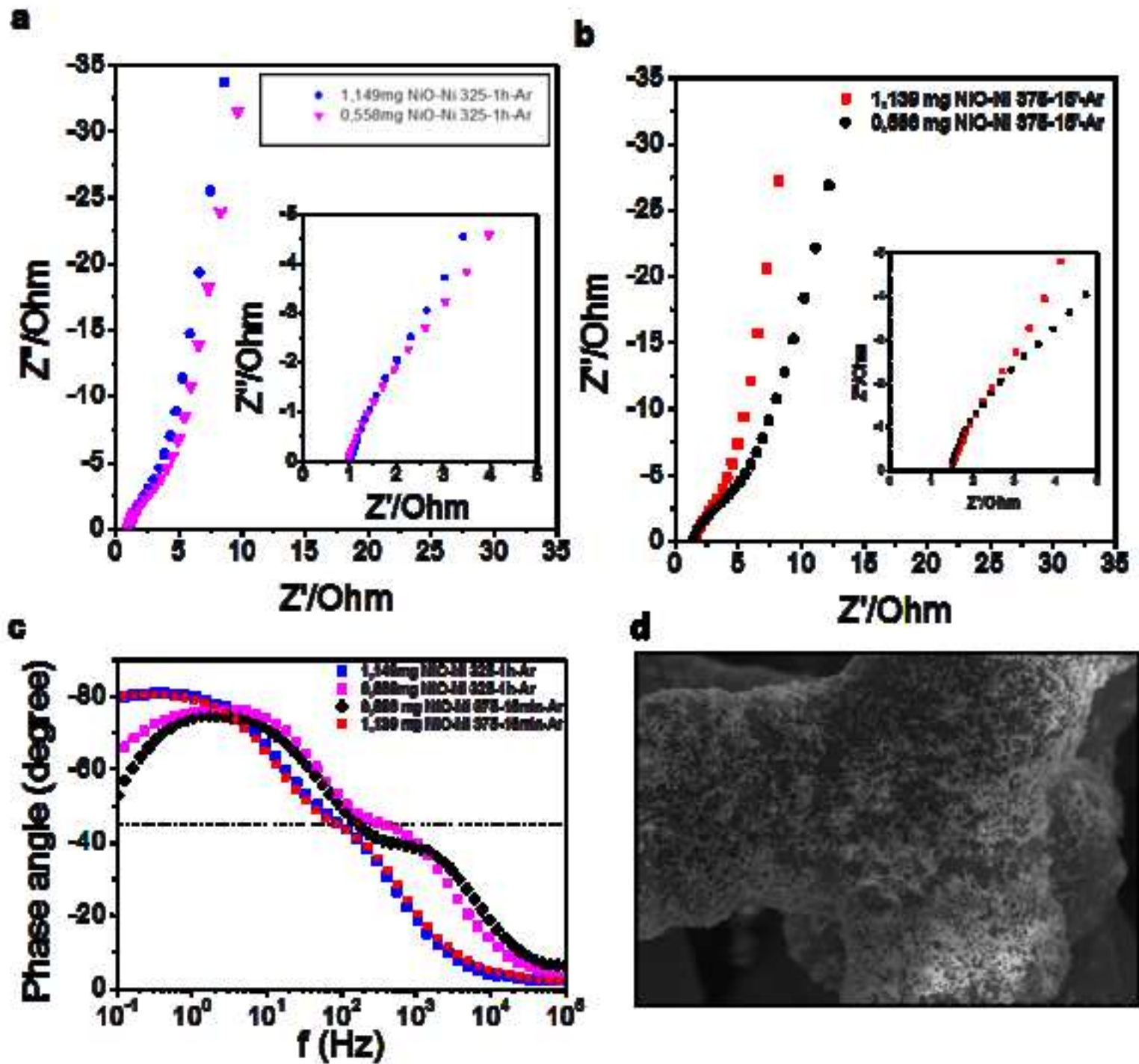












7

Other Research Merits



Original Article

A colloidal approach to prepare binder and crack-free TiO₂ multilayer coatings from particulate suspensions: Application in DSSCsZ. Gonzalez^{a,*}, J. Yus^a, A.J. Sanchez-Herencia^a, J. Dewalque^b, L. Mancieri^b, C. Henrist^b, B. Ferrari^a^a Instituto de Ceramica y Vidrio, CSIC, Kelsen 5, 28049 Madrid, Spain^b GREEnMat, UR CESAM, University of Liège, Allée du Six Août 13, B-4000 Liège, Belgium

ARTICLE INFO

Keywords:

TiO₂ coatings
Particulate suspensions
Colloidal processing
Crack-free
DSSCs

ABSTRACT

A porous well-consolidated and crack-free TiO₂ multilayer coatings have been manufactured from a colloidal approach based on the preparation of particulate suspensions for DSSC. The study of the suspension parameters to optimize dispersion and stabilization of the TiO₂ nanoparticle in the liquid media as well as a thermal stabilization step between the layers have been defined as two key points in the processing method to obtain interconnected microstructures, free of defects and heterogeneities, that prevent the application of an additional scattering layer or any kind of specific or clean conditions during deposition. The sintering process at low temperature, 450°C, has allowed obtaining open microarchitectures avoiding the complete densification and favoring the dye adsorption. A thickness of 12.8 μm resulted in a successful dye loading of 4.52×10^{-10} mol·mm⁻² and a photoefficiency of 5.7%, both in the range of the others particulate systems. EIS measurements were also made to study the transfer charge phenomena.

1. Introduction

Dye sensitized solar cells (DSSCs), also known as Grätzel cells by the name of their inventor have received special attention in recent years owing to offer an efficient and easily implementable photovoltaic technology for future energy supply. In comparison with conventional silicon photovoltaic cells, DSSCs exhibit some specific advantages including easy fabrication procedures, low manufacturing cost and compatibility with flexible substrates [1,2].

A typical DSSC is composed of photoanode, counter electrode, electrolyte and photo-sensitizer (dye). Among them, the photoanode plays an important role to achieve high conversion efficiency as it collects the photo-excited electrons produced from the dye molecules under light exposure. Upon light irradiation, the sensitizer becomes photo-excited and injects electrons into the conduction band (CB) of photoanode. The electrons pass through the external electric circuit until reaching the counter electrode where the oxidized component of the electrolyte (redox couple) is reduced. This reduced component of redox couple in the electrolyte oxidizes the dye regenerating its capacity to the photo-excitation [3,4].

Usually, photoanodes are made of metal oxide semiconductors such as TiO₂, ZnO, Nb₂O₅, SnO₂, etc. which can be prepared through simple

and cost effective solution processing route [5]. The transfer of electrons and holes in the semiconductor nanomaterial is primarily governed by the quantum confinement and the transport properties related to phonons, which are largely affected by the size, crystallinity and morphology [6]. The major drawback of these materials arise from the rapid charge recombination of the electron–hole pairs (thereby suppressing the quantum efficiency) and their wide band gap, which limits light absorption to ultraviolet region only (wavelength < 390 nm) and thus limits the practical applications for solar light harvesting. Many strategies have been described in the literature to extend the visible light activity ranges [7] including metal, or even nonmetal doping of the semiconductor.

In addition to the materials composition and characteristic, it is also relevant to design the micro-architecture of the nanocomposite films that would to lower the recombination currents, enhance the light absorption and ensure a good electric connection. All of these phenomena are often considered to be mutually antagonistic, which makes the attempt of balancing their conflicting requirements a research challenge [8].

Different compositions and deposition methods have been intensely explored for DSSC applications [9]. Highly porous thin films with accessible pores have been developed in comparison to nanocrystalline

* Corresponding author.

E-mail address: zgonzalez@icv.csic.es (Z. Gonzalez).

films prepared by conventional techniques such as doctor blade, screen printing, etc. Mesoporous thin films are usually obtained by surfactant assisted sol-gel techniques known as the evaporation-induced self-assembly (EISA) or the evaporation-induced micelles packing (EIMP) [10]. However, they require complex synthesis procedures with numerous steps to overcome the poor quantity of active material and the limited reactive surface area resulting from a small thickness. In this case, it is necessary to increase the film thickness to obtain better photovoltaic performances [11]. Some authors have already studied the photoresponse of a coating made by a multilayer deposition from a templated sol [12–14], but the methods employed for the preparation of mesoporous films suffered from a large time consuming process to get thick films with crack-free microstructures. Recently, Keshavarzi et al. [15] have achieved to reduce the processing time for a wormlike mesoporous TiO_2 film by optimizing the number of calcination steps. However, the thickness was only of 5.7 μm . As alternative to the sol-gel techniques, several groups have studied the photovoltaic behavior of DSSC fabricated directly by deposition of particulate TiO_2 suspensions (prepared from commercial TiO_2 powder) on conducting glasses, which allow obtaining thicker coatings with less consumption time. For these photoanodes, the effectiveness of the coating depends on the physical properties of the respective slurry/paste such as viscosity, nature of binder, solvent type etc. However, not special attention has been paid to the processing variables and any mature protocol has been reported on the preparation of the slurry/paste and the photoanode fabrication [16]. Ito et al. reported a high photoresponse when the thickness of the photoanodes was increased by piling consecutive coating layers of a paste based on commercial TiO_2 powder [17]. However they applied the additional so called TiO_2 scattering layer to reduce the defects and cracks in the microstructure electrode. Fan et al. reported the preparation of coatings at low temperature with a binder-free paste [18]. They mixed the commercial NPs with other additional TiO_2 particles synthesized by a hydrothermal method. Other authors have also evaluated the performance of TiO_2 thick films made with modified commercial particles. Liu et al. described the effect of ethyl cellulose content in pastes to prepare 14.5 μm -thick [19]. Pan et al. reported the surface modification of particles with ethylene glycol, citric acid and propylene carbonate for the preparation of 14.3 μm -thick photoanodes [20]. Nevertheless, the colloidal stability, the dispersion of particles or the paste viscosities were not determined and no thermal stabilization step or thickness studies were carried out.

Earlier reports suggest the need to address the development of new strategies to control the nanoparticles arrangement during film growth, nanoparticles compaction and/or consolidation structures to achieve higher performance. In the late eighties, advances in colloidal chemistry knowledge have provided the required milestones to successfully apply the colloidal processing methods to the reliable manufacture of nanostructures with specific properties. The colloidal approach of particulate suspensions used herein involves the manipulation and control of the interparticle forces in the liquid media. This is a key step to break down weak agglomerates, stabilize and facilitate powders mixing, removing heterogeneities and defects that degrade relevant properties [21]. Moreover, it is critical to fit processing additives that modify the viscosity, flow, surface tension, wettability, etc., adapting the rheological behavior to the manufacturing technique [22] and controlling the particles assembly [23].

In this work, a colloidal approach of optimized particulate suspensions has been proposed to prepare binder-free TiO_2 coatings based on the improvement of the nanoparticles packing and connectivity through a multilayer system. The suspension and the processing parameters were optimized and short thermal stabilization steps have been applied to promote the crack-free microstructures. The resulting TiO_2 coatings were evaluated in terms of homogeneity (SEM), dye loading (UV-VIS spectroscopy) and charge transfer resistance (Electrochemical impedance spectroscopy). Finally their performance in liquid DSSCs was tested.

2. Experimental

TiO_2 colloidal suspension, TCS, was prepared and optimized to be used as photoactive phase to determine the influence of the colloidal processing in the fabrication of photoelectrodes for DSSC. Besides, a mixture of commercial TiO_2 Paste (Dyesol - DSL 18NR-T, Queanbeyan, Australia) and terpinol was used as reference paste, further reorted as TRP.

The TCS was formulated based on the surface modification of as-received TiO_2 nanopowder (Aeroxide P25, Evonik Degussa GmbH, Germany) in deionized water. As-received commercial nanoparticles (NP) were characterized by He pycnometer (Mettler, Multipycnometer, Quantachrome Co., USA) to determine their density, and by Physisorption Analyzer (ASAP 2020, Micromeritics, USA) to measure the specific surface area. Polyethilenimine (PEI, Mw 25,000 mol/g, Aldrich, Germany) was used as stabilizer additive. The particle size distribution was determined by Dynamic Light Scattering (DLS) using a ZetasizerNano ZS (Malvern, UK) for TiO_2 concentration ranging between 0.001–0.1 g/L. The conditions for NP dispersion and suspension stability were then determined in terms of zeta potential and viscosity, optimizing the pH and the amount of stabilizer.

Differential Thermal Analysis (DTA) and Thermogravimetric Analysis (TGA) (Perkin Elmer, USA) were used to study the thermal evolution of NP as well as to determine the calcination temperature to retain the anatase phase. Tests were made in air atmosphere with constant heating rate of 10 $^{\circ}\text{C}/\text{min}$ up to temperature of 1000 $^{\circ}\text{C}$. A TG analysis was also performed under similar conditions with PEI to determine its temperature of decomposition in air.

Zeta potential was measured by laser Doppler velocimetry in a ZetasizerNano ZS (Malvern, UK). The zeta potential evolution of NP with pH was determined for suspensions with concentrations of 0.1 g/l using 10^{-2} M KCl as solvent and inert electrolyte, so as to maintain the ionic strength of the medium. The pH adjustment of the suspensions was carried out by addition of small quantities of 0.1 M HNO_3 or Tetramethylammonium Hydroxide (TMAH) and controlled with a pH probe (Metrohm AG, Germany). The zeta potential saturation curve determined for the addition of PEI was measured without the inert electrolyte at pH 8. Before each measurement, NP suspensions was dispersed and homogenized by sonication, using a UP400S Ultrasonication probe (Hielscher, Germany) for an optimized period of 30 s.

Rheology of NP suspensions was measured in a Haake Mars rheometer (Thermo Scientific, Germany) with a double-cone plate fix of 60 mm of diameter and an angle of 2 $^{\circ}$ (DC60/2 $^{\circ}$). Tests were performed in a control rate mode (CR) shearing up from 0 to 1000 s^{-1} in 2 min, dwelling at 1000 s^{-1} for 1 min and shearing down to 0 s^{-1} in 2 min and control stress mode (CS) increasing stress from 0 to 15 Pa in 2 min and decreasing to 0 Pa in the same time. All tests were done at a constant temperature of 23 \pm 0.5 $^{\circ}\text{C}$. Rheograms were determined to establish the optimal addition of PEI and adjust the milling time. For that, suspensions with a solid content of 3 vol.% were stabilized with amounts of PEI ranging between 3–9 wt.% (referred to powder) and suspensions with a 7.4 vol.% of solid content were milled in a ball mill during times ranging between 30–120 min (using Al_2O_3 balls of 1 cm in diameter).

NP suspensions were formulated at optimal dispersion conditions, and then centrifuged and re-dispersed in ethanol to achieve the 2 vol.% of solid contents for the TCS.

For comparative purposes regarding to the photoresponse, the TCS shaping into coatings was done by dip-coating technique with a withdrawal rate of 2.5 mm/s, whereas the TRP was processed by a standard spin-coating procedure. In both cases FTO conducting glass (Dyesol, 15 Ω/sq) was used as substrate. The thickness of the coatings was increased by a sequential deposition of several layers where a thermal stabilization step between each coating was made by heating the fresh film during 10 min on a hot plate at 200 $^{\circ}\text{C}$.

The TiO_2 coatings were further sintered in air at 450 $^{\circ}\text{C}$ for 15 min,

with heating and cooling rates of 5 °C/min. The films microstructure and thickness were characterized by FEG-ESEM XL30 (FEI) with an accelerating voltage of 5 kV under high vacuum and by FESEM in an S-4700 microscope (Hitachi, JAPAN). The identification of the crystal phases of the coatings has been carried out by X-ray diffraction (XRD) with a Siemens D5000 diffractometer (Germany) with a Kristalloflex 710 generator ($K\alpha(\text{Cu}) \lambda = 1.5405 \text{ \AA}$; 40 kV; 30 mA; $2\theta = 5\text{--}70$).

TiO_2 coatings were sensitized by a Ruthenium complex-based dye, N-719 dye (Solaronix), dissolved in ethanolup to $2.7 \times 10^{-4} \text{ M}$. The coatings were cleaned by UV-O3 for 15 min right before the dye adsorption. Electrodes were immersed in the dye solution overnight at room temperature.

The dye loading of the shaped electrodes was measured by UV–vis spectroscopy with a Perkin Elmer UV–vis Spectrometer Lambda 14 P. The absorbance values of the aqueous solutions (10^{-3} M of potassium hydroxide (KOH)) where dye was previously desorbed were analyzed. A calibration curve was used to calculate the experimental extinction coefficient of N-719 dye, which is $12,900 (\text{mol/L})^{-1} \text{ cm}^{-1}$ at 500 nm. For the dye loading measurements, the area of all the coatings was normalized and determined by image analysis using the GIMP software.

The assembly of the DSSCs was carried out by a conventional procedure at room temperature. Counter electrodes were composed of a FTO conducting glass substrate (Dyesol, $15 \Omega/\text{sq}$) coated with a platinum layer to catalyze electron transfer. The Pt coating was obtained by sputtering performed at 30 mA intensity during 80 s and at a working distance of 3 cm. The thickness of the platinum layer was of approximately 29 nm, determined by spectroscopic ellipsometry.

The electrodes were separated by a polymer spacer SX-1170-60 (60 μm -thick) applied under spring pressure and heating (100 °C 30 min in an oven). A home-made electrolyte solution composed of 0.6 M 1-butyl-3-methylimidazolium iodide (Aldrich Chemistry), 0.03 M iodine (Sigma-Aldrich), 0.1 guanidine thiocyanate (Sigma-Aldrich) and 0.5 M 4-tert-butylpyridine (Aldrich Chemistry) in acetonitrile n oven). A home-made electrolyte solution composed of 0.6 M 1-butyl-3-methylimidazolium iodide (Aldrich Chemistry), 0.03 M iodine (Sigma-Aldrich), 0.1 guanidine thiocyanate (Sigma-Aldrich) and 0.5 M 4-tert-butylpyridine (Aldrich Chemistry) in acetonitrile (ABCR GmbH and Co.)/valeronitrile (Aldrich Chemistry) (85/15, v/v) was prepared and introduced via vacuum backfilling in a hole drilled in the Pt-coated FTO counter-electrode. The hole was sealed with SX-1170-60 polymer and a cover-glass.

Photovoltaic performances were evaluated into a class A solar simulator purchased from Newport Spectra Physics coupled with a Keithley 2400 SourceMeter. Photocurrent-voltage curves were measured under 0.7 SUN simulated illumination (filter AM 1.5). The electrode active area was set to 0.2064 cm^2 with a mask. Electrochemical impedance spectroscopy was performed using a BioLogic SP-200 potentiostat (Science Instrument) and data were analyzed with the EC-Lab software. A sinusoidal potential perturbation was applied to the cell and the current variation response was recorded. EIS spectra were measured over a frequency range of 10^{-1} to 10^6 Hz , with 10 mV sinusoidal modulation signal. Measurements were performed in the dark, at room temperature by applying a bias equal to the V_{OC} value determined from the I–V curves. Photovoltaic and EIS measurements were repeated several times.

3. Results

TiO_2 nanopowders have been widely studied for shaping photoelectrodes. Examples in the literature describe a high variability of commercially-available powders in terms of particle size and percentage of anatase and rutile phases. Different authors have characterized the same materials obtaining results with slight desviations. The P25 Degussa powders described in [18,19] displayed 70% anatase and 30% rutile with a particle size of 24 nm; on the other hand, the P25 Degussa powder used in [17] presented an average size of 30 nm by BET, 80%

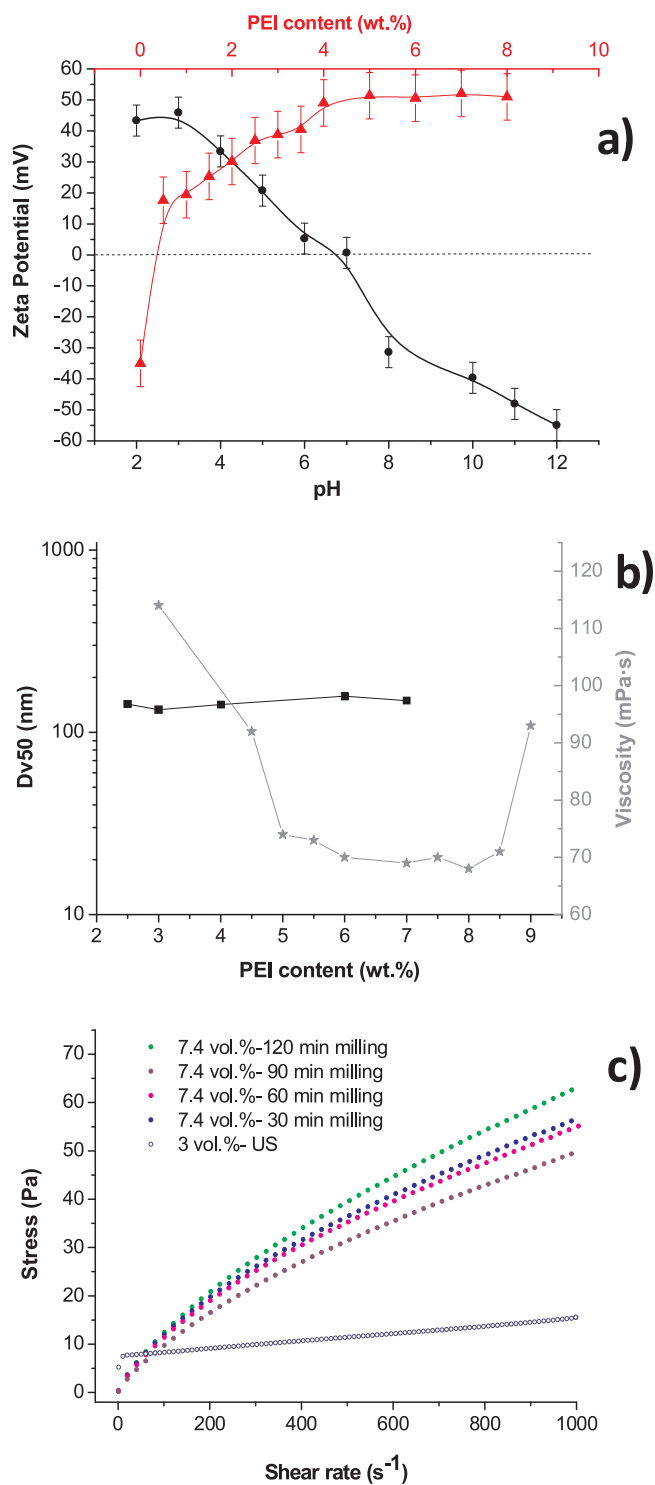


Fig. 1. a) Evolution of the zeta potential of TiO_2 NPs in aqueous suspensions varying the pH ($2 < \text{pH} < 12$) and the addition of PEI (ranging from 0.5 to 8 wt.%) (a), evolution of the mean particle size (Dv50) and viscosity (at a shear rate of 100 s^{-1}) of the TiO_2 NPs in 3 vol.% aqueous suspensions with the addition of PEI at pH 8 (b) and rheograms of aqueous suspensions of TiO_2 NPs modified with 6 wt.% of PEI with 3 and 7.4 vol.% of solid contents dispersed by ultrasounds and ball milling respectively (c).

anatase (21 nm) and 20% rutile (50 nm). In these cases, the SEM pictures of the same powder showed smaller particles of anatase (20 nm) and rutile (40 nm); in reference [20], the size of the managed P25 nanopowder was of 20–30 nm, with a surface area of $50 \text{ m}^2/\text{g}$. In comparison with these studies, the Aeroxide P25 powder used herein (NPs)

has a density of 4.2 g/cm^3 and a specific surface area of $50 \pm 15 \text{ m}^2/\text{g}$. Two crystallographic phases corresponding to 95% anatase and 5% rutile were identified by XRD analysis.

In order to fit the optimal conditions for colloidal processing, the evolution of the zeta potential of NPs in deionized water is firstly examined. Fig. 1a shows the values of zeta potential for a wide range of pH values ($2 < \text{pH} < 12$). TiO_2 NPs have the isoelectric point at pH 6, exhibiting a positive charge for $\text{pH} < 6$ and a negative surface charge for pH values over the isoelectric point. The zeta potential at pH 8 is negative with an absolute value around 30–35 mV. These are ideal conditions to adsorb on the surface a branched polyethylenimine with a molecular weight of $25,000 \text{ g mol}^{-1}$ (pKa 8.6), widely protonated at this pH [24]. The adsorption of the cationic polyelectrolyte onto the TiO_2 NPs surface and its ionization state can be followed also by zeta potential measurements. Fig. 1a additionally shows the evolution of the zeta potential of NPs suspensions with the addition of PEI (wt. %). The strongly negative surface of NPs at pH 8 turns to positive with the addition of an amount of PEI as small as 0.5 wt. % related to the solid content of the suspension. The NPs become more positively charged with increasing PEI addition, reaching a maximum of 50 mV for the addition 6 wt. % of the stabilizer.

The particle size distribution of TiO_2 NPs in aqueous suspensions is determined in Fig. 1b for different additions of PEI (2.5–7 wt. %). The particle population has a mean particle size (Dv50) ranging between 130–160 nm. These particle size values do not significantly changes with the addition of PEI in the values recorded. Even though the results indicated that primary particle size of those NPs (50 nm) cannot be achieved in aqueous suspensions, the level of particle stabilization determined by the absolute zeta potential value (50 mV) was successful. Fig. 1b also displays the viscosity values of 3 vol. % TiO_2 NPs suspensions stabilized with increasing amounts of PEI (3–9 wt. %) at pH 8. The values are taken at shear rates of 100 s^{-1} from the corresponding flux curves (included as supplementary information, Fig. S2S). All suspensions exhibit a thinning behavior leading to viscosities in the range of 10–100 mPa s for the mentioned shear rates, except for the suspension with 3 wt. % of PEI, which present a value out of this range. The suspension viscosity decreases with the addition of PEI down to reach a plateau, between 6–8 wt.%, where it stabilizes. Although the dilution effect provoked by the stabilizer incorporation the addition of 9 wt.% made the viscosity increase again, therefore the 6 wt. % of PEI is selected to prepare the suspensions.

Fig. 1c shows the rheograms of TiO_2 suspensions modified with 6 wt. % of PEI and milled for 30, 60, 90 and 120 min. At low solid content as 3 vol.%, viscosity is too low and the rheograms do not show any significant change. For that reason, a solid content of 7.4 vol.% was choose to clearly evaluate the signal variations. Higher solid content than 7.4 vol.% makes the suspension difficult to handle. The lowest shear stress values are reached when the milling time is 90 min and longer times results in an increase of the stress value.

Suspensions prepared on the better conditions of dispersion (6 wt. % of PEI) and milling (90 min.) were centrifuged in order to separate surface modified NPs from water media. Nevertheless, the suspension was never completely dried to avoid the particle flocculation. The water is substituted by ethanol as solvent in order to improve the drying process during the shaping. 30 s of ultrasounds are applied to favor the particles re-dispersion in ethanol. Processing in ethanol provide the shaping with a better thickness control as well as a uniform and quick drying process of the layers. Both the solid contents of the suspensions and the withdrawal rate of the dip-coating were adjusted to obtain crack-free layers after drying and calcining. 2 vol. % in ethanol and 2.5 mm/s are selected to prepare the coatings.

The dispersant (PEI) and the as-received TiO_2 powder are thermally analyzed to study the possible effects on the calcining and sintering treatments and their possible influence on the structure of the final coatings. Fig. 2 shows the TGA and DTA-TGA analysis of the PEI and TiO_2 NPs respectively.

The TGA of the PEI (without TiO_2 particles) in Fig. 2a displays a weight loss of 100% between 250 and 400°C , corresponding to organic stabilizer removal which means that a thermal treatment above this temperature would result in binder-free coatings. The polyelectrolyte is completely removed and any remainder would be found at the coating after sintering over 400°C . Consequently, the photoresponse or the transport electron charge between particles will not be affected by any possible interference caused by significant residues of the dispersant.

On the other hand, the thermal analysis of TiO_2 powder is showed in Fig. 2b. In this case, the weight loss is extremely low, ($< 2\%$) and there are no appreciable differences with similar reported studies in the literature. For example Di Paola, A. et al. [25] has identified discrete steps in weight loss in relation to the different OH groups: one, in the $30\text{--}120^\circ\text{C}$ range, due to the physically adsorbed water and others, in the $120\text{--}300^\circ\text{C}$ and $300\text{--}600^\circ\text{C}$ ranges, related to weakly bonded OH groups and strongly bonded OH groups, respectively. In addition, a wide peak was identified between $600\text{--}900^\circ\text{C}$ in the DTA curve, and attributed to the phase transformation from anatase to rutile. In order to assure de-binding and simultaneously avoid the phase transformation of TiO_2 , a temperature within the range $400\text{--}600^\circ\text{C}$ could be selected. In this sense 450°C was selected as sintering temperature for the final multilayer systems in a muffle, while a thermal treatment of calcination of 200°C in a heating plate was applied to dry and densify the NPs arrangement after each dip-coating.

To analyze the suitability and the photovoltaic performance of the TCS suspensions, a multilayer strategy is followed to prepare the coatings. A dip coating procedure followed by a thermal stabilization step were repeated for several times (3, 6, 9 and 16 layers) to shape the mentioned coatings. Fig. 3 shows the cross section and top views micrographs of a 3 layers TCS sample after a final thermal treatment at 450°C .

As a result of successful suspension optimization, the cross section micrographs 3a and 3b indicate a homogeneous thickness while in top view micrographs 3c and 3d it can be observed a crack-free coating on the glass surface. The details at high magnification seen in Fig. 3b and d displayed that the adjustments on particles stabilization, solid content, viscosity and the subsequent thermal stabilization steps at 200°C and the sintering treatment at 450°C resulted in crack-free microstructures and a high level of consolidation.

XRD analysis of the sintered coatings (Fig. 1S) was also carried out to determine the ratio of the crystallographic phases (anatase:rutile). Slight variations, from 95.0% to 93.7% for anatase and from 5.0% to 6.3% for rutile, were determined before and after the applied thermal treatment. In spite of the DTA-TGA analysis showed that the full phase transformation occurs above of the selected temperature of sintering, 450°C , the percentage of photoactive phase was partially reduced due to the heating and cooling rates, remaining the TiO_2 coatings under relatively high temperature a considerable time. According to the literature this fact can limit the process.

In addition, the microstructure of this sample is also compared with a coating made of TRP in order to evaluate the influence of the film morphology in the final photoresponse, Fig. 4a. Both samples were prepared with the same thickness onto FTO substrates and thermally treated under the same conditions. The micrograph of the TRP sintered sample showed some microstructural differences in respect to the TCS coating. The film made with the reference paste presented more homogeneity and continuity than the coating made with the TCS (Fig. 4a). While the first displayed a high uniformity, the second one presented a wrinkled appearance with higher exposed surface area.

Both TCS and TRP based TiO_2 photoanodes were used to fabricate DSSCs and their performance was evaluated. The IV curves registered for the corresponding cells are shown in Fig. 4b.

Table 1 collects the photovoltaic parameters obtained from the I–V curves (Fig. 4b) for the TCR and TRP samples.

The open circuit voltage (V_{oc}), the short-circuit current density (J_{sc}) and the fill factor (FF) values of the TCS sample were higher than

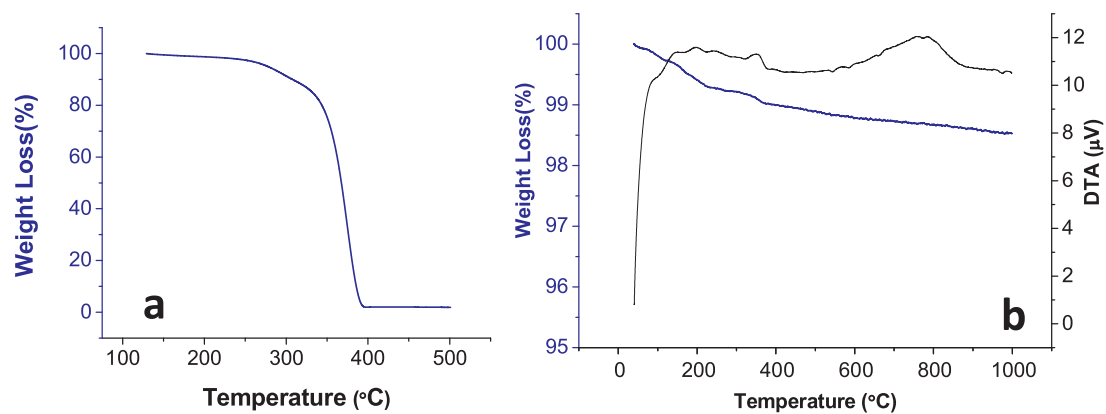


Fig. 2. TGA of PEI a) and DTA-TGA of the as- received TiO₂ NPs b).

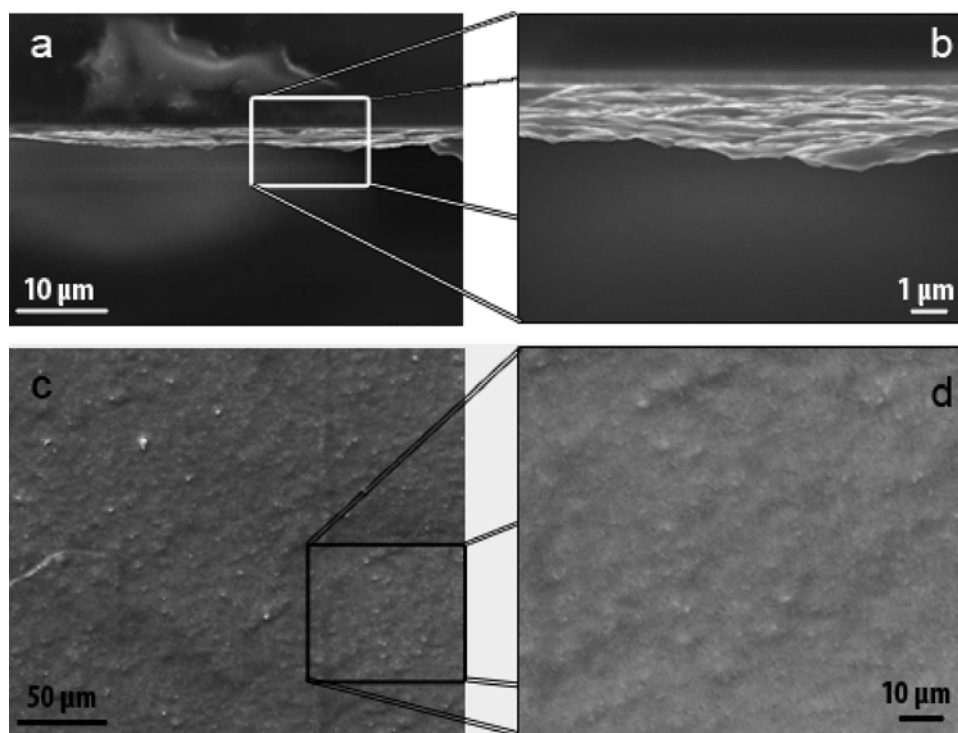


Fig. 3. Low and high magnification SEM images of the cross section (a) and (b) and top view (c) and (d) of the TiO₂ coatings obtained by depositing 3 layers of TCS onto FTO.

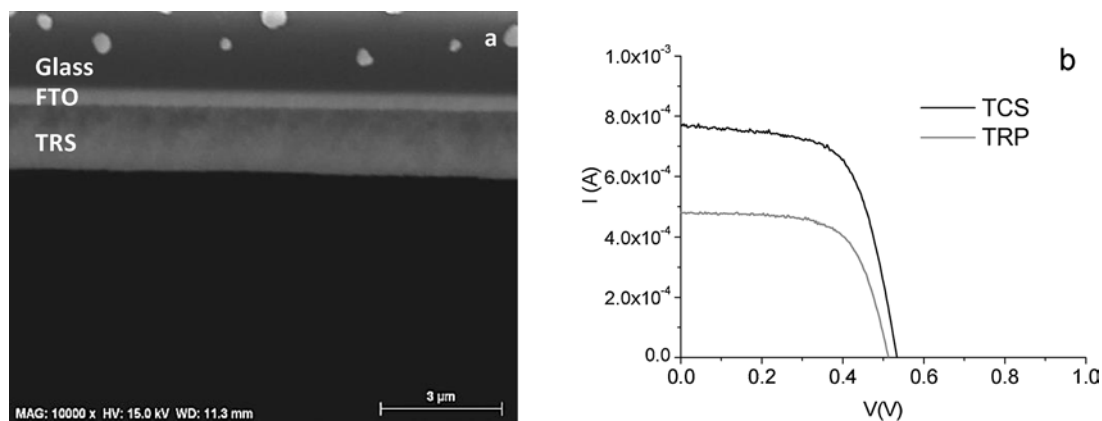


Fig. 4. SEM cross section of the microstructure of the coating made with TRP (a) and photocurrent vs voltage curves of the assembled DSSCs made with TCS and TRP (b).

Table 1

DSSCs parameters for the cells based on TCS and TRP coatings. Film thickness is also mentioned in the table.

Sample	Thickness (μm)	Voc (V)	Jsc (mA cm^{-2})	FF (%)	η (%)
TCS	1.88	0.57	2.52	67.8	1.95
TRP	1.85	0.51	2.29	64.8	1.18

V_{oc}: open circuit voltage; J_{sc}: short-circuit current density; FF: Fill Factor; η : Efficiency.

those of the TRP sample leading to higher conversion efficiency. This is mainly attributed to the higher accessible surface area in meso-structured films, along with a better control on the pore diameter and connectivity, favoring a better dye loading and electrolyte impregnation.

After proving that considerable conversion efficiency is achieved with 3 layers, the cells efficiency was further improved with thicker coatings made from several layers of TCS. Fig. 5 shows the cross section micrographs of those coatings made with 6, 9 and 16 layers of TCS onto FTO and sintered at 450°C.

Although all samples were sintered under the same thermal

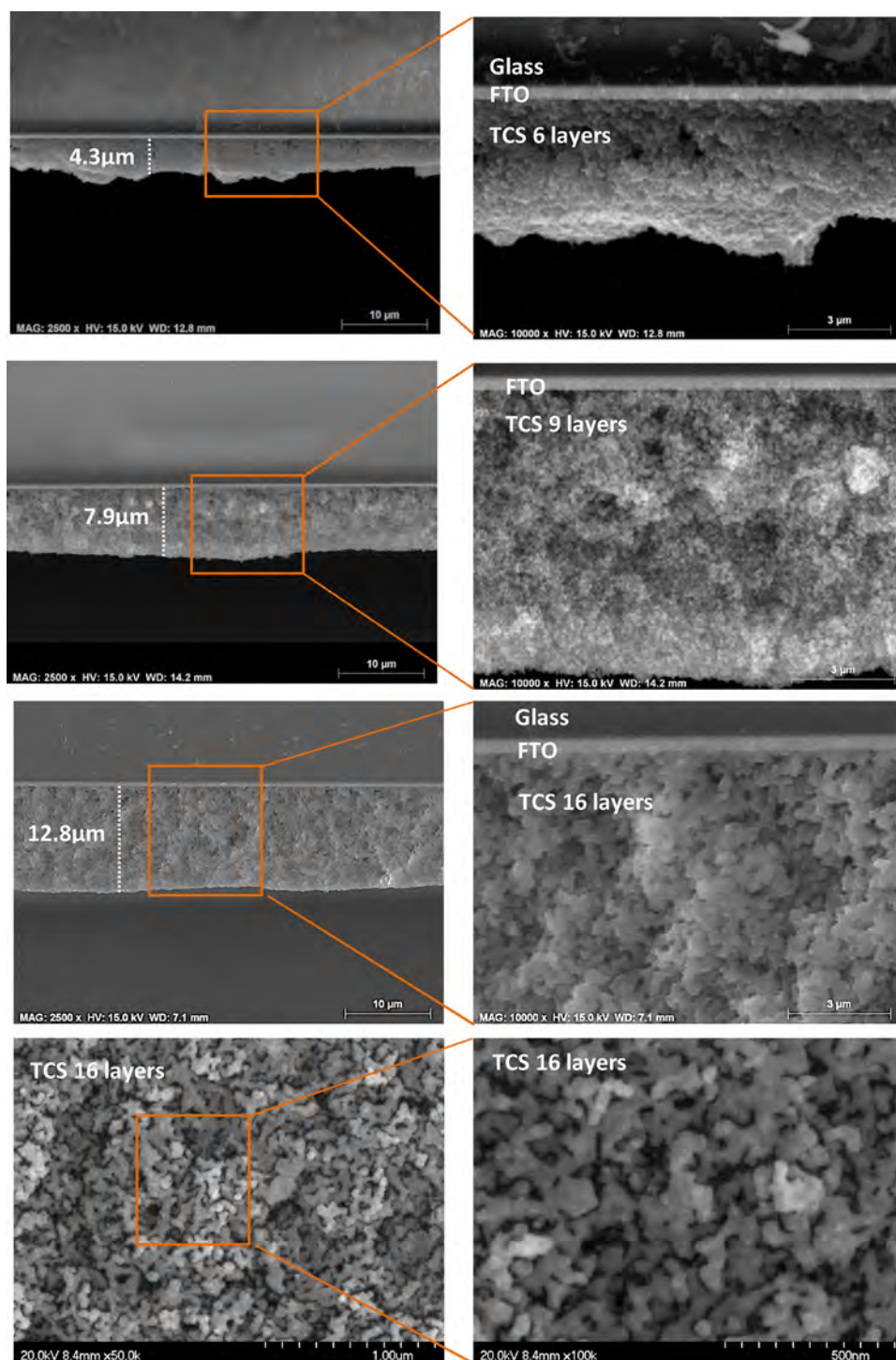


Fig. 5. SEM cross section views of the TCS coatings (6, 9 and 16 layers) at different magnifications.

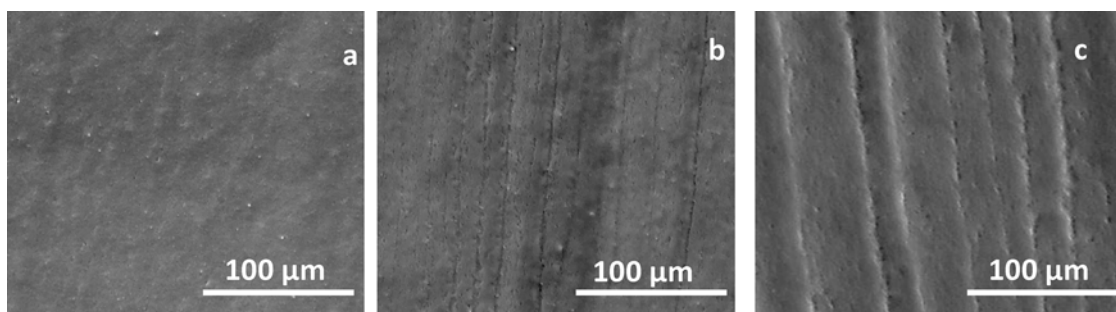


Fig. 6. SEM top view of the coatings made with 6, 9 and 16 layers TCS onto FTO.

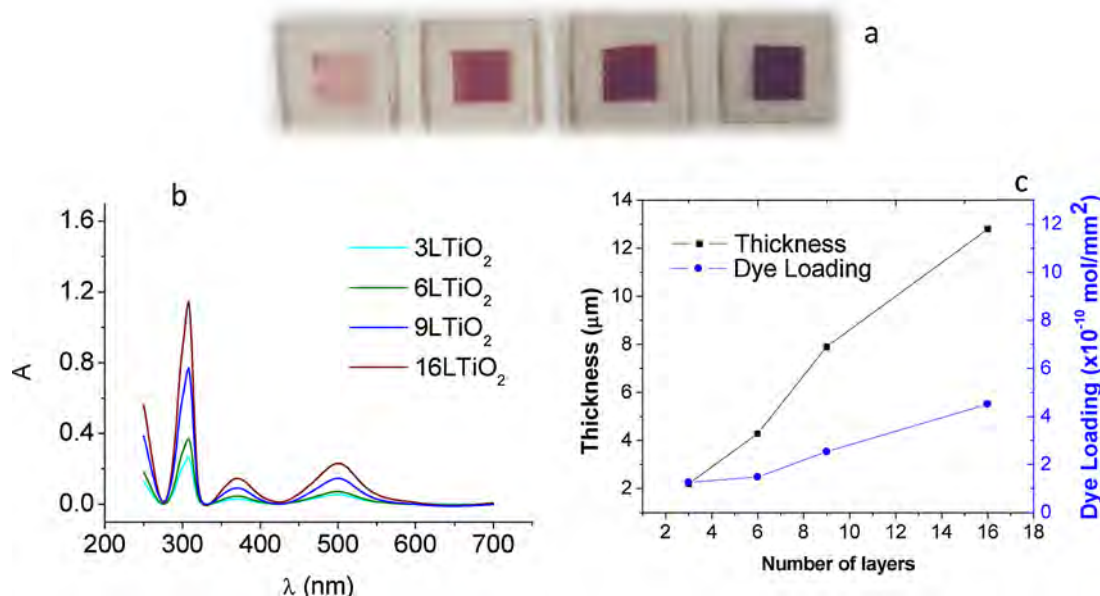


Fig. 7. Picture of the dye sensitized photoelectrodes made with 3, 6, 9 and 16 layers of TCS (a), UV-vis spectrum of the desorption solutions of the samples (b) and evolution of thickness and dye loading with the number of layers (c).

Table 2

Dye loading and cell performances of DSSCs comprising the TCS electrodes with different thickness. Layer thickness is also shown in the table.

TCS	Thickness (μm)	Dye Loading (mol mm ⁻²)	V _{oc} (V)	J _{sc} (mAcm ⁻²)	FF(%)	η (%)
3 layers	2.2	1.26×10^{-10}	0.75	2.4	67.2	1.9
6 layers	4.3	1.48×10^{-10}	0.72	3.6	54.3	2.3
9 layers	7.9	2.54×10^{-10}	0.70	5.2	64.5	3.6
16 layers	12.8	4.52×10^{-10}	0.71	8.7	62.0	5.7

V_{oc}: open circuit voltage; J_{sc}: short-circuit current density; FF: Fill Factor; η: Efficiency.

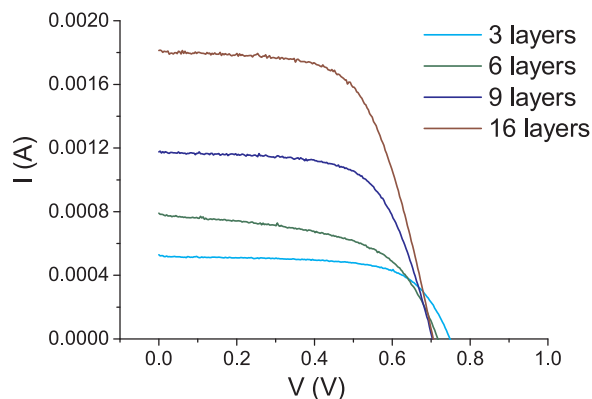


Fig. 8. I-V curves registered in light of the DSSCs made with 3, 6, 9 and 16 layers of TCS.

treatment, the visual consolidation level of the microstructures was significantly different with the increase of thickness. The micrographs, at higher magnification, corresponding to the sample made with 16 layers showed the details of the consolidated microstructures after the thermal treatment.

It is reported that the application of successive thermal steps during the deposition process leads to excessive grain growth and sintering, with a subsequent decrease in the roughness factor [26,27]. However, the packing density of our coatings made with 3 layers, (Fig. 3) was significant higher than the coatings made with 6, 9 and 16 layers, which present more opened porosity, which is directly related to the dye adsorption. The open porosity favors the impregnation of the dye and the electrolyte and eventually could improve the photovoltaic performance of the assembled DSSCs. Nevertheless, the decrease of consolidation level could affect the charge transfer along the microstructure and therefore an intermediate compromise between porosity and packing

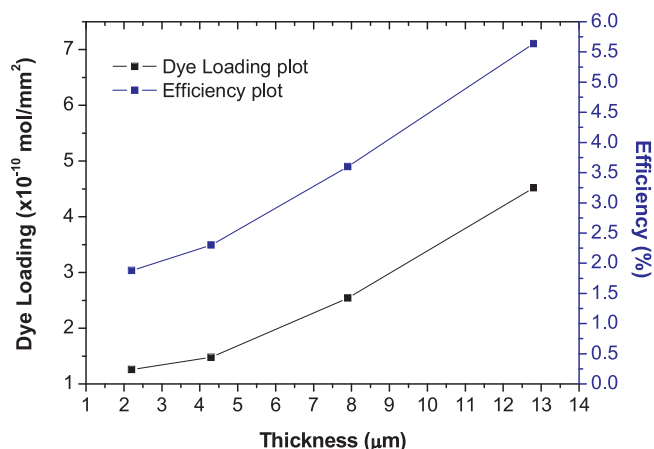


Fig. 9. Dye loading expressed in moles of N-719 dye per mm² of projected electrode area (left) and efficiency evolution (right) with the film thickness.

density should be reached.

In addition, top view micrographs of these coating were also analyzed at very low magnification to probe that the increase of thickness did not affect the surface homogeneity. The obtained crack-free microstructures (Fig. 6) with a uniformly distributed porosity confirmed the benefits of the colloidal approach, either by the suspension optimization and/or the application of the thermal stabilization steps at 200°C carried out between each layer during the dip coating process. The obtained microstructures confirmed that the adjustment of the TCS avoid cracking for overpass the critical thickness for both the drying and sintering processes. A little rippling was observed above 9 layers caused by the withdrawal in the dip coating process.

The influence of the microstructural features, such as the thickness and porosity, and hence the exposed surface area, on the dye loading and therefore on the photovoltaic performance of the assembled cells was also evaluated. Fig. 7 shows a picture of the TCS coatings on the FTO conducting glass after the dye absorption (Fig. 7a) as well as the UV–vis ible spectrum corresponding to the desorption solutions for the 3, 6, 9 and 16 layer TCS samples (Fig. 7b) and the thickness and the dye loading per area unit (Fig. 7c).

The increase in the color intensity of the coatings means that the impregnation of the dye was higher when the thickness increased as confirmed by the absorption spectra. The slope of the thickness curve was more pronounced than the slope of the dye curve (Fig. 7c), which means the multilayer system is more densified with the increase of the number of layers and the dye impregnation is not completely proportional.

Table 2 collects the dye loading values of the prepared samples and the photovoltaic parameters extracted from the I–V curves (Fig. 8).

It can be seen that, as the film thickness increases, the solar cells exhibit a continuous improvement of the J_{sc} and the η values, when the film thickness increase from 3 to 16 layers, while the V_{oc} and the FF slightly decrease. The J_{sc} parameter is known to be largely determined by the dye loading and thus the surface area and the pores connectivity. It has to be noted that from 3 to 16 layers the increment of J_{sc} in a factor

of 3.6 is a similar increment that in the dye loading per area, meaning that, in addition to the dye loading increment with the film thickness reported for the materials here processed (Fig. 7c), That confirms that the dye impregnation within the microarchitecture of the coatings was successful and thus presented an excellent pore accessibility. In the case V_{oc} values there is a slightly decrease of 5% when the thickness increases due to the longer path of photogenerated electrons to reach the collecting electrode. This slightly decrement confirms the microscopic observations that there are no appreciable interface between layers as a consequence of the high homogeneity of the suspension and the adequate calcining treatment that promotes firstly the adhesion between layers during the sequential dipping process, and later the full consolidation of the multilayer structure after sintering. Additionally, Fig. 9 shows a linear progress of the dye loading and the efficiencies values with the film thickness. This performance means that our coatings are far from reaching the typical solar conversion plateau (non-proportional behavior) described in the literature and therefore they still have improvement capability with a photovoltaic yield above 5.7%.

Efficiency is in the range of similar coatings processed from nanoparticles in suspension using commercial powder. Table 3 compares the results showed in the most recent publications to compare them with the results of coatings fully shaped from commercial TiO₂ by the described simple method. Important coating details, such as thickness, processing method, photoactive nanostructures and the intercalation of the so called scattering layer, were considered. In these manuscripts any specific description dealing with the nanoparticles stabilization and/or suspension optimization was reported. Furthermore, in some cases the heterogeneity of the resulting coatings produces cracking and connectivity lacks in their microarchitectures, which difficult the achievement of an available, controllable and effective range of thicknesses built on commercial nanopowders, and consequently many times the mixture of the commercial nanopowder with synthesized TiO₂-nanostructures, the application of a sol-gel healing coating or the application of a dense scattering layer is necessary to increase the photo-efficiency.

Furthermore, the internal resistances and the charge transport properties were also studied by electrochemical impedance spectroscopy (EIS). Fig. 10 show the Nyquist plots of the TCS coatings with different thicknesses measured in dark conditions. The equivalent circuit used to fit the data is described as follows:

$$R_s + \frac{R_1}{Q_1} + \frac{R_2}{Q_2} + Q_3$$

where + is used for series connection and/or parallel connection. Here R_s is the resistance of the contacts and electrolyte, R_1/Q_1 is attributed to the FTO/ electrolyte interface, with an extra contribution expected from the FTO/TiO₂ interface [28], whereas R_2/Q_2 is the response of the TiO₂/electrolyte interface.

The straight sloping line in the low frequency region is associated to Q_3 and it is related to the ions diffusion in the microstructure. The EIS curves were fitted by the Z-fit software (EC-Lab v10.4) and the results are shown in Table 4.

The R_s and R_1 were almost the same among samples, showing slight resistance variations, which are associated to the slight different

Table 3

Comparative of the efficiency values obtained in other similar works based on particulate suspensions.

Efficiency (%)	Thickness (μm)	Processing Method	Additional Info	Ref.
9.2	17.0	Screen-printing	Scattering layer of 5.7 μm	[17]
4.6	9.0	Doctor Blade	Commercial powder mixed with synthesized particles	[18]
7.5	14.5	Multilayer Screen-printing	Ethyl Cellulose as Pore former	[19]
5.5	14.3	Doctor Blade	High surface area anatase TiO ₂ or TiO ₂ sol are added into pure commercial paste	[20]
5.7	12.8	Multilayer sequential dip coating + thermal stabilization step	—	Our work

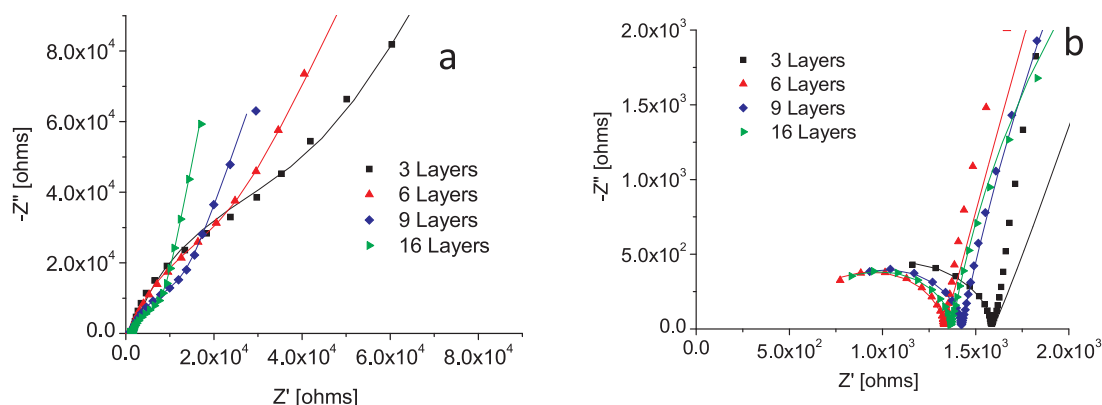


Fig. 10. Nyquist plots of the TCS coatings for different thickness, measured in dark in the 10^{-1} to 10^6 Hz frequency range, using 0.5 mol/L Na_2SO_4 as electrolyte. Fig. 10b shows a magnified view in the high frequency range. Experimental data are represented by symbols and solid lines correspond to the fitted curves.

Table 4

Results of the fitting of the EIS spectra of the TCS coatings with different thickness.

Sample	R_s (Ω)	R_1 (Ω)	Q_1 ($\Omega \cdot \text{cm}^2 \cdot \text{s}^{-(1-a)}$)	R_2 (K Ω)	Q_2 ($\Omega \cdot \text{cm}^2 \cdot \text{s}^{-(1-a)}$)	Q_3 ($\Omega \cdot \text{cm}^2 \cdot \text{s}^{-(1-a)}$)
3 layers	598	994	$0.8 \cdot 10^{-9}$	28.5	$6.2 \cdot 10^{-6}$	$10.5 \cdot 10^{-6}$
6 layers	550	774	$0.8 \cdot 10^{-9}$	16.2	$7.5 \cdot 10^{-6}$	$11.6 \cdot 10^{-6}$
9 layers	619	800	$0.5 \cdot 10^{-9}$	9.2	$6.4 \cdot 10^{-6}$	$13.2 \cdot 10^{-6}$
16 layers	582	790	$0.8 \cdot 10^{-9}$	6.3	$7.0 \cdot 10^{-6}$	$13.9 \cdot 10^{-6}$

contacts/FTO and TiO_2 /FTO resistances. Contrarily to the literature [29], it has been found that the charge transport resistance (R_2) decreased as the thickness increases from 3 to 16 layers. This increment in the conductance is the result of a better electron percolation through the TiO_2 as a consequence of the developed colloidal approach as well as the sequential thermal steps applied during the shaping and the well-defined sintering process which provide better particle connectivity. On the other hand, a steeper slope at low frequency signifies higher ion-diffusion rate and an capacitive behavior which means lower resistance values [30]. This is explained by the fact that after the sintering process, the microstructure of the thinnest coating, (Fig. 3a, b) was closer than the thickest film (Fig. 5e, f). The increase of the number of layers facilitated the transport and intercalation of ions through the TiO_2 microstructure.

4. Conclusions

Well connected and crack-free TiO_2 multilayer coatings were successfully prepared by a colloidal approach consisting in depositing a particulate suspension by sequential dip-coating. The optimization of the suspension combined with the use of the sequential multilayer dipping system with thermal stabilization steps between layers allow obtaining interconnected microstructures without appreciable defects and heterogeneities in the shaped material nor between the interfaces. The Titania Colloidal Suspension (TCS) was formulated using a surface modified powder with 6.5% wt. of PEI as dispersant and a 2% vol. of solid content in ethanol. The described sequential stabilization allows larger drying and sintering critical thicknesses than in the one step layer.

The multilayer strategy allows for obtaining coatings with high thickness values (above $12.8 \mu\text{m}$). The increase of the thickness from 3 to 16 layers did not produce the complete densification of the microstructures, thus open and uniformly distributed porosities have been obtained along the thicknesses of the coatings. This has allowed the homogeneous and proportional dye adsorption ($4.52 \times 10^{-10} \text{ mol} \cdot \text{mm}^{-2}$) improving the photoefficiency (up to 5.7%) and decreasing the electron charge transfer resistance. Although the photovoltaic parameters of our thicker coatings are in the range of others particulate systems previously reported, our alternative proposed route still have

improvement capability because it avoid the microstructure cracking and did not require of the additional scattering layer to achieve a good charge transfer along the coating. The previous optimization of the TiO_2 colloidal suspension and the application of the thermal stabilization steps between layers could be also considered in the case of applying other processing methodology and they would be compatible with other scalable colloidal techniques, such as the screen printing.

Acknowledgements

Authors acknowledge the support to the projects S2013/MIT-2862 (Comunidad de Madrid) and MAT2015-70780-C4-1 (MINECO/FEDER). Z. Gonzalez acknowledges to the European Ceramic Society for the funds of the “Frontiers of Research” program and also to the Spanish Ministry of Economy and Competitiveness for the Postdoctoral Fellowship: IJCI-2016-28538. J. Yus acknowledges to the Comunidad de Madrid the support from the Youth Employment Initiative, CAMPD17_ICV_002.

Appendix A. Supplementary data

Supplementary material related to this article can be found, in the online version, at doi:<https://doi.org/10.1016/j.jeurceramsoc.2018.09.018>.

References

- [1] J. Gong, K. Sumathy, Q. Qiao, Z. Zhou, Review on dye-sensitized solar cells (DSSCs): advanced techniques and research trends, *Renew. Sustain. Energy Rev.* 68 (2017) 234–246.
- [2] S. Mozaffari, M.R. Nateghi, M.B. Zarandi, An overview of the Challenges in the commercialization of dye sensitized solar cells, *Renew. Sustain. Energy Rev.* 71 (2017) 675–686.
- [3] A. Hagfeldt, G. Boschloo, L. Sun, L. Kloo, H. Pettersson, Dye-sensitized solar cells, *Chem. Rev.* 110 (2010) 6595–6663.
- [4] B. O'Regan, M. Grätzel, A low-cost, high-efficiency solar cell based on dye-sensitized colloidal TiO_2 films, *Nature* 353 (1991) 737–740.
- [5] M. Ye, X. Wen, M. Wang, J. Iocozzia, N. Zhang, C. Lin, et al., Recent advances in dye-sensitized solar cells: from photoanodes, sensitizers and electrolytes to counter electrodes, *Mater. Today* 18 (2015) 155–162.
- [6] N. Kinadjian, M. Le Behec, C. Henrist, E. Prouzet, S. Lacombe, R. Backov, Varying TiO_2 macroscopic fiber morphologies toward tuning their photocatalytic properties,

- ACS Appl. Mater. Interfaces 6 (2014) 11211–11218.
- [7] S. Banerjee, S.C. Pillai, P. Falaras, K.E. O'Shea, J.A. Byrne, D.D. Dionysiou, New insights into the mechanism of visible light photocatalysis, *J. Phys. Chem. Lett.* 5 (2014) 2543–2554.
- [8] A. Taleb, F. Mesguich, A. Hérisan, C. Colbeau-Justin, X. Yanpeng, P. Dubot, Optimized TiO₂ nanoparticle packing for DSSC photovoltaic applications, *Sol. Energy Mater. Sol. Cells* 148 (2016) 52–59.
- [9] S. Ahmadi, N. Asim, M.A. Alghoul, F.Y. Hammadi, K. Saeedfar, N.A. Ludin, et al., The role of physical techniques on the preparation of photoanodes for dye sensitized solar cells, *Int. J. Photoenergy* 2014 (2014).
- [10] C. Sanchez, C. Boissière, D. Grosso, C. Laberty, L. Nicole, Design, synthesis, and properties of inorganic and hybrid thin films having periodically organized nanoporosity, *Chem. Mater.* 20 (2008) 682–737.
- [11] J. Dewalque, R. Cloots, F. Mathis, O. Dubreuil, N. Krins, C. Henrist, TiO₂ multilayer thick films (up to 4 μm) with ordered mesoporosity: Influence of template on the film mesostructure and use as high efficiency photoelectrode in DSSCs, *J. Mater. Chem.* 21 (2011) 7356–7363.
- [12] R. Keshavarzi, V. Mirkhani, M. Moghadam, S. Tangestaninejad, I. Mohammadpoor-Baltork, Highly efficient dye sensitized solar cells based on ordered and disordered mesoporous titania thick templated films, *J. Mater. Chem. A* 3 (2015) 2294–2304.
- [13] H. Zhang, W. Wang, H. Liu, R. Wang, Y. Chen, Z. Wang, Effects of TiO₂ film thickness on photovoltaic properties of dye-sensitized solar cell and its enhanced performance by graphene combination, *Mater. Res. Bull.* 49 (2014) 126–131.
- [14] M.C. Kao, H.Z. Chen, S.L. Young, C.Y. Kung, C.C. Lin, The effects of the thickness of TiO₂ films on the performance of dye-sensitized solar cells, *Thin Solid Films* 517 (2009) 5096–5099.
- [15] R. Keshavarzi, A. Jamshidvand, V. Mirkhani, S. Tangestaninejad, M. Moghadam, I. Mohammadpoor-Baltork, The effect of the number of calcination steps on preparing crack free titania thick templated films for use in dye sensitized solar cells, *Mater. Sci. Semicond. Process.* 73 (2018) 99–105.
- [16] D. Sengupta, P. Das, B. Mondal, K. Mukherjee, Effects of doping, morphology and film-thickness of photo-anode materials for dye sensitized solar cell application - a review, *Renew. Sustain. Energy Rev.* 60 (2016) 356–376.
- [17] S. Ito, P. Chen, P. Comte, M.K. Nazeeruddin, P. Liska, P. Péchy, et al., Fabrication of screen-printing pastes from TiO₂ powders for dye-sensitized solar cells, *Prog. Photovoltaics Res. Appl.* 15 (2007) 603–612.
- [18] K. Fan, C. Gong, T. Peng, J. Chen, J. Xia, A novel preparation of small TiO₂ nanoparticle and its application to dye-sensitized solar cells with binder-free paste at low temperature, *Nanoscale* 3 (2011) 3900–3906.
- [19] T.-C. Liu, C.-C. Wu, C.-H. Huang, C.-M. Chen, Effects of ethyl cellulose on performance of titania photoanode for dye-sensitized solar cells, *J. Korean Inst. Electr. Electron. Mater. Eng.* 45 (2016) 6192–6199.
- [20] M. Pan, N. Huang, X. Zhao, J. Fu, X. Zhong, Enhanced efficiency of dye-sensitized solar cell by high surface area anatase-TiO₂-modified P25 paste, *J. Nanomater.* 2013 (2013).
- [21] G.V. Franks, C. Tallon, A.R. Studart, M.L. Sesso, S. Leo, Colloidal processing: enabling complex shaped ceramics with unique multiscale structures, *J. Am. Ceram. Soc.* 100 (2017) 458–490.
- [22] J. Deckers, J. Vleugels, J.-P. Kruth, Additive manufacturing of ceramics: a review, *J. Ceram. Sci. Technol.* 5 (2014) 245–260.
- [23] Z. Gonzalez, J. Yus, A. Caballero, J. Morales, A.J. Sanchez-Herencia, B. Ferrari, Electrochemical performance of pseudo-capacitor electrodes fabricated by Electrophoretic Deposition inducing Ni(OH)₂ nanoplatelets agglomeration by Layer-by-Layer, *Electrochim. Acta* 247 (2017) 333–343.
- [24] Z. Gonzalez, C. Filiatre, C.C. Buron, A.J. Sanchez-Herencia, B. Ferrari, Electrophoretic deposition of Ni(OH)₂ nanoplatelets modified by polyelectrolyte multilayers: study of the coatings formation in a laminar flow cell, *J. Electrochem. Soc.* 164 (2017) D436–D444.
- [25] A. Di Paola, M. Bellardita, L. Palmisano, Z. Barbieriková, V. Brezová, Influence of crystallinity and OH surface density on the photocatalytic activity of TiO₂ powders, *J. Photochem. Photobiol. A: Chem.* 273 (2014) 59–67.
- [26] J. Dewalque, R. Cloots, O. Dubreuil, N. Krins, B. Vertruyen, C. Henrist, Microstructural evolution of a TiO₂ mesoporous single layer film under calcination: effect of stabilization and repeated thermal treatments on the film crystallization and surface area, *Thin Solid Films* 520 (2012) 5272–5276.
- [27] J. Procházka, L. Kavan, V. Shklover, M. Zúkalová, O. Frank, M. Kalbáč, et al., Multilayer films from templated TiO₂ and structural changes during their thermal treatment, *Chem. Mater.* 20 (2008) 2985–2993.
- [28] S. Phadke, A. Du Pasquier, D.P. Birnie, Enhanced Electron transport through template-derived pore channels in dye-sensitized solar cells, *J. Phys. Chem. C* 115 (2011) 18342–18347.
- [29] C.-P. Hsu, K.-M. Lee, J.T.-W. Huang, C.-Y. Lin, C.-H. Lee, L.-P. Wang, et al., EIS analysis on low temperature fabrication of TiO₂ porous films for dye-sensitized solar cells, *Electrochim. Acta* 53 (2008) 7514–7522.
- [30] J. Huang, J. Zhu, K. Cheng, Y. Xu, D. Cao, G. Wang, Preparation of Co₃O₄ nanowires grown on nickel foam with superior electrochemical capacitance, *Electrochim. Acta* 75 (2012) 273–278.



3D Printing of Photocatalytic Filters Using a Biopolymer to Immobilize TiO₂ Nanoparticles

A. Sangiorgi,¹ Z. Gonzalez,² A. Ferrandez-Montero,² J. Yus,² A. J. Sanchez-Herencia,² C. Galassi,¹ A. Sanson,¹ and B. Ferrari^{1,2,z}

¹CNR-ISTEC, Institute of Science and Technology for Ceramics, National Research Council, 48018 Faenza, Italy

²Instituto de Ceramica y Vidrio, CSIC, 28049 Madrid, Spain

Titanium oxide-based photocatalytic filters were produced by Fused Deposition Modelling (FDM) using biopolymers obtained from renewable biomass resources. The thermoplastic route allows shaping composites through the immobilization of photoactive TiO₂ nanoparticles in an environmentally friendly bioplastic such as the polylactic acid (PLA). Composites with an inorganic charge of 30 wt% of TiO₂ nanoparticles (NPs) exhibit a 100% methyl orange (MO) degradation after 24 h of light exposition due to the extremely uniform dispersion of the nanophase within the polymer matrix in the FDM feedstock. Surface modification of TiO₂ NPs allows the optimization of the colloidal dispersion and stabilization of the inorganic charge in a PLA solution and hence, the optimal distribution of nano-photoactive points in the TiO₂/PLA filaments and scaffolds. The proposed new route of processing improves the dispersion of nano-charges comparing with the traditional thermo-pressing routes used for mixing thermoplastics based composites, avoiding the thermal degradation of the polymer and providing a customised product. In this manuscript the evolution of photodegradation with the increase of TiO₂ content in the composite and the variation of the filter geometry was evaluated.

© The Author(s) 2019. Published by ECS. This is an open access article distributed under the terms of the Creative Commons Attribution 4.0 License (CC BY, <http://creativecommons.org/licenses/by/4.0/>), which permits unrestricted reuse of the work in any medium, provided the original work is properly cited. [DOI: 10.1149/2.0341905jes]



Manuscript submitted November 16, 2018; revised manuscript received January 7, 2019. Published February 27, 2019. *This paper is part of the JES Focus Issue on Semiconductor Electrochemistry and Photoelectrochemistry in Honor of Krishnan Rajeshwar.*

Energy and environmental issues are among the most dramatic and urgent challenges that modern society has to face. Realizing that, researchers are spending lot of effort on more eco-friendly alternative technologies for many daily life areas. Among them, sustainable energy production and pollutant removal are two of the areas in which intense research is being carried out. Semiconductor-assisted photocatalysis (mainly based on Titanium dioxide, TiO₂) is a well-established technique for water and air pollutants degradation. It is recognized as a predominant advanced oxidation process (AOP) thanks to its efficiency and eco-friendliness.^{1,2} In particular, AOP techniques of water purification mainly rely on the generation of *OH radicals and their homogeneous attack on organic molecules. About the latter, the spectrum of compounds that are susceptible to this approach includes dyes, pesticides, cosmetics, and more. TiO₂, owing to its characteristics, is the most frequently used photocatalyst in water purification processes. It is relatively cheap, water insoluble, non-toxic and highly resistant to different chemicals. In the anatase form, it shows also the highest photocatalytic activity and resistance to so-called anodic photocorrosion. However, the application of TiO₂ in form of suspended powder in contaminated water requires further additional operations for the separation after photocatalysis. To avoid this relevant technological inconvenience, several solutions are proposed, which enable the photocatalyst to be immobilised. The TiO₂ immobilization on various substrates is an interesting research area within the photocatalytic water treatment field.³ Furthermore, there are additional advantages achievable such as increasing the absorption properties,⁴⁻⁶ and surface hydroxyl groups or reducing the charge recombination.⁷

Immobilization of TiO₂ can be done on powder and pellet substrates,⁴⁻⁶ on rigid/thick substrates or on soft/thin materials.⁸⁻¹⁴ Some examples of powder/pellet substrates include activated carbon,⁵ magnesium-aluminum silicates⁶ and volcanic ash.⁴ The deposition of fine TiO₂ powder on rigid glass surfaces is a quite accepted method. It is commonly accomplished by the simple coverage of the surface with water suspended titania powder and the relative drying. The as-prepared films strongly adhere to the glass due to TiO₂ electrostatic charge (the glass surface is usually negatively charged). TiO₂ immobilized on soft substrates are normally referred as TiO₂ films, membranes or filters. Some examples include TiO₂ immobilized on porous

Al₂O₃,⁹⁻¹¹ glass filter,¹³ polyvinylidene difluoride,¹² sponge⁸ and cellulose fibres.¹⁴ Various techniques, such as electrospinning,^{13,14} film casting,¹² chemical vapour deposition,^{10,11} slip and dip-coating,⁹ have been investigated to achieve the TiO₂ immobilization on soft substrates. Although many efforts have been spent to develop these functional filters, further research work is still needed to better understand both their operation and design. The latter is an important aspect in order to produce highly performing devices because it can produce, for e.g., fluid flux enhancements or fouling mitigation. The mentioned filter production techniques, such as slip or dip-coating, allow producing membranes with simple geometries, mainly with planar configuration. Thus, in order to overcome this limitation, we considered Additive Manufacturing (or three-dimensional printing) as a promising shaping technique.

Since the first technique for 3D printing became available in the late 1980s and was used to fabricate models and prototypes,¹⁵ AM technology has experienced more than 20 years of development and today is one of the rapidly developing advanced manufacturing techniques in the world due to its process flexibility, its ability to create complex structures and rapid response to design alterations. The 3D printing term indicates a class of technologies such as stereolithography (SLA), selective laser sintering (SLS), syringe extrusion, fused deposition modeling (FDM)/fused filament fabrication (FFF), etc. FDM is the one where a temperature controlled head extrudes a thermoplastic material (at temperatures above its glass transition temperature, T_g) layer by layer. In this process, the material changes from a solid to a semi liquid state during the extrusion process and follows the path of a computer aided system.¹⁶ The common materials used in FDM process are acrylonitrile butadiene styrene (ABS),¹⁷ polycarbonate (PC), polylactic acid (PLA), polyvinyl alcohol (PVA), etc.¹⁸ However, it is well-known that one way to lend active chemistry to 3D printed thermoplastic objects is to incorporate inorganic nanoparticles into the polymer filaments. In this way, FDM technology was found to be a potential method for the fabrication of electronic sensors based on conductive carbon black filled poly (caprolactone) (PCL) filaments.^{16,19} Carbon nanotubes have been used to reinforce thermoplastic polyurethane filaments and to induce electrical conductivity.²⁰⁻²² Finally, there has been interest to design and fabricate filaments and then devices, for space-based applications.^{16,23,24}

Although recent works on TiO₂-polymer nanocomposites, especially for biodegradable implants applications,^{25,26} can be found in

^zE-mail: bferrari@icv.csic.es

literature, up to our knowledge there is no 3D TiO₂-based composites where the amount of the inorganic nanophase exceeds 5 wt%. In this paper, we focus on the fabrication and characterization of composite filaments for FDM production of 3D photocatalytic filters. In this environmental friendly approach we selected PLA as polymer matrix, since it is a biopolymer obtained from renewable biomass resources, to have fashioning complex shaped photocatalytic filters. The TiO₂-PLA filaments were initially prepared with 15–30 wt% of TiO₂ nanoparticles (NPs) and tested in the photodegradation of methyl orange (MO) to demonstrate its photocatalytic activity.

Materials and Methods

All chemicals were of reagent grade and used without any further purification. The as-received TiO₂ nanopowder (Aeroxide P25, Evonik Degussa GmbH, Germany) with a density of 4.2 g/cm³, a specific surface area of 50 ± 15 m²/g and an anatase:rutile ratio of 80:20, was dispersed in deionized water to prepare a stable TiO₂ water-based suspension formulated with a 6 vol.% of solid content by adding 6 wt% (referred to powder) of a stabilizer such as the branched polyethylenimine (PEI, pK_a 8.6, Mw 25,000 mol/g, Aldrich, Germany) at pH 8. Modified TiO₂ NPs by PEI coverage in suspension were then ball-milled for 90 minutes (using Al₂O₃ balls of 1 cm in diameter) and subsequently centrifuged at 4000 rpm for 15 minutes in order to remove the aqueous solvent.

The procedure used for the particles dispersion and the adsorption of PEI onto the NPs surfaces has been described previously elsewhere.²⁷ However, to improve the centrifugation of well dispersed NPs, the conditions for the suspension coagulation were stabilised. In this sense, the modification of the zeta potential for TiO₂ NPs induced by the absorption of PEI was determined in a wider pH range (2–12) using the laser Doppler velocimetry technique in a ZetasizerNano ZS (Malvern, UK), and then compared to zeta potential determination in a similar pH range for the bare nanopowder. The pH adjustment of the suspensions was carried out by addition of small quantities of 0.1 M HNO₃ or Tetramethylammonium Hydroxide (TMAH) and controlled with a pH probe (Metrohm AG, Germany). The particle size distribution of the PEI-TiO₂ NPs was also characterized by Dynamic Light Scattering (DLS) by using the ZetasizerNano ZS (Malvern, UK) for concentration ranging between 0.001–0.1 g/L. All the mentioned suspensions were sonicated before each measurement using a UP400S Ultrasonication probe (Hielscher, Germany) for an optimized period of 30 s.

Two different compositions of PLA:TiO₂ (85:15 and 70:30) were prepared by mixing a specific amount of the modified PEI-TiO₂ NPs (still wet after centrifugation) with a certain volume of a polylactic acid (PLA) solution, that was prepared at 80 g/L dissolving, at 40°C under magnetic stirring, polymer pellets (PLA 2003D with D-isomer content of 4.25% provided by Natureworks (USA) in tetrahydrofuran (THF, Panreac Germany).

A vigorous mechanical stirring step coupled with a US treatment (30–60 seconds) were applied to obtain a homogeneous mix which was loaded in a conventional rotary evaporator to remove THF under reduced pressure. The resulting powder was completely dried in a laboratory stove at 80°C and milled later in a blade grinder to reduce the PLA:PEI-TiO₂ granules size. The latter were extruded at temperatures ranging 185–187°C using a homemade single screw extruder to manufacture FDM filaments with a suitable diameter (2.5–3 mm). The morphology and shape of the modified PEI-TiO₂ NPs, the PLA:PEI-TiO₂ composite granules and, finally, the filaments were examined by a field emission scanning electron microscope (FESEM Hitachi S-4700, Japan).

The extruded filaments were employed for manufacturing scaffolds by FDM using a conventional 3D printer (Prusa I3 with the Repetier software) with a nozzle diameter ranging between 0.3–0.5 mm. These filters were designed with a CAD software and printed varying parameters such as: filter diameter (10, 14 and 2 mm), scaffold height (number of printed layers: 4 or 8) and the infill (20–40%). The bed and nozzle temperatures were fixed at 55 and 185°C respectively, with a

filament feed rate of 40 mm/s. The printed filters were characterized by a Tabletop Scanning Electron Microscope (SEM, Hitachi TM-1000).

Thermogravimetric Analysis (TGA) (Perkin Elmer, USA) was used to study the thermal evolution of the PLA:PEI-TiO₂ composites. Tests were performed in air atmosphere with a constant heating rate of 5°C/min up to 600°C. The identification of the crystal phases of the samples was carried out by X-ray diffraction (XRD) with a Siemens D5000 diffractometer (Germany) with a Kristalloflex 710 generator (K α (Cu) λ = 1.5405 Å; 40 kV; 30 mA; 2θ = 5–70).

Finally, the photocatalytic activity of the scaffolds was evaluated by the degradation of methyl orange (MO) in aqueous solution.²⁸ The used light source (Oriel, model 96000) is equipped with a solar light simulating Xe-arc lamp (Osram XBO 450 W) with commercial AM 6197 filter. The tests were performed using 25 mL of MO aqueous solution with a concentration of 3 mg/L. The pH of the solution was adjusted to 2 using HCl. The quartz reactor vessel was plugged to prevent MO solution evaporation. First, photolysis and dark tests (adsorption) were performed to confirm that the MO degradation is only associated with the PLA:PEI-TiO₂ scaffolds and not to light irradiation and/or adsorption. Photocatalytic measurements were performed introducing the PLA:PEI-TiO₂ scaffolds in the MO solution that was maintained under continuous stirring and irradiation. Degradation phenomena were monitored using a home-made system described previously elsewhere.²⁸ A narrow bandpass filter centered at 500 nm and bandwidth of 10 nm (Thorlabs, FB-500-10 full width at half maximum) was placed in front of a biased Silicon Photodetector (Thorlabs DET100A). The filter limits allow the light transmission in a wavelength range that matches the absorption band of MO (508 nm). Therefore, the intensity of light at the detector allows measuring the degradation of MO. All the elements were installed on an optical table to ensure stability and also, optically isolated in the dark to avoid the presence of other light sources. The output signal from the detector (voltage) was sent to a Keithley 2010 multimeter where it was recorded every 10 min using a Visual Basic homemade code.

Results and Discussion

The stabilization of TiO₂ NPs in deionized water was firstly examined through zeta potential measurements. Figure 1a shows the variation of the zeta potential as a function of pH for bare NPs and also for NPs covered with the polyelectrolyte PEI as dispersant additive (PEI-TiO₂). Two zones of maximum stability were displayed in the curve corresponding to the bare TiO₂, where the surface charge is enough to provide repulsive interactions among the particles, far from the isoelectric point (IEP) located at pH 7. One zone was located at acid pH (2–4) with zeta potential values close to +40 mV and the other at basic pH (8–12) with values ranging from –30 to –50 mV. Although the surface charge balance of NPs was slightly higher at other pH values, the working pH was fixed in at 8 for the PEI adsorption, since it is more efficient in these conditions. The PEI used is a branched chain with primary, binary and ternary amino groups that maintains highly protonated (charged) at pH 8 favouring the additive adsorption on negative TiO₂ surfaces. Consequently after PEI addition, the PEI-TiO₂ suspension (at pH 8) exhibits a zeta potential of +66 mV, due to the adsorbed protonated PEI, and a shear-thinning behavior with a manageable viscosity of 70 mPa s (at shear rate of 100 s^{–1}).²⁷

Moreover, the DLS measurements were also performed to determine the particle size after the surface modification. Figure 1b shows the particle size distribution of the PEI-TiO₂ NPs where one narrow peak, centred on 120 nm (D_{V50}) was observed as additionally confirmed by the cumulative volume % curve. Despite the high dispersion obtained, the modified particles presented a slight trend to the agglomeration as confirmed by the BET diameter (D_{BET}). This parameter is calculated from the powder morphological properties, specific surface area, SSA, and density, ρ , ($D_{BET} = 6/\rho \cdot SSA$), and allows the evaluation of the effect of the polyelectrolyte on the particles dispersion. A value of D_{BET} close to 30 nm was obtained, which means that the PEI-TiO₂ NPs presented a relatively low agglomeration factor of 3 ($F_{ag} = D_{V50}/D_{BET}$). Figure 1c shows the morphological

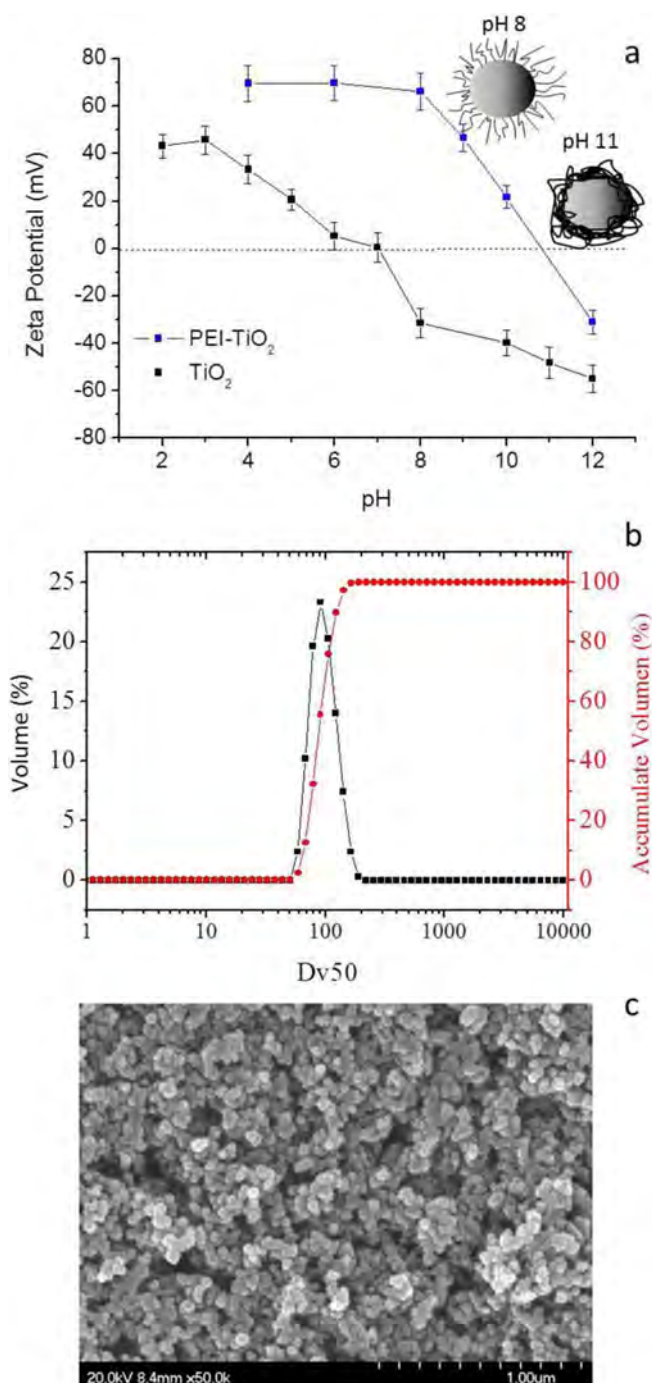


Figure 1. (a) Evolution of the zeta potential of bare-TiO₂ and modified PEI-TiO₂ NPs in aqueous suspension varying the pH (2 < pH < 12); (b) Size distribution of the modified PEI-TiO₂ NPs and; (c) FESEM image of the modified PEI-TiO₂ NPs.

characterization of the modified powder by FESEM that confirms the presence of small particles agglomerates around 100–150 nm. Although the size of the TiO₂ agglomerates maintains in the nanometric range, the dispersion of TiO₂ in the PLA matrix could be limited which can affect the photoactive efficiency of the 3D printed pieces.

The variation of the zeta potential as a function of pH was also examined after PEI adsorption at pH 8. The global charge balance at the particle surfaces was completely modified appearing positive up to pH 11 after which the surface charge became negative. The variation of zeta potential induced by the PEI on the TiO₂ NPs can

be explained by the way in which the polyelectrolyte chain interacts with the particle surface (through tail or train conformations), which depends on its pK_a value, ionic strength, used solvent or molecular architecture.²⁹ The amino groups of the PEI structure present a high degree of ionization when the working pH < pK_a (tail) and a lower degree when the working pH > pK_a (train). The sketches in Figure 1a illustrate both configurations. The zeta potential value of the PEI-TiO₂ at pH 8 was +66 mV while the increase of the pH toward higher basic values reduced the global charge, neutralizing the surface, to achieve the IEP of the system, where NPs are unstable and the system should coagulate.

In order to prepare the polymeric nanocomposite or feedstock for the extrusion of PLA/PEI-TiO₂ filaments,³⁰ the TiO₂ NPs were firstly stabilized in aqueous suspensions by the addition of PEI, and then flocculated by varying the pH up to 11 to centrifuge them. The formation of TiO₂ agglomerates (100–150 nm), as well as its low zeta potential at pH 11, favours TiO₂ NPs flocculation and centrifugation. The wet flocculated PEI-TiO₂ nanopowder was then mixed and re-dispersed in the PLA solution in THF under mechanical stirring. Figure 2a shows a scheme of the complete process. The as-prepared PLA/PEI-TiO₂ suspension was then gently dried under reduced pressure obtaining PLA/PEI-TiO₂ composite granules which were grinded in a blade grinder to reduce their size and to adapt them to the extruder conditions. These granules were then extruded in a single screw extruder with a thermal pass of only 10 cm at temperatures ranging from 185–187°C, obtaining composite filaments with homogeneous diameters lower than 1.75 mm, which were used as the PLA/PEI-TiO₂ composite feedstock for printing. Figure 2b displays the pictures of the obtained composites, both powder and filaments, for a specific composition of 85:15 (wt/wt) PLA:PEI-TiO₂.

In deep microstructural analysis of the granules, filaments and scaffolds were also characterised by FESEM. Micrographs in Figures 3a and 3b show a low magnification image of a PLA/PEI-TiO₂ granule, where the inorganic nanoparticles (white arrows) are just slightly agglomerated but homogeneously distributed in the blend surrounding PLA (blue arrows). This well dispersed composite makes PLA/PEI-TiO₂ granules suitable candidates for the production of FDM filaments with an isotropic composition. Figure 3c shows an image of the cross section of an extruded filament (185–187°C) which fulfils the requirements for printing. Although the appearance of the fracture surface is mostly plastic due to the high percentage of the polymer (85:15 (wt/wt) PLA:PEI-TiO₂), NPs agglomerates of 100–150 nm, still visible at such magnification, appear to be well-distributed inside the filament (white arrows). The PEI-TiO₂ NPs distribution in the PLA matrix is retained after printing at 185°C. The micrographs of the PLA/PEI-TiO₂ scaffold in Figure 3d display the dense structure of the rods with inorganic NPs distributed both at the rod surfaces and inside parts.

Figure 4a shows the XRD spectra of the 85:15 (wt/wt) PLA:PEI-TiO₂ granules and scaffolds. The pattern of the granules is characteristic of a mixture of TiO₂ and a crystalline polymer, where the diffractions at 20.7° and 22.9° indicate the presence of the α-phase of PLA (Figure 4b).³¹ The diffractogram of the scaffold shows the presence of amorphous PLA (from the wide band at 20°) derived by the thermal treatments during the extrusion and printing processes. On the other hand, the TiO₂ phase maintains in both cases the expected ratio of anatase and rutile 95% and 5%, compatible with the P25 nanopowder composition. These results evidence the effect of TiO₂ NPs as nucleant agent for the polymer matrix. When the composites are processed from the stable suspension of PEI-TiO₂ NPs in a PLA solution in fact, the excellent dispersion of PEI modified TiO₂ NPs induces the precipitation of pure crystalline PLA over the inorganic seeds during drying.³² However, for the extrusion process, the PLA-TiO₂ granules are melted and then deposited: the XRD analysis clearly shows that the polymer preserved the amorphous state after solidification. PLA is in fact a biopolymer that does not crystallize from melting and therefore the thermal processing erases the matrix crystallinity.

Two different PLA/PEI-TiO₂ composites were used to prepare the feedstock granule-like: 85:15 and 70:30 (wt/wt PLA:PEI-TiO₂), labelled respectively 15TiO₂ and 30TiO₂. The same printing parameters

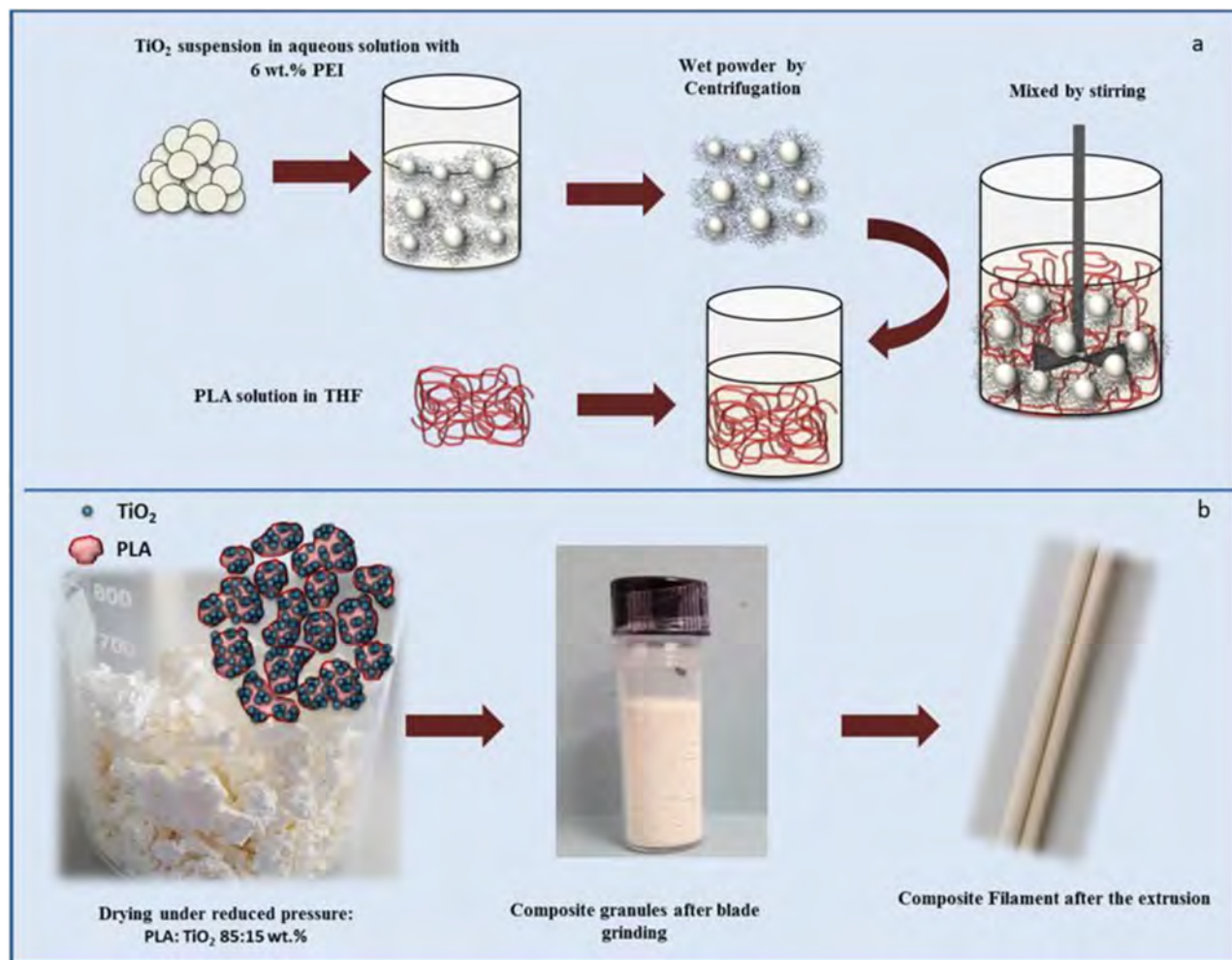


Figure 2. (a) Scheme of the process for the preparation of modified PEI- TiO_2 suspension in PLA and; (b) Pictures of the resulting dried composite, PLA/PEI- TiO_2 granules, after and before blade grinding as well as the composite filament after the extrusion.

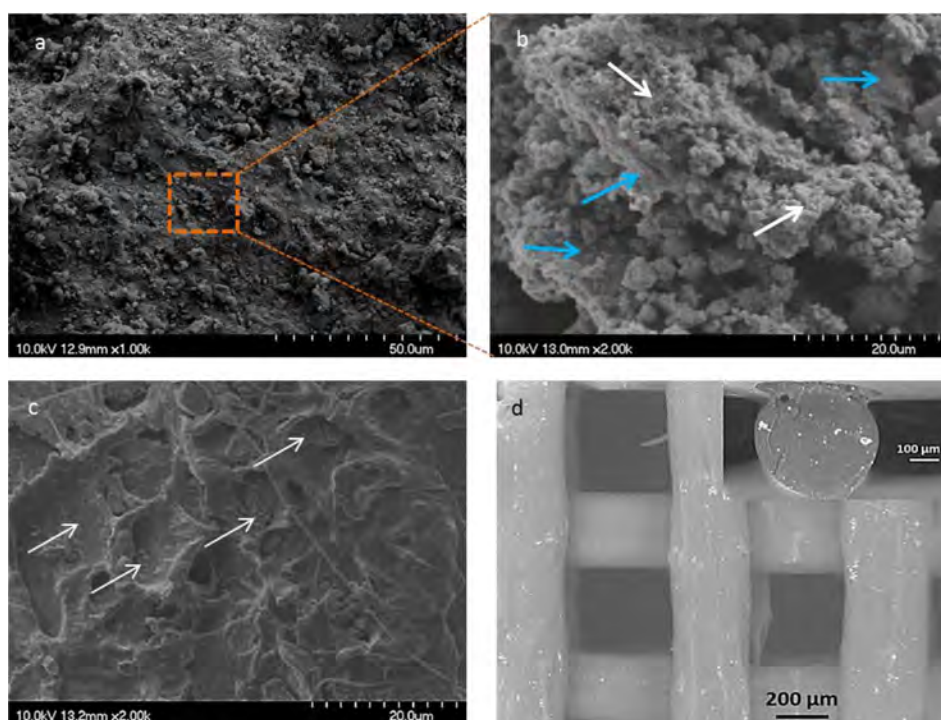


Figure 3. (a, b) FESEM images of the PLA/PEI- TiO_2 granules at different magnifications, where blue and white arrows point to the PLA and TiO_2 aggregates, respectively; (c) FESEM image of the cross section of a PLA/PEI- TiO_2 filament and; (d) SEM image of the top view of a filter including (inset) the detail of the rod cross-section. All images correspond to the composite 85:15 (wt/wt) PLA:PEI- TiO_2 .

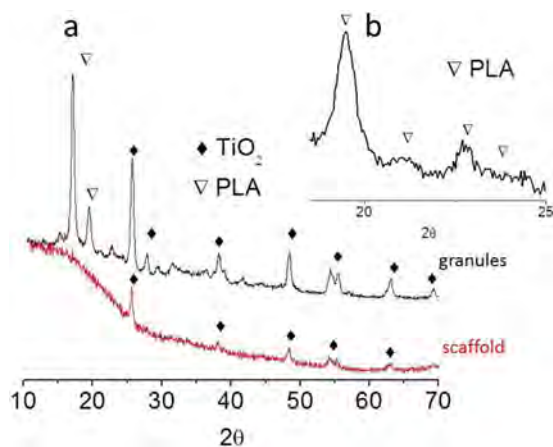


Figure 4. (a) XRD spectra of the granules and scaffold of the composite 85:15 (wt/wt) PLA:PEI-TiO₂ and; (b) detail of the peaks associated with the α crystalline phase in the granules scanning.

(a printing nozzle of 0.5 mm in diameter, a filament feed rate of 40 mm/s and, a bed and nozzle temperatures of 55 and 185°C respectively), were used to produce different filters designs: in particular filters with diameters of 10, 14 and 20 mm, heights of 4 or 8 layers and, infills ranging 20–40% (which defines the free space left on the designed piece). Table I summarizes the most relevant printing conditions while Figure 5 shows the CAD printing shapes corresponding to the explored printing parameters: scaffold diameter, number of layers and infill. Table I also includes the calculated dimensions of the scaffold: height and the height \times length of the structure holes, (considering the CAD models which define the number of bars and holes of the designed scaffold structure, the nozzle diameter (0.4 mm) which define the diameter of the printed bars), the diameter of the filter (10, 14 and 20 mm) and the number of layers (4 and 8 layers).

Figure 6a quantifies the MO photodegradation capability respectively of 15TiO₂ and 30TiO₂ filters, F1 and F5 in Table I, while their microstructure is reported in Figures 6c–6h. It is important to consider that both filters were printed following the same CAD model (F1 and F5 in Figure 5) having 8 layers and 10 mm of diameter. The preliminary photolysis and dark tests showed that neither photolysis nor adsorption processes occur. Plots in Figure 6a show that the designed porosity is higher enough to be infiltrated by the MO solution, and more than 50% MO degradation is recorded after 24 h with both compositions.

According to a great number of researchers, the rates of photocatalytic oxidation of various dyes, MO included, over illuminated TiO₂ fitted the Langmuir-Hinshelwood kinetics model:³³

$$r = \frac{dC}{dt} = \frac{kKC}{1 + KC} \quad [1]$$

where r is the oxidation rate of the reactant, C is the concentration of the reactant, t the illumination time, k the reaction rate constant, and K is the adsorption coefficient of the reactant. When the initial chemical concentration of the dye (C_0) is low, the above equation can be simplified to an apparent first-order equation:

$$\ln\left(\frac{C_0}{C}\right) = kt \quad [2]$$

The plots of $\ln(C_0/C)$ versus time (t) represent a straight line with a slope k that is the apparent first-order rate reaction constant.³⁴ These considerations are valid for TiO₂ as powder samples or immobilized in a film or coating form. In this stage of the study, we assume to be in the same conditions to evaluate the MO degradation kinetic in presence of the hybrid filters. The obtained plots (Figure 6b) confirm that the MO degradation follows a first-order kinetic model, although it is important to note that the 30TiO₂ filters achieve this degradation regimen after 5 h. Moreover, k values demonstrate that the F1 (15TiO₂) filter exhibits better photocatalytic behavior in degrading MO. The differences in the reaction rates, or in the photocatalytic behavior, are usually associated with changes of the structure, texture and porosity of the microstructure.²⁸

Comparing the two filters, the F5 (30TiO₂) shows less effectiveness in degrading the MO solution. Figures 6c–6h show the SEM images of the top view and the cross section of both filters F1 (c, e and g) and F5 (d, f and h) at different magnifications. Figures 6c and 6d illustrate the 3D periodic structures composed, especially in the F1 case, by smooth surfaces and quite uniform cylindrical rods. However, observing the cross section of the scaffolds (Figures 6e–6h) the incorporation of a double amount of TiO₂ NPs promotes a partial collapse of the porous structure. Although the bed and nozzle temperature are kept constant for both composites, a regular printing is impeded by the presence of a higher inorganic charge amount finely dispersed within the PLA matrix. Irregular printing leads to the deposition of asymmetrical rods reducing and sometimes closing the pre-designed porosity of the filter, and then, lowering the filter surface area exposed to the dye molecules.

F1 and F5 filters dimensions are far from that designed (see Figure 5 and Table I). The whole scaffold height decreases down to 2.75 mm, instead of the designed 3.20 mm, since the holes height decreases down to 0.32 mm (versus 0.4 mm at the CAD model) due to the deformation of the bars during the layer-by-layer printing, evidenced in Figure 6e. Similarly the bars also deform acquiring lengths up to 0.59 mm (versus 0.4 mm at the CAD model), while the holes length decreases, ranging 0.43–0.56 mm. Consequently the porosity decreases in F1 (15TiO₂) filter if it is compared with the reference structure in Figure 5. This effect is more pronounced in the F5 filter (30TiO₂ in Figure 6f). In fact the F5 scaffold height reduces to 2.00 mm. At higher magnifications, the reduction of the spaces between bars in different layers, as well as the decreasing (even inexistent) spaces between bars in the same layer, are evident. Comparing the structures in Figures 6g and 6h also demonstrates that an increase of the NPs amount leads more defects inside the rods core (closed porosity) while the increase on NPs doesn't take place necessarily in the bars surface, and can reduce the photocatalytic effectivity. In view of the FESEM results,

Table I. Summary of the PLA/PEI-TiO₂ filters characteristics processed by FDM.

Filter	Label	Diameter (mm)	Number of layers	Infill (%)	Height* (mm)	Hole dimensions* (mm): height \times length	Weight (g)
F1	15TiO ₂	10	8	40	3.2	0.4 \times 0.80	0.12
F2		14	4	30	1.2	0.3 \times 0.40	0.13
F3		14	4	25	1.2	0.3 \times 0.75	0.11
F4		14	4	20	1.2	0.3 \times 0.96	0.08
F5	30TiO ₂	10	8	40	3.2	0.4 \times 0.80	0.12
F6		14	4	40	1.6	0.4 \times 0.73	0.14
F7		20	4	40	1.6	0.4 \times 0.82	0.18

*Calculated dimensions considering printing design parameters and CAD models in Figure 5.

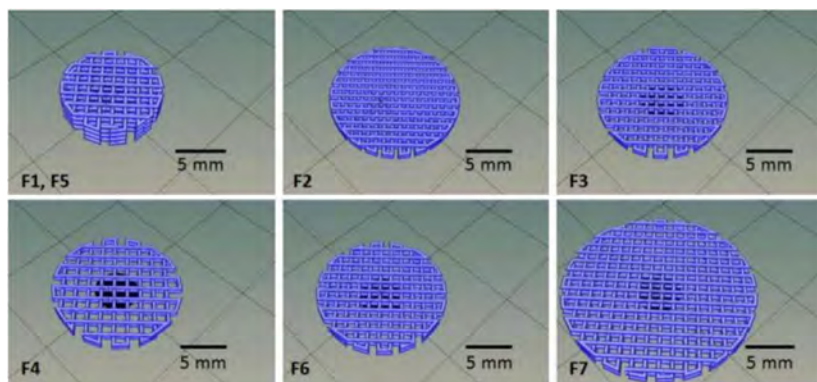


Figure 5. CAD models of the filters in Table I.

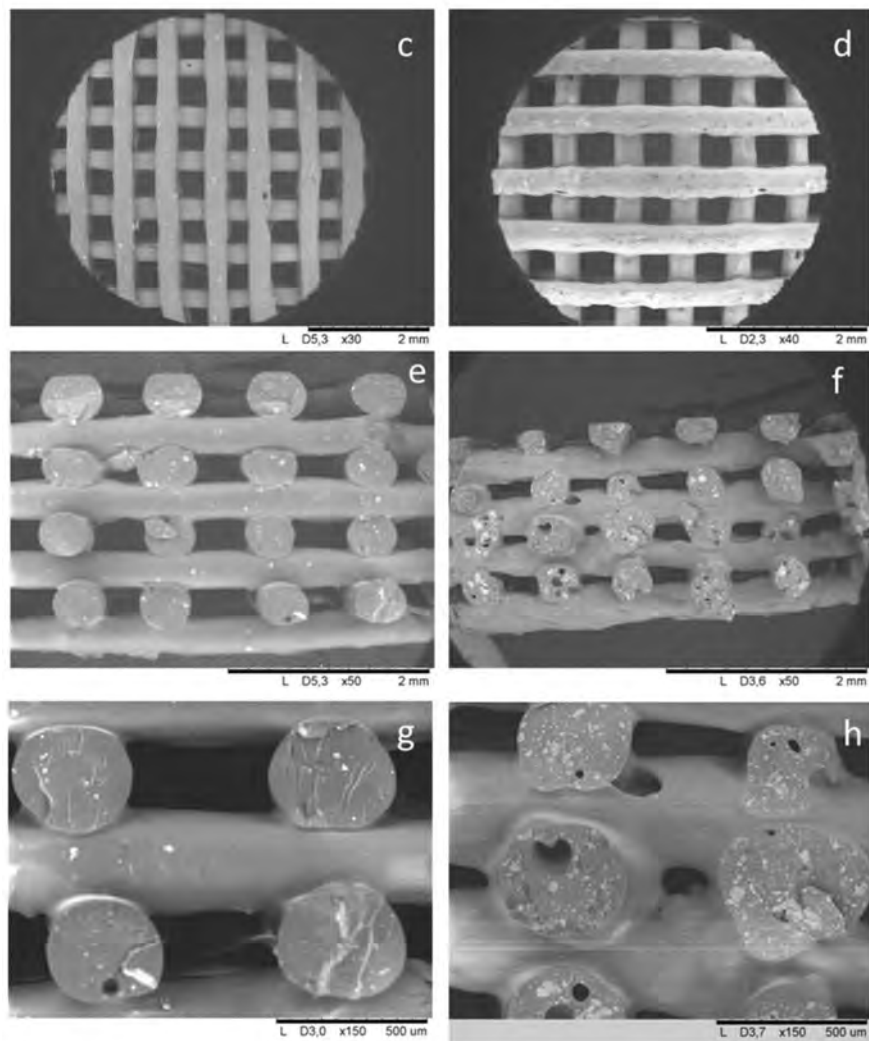
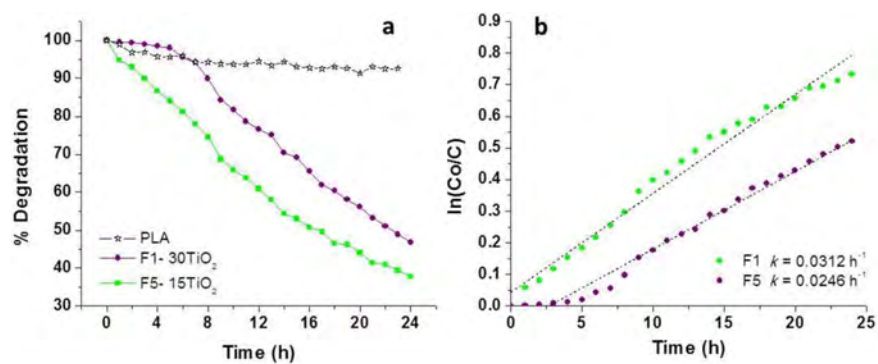


Figure 6. (a, b) Photodegradation of MO and kinetics of F1 and F5 filters; (c, e, g) FESEM images of the F1 filter; (d, f, h) FESEM images of the F5 filter at different magnifications.

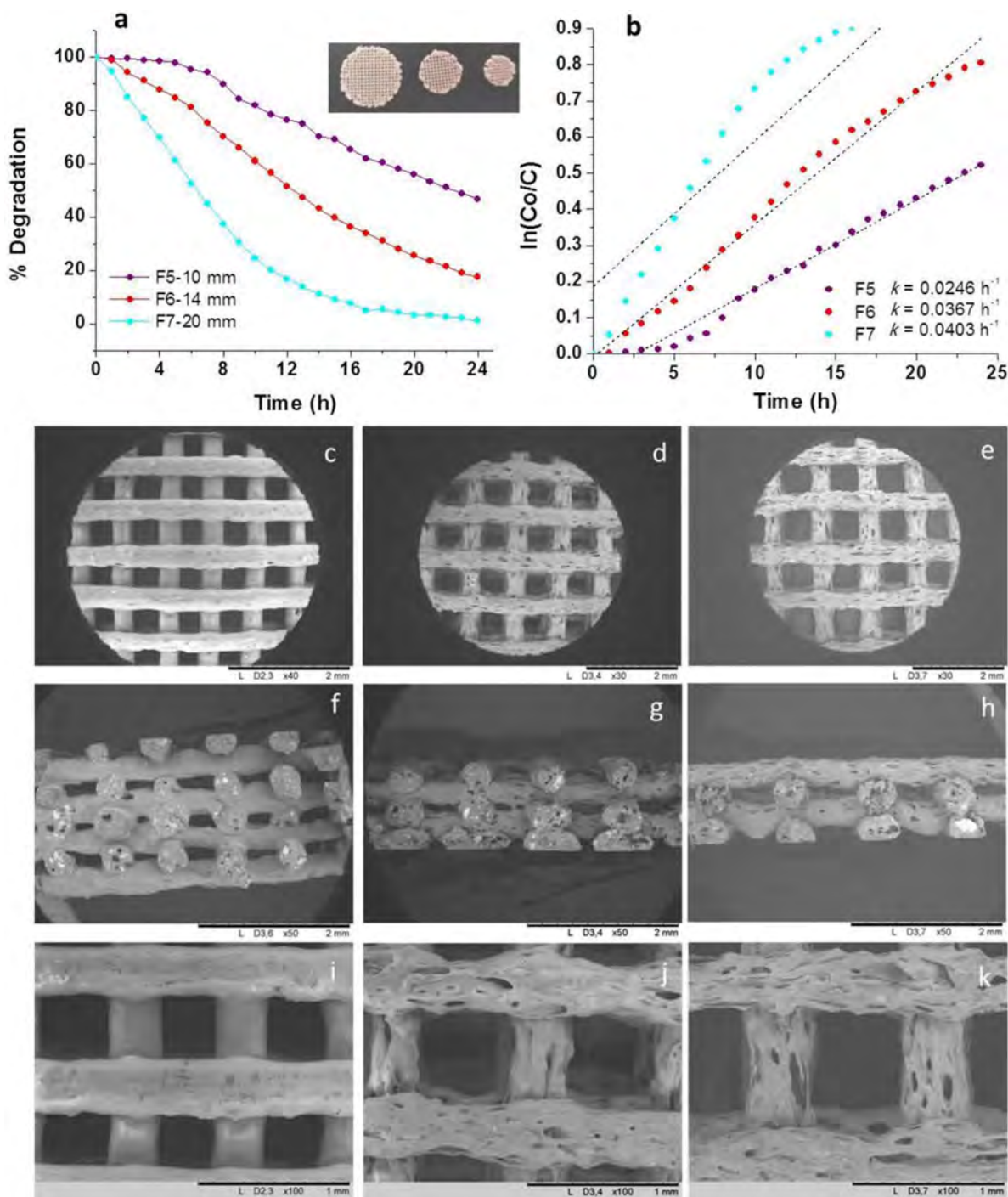


Figure 7. (a, b) Photodegradation of MO and kinetics of F5, F6 and F7 filters; (c, f, i) FESEM images of the F5 filter; (d, g, j) FESEM images of the F6 filter; (e, h, k) FESEM images of the F7 filter at different magnifications.

degradation kinetics could be affected by the fact that the NPs imbibed in the composite are partially available at the surface of the filter rods, but also the structure collapse impedes the homogeneous irradiation of all the structure due to partial shading effects between each other bars.

Figures 7a and 7b quantified the MO photodegradation of 30TiO₂ filters designed with 40% infill using nozzles of 0.4 mm of diameter, scaffold diameters of 10, 14 and 20 mm, and 8 or 4 layers, exhibiting weights ranging 0.12–0.18 g, corresponding to the filter F5, F6 and F7 in Table 1, which SEM images are showed in Figures 7c–7h and insets, respectively.

The F7 filter (20 mm in diameter and 4 layers) shows the highest efficiency in degrading the MO solution, after 20 hours, a total degradation of the dye molecules is achieved. This effect is ascribed to the potential higher exposed surface area and the higher amount of TiO₂ NPs included in the three-dimensional structure. Although scaffold bars maintain their diameter, the holes length differs from the CAD model (Figure 5 and Table 1) similarly to what occurs in the F5 filter, that corresponds to the same feedstock composition (30TiO₂). However, the wall-roughness of the rods plays an important role on the filters behavior. Comparing the Figures 7i, 7j and 7k, extremely rough surfaces are illustrated going from the F5 (10 mm in diameter and 8

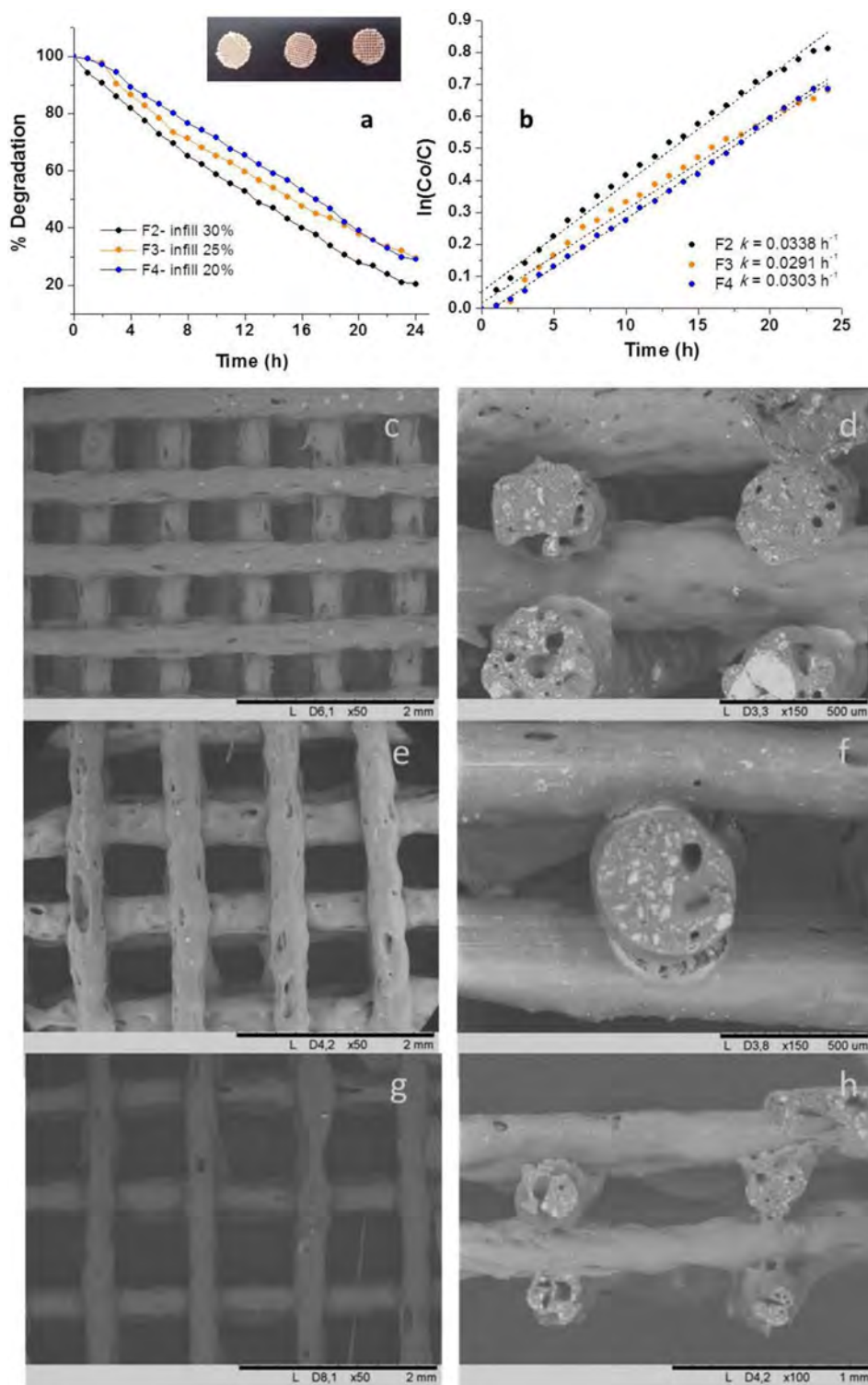


Figure 8. (a, b) Photodegradation of MO and kinetics of F2, F3 and F4 filters; (c, d) FESEM images of the F2 filter; (e, f) FESEM images of the F3 filter; (g, h) FESEM images of the F4 filter at different magnifications.

layers) to the F7 sample, probably indicating a scale-up effect during the FDM deposition of the largest one. However, this microstructure composed of superficial voids and irregular surfaces perfectly matches the requirements needed to have a higher surface area in contact with the dye solution, thus justifying the good photocatalytic performance of the F7 filter. The kinetics of MO photodegradation obtained using these filters (Figure 7b) confirm that the F7 filter is the most performing one, however, looking at the relative curves, only the F6 filter follows a first-order kinetic model as well as F5 filter after the first 5 h. F7

shows a different behavior that is ascribed to its unique microstructure, illustrated in Figures 7e, 7h and 7k.

Figures 8a and 8b report the MO photodegradation of 15TiO₂ filters designed with a diameter of 14 mm and 4 layers varying the infill from 30% to 20% (nozzle diameter of 0.3 mm). They exhibit weights ranging 0.13–0.08 g, corresponding to the filter F2, F3 and F4 in Table I respectively, which pictures are showed in the inset. In terms of photocatalytic degradation of the MO solution, higher infill % values lead to the best performance, as in the F2 case (30%). The initial dye concentration is reduced of about 80% during the test. In this case,

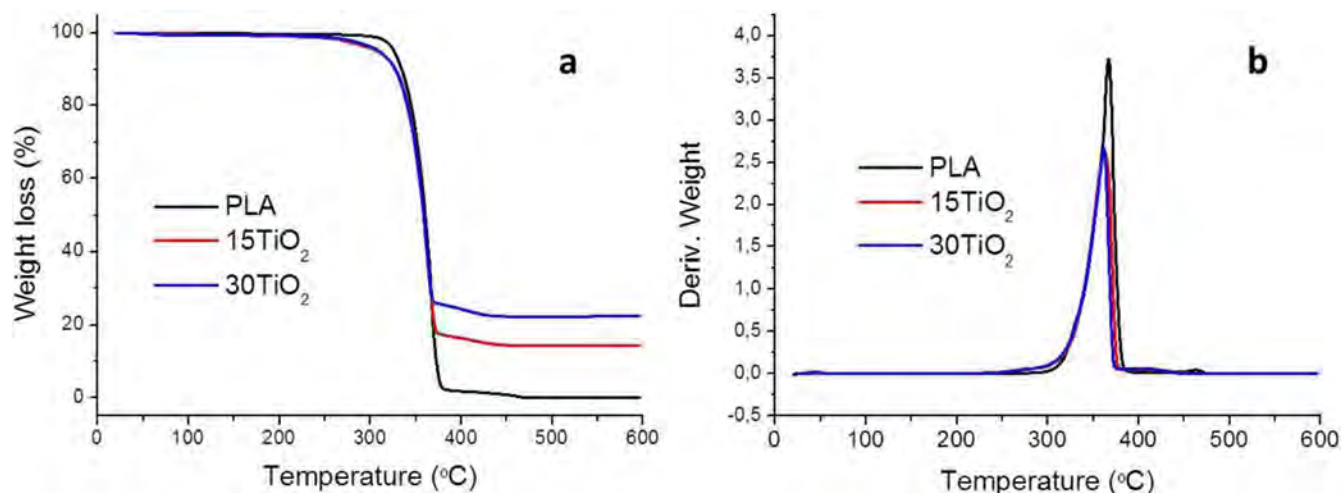


Figure 9. (a) Thermograms and (b) TGA derivate of F3 (15TiO₂) and F7 (30TiO₂) filters.

all the samples follow a first-order kinetic model with the F2 filter showing the highest k value, equal to 0.0338 h^{-1} . Keeping constant the rods wall roughness (Figures 8c, 8e and 8g) this trend mainly relies on the major amount of TiO₂ present on the F2 filter, because of the higher mass, and thus the higher presence of photocatalytic sites. Figures 8c–8h report the SEM images of the top view and the cross section of the filters F2 (c and d), F3 (e and f) and F4 (g and h) (in Table I). All the micrographs reported in Figures 8c–8h show 3D structures composed of well-aligned rods that maintain their initial shape even without support of the underlying layer.

Finally, the stability of PLA/PEI-TiO₂ composites was measured by thermogravimetric test after the photodegradation test. Figure 9 illustrates the TGA (Figure 9a) and their respective derivative thermograms (DTGA) curves (Figure 9b) of pure PLA and both, 15TiO₂ (F3, Figure 8a) and 30TiO₂ (F7, Figure 7a) filters, able to degrade the 70% and 100% of MO after 24 h, respectively. Weight losses of the polymer and composites take place between 250 and 450°C, with a maximum rate around 350°C, evidencing that the composites degrade similarly to PLA. That means that the PLA matrix of the composites at least maintains its thermal properties after a double thermal process (extrusion and printing). The inorganic residue of the filters decomposition at 450°C is 15 and 25% of 15TiO₂ and 30TiO₂ composites, respectively, evidencing a slight loose of TiO₂ content of the 30TiO₂ filters during their double thermal processing, i.e. at the extrusion of the composites filaments and the FDM printing of filters.

The results of a detailed study of the filters after operation, in particular the initial degradation temperature (T_0), the maximum degradation temperature (T_{max}) and the final degradation temperature (T_e) data, are summarized in Table II. The maximum peaks in the DTGA curves represent the temperatures at maximum degradation rates (T_{max}). Although the PLA is a biodegradable polymer its degradation properties are influenced by different factors such as polymer crystallinity, chemical bond, temperature or UV radiation.³⁵ The results show that the composite thermal degradation happens at practically the same temperature as the pure PLA therefore no photodegradation of the polymer matrix is observed, induced by the TiO₂ nanoparticles, since

MO is more susceptible to oxidation. Moreover, contrary to what could be expected, the PLA matrix doesn't seem to be degraded after 24 h dipped in a MO aqueous solution. In this sense, the heat barrier role of TiO₂ particles³⁶ in these composites should be considered since the inorganic load addition could mask in the thermal tests a slightly PLA degradation by dissolution in the aqueous solvent during the photodegradation test. On the other hand, the improvement of mechanical properties could be expected due to the increase of the content on TiO₂ in the feedstock.³⁷ However a higher amount of inorganic particles in the polymeric matrix promotes printing irregularities such as the closed porosity and voids at the bars core as well as the formation of the wall-porosity. Although these last microstructural defects step up the photocatalytic activity of the filters they could compromise the mechanical properties improvement. Consequently, once the thermal degradation of the polymeric matrix has been avoided by substituting the thermal mixing of the PLA and TiO₂ NPs by the proposed colloidal processing for the feedstock preparation, further research should be addressed to optimize the filters mechanical properties while maintaining their photocatalytic performance. In view of the obtained results, we can assume that it is possible to process scaffolds with an improved photocatalytic response retaining the composite structure at least during the photodegradation test, and hence keeping immobilized the photocatalyst.

Conclusions

Eco-friendly and biopolymer-based composites, able to photodegrade an organic molecule, were designed for 3D printing of photocatalytic filters. 3D scaffolds with an engineered microstructure and containing immobilized TiO₂ NPs in PLA, were for the first time printed by fused filament fabrication or fused deposition modeling (FDM) with low-cost 3D printers. FDM allows the manufacture of customized 3D pieces, and in this work, the variation of the 3D scaffold geometry, by manipulating the printer parameters, leads to achieve the 100% degradation of MO for 70:30 (wt/wt) PLA:PEI-TiO₂ composites.

New polymer composites were produced by incorporating modified PEI-TiO₂ NPs in a thermoplastic biopolymer such as PLA. PEI adsorption onto the nanopowders surface provides the needed stability to disperse NPs during the whole process, from the mixture of the PLA and TiO₂ NPs in a THF suspension to the final homogeneous distribution of TiO₂ in the PLA matrix at the FDM scaffolds. Moreover, the surface modification of the TiO₂ NPs allows increasing the inorganic loading of the polymer minimizing charge losses during the manufacturing of filaments and scaffolds by the extrusion and printing for the composites formulated with the highest TiO₂ contents (70:30 (wt/wt) PLA:PEI-TiO₂). The increase of the inorganic charge

Table II. Thermal degradation temperatures: initial degradation (T_0), maximum degradation (T_{max}) and the end of degradation (T_e) temperatures.

	T_0 (°C)	T_{max} (°C)	T_e (°C)
PLA	338	368	376
15TiO ₂	336	361	371
30TiO ₂	336	362	368

in the polymer as well as the scaling up parameters used produce to a valuable wall roughness/porosity in the scaffolds rods that propitiates the photocatalysis.

Acknowledgments

Authors acknowledge the support to the projects S2018/NMT-4411 (Comunidad de Madrid) and MAT2015-70780-C4-1 (MINECO/FEDER). Z. Gonzalez acknowledges the Spanish Ministry of Economy and Competitiveness for the Postdoctoral Fellowship: IJCI-2016-28538. J. Yus acknowledges to the Comunidad de Madrid the support from the Youth Employment Initiative, CAMPD17_ICV_002. The authors thank ECERS for funding on Mobility Project JECS Trust Contract number: 2017294.

ORCID

B. Ferrari  <https://orcid.org/0000-0003-3377-6844>

References

1. A. Sobczykński and A. Dobosz, *Polish J. Environ. Stud.*, **10**, 195 (2001).
2. O. Legrini, E. Oliveros, and A. M. Braun, *Chem. Rev.*, **93**, 671 (1993).
3. A. Y. Shan, T. I. M. Ghazi, and S. A. Rashid, *Appl. Catal. A Gen.*, **389**, 1 (2010).
4. P. Esparza, M. E. Borges, L. Díaz, M. C. Alvarez-Galván, and J. L. G. Fierro, *Appl. Catal. A Gen.*, **388**, 7 (2010).
5. B. Zhu and L. Zou, *J. Environ. Manage.*, **90**, 3217 (2009).
6. L. Jin and B. Dai, *Appl. Surf. Sci.*, **258**, 3386 (2012).
7. E. Stathatos, D. Papoulis, C. A. Aggelopoulos, D. Panagiotaras, and A. Nikolopoulou, *J. Hazard. Mater.*, **211–212**, 68 (2012).
8. G. Li, S. Park, D. W. Kang, R. Krajmalnik-Brown, and B. E. Rittmann, *Environ. Sci. Technol.*, **45**, 8359 (2011).
9. L. Djafer, A. Ayral, and A. Ouagued, *Sep. Purif. Technol.*, **75**, 198 (2010).
10. C. P. Athanasekou et al., *J. Memb. Sci.*, **392–393**, 192 (2012).
11. G. E. Romanos et al., *J. Hazard. Mater.*, **211–212**, 304 (2012).
12. R. A. Damodar, S.-J. You, and H.-H. Chou, *J. Hazard. Mater.*, **172**, 1321 (2009).
13. L. Liu, Z. Liu, H. Bai, and D. D. Sun, *Water Res.*, **46**, 1101 (2012).
14. N. M. Bedford, M. Pelaez, C. Han, D. D. Dionysiou, and A. J. Steckl, *J. Mater. Chem.*, **22**, 12666 (2012).
15. D. L. Bourell, M. H. L., J. W. Barlow, J. J. Beaman, and C. R. Deckard, (1991).
16. K. Prashantha and F. Roger, *J. Macromol. Sci. Part A Pure Appl. Chem.*, **54**, 24 (2017).
17. M. R. Skorski, J. M. Esenther, Z. Ahmed, A. E. Miller, and M. R. Hartings, *Sci. Technol. Adv. Mater.*, **17**, 89 (2016).
18. L. E. Murr et al., *Philos. Trans. R. Soc. A Math. Phys. Eng. Sci.*, **368**, 1999 LP-2032 (2010).
19. S. J. Leigh, R. J. Bradley, C. P. Purssell, D. R. Billson, and D. A. Hutchins, *PLoS One*, **7**, e49365 (2012).
20. W. Zhong, F. Li, Z. Zhang, L. Song, and Z. Li, *Mater. Sci. Eng. A*, **301**, 125 (2001).
21. F. Ning, W. Cong, J. Qiu, J. Wei, and S. Wang, *Compos. Part B Eng.*, **80**, 369 (2015).
22. Y. Wu, D. Isakov, and P. S. Grant, *Materials (Basel)*, **10** (2017).
23. C. Shemelya et al., *IEEE Sens. J.*, **15**, 1280 (2015).
24. C. M. Shemelya et al., *J. Electron. Mater.*, **44**, 2598 (2015).
25. M. S. de, S. B. Monteiro, and M. I. B. Tavares, *Adv. Nanoparticles*, **07**, 11 (2018).
26. A. Muñoz-Bonilla et al., *Int. J. Mol. Sci.*, **14**, 9249 (2013).
27. Z. Gonzalez et al., *J. Eur. Ceram. Soc.*, **39**, 366 (2019).
28. Y. Castro and A. Durán, *J. Sol-Gel Sci. Technol.*, **78**, 482 (2016).
29. J. A. Lewis, *J. Am. Ceram. Soc.*, **83**, 2341 (2004).
30. A. Ferrandez-Montero, A. Ferrari, B. Sanchez-Herencia, A. J. Gonzalez, Z. Gonzalez, F. J. Yus, J. Lieblich, and J. L. Gonzalez, *ESI1641.1356, Regist. Date 24/05/2018*, 2–33.
31. P. Pan, B. Zhu, W. Kai, T. Dong, and Y. Inoue, *J. Appl. Polym. Sci.*, **107**, 54 (2008).
32. H. Salas-Papayanopolos, A. B. Morales-Cepeda, S. Sanchez, P. G. Lafleur, and I. Gomez, *Polym. Bull.*, **74**, 4799 (2017).
33. Y. Li, X. Li, J. Li, and J. Yin, *Water Res.*, **40**, 1119 (2006).
34. M. N. Rashed and A. A. El-Amin, **2**, 73 (2007).
35. R. Auras, L. T. Lim, S. E. M. Selke, and H. Tsuji, *Poly-lactic acid. Synthesis, Structures, Properties, and Applications*, John Wiley & Sons, Inc., New Jersey, (2010).
36. H. Zhang et al., *RSC Adv.*, **5**, 4639 (2015).
37. Y. Luo et al., *J. App. Polym. Sci.*, **46509**, 1 (2018).

Justificante de presentación electrónica de solicitud de patente

Este documento es un justificante de que se ha recibido una solicitud española de patente por vía electrónica utilizando la conexión segura de la O.E.P.M. De acuerdo con lo dispuesto en el art. 16.1 del Reglamento de ejecución de la Ley 24/2015 de Patentes, se han asignado a su solicitud un número de expediente y una fecha de recepción de forma automática. La fecha de presentación de la solicitud a la que se refiere el art. 24 de la Ley le será comunicada posteriormente.

Número de solicitud:	P201830503	
Fecha de recepción:	24 mayo 2018, 14:22 (CEST)	
Oficina receptora:	OEPM Madrid	
Su referencia:	ES1641.1356	
Solicitante:	CONSEJO SUPERIOR DE INVESTIGACIONES CIENTÍFICAS	
Número de solicitantes:	1	
País:	ES	
Título:	Procedimiento de obtención de una pieza por modelado por deposición de hilo fundido	
Documentos enviados:	Descripcion-1.pdf (18 p.) Reivindicaciones-1.pdf (3 p.) Dibujos-1.pdf (10 p.) Resumen-1.pdf (1 p.) OLF-ARCHIVE.zip FEERCPT-1.pdf (1 p.) FEERCPT-2.pdf (1 p.)	package-data.xml es-request.xml application-body.xml es-fee-sheet.xml feesheet.pdf request.pdf
Enviados por:	C=ES,O=PONS PATENTES Y MARCAS INTERNACIONAL SL,2.5.4.97=#0C0F56415445532D423834393231373039,CN=50534279 J ANGEL PONS (R: B84921709),SN=PONS ARIÑO,givenName=ANGEL,serialNumber=IDCES-50534279J,descriptio n=Ref:AEAT/AEAT0297/PUESTO 1/40639/05102016093524	
Fecha y hora de recepción:	24 mayo 2018, 14:22 (CEST)	
Codificación del envío:	46:67:C3:57:D5:48:C5:52:E2:79:19:20:08:F1:F0:80:AE:C8:51:3C	

AVISO IMPORTANTE

Las tasas pagaderas al solicitar y durante la tramitación de una patente o un modelo de utilidad son las que se recogen en el Apartado "Tasas y precios públicos" de la página web de la OEPM (http://www.oepm.es/es/propiedad_industrial/tasas/). Consecuentemente, si recibe una comunicación informándole de la necesidad de hacer un pago por la inscripción de su patente o su modelo de utilidad en un "registro central" o en un "registro de internet" posiblemente se trate de un fraude.

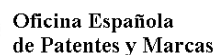
La anotación en este tipo de autodenominados "registros" no despliega ningún tipo de eficacia jurídica ni tiene carácter oficial.

En estos casos le aconsejamos que se ponga en contacto con la Oficina Española de Patentes y Marcas en el correo electrónico informacion@oepm.es.

ADVERTENCIA: POR DISPOSICIÓN LEGAL LOS DATOS CONTENIDOS EN ESTA SOLICITUD PODRÁN SER PUBLICADOS EN EL BOLETÍN OFICIAL DE LA PROPIEDAD INDUSTRIAL E INSCRITOS EN EL REGISTRO DE PATENTES DE LA OEPM, SIENDO AMBAS BASES DE DATOS DE CARÁCTER PÚBLICO Y ACCESIBLES VÍA REDES MUNDIALES DE INFORMÁTICA.

Para cualquier aclaración puede contactar con la O.E.P.M.

/Madrid, Oficina Receptora/



(1) MODALIDAD:		PATENTE DE INVENCION MODELO DE UTILIDAD	[X] []
(2) FORMULARIO 5101. TIPO DE SOLICITUD:		PRIMERA PRESENTACION SOLICITUD DIVISIONAL CAMBIO DE MODALIDAD TRANSFORMACION SOLICITUD PATENTE EUROPEA PCT: ENTRADA FASE NACIONAL	[X] [] [] [] []
(3) EXP. PRINCIPAL O DE ORIGEN:		MODALIDAD: N.º SOLICITUD: FECHA SOLICITUD:	
(4) LUGAR DE PRESENTACION:			OEPM, Presentación Electrónica
(5-1) SOLICITANTE 1:		DENOMINACION SOCIAL: UNIVERSIDAD PUBLICA NACIONALIDAD: CODIGO PAIS: NIF/NIE/PASAPORTE: CNAE: PYME: DOMICILIO: LOCALIDAD: PROVINCIA: CODIGO POSTAL: PAIS RESIDENCIA: CODIGO PAIS: TELEFONO: FAX: CORREO ELECTRONICO: EMPRENDEDOR: PERSONA DE CONTACTO: MODO DE OBTENCION DEL DERECHO: INVENCION LABORAL: CONTRATO: SUCESSION: PORCENTAJE DE TITULARIDAD:	CONSEJO SUPERIOR DE INVESTIGACIONES CIENTIFICAS [] España ES Q2818002D C/ Serrano, 117 Madrid 28 Madrid 28006 España ES [] [X] [] [] 100,00 %
(6-1) INVENTOR 1:		APELLIDOS: NOMBRE: NACIONALIDAD: CODIGO PAIS: NIF/NIE/PASAPORTE: DOMICILIO: LOCALIDAD: PROVINCIA: CODIGO POSTAL: PAIS RESIDENCIA: CODIGO PAIS:	Ferrández Montero Ana España ES 49101248-C Av. de Gregorio del Amo, 8 Madrid 28 Madrid 28040 España ES

	TELÉFONO:	
	FAX:	
	CORREO ELECTRÓNICO:	
	EL INVENTOR RENUNCIA A SER MENCIONADO:	[]
(6-2) INVENTOR 2:		
	APELLIDOS:	Ferrari Fernández
	NOMBRE:	Begoña
	NACIONALIDAD:	España
	CÓDIGO PAÍS:	ES
	NIF/NIE/PASAPORTE:	05276149-H
	DOMICILIO:	C/Kelsen 5. Campus de Cantoblanco.
	LOCALIDAD:	Madrid
	PROVINCIA:	28 Madrid
	CÓDIGO POSTAL:	28049
	PAÍS RESIDENCIA:	España
	CÓDIGO PAÍS:	ES
	TELÉFONO:	
	FAX:	
	CORREO ELECTRÓNICO:	
	EL INVENTOR RENUNCIA A SER MENCIONADO:	[]
(6-3) INVENTOR 3:		
	APELLIDOS:	Sánchez Herencia
	NOMBRE:	Antonio Javier
	NACIONALIDAD:	España
	CÓDIGO PAÍS:	ES
	NIF/NIE/PASAPORTE:	02872849-B
	DOMICILIO:	C/Kelsen 5. Campus de Cantoblanco.
	LOCALIDAD:	Madrid
	PROVINCIA:	28 Madrid
	CÓDIGO POSTAL:	28049
	PAÍS RESIDENCIA:	España
	CÓDIGO PAÍS:	ES
	TELÉFONO:	
	FAX:	
	CORREO ELECTRÓNICO:	
	EL INVENTOR RENUNCIA A SER MENCIONADO:	[]
(6-4) INVENTOR 4:		
	APELLIDOS:	González Granados
	NOMBRE:	Zoilo
	NACIONALIDAD:	España
	CÓDIGO PAÍS:	ES
	NIF/NIE/PASAPORTE:	44371652-Y
	DOMICILIO:	C/Kelsen 5. Campus de Cantoblanco.
	LOCALIDAD:	Madrid
	PROVINCIA:	28 Madrid
	CÓDIGO POSTAL:	28049
	PAÍS RESIDENCIA:	España
	CÓDIGO PAÍS:	ES
	TELÉFONO:	
	FAX:	
	CORREO ELECTRÓNICO:	
	EL INVENTOR RENUNCIA A SER MENCIONADO:	[]
(6-5) INVENTOR 5:		
	APELLIDOS:	González López
	NOMBRE:	Francisco Javier
	NACIONALIDAD:	España
	CÓDIGO PAÍS:	ES
	NIF/NIE/PASAPORTE:	47462975-Z
	DOMICILIO:	C/Kelsen 5. Campus de

<p>(6-6) INVENTOR 6:</p>	<p>LOCALIDAD: Cantoblanco. PROVINCIA: Madrid CÓDIGO POSTAL: 28049 PAÍS RESIDENCIA: España CÓDIGO PAÍS: ES TELÉFONO: FAX: CORREO ELECTRÓNICO: EL INVENTOR RENUNCIA A SER MENCIONADO: []</p>
<p>(6-7) INVENTOR 7:</p>	<p>APELLIDOS: Yus Domínguez NOMBRE: Joaquín Luis NACIONALIDAD: España CÓDIGO PAÍS: ES NIF/NIE/PASAPORTE: 51121664-R</p> <p>DOMICILIO: C/Kelsen 5. Campus de Cantoblanco. LOCALIDAD: Madrid PROVINCIA: 28 Madrid CÓDIGO POSTAL: 28049 PAÍS RESIDENCIA: España CÓDIGO PAÍS: ES TELÉFONO: FAX: CORREO ELECTRÓNICO: EL INVENTOR RENUNCIA A SER MENCIONADO: []</p>
<p>(6-8) INVENTOR 8:</p>	<p>APELLIDOS: González Carrasco NOMBRE: Jose Luis NACIONALIDAD: España CÓDIGO PAÍS: ES NIF/NIE/PASAPORTE: 50795495-H</p> <p>DOMICILIO: Av. de Gregorio del Amo, 8 LOCALIDAD: Madrid PROVINCIA: 28 Madrid CÓDIGO POSTAL: 28040 PAÍS RESIDENCIA: España CÓDIGO PAÍS: ES TELÉFONO: FAX: CORREO ELECTRÓNICO: EL INVENTOR RENUNCIA A SER MENCIONADO: []</p>
<p>(7) TÍTULO DE LA INVENCION:</p>	<p>APELLIDOS: Lieblich Rodríguez NOMBRE: Marcela NACIONALIDAD: España CÓDIGO PAÍS: ES NIF/NIE/PASAPORTE: 02622175-Z</p> <p>DOMICILIO: Av. de Gregorio del Amo, 8 LOCALIDAD: Madrid PROVINCIA: 28 Madrid CÓDIGO POSTAL: 28040 PAÍS RESIDENCIA: España CÓDIGO PAÍS: ES TELÉFONO: FAX: CORREO ELECTRÓNICO: EL INVENTOR RENUNCIA A SER MENCIONADO: []</p>
	<p>Procedimiento de obtención de una pieza por modelado por deposición de hilo fundido</p>

(8) NÚMERO DE INFORME TECNOLÓGICO DE PATENTES (ITP):		
(9) SOLICITA LA INCLUSIÓN EN EL PROCEDIMIENTO ACELERADO DE CONCESIÓN	SI NO	<input type="checkbox"/> <input checked="" type="checkbox"/>
(10) EFECTUADO DEPÓSITO DE MATERIA BIOLÓGICA:	SI NO	<input type="checkbox"/> <input checked="" type="checkbox"/>
(11) DEPÓSITO:	REFERENCIA DE IDENTIFICACIÓN: INSTITUCIÓN DE DEPÓSITO: NÚMERO DE DEPÓSITO: ORÍGEN BIOLÓGICO:	
(12) RECURSO GENÉTICO:	NÚMERO DE REGISTRO: NÚMERO DE CERTIFICADO DE ACCESO AL RECURSO: UTILIZACIÓN DEL RECURSO GENÉTICO: CONOCIMIENTO TRADICIONAL ASOCIADO A UN RECURSO GENÉTICO:	
(13) DECLARACIONES RELATIVAS A LA LISTA DE SECUENCIAS:	LA LISTA DE SECUENCIAS NO VA MÁS ALLÁ DEL CONTENIDO DE LA SOLICITUD LA LISTA DE SECUENCIAS EN FORMATO PDF Y ASCII SON IDENTICOS	<input type="checkbox"/> <input type="checkbox"/>
(14) EXPOSICIONES OFICIALES:	NOMBRE: LUGAR: FECHA:	
(15) DECLARACIONES DE PRIORIDAD:	PAÍS DE ORIGEN: CÓDIGO PAÍS: NÚMERO: FECHA:	
(16) REMISIÓN A UNA SOLICITUD ANTERIOR:	PAÍS DE ORIGEN: CÓDIGO PAÍS: NÚMERO: FECHA:	
(17) AGENTE DE PROPIEDAD INDUSTRIAL:	APELLIDOS: NOMBRE: CÓDIGO DE AGENTE: NÚMERO DE PODER:	PONS ARIÑO ÁNGEL 0499/5 20081765
(18) DIRECCIÓN A EFECTOS DE COMUNICACIONES: DIRECCIÓN ASOCIADA AL PRIMER SOLICITANTE	DOMICILIO: LOCALIDAD: PROVINCIA: CÓDIGO POSTAL: PAÍS RESIDENCIA: CÓDIGO PAÍS: TELÉFONO: FAX: CORREO ELECTRÓNICO: MEDIO PREFERENTE DE COMUNICACIÓN	
(19) RELACIÓN DE DOCUMENTOS QUE SE ACOMPAÑAN:	DESCRIPCIÓN: REIVINDICACIONES: DIBUJOS: RESUMEN:	<input checked="" type="checkbox"/> N.º de páginas: 18 <input checked="" type="checkbox"/> N.º reivindicaciones: 17 <input checked="" type="checkbox"/> N.º de dibujos: 10 <input checked="" type="checkbox"/> N.º de páginas: 1

<p>FIGURA(S) A PUBLICAR CON EL RESUMEN: ARCHIVO DE PRECONVERSION: DOCUMENTO DE REPRESENTACIÓN: JUSTIFICANTE DE PAGO (1): JUSTIFICANTE DE PAGO (2): LISTA DE SECUENCIAS PDF: ARCHIVO PARA LA BUSQUEDA DE LS: OTROS (Aparecerán detallados):</p>	<p><input checked="" type="checkbox"/> N.º de figura(s): <input checked="" type="checkbox"/> <input type="checkbox"/> N.º de páginas: <input checked="" type="checkbox"/> N.º de páginas: 1 <input checked="" type="checkbox"/> N.º de páginas: 1 <input type="checkbox"/> N.º de páginas: <input type="checkbox"/></p>
<p>(20) EL SOLICITANTE SE ACOGE A LA REDUCCIÓN DE TASAS PARA EMPRENDEDORES PREVISTA EN EL ART. 186 DE LA LEY 24/2015 DE PATENTES Y, A TAL EFECTO, APORTA LA SIGUIENTE DOCUMENTACIÓN ADJUNTA:</p>	<p><input type="checkbox"/></p>
<p>(21) NOTAS:</p>	
<p>(22) FIRMA:</p> <p style="text-align: right;">FIRMA DEL SOLICITANTE O REPRESENTANTE: LUGAR DE FIRMA: FECHA DE FIRMA:</p>	<p>50534279J ANGEL PONS (R: B84921709) MADRID 24 Mayo 2018</p>

Identificación

Ejercicio: 2018
Nro Justificante: 7915114811572

Sujeto Pasivo

NIF:
Apellidos y Nombre o Razón Social:
Correo electrónico: agueda.lopez@ponsip.com

Agente o Representante legal

NIF: 50534279J
Apellidos y Nombre o Razón Social: ANGEL PONS ARIÑO
Código de Agente o Representante 0499

Autoliquidación

Titular del expediente si es distinto del pagador: CSIC
Modalidad Expediente: P Número Tipo
Clave: IE01 Año: 2018 Concepto: SOL. DE INVENCION O REHABILITACIÓN POR INTERNET
Unidades: 1 Importe: 85,32



Referencia OEPM: 88181134917 909992100200188181134917

Declarante

Fecha: 24/05/18 13:29
Firma: ANGEL PONS ARIÑO

Ingreso

Importe en 85,32 Adeudo en ☐
NRC Asignado: 7915114811572000000001

Modelo 791

- (1) Solo cuando el pago se realice con cargo a la cuenta corriente del representante o agente.
(2) En el caso de que tenga asignado un número por la OEPM.
(3) En el caso de patentes europeas, se pondrá una P si es el número de publicación o una S si es el número de solicitud.

Identificación

Ejercicio: 2018
Nro Justificante: 7915114811694

Sujeto Pasivo

NIF:
Apellidos y Nombre o Razón Social:
Correo electrónico: agueda.lopez@ponsip.com

Agente o Representante legal

NIF: 50534279J
Apellidos y Nombre o Razón Social: ANGEL PONS ARIÑO
Código de Agente o Representante 0499

Autoliquidación

Titular del expediente si es distinto del pagador: CSIC
Modalidad Expediente: P Número Tipo
Clave: IE04 Año: 2018 Concepto: SOLICITUD I.E.T. INTERNET
Unidades: 1 Importe: 581,95




Referencia OEPM: 88181136713 909992100200188181136713

Declarante

Fecha: 24/05/18 13:35
Firma: ANGEL PONS ARIÑO

Ingreso

Importe en 581,95 Adeudo en 
NRC Asignado: 7915114811694000000001

Modelo 791

- (1) Solo cuando el pago se realice con cargo a la cuenta corriente del representante o agente.
(2) En el caso de que tenga asignado un número por la OEPM.
(3) En el caso de patentes europeas, se pondrá una P si es el número de publicación o una S si es el número de solicitud.



OFICINA ESPAÑOLA DE PATENTES Y MARCAS		
Hoja informativa sobre pago de tasas de una solicitud de patente o modelo de utilidad		
1. REFERENCIA DE SOLICITUD	ES1641.1356	
2. TASAS	Importe (en euros)	
Concepto	Código de barras asignado	Importe
IE01 - Solicitud de demanda de depósito o de rehabilitación.	88181134917	85,32
IE02 - Solicitud de cambio de modalidad en la protección		0,00
IE04 - Petición IET	88181136713	581,95
IE06 - Prioridad extranjera (0)		0,00
IE22 - Solicitud de examen sustantivo		0,00
Importe total		667,27
Importe abonado		667,27

Se ha aplicado el 15% de descuento sobre la tasa de solicitud de acuerdo con la D. Adic. 8.2 Ley de Marcas.

DESCRIPCIÓN

Procedimiento de obtención de una pieza por modelado por deposición de hilo fundido

5

La presente invención se refiere a un procedimiento de obtención de una pieza de material compuesto o una pieza cerámica y/o metálica por modelado por deposición de hilo fundido.

10

La presente invención se puede encuadrar en el área de la ciencia de los materiales y por tanto es de interés para industrias que fabrican materiales compuestos de matriz polimérica, cerámica y metal para aplicaciones en aeronáutica, en la producción de biomateriales, dispositivos de generación/almacenamiento energético y materiales refractarios utilizados en condiciones severas de servicio.

15

ANTECEDENTES DE LA INVENCION

20

El procesamiento de materiales compuestos mediante técnicas de prototipado rápido ha experimentado un desarrollo exponencial en los últimos años, debido a la posibilidad que ofrece estas técnicas de obtener geometrías complejas o formas personalizadas, sin necesidad de recurrir al empleo de moldes, que graban y lastran los costes y tiempos de fabricación.

25

Del abanico de tecnologías de impresión 3D disponibles, las tecnologías aditivas de moldeo por fusión (en inglés Fused Deposition Modeling, FDM, or Fused Filament Fabrication, FFF) gozan de una serie de ventajas que las sitúan a la cabeza de la manufactura aditiva. Se trata de una metodología aplicable a una amplia variedad de materiales basada en el uso de polímeros termoplásticos como son ácido poliláctico, acetonitrilo-butadieno-estireno, nylon etc., que pueden actuar como material único, matriz o estructurador, dependiendo de la cantidad de termoplástico que contenga la pieza final impresa y/o sinterizada.

30

La limitación intrínseca de la impresión por fusión tiene su origen en las propiedades térmicas del polímero termoplástico utilizado. De forma análoga a como se hace en

otros procesos industriales de fabricación de piezas por fusión, tales como el moldeo por Inyección [Preparation of articles using metal injection molding. US 20020144571 A1. EP 0465940 A3], el mezclado de las diferentes fases que forman el material compuesto final, se realiza de forma convencional en una mezcladora de doble uso, 5 donde el polímero termoplástico llega a fundir, superando en todos los casos su temperatura de transición vítrea (T_g) y fusión (T_m) durante el tiempo de procesado de la mezcla de partida o de la materia prima compuesta. Es más, para asegurar la homogeneidad de la mezcla final, el proceso de mezclado de las diferentes materias primas lleva asociado un proceso de molturación y un segundo mezclado por fusión, 10 repitiéndose este protocolo de molturación y mezclado tantas veces sea necesario. Es por todo ello que el proceso convencional de mezclado por fusión, en ocasiones, puede provocar la degradación térmica del material y/o la mezcla final.

Esta limitación se agrava en la impresión de un material compuesto orgánico-inorgánico, donde el termoplástico es la matriz o el aditivo estructurador del proceso, 15 ya que los puntos de fusión (T_m) y las temperaturas de transición vítrea (T_g) de los materiales inorgánicos están muy por encima de los rangos de temperatura que habitualmente se emplean en los procedimientos de mezclado convencional (250-270 °C). Además, en el mezclado por fusión, las partículas inorgánicas se mezclan con el 20 polímero termoplástico fundido, y la elevada viscosidad de estas mezclas (> 100 Pa·s) limita tanto la cantidad de partículas inorgánicas como su dispersión en la matriz/estructurador termoplástico. Es por ello, que en muchas ocasiones la técnica aditiva no puede aplicarse de manera directa en la impresión de piezas con alta carga de partículas inorgánicas. En consecuencia, la precisión en la impresión disminuye y 25 compromete el acabado final de la pieza impresa. Pero además, en el caso de la fabricación por impresión de piezas 100 % inorgánicas, la cantidad de polímero termoplástico para imprimir satisfactoriamente es por lo general tan elevada (> 30 % en volumen), que lastra la consistencia e integridad mecánica de la pieza durante los procesos de contracción de volumen generados durante el tratamiento térmico de 30 sinterización que consolidan la estructura inorgánica de las piezas fabricadas.

La investigación realizada hasta la fecha en las técnicas de impresión se centra en la mejora de parámetros relacionados con el acabado superficial, la precisión dimensional, las propiedades mecánicas o la eficiencia del proceso. En la impresión 35 por fusión, con objeto de paliar las limitaciones del proceso indicadas anteriormente,

se han propuesto modificaciones sobre proceso de extrusión, como variaciones de las velocidades de dosificación 3D y de alimentación de filamentos, cambios de gradientes de presión y temperatura, modificación de los diseños de boquilla, estudios de las viscosidades de los fundidos, adición de estabilizadores u otros aditivos, planificación de trayectorias, orientación de piezas, etc. [S.C. Ligon, R. Liska, J. Stampfl, M. Gurr, R. Mülhaupt, *Polymers for 3D Printing and Customized Additive Manufacturing*, Chem. Rev. 117 (2017) 10212–10290. doi:10.1021/acs.chemrev.7b00074]. Sin embargo, los esfuerzos dedicados al estudio del proceso de mezclado son escasos, aun siendo especialmente relevantes, ya que la dispersión de partículas inorgánicas en el polímero afecta directamente a la homogeneidad de los hilos extruidos, y por consiguiente a las propiedades específicas del material final. De hecho se ha demostrado que el paso de materiales compuestos en estado semifundido (en forma de gránulos o hilo) a través de una boquilla puede romper, cortar o aglomerar las partículas. Este último efecto de aglomeración podría acentuarse al emplear partículas de tamaño nanométrico, provocando la pérdida de propiedades mecánicas, ya que el efecto que produce la cizalla en el material impreso es función directa del área de la unión partícula-polímero.

Convencionalmente, en la impresión de materiales híbridos termoplástico e inorgánico, tras el mezclado de las materias primas, el material molturado o granceado se hace pasar por una extrusora, en la que la mezcla fundida pasa por una boquilla con un diámetro específico, y al enfriarse adquiere forma de hilo, siendo el hilo la forma de alimentación convencional de la impresión por fusión [Ji Hongbing; Dai Wen; Zeng Yongbin, *Metal or ceramic consumable item for FDM 3D printing, preparation method for metal or ceramic consumable item and finished product printing method*, CN105665697, 2016].

En una revisión bibliográfica sobre la producción de hilos o materia prima híbrida para impresión por fusión [S. Singh, S. Ramakrishna, R. Singh, *Material issues in additive manufacturing: A review*, J. Manuf. Process. 25 (2017) 185–200. doi:10.1016/j.jmapro.2016.11.006], se describen aspectos básicos como la proporción de los materiales constituyentes, la composición y naturaleza de los mismos, etc., y su efectos en las propiedades mecánicas de los materiales fabricados. Pero también recoge, de qué manera diferentes autores han propuesto rutas alternativas para el mezclado, como el uso de una molienda previa a la extrusión, en molino centrífugo [M.

Nikzad, S.H. Masood, I. Sbarski, Thermo-mechanical properties of a highly filled polymeric composites for Fused Deposition Modeling, Mater. Des. 32 (2011) 3448–3456. doi:10.1016/j.matdes.2011.01.056], la molienda criogénica, o empleando una extrusora de un solo tornillo y con un premezclado en vía seca de las materias primas [S.H. Masood, W.Q. Song, Development of new metal/polymer materials for rapid tooling using Fused deposition modelling, Mater. Des. 25 (2004) 587–594. doi:10.1016/j.matdes.2004.02.009].

En otros trabajos más recientes se han llevado a cabo metodologías de mezclado más novedosas en medio líquido. M. Thuyet-Nguyen et al. han preparado una mezcla Ni/ABS por drop casting usando una relación en peso de 2:1 y 1:1 [M. Thuyet-Nguyen, H. Hai-Nguyen, W.J. Kim, H.Y. Kim, J.-C. Kim, Synthesis and characterization of magnetic of Ni/ABS nanocomposites by electrical explosion of wire in liquid and solution blending methods, Met. Mater. Int. 23 (2017) 391–396. doi:10.1007/s12540-017-6533-z], mientras que J. Canales et al. han patentado un procedimiento para la obtención de hilos a partir de barbotinas con una composición de entre un 30-70% en peso de material cerámico, que incorporan una mezcla polimérica de formulación compleja, y la impresión se basa en la presencia de agentes gelificantes, que retienen su estructura por encima de la Tg [Canales Vázquez Jesús; Sánchez Bravo Gloria Begoña ; Marín Rueda Juan Ramón; Yagüe Alcaraz Vicente; López López Juan José, Method for Obtaining Ceramic Barbotine for the Production of Filaments for 3D-FDM Printing, Barbotine Obtained using SAID Method, and Ceramic Filaments, WO2017191340, 2017]. Ninguno de los procesos propuestos contempla la etapa de estabilización y/o dispersión de las partículas inorgánicas en el medio líquido y fundente.

En la impresión de materiales compuestos y puramente inorgánicos, la problemática fundamental radica en la obtención de una materia prima en forma de hilo, con alta carga inorgánica, de metal o cerámica, homogéneamente dispersa en el polímero, para la impresión por fusión de piezas consistentes, con propiedades finales, densidades, propiedades mecánicas y funcionales, reproducibles. Por ello es necesario desarrollar nuevos procedimientos.

DESCRIPCIÓN DE LA INVENCION

La presente invención se refiere a un procedimiento para la obtención de una pieza con una composición seleccionada de entre un material puramente cerámico o metálico y un material compuesto, por modelado por deposición de hilo fundido.

- 5 El procedimiento de la presente invención tiene especial interés para el usuario final, para industrias que fabrican materiales compuestos de matriz polimérica, en aplicaciones que abarcan desde la aeronáutica a los biomateriales, y materiales inorgánicos (cerámica y/o metal o compuestos de matriz metálica y/o cerámica) en dispositivos de generación/almacenamiento energético, biomateriales y, metales y
- 10 compuestos refractarios utilizados en condiciones severas de servicio. Incide además de forma relevante en sectores industriales dedicados a la fabricación y comercialización de materia prima procesada y/o comercialización de soluciones ingenieriles de bienes de equipo.
- 15 En un primer aspecto, la presente invención se refiere a un procedimiento de obtención de una pieza por modelado por deposición de hilo fundido (a partir de aquí “procedimiento de la invención”) que comprende las siguientes etapas:
- a) preparar una suspensión dispersa y estable de partículas inorgánicas,
 - b) eliminar el disolvente de la suspensión obtenida en la etapa (a),
 - 20 c) redispersar el producto obtenido en la etapa (b) en una disolución polimérica que comprende al menos un termoplástico,
 - d) secar el producto obtenido en la etapa (c) en ausencia de temperatura,
 - e) determinar la ventana de extrusión del producto obtenido en la etapa (d)
 - f) extruir el producto de la etapa (d) en un rango de temperaturas de entre la
 - 25 temperatura de fusión y la temperatura inicial de descomposición, obtenidas en la etapa (e), e
 - g) imprimir las piezas 3D utilizando el producto obtenido en la etapa (f) mediante la técnica de modelado por deposición de hilo fundido.
- 30 La etapa (a) del procedimiento de la invención se refiere a la preparación de una suspensión dispersa y estable de partículas inorgánicas.

Cualquier disolvente puede ser utilizado para preparar la suspensión, incluso agua.

Las partículas inorgánicas utilizadas en la etapa (a) son polvo metálico, polvo cerámico o una combinación de los mismos. Dichas partículas inorgánicas pueden tener cualquier tamaño que la técnica de modelado de deposición de hilo permita, incluido el tamaño nanométrico. Además, las partículas inorgánicas de la etapa (a) de la presente invención pueden tener cualquier forma.

Ejemplo preferido de partículas inorgánicas de polvo metálico son

- metales biocompatibles como son el hierro, el magnesio, el titanio,
- metales refractarios como el níquel, el titanio y el cobalto y
- y una combinación de los mismos

Ejemplos preferidos de partículas inorgánicas de polvo cerámico son:

- cerámicas bioactivas como son la hidroxiapatita y el biovidrio,
- cerámicas semiconductoras como son dióxido de titanio y el óxido de zinc,
- cerámicas de elevada resistencia química en condiciones extremas como son la alúmina, la zircona, los nitruros y los carburos y
- cualquiera de sus combinaciones.

Cabe señalar que las partículas inorgánicas se dispersan por medios mecánicos o sónicos en la suspensión.

La etapa (b) del procedimiento de la invención se refiere a la eliminación del disolvente de la suspensión obtenida en la etapa (a).

Preferiblemente, dicha etapa (b) se lleva a cabo mediante centrifugación o filtración.

La etapa (c) del procedimiento de la invención trata de redispersar el producto obtenido en la etapa (b) con una disolución polimérica que comprende

- al menos un polímero o un copolímero termoplástico.

Ejemplos de polímeros o copolímeros termoestables son el polietileno, el ácido poliláctico, el polietilenglicol, la policaprolactona, el nylon, el acrilonitrilo y el butadieno estireno.

En una realización preferida del procedimiento de la presente invención, la disolución

polimérica de la etapa (c) comprende además un plastificante, un colorante o un antiespumante.

5 Cabe señalar que las partículas inorgánicas se redispersan por medios mecánicos o sónicos en la suspensión.

La etapa (d) del procedimiento de la presente invención se refiere al secado del producto obtenido en la etapa (c) en ausencia de temperatura para evitar el deterioro de la matriz polimérica termoestable. Dicha etapa (d) se lleva a cabo bajo presión
10 reducida en un rotavapor o mediante congelación-sublimación.

En la etapa (e) del procedimiento de la presente invención se lleva a cabo la determinación de la ventana de extrusión del producto obtenido en la etapa (d). Llevar a cabo esta determinación supone una ventaja puesto que optimiza el procedimiento
15 de extrusión que le sigue.

Se entiende como “ventana de extrusión” como aquellas temperaturas que son necesarias conocer para poder concretar el rango de temperaturas al que se puede llevar a cabo el modelado por deposición de hilo fundido. Concretamente, las
20 temperaturas a determinar son las siguientes:

- temperatura de fusión
- temperatura inicial de la descomposición

La determinación de la ventana de extrusión se lleva preferiblemente a cabo mediante
25 termogravimetría y/o calorimetría diferencial de barrido.

En la etapa (f) del procedimiento de la invención, la extrusión del producto obtenido en la etapa (d) se lleva a cabo en un rango de temperaturas de entre la temperatura de fusión y la temperatura inicial de descomposición obtenidas en la etapa (e). Dentro de
30 este rango de temperaturas, los parámetros de impresión tales como

- El diámetro de la tobera de entrada
- El diámetro de tobera de salida
- El diámetro del hilo fundido
- La altura desde la cual se lleva a cabo la deposición
- 35 • La velocidad de impresión o deposición

- Etc.

se pueden seleccionar con facilidad.

5 Por ejemplo, una ventaja que supone el procedimiento de la presente invención sería que la etapa (f) se puede llevar a cabo con cualquier tobera de salida, puesto que los parámetros térmicos de la mezcla de partida se han determinado con anterioridad para la composición concreta.

10 La última etapa del procedimiento de la invención, la etapa (g) se refiere a la impresión de las piezas 3D utilizando el producto obtenido en la etapa (f) mediante la técnica de modelado por deposición de hilo fundido.

15 Por “modelado de deposición de hilo” se entiende, en la presente invención, como aquella técnica de modelado por deposición de una mezcla fundida, en la que se utiliza una técnica aditiva, de forma que depositando el material en una o varias capas sucesivas se conforma a una pieza o material impreso.

20 Una ventaja que supone el procedimiento de la presente invención, por ejemplo, sería que la etapa (g) también se puede llevar a cabo con cualquier tobera de entrada, ya que el diámetro del hilo se ha definido en la etapa (f) de extrusión, y cualquier boquilla de salida, puesto que los parámetros térmicos de la mezcla de partida se han determinado con anterioridad para la composición concreta.

25 En la presente invención, la pieza que se obtiene es un material compuesto, una pieza puramente cerámica, una pieza puramente metálica o una pieza formada por una mezcla cerámico-metal.

Cuando la pieza que se obtiene es puramente cerámica, puramente metálica o es una pieza formada por una mezcla cerámico-metal:

- 30
- la etapa (a) de preparación de una suspensión dispersa y estable de partículas inorgánicas se lleva a cabo por adsorción en superficie de un estabilizante/dispersante ha de ser de naturaleza tal que prime la dispersión homogénea y estable de las partículas inorgánicas en la matriz polimérica, siendo preferiblemente un polímero surfactante o un polielectrolito,
- 35
- y el procedimiento comprende las siguientes etapas adicionales:

(h), tras la etapa (g), de eliminación del polímero que comprende el producto obtenido en la etapa (g) mediante disolución o descomposición térmica, y
(i) sinterizar el producto obtenido en la etapa (h).

5 Ejemplos de surfactante son el dodecilsulfato, la oleimina y el bromuro de hexadeciltrimetilamonio.

Ejemplos de polielectrolito son un poliacrilato, un citrato o una poliamina.

10 En una realización preferida del procedimiento de la presente invención,
• cuando la pieza es puramente cerámica, puramente metálica o es una pieza formada por una mezcla cerámico-metal y
• cuando la pieza es porosa,
el porcentaje en volumen de las partículas inorgánicas en la mezcla obtenida en la
15 etapa (d) es mayor del 30 %.

En otra realización preferida del procedimiento de la presente invención,
• cuando la pieza es puramente cerámica, puramente metálica o es una pieza formada por una mezcla cerámico-metal y
20 • cuando la pieza es densa,
el porcentaje en volumen de las partículas inorgánicas en la mezcla obtenida en la etapa (d) es mayor del 50 %.

Cuando la pieza que se obtiene es un material compuesto:
25 • la etapa (a) de preparación de una suspensión dispersa y estable de partículas inorgánicas se lleva a cabo por adsorción en superficie de un estabilizante/dispersante ha de ser de naturaleza tal que prime la dispersión homogénea y estable de las partículas inorgánicas en la matriz polimérica, siendo preferiblemente un polielectrolito que se escoge en función del grupo
30 funcional para que reaccione con la matriz polimérica termoestable.
• el porcentaje en volumen de las partículas inorgánicas en la mezcla obtenida en la etapa (d) es mayor del 1 %.

Como se ha mencionado anteriormente, ejemplos de polímeros o copolímeros
35 termoestables que forman parte de la pieza de material compuesto son el polietileno,

el ácido poliláctico, el polietilenglicol, la policaprolactona, el nylon, el acrilonitrilo y el butadieno estireno.

5 Ejemplos de polielectrolitos de estos polímeros o copolímeros termoestables son los poliacrilatos, los citratos o las poliaminas.

Una ventaja que supone el procedimiento de obtención de la presente invención, por ejemplo, sería que desde la etapa (c) las partículas interaccionan con la mezcla polimérica, ya que las partículas tienen en superficie el estabilizante/dispersante adsorbido en la etapa (a) que se ha seleccionado en función de su interacción en la redispersión de la etapa (c) con los polímeros en disolución.

Otra ventaja que supone el procedimiento de la presente invención, por ejemplo, sería que la etapa (c) se lleva a cabo a temperatura ambiente, lo que preserva las propiedades de la matriz polimérica en la pieza final de material compuesto.

En una realización preferida del procedimiento de la presente invención, el porcentaje en volumen de las partículas inorgánicas en la mezcla obtenida en la etapa (d) es mayor del 10 %, preferentemente mayor del 15 %.

20 A lo largo de la descripción y las reivindicaciones la palabra "comprende" y sus variantes no pretenden excluir otras características técnicas, aditivos, componentes o pasos. Para los expertos en la materia, otros objetos, ventajas y características de la invención se desprenderán en parte de la descripción y en parte de la práctica de la invención. Los siguientes ejemplos y figuras se proporcionan a modo de ilustración, y no se pretende que sean limitativos de la presente invención.

BREVE DESCRIPCIÓN DE LAS FIGURAS

Figura 1. Micrografías obtenidas por microscopía electrónica de barrido a diferentes magnificaciones de la estructura 3D en forma de andamio de la pieza final, impresa a partir del hilo de composición (1) del ejemplo 1: 1A, imagen general de la estructura del andamio, 1B, micrografía de la sección transversal de una de las vigas y, 1C, un detalle de la microestructura de esta sección.

Figura 2. Gráficas del análisis termogravimétrico (2A) y de la calorimetría diferencial de barrido (2B) de la mezcla de partida de la composición (1) del ejemplo 1, obtenida en forma de gránulo tras el secado de la etapa (d). En las gráficas se ha señalado con una flecha la temperatura inicial de descomposición (en 2A) y la temperatura de fusión (en 2B).

Figura 3. Imágenes de la mezcla de partida de la composición (2) del ejemplo 1, obtenida en forma de gránulo tras el secado: 3A, fotografía de los gránulos y, 3B, micrografía de detalle de la microestructura de los gránulos obtenida por microscopía electrónica de barrido.

Figura 4. Imágenes del hilo de composición (2) del ejemplo 1, obtenido tras la extrusión: 4A, fotografía el hilo y, 4B, micrografía de la sección transversal del hilo obtenida por microscopía electrónica de barrido.

Figura 5. Imagen de la estructura tridimensional en forma de andamio de la pieza final, impresa a partir de hilo de composición (2) del ejemplo 1.

Figura 6. Imágenes de la estructura 3D en forma de andamio de la pieza final, impresa a partir de hilo de composición (3) del ejemplo 1: 6A, fotografía de la pieza final y, 6B, micrografía del detalle de la microestructura obtenida por microscopía electrónica de barrido.

Figura 7. Micrografías obtenidas por microscopía electrónica de barrido a diferentes magnificaciones de la estructura 3D en forma de andamio de la pieza final, impresa a partir del hilo de composición (1) del ejemplo 2: 7A, imagen general de la estructura del andamio de la pieza impresa, 7B, micrografía de la sección transversal de una de las vigas y, 7C y 7D, detalles de la microestructura de la sección.

Figura 8. Imágenes de la estructura tridimensional en forma de andamio de la pieza final obtenida tras el tratamiento térmico, e impresa a partir de hilo de composición (1) del ejemplo 2: 8A, fotografía de la pieza final y, 8B, micrografía de la estructura general del andamio de la pieza final y, 8C, micrografía del detalle de la microestructura de la sección transversal de una de las vigas, obtenidas por microscopía electrónica de barrido.

Figura 9. Micrografías obtenidas por microscopía electrónica de barrido a diferentes magnificaciones del detalle de la microestructura de la sección transversal de un hilo extruido a partir de la composición (2) del ejemplo 2: 9A, antes del tratamiento térmico y, 9B, tras el tratamiento térmico.

Figura 10. Imágenes de la mezcla de partida de la composición (3) del ejemplo 2, obtenida en forma de gránulo tras el secado: 10A, fotografía de los gránulos y, 10B y 10C, micrografías de detalle de la microestructura de los gránulos obtenidas por microscopía electrónica de barrido.

EJEMPLOS

A continuación se ilustrará la invención mediante unos ensayos realizados por los inventores, que pone de manifiesto la efectividad del producto de la invención.

Ejemplo 1: Impresión de piezas finales de un material compuesto.

Se preparan suspensiones de partículas metálicas/cerámicas añadiendo un polielectrolito catiónico como estabilizante/dispersante, tales como:

(1) Partículas de hidroxiapatita (HA), con un tamaño medio de partícula de 2 μm , con una concentración < 35 % en volumen en medio acuoso a un pH fijo de 8, adicionando tetrametil amonio (HTMA). A esta suspensión se le añade polietilenimina (PEI > 25.000 KDa) en una proporción del 0,2 % en peso con respecto al peso del polvo cerámico. La mezcla se somete a un proceso de molienda de homogenización de 45 min.

(2) Partículas de Magnesio metálico (Mg), con un tamaño de partícula medio de 25 μm , con una concentración < 35 % en volumen en medio acuoso a un pH fijo de 12, adicionando tetrametil amonio (HTMA). A esta suspensión se le adiciona polietilenimina (PEI > 25.000 KDa) en una proporción del 0,2 % en peso con respecto al peso de Mg, y posteriormente la mezcla se somete a un proceso de molienda de homogeneización de 45 min.

(3) Nanotubos de Halosita (NTH), con diámetro medio < 30 nm y una longitud < 150 µm, con una concentración de 100 g/L en medio acuoso. A esta suspensión se le añade polietilenimina (PEI > 25.000 KDa) en una proporción del 2 % en peso con respecto al peso del polvo cerámico, y posteriormente la mezcla se dispersa aplicando 1 min de ultrasonidos con una sonda de 400 W de potencia

Las suspensiones resultantes se centrifugan 2 veces, una primera vez para eliminar el agua y cambiar el disolvente por tetrahidrofurano (THF), y una segunda vez para eliminar este último disolvente orgánico. Las partículas modificadas con el polielectrolito, se añaden bajo agitación mecánica a una disolución de polímeros en THF en la proporción deseada, siendo tal proporción en:

(1) 15 /85 en volumen de HA / PLA.

(2) 7 /93 en volumen de Mg / Polímero, siendo el polímero una mezcla de un termoplástico como el ácido poliláctico (PLA) y plastificante polietilenglicol (PEG-400) en un ratio 95 / 5 en volumen PLA/PEG-400.

(3) 1 /99 en volumen de HNT / PLA.

Se aplica ultrasonidos para dispersar y homogeneizar la suspensión.

Durante el secado, el disolvente se elimina bajo presión reducida, recuperando el disolvente, y obteniendo la mezcla de partida en forma de gránulos. Para asegurar la eliminación completa del disolvente, los gránulos se secan en estufa a 60 °C durante al menos 24 h.

Para determinar el rango térmico de trabajo, se determinaron la temperatura de fusión, y la temperatura inicial de descomposición de la mezcla, por calorimetría diferencial de barrido (DSC) y análisis térmogravimétrico (ATG), respectivamente, siendo los márgenes de impresión de:

(1) 152 °C y 212 °C, para los materiales compuestos HA / Polímero

(2) 149 °C y 264 °C, para los materiales compuestos Mg / Polímero

(3) 150 °C y 265 °C, para los materiales compuestos HNT / PLA

5 Las mezclas se extruyeron a una temperatura entre 155 °C y 200 °C, en una extrusora de un solo uso con una boquilla de salida de 2,00 mm de diámetro, para obtener filamento con un diámetro inferior a 3,00 mm.

10 Con el hilo extruido de cada composición se imprime una pieza tridimensional con una impresora 3D convencional a la que se ha acoplado un cabezal con una entrada de 3,00 mm y una boquilla de salida de 0,3 mm, manteniendo una temperatura de plato 60 °C, y una temperatura de la boquilla de:

(1) 160 °C, para los materiales compuestos HA / Polímero

15 (2) 155 °C, para los materiales compuestos Mg / Polímero

(3) 182 °C, para los materiales compuestos HNT / PLA

20 La figura 1 muestra micrográficas a diferentes magnificaciones de la estructura de la pieza 3D final, impresa a partir de la mezcla de partida de composición (1): 15 / 85 en volumen de HA / PLA. En el detalle (1C) puede apreciarse la dispersión de la HA e la matriz polimérica.

25 La figura 2 muestra los ATG (2A) y DSC (2B) de los gránulos de composición (1): 15 / 85 en volumen de HA / PLA. En ambos gráficos se han señalado las temperaturas que determinan la ventana térmica: la temperatura de fusión, y la temperatura de inicio de degradación.

30 La figura 3A muestra una fotografía de la mezcla de partida en forma de gránulos, y la figura 3B muestra una micrografía de detalle, de la mezcla de composición (2): 7 / 93 en volumen de Mg / Polímero, donde se aprecia como una partícula de Mg está rodeada de polímero.

35 La figura 4A muestra una fotografía del hilo extruido a partir de la mezcla de composición (2) que se muestra en la figura 3, y una micrografía de la sección

transversal del mismo en la que se observa la dispersión del Mg en la matriz polimérica.

La figura 5 muestra una pieza 3D final impresa en forma de andamio, a partir de hilo
5 mostrado en la figura 4, obtenido a partir de la mezcla de partida de composición (2).

La figura 6A muestra una fotografía de una pieza tridimensional final, impresa en forma
de andamio y la figura 6B muestra una micrografía con la microestructura del material
compuesto (3), en la que se observa la dispersión de los NTH en la matriz de PLA.
10

Ejemplo 2: Impresión de piezas finales de un material 100% cerámico

Se preparan suspensiones de partículas cerámicas añadiendo un polielectrolito
catiónico como estabilizante/dispersante, tales como:

15 (1) Partículas de hidroxiapatita (HA), con un tamaño medio de partícula de 2 μm ,
con una concentración < 35 % en volumen en medio acuoso a un pH fijo de 8,
adicionando tetrametil amonio (HTMA). A esta suspensión se le añade
polietilenimina (PEI > 25.000 KDa) en una proporción del 0,2 % en peso con
20 respecto al peso del polvo cerámico. La mezcla se somete a un proceso de
molienda de homogenización de 45 min.

(2) Partículas de Alúmina (Al_2O_3), con un tamaño medio de partícula de 0,5 μm ,
con una concentración < 37 % en volumen en medio líquido. A esta suspensión
25 se le añade un polielectrolito aniónico como estabilizante, la sal amónica de un
ácido poliacrílico (PAA) en una proporción del 1 % en peso con respecto al peso
del polvo cerámico, y posteriormente la mezcla se somete a un proceso de
molienda de homogeneización de 2 h.

30 (3) Nanopartículas de Óxido de Zinc (ZnO), con un tamaño medio de partícula de
< 30 nm, con una concentración < 5 % en volumen en medio acuoso. A esta
suspensión se le añade un surfactante como estabilizante, el bromuro de
hexadeciltrimetilamonio (CTAB), en una proporción del 3 % en peso con
respecto al peso del polvo cerámico, y posteriormente la mezcla se dispersa
35 aplicando 1 min de ultrasonidos con una sonda de 400 W de potencia.

Las suspensiones resultantes se centrifugan 2 veces, una primera vez para eliminar el agua y cambiar el disolvente por tetrahidrofurano (THF), y una segunda vez para eliminar este último disolvente orgánico. Las partículas modificadas con el polielectrolito, se añaden bajo agitación mecánica a una disolución de polímeros en THF en la proporción deseada, siendo tal proporción en:

(1) 40 / 60 en volumen de HA / Polímero, siendo el polímero una mezcla de un termoplástico como el ácido poliláctico (PLA) y plastificante polietilenglicol (PEG-400) en un ratio 95,3 / 4,7 en volumen PLA / PEG-400.

(2) 50 / 50 en volumen de Al_2O_3 / Polímero, siendo el polímero una mezcla de un termoplástico como el ácido poliláctico (PLA) y plastificante polietilenglicol (PEG-400) en un ratio 80 / 20 en volumen PLA / PEG-400.

(3) 30 / 70 en volumen de ZnO / PLA.

Se aplica ultrasonidos para dispersar y homogeneizar la suspensión.

Durante el secado, el disolvente se elimina bajo presión reducida, recuperando el disolvente, y obteniendo la mezcla de partida en forma de gránulos. Para asegurar la eliminación completa del disolvente, los gránulos se secan en estufa a 60 °C durante al menos 24 h.

Para determinar el rango térmico de trabajo, se determinaron la temperatura de fusión, y la temperatura inicial de descomposición de la mezcla, tal y como se describe en el ejemplo 1.

Las mezclas (1) y (2) se extruyeron a una temperatura entre 160 °C y 200 °C, en una extrusora de un solo uso con una boquilla de salida de 2,00 mm de diámetro, para obtener filamento con un diámetro inferior a 3,00 mm.

El hilo extruido a partir de la mezcla (2) se sometió a un tratamiento térmico, para descomponer térmicamente la fase polimérica y consolidar/densificar la estructura cerámica; manteniendo constante una temperatura punta de 1550 °C durante 60 min,

con rampas de calentamiento y enfriamiento de 5 °C/min. Tras el tratamiento térmico se obtuvieron hilos de composición 100% Al_2O_3 densos.

5 Con el hilo extruido a partir de la mezcla (1), se imprime una pieza tridimensional con una impresora 3D convencional a la que se ha acoplado un cabezal con una entrada de 3,00 mm y una boquilla de salida de 0,3 mm, manteniendo una temperatura de plato 60 °C, y una temperatura de la boquilla de 160 °C, para los materiales compuestos HA / Polímero

10 El material impreso se sometió a un tratamiento térmico, para descomponer térmicamente la fase polimérica y consolidar/densificar la estructura cerámica; manteniendo constante una temperatura punta de 1250 °C durante 90 min, con rampas de calentamiento y enfriamiento de 5 °C/min. Tras el tratamiento térmico se obtuvo una pieza tridimensional de composición 100 % HA de estructura porosa.

15 La figura 7 muestra micrografías a diferentes magnificaciones de la estructura del material impreso en forma de andamio a partir de la mezcla de partida de composición (1). El detalle de la figura 7A muestra la superficie rugosa del material. El detalle de la figura 7B muestra el diámetro de la barra de aproximadamente 2 mm. En el detalle de la figura 7D puede apreciarse la dispersión de las partículas de HA en la matriz polimérica. En el detalle de la figura 7C puede apreciarse que con el ratio en volumen 40 / 60 HA / Polímero, las partículas de HA están en contacto formando una red de compactación, lo que posibilitará la consolidación del material cerámico durante la sinterización, y su estabilidad estructural una vez eliminado el polímero en el proceso

20

25 térmico.

La figura 8 muestra una fotografía de la pieza final obtenido al tratar térmicamente el material mostrado en la figura 7. La figura 8A muestra la pieza final 100 % HA de estructura porosa obtenida tras la sinterización, mientras que la figura 8B muestra la micrografía de la estructura del andamio, y la figura 8C muestra un detalle de la microestructura 100 % HA porosa, de la pieza cerámica ya consolidada.

30

La figura 9 muestra en detalle las microestructuras del hilo obtenido a partir de la composición (2), antes (9A) y después (9B) del tratamiento térmico de sinterización.

35 En esta última se observa la microestructura densa 100% Al_2O_3 densa obtenida tras el

tratamiento térmico.

La figura 10 muestra una fotografía (10A) y micrografías (10B y 10C) de los gránulos obtenidos a partir de la mezcla de composición (3). En el detalle de la micrografía de
5 figura 10C muestra la dispersión homogénea de la fase nanométrica y la fase polimérica.

10

REIVINDICACIONES

- 1- Un procedimiento de obtención de una pieza por modelado por deposición de hilo fundido que comprende las siguientes etapas:
- 5 a) preparar una suspensión dispersa y estable de partículas inorgánicas,
 - b) eliminar el disolvente de la suspensión obtenida en la etapa (a),
 - c) redispersar el producto obtenido en la etapa (b) en una disolución polimérica que comprende al menos un polímero o copolímero termoplástico,
 - d) secar el producto obtenido en la etapa (c) bajo presión reducida en un
 - 10 rotavapor o mediante congelación-sublimación,
 - e) determinar la ventana de extrusión del producto obtenido en la etapa (d),
 - f) extruir el producto de la etapa (d) en un rango de temperaturas de entre la temperatura de fusión y la temperatura inicial de descomposición, y
 - g) imprimir las piezas 3D utilizando el producto obtenido en la etapa (f)
 - 15 mediante la técnica de modelado por deposición de hilo fundido.
2. El procedimiento según la reivindicación 1, donde las partículas inorgánicas son polvo metálico, polvo cerámico o una combinación de los mismos.
- 20 3. El procedimiento según cualquiera de las reivindicaciones 1 ó 2, donde las partículas inorgánicas son polvo metálico seleccionado de entre metales biocompatibles, metales refractarios y una combinación de los mismos.
4. El procedimiento según cualquiera de las reivindicaciones 1 ó 2, donde las
- 25 partículas inorgánicas son polvo cerámico seleccionado de entre cerámicas bioactivas, cerámicas semiconductoras, cerámicas de elevada resistencia química en condiciones extremas y cualquiera de sus combinaciones.
5. El procedimiento según cualquiera de las reivindicaciones 1 a 4, donde la etapa (b)
- 30 se lleva a cabo mediante centrifugado o filtración.
6. El procedimiento según cualquiera de las reivindicaciones 1 a 5, donde la etapa (c) se lleva a cabo mediante la mezcla y redispersión de las partículas inorgánicas en la mezcla polimérica mediante medios mecánicos o sónicos.

35

7. El procedimiento según cualquiera de las reivindicaciones 1 a 6, donde el termoplástico se selecciona de entre el polietileno, el ácido poliláctico, el polietilenglicol, la policaprolactona, el nylon, el acrilonitrilo y el butadieno estireno.
- 5 8. El procedimiento según cualquiera de las reivindicaciones 1 a 7, donde la disolución polimérica de la etapa (c) comprende además un plastificante, un colorante o un antiespumante.
9. El procedimiento según cualquiera de las reivindicaciones 1 a 8, donde la etapa (e)
- 10 se lleva a cabo mediante termogravimetría y/o calorimetría diferencial de barrido.
10. El procedimiento según cualquiera de las reivindicaciones 1 a 9, donde
- la pieza es puramente cerámica, puramente metálica o es una pieza formada por una mezcla cerámico-metal
 - 15 • la etapa (a) se lleva a cabo por adsorción en superficie de un surfactante o un polielectrolito, el procedimiento comprende las siguientes etapas adicionales: (h), tras la etapa (g), de eliminación del polímero que comprende el producto obtenido en la etapa (g) mediante disolución o descomposición térmica, y (i) sinterizar el producto obtenido en la etapa (h).
- 20
11. El procedimiento según la reivindicación 10, donde el surfactante de la etapa (a) se selecciona de entre dodecilsulfato, oleimina y bromuro de hexadeciltrimetilamonio.
12. El procedimiento según la reivindicación 10, donde el polielectrolito de la etapa (a)
- 25 se selecciona de entre un poliacrilato, un citrato o una poliamina.
13. El procedimiento según cualquiera de las reivindicaciones 10 a 12, donde la pieza es porosa y el porcentaje en volumen de las partículas inorgánicas en la mezcla obtenida en la etapa (d) es mayor del 30 %.
- 30
14. El procedimiento según cualquiera de las reivindicaciones 10 a 12, donde la pieza es densa y el porcentaje en volumen de las partículas inorgánicas en la mezcla obtenida en la etapa (d) es mayor del 50 %.
- 35 15. El procedimiento según cualquiera de las reivindicaciones 1 a 9, donde

- la pieza es un material compuesto,
- la etapa (a) se lleva a cabo por adsorción en superficie de un polielectrolito y
- el porcentaje en volumen de las partículas inorgánicas en la mezcla obtenida en la etapa (d) es mayor del 1 %.

5

16. El procedimiento según la reivindicación 15, donde el polielectrolito de la etapa (a) se selecciona de entre un poliacrilato, un citrato o una poliamina.

10 17. El procedimiento según cualquiera de las reivindicaciones 15 ó 16, donde el porcentaje en volumen de las partículas inorgánicas en la mezcla obtenida en la etapa (d) es mayor del 15 %.

15

DIBUJOS

Figura 1

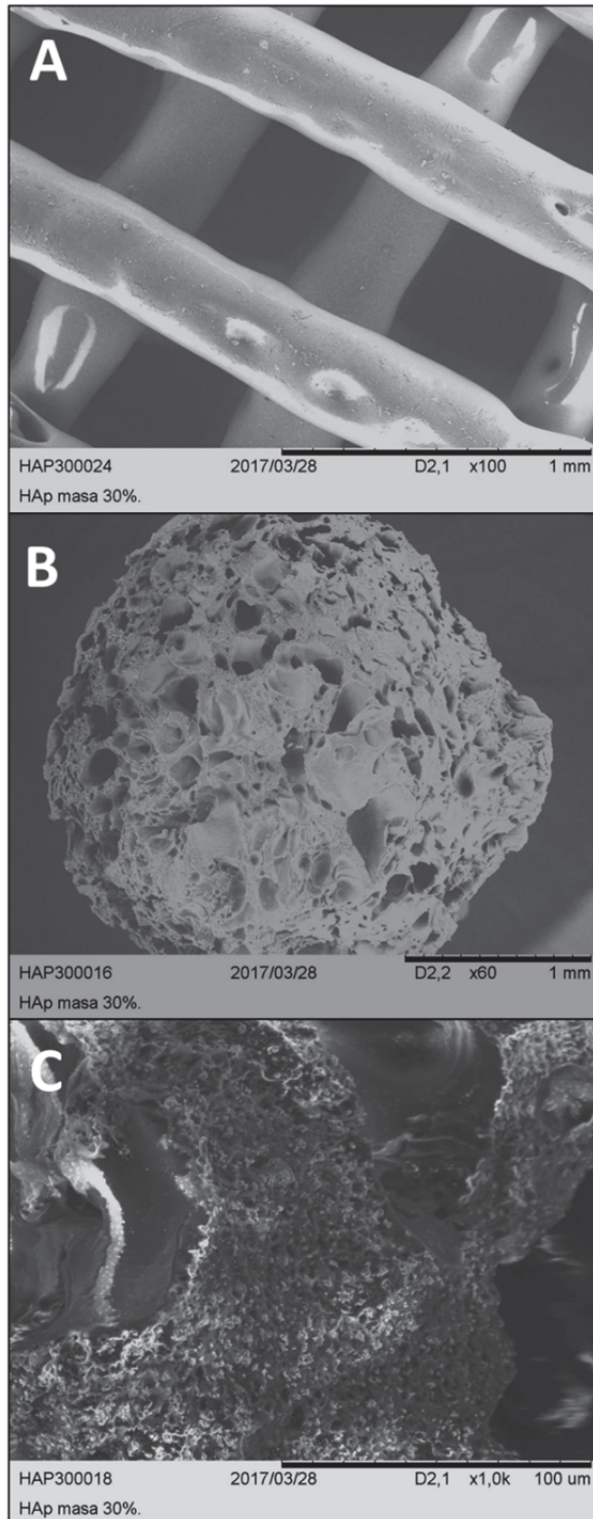


Figura 2

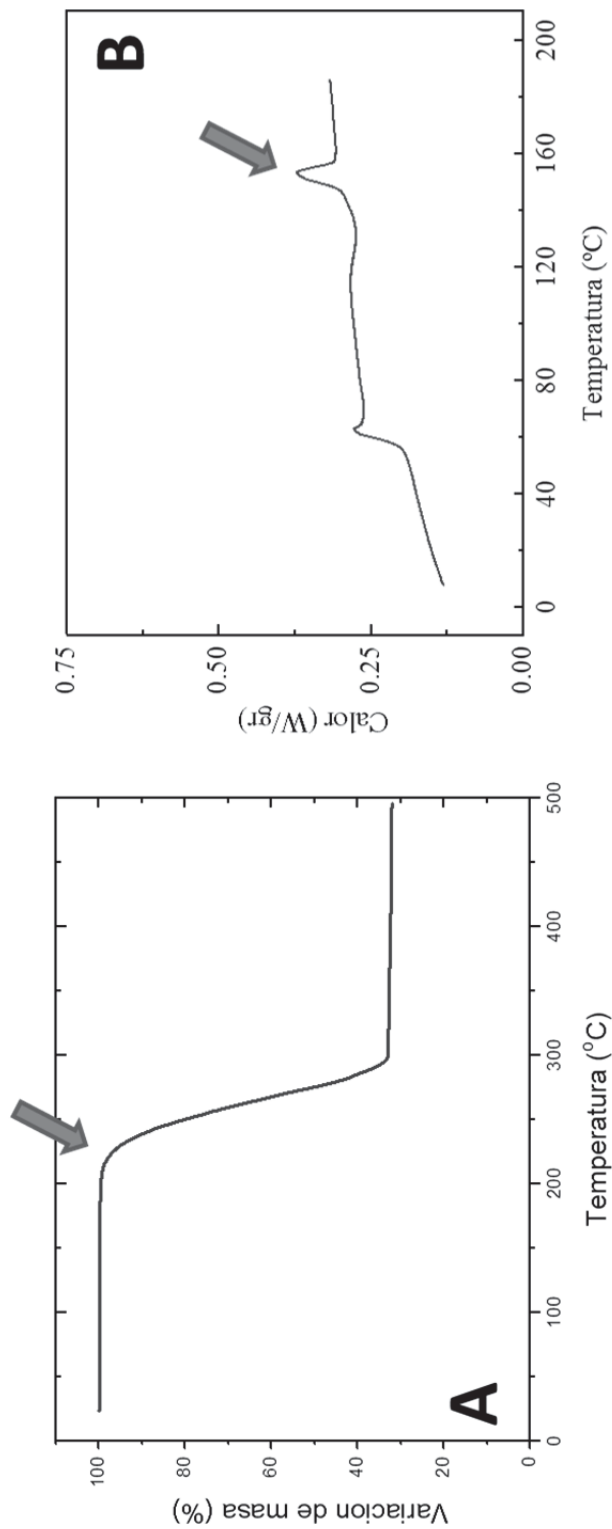


Figura 3

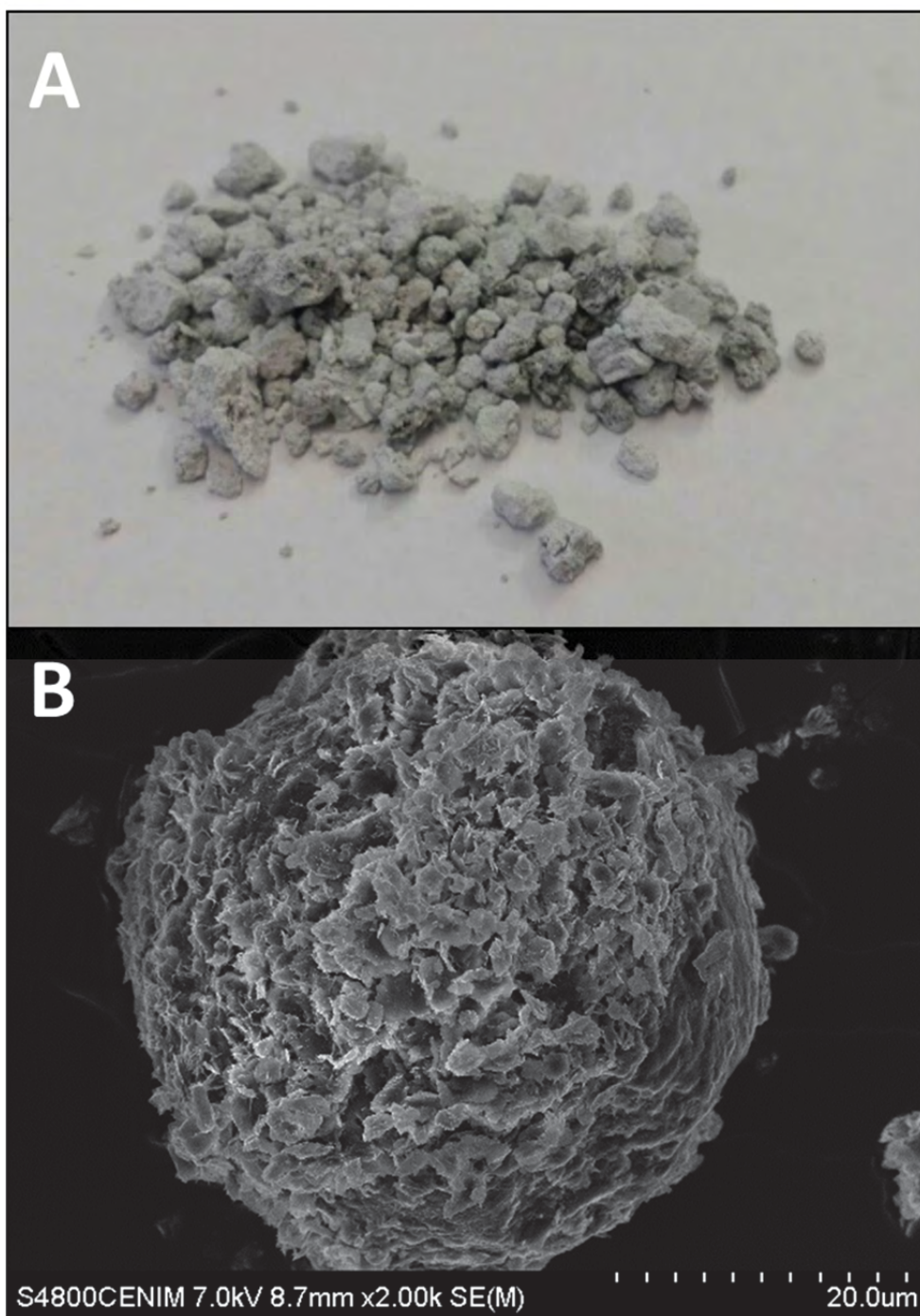


Figura 4

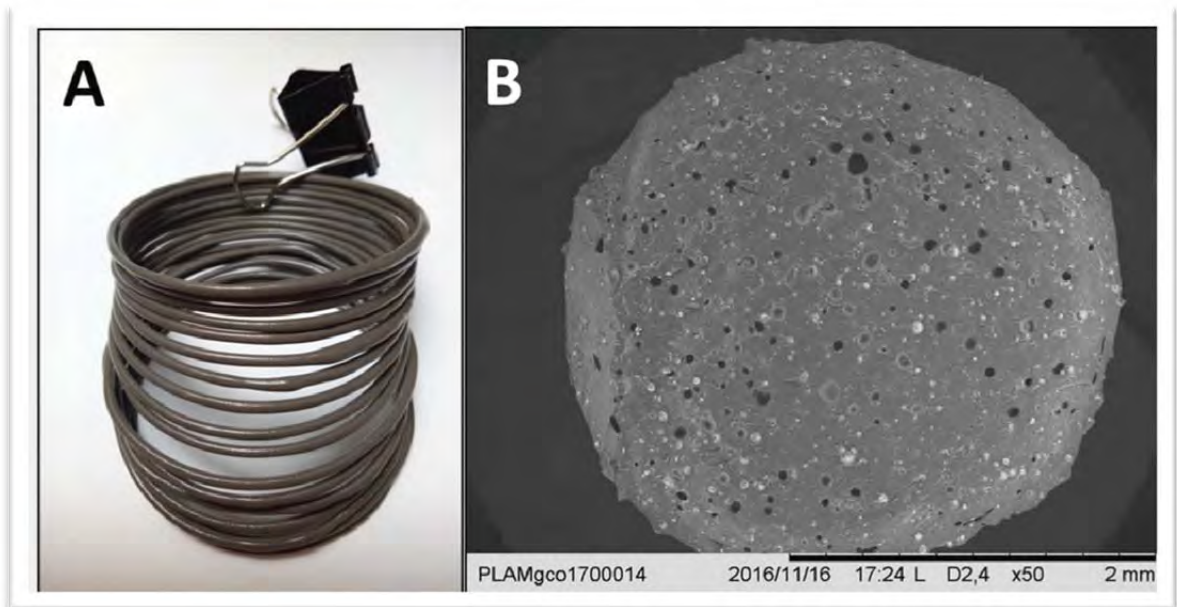


Figura 5

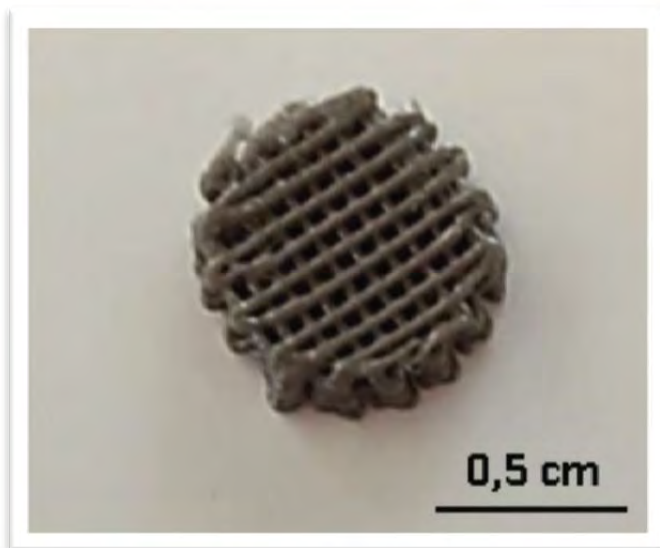


Figura 6

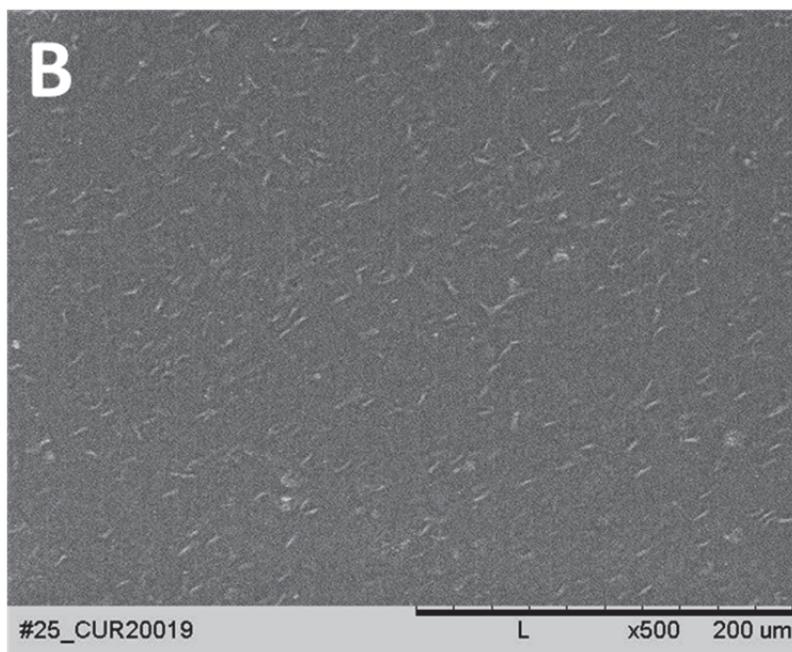
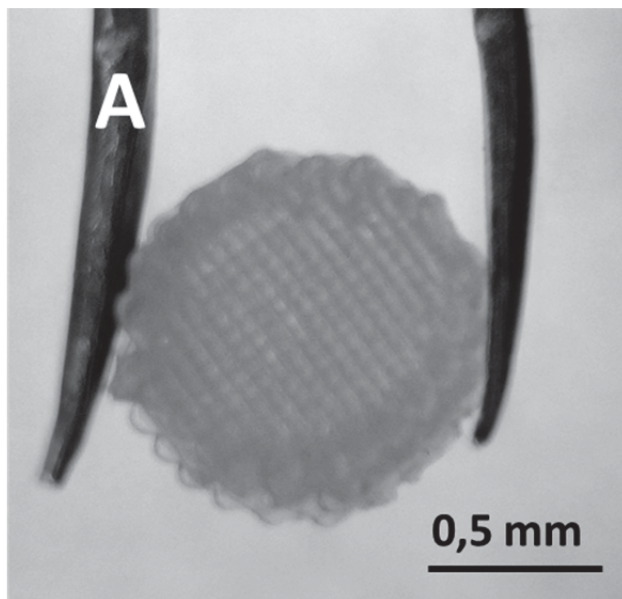


Figura 7

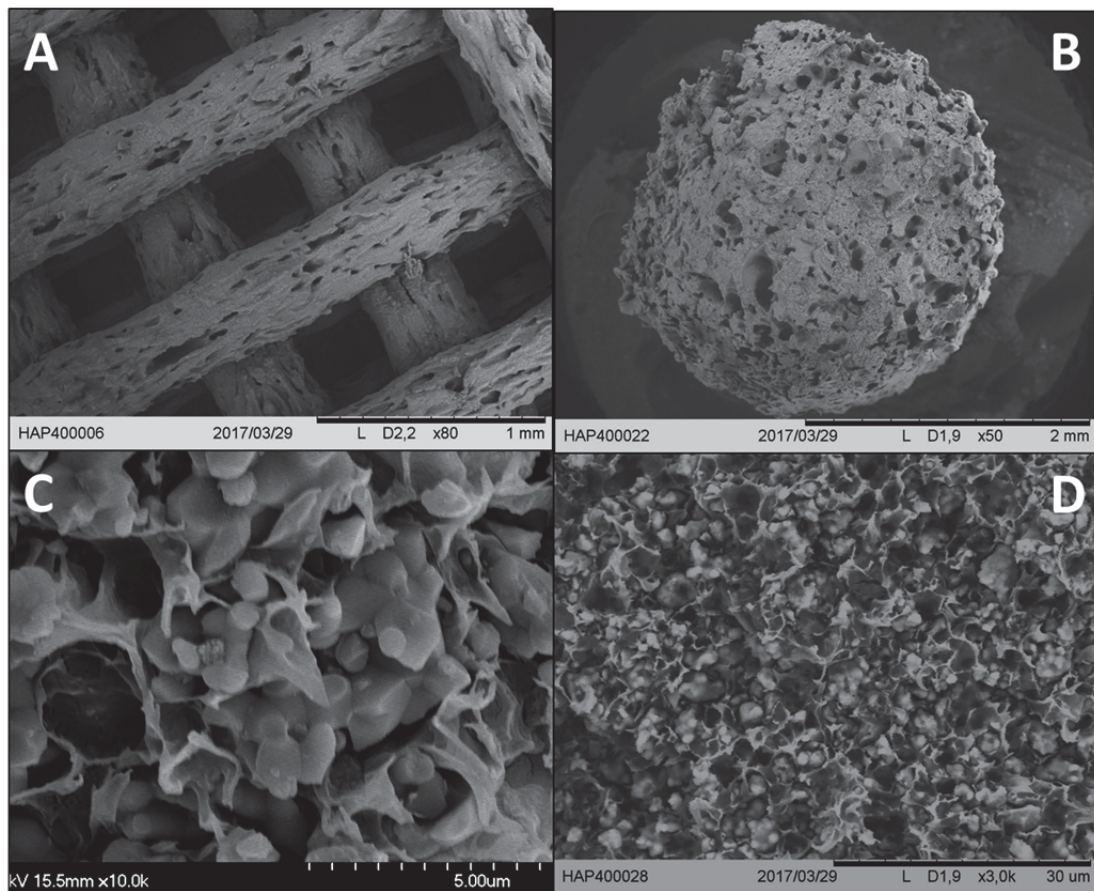


Figura 8

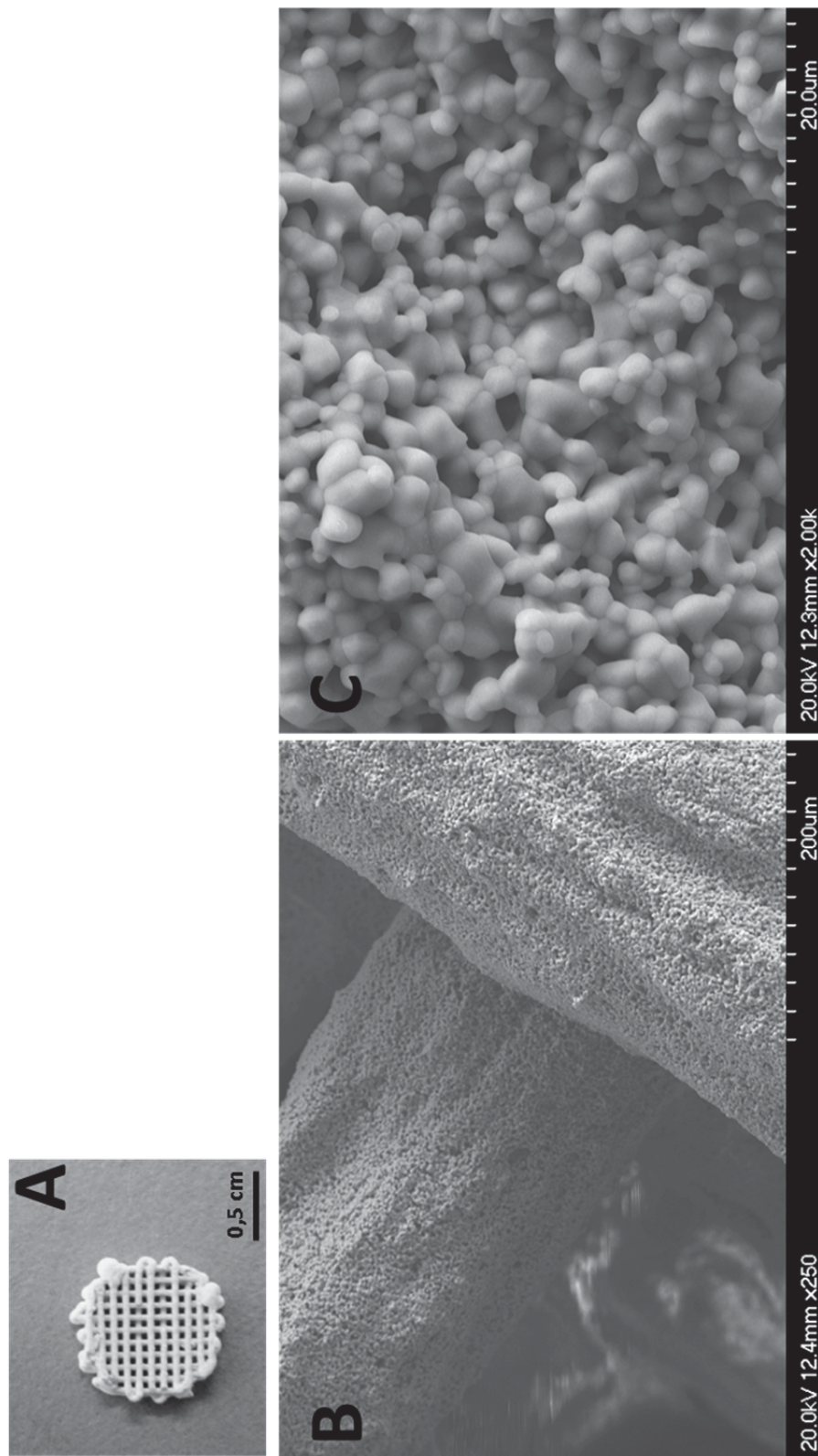


Figura 9

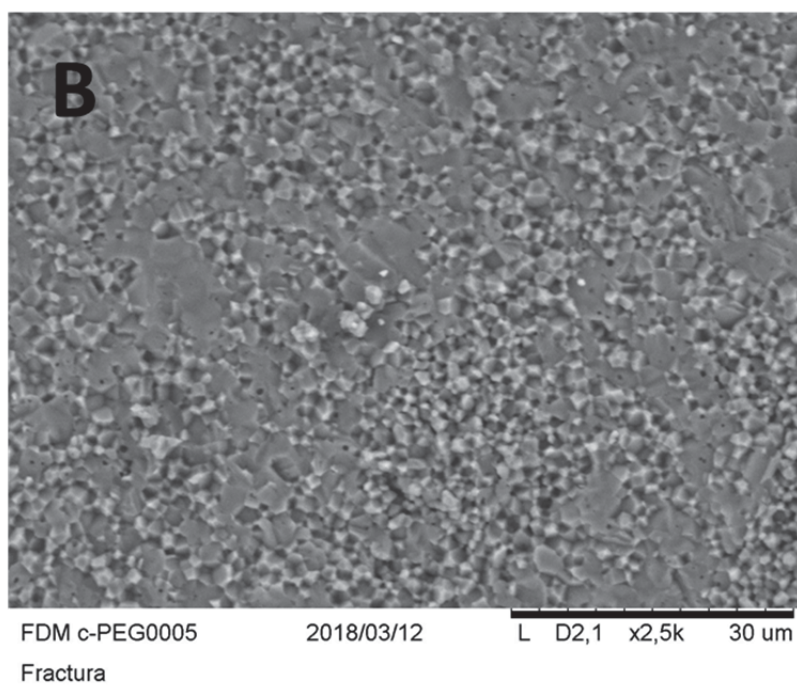
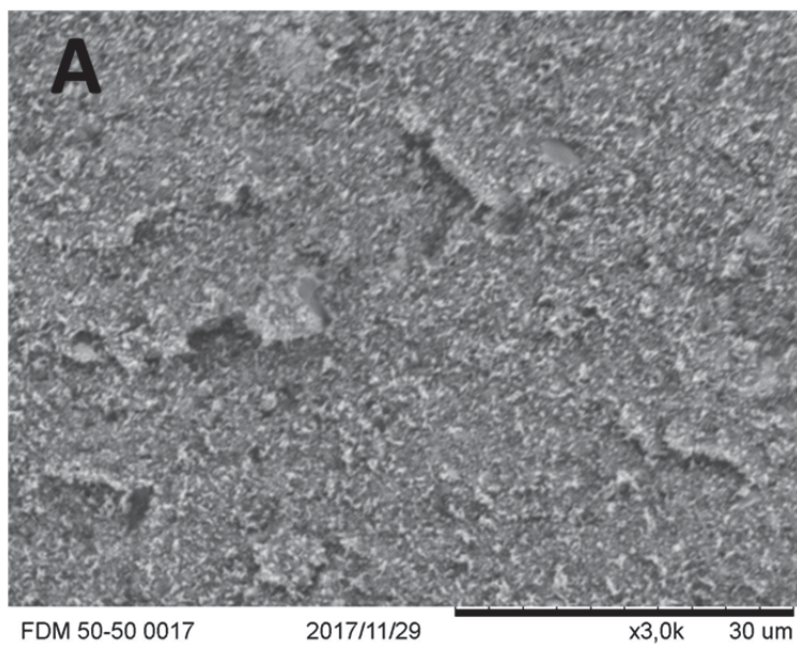
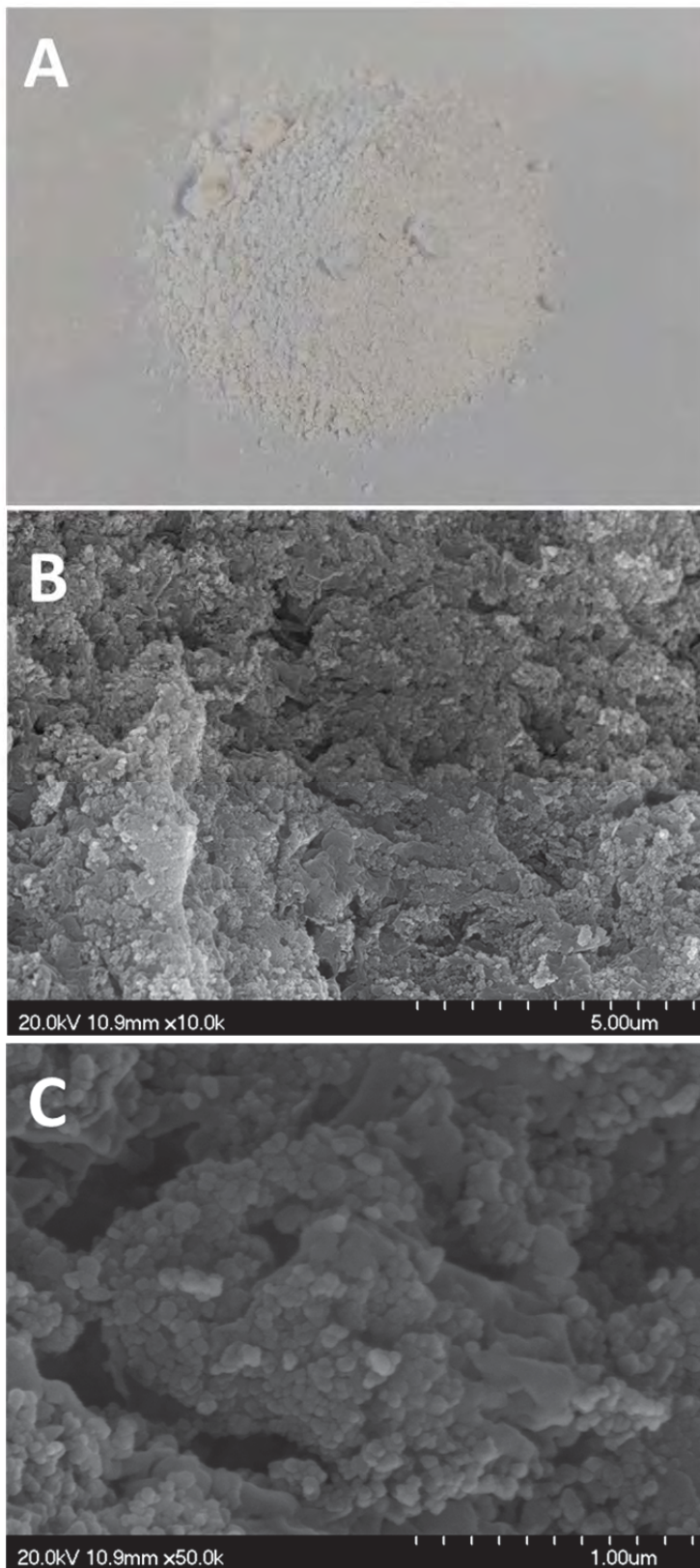


Figura 10



RESUMEN

Procedimiento de obtención de una pieza por modelado por deposición de hilo fundido

La presente invención se refiere a un procedimiento de obtención de una pieza de material compuesto o una pieza cerámica y/o metálica por modelado por deposición de hilo fundido. La presente invención se puede encuadrar en el área de la ciencia de los materiales y por tanto es de interés para industrias que fabrican materiales compuestos de matriz polimérica, cerámica y metal para aplicaciones en aeronáutica, en la producción de biomateriales, dispositivos de generación/almacenamiento energético y materiales refractarios utilizados en condiciones severas de servicio.



TRATADO DE COOPERACIÓN EN MATERIA DE PATENTES NOTIFICACIÓN DE LA RECEPCIÓN DE LOS DOCUMENTOS QUE CONSTITUYEN SUPUESTAMENTE UNA SOLICITUD INTERNACIONAL PRESENTADA DE FORMA ELECTRÓNICA.

(Instrucciones Administrativas del PCT, Parte Séptima)

- 1.-Se notifica al solicitante que la Oficina Receptora ha recibido en la fecha de recepción indicada más abajo, los documentos que supuestamente constituyen una solicitud internacional.
- 2.-Se llama la atención del solicitante sobre el hecho de que la Oficina Receptora no ha comprobado aún si estos documentos satisfacen las condiciones del art. 11.1, es decir, si cumple los requisitos para que le sea atribuida una fecha de presentación internacional. En cuanto la Oficina Receptora haya comprobado los documentos, avisará al solicitante.
- 3.-El número de la supuesta solicitud internacional indicado más abajo ha sido otorgado automáticamente a estos documentos. Se invita al solicitante a mencionar este número en toda la correspondencia con la Oficina Receptora.

Número de presentación	300319896	
Solicitud Número PCT	PCT/ES2019/070348	
Fecha de recepción	24 mayo 2019	
Oficina Receptora	Oficina Española de Patentes y Marcas, Madrid	
Referencia del expediente del solicitante o mandatario	PCT1641.1356	
Solicitante	CONSEJO SUPERIOR DE INVESTIGACIONES CIENTÍFICAS	
Número de solicitantes	1	
País	ES	
Título de la invención	PROCEDIMIENTO DE OBTENCIÓN DE UNA PIEZA POR MODELADO POR DEPOSICIÓN DE HILO FUNDIDO	
Documentos presentados	eolf-pkda.xml eolf-appb.xml eolf-vlog.xml eolf-appb-P000002.pdf (3 p.)	eolf-requ.xml eolf-fees.xml eolf-appb-P000001.pdf (17 p.) eolf-appb-P000003.pdf (1 p.)

	eolf-abst.txt	eolf-appb-P000004.pdf (9 p.)
Presentado por	C=ES,O=PONS PATENTES Y MARCAS INTERNACIONAL SL,2.5.4.97=#0C0F56415445532D423834393231373039,CN=50534279J ANGEL PONS (R: B84921709),SN=PONS ARIÑO,givenName=ANGEL,serialNumber=IDCES-50534279J,description= Ref:AEAT/AEAT0297/PUESTO 1/40639/21092018091901	
Método de Transmisión	Online	
Fecha y hora de expedición del recibo	24 mayo 2019, 13:07 (CEST)	
Información oficial condensada de la presentación	CE:08:B2:DF:AC:2E:53:9C:62:FF:21:49:51:E8:00:74:85:0D:EB:84	

/Madrid, Oficina Receptora/

PETITORIO PCT

(original en formato electrónico)

0	Para uso de la oficina receptora únicamente	
0-1	Solicitud internacional No.	
0-2	Fecha de presentación internacional	
0-3	Nombre de la Oficina receptora y "Solicitud Internacional PCT"	
0-4	Formulario PCT/RO/101 Petitorio PCT	
0-4-1	Preparado usando	PCT Online Filing Version 3.51.000.263e MT/FOP 20141031/0.20.5.20
0-5	Petición El abajo firmante pide que la presente solicitud internacional sea tramitada con arreglo al Tratado de Cooperación en materia de Patentes	
0-6	Oficina receptora (indicada por el solicitante)	Oficina Española de Patentes y Marcas (RO/ES)
0-7	Referencia al expediente del solicitante o del mandatario	PCT1641.1356
I	Título de la invención	PROCEDIMIENTO DE OBTENCIÓN DE UNA PIEZA POR MODELADO POR DEPOSICIÓN DE HILO FUNDIDO
II	Solicitante	
II-1	Esta persona es:	Solicitante únicamente
II-2	Solicitante para	Todos los Estados designados
II-4	Nombre	CONSEJO SUPERIOR DE INVESTIGACIONES CIENTÍFICAS
II-5	Dirección	C/ Serrano, 117 28006 Madrid España
II-6	Estado de nacionalidad	ES
II-7	Estado de domicilio	ES
III-1	Solicitante y/o inventor	
III-1-1	Esta persona es:	Inventor únicamente
III-1-3	Inventor para	Todos los Estados designados
III-1-4	Nombre (APELLIDOS, Nombre)	FERRÁNDEZ MONTERO, Ana
III-1-5	Dirección	Av. de Gregorio del Amo, 8 28040 Madrid España

PETITORIO PCT

(original en formato electrónico)

III-2	Solicitante y/o inventor	
III-2-1	Esta persona es:	Inventor únicamente
III-2-3	Inventor para	Todos los Estados designados
III-2-4	Nombre (APELLIDOS, Nombre)	FERRARI FERNÁNDEZ, Begoña
III-2-5	Dirección	C/Kelsen, 5 Campus de Cantoblanco 28049 Madrid España
III-3	Solicitante y/o inventor	
III-3-1	Esta persona es:	Inventor únicamente
III-3-3	Inventor para	Todos los Estados designados
III-3-4	Nombre (APELLIDOS, Nombre)	SÁNCHEZ HERENCIA, Antonio Javier
III-3-5	Dirección	C/Kelsen, 5 Campus de Cantoblanco 28049 Madrid España
III-4	Solicitante y/o inventor	
III-4-1	Esta persona es:	Inventor únicamente
III-4-3	Inventor para	Todos los Estados designados
III-4-4	Nombre (APELLIDOS, Nombre)	GONZÁLEZ GRANADOS, Zoilo
III-4-5	Dirección	C/Kelsen, 5 Campus de Cantoblanco 28049 Madrid España
III-5	Solicitante y/o inventor	
III-5-1	Esta persona es:	Inventor únicamente
III-5-3	Inventor para	Todos los Estados designados
III-5-4	Nombre (APELLIDOS, Nombre)	GONZÁLEZ LÓPEZ, Francisco Javier
III-5-5	Dirección	C/Kelsen, 5 Campus de Cantoblanco 28049 Madrid España
III-6	Solicitante y/o inventor	
III-6-1	Esta persona es:	Inventor únicamente
III-6-3	Inventor para	Todos los Estados designados
III-6-4	Nombre (APELLIDOS, Nombre)	YUS DOMÍNGUEZ, Joaquín Luis
III-6-5	Dirección	C/Kelsen, 5 Campus de Cantoblanco 28049 Madrid España

PETITORIO PCT

(original en formato electrónico)

III-7	Solicitante y/o inventor	
III-7-1	Esta persona es:	Inventor únicamente
III-7-3	Inventor para	Todos los Estados designados
III-7-4	Nombre (APELLIDOS, Nombre)	GONZÁLEZ CARRASCO, Jose Luis
III-7-5	Dirección	Av. de Gregorio del Amo, 8 28040 Madrid España
III-8	Solicitante y/o inventor	
III-8-1	Esta persona es:	Inventor únicamente
III-8-3	Inventor para	Todos los Estados designados
III-8-4	Nombre (APELLIDOS, Nombre)	LIEBLICH RODRÍGUEZ, Marcela
III-8-5	Dirección	Av. de Gregorio del Amo, 8 28040 Madrid España
IV-1	Mandatario o representante común; o dirección para la correspondencia	
	La persona identificada a continuación se nombra/ha sido nombrada para actuar en nombre del/de los solicitante(s) ante las administraciones internacionales competentes como:	Mandatario
IV-1-1	Nombre (APELLIDOS, Nombre)	PONS ARIÑO, Ángel
IV-1-2	Dirección	Glorieta de Rubén Darío, 4 28010 Madrid España
IV-1-3	No. de teléfono	91 700 76 00
IV-1-4	No. de facsímil	91 308 61 03
IV-1-5	Correo electrónico	patentesdpto@pons.es
IV-1-5(a)	Autorización a utilizar el correo-e) Se autoriza a la Oficina receptora, la Administración de búsqueda internacional, la Oficina Internacional y la Administración de examen preliminar internacional a utilizar esta dirección de correo-e para enviar notificaciones relativas a la presente solicitud internacional, si dichas oficinas así lo desean:	por correo electrónico exclusivamente (no se enviará ninguna notificación en papel)
V	DESIGNACIONES	
V-1	Según la Regla 4.9.a), la presentación de este petitorio constituye la designación de todos los Estados contratantes vinculados por el PCT en la fecha de presentación internacional a efectos de todo tipo de protección disponible y, cuando proceda, de la concesión tanto de patentes regionales como de patentes nacionales.	
VI-1	Reivindicación de prioridad de una solicitud nacional anterior	
VI-1-1	Fecha de presentación	24 mayo 2018 (24.05.2018)
VI-1-2	Número	P201830503
VI-1-3	País o miembro de la OMC	ES
VI-2	Petición de documento de prioridad	
	Se ruega a la Oficina receptora que prepare y transmita a la Oficina Internacional una copia certificada de la(s) solicitud(es) anterior(es) identificada(s) supra como punto(s):	VI-1

PETITORIO PCT

(original en formato electrónico)

VI-3	Incorporación por referencia : cuando un elemento de la solicitud internacional mencionado en el Artículo 11.1)iii)d) o e) o una parte de la descripción, de las reivindicaciones o de los dibujos mencionada en la Regla 20.5.a) no está contenido en otro lugar en esta solicitud internacional pero figura íntegramente en una solicitud anterior cuya prioridad se reivindica en la fecha en la que uno o varios elementos mencionados en el Artículo 11.1)iii) fueron recibidos inicialmente por la Oficina receptora, ese elemento o esa parte, a reserva de confirmación según la Regla 20.6, se incorporará por referencia en esta solicitud internacional a los efectos de la Regla 20.6.		
VII-1	Administración encargada de la búsqueda internacional elegida	Oficina Europea de Patentes (OEP) (ISA/EP)	
VIII	Declaraciones	Número de declaraciones	
VIII-1	Declaración sobre la identidad del inventor	—	
VIII-2	Declaración sobre el derecho del solicitante, en la fecha de presentación internacional, para solicitar y que le sea concedida una patente	—	
VIII-3	Declaración sobre el derecho del solicitante, en la fecha de presentación internacional, a reivindicar la prioridad de la solicitud anterior	—	
VIII-4	Declaración sobre la calidad de inventor (sólo para la designación de los Estados Unidos de América)	—	
VIII-5	Declaración sobre las divulgaciones no perjudiciales o las excepciones a la falta de novedad	—	
IX	Lista de verificación	Número de hojas	Fichero(s) electrónico(s) adjunto(s)
IX-1	Petitorio (incluidas las hojas de declaración)	5	✓
IX-2	Descripción	17	✓
IX-3	Reivindicaciones	3	✓
IX-4	Resumen	1	✓
IX-5	Dibujos	9	✓
IX-7	TOTAL	35	
	Elementos de acompañamiento	Documento(s) en papel adjunto(s)	Fichero(s) electrónico(s) adjunto(s)
IX-8	Hoja de cálculo de tasas	—	✓
IX-20	Figura de los dibujos que debe acompañar el resumen		
IX-21	Idioma de presentación de la solicitud internacional	español	
X-1	Firma del solicitante , del mandatario o del representante común	(PKCS7 Firma Digital)	
X-1-1	Nombre (APELLIDOS, Nombre)	PONS ARIÑO, Ángel	
X-1-3	Calidad (si tal calidad no es obvia al leer el petitorio)	(Representante)	

PETITORIO PCT

(original en formato electrónico)

PARA USO DE LA OFICINA RECEPTORA ÚNICAMENTE

10-1	Fecha efectiva de recepción de la pretendida solicitud internacional	
10-2	Dibujos:	
10-2-1	Recibido	
10-2-2	No recibido	
10-3	Fecha efectiva de recepción, rectificadora en razón de la recepción ulterior pero dentro del plazo, de documentos o de dibujos que completan la pretendida solicitud internacional	
10-4	Fecha de recepción, dentro del plazo, de las correcciones requeridas según el Artículo 11(2) del PCT	
10-5	Administración encargada de la búsqueda internacional	ISA/EP
10-6	Transmisión de la copia para la búsqueda diferida hasta que se pague la tasa de búsqueda	

PARA USO DE LA OFICINA INTERNACIONAL ÚNICAMENTE

11-1	Fecha de recepción del ejemplar original por la Oficina Internacional	
------	---	--

PCT (ANEXO - HOJA DE CALCULO DE TASAS)

(original en formato electrónico)

(Esta hoja no forma parte de la solicitud internacional y no cuenta como una de sus hojas)

0	Para uso de la oficina receptora únicamente			
0-1	Solicitud internacional No.			
0-2	Sello con la fecha de la Oficina receptora			
0-4	Formulario PCT/RO/101 (Anexo) Hoja de cálculo de tasas PCT			
0-4-1	Preparado usando	PCT Online Filing Version 3.51.000.263e MT/FOP 20141031/0.20.5.20		
0-9	Referencia al expediente del solicitante o del mandatario	PCT1641.1356		
2	Solicitante	CONSEJO SUPERIOR DE INVESTIGACIONES CIENTÍFICAS		
12	Calculo de las tasas prescritas	Importe de la tasa/ multiplicador	Importes totales (EUR)	
12-1	Tasa de transmisión T	⇒	74.25	
12-2-1	Tasa de búsqueda S	⇒	1775	
12-2-2	Búsqueda internacional a efectuar por	EP		
12-3	Tasa de presentación internacional (30 primeras hojas) i1	1169		
12-4	Hojas restantes	5		
12-5	Cantidad adicional (X)	13		
12-6	Total de la cantidad adicional i2	65		
12-7	i1 + i2 = i	1234		
12-12	Réducción por presentación electrónica (imagen) R	-176		
12-13	Total de la tasa de presentación internacional (i-R) I	⇒	1058	
12-14	Tasa por documento de prioridad			
	Número de documentos de prioridad solicitados	1		
12-15	Tasa por documento (X)	29.69		
12-16	Total de la tasa por documento de prioridad: P	⇒	29.69	
12-17	Tasa por la restauración del derecho de prioridad RP			
	Número de las peticiones de restauración del derecho de prioridad	0		
	Total de las tasas por la restauración del derecho de prioridad			
12-19	TOTAL DE LAS TASAS PAGADERAS (T+S+I+P+RP)	⇒	2936.94	
12-21	Modo de pago:	Otro : no se realiza el pago en este momento		